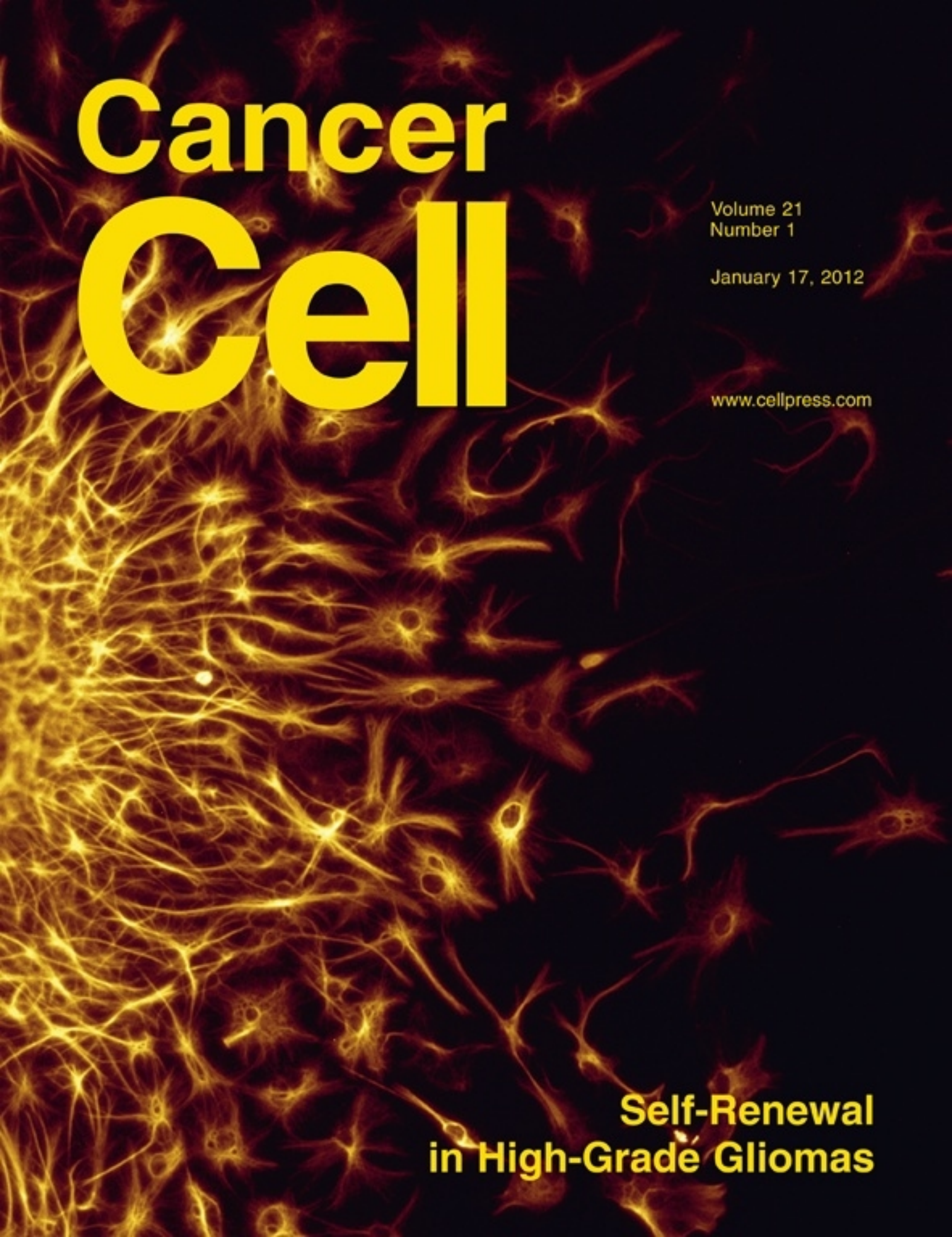
Cancer
Cell
Volume 21
Number 1
January 17, 2012
www.cellpress.com
Self-Renewal
in High-Grade Gliomas

Spheres without Influence: Dissociating In Vitro Self-Renewal from Tumorigenic Potential in Glioma

Tracy-Ann Read[1] and Robert J. Wechsler-Reya[2,*]
[1]Department of Neurosurgery, Emory University School of Medicine, Atlanta, GA 30322, USA
[2]Tumor Development Program, Sanford-Burnham Medical Research Institute, La Jolla, CA 92037, USA
*Correspondence: rwreya@sanfordburnham.org
DOI 10.1016/j.ccr.2011.12.011

The capacity for self-renewal is thought to be a critical property of tumor-initiating cells. This capacity is often associated with the ability to generate spheres in vitro. In this issue of *Cancer Cell*, Barrett et al. show that cells lacking sphere-forming ability can still be very efficient at propagating tumors.

One of the great frustrations of current cancer therapy is that the disease often returns even after aggressive surgery, radiation, and chemotherapy. Consequently, the discovery of unique populations of tumor cells that may be responsible for recurrence—and that could be targeted to prevent it–has garnered a great deal of interest. These cells, termed tumor-initiating cells (TICs) or cancer stem cells, were originally defined based on their ability to reinitiate tumors following transplantation. However, studies from a variety of systems have shown that TICs frequently share characteristics with normal stem cells, including marker expression, ability to self-renew, and ability to give rise to progeny of multiple lineages. Because FACS analysis and in vitro assays of self-renewal are much simpler than in vivo studies of tumorigenicity, the former are sometimes used as a surrogate for the latter.

One system in which TICs have been studied extensively is glioma. Numerous reports have suggested that glioma intiating cells share markers with neural stem cells (NSCs), and that when cultured at low density in the presence of growth factors, they can give rise to clonally-derived "tumorspheres," analogous to the neurospheres generated when NSCs are cultured under similar conditions. In fact, the ability of glioma cells to self-renew under neurosphere conditions has prompted many investigators to propagate patient samples as spheres rather than as traditional adherent cell lines (Galli et al., 2004; Lee et al., 2006). However, the assumption that all gliomas can be propagated by stem-like sphere-forming cells has not been carefully tested.

In this issue of *Cancer Cell*, Barrett et al. (Barrett et al., 2012) show that in a subset of gliomas, cells that lack stem cell markers and are unable to form spheres are more tumorigenic than cells that have these properties.

The investigators used a model of glioma in which mice lacking the *Arf* tumor suppressor gene were injected with viruses encoding platelet-derived growth factor (PDGF) or its downstream signaling mediator KRAS (Fomchenko et al., 2011). Because the PDGF pathway is aberrantly activated in the "proneural" form of human glioma (Verhaak et al., 2010), this model has been used to study that subtype of the disease. To investigate the relationship between self-renewal and tumor initiation, they crossed their animals with *Id1*^{VenusYFP} reporter mice (Nam and Benezra, 2009). This allowed them to separate cells based on expression of Id1, a transcriptional regulator that has been shown to control self-renewal in NSCs. Consistent with the role of Id1 in NSCs, Id1^{high} cells (which represented <1% of tumor cells) were enriched in expression of stem cell markers (e.g., Prominin-1/CD133), and were very efficient at sphere formation. In contrast, Id1^{low} cells expressed progenitor markers (e.g., Olig2, Mash1, NG2), and showed minimal self-renewal capacity in the sphere assay (Figure 1).

The investigators then sorted Id1^{high} and Id1^{low} tumor cells and tested their ability to give rise to tumors following transplantation. Surprisingly, the ability to form spheres in vitro did not correlate with in vivo tumorigenic potential. Although Id1^{high} and Id1^{low} cells could both generate tumors, Id1^{low} cells did so much more quickly and with higher penetrance. For example, in the KRAS-driven model of glioma, Id1^{low} cells generated tumors in 52% of mice, with a latency of 37 days, whereas Id1^{high} cells gave rise to tumors in only 5% of mice, with a latency of 119 days. These studies suggested that sphere-forming cells are not necessarily more tumorigenic.

To determine if Id1 function is required for tumor growth, Barrett et al. (2012) crossed their animals to *Id1* knockout mice or to mice expressing a conditional allele of *Id1* that could be deleted using Cre recombinase. In both cases, they found that loss of Id1 dramatically impaired sphere formation but did not affect tumorigenicity. In contrast, knockdown of Olig2 (a progenitor marker that is enriched in Id1^{low} cells and has been shown to be required for glioma formation [Ligon et al., 2007]) significantly impaired tumor formation. These studies reinforce the notion that in vitro self-renewal may not be linked to tumorigenic potential.

The disconnect between sphere formation and tumorgenicity has a number of important implications. First, it highlights the fact that not all tumor-propagating cells resemble stem cells. Whereas normal NSCs expand when cultured under neurosphere conditions, normal progenitors typically do not. Thus, tumors that are propagated by progenitor-like TICs would not be expected to grow under these conditions. This is supported by studies of tumors in *Patched* mutant mice, a model for Sonic hedgehog-driven medulloblastoma; these tumors are propagated by progenitor-like CD15^{+} cells that

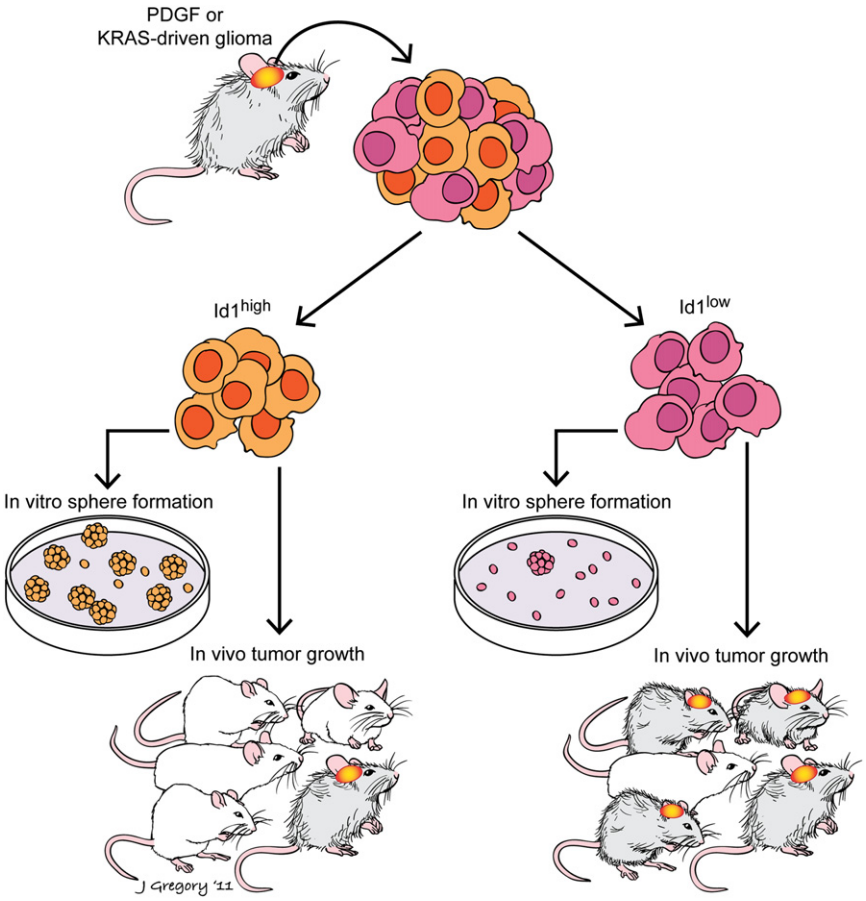

Figure 1. Distinct Populations of Cells Mediate Sphere Formation and Tumor Initiation
PDGF- and KRAS-driven gliomas contain mixtures of cells expressing high and low levels of the transcription factor Id1. Id1^{high} cells (orange) are much more efficient than Id1^{low} cells (pink) at forming self-renewing spheres in vitro. In contrast, Id1^{low} cells are much more efficient at forming tumors following transplantation into mice. (Illustration by Jill Gregory.)

do not grow, or even survive, under neurosphere conditions (Read et al., 2009). Importantly, if not all TICs can form spheres, using this approach to expand patient tumor samples might result in a significant selection bias; only tumors that can form spheres would be available for study. Indeed, one recent study noted that only half of primary gliomas were able to give rise to tumorsphere lines (Chen et al., 2010).

Even when tumors can be grown under sphere-forming conditions, the cells that grow out may not be representative of the original tumor. As Barrett et al. (2012) show, these conditions may select for subpopulations of cells (i.e., Id^{high} cells) that do not represent the full tumorigenic potential of the original tumor. In addition to selection, culturing cells at low density in the presence of growth factors may change their behavior. This was shown many years ago for NSCs, which can undergo marked changes in cell fate potential when cultured under neurosphere conditions (Gabay et al., 2003). Barrett et al. (2012) provide further evidence for this, by showing that glioma cells cultured as spheres undergo changes in marker expression (including Id1 and Olig2) and lose the ability to generate tumors upon transplantation. The fact that culture conditions can dramatically alter tumorigenic potential raises cautions about using tumorspheres to screen for drugs that might be effective at killing tumors in patients.

One possible interpretation of the disconnect between sphere-forming capacity and tumorigenic potential is that tumor initiation does not depend on self-renewal. However, the fact that Id1^{low} cells cannot form spheres in vitro does not necessarily mean that they cannot self-renew. It is possible that under the appropriate culture conditions, these cells might show extensive self-renewal. More importantly, the fact that Id1^{low} cells can form tumors following transplantation indicates that they are capable of significant expansion in vivo. The degree to which this expansion involves self-renewal (e.g., by asymmetric division) versus differentiation remains to be determined. Moreover, the ability of Id1^{low} tumor cells to serially transplant tumors without exhausting—another measure of in vivo self-renewal–has not been tested. Further studies may shed light on the capacity of Id1^{low} tumor cells to self-renew in vivo.

It is important to note that these studies focus on a specific subtype of glioma and that other forms of glioma may be propagated by stem-like, sphere-forming cells. At the same time, it is worth considering whether other types of cancer that are propagated as spheres might be subject to the same caveats raised by these studies. As convenient as cultured cell lines can be for studying tumor biology, it is critical to remember that tumors only grow in living animals. Finding ways to make them stop growing often requires moving beyond the in vitro sphere and into the complex in vivo microenvironment.

REFERENCES

Barrett, L.E., Granhot, Z., Coker, C., Iavarone, A., Hambardzumyan, D., Holland, E.C., Nam, H.-S., and Benezra, R. (2012). Cancer Cell *21*, this issue, 11–24.

Chen, R., Nishimura, M.C., Bumbaca, S.M., Kharbanda, S., Forrest, W.F., Kasman, I.M., Greve, J.M., Soriano, R.H., Gilmour, L.L., Rivers, C.S., et al. (2010). Cancer Cell *17*, 362–375.

Fomchenko, E.I., Dougherty, J.D., Helmy, K.Y., Katz, A.M., Pietras, A., Brennan, C., Huse, J.T., Milosevic, A., and Holland, E.C. (2011). PLoS ONE *6*, e20605.

Gabay, L., Lowell, S., Rubin, L.L., and Anderson, D.J. (2003). Neuron *40*, 485–499.

Galli, R., Binda, E., Orfanelli, U., Cipelletti, B., Gritti, A., De Vitis, S., Fiocco, R., Foroni, C., Dimeco, F., and Vescovi, A. (2004). Cancer Res. *64*, 7011–7021.

Lee, J., Kotliarova, S., Kotliarov, Y., Li, A., Su, Q., Donin, N.M., Pastorino, S., Purow, B.W., Christopher, N., Zhang, W., et al. (2006). Cancer Cell *9*, 391–403.

Ligon, K.L., Huillard, E., Mehta, S., Kesari, S., Liu, H., Alberta, J.A., Bachoo, R.M., Kane, M., Louis, D.N., Depinho, R.A., et al. (2007). Neuron *53*, 503–517.

Nam, H.S., and Benezra, R. (2009). Cell Stem Cell *5*, 515–526.

Read, T.A., Fogarty, M.P., Markant, S.L., McLendon, R.E., Wei, Z., Ellison, D.W., Febbo, P.G., and Wechsler-Reya, R.J. (2009). Cancer Cell *15*, 135–147.

Verhaak, R.G., Hoadley, K.A., Purdom, E., Wang, V., Qi, Y., Wilkerson, M.D., Miller, C.R., Ding, L., Golub, T., Mesirov, J.P., et al; Cancer Genome Atlas Research Network. (2010). Cancer Cell *17*, 98–110.

Mdm2's Dilemma: To Degrade or To Translate p53?

Pierre-Jacques Hamard[1] and James J. Manfredi[1,*]
[1]Department of Oncological Sciences, Mount Sinai School of Medicine, New York, NY 10029, USA
*Correspondence: james.manfredi@mssm.edu
DOI 10.1016/j.ccr.2011.12.018

In this issue of *Cancer Cell*, Gajjar et al. provide insight into how Mdm2 can both inhibit and enhance p53 activity. In the basal setting, Mdm2 binds p53 and promotes p53 degradation. Under stress conditions, ATM-dependent phosphorylation of Mdm2 results in its recruitment to p53 mRNA, thereby stimulating p53 translation.

The p53 tumor suppressor is a transcription factor that is induced in response to a variety of stress signals (Kruse and Gu, 2009). Under normal conditions, the p53 protein is kept at low levels in cells by ubiquitination-dependent proteosomal degradation mediated by its negative regulator, the E3 ubiquitin ligase Mdm2 (Figure 1A). Mdm2 is also a p53 transcriptional target and thus participates in a negative feedback loop with p53. Stress-mediated upregulation of Mdm2 has been considered a means by which p53 is able to regulate the duration and amplitude of its cellular effects.

In response to activation of specific oncogenic pathways, the ARF tumor suppressor is upregulated. ARF, in turn, interferes with Mdm2-dependent inhibition of p53 (Manfredi, 2010) (Figure 1B). In contrast, stimulation of the p53 pathway by genotoxic stress involves the DNA damage-activated kinase ATM, which has been shown to directly phosphorylate both p53 and Mdm2 (Kruse and Gu, 2009; Manfredi, 2010) (Figure 1C). The significance of ATM-dependent phosphorylation of Mdm2 was confirmed by the observation that phosphorylation of serine 395 on Mdm2 led to impaired p53 degradation (Maya et al., 2001). Biochemical studies have indicated that this is likely due to altered oligomerization, thereby attenuating the processivity of the E3 ligase activity of Mdm2 (Cheng et al., 2009). DNA damage has also been shown to induce the relocalization of Mdm2 to the nucleolus (Bernardi et al., 2004). It has been proposed that a nucleotide-binding motif within the Mdm2 E3 ligase RING domain facilitates nucleolar localization of Mdm2 (Poyurovsky et al., 2003). Candeias et al. (2008) then made the surprising observation that the p53 mRNA itself was able to interact directly with the RING domain of Mdm2. This interaction impaired the E3 ligase activity of Mdm2 and promoted p53 mRNA translation. It was unclear, however, under what biological settings such an interaction would have relevance.

In this issue of *Cancer Cell*, Gajjar et al. (2012) provide important insight by demonstrating that the DNA damage- and ATM-dependent phosphorylation of Mdm2 on serine 395 promotes the interaction of Mdm2 with p53 mRNA. This, in turn, is needed for p53 stabilization and apoptotic activity (Gajjar et al., 2012) (Figure 1D). By means of RNAi and overexpression experiments, these authors show that both ATM and Mdm2 are required to achieve full p53 apoptotic activity after DNA damage. Use of an Mdm2 isoform that does not bind to the p53 protein shows that a protein-protein interaction between Mdm2 and p53 is remarkably dispensable for this. It was further demonstrated that the interaction between p53 mRNA and the Mdm2 RING domain is necessary for p53-dependent apoptosis after genotoxic stress. Studies using a mutated p53 mRNA that no longer binds Mdm2 confirmed findings with a mutant Mdm2 protein that has a reduced affinity for the mRNA. These intriguing results support the notion that ATM-mediated phosphorylation of Mdm2 at serine 395 promotes allosteric changes in the RING domain, which in turn facilitate p53 mRNA binding. Finally, Gajjar et al. (2012) show that after DNA damage, the interaction between Mdm2 and p53 mRNA impairs Mdm2-dependent ubiquitination of p53. Thus, it is argued that the p53 mRNA-MDM2 interaction not only increases p53 translation but also inhibits p53 protein degradation as well.

In sum, this study demonstrates that Mdm2 can act as a positive regulator of p53 activity after genotoxic stress. It further provides an additional novel explanation for why Mdm2 is transcriptionally upregulated by p53 after DNA damage.

The finding that p53 mRNA relocalizes with Mdm2 in the nucleolus after DNA damage is especially interesting since the nucleolus is generally thought of as the site of ribosomal RNA transcription.

Lee, J., Kotliarova, S., Kotliarov, Y., Li, A., Su, Q., Donin, N.M., Pastorino, S., Purow, B.W., Christopher, N., Zhang, W., et al. (2006). Cancer Cell *9*, 391–403.

Ligon, K.L., Huillard, E., Mehta, S., Kesari, S., Liu, H., Alberta, J.A., Bachoo, R.M., Kane, M., Louis, D.N., Depinho, R.A., et al. (2007). Neuron *53*, 503–517.

Nam, H.S., and Benezra, R. (2009). Cell Stem Cell *5*, 515–526.

Read, T.A., Fogarty, M.P., Markant, S.L., McLendon, R.E., Wei, Z., Ellison, D.W., Febbo, P.G., and Wechsler-Reya, R.J. (2009). Cancer Cell *15*, 135–147.

Verhaak, R.G., Hoadley, K.A., Purdom, E., Wang, V., Qi, Y., Wilkerson, M.D., Miller, C.R., Ding, L., Golub, T., Mesirov, J.P., et al; Cancer Genome Atlas Research Network. (2010). Cancer Cell *17*, 98–110.

Mdm2's Dilemma: To Degrade or To Translate p53?

Pierre-Jacques Hamard[1] and James J. Manfredi[1,*]
[1]Department of Oncological Sciences, Mount Sinai School of Medicine, New York, NY 10029, USA
*Correspondence: james.manfredi@mssm.edu
DOI 10.1016/j.ccr.2011.12.018

In this issue of *Cancer Cell*, Gajjar et al. provide insight into how Mdm2 can both inhibit and enhance p53 activity. In the basal setting, Mdm2 binds p53 and promotes p53 degradation. Under stress conditions, ATM-dependent phosphorylation of Mdm2 results in its recruitment to p53 mRNA, thereby stimulating p53 translation.

The p53 tumor suppressor is a transcription factor that is induced in response to a variety of stress signals (Kruse and Gu, 2009). Under normal conditions, the p53 protein is kept at low levels in cells by ubiquitination-dependent proteosomal degradation mediated by its negative regulator, the E3 ubiquitin ligase Mdm2 (Figure 1A). Mdm2 is also a p53 transcriptional target and thus participates in a negative feedback loop with p53. Stress-mediated upregulation of Mdm2 has been considered a means by which p53 is able to regulate the duration and amplitude of its cellular effects.

In response to activation of specific oncogenic pathways, the ARF tumor suppressor is upregulated. ARF, in turn, interferes with Mdm2-dependent inhibition of p53 (Manfredi, 2010) (Figure 1B). In contrast, stimulation of the p53 pathway by genotoxic stress involves the DNA damage-activated kinase ATM, which has been shown to directly phosphorylate both p53 and Mdm2 (Kruse and Gu, 2009; Manfredi, 2010) (Figure 1C). The significance of ATM-dependent phosphorylation of Mdm2 was confirmed by the observation that phosphorylation of serine 395 on Mdm2 led to impaired p53 degradation (Maya et al., 2001). Biochemical studies have indicated that this is likely due to altered oligomerization, thereby attenuating the processivity of the E3 ligase activity of Mdm2 (Cheng et al., 2009). DNA damage has also been shown to induce the relocalization of Mdm2 to the nucleolus (Bernardi et al., 2004). It has been proposed that a nucleotide-binding motif within the Mdm2 E3 ligase RING domain facilitates nucleolar localization of Mdm2 (Poyurovsky et al., 2003). Candeias et al. (2008) then made the surprising observation that the p53 mRNA itself was able to interact directly with the RING domain of Mdm2. This interaction impaired the E3 ligase activity of Mdm2 and promoted p53 mRNA translation. It was unclear, however, under what biological settings such an interaction would have relevance.

In this issue of *Cancer Cell*, Gajjar et al. (2012) provide important insight by demonstrating that the DNA damage- and ATM-dependent phosphorylation of Mdm2 on serine 395 promotes the interaction of Mdm2 with p53 mRNA. This, in turn, is needed for p53 stabilization and apoptotic activity (Gajjar et al., 2012) (Figure 1D). By means of RNAi and overexpression experiments, these authors show that both ATM and Mdm2 are required to achieve full p53 apoptotic activity after DNA damage. Use of an Mdm2 isoform that does not bind to the p53 protein shows that a protein-protein interaction between Mdm2 and p53 is remarkably dispensable for this. It was further demonstrated that the interaction between p53 mRNA and the Mdm2 RING domain is necessary for p53-dependent apoptosis after genotoxic stress. Studies using a mutated p53 mRNA that no longer binds Mdm2 confirmed findings with a mutant Mdm2 protein that has a reduced affinity for the mRNA. These intriguing results support the notion that ATM-mediated phosphorylation of Mdm2 at serine 395 promotes allosteric changes in the RING domain, which in turn facilitate p53 mRNA binding. Finally, Gajjar et al. (2012) show that after DNA damage, the interaction between Mdm2 and p53 mRNA impairs Mdm2-dependent ubiquitination of p53. Thus, it is argued that the p53 mRNA-MDM2 interaction not only increases p53 translation but also inhibits p53 protein degradation as well.

In sum, this study demonstrates that Mdm2 can act as a positive regulator of p53 activity after genotoxic stress. It further provides an additional novel explanation for why Mdm2 is transcriptionally upregulated by p53 after DNA damage.

The finding that p53 mRNA relocalizes with Mdm2 in the nucleolus after DNA damage is especially interesting since the nucleolus is generally thought of as the site of ribosomal RNA transcription.

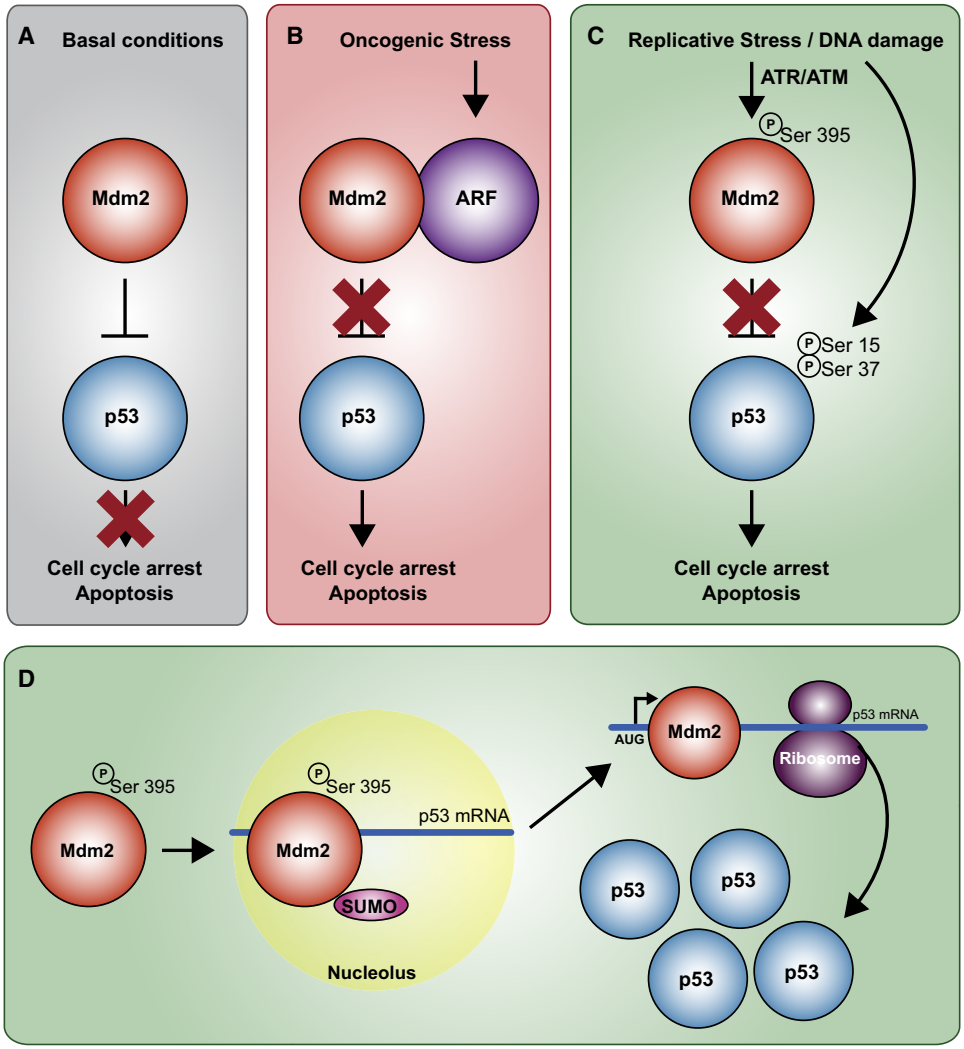

Figure 1. Mdm2 Acts as a Positive or Negative Regulator of p53 Activity in Response to Different Stresses

(A) Under basal conditions, Mdm2 inhibits p53 function by ubiquitination of p53 through its E3 ubiquitin ligase activity, leading to proteosomal-dependent degradation of p53, and by direct interference with the ability of p53 to act as a transcription factor.

(B) Oncogenic signaling has been shown to upregulate ARF at the transcriptional level. ARF binds to Mdm2 and inhibits its E3 ubiquitin ligase activity, thereby increasing p53 protein levels by alleviating proteosomal-dependent degradation of p53. In this case, Mdm2 behaves as an oncogene. In certain cancers, Mdm2 is indeed overexpressed.

(C) Other signals such as replicative stress or DNA damage activate the ATM or ATR kinases. ATM, in particular, has been shown to phosphorylate both p53 and Mdm2 and stabilize p53. The phosphorylation of p53 on serine 15 and serine 37 inhibits its interaction with Mdm2, and the phosphorylation of Mdm2 on serine 395 impairs Mdm2-mediated p53 degradation.

(D) Gajjar et al. (2012) demonstrate that phosphorylation of Mdm2 on serine 395 induces the binding of p53 mRNA to the RING domain of Mdm2, the sumoylation of Mdm2, and the relocalization of Mdm2 to the nucleolus. This p53 mRNA-Mdm2 interaction enhances p53 translation and inhibits Mdm2 E3 ubiquitin ligase activity toward p53 protein (Gajjar et al., 2012). Overall, phosphorylated Mdm2 on serine 395 is a positive regulator of p53. In this case, Mdm2 acts as a tumor suppressor.

However, several studies support the idea that it might also be involved in the processing or nuclear export of specific messenger RNAs (Pederson, 2011). Nevertheless, little is known about the relationship between mRNA and the nucleolus. The present study rekindles the idea that the nucleolus and mRNA processing are functionally connected.

While these nucleolar events are intriguing, the key outcome is an enhancement of p53 protein synthesis, a process that occurs in the cytoplasm. With this in mind, a molecular explanation is still needed for how p53 mRNA is then relocated from the nucleolus to the cytoplasm. In their previous study, Candeias et al. (2008) showed that Mdm2 is associated with polysomes in the cytoplasm, raising the intriguing possibility that Mdm2 is actually exported to the cytoplasm along with p53 mRNA and that Mdm2 may enhance p53 translation once there. Mdm2 is known to interact with several ribosomal proteins (Zhang and Lu, 2009). These interactions may indeed be at play in this process. The molecular mechanism by which the transient Mdm2-dependent nucleolar targeting of p53 mRNA enhances its translation also remains to be explored.

In summary, the significance of the study lies not only in its elucidation of a new role for p53-mediated induction of

Mdm2 after DNA damage, it begins to provide a molecular explanation for how Mdm2 may act either as an oncogene or a tumor suppressor, depending upon the particular context (Manfredi, 2010). This latter notion has important implications for the prognosis and treatment of tumors with aberrant Mdm2 expression.

REFERENCES

Bernardi, R., Scaglioni, P.P., Bergmann, S., Horn, H.F., Vousden, K.H., and Pandolfi, P.P. (2004). Nat. Cell Biol. *6*, 665–672.

Candeias, M.M., Malbert-Colas, L., Powell, D.J., Daskalogianni, C., Maslon, M.M., Naski, N., Bourougaa, K., Calvo, F., and Fåhraeus, R. (2008). Nat. Cell Biol. *10*, 1098–1105.

Cheng, Q., Chen, L., Li, Z., Lane, W.S., and Chen, J. (2009). EMBO J. *28*, 3857–3867.

Gajjar, M., Candeias, M.M., Malbert-Colas, L., Mazars, A., Fujita, J., Olivares-Illana, V., and Fåhraeus, R. (2012). Cancer Cell *21*, this issue, 25–35.

Kruse, J.P., and Gu, W. (2009). Cell *137*, 609–622.

Manfredi, J.J. (2010). Genes Dev. *24*, 1580–1589.

Maya, R., Balass, M., Kim, S.T., Shkedy, D., Leal, J.F., Shifman, O., Moas, M., Buschmann, T., Ronai, Z., Shiloh, Y., et al. (2001). Genes Dev. *15*, 1067–1077.

Pederson, T. (2011). Cold Spring Harb. Perspect. Biol. *3*, a000638.

Poyurovsky, M.V., Jacq, X., Ma, C., Karni-Schmidt, O., Parker, P.J., Chalfie, M., Manley, J.L., and Prives, C. (2003). Mol. Cell *12*, 875–887.

Zhang, Y., and Lu, H. (2009). Cancer Cell *16*, 369–377.

Polycomb Regulates NF-κB Signaling in Cancer through miRNA

Iris Uribesalgo,[1] Cecilia Ballaré,[1] and Luciano Di Croce[1,2,*]
[1]Centre de Regulació Genòmica (CRG) and UPF, 08003 Barcelona, Spain
[2]Institució Catalana de Recerca i Estudis Avançats (ICREA), 08010 Barcelona, Spain
*Correspondence: luciano.dicroce@crg.es
DOI 10.1016/j.ccr.2011.12.019

The mechanisms leading to the constitutive activation of NF-κB in cancers and the pathways upstream and downstream of this activation are not fully understood. In this issue of *Cancer Cell*, Yamagishi et al. demonstrate that Polycomb-mediated silencing of miR-31 is implicated in the aberrant activation of NF-κB signaling in tumors.

Differential gene expression distinguishes one cell type from another and enables cells to build specialized tissues. Once a cell fate decision is made, the cell must be able to silence the transcriptional programs that could potentially lead to other lineages, because the DNA content of all cells is the same. Epigenetic factors play a crucial role in this type of gene expression regulation. The Polycomb group of proteins plays a pivotal role in silencing and in the long-term repression of genes implicated in cell fate decisions (Richly et al., 2010). Polycomb proteins belong either to Polycomb repressive complex 1 (PRC1) or PRC2. The PRC2 component EZH2 methylates lysine 27 of histone H3, which attracts the PRC1 complex; the presence of both PRC1 and PRC2 at promoter regions leads to transcriptional silencing (Richly et al., 2011).

It is now clear that, in addition to epigenetic complexes, microRNAs (miRNAs) also contribute greatly to posttranscriptional gene regulation. miRNAs are endogenous, short (~23 nt) RNAs that suppress gene expression via sequence-specific interactions with the 3′ untranslated regions of related mRNA targets. miRNAs affect gene silencing via both translational inhibition and mRNA degradation. Several miRNAs have been reported to have a direct role in oncogenesis, and indeed, abnormal miRNA expression is a common feature of diverse types of cancers, suggesting potential diagnostic or prognostic biomarker uses.

The NF-κB transcription factor family regulates the expression of diverse genes involved in development, cell growth, immune responses, apoptosis, and neoplastic transformation. Activation of NF-κB is a tightly regulated event. In non-malignant cells, NF-κB is activated only after appropriate stimulation, after which it transiently upregulates the transcription of its target genes. In tumor cells, different types of molecular alterations may result in an impaired regulation of NF-κB activation and deregulated expression of target genes due to constitutively active NF-κB. Recent studies have also demonstrated that miRNAs modulate NF-κB signaling in both normal and pathological scenarios (Lu et al., 2011; Ma et al., 2011).

Adult T cell leukemia/lymphoma (ATL) is an aggressive neoplasm of mature $CD4^+$ T lymphocytes caused by the human T cell leukemia/lymphoma virus type 1 (HTLV-1) infection. Aberrant activation of NF-κB stimulates cell growth and anti-apoptotic responses in ATL cells and thus directly participates in ATL pathogenesis. Recently, correlations between the epigenetic machinery, NF-κB activation, and ATL pathology have been suggested (Sasaki et al., 2011). However, mechanistic insights are lacking. Tax, an

Mdm2 after DNA damage, it begins to provide a molecular explanation for how Mdm2 may act either as an oncogene or a tumor suppressor, depending upon the particular context (Manfredi, 2010). This latter notion has important implications for the prognosis and treatment of tumors with aberrant Mdm2 expression.

REFERENCES

Bernardi, R., Scaglioni, P.P., Bergmann, S., Horn, H.F., Vousden, K.H., and Pandolfi, P.P. (2004). Nat. Cell Biol. *6*, 665–672.

Candeias, M.M., Malbert-Colas, L., Powell, D.J., Daskalogianni, C., Maslon, M.M., Naski, N., Bourougaa, K., Calvo, F., and Fåhraeus, R. (2008). Nat. Cell Biol. *10*, 1098–1105.

Cheng, Q., Chen, L., Li, Z., Lane, W.S., and Chen, J. (2009). EMBO J. *28*, 3857–3867.

Gajjar, M., Candeias, M.M., Malbert-Colas, L., Mazars, A., Fujita, J., Olivares-Illana, V., and Fåhraeus, R. (2012). Cancer Cell *21*, this issue, 25–35.

Kruse, J.P., and Gu, W. (2009). Cell *137*, 609–622.

Manfredi, J.J. (2010). Genes Dev. *24*, 1580–1589.

Maya, R., Balass, M., Kim, S.T., Shkedy, D., Leal, J.F., Shifman, O., Moas, M., Buschmann, T., Ronai, Z., Shiloh, Y., et al. (2001). Genes Dev. *15*, 1067–1077.

Pederson, T. (2011). Cold Spring Harb. Perspect. Biol. *3*, a000638.

Poyurovsky, M.V., Jacq, X., Ma, C., Karni-Schmidt, O., Parker, P.J., Chalfie, M., Manley, J.L., and Prives, C. (2003). Mol. Cell *12*, 875–887.

Zhang, Y., and Lu, H. (2009). Cancer Cell *16*, 369–377.

Polycomb Regulates NF-κB Signaling in Cancer through miRNA

Iris Uribesalgo,[1] Cecilia Ballaré,[1] and Luciano Di Croce[1,2,*]
[1]Centre de Regulació Genòmica (CRG) and UPF, 08003 Barcelona, Spain
[2]Institució Catalana de Recerca i Estudis Avançats (ICREA), 08010 Barcelona, Spain
*Correspondence: luciano.dicroce@crg.es
DOI 10.1016/j.ccr.2011.12.019

The mechanisms leading to the constitutive activation of NF-κB in cancers and the pathways upstream and downstream of this activation are not fully understood. In this issue of *Cancer Cell*, Yamagishi et al. demonstrate that Polycomb-mediated silencing of miR-31 is implicated in the aberrant activation of NF-κB signaling in tumors.

Differential gene expression distinguishes one cell type from another and enables cells to build specialized tissues. Once a cell fate decision is made, the cell must be able to silence the transcriptional programs that could potentially lead to other lineages, because the DNA content of all cells is the same. Epigenetic factors play a crucial role in this type of gene expression regulation. The Polycomb group of proteins plays a pivotal role in silencing and in the long-term repression of genes implicated in cell fate decisions (Richly et al., 2010). Polycomb proteins belong either to Polycomb repressive complex 1 (PRC1) or PRC2. The PRC2 component EZH2 methylates lysine 27 of histone H3, which attracts the PRC1 complex; the presence of both PRC1 and PRC2 at promoter regions leads to transcriptional silencing (Richly et al., 2011).

It is now clear that, in addition to epigenetic complexes, microRNAs (miRNAs) also contribute greatly to posttranscriptional gene regulation. miRNAs are endogenous, short (~23 nt) RNAs that suppress gene expression via sequence-specific interactions with the 3′ untranslated regions of related mRNA targets. miRNAs affect gene silencing via both translational inhibition and mRNA degradation. Several miRNAs have been reported to have a direct role in oncogenesis, and indeed, abnormal miRNA expression is a common feature of diverse types of cancers, suggesting potential diagnostic or prognostic biomarker uses.

The NF-κB transcription factor family regulates the expression of diverse genes involved in development, cell growth, immune responses, apoptosis, and neoplastic transformation. Activation of NF-κB is a tightly regulated event. In non-malignant cells, NF-κB is activated only after appropriate stimulation, after which it transiently upregulates the transcription of its target genes. In tumor cells, different types of molecular alterations may result in an impaired regulation of NF-κB activation and deregulated expression of target genes due to constitutively active NF-κB. Recent studies have also demonstrated that miRNAs modulate NF-κB signaling in both normal and pathological scenarios (Lu et al., 2011; Ma et al., 2011).

Adult T cell leukemia/lymphoma (ATL) is an aggressive neoplasm of mature $CD4^+$ T lymphocytes caused by the human T cell leukemia/lymphoma virus type 1 (HTLV-1) infection. Aberrant activation of NF-κB stimulates cell growth and anti-apoptotic responses in ATL cells and thus directly participates in ATL pathogenesis. Recently, correlations between the epigenetic machinery, NF-κB activation, and ATL pathology have been suggested (Sasaki et al., 2011). However, mechanistic insights are lacking. Tax, an

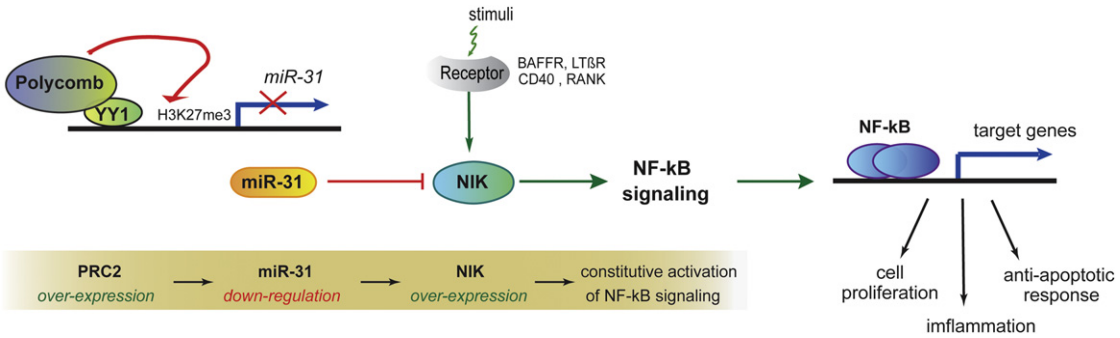

Figure 1. Polycomb-Mediated Silencing of miR-31 Activates the NF-κB Pathway
miR-31 negatively regulates the non-canonical NF-κB pathway by targeting the NIK. Polycomb can modulate NF-κB signaling via miR-31 regulation. PRC2 is recruited by YY1 to a region upstream of the miR-31 locus and epigenetically silences miR-31 expression. In ATL cells, overexpression of PCR2 components leads to miR-31 repression, NIK upregulation, and constitutive activation of NF-κB signaling.

HTLV-1 regulatory protein, has also been reported to activate the NF-κB pathway. Tax expression is required at the early stages of cellular transformation, but Tax is not expressed in the later states. In this issue of *Cancer Cell*, Yamagishi et al. (2012) describe a Tax-independent mechanism by which NF-κB is aberrantly activated in ATL cells through a PRC2-dependent miR-31 epigenetic silencing.

Given the poor understanding of the molecular basis of ATL development, Yamagishi et al. (2012) initially characterized the genetic and epigenetic background of the ATL disease. The authors demonstrated by miRNA expression microarray analyses that miR-31 is downregulated in all primary ATL samples; this suggests that miR-31 loss is a prerequisite for ATL development. Using computational algorithms and gene expression microarray analyses of ATL primary samples, the authors revealed that the NF-κB-inducing kinase (NIK) is a downstream target of miR-31. Intriguingly, NIK plays a central role in activating non-canonical NF-κB signaling and has been implicated in ATL pathogenesis (Saitoh et al., 2008).

The Weinberg lab previously demonstrated that miR-31 plays a suppressive role in breast cancer metastasis (Valastyan et al., 2009). Although miR-31 can concomitantly repress multiple prometastatic targets in breast tumors, miR-31's impact on metastasis was shown to be mediated through a small cohort of these targets. Accordingly, Yamagishi et al. (2012) now provide evidence for a high specificity of NIK regulation by miR-31 in ATL. First, NIK knockdown and miR-31 ectopic expression produced similar effects in ATL cells, such as triggering an apoptotic response and attenuating cell proliferation. Second, expression of a miR-31-resistant NIK mutant into miR-31-expressing ATL cells impaired their ability to enter apoptosis. These results emphasize the ability of miRNAs to exert their effect by modulating a precise and modest number of downstream targets in several cell types and broaden the anti-carcinogenic role of miR-31 in different types of cancers.

Computational analysis identified YY1 binding motifs upstream of the miR-31 region in both human and mouse. As the YY1 motifs have been previously shown to be involved in PRC2 recruitment, the authors propose that YY1 targets PRC2 to the miR-31 locus and thus induces its epigenetic silencing. This in turn leads to increased intracellular levels of NIK and triggers NF-κB activation (Figure 1). Interestingly, high levels of several Polycomb proteins and YY1 have been reported together in primary ATL samples (Sasaki et al., 2011). These results complement the data from Yamagishi et al. (2012) and highlight a novel pathway in ATL that is triggered by an aberrant overexpression of PRC2 complex, leading to an epigenetic-directed activation of the NF-κB pathway. It is now relevant to understand how the PRC2 complex is deregulated in ATL.

Understanding the regulatory mechanisms involving Polycomb proteins is highly relevant considering their important roles in both normal and cancer cells. In this respect, the Yamagishi study emphasizes two interesting mechanistic features of PRC2: first, its ability to regulate miRNA expression in human lymphocytes, as previously showed in *Drosophila* and in mouse ES cells (Enderle et al., 2011; Marson et al., 2008); and second, its ability to be recruited by YY1. Indeed, as Polycomb response elements have not been identified in mammals, several studies have identified a handful of PRC2 recruiters that could be cell type-specific. It would be of interest to study if YY1 binding sites are frequently present in miRNAs that are silenced by PRC2 and whether this is cell-specific.

Strikingly, 12.5% of the ATL cases studied by Yamagishi et al. (2012) had genomic deletions of the region where the human gene that encodes miR-31, *hsa-miR-31*, is located. Correspondingly, several ATL cases with no genetic deletion at *hsa-miR-31* presented a severe downregulation of miR-31 expression. Thus, this study also opens the possibility to monitor the expression of miR-31 as clinical biomarkers for ATL. Furthermore, the miRNA expression signature in ATL cells presented in this study revealed 59 other miRNAs to be downregulated, some of which have known tumor-suppressive functions. These might also be relevant for ATL pathogenesis and warrant further investigation.

The findings by Yamagishi et al. (2012) further our understanding of the highly complex transformation phenotype and oncogenic synergism in ATL. Recent data highlighted the relevance of NF-κB activation in Notch1-induced T cell acute lymphoblastic leukemia and its potential as a therapeutic target (Espinosa et al., 2010). The crosstalk between NF-κB and Polycomb-mediated silencing of miRNAs

described here opens new therapeutic possibilities for ATL treatment. Targeting Polycomb activity, restoring the tumor suppressor miR-31, or inhibiting NIK are all attractive potential strategies for eliminating ATL tumor cells. Furthermore, the described involvement of miR-31 in breast cancer cells (Valastyan et al., 2009) raises the question of whether miR-31 silencing through PRC2 occurs in other type of tumors and whether these pathways could be also be targets for molecular therapies in those malignancies. Finally, from a basic biology viewpoint, the novel mechanism described by Yamagishi et al. (2012) might have a wider role in normal cells, given the ubiquitous roles of NF-κB, Polycomb, and miRNAs in several tissues.

REFERENCES

Enderle, D., Beisel, C., Stadler, M.B., Gerstung, M., Athri, P., and Paro, R. (2011). Genome Res. *21*, 216–226.

Espinosa, L., Cathelin, S., D'Altri, T., Trimarchi, T., Statnikov, A., Guiu, J., Rodilla, V., Inglés-Esteve, J., Nomdedeu, J., Bellosillo, B., et al. (2010). Cancer Cell *18*, 268–281.

Lu, Z., Li, Y., Takwi, A., Li, B., Zhang, J., Conklin, D.J., Young, K.H., Martin, R., and Li, Y. (2011). EMBO J. *30*, 57–67.

Ma, X., Becker Buscaglia, L.E., Barker, J.R., and Li, Y. (2011). J. Mol. Cell. Biol. *3*, 159–166.

Marson, A., Levine, S.S., Cole, M.F., Frampton, G.M., Brambrink, T., Johnstone, S., Guenther, M.G., Johnston, W.K., Wernig, M., Newman, J., et al. (2008). Cell *134*, 521–533.

Richly, H., Rocha-Viegas, L., Ribeiro, J.D., Demajo, S., Gundem, G., Lopez-Bigas, N., Nakagawa, T., Rospert, S., Ito, T., and Di Croce, L. (2010). Nature *468*, 1124–1128.

Richly, H., Aloia, L., and Di Croce, L. (2011). Cell Death Dis *2*, e204.

Saitoh, Y., Yamamoto, N., Dewan, M.Z., Sugimoto, H., Martinez Bruyn, V.J., Iwasaki, Y., Matsubara, K., Qi, X., Saitoh, T., Imoto, I., et al. (2008). Blood *111*, 5118–5129.

Sasaki, D., Imaizumi, Y., Hasegawa, H., Osaka, A., Tsukasaki, K., Choi, Y.L., Mano, H., Marquez, V.E., Hayashi, T., Yanagihara, K., et al. (2011). Haematologica *96*, 712–719.

Valastyan, S., Benaich, N., Chang, A., Reinhardt, F., and Weinberg, R.A. (2009). Genes Dev. *23*, 2592–2597.

Yamagishi, M., Nakano, K., Miyake, A., Yamochi, T., Kagami, Y., Tsutsumi, A., Matsuda, Y., Sato-Otsubo, A., Muto, S., Utsunomiya, A., et al. (2012). Cancer Cell *21*, this issue, 121–135.

How to Fool a Wonder Drug: Truncate and Dimerize

Miriam Molina-Arcas[1] and Julian Downward[1,*]
[1]Signal Transduction Laboratory, Cancer Research UK London Research Institute, 44 Lincoln's Inn Fields, London WC2A 3LY, UK
*Correspondence: julian.downward@cancer.org.uk
DOI 10.1016/j.ccr.2011.12.017

In a recent paper, Poulikakos et al. describe a new and potentially common mechanism whereby melanomas develop resistance to the BRAF inhibitor vemurafenib by expressing truncated forms of BRAF(V600E) that can dimerize in the absence of activated RAS. Will it be possible to block this with improved BRAF inhibitor design?

Metastatic melanoma has long been renowned for being extremely difficult to treat effectively. However, the last few years have witnessed dramatic changes to the landscape of this disease. In 2002, it was discovered that over 50% of melanomas harbor activating mutations, most commonly V600E, in the gene encoding the protein kinase BRAF, which lead to constitutive activation of the RAF/MEK/ERK pro-proliferative signaling pathway (Davies et al., 2002). Within a few years, the first selective BRAF inhibitor was in clinical trials producing highly encouraging results. In a phase I clinical trial, the BRAF(V600E) selective inhibitor vemurafenib (PLX4032) resulted in complete or partial regression in the majority of melanoma patients harboring the BRAF(V600E) mutation (Flaherty et al., 2010). However, the excitement from this spectacular result was soon tempered as resistance to the therapy quickly developed, resulting in response durations of only 2 to 18 months.

Vemurafenib is only effective in BRAF mutant cells. In normal tissues and in cells where the RAF/MEK/ERK pathway is activated by mutation of the upstream RAS signaling proteins, vemurafenib actually enhances signaling. Key to understanding this surprising result is the fact that RAF isoforms BRAF and CRAF normally homo- or heterodimerize following activation of RAS proteins. RAF inhibitor binding appears to cause a conformational change that promotes the formation of BRAF-CRAF or CRAF-CRAF dimers in which the drug-inactivated molecule is able to induce activation of its drug-free partner within the dimer. On the other hand, in cells harboring BRAF(V600E), the levels of activated RAS (GTP bound) are insufficient to induce dimer formation, so BRAF(V600E) signals only as a monomer and the inhibitor can completely block its kinase activity (Hatzivassiliou et al., 2010; Heidorn et al., 2010; Poulikakos et al., 2010) (Figure 1).

This model suggests that molecular lesions that enhance RAF dimerization in tumor cells will increase RAF activity upon drug treatment and promote tumor resistance. Poulikakos et al. 2011 have now found evidence for the operation of just such a mechanism in vemurafenib-resistant, BRAF(V600E) mutant melanoma cell lines, and patient samples. The authors generated resistant cell lines by exposing a BRAF(V600E) melanoma

described here opens new therapeutic possibilities for ATL treatment. Targeting Polycomb activity, restoring the tumor suppressor miR-31, or inhibiting NIK are all attractive potential strategies for eliminating ATL tumor cells. Furthermore, the described involvement of miR-31 in breast cancer cells (Valastyan et al., 2009) raises the question of whether miR-31 silencing through PRC2 occurs in other type of tumors and whether these pathways could be also be targets for molecular therapies in those malignancies. Finally, from a basic biology viewpoint, the novel mechanism described by Yamagishi et al. (2012) might have a wider role in normal cells, given the ubiquitous roles of NF-κB, Polycomb, and miRNAs in several tissues.

REFERENCES

Enderle, D., Beisel, C., Stadler, M.B., Gerstung, M., Athri, P., and Paro, R. (2011). Genome Res. *21*, 216–226.

Espinosa, L., Cathelin, S., D'Altri, T., Trimarchi, T., Statnikov, A., Guiu, J., Rodilla, V., Inglés-Esteve, J., Nomdedeu, J., Bellosillo, B., et al. (2010). Cancer Cell *18*, 268–281.

Lu, Z., Li, Y., Takwi, A., Li, B., Zhang, J., Conklin, D.J., Young, K.H., Martin, R., and Li, Y. (2011). EMBO J. *30*, 57–67.

Ma, X., Becker Buscaglia, L.E., Barker, J.R., and Li, Y. (2011). J. Mol. Cell. Biol. *3*, 159–166.

Marson, A., Levine, S.S., Cole, M.F., Frampton, G.M., Brambrink, T., Johnstone, S., Guenther, M.G., Johnston, W.K., Wernig, M., Newman, J., et al. (2008). Cell *134*, 521–533.

Richly, H., Rocha-Viegas, L., Ribeiro, J.D., Demajo, S., Gundem, G., Lopez-Bigas, N., Nakagawa, T., Rospert, S., Ito, T., and Di Croce, L. (2010). Nature *468*, 1124–1128.

Richly, H., Aloia, L., and Di Croce, L. (2011). Cell Death Dis *2*, e204.

Saitoh, Y., Yamamoto, N., Dewan, M.Z., Sugimoto, H., Martinez Bruyn, V.J., Iwasaki, Y., Matsubara, K., Qi, X., Saitoh, T., Imoto, I., et al. (2008). Blood *111*, 5118–5129.

Sasaki, D., Imaizumi, Y., Hasegawa, H., Osaka, A., Tsukasaki, K., Choi, Y.L., Mano, H., Marquez, V.E., Hayashi, T., Yanagihara, K., et al. (2011). Haematologica *96*, 712–719.

Valastyan, S., Benaich, N., Chang, A., Reinhardt, F., and Weinberg, R.A. (2009). Genes Dev. *23*, 2592–2597.

Yamagishi, M., Nakano, K., Miyake, A., Yamochi, T., Kagami, Y., Tsutsumi, A., Matsuda, Y., Sato-Otsubo, A., Muto, S., Utsunomiya, A., et al. (2012). Cancer Cell *21*, this issue, 121–135.

How to Fool a Wonder Drug: Truncate and Dimerize

Miriam Molina-Arcas[1] and Julian Downward[1,*]
[1]Signal Transduction Laboratory, Cancer Research UK London Research Institute, 44 Lincoln's Inn Fields, London WC2A 3LY, UK
*Correspondence: julian.downward@cancer.org.uk
DOI 10.1016/j.ccr.2011.12.017

In a recent paper, Poulikakos et al. describe a new and potentially common mechanism whereby melanomas develop resistance to the BRAF inhibitor vemurafenib by expressing truncated forms of BRAF(V600E) that can dimerize in the absence of activated RAS. Will it be possible to block this with improved BRAF inhibitor design?

Metastatic melanoma has long been renowned for being extremely difficult to treat effectively. However, the last few years have witnessed dramatic changes to the landscape of this disease. In 2002, it was discovered that over 50% of melanomas harbor activating mutations, most commonly V600E, in the gene encoding the protein kinase BRAF, which lead to constitutive activation of the RAF/MEK/ERK pro-proliferative signaling pathway (Davies et al., 2002). Within a few years, the first selective BRAF inhibitor was in clinical trials producing highly encouraging results. In a phase I clinical trial, the BRAF(V600E) selective inhibitor vemurafenib (PLX4032) resulted in complete or partial regression in the majority of melanoma patients harboring the BRAF(V600E) mutation (Flaherty et al., 2010). However, the excitement from this spectacular result was soon tempered as resistance to the therapy quickly developed, resulting in response durations of only 2 to 18 months.

Vemurafenib is only effective in BRAF mutant cells. In normal tissues and in cells where the RAF/MEK/ERK pathway is activated by mutation of the upstream RAS signaling proteins, vemurafenib actually enhances signaling. Key to understanding this surprising result is the fact that RAF isoforms BRAF and CRAF normally homo- or heterodimerize following activation of RAS proteins. RAF inhibitor binding appears to cause a conformational change that promotes the formation of BRAF-CRAF or CRAF-CRAF dimers in which the drug-inactivated molecule is able to induce activation of its drug-free partner within the dimer. On the other hand, in cells harboring BRAF(V600E), the levels of activated RAS (GTP bound) are insufficient to induce dimer formation, so BRAF(V600E) signals only as a monomer and the inhibitor can completely block its kinase activity (Hatzivassiliou et al., 2010; Heidorn et al., 2010; Poulikakos et al., 2010) (Figure 1).

This model suggests that molecular lesions that enhance RAF dimerization in tumor cells will increase RAF activity upon drug treatment and promote tumor resistance. Poulikakos et al. 2011 have now found evidence for the operation of just such a mechanism in vemurafenib-resistant, BRAF(V600E) mutant melanoma cell lines, and patient samples. The authors generated resistant cell lines by exposing a BRAF(V600E) melanoma

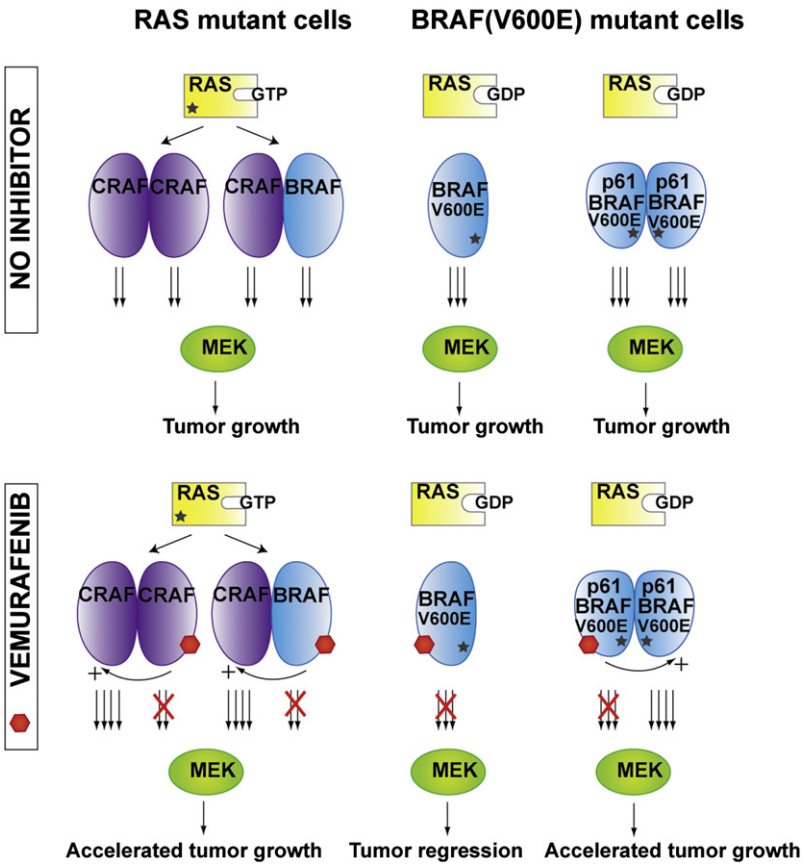

Figure 1. Effects of RAF Inhibitors on Cells with BRAF or RAS Mutations
Active GTP-bound RAS promotes the formation of homo- and heterodimers, but BRAF(V600E) signals primarily as a monomer in BRAF(V600E) mutant cells because the levels of RAS-GTP are low. In contrast, the BRAF(V600E) splice variant p61BRAF(V600E) lacks domains necessary for RAS interaction and for preventing RAS-independent dimerization. When melanoma cells are treated with a BRAF inhibitor, BRAF(V600E) is inhibited, leading to tumor regression. However, when RAF isoforms form dimers, either due to RAS mutation or BRAF truncation, the drug-inactivated kinase subunit induces the transactivation of the drug-free kinase subunit in the dimmer, resulting in continued activation of downstream pro-proliferative signaling.

line to a high dose of vemurafenib in vitro. In three of five resistant clones obtained, they detected a smaller BRAF transcript that contained both the V600E mutation and an in-frame deletion of exons 4–8, resulting in expression of a BRAF variant lacking domains necessary for interaction with RAS. This deletion also removes sequences that inhibit BRAF dimerization in the absence of RAS binding, allowing dimerization of this variant in a RAS-independent manner. Thus, this truncation results in a constitutively activated BRAF(V600E) dimer rather than the BRAF(V600E) monomer found in the parental cells. The dimer displays the transactivation of the drug-free subunit by the drug-bound subunit that has been observed for other RAF dimers (Hatzivassiliou et al., 2010; Heidorn et al., 2010; Poulikakos et al., 2010), reducing sensitivity to vemurafenib by 100-fold.

Acknowledging that generation of resistant cell lines by drug exposure in vitro may have its limitations, Poulikakos et al. 2011 went on to demonstrate the importance of this resistance mechanism in the clinic. The authors analyzed tumors from 19 BRAF(V600E) mutant melanoma patients with acquired resistance to vemurafenib and identified a total of four shorter BRAF transcript variants in 6 of them. All these splicing variants lack minimally exons 4–8, one of which was identical to that seen in the cell lines. As yet, it is unclear how these variants were generated: could they be caused by mutations at the splice junctions or perhaps epigenetic changes?

This BRAF inhibitor resistance mechanism is the first identified that involves a structural change in BRAF itself, bringing BRAF more in line with resistance mechanisms commonly seen when pharmacologically targeting other oncogenes, such as activated EGFR or BCR-ABL. Several other mechanisms of resistance to RAF inhibitors have been previously reported, but in each study, only a very small group of tumor samples has been analyzed, making it hard to assess their relative importance in the clinic. Poulikakos et al. 2011 have analyzed the largest cohort of tumor samples thus far, with 19 patients, of which 6 had BRAF splice variants and 4 had mutations in NRAS, suggesting that both BRAF and NRAS mutations are likely to play major roles in the development of resistance. A mutation in NRAS had previously been identified as a resistance mechanism (Nazarian et al., 2010). Other possibly rarer molecular events reported previously that may also reactivate RAF/MEK/ERK signaling include enhancement of MAP3K8 (Cot1/Tpl2) mRNA levels (Johannessen et al., 2010) and an activating mutation in MEK1 (Wagle et al., 2011). Alterations that activate PI3K pathway signaling, including increased expression of PDGFRβ or IGF-1R levels or deletion of PTEN, have also been detected (Nazarian et al., 2010).

Drug resistance is arguably the biggest challenge blocking progress toward better outcomes in cancer treatment. Obviously, the importance of identifying drug resistance mechanisms lies in the possibility of developing better drugs or drug combinations to overcome resistance. For BRAF mutant melanoma, many resistance mechanisms result in ERK pathway reactivation, suggesting that inhibition of the pathway downstream of RAF using MEK inhibitors could overcome acquired resistance and might also have value in combination with vemurafenib to limit the development of resistance. However, MEK inhibitors have yet to prove their worth in the clinic. Perhaps a more interesting approach to tackling resistance is the development of new RAF inhibitors. The ideal drug would be one that was specific for oncogenic BRAF but would not transactivate CRAF or truncated BRAF, but achieving this may be quite a challenge for drug developers. Existing BRAF inhibitors also have some activity toward CRAF, and it is possible that

the transactivation has actually been selected in the drug development process because it circumvents potential systemic toxicity associated with pan-RAF inhibition.

Vemurafenib resistance often develops rapidly and multiple resistant tumor nodules usually appear at the same time (Wagle et al., 2011). The efficacy of RAF inhibitors depend on almost complete inhibition of ERK signaling; partial RAF inhibition or small changes that increase pathway activity can produce resistance. One possible reason for the rapid simultaneous appearance of resistant nodules is the existence of minor populations of resistant cells in the original tumors prior to treatment that can overtake the drug-sensitive populations. If this is the case, emergence of a single resistance mechanism should be seen if several different resistant lesions from the same patient are analyzed. More worrying is the possibility that tumor cells can escape destruction via any of a plethora of relatively easily accessed routes, so that each different resistant lesion in a patient is using a different mechanism. It has been suggested that tumor heterogeneity and changes in drug response can be mediated by epigenetic changes (Sharma et al., 2010), leading to changes in expression of some genes and potentially splicing alterations. This suggests that combination treatment with epigenetic modulators such as histone deacetylase inhibitors could be tested to overcome RAF inhibitor-mediated resistance.

The extremely rapid progress in understanding BRAF inhibitor resistance mechanisms raises hopes that the partial success of targeted agents like vemurafenib may soon lead to more lasting patient benefit. However, the complexity seen in the BRAF signaling network response to these drugs and the ease with which tumors develop resistance to them suggests that there will be many more unexpected twists to this story before metastatic melanoma can be considered beaten.

REFERENCES

Davies, H., Bignell, G.R., Cox, C., Stephens, P., Edkins, S., Clegg, S., Teague, J., Woffendin, H., Garnett, M.J., Bottomley, W., et al. (2002). Nature *417*, 949–954.

Flaherty, K.T., Puzanov, I., Kim, K.B., Ribas, A., McArthur, G.A., Sosman, J.A., O'Dwyer, P.J., Lee, R.J., Grippo, J.F., Nolop, K., and Chapman, P.B. (2010). N. Engl. J. Med. *363*, 809–819.

Hatzivassiliou, G., Song, K., Yen, I., Brandhuber, B.J., Anderson, D.J., Alvarado, R., Ludlam, M.J., Stokoe, D., Gloor, S.L., Vigers, G., et al. (2010). Nature *464*, 431–435.

Heidorn, S.J., Milagre, C., Whittaker, S., Nourry, A., Niculescu-Duvas, I., Dhomen, N., Hussain, J., Reis-Filho, J.S., Springer, C.J., Pritchard, C., and Marais, R. (2010). Cell *140*, 209–221.

Johannessen, C.M., Boehm, J.S., Kim, S.Y., Thomas, S.R., Wardwell, L., Johnson, L.A., Emery, C.M., Stransky, N., Cogdill, A.P., Barretina, J., et al. (2010). Nature *468*, 968–972.

Nazarian, R., Shi, H., Wang, Q., Kong, X., Koya, R.C., Lee, H., Chen, Z., Lee, M.K., Attar, N., Sazegar, H., et al. (2010). Nature *468*, 973–977.

Poulikakos, P.I., Persaud, Y., Janakiraman, M., Kong, X., Ng, C., Moriceau, G., Shi, H., Atefi, M., Titz, B., Gabay, M.T., et al. (2011). Nature *480*, 387–390.

Poulikakos, P.I., Zhang, C., Bollag, G., Shokat, K.M., and Rosen, N. (2010). Nature *464*, 427–430.

Sharma, S.V., Lee, D.Y., Li, B., Quinlan, M.P., Takahashi, F., Maheswaran, S., McDermott, U., Azizian, N., Zou, L., Fischbach, M.A., et al. (2010). Cell *141*, 69–80.

Wagle, N., Emery, C., Berger, M.F., Davis, M.J., Sawyer, A., Pochanard, P., Kehoe, S.M., Johannessen, C.M., Macconaill, L.E., Hahn, W.C., et al. (2011). J. Clin. Oncol. *29*, 3085–3096.

Cancer Cell
Article

Self-Renewal Does Not Predict Tumor Growth Potential in Mouse Models of High-Grade Glioma

Lindy E. Barrett,[1] Zvi Granot,[1] Courtney Coker,[1] Antonio Iavarone,[2] Dolores Hambardzumyan,[3] Eric C. Holland,[1] Hyung-song Nam,[1,4] and Robert Benezra[1,*]
[1]Department of Cancer Biology and Genetics, Memorial Sloan-Kettering Cancer Center, New York, NY 10021, USA
[2]Institute for Cancer Genetics, Department of Neurology, Columbia University Medical Center, New York, NY 10032, USA
[3]Department of Stem Cell Biology and Regenerative Medicine, Cleveland Clinic, Cleveland, OH 44195, USA
[4]Present address: Howard Hughes Medical Institute and Department of Human Genetics, University of Utah School of Medicine, Salt Lake City, UT 84112, USA
*Correspondence: r-benezra@ski.mskcc.org
DOI 10.1016/j.ccr.2011.11.025

SUMMARY

Within high-grade gliomas, the precise identities and functional roles of stem-like cells remain unclear. In the normal neurogenic niche, *ID* (*Inhibitor of DNA-binding*) genes maintain self-renewal and multipotency of adult neural stem cells. Using PDGF- and KRAS-driven murine models of gliomagenesis, we show that high Id1 expression (Id1^{high}) identifies tumor cells with high self-renewal capacity, while low Id1 expression (Id1^{low}) identifies tumor cells with proliferative potential but limited self-renewal capacity. Surprisingly, Id1^{low} cells generate tumors more rapidly and with higher penetrance than Id1^{high} cells. Further, eliminating tumor cell self-renewal through deletion of Id1 has modest effects on animal survival, while knockdown of Olig2 within Id1^{low} cells has a significant survival benefit, underscoring the importance of non-self-renewing lineages in disease progression.

INTRODUCTION

High-grade gliomas (WHO Grade III, IV astrocytomas) are among the most lethal types of solid tumors, with significant cellular and genetic heterogeneity complicating treatment efforts (Terzis et al., 2006). Since the discovery of glioma cells with properties reminiscent of neural stem cells, including the capacity to self-renew, there has been a great deal of interest in elucidating their contributions to tumorigenesis. Self-renewal in normal and tumor stem cells occurs when a cell divides to produce at least one daughter cell with the same developmental potential as itself, thus maintaining multipotency (He et al., 2009). This is in contrast to proliferation, which refers to cell divisions regardless of developmental potential (He et al., 2009). Within the subventricular zone (SVZ), normal adult neural stem cells (also referred to as "type B cells") are rare, slow-cycling and self-renewing cells that give rise to more rapid cycling transit amplifying cells ("type C cells"), which then give rise to more differentiated neuroblasts ("type A cells") (Doetsch et al., 1997). Glioma stem cells, likened to type B cells, are defined by their capacity to (1) self-renew in vitro, (2) transplant tumors in vivo, and (3) generate tumors that recapitulate the heterogeneity of the parental tumors (Stiles and Rowitch, 2008). The degree to which glioma stem cells resemble neural stem cells, and the degree to which the normal lineage hierarchy is maintained in brain tumors remain unanswered questions.

The cancer stem cell hypothesis predicts that stem cells are responsible for tumor initiation and preferentially drive tumor growth, and indeed, many studies use the term "glioma-initiating cell" (GIC) interchangeably with "glioma-stem cell" (GSC). However, whether stem-like cells are uniquely qualified in their ability to transplant disease, or whether other, more differentiated,

Significance

High-grade gliomas are typified by poor therapeutic response and rapid lethality. Using two mouse models of gliomagenesis, we identify and isolate two distinct stem- and progenitor-like tumor cell populations using a single marker, Id1. Id1^{high} glioma cells self-renew, giving rise to consistent proportions of differentiated lineages, while Id1^{low} cells have limited self-renewal capacity but retain proliferative potential. Although both populations transplant disease, Id1^{low} cells are more tumorigenic compared to Id1^{high} cells. Further, inhibiting the bHLH transcription factor Olig2 within Id1^{low} cells significantly prolongs the survival of tumor-bearing mice, while eliminating self-renewal of Id1^{high} cells has modest effects. These results have important implications for therapeutic strategies that seek to target stem- or progenitor- like cells within different subclasses of high-grade gliomas.

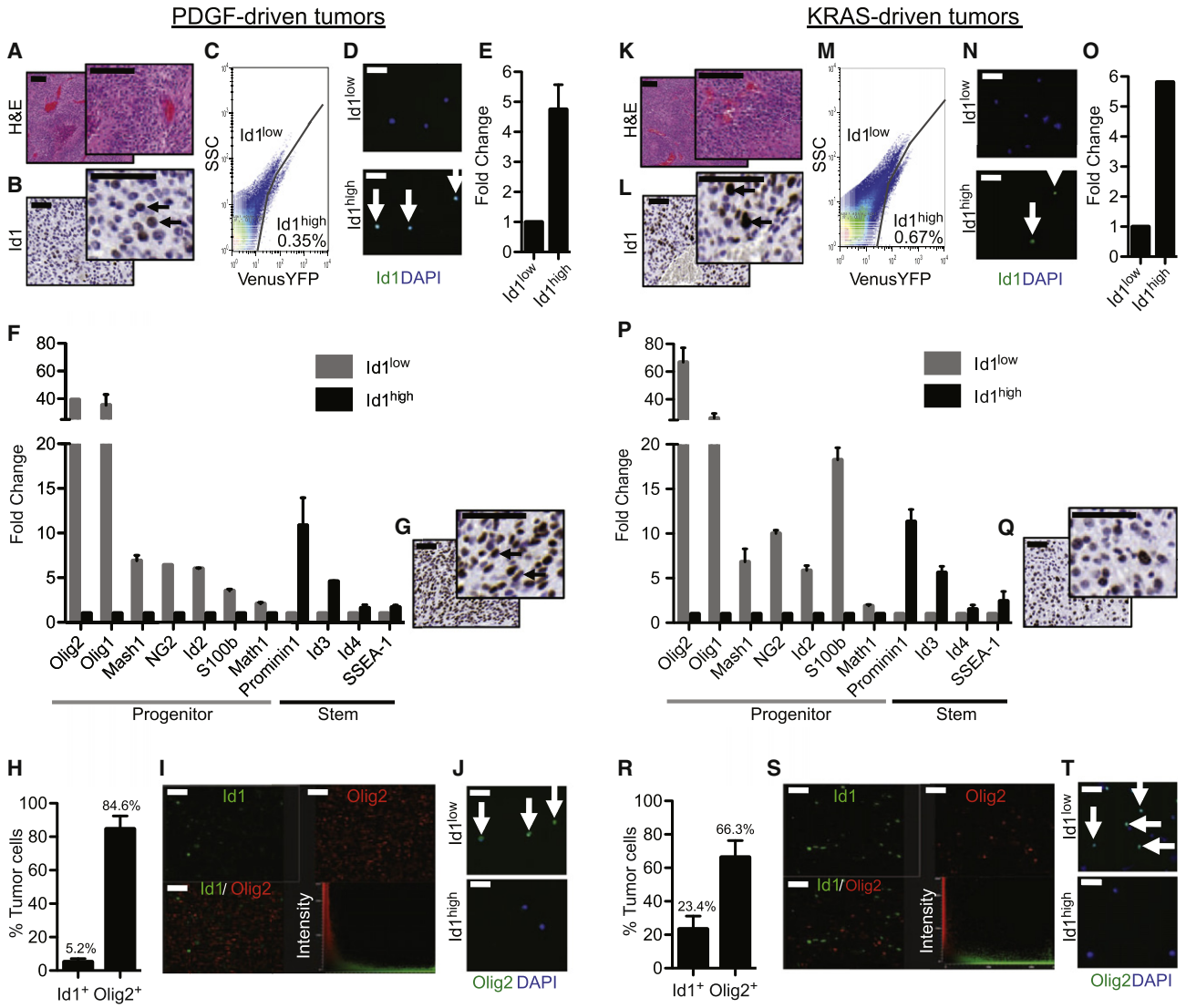

Figure 1. Tumors Can Be Separated into Id1^{high} and Id1^{low} Cell Populations

(A) Tumors were initiated with RCAS-PDGFB in Nestin-tva; Arf$^{-/-}$ mice (A–J). Staining with hematoxylin and eosin (H&E) shows high-grade features. Scale bars = 100 μm.

(B) Immunohistochemistry for Id1 reveals Id1+ cells within the tumor (arrows). Scale bars = 50 μm.

(C) FACS plot from Nestin-tva;Arf$^{-/-}$;Id1^{VenusYFP} tumors. Gray line indicates gate for VenusYFP signal.

(D) Id1 immunostaining on sorted Id1^{low} (top) and Id1^{high} (bottom) cells reveals Id1 expression restricted to the Id1^{high} cell population (arrows). Cells were counterstained with DAPI. Scale bars = 50 μm.

(E) Quantitative RT-PCR reveals enhanced Id1 expression in Id1^{high} compared to Id1^{low} cells.

(F) Quantitative RT-PCR for Olig2, Olig1, Mash1, NG2, Id2, S100b, Math1, Prominin1, Id3, Id4, SSEA-1 from Id1^{low} (gray bars) and Id1^{high} (black bars) sorted cells.

(G) Immunohistochemistry for Olig2 reveals a frequent expression pattern of Olig2+ cells (arrows). Scale bars = 50 μm.

(H) Graph shows percentage of Id1+ and Olig2+ tumor cells from PDGF-driven tumors.

(I) Immunostaining for Id1 (green), Olig2 (red) and spectral analysis showing intensity in red channel and green channels. Scale bars = 50 μm.

(J) Olig2 immunostaining on sorted Id1^{low} (top) and Id1^{high} (bottom) cells reveals Olig2 expression restricted to the Id1^{low} cell population (arrows). Cells were counterstained with DAPI. Scale bars = 50 μm.

(K) Tumors were initiated with RCAS-KRAS in Nestin-tva; Arf$^{-/-}$ mice (K-T). Staining with H&E shows high-grade features. Scale bars = 100 μm.

(L) Immunohistochemistry for Id1 reveals Id1+ cells within the tumor (arrows). Scale bars = 50 μm.

(M) FACS plot from Nestin-tva;Arf$^{-/-}$;Id1^{VenusYFP} tumors. Gray line indicates gate for VenusYFP signal.

(N) Id1 immunostaining on sorted Id1^{low} (top) and Id1^{high} (bottom) cells reveals Id1 expression restricted to the Id1^{high} cell population (arrows). Cells were counterstained with DAPI. Scale bars = 50 μm.

(O) Quantitative RT-PCR reveals enhanced Id1 expression in Id1^{high} compared to Id1^{low} cells.

(P) Quantitative RT-PCR for Olig2, Olig1, Mash1, NG2, Id2, S100b, Math1, Prominin1, Id3, Id4, SSEA-1 from Id1^{low} (gray bars) and Id1^{high} (black bars) sorted cells.

(Q) Immunohistochemistry for Olig2 reveals a frequent expression pattern of Olig2+ cells (arrows). Scale bars = 50 μm.

(R) Graph shows percentage of Id1+ and Olig2+ tumor cells from KRAS-driven tumors.

non-self-renewing lineages possess this capacity, remains controversial (Alcantara Llaguno et al., 2009; Chow et al., 2011; Lindberg et al., 2009; Prestegarden and Enger, 2010; Stiles and Rowitch, 2008). In other types of brain tumors, including medulloblastoma (Yang et al., 2008) and oligodendroglioma (Persson et al., 2010), cell lineages that express progenitor markers but are incapable of self-renewal in vitro have been shown to transplant disease. Further, oligodendrocyte precursor cells (OPCs) were recently identified as likely cells-of-origin in a p53/Nf1 mouse model of gliomagenesis, as lineage-analysis revealed this population to have the most dramatic growth expansion prior to malignancy (Liu et al., 2011). Adding to the complexity, it has been hypothesized that more differentiated cells may dedifferentiate and acquire a stem cell phenotype during the course of tumorigenesis (Kang et al., 2006). How frequently this occurs in vivo and whether the acquisition of self-renewal and "stemness" is a requisite for tumorigenic potential requires further investigation.

Critical to the analysis of high-grade gliomas is the identification of markers to definitively isolate and functionally characterize the distinct lineages. CD133 (Prominin-1) is the most common antigen used to identify glioma stem cells, but studies have shown that both $CD133^+$ and $CD133^-$ cells can self-renew and generate histologically distinct tumors (Beier et al., 2007; Chen et al., 2010; Clément et al., 2009; Wang et al., 2008), arguing against CD133 as a specific marker of glioma stem cells. Other studies have used the side population (SP) to define the stem-cell fraction, although this also identifies a heterogeneous population of both self-renewing and non self-renewing lineages (Broadley et al., 2011). The *ID (Inhibitor of DNA-binding)* genes are dominant negative regulators of basic helix-loop-helix transcription factors (Perk et al., 2005) with established roles in embryonic stem cell self-renewal (Romero-Lanman et al., 2011; Ying et al., 2003). Following development, Id1 continues to regulate self-renewal and differentiation in multiple somatic stem cell populations, including adult neural stem cells. High levels of Id1 identify type B adult neural stem cells within neurogenic niches, and Id1 and Id3 are required to maintain the self-renewal capacity of this cell population (Nam and Benezra, 2009). During lineage commitment, Id1 protein levels decrease as progenitor markers become more highly expressed (Nam and Benezra, 2009). While Id1 expression is low to absent in nonneurogenic regions of the normal adult brain, Id1 expression is upregulated in multiple subtypes of human and mouse gliomas (Anido et al., 2010; Vandeputte et al., 2002). Because high levels of Id1 identify self-renewing type B cells in the normal neurogenic niche, we hypothesized that high levels of Id1 could similarly identify glioma cells with a stem-cell phenotype.

Large-scale sequencing projects have identified alterations that frequently occur in human high-grade gliomas, including *PDGFRA* amplification (13%), alterations in RTK/RAS/PI(3)K signaling (88%) and *CDKN2A/Arf* homozygous deletion or mutation (49%) (Network, 2008). This has led to the generation of subclasses based upon specific genomic and proteomic signatures (Brennan et al., 2009; Huse et al., 2011; Network, 2008). Although studies differ with regard to subclass identity and nomenclature, broadly speaking, tumors with aberrant PDGFR signaling have been grouped in the Proneural subclass, and tumors with mutation and/or deletion of *NF1* have been grouped in the Mesenchymal subclass. The PDGFR/Proneural subclass has a well-established RCAS/tva-based mouse model, where adult *Nestin-tva;Arf*$^{-/-}$ mice are stereotaxically injected with RCAS-PDGFB into the SVZ, generating gliomas with near complete penetrance (Hambardzumyan et al., 2009, 2011). Tumors can also be initiated using constitutively active mutant KRAS, as KRAS has been shown to cooperate with tumor suppressor loss to generate gliomas (Uhrbom and Holland, 2001; Uhrbom et al., 2005). Tumors driven by either PDGF or KRAS show a histopathology that closely mimics human tumors, as well as high-grade features, including pseudopalisading necrosis and microvascular proliferation (Hambardzumyan et al., 2009, 2011; Uhrbom and Holland, 2001; Uhrbom et al., 2005).

Here, we test a central tenet of the cancer stem cell hypothesis, that self-renewal capacity is required for disease transplantation and is a key predictor of tumor growth potential, in PDGF- and KRAS-driven murine glioma models.

RESULTS

PDGF- and KRAS-Driven Tumors Can Be Separated into $Id1^{high}$ and $Id1^{low}$ Cell Populations

As shown in Figures 1A and 1B, tumors initiated with PDGF displayed high-grade features and upregulated Id1 expression, similar to what is observed in human high-grade gliomas (Figures S1A and S1B available online). In order to isolate and further characterize live tumor cells with high Id1 expression, we generated *Nestin-tva;Arf*$^{-/-}$*;Id1*^{VenusYFP} mice, where endogenous Id1 is fused to fluorescent VenusYFP and faithfully reports endogenous Id1 protein levels (Nam and Benezra, 2009). Following initiation with PDGF, tumors were dissociated and sorted based on VenusYFP expression into cell populations with high levels of VenusYFP (further referred to as $Id1^{high}$) and cell populations with undetectable levels of VenusYFP (further referred to as $Id1^{low}$) (Figure 1C). Post-sort analysis was used to confirm the absence of VenusYFP signal in the $Id1^{low}$ fraction (Figure S1C) and $Id1^{high}$ cells were, on average, 0.35% of the total sorted population, including stromal cells (Figure 1C). Immunostaining (Figure 1D) and RT-PCR (Figure 1E) confirmed Id1 expression in freshly sorted $Id1^{high}$ cells and low to undetectable levels of Id1 expression in freshly sorted $Id1^{low}$ cells. The stem-associated markers Prominin-1 and Id3 were more highly expressed in $Id1^{high}$ cells compared to $Id1^{low}$ cells (Figure 1F). In contrast, multiple progenitor-associated markers, including Olig2, Mash1, NG2, and Id2 were more highly expressed in $Id1^{low}$ cells compared to $Id1^{high}$ cells (Figure 1F).

Olig2 is known to regulate proliferation in neural progenitors (Ligon et al., 2007; Sun et al., 2011) and is expressed in multiple lineages, including type C cells in the normal neurogenic niche

(S) Immunostaining for Id1 (green), Olig2 (red) and spectral analysis showing intensity in red channel and green channels. Scale bars = 50 μm.
(T) Olig2 immunostaining on sorted $Id1^{low}$ (top) and $Id1^{high}$ (bottom) cells reveals Olig2 expression restricted to the $Id1^{low}$ cell population (arrows). Cells were counterstained with DAPI. Scale bars = 50 μm.
Error bars represent mean ± SD. See also Figure S1.

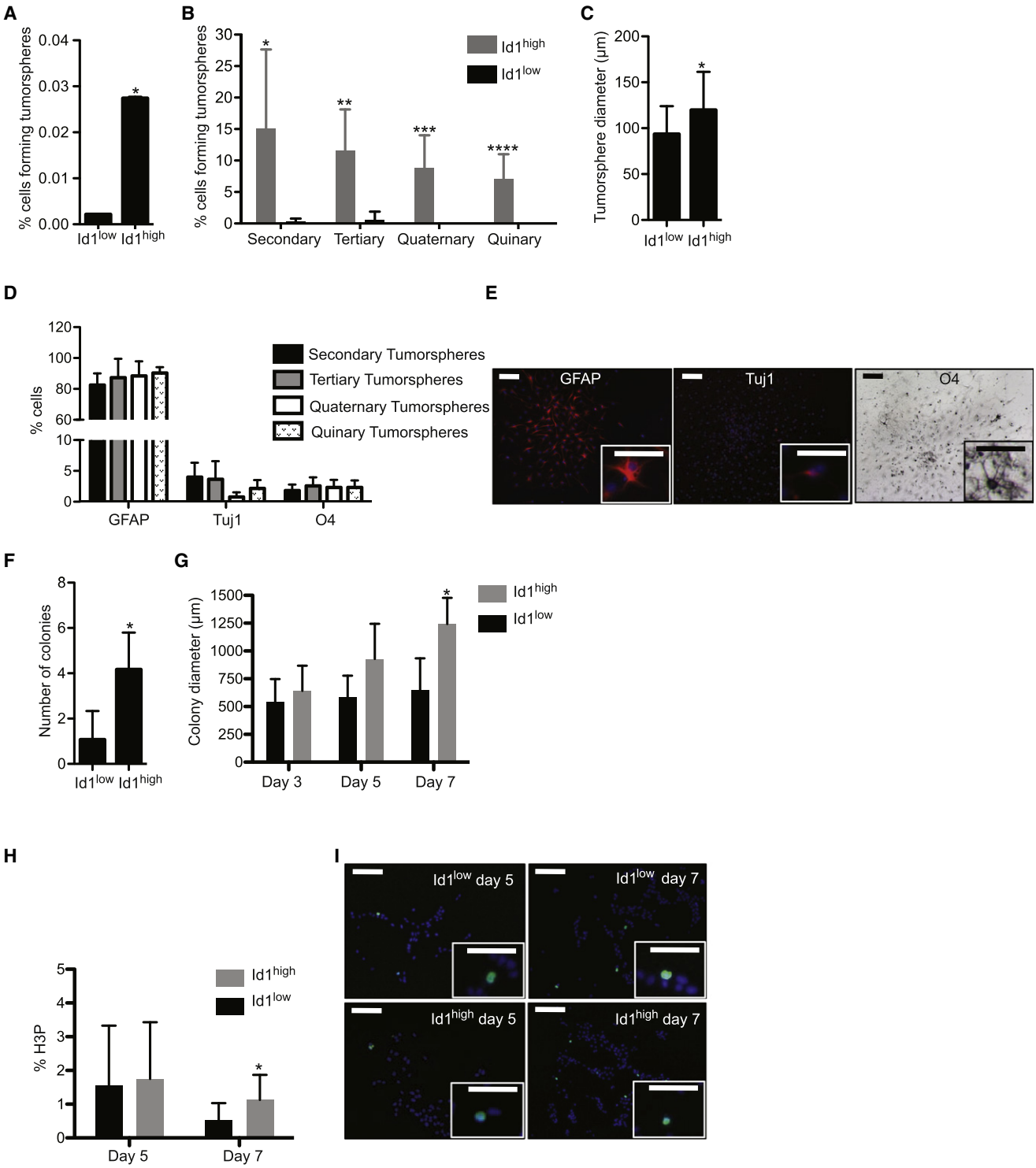

Figure 2. Id1^{high} Cells Are Characterized by High Self-Renewal Capacity, while Id1^{low} Cells Are Characterized By Limited Self-Renewal Capacity

(A) Percentage of sorted Id1^{high} and Id1^{low} cells forming primary tumorspheres from PDGF-driven tumors (10 cells/μl; *p = 2.37 × 10^{-7}).

(B) Percentage of sorted Id1^{high} (gray bars) and Id1^{low} (black bars) cells forming secondary, tertiary, quaternary and quinary tumorspheres from PDGF-driven tumors (1 cell/well; *p = 0.026, **p = 0.0084, ***p = 0.01, ****p = 0.007).

(C) Tumorsphere diameter was measured after 7 days in vitro for Id1^{low} (n = 60) and Id1^{high} (n = 128) tumorspheres (*p = 1.66 × 10^{-5}) from PDGF-driven tumors.

(D) Id1^{high} cells were used to generate secondary, tertiary, quaternary and quinary tumorspheres, which were then differentiated and the percentage of cells from individual tumorspheres that expressed GFAP, Tuj1, and O4 were quantified.

and mature oligodendrocytes (Menn et al., 2006). Olig2 is also expressed in all subtypes of malignant glioma (Ligon et al., 2004), leading us to more closely examine Olig2 expression in our model. Within PDGF-driven tumors, we observed high levels of Olig2 expression (Figure 1G), consistent with what is observed in human gliomas (Figures S1D and S1E) including those from the PDGFR subclass (Verhaak et al., 2010). By IHC, 5.2% of tumor cells had detectable levels of Id1 expression and 84.6% of cells had detectable levels of Olig2 expression (Figure 1H). Sorted Id1^{high} cells make up a subset of the total Id1-expressing population, as Id1 is expressed in varying levels in both tumor cells and stromal cells. Importantly, Olig2 and Id1 showed a largely mutually exclusive expression pattern (Figure 1I). Of Id1-expressing tumor cells, only 6.1% showed some level of Olig2 expression (Figure S1F). In the normal neurogenic niche, Id1 levels decrease and progenitor markers increase as cells transition from a type B cell to a type C cell phenotype (Nam and Benezra, 2009), and this population overlap within tumors may reflect a similar phenomenon. Importantly, we did not detect Olig2 protein expression in the sorted Id1^{high} population, and found significant Olig2 protein expression in the sorted Id1^{low} population (Figure 1J).

In order to test the generality of our results, we examined tumors driven by RCAS mutant KRAS using *Nestin-tva; Arf*$^{-/-}$*; Id1*^{VenusYFP} mice. As shown in Figures 1K and 1L, KRAS-driven tumors also displayed high-grade features and upregulated Id1 expression. By FACS, Id1^{high} cells represented, on average, 0.67% of the total sorted population including stromal cells (Figure 1M). Immunostaining (Figure 1N) and RT-PCR (Figure 1O) confirmed Id1 expression in freshly sorted Id1^{high} cells and low to undetectable levels of Id1 expression in freshly sorted Id1^{low} cells. Id1^{high} and Id1^{low} cells from KRAS-driven tumors showed a lineage-marker profile similar to what was observed from PDGF-driven tumors (Figure 1P). Compared to PDGF-driven tumors, KRAS-driven tumors had more Id1-expressing cells by IHC and fewer Olig2-expressing cells, with 23.4% of tumor cells expressing Id1 and 66.3% of tumor cells expressing Olig2 (Figures 1Q and 1R). Coimmunostaining for Id1 and Olig2 again revealed a largely mutually exclusive expression pattern (Figure 1S). Importantly, we did not detect Olig2 protein expression in the sorted Id1^{high} cells, and found significant Olig2 protein expression in the sorted Id1^{low} cells (Figure 1T). Thus, in both PDGF- and KRAS-driven tumors, sorted Id1^{high} cells were characterized by high levels of the neural stem cell marker Id1, and an absence of common progenitor-associated markers. While Id1^{low} cells represented heterogeneous tumor bulk, they were characterized by high levels of Olig2 and other progenitor-associated markers.

We further characterized the expression of Id1 and several lineage markers using human glioma tissue microarrays (TMAs). Here, we found that a subset of Id1-expressing cells also expressed the putative stem-cell marker CD133, although we observed both CD133^{+}/Id1^{-} and CD133^{-}/Id1^{+} cells (Figure S1G). While Id1 and Olig2 showed a largely exclusive expression pattern in the PDGF- and KRAS-driven murine models, we identified two distinct groups from the human TMAs: one group showed a largely exclusive expression pattern between Id1 and Olig2, while the other group showed a high-degree of overlap between the two proteins (Figures S1D and S1E). We speculate that differences may exist in the Id1/Olig2 lineage relationship, and expression of stem and progenitor cells generally, within distinct subtypes of high-grade gliomas.

Id1^{high} Tumor Cells Have Stem Cell Properties, while Id1^{low} Tumor Cells Resemble Progenitor Cells

We hypothesized that high levels of Id1 would identify tumor cells with a stem cell phenotype, similar to what is observed in type B cells of the normal neurogenic niche. To assess the self-renewal capacity of Id1^{high} and Id1^{low} glioma cells, we plated cells at clonal density in the presence of epidermal growth factor (EGF) and fibroblast growth factor (FGF) and characterized tumorsphere formation and colony formation in vitro. From PDGF-driven tumors, freshly sorted Id1^{high} cells showed a 12.8-fold enhancement in primary tumorsphere formation compared to Id1^{low} cells (Figure 2A; 10 cells/μl). Similar results were obtained when cells were plated to form tumorspheres prior to sorting to eliminate stroma and then dissociated, sorted into Id1^{high} and Id1^{low} populations and replated to form tumorspheres (Figure S2A; 10 cells/μl). Primary tumorspheres were dissociated and plated at clonal density (1 cell/well) over serial passages. From Id1^{high} primary tumorspheres, 15.06% of single cells formed secondary tumorspheres, of which 11.62% of single cells formed tertiary tumorspheres, 8.82% of single cells formed quaternary tumorspheres, and 7.10% of single cells formed quinary tumorspheres (Figure 2B). By contrast, from Id1^{low} primary tumorspheres, 0.33% of single cells formed secondary tumorspheres, of which 0.625% of single cells formed tertiary tumorspheres, with no generation of tumorspheres over additional passages (Figure 2B). Id1^{high} cells generated tumorspheres that were marginally larger than those generated from Id1^{low} cells (Figure 2C). Similar results were observed in KRAS-driven tumors, where Id1^{high} cells showed a 7.5-fold enhancement in primary tumorsphere formation compared to Id1^{low} cells (Figure S2B; 10 cells/μl). From Id1^{high} primary tumorspheres, 7.67% of cells formed secondary tumorspheres, 1.85% of cells formed tertiary tumorspheres, and 0.267% of cells formed quaternary tumorspheres (plated 0.5 cells/μl; Figure S2C). By contrast, we were unable to generate secondary tumorspheres

(E) Representative images of tumorspheres generated from Id1^{high} cells that were differentiated and stained for GFAP, Tuj1, and O4. Scale bars = 100 μm for main images, 50 μm for insets. Cells were counterstained with DAPI in fluorescent images.
(F) Number of adherent colonies formed after 7 days in vitro from Id1^{low} cells (n = 14) compared to Id1^{high} cells (n = 24) (0.5 cells/μl; *p = 5.29 × 10^{-7}).
(G) Diameter of adherent colonies measured after 3 days (p = 0.38; n = 17), 5 days (p = 0.04; n = 27) and 7 days (*p = 6.39 × 10^{-5}; n = 14) from Id1^{low} cells (black bars) compared to Id1^{high} cells (gray bars).
(H) Percentage of phosphohistone H3 expressing cells within adherent colonies from Id1^{low} cells (black bars) compared to Id1^{high} cells (gray bars) after 5 days (p = 0.75; n = 16) or 7 days (*p = 0.014; n = 35).
(I) Representative images of Id1^{low} and Id1^{high} adherent colonies after 5 or 7 days stained for H3P (green) and counterstained with DAPI. Scale bars = 100 μm for main images, 50 μm for insets.
Error bars represent mean ± SD. See also Figure S2.

from the Id1^{low} primary tumorspheres at this plating density (Figure S2C).

Id1^{low} secondary tumorspheres, as well as Id1^{high} secondary, tertiary, quaternary, and quinary tumorspheres from the PDGF-driven model were plated under conditions to favor differentiation, and the resultant progeny were quantified. While undifferentiated tumorspheres showed low to absent expression of GFAP, O4, and Tuj1 (Figures S2D and S2E), individual Id1^{high} secondary tumorspheres primarily generated GFAP-expressing astrocytes upon differentiation, with less frequent but consistent generation of O4-expressing oligodendrocytes and Tuj1-expressing neurons (Figures 2D and 2E; Figure S2F). Essentially all individual Id1^{high} tumorspheres showed similar percentages of cells expressing these markers. We also observed similar proportions of GFAP-, O4-, and Tuj1-expressing cells from Id1^{high} tumorspheres at tertiary, quaternary, and quinary passages (Figure 2D; Figure S2F), consistent with these populations undergoing self-renewal events, rather than physical events such as in vitro fusion. The fact that the Id1^{high} population primarily differentiated into GFAP-expressing cells is also consistent with studies showing a role for Id1 in restraining neural differentiation (Ying et al., 2003). Id1^{low} secondary tumorspheres, by contrast, showed a high degree of variability with regards to their differentiation potential: 37.5% primarily generated GFAP-expressing cells, 43.75% primarily generated Tuj1-expressing cells, and 18.75% generated roughly equal numbers of GFAP- and Tuj1-expressing cells (n = 16; Figure S2G). The generation of O4-expressing cells was sporadic, found within approximately 18% of differentiated Id1^{low} secondary tumorspheres (Figure S2G). Thus, Id1^{high} glioma cells displayed a classic stem-cell phenotype in vitro, while Id1^{low} glioma cells, depleted of stromal cells, were found to possess limited self-renewal capacity.

Id1^{low} and Id1^{high} cells derived from PDGF-driven tumors were also plated at clonal density (0.5 cells/μl) as adherent monolayers using the same mitogenic conditions as in the nonadherent tumorsphere assays. Id1^{high} cells generated colonies more frequently than Id1^{low} cells (Figure 2F), and generated colonies that were marginally larger than those generated from Id1^{low} cells (Figure 2G), paralleling our tumorsphere data (Figures 2A–2C). We did not observe significant differences in expression of cleaved caspase-3 between colonies generated from Id1^{low} and Id1^{high} cells (data not shown), nor did we observe differences in H3P expression after 5 days in vitro (Figures 2H and 2I). Id1^{high} colonies did show approximately 2-fold greater H3P expression at 7 days in vitro suggesting a modest proliferative advantage (Figures 2H and 2I). Nonetheless, both Id1^{low} and Id1^{high} cells were capable of proliferation, suggesting that the dramatic differences in tumorsphere formation between the Id1^{low} and Id1^{high} cell populations were due largely to differences in self-renewal capacity, as opposed to an inability of the Id1^{low} cells to proliferate under the conditions used in our assays.

Id1^{low} Cells More Efficiently Transplant Disease than Id1^{high} Cells

We next probed the capacity of Id1^{low} and Id1^{high} glioma cells to transplant disease by injecting 1.0 × 10^3 freshly sorted cells into the cortex of adult Nude/NCr host mice. From PDGF-driven tumors, both Id1^{low} and Id1^{high} cells were capable of generating high-grade gliomas (Figures 3A and 3B). However, Id1^{low} cells generated tumors more quickly and with higher penetrance: mice injected with 1.0 × 10^3 Id1^{low} cells had a median survival of 35.5 days compared to mice injected with 1.0 × 10^3 Id1^{high} cells, which had a median survival of 62 days (Figure 3A). Tumors were generated in 73.7% of mice injected with 1.0 × 10^3 Id1^{low} cells compared to 46.7% of mice injected with 1.0 × 10^3 Id1^{high} cells (Figure 3A). We were unable to generate tumors with 1.0 × 10^3 cells from either Id1^{low} or Id1^{high} cells when they were plated in vitro prior to transplantation (data not shown). Plating cells in vitro also led to changes in Id1 and Olig2 expression (Figures S3A–S3C), and we therefore injected freshly sorted cells in all experiments, allowing us to avoid in vitro selection bias and analyze the lineages in a minimally perturbed state. We also performed the same experiments using 1.0 × 10^3 Id1^{high} or Id1^{low} cells isolated from KRAS-driven tumors. Here, 52.6% of mice injected with 1.0 × 10^3 Id1^{low} cells developed high-grade tumors, with a median survival of 37 days (Figure 3C), while 1 of 19 mice (5.3%) injected with 1.0 × 10^3 Id1^{high} cells developed a low-grade tumor with a survival of 119 days (Figure 3C). Therefore, in both PDGF- and KRAS-driven tumors, Id1^{low} cells generated tumors more quickly and with higher penetrance than Id1^{high} cells.

Tumors initiated with either Id1^{low} or Id1^{high} cells expressed Nestin, GFAP, and Tuj1 (Figures S3D and S3E), although the majority of tumor cells expressed Olig2 (Figures 3B and 3D). The fact that Id1^{high} cells did not express Olig2 upon isolation indicates that Id1-expressing tumor cells were generating Olig2-expressing tumor cells in vivo. This is consistent with studies in the normal SVZ, which show that type B cells can generate oligodendrocyte lineages (Jackson et al., 2006; Menn et al., 2006), and with the observation that Id1^{high} B-type cells give rise to Id1^{low} (Mash1$^+$, Olig2$^+$) progenitor cells (Nam and Benezra, 2009). Surprisingly, both Id1^{low} and Id1^{high} cells generated tumors with Id1 expression (Figures 3B and 3D).

To determine the source of Id1 expression in tumors initiated with Id1^{low} cells, we injected 1.0 × 10^3 Id1^{low} cells from the PDGF-driven model into the cortex of *ubc-GFP;NOD-SCID* mice, which express GFP in all cells (Figure 4A). Immunostaining for Id1 revealed that Id1 expression was restricted to GFP expressing cells (Figure 4B). We did not observe Id1-expressing/GFP-nonexpressing cells (Figure 4C), indicating that the Id1 expressing cells were in fact host-derived. In contrast to Id1, immunostaining for Olig2 did not colocalize with GFP, indicating that the Olig2 expressing cells were coming from the initiating cell population (Figures 4D and 4E). We also observed recruitment using cells isolated from the KRAS-driven model (Figure S4A). These data are consistent with studies in other model systems showing that cells recruited from the normal brain parenchyma can contribute to glioma heterogeneity (Assanah et al., 2006). To determine whether Id1 expression in the recruited population was important for tumor growth, we injected 1.0 × 10^3 Id1^{low} cells from PDGF-driven tumors into the cortex of Id1$^{-/-}$ mice. These mice also developed tumors (Figure S4B), indicating that Id1 expression in the recruited cells was not essential for tumorigenic potential. Further, both Id1^{low} and Id1^{high} cells led to recruitment of similar numbers of cells (Figure S4C), suggesting that the differences in tumor initiation between Id1^{low} and Id1^{high} cells were not due to their relative capacity for recruitment. Most importantly, Id1^{low} cells were

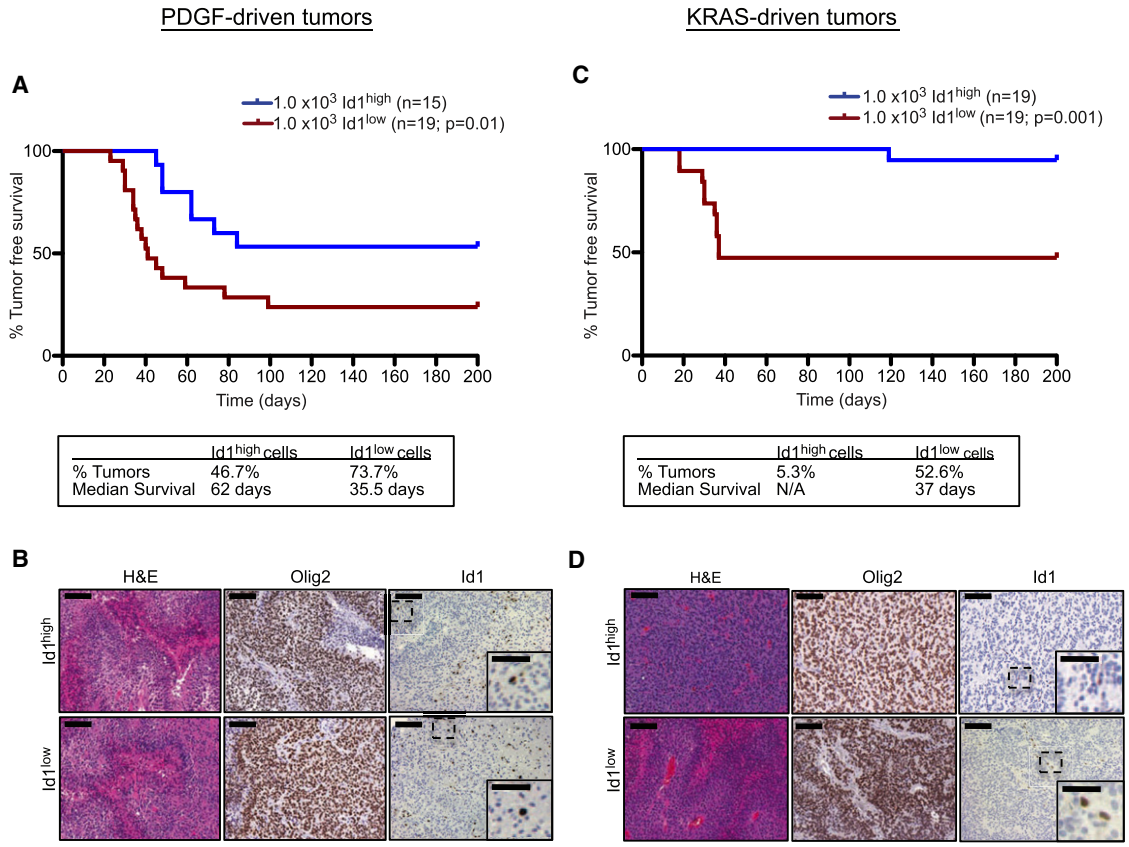

Figure 3. Id1^{low} Cells Transplant Disease More Efficiently than Id1^{high} Cells

(A) Kaplan-Meier analysis comparing mice injected with 1.0 × 10^3 Id1^{low} cells (n = 19; red line) or 1.0 × 10^3 Id1^{high} cells (n = 15; blue line) from PDGF-driven tumors. Chart shows percentage of mice that developed tumors and median survival.

(B) Representative images of H&E, Olig2 and Id1 immunohistochemistry for tumors generated with either Id1^{low} (bottom) or Id1^{high} (top) cells from PDGF-driven tumors. Scale bars = 100 μm for main images, 50 μm for insets.

(C) Kaplan-Meier analysis comparing mice injected with 1.0 × 10^3 Id1^{low} cells (n = 19; red line) or 1.0 × 10^3 Id1^{high} cells (n = 19; blue line) from KRAS-driven tumors. Chart shows percentage of mice that developed tumors and median survival.

(D) Representative images of H&E, Olig2 and Id1 immunohistochemistry for tumors generated with Id1^{low} (bottom) or Id1^{high} (top) cells from KRAS-driven tumors. Scale bars = 100 μm for main images, 50 μm for insets. See also Figure S3.

not reverting to an Id1-expressing state during the course of tumorigenesis and therefore this type of conversion could not explain the tumorigenic potential of the Id1^{low} cell population.

Inhibiting the Self-Renewal Capacity of Id1^{high} Cells Has Modest Effects on Tumor Growth

To determine how a reduction in self-renewal capacity would impact tumor growth, we generated *Nestin-tva;Arf*$^{-/-}$ mice with the following genotypes: *Id1*$^{+/+}$;*Id3*$^{+/+}$, *Id1*$^{-/-}$;*Id3*$^{+/+}$, and *Id1*$^{-/-}$;*Id3*$^{+/-}$. As shown in Figure 5, loss of Id1 led to dramatic reductions in tumor cell self-renewal capacity. *Id1*$^{-/-}$;*Id3*$^{+/+}$ and *Id1*$^{-/-}$;*Id3*$^{+/-}$ mice had a 5- to 10-fold reduction in primary tumorsphere formation compared to *Id1*$^{+/+}$;*Id3*$^{+/+}$ mice (Figure 5A; 10 cells/μl). From *Id1*$^{+/+}$;*Id3*$^{+/+}$ mice, 19.8% of cells formed secondary tumorspheres, compared to 0.067% of cells from *Id1*$^{-/-}$;*Id3*$^{+/+}$ mice and 0.21% of cells from *Id1*$^{-/-}$;*Id3*$^{+/-}$ mice (Figure 5B; 1 cell/well). *Id1*$^{+/+}$ *Id3*$^{+/+}$ tumorspheres primarily differentiated into GFAP-expressing cells, with less frequent but consistent generation of O4- and Tuj1-expressing cells (Figures 5C and 5D). We observed similar proportions of GFAP-, O4-, and Tuj1-expressing cells from secondary and tertiary tumorspheres (Figures 5C and 5D), and a pattern of differentiation closely paralleling that of Id1^{high} tumorspheres (Figures 2D and 2E).

Cells from *Id1*$^{+/+}$;*Id3*$^{+/+}$ and *Id1*$^{-/-}$;*Id3*$^{+/-}$ mice were also plated as adherent monolayers at clonal density (0.5 cells/μl). Cells plated from *Id1*$^{-/-}$;*Id3*$^{+/-}$ tumors generated fewer adherent colonies than cells plated from *Id1*$^{+/+}$;*Id3*$^{+/+}$ tumors (Figure 5E) and while the average H3P expression in *Id1*$^{-/-}$;*Id3*$^{+/-}$ colonies was slightly lower compared to *Id1*$^{+/+}$;*Id3*$^{+/+}$ colonies at 7 days in vitro, these differences were not statistically significant (Figure 5F). Thus, both cell populations were capable of proliferation in vitro.

The reduction in self-renewal capacity with Id loss mirrors the effects of Id loss in normal adult neural stem cells (Nam and Benezra, 2009). However, we observed only modest effects of Id loss on tumor-free survival (Figure 5G). Similar effects on tumor-free survival were observed following conditional loss of Id1 in *Nestin-tva;Arf*$^{-/-}$ mice: after coinjection of RCAS-PDGFB and RCAS-Cre, *Id1*$^{+/+}$;*Id3*$^{+/+}$ mice had a median survival of 28 days and *Id1*$^{flox/flox}$;*Id3*$^{+/+}$ mice had a median survival of

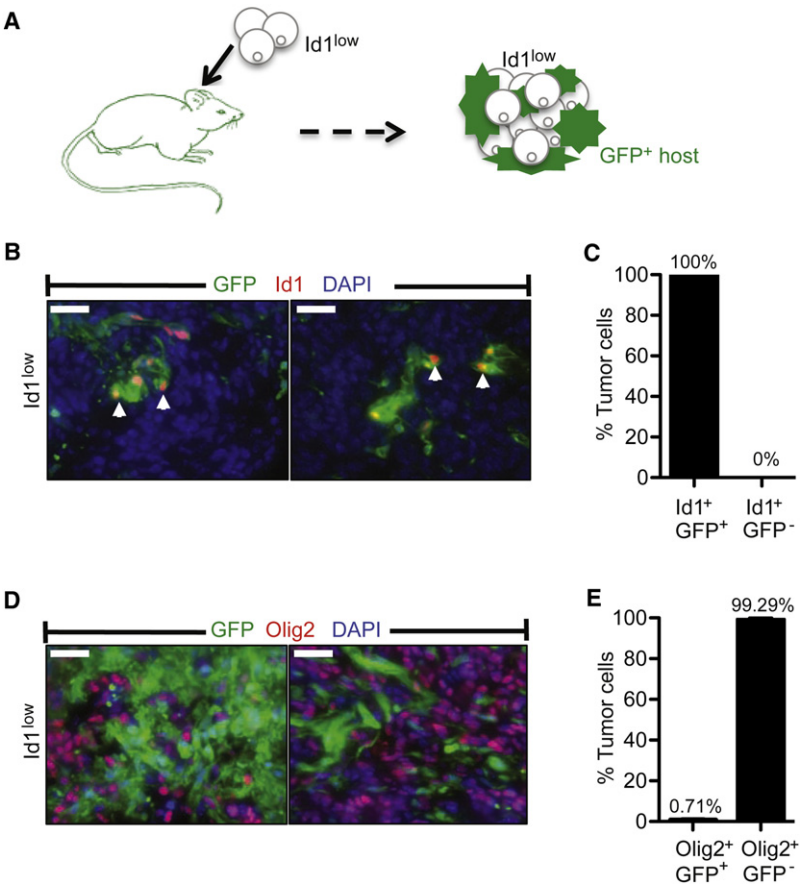

Figure 4. Id1^{low} Cells Do Not Revert to an Id1-Expressing State In Vivo

(A) Schematic illustrating the injection of Id1^{low} (nonfluorescent) cells into ubc-GFP;NOD-SCID host mice.

(B) Two representative images showing coimmunostaining for GFP and Id1. Note the presence of Id1^{+}/GFP^{+} cells (arrowheads). Tissue was counterstained with DAPI. Scale bars = 50 μm.

(C) Percentage of tumor cells that were Id1+/GFP+ compared to Id1^{+}/GFP^{-} (n = 4 mice, >900 Id1^{+} cells).

(D) Two representative images showing coimmunostaining for GFP and Olig2. Tissue was counterstained with DAPI. Scale bars = 50 μm.

(E) Percentage of tumor cells that were Olig2+/GFP+ compared to Olig2^{+}/GFP^{-} (n = 4 mice, >900 Olig2+ cells). Error bars represent mean ± SD. See also Figure S4.

34 days (Figure S5). In normal adult neural stem cells, Id1 and Id3 show redundancy of function at the level of self-renewal (Nam and Benezra, 2009). We therefore probed the effects of combined Id1 and Id3 loss to eliminated potential compensation between Id proteins. *Nestin-tva;Arf*$^{-/-}$ *Id1*$^{flox/flox}$*; Id3*$^{-/-}$ mice injected with RCAS-PDGFB and RCAS-Cre had a median survival no different from control animals (28 days; Figure S5).

Id1^{low} tumor cells showed significant growth potential in vivo (Figure 3), and we hypothesized that inhibiting the growth of the Id1^{low} population might confer a more significant survival benefit. As Olig2 is a known mediator of glioma growth in cell line models, we inserted an H1 promoter driving Olig2 shRNA downstream of PDGFB in the RCAS vector (Figures S6A and S6B). Using RCAS-PDGFB;Olig2-shRNA or RCAS-PDGFB; shRNA-Control constructs to initiate tumors, we found that Olig2 knockdown significantly increased tumor-free survival (Figure 6A). Olig2 knockdown was confirmed in tumors that were removed at early time points from presymptomatic mice (Figure 6B). Tumors that grew out from the Olig2 shRNA condition expressed Olig2 (Figure 6C), consistent with previous reports showing a significant role for Olig2 in human and mouse gliomas (Ligon et al., 2007; Mehta et al., 2011). To further explore the relationship between Id1 and Olig2, primary mouse glioma cells were transiently transfected with Id1 siRNA, Olig2 siRNA or Control siRNA. Knockdown of Id1 did not affect Olig2 expression levels, and knockdown of Olig2 did not affect Id1 expression levels (Figure S6C), suggesting that neither gene directly represses the other in our model system.

To begin to explore the role of Id1 and stem-like cells in human high-grade gliomas, we analyzed survival data from The Cancer Genome Atlas for each of the identified subtypes (Verhaak et al., 2010) based on Id1 expression for patients diagnosed with primary GBMs. Patients were subdivided into those with high Id1 expression (top 50%) and those with low Id1 expression (bottom 50%), compared to the unfiltered data set (Figures 7A–7D). Within the Proneural subclass, patients with high Id1 expression had a median survival of 22.015 months, compared to patients with low Id1 expression, which had a median survival of 6.015 months (Figure 7D). No significant differences in survival were observed for the Classical, Mesenchymal and Neural subtypes when subdivided by Id1 expression (Figures 7A–7C). As the PDGF-driven murine model most closely mimics the Proneural subclass, this human data, while correlative, is consistent with our finding that low Id1 expression identifies a more aggressive tumor cell population in this subtype.

DISCUSSION

Self-renewal is the defining characteristic of both normal and cancer stem cells. It has been postulated that glioma cells with stem cell properties preferentially transplant disease and contribute disproportionately to tumor growth compared to other, more differentiated lineages. Our results argue against this stringent interpretation of the cancer stem cell hypothesis. Using a marker of normal adult neural stem cells, we identified glioma cells with high self-renewal capacity and compared their tumorigenic potential to that of low self-renewing lineages. We found that in PDGF- and KRAS- driven mouse glioma models, both cell populations were capable of transplanting disease, and cells with low self-renewal capacity were actually more tumorigenic. Thus, GICs cannot be exclusively identified by self-renewal or "stemness."

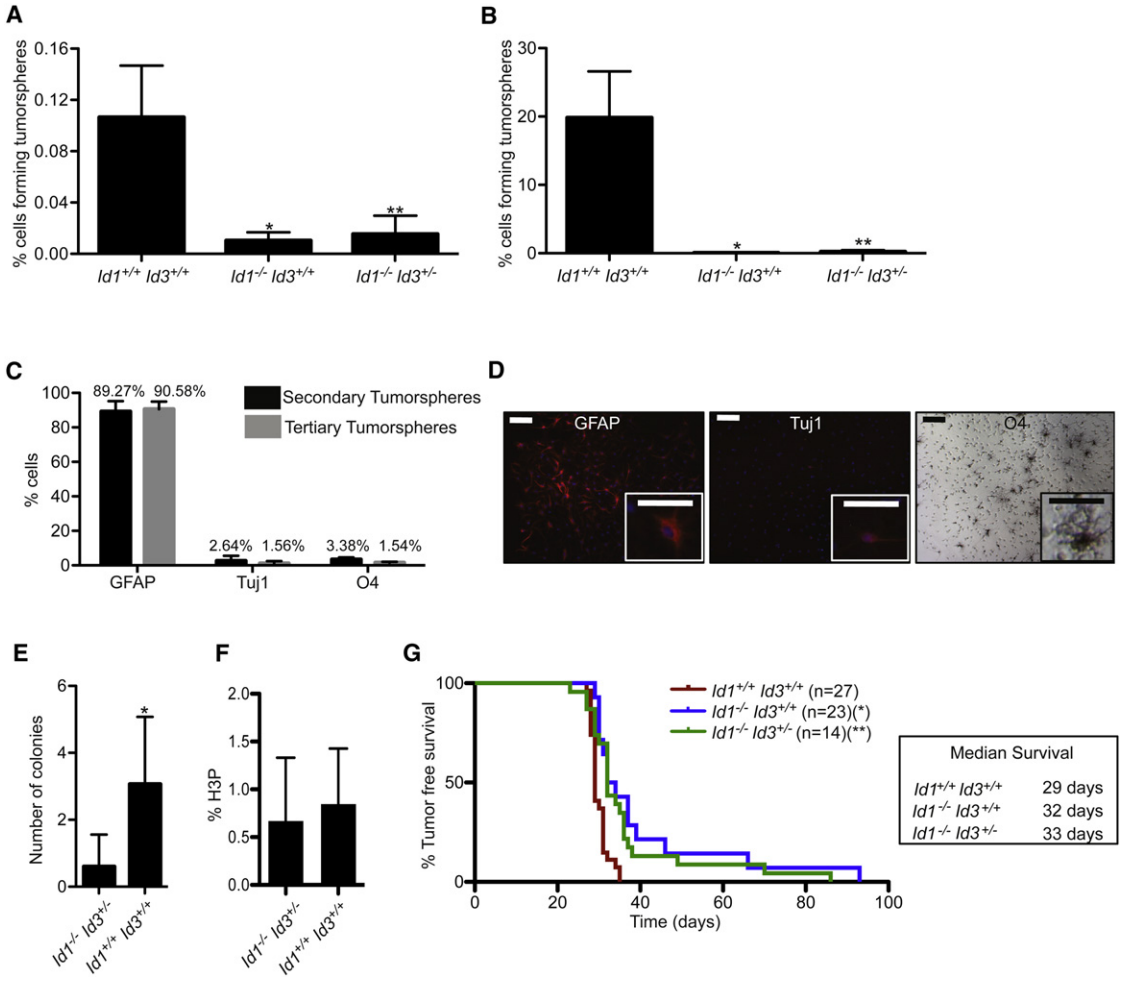

Figure 5. Id1-Loss Significantly Impacts Tumor Cell Self-Renewal but Has Only Modest Effects on Tumor-Free Survival

(A) Percentage of cells forming primary tumorspheres from PDGF-driven tumors (10 cells/μl) using *Nestin-tva;Arf*$^{-/-}$ *;Id1*$^{-/-}$*;Id3*$^{+/+}$ mice (n = 4; *p = 0.0017), *Nestin-tva;Arf*$^{-/-}$ *;Id1*$^{-/-}$*;Id3*$^{+/-}$ mice (n = 5; **p = 0.001) and *Nestin-tva;Arf*$^{-/-}$ *;Id1*$^{+/+}$*;Id3*$^{+/+}$ mice (n = 6).

(B) Percentage of cells forming secondary tumorspheres from PDGF-driven tumors (0.5 cells/μl) using *Nestin-tva;Arf*$^{-/-}$ *;Id1*$^{-/-}$*;Id3*$^{+/+}$ mice (n = 3; *p = 0.0044), *Nestin-tva;Arf*$^{-/-}$ *; Id1*$^{-/-}$*;Id3*$^{+/-}$ mice (n = 5; **p = 0.0003) and *Nestin-tva;Arf*$^{-/-}$ *;Id1*$^{+/+}$*;Id3*$^{+/+}$ mice (n = 4).

(C) Percentage of cells from secondary or tertiary tumorspheres that differentiated into GFAP, Tuj1, and O4 expressing cells. Tumorspheres were generated from *Nestin-tva;Arf*$^{-/-}$ *;Id1*$^{+/+}$*;Id3*$^{+/+}$ mice.

(D) Representative images of tumorspheres generated from *Id1*$^{+/+}$*;Id3*$^{+/+}$ cells, differentiated, and stained for GFAP, Tuj1, and O4. Scale bars = 100 μm for main images, 50 μm for insets. Cells were counterstained with DAPI in fluorescent images.

(E) Number of adherent colonies formed after 7 days in vitro from *Id1*$^{+/+}$*;Id3*$^{+/+}$ cells compared to *Id1*$^{-/-}$*;Id3*$^{+/-}$ cells (0.5 cells/μl; *p = 4.98 × 10^{-8}).

(F) Percentage of phosphohistone H3 (H3P) expressing cells within adherent colonies from *Id1*$^{+/+}$ *Id3*$^{+/+}$ compared to *Id1*$^{-/-}$ *Id3*$^{+/-}$ mice after 7 days in vitro (p = 0.44).

(G) Kaplan-Meier analysis comparing *Nestin-tva;Arf*$^{-/-}$ *;Id1*$^{+/+}$*;Id3*$^{+/+}$ mice (n = 27) with *Nestin-tva;Arf*$^{-/-}$ *;Id1*$^{-/-}$*;Id3*$^{+/+}$ mice (n = 23; *p = 0.0003) and *Nestin-tva;Arf*$^{-/-}$ *;Id1*$^{-/-}$*;Id3*$^{+/-}$ mice (n = 14; **p = 0.0003). Tumors were initiated with PDGF. Chart shows median survival.

Error bars represent mean ± SD. See also Figure S5.

Using Id1 to Identify Stem-Like Glioma Cells

Unlike the clearly defined, marker restricted lineages that exist in the hematopoietic system, stem and progenitor cells in the normal neurogenic niche and in brain tumors remain relatively ill-defined, complicating efforts to assign functional roles to these cell populations. While many studies use CD133 (Prominin 1) to identify glioma stem cells, CD133^{-} cells can also self-renew, suggesting that CD133 expression alone does not definitively identify glioma stem cells. High Id1 expression identifies type B cells in the normal neurogenic niche, and Id1 levels decrease gradually during lineage commitment (Nam and Benezra, 2009). Reversion from an Id1^{low} to an Id1^{high} state is never observed, and we have therefore taken advantage of the Id1-VenusYFP knockin strain to isolate cells with high levels of Id1 within murine gliomas, and specifically identify the stem-like fraction.

We define self-renewal capacity by the ability of cells to form multipotent tumorspheres of consistent progeny over serial passages when plated at clonal density in serum-free, adherent-free conditions. While definitive assays for self-renewal remain

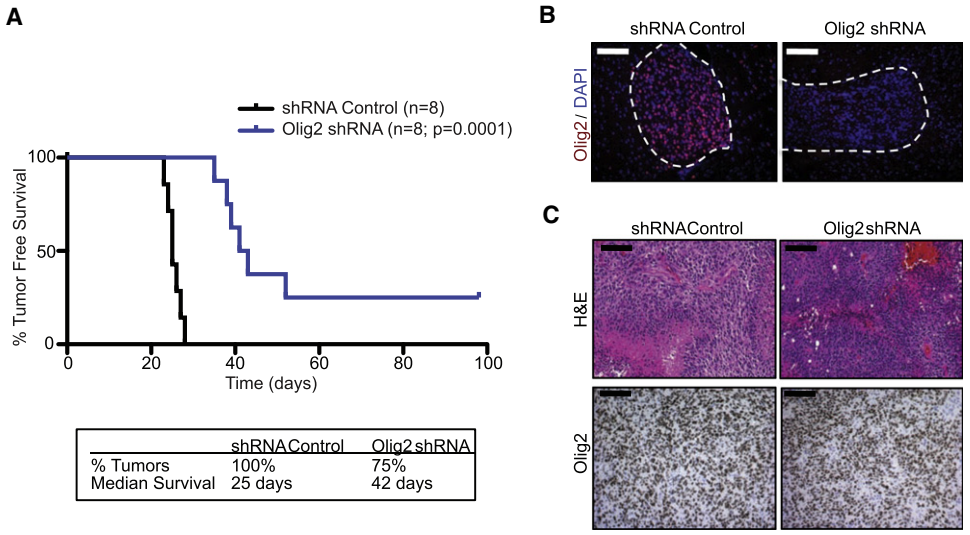

Figure 6. Targeting Id1^{low} Progenitor-Like Cells via Knockdown of Olig2 Shows a Significant Survival Benefit

(A) Kaplan-Meier analysis comparing *Nestin-tva;Arf*$^{-/-}$ mice injected with RCAS-PDGFB-shRNA Control or RCAS-PDGFB-Olig2 shRNA. Chart shows percentage of mice that developed tumors and median survival.

(B) Olig2 immunostaining from tumors (dotted line) generated with shRNA Control or Olig2 shRNA. Tumors were analyzed from pre-symptomatic mice. Tissue was counterstained with DAPI. Scale bars = 100 μm.

(C) H&E and Olig2 immunohistochemistry from tumors generated with shRNA Control or Olig2 shRNA. Tumors were analyzed when mice became symptomatic. Scale bars = 100 μm. See also Figure S6.

a matter of controversy, the ability of a glioma cell to form a tumorsphere under defined conditions has historically been used as an in vitro measure of self-renewal (Galli et al., 2004; Pastrana et al., 2011; Singh et al., 2003, 2004). A recent review by Pastrana et al. (2011) highlights a number of important considerations for the design and interpretation of sphere-formation assays. Importantly, we sorted fluorescent cells directly from transgenic mice, eliminating issues related to antibody labeling and antigen presentation. We also plated cells in identical mitogenic conditions and used clonal densities to reduce the likelihood of aggregations. Further, we confirmed the multipotency and proliferation potential of our cell populations. Under these experimental conditions, Id1^{high} glioma cells were characterized by high self-renewal capacity, giving rise to tumorspheres with similar proportions of differentiated progeny over multiple passages, and thus maintaining multipotency. Id1^{high} cells also gave rise to heterogeneous tumors in vivo, fulfilling the criteria of glioma stem cells. By contrast, Id1^{low} glioma cells were characterized by low self-renewal capacity, generating tumorspheres with variable proportions of differentiated progeny. Undifferentiated Id1^{low} cells also expressed progenitor markers (including high levels of Olig2), and had the ability to generate heterogeneous tumors in vivo, making them more characteristic of multipotent progenitors. It has been hypothesized that, within tumors, Olig2 may represent a transition from a type B cell to a type C cell, although Olig2 is also expressed in more differentiated lineages (Ligon et al., 2007). Taken together, our data suggest that Id1^{high} glioma cells resemble type B cells, at or near the top of the lineage hierarchy, while Id1^{low} cells more closely resemble type C cells.

Tumor Cell Self-Renewal Does Not Predict Tumor Growth Potential

Our data show that Id1^{low} glioma cells resembling type C cells have greater tumorigenic potential than Id1^{high} glioma cells reminiscent of type B cells in PDGF- and KRAS-driven tumors (Figure 8). Although it is important to note that both populations were capable of transplanting disease, we were surprised to find that Id1^{low} cells generated tumors more quickly and with higher penetrance, indicating that self-renewal did not cosegregate with tumorigenic potential. Thus, the ability of a glioma cell to proliferate even while changing state (as seen in the Id1^{low} population) appears in this model system to be compatible with the ability to transplant disease efficiently.

Id1^{high} cells generated tumors with high levels of Olig2 expression, which is consistent with acquisition of Olig2 in the Id1^{high} population being a critical factor in its tumorigenic potential, and previous studies have indeed shown an essential role for Olig2 in gliomagenesis (Ligon et al., 2007). While Id1^{high} cells were capable of generating tumors with Olig2 expression, Id1^{low} cells never reverted to an Id1-expressing state. Therefore, the lineage hierarchy of the normal neurogenic niche, which proceeds unidirectionally from stem cell to progenitor cell, was also maintained in our murine glioma models. We found no evidence for interconversion from an Id1^{low} progenitor state to an Id1^{high} stem-like state, although such dedifferentiation has been reported in in vitro systems (Kondo and Raff, 2000) and may occur under other oncogenic conditions. Thus, Id1^{low} cells need not dedifferentiate and acquire Id1 expression in order to transplant disease. Our results also suggest that Id1^{high} cells present in PDGF-driven gliomas likely arise from stem cell pools,

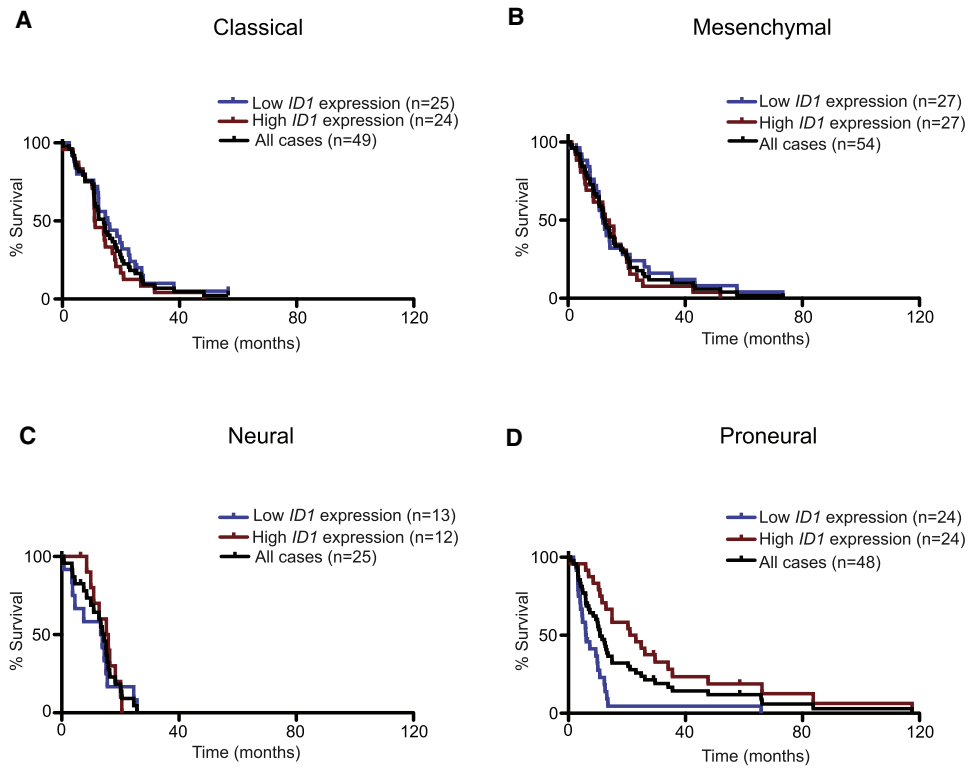

Figure 7. *ID1* Expression Levels Correlate with Survival of Human Patients within the Proneural Subclass of High-Grade Gliomas

Kaplan Meier analysis based on *ID1* expression using data from each of the four TCGA identified subtypes of primary GBM: (A) Classical ($p = 0.20$), (B) Mesenchymal ($p = 0.43$), (C) Neural ($p = 0.65$), and (D) Proneural. For the proneural subtype, the medium survival of patients with low and high Id1 expressing tumors are 6.015 months and 22.015 months, respectively ($p < 0.0001$).

rather than from expanding progenitor pools that revert to an $Id1^{high}$ state.

The Id1-expressing cells observed in tumors generated from $Id1^{low}$ cells were derived exclusively from the host, and Fomchenko et al. (2011) recently found significant roles for recruited cells in PDGF-driven murine gliomas. These cells were shown to aid in disease transplantation and had the capacity to become independent of the initiating oncogene (Fomchenko et al., 2011). We found that Id1 expression in the recruited population was not required for tumor growth, which was largely unaffected when $Id1^{low}$ cells were transplanted into an $Id1^{-/-}$ background. Our Id1-knockout studies further support the idea that Id1 expression and self-renewal capacity is not essential for tumor growth. If tumors were dependent upon self-renewal for their growth potential, we would expect that knockout of Id1, which significantly impacted tumorsphere formation, would have a greater impact on overall survival than observed. Our Olig2-knockdown studies lend further support to the notion that progenitor cell lineages may make greater contributions to tumor growth in PDGF-driven gliomas.

ID Genes in High-Grade Gliomas

We have isolated glioma cells that express high levels of Id1, and find that they represent a highly self-renewing population of tumor cells, allowing us to probe the role of self-renewal in glioma growth, rather than the role of *ID* genes in glioma biology generally. However, multiple *ID* genes are upregulated in high-grade gliomas and implicated in glioma pathogenesis (Vandeputte et al., 2002), and *ID* genes are known to have roles in tumor biology beyond self-renewal, including neoangiogenesis and regulation of cell-cycle (Perk et al., 2005). Recently, Anido et al. (2010) isolated a $CD44^{high}$ cell population from human patient derived glioma cells characterized by high levels of Id1 expression, TGF-ß-responsiveness and stem-like properties. These data are consistent with our results showing a role for Id1 in glioma cell self-renewal, and points to TGF-ß as a likely upstream regulator of Id1. While Id3 cosegregated with Id1 in our assays, Id2 and Id4 did not. It is likely that Id1/Id3 and Id2 and Id4 are expressed in different cell types and possess different functional roles depending on the specific tumorigenic context. While the effects of loss of Id1/3 on overall survival were modest in our model systems, it is possible that targeting additional Id proteins would yield a more dramatic effect, as this may impact both stem- and progenitor-like cell populations. In fact, recent studies indicate that combined loss of Id1, Id2, and Id3 impacts glioma cell self-renewal as well as proliferation, leading to a significant delay in tumor progression (A.I., unpublished observations). Our finding that multiple lineages are capable of transplanting disease suggests that targeting a single cell population alone may not yield optimal therapeutic effects in these tumor subtypes.

Relevance to Human Disease

This work raises a number of questions regarding the origin and propagation of human high-grade gliomas. We know that

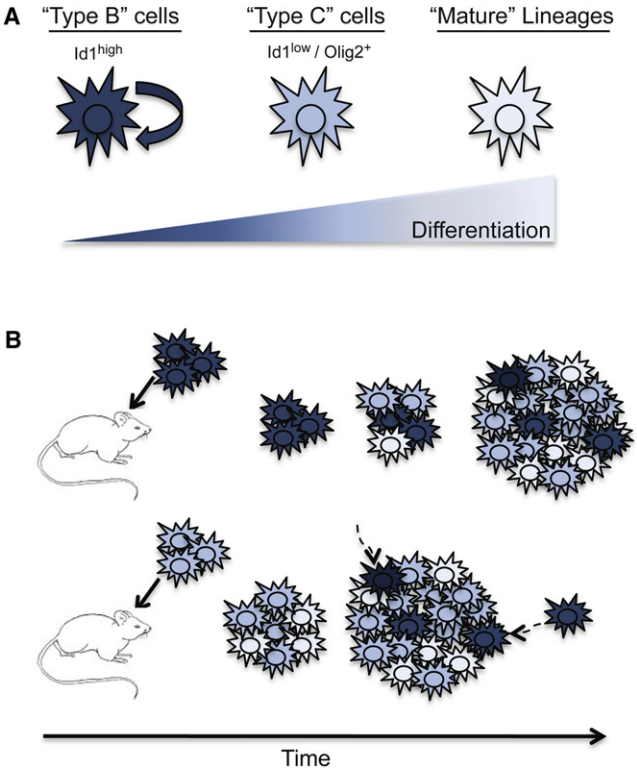

Figure 8. Proposed Model of High and Low Self-Renewing Lineages in Gliomagenesis

(A) Model depicting Id1^{high} cells, Id1^{low}/Olig2^{+} cells, and mature lineages.
(B) Comparison of Id1^{high} cells and Id1^{low}/Olig2^{+} cells in disease transplantation. Arrow represents recruitment of Id1-expressing cells to the tumor bulk.

multiple subclasses of human gliomas show a similar pattern of Id1 and Olig2 upregulation (Anido et al., 2010; Ligon et al., 2007; Vandeputte et al., 2002) and studies exploring at the effects of Olig2 knockdown in primary human glioma cells also show a significant delay in tumor development upon orthotopic transplantation (Mehta et al., 2011), consistent with our mouse knockdown experiments. Further, data from TCGA suggest that, within the Proneural subclass, high Id1 expression is associated with a better survival outcome. As gliomas are highly heterogeneous tumors that can be classified into multiple subtypes, further work will be required to determine the role of self-renewing, stem-like cells in tumors generated with other mutations and amplifications as well as the relative response of these different cell populations to radiation and chemotherapy. It is possible that stem-like and progenitor-like cells have different contributions to tumorigenesis depending on the oncogenic context, and a careful analysis of these cell populations in additional tumor subtypes will be important for determining the optimal cell populations for therapeutic targeting.

EXPERIMENTAL PROCEDURES

In Vivo Models

Nestin-tva; Arf$^{-/-}$ mice (Hambardzumyan et al., 2009), Id1^{VenusYFP} mice, Id1$^{flox/flox}$ mice (Nam and Benezra, 2009), and Id1$^{-/-}$ mice (Lyden et al., 1999) have been described. ubc-GFP mice were crossed with NOD-SCID mice to generate ubc-GFP;NOD-SCIDs. All mouse experiments were approved by MSKCC's Institutional Animal Care and Use Committee (IACUC).

Immunostaining

The following primary antibodies were used: Id1 (Biocheck), Id3 (Biocheck), Olig2 (Millipore), MAP2 (Millipore), GFAP (Millipore), Tuj1 (mouse, Millipore), Tuj1 (rabbit, Covance), O4 (Millipore), Nestin (BD Biosciences), phosphorylated histone H3 (H3P; Sigma), Cleaved Caspase 3 (Cell Signaling Technology), CD133 (Miltenyi Biotech), and GFP (Abcam).

Flow Cytometry

Cells were sorted for VenusYFP expression with PI exclusion at our FACS facility using a MoFlo cell sorter (Cytomation).

In Vitro Tumorsphere Assays

Tumors were papain digested (Worthington Biochemical), triturated and cells were plated for in vitro analysis in Neurocult Stem Cell Basal Media with Proliferation Supplements, 20 ng/ml EGF, 10 ng/ml FGF, and 2 μg/ml heparin (Stem Cell Technologies).

TCGA Kaplan-Meier Analysis

Id1 expression data were retrieved from the MSKCC cBio Cancer Genomics Portal (http://www.cbioportal.org/public-portal/). Patients were subdivided into high Id1 expression (top 50%) and low expression (bottom 50%) for analysis.

Statistics

Kaplan-Meier survival curves were generated with Prism software. All experiments were carried out in triplicate or greater. All p values are two-tailed and p values < 0.05 were considered significant. Data are shown as mean ± SD.

SUPPLEMENTAL INFORMATION

Supplemental Information includes six figures and Supplemental Experimental Procedures and can be found with this article online at doi:10.1016/j.ccr.2011.11.025.

ACKNOWLEDGMENTS

The authors thank members of the Benezra laboratory; E. Fomchenko, K. Pitter, and T. Ozawa for technical advice and reagents; The Laboratory of Comparative Pathology, Flow Cytometry Core Facility and Molecular Cytology Core Facility (MSKCC). Funding was provided through the Brain Tumor Center, MSKCC (L.E.B.), Ladies Auxiliary to the Veterans of Foreign Wars Postdoctoral Cancer Research Fellowship (L.E.B.), and the Kleberg Foundation (R.B.).

Received: June 28, 2011
Revised: October 20, 2011
Accepted: November 29, 2011
Published: January 17, 2012

REFERENCES

Alcantara Llaguno, S., Chen, J., Kwon, C.H., Jackson, E.L., Li, Y., Burns, D.K., Alvarez-Buylla, A., and Parada, L.F. (2009). Malignant astrocytomas originate from neural stem/progenitor cells in a somatic tumor suppressor mouse model. Cancer Cell *15*, 45–56.

Anido, J., Sáez-Borderías, A., Gonzàlez-Juncà, A., Rodón, L., Folch, G., Carmona, M.A., Prieto-Sánchez, R.M., Barba, I., Martínez-Sáez, E., Prudkin, L., et al. (2010). TGF-β Receptor Inhibitors Target the CD44(high)/Id1(high) Glioma-Initiating Cell Population in Human Glioblastoma. Cancer Cell *18*, 655–668.

Assanah, M., Lochhead, R., Ogden, A., Bruce, J., Goldman, J., and Canoll, P. (2006). Glial progenitors in adult white matter are driven to form

malignant gliomas by platelet-derived growth factor-expressing retroviruses. J. Neurosci. *26*, 6781–6790.

Beier, D., Hau, P., Proescholdt, M., Lohmeier, A., Wischhusen, J., Oefner, P.J., Aigner, L., Brawanski, A., Bogdahn, U., and Beier, C.P. (2007). CD133(+) and CD133(-) glioblastoma-derived cancer stem cells show differential growth characteristics and molecular profiles. Cancer Res. *67*, 4010–4015.

Brennan, C., Momota, H., Hambardzumyan, D., Ozawa, T., Tandon, A., Pedraza, A., and Holland, E. (2009). Glioblastoma subclasses can be defined by activity among signal transduction pathways and associated genomic alterations. PLoS ONE *4*, e7752.

Broadley, K.W., Hunn, M.K., Farrand, K.J., Price, K.M., Grasso, C., Miller, R.J., Hermans, I.F., and McConnell, M.J. (2011). Side population is not necessary or sufficient for a cancer stem cell phenotype in glioblastoma multiforme. Stem Cells *29*, 452–461.

Chen, R., Nishimura, M.C., Bumbaca, S.M., Kharbanda, S., Forrest, W.F., Kasman, I.M., Greve, J.M., Soriano, R.H., Gilmour, L.L., Rivers, C.S., et al. (2010). A hierarchy of self-renewing tumor-initiating cell types in glioblastoma. Cancer Cell *17*, 362–375.

Chow, L.M., Endersby, R., Zhu, X., Rankin, S., Qu, C., Zhang, J., Broniscer, A., Ellison, D.W., and Baker, S.J. (2011). Cooperativity within and among Pten, p53, and Rb pathways induces high-grade astrocytoma in adult brain. Cancer Cell *19*, 305–316.

Clément, V., Dutoit, V., Marino, D., Dietrich, P.Y., and Radovanovic, I. (2009). Limits of CD133 as a marker of glioma self-renewing cells. Int. J. Cancer *125*, 244–248.

Doetsch, F., García-Verdugo, J.M., and Alvarez-Buylla, A. (1997). Cellular composition and three-dimensional organization of the subventricular germinal zone in the adult mammalian brain. J. Neurosci. *17*, 5046–5061.

Fomchenko, E.I., Dougherty, J.D., Helmy, K.Y., Katz, A.M., Pietras, A., Brennan, C., Huse, J.T., Milosevic, A., and Holland, E.C. (2011). Recruited cells can become transformed and overtake PDGF-induced murine gliomas in vivo during tumor progression. PLoS ONE *6*, e20605.

Galli, R., Binda, E., Orfanelli, U., Cipelletti, B., Gritti, A., De Vitis, S., Fiocco, R., Foroni, C., Dimeco, F., and Vescovi, A. (2004). Isolation and characterization of tumorigenic, stem-like neural precursors from human glioblastoma. Cancer Res. *64*, 7011–7021.

Hambardzumyan, D., Amankulor, N.M., Helmy, K.Y., Becher, O.J., and Holland, E.C. (2009). Modeling Adult Gliomas Using RCAS/t-va Technology. Transl Oncol *2*, 89–95.

Hambardzumyan, D., Parada, L.F., Holland, E.C., and Charest, A. (2011). Genetic modeling of gliomas in mice: new tools to tackle old problems. Glia *59*, 1155–1168.

He, S., Nakada, D., and Morrison, S.J. (2009). Mechanisms of stem cell self-renewal. Annu. Rev. Cell Dev. Biol. *25*, 377–406.

Huse, J.T., Phillips, H.S., and Brennan, C.W. (2011). Molecular subclassification of diffuse gliomas: seeing order in the chaos. Glia *59*, 1190–1199.

Jackson, E.L., Garcia-Verdugo, J.M., Gil-Perotin, S., Roy, M., Quinones-Hinojosa, A., VandenBerg, S., and Alvarez-Buylla, A. (2006). PDGFR alpha-positive B cells are neural stem cells in the adult SVZ that form glioma-like growths in response to increased PDGF signaling. Neuron *51*, 187–199.

Kang, S.K., Park, J.B., and Cha, S.H. (2006). Multipotent, dedifferentiated cancer stem-like cells from brain gliomas. Stem Cells Dev. *15*, 423–435.

Kondo, T., and Raff, M. (2000). Oligodendrocyte precursor cells reprogrammed to become multipotent CNS stem cells. Science *289*, 1754–1757.

Ligon, K.L., Alberta, J.A., Kho, A.T., Weiss, J., Kwaan, M.R., Nutt, C.L., Louis, D.N., Stiles, C.D., and Rowitch, D.H. (2004). The oligodendroglial lineage marker OLIG2 is universally expressed in diffuse gliomas. J. Neuropathol. Exp. Neurol. *63*, 499–509.

Ligon, K.L., Huillard, E., Mehta, S., Kesari, S., Liu, H., Alberta, J.A., Bachoo, R.M., Kane, M., Louis, D.N., Depinho, R.A., et al. (2007). Olig2-regulated lineage-restricted pathway controls replication competence in neural stem cells and malignant glioma. Neuron *53*, 503–517.

Lindberg, N., Kastemar, M., Olofsson, T., Smits, A., and Uhrbom, L. (2009). Oligodendrocyte progenitor cells can act as cell of origin for experimental glioma. Oncogene *28*, 2266–2275.

Liu, C., Sage, J.C., Miller, M.R., Verhaak, R.G., Hippenmeyer, S., Vogel, H., Foreman, O., Bronson, R.T., Nishiyama, A., Luo, L., and Zong, H. (2011). Mosaic analysis with double markers reveals tumor cell of origin in glioma. Cell *146*, 209–221.

Lyden, D., Young, A.Z., Zagzag, D., Yan, W., Gerald, W., O'Reilly, R., Bader, B.L., Hynes, R.O., Zhuang, Y., Manova, K., and Benezra, R. (1999). Id1 and Id3 are required for neurogenesis, angiogenesis and vascularization of tumour xenografts. Nature *401*, 670–677.

Mehta, S., Huillard, E., Kesari, S., Maire, C.L., Golebiowski, D., Harrington, E.P., Alberta, J.A., Kane, M.F., Theisen, M., Ligon, K.L., et al. (2011). The central nervous system-restricted transcription factor Olig2 opposes p53 responses to genotoxic damage in neural progenitors and malignant glioma. Cancer Cell *19*, 359–371.

Menn, B., Garcia-Verdugo, J.M., Yaschine, C., Gonzalez-Perez, O., Rowitch, D., and Alvarez-Buylla, A. (2006). Origin of oligodendrocytes in the subventricular zone of the adult brain. J. Neurosci. *26*, 7907–7918.

Nam, H.S., and Benezra, R. (2009). High levels of Id1 expression define B1 type adult neural stem cells. Cell Stem Cell *5*, 515–526.

Network, T.C.G.A.T.R.; Cancer Genome Atlas Research Network. (2008). Comprehensive genomic characterization defines human glioblastoma genes and core pathways. Nature *455*, 1061–1068.

Pastrana, E., Silva-Vargas, V., and Doetsch, F. (2011). Eyes wide open: a critical review of sphere-formation as an assay for stem cells. Cell Stem Cell *8*, 486–498.

Perk, J., Iavarone, A., and Benezra, R. (2005). Id family of helix-loop-helix proteins in cancer. Nat. Rev. Cancer *5*, 603–614.

Persson, A.I., Petritsch, C., Swartling, F.J., Itsara, M., Sim, F.J., Auvergne, R., Goldenberg, D.D., Vandenberg, S.R., Nguyen, K.N., Yakovenko, S., et al. (2010). Non-stem cell origin for oligodendroglioma. Cancer Cell *18*, 669–682.

Prestegarden, L., and Enger, P.O. (2010). Cancer stem cells in the central nervous system—a critical review. Cancer Res. *70*, 8255–8258.

Romero-Lanman, E.E., Pavlovic, S., Amlani, B., Chin, Y., and Benezra, R. (2011). Id1 maintains embryonic stem cell self-renewal by up-regulation of Nanog and repression of Brachyury expression. Stem Cells Dev. 10.1089/scd.2011.0428.

Singh, S.K., Clarke, I.D., Terasaki, M., Bonn, V.E., Hawkins, C., Squire, J., and Dirks, P.B. (2003). Identification of a cancer stem cell in human brain tumors. Cancer Res. *63*, 5821–5828.

Singh, S.K., Hawkins, C., Clarke, I.D., Squire, J.A., Bayani, J., Hide, T., Henkelman, R.M., Cusimano, M.D., and Dirks, P.B. (2004). Identification of human brain tumour initiating cells. Nature *432*, 396–401.

Stiles, C.D., and Rowitch, D.H. (2008). Glioma stem cells: a midterm exam. Neuron *58*, 832–846.

Sun, Y., Meijer, D.H., Alberta, J.A., Mehta, S., Kane, M.F., Tien, A.C., Fu, H., Petryniak, M.A., Potter, G.B., Liu, Z., et al. (2011). Phosphorylation state of Olig2 regulates proliferation of neural progenitors. Neuron *69*, 906–917.

Terzis, A.J., Niclou, S.P., Rajcevic, U., Danzeisen, C., and Bjerkvig, R. (2006). Cell therapies for glioblastoma. Expert Opin. Biol. Ther. *6*, 739–749.

Uhrbom, L., and Holland, E.C. (2001). Modeling gliomagenesis with somatic cell gene transfer using retroviral vectors. J. Neurooncol. *53*, 297–305.

Uhrbom, L., Kastemar, M., Johansson, F.K., Westermark, B., and Holland, E.C. (2005). Cell type-specific tumor suppression by Ink4a and Arf in Kras-induced mouse gliomagenesis. Cancer Res. *65*, 2065–2069.

Vandeputte, D.A., Troost, D., Leenstra, S., Ijlst-Keizers, H., Ramkema, M., Bosch, D.A., Baas, F., Das, N.K., and Aronica, E. (2002). Expression and distribution of id helix-loop-helix proteins in human astrocytic tumors. Glia *38*, 329–338.

Verhaak, R.G., Hoadley, K.A., Purdom, E., Wang, V., Qi, Y., Wilkerson, M.D., Miller, C.R., Ding, L., Golub, T., Mesirov, J.P., et al; Cancer Genome Atlas Research Network. (2010). Integrated genomic analysis identifies clinically

relevant subtypes of glioblastoma characterized by abnormalities in PDGFRA, IDH1, EGFR, and NF1. Cancer Cell *17*, 98–110.

Wang, J., Sakariassen, P.O., Tsinkalovsky, O., Immervoll, H., Bøe, S.O., Svendsen, A., Prestegarden, L., Røsland, G., Thorsen, F., Stuhr, L., et al. (2008). CD133 negative glioma cells form tumors in nude rats and give rise to CD133 positive cells. Int. J. Cancer *122*, 761–768.

Yang, Z.J., Ellis, T., Markant, S.L., Read, T.A., Kessler, J.D., Bourboulas, M., Schüller, U., Machold, R., Fishell, G., Rowitch, D.H., et al. (2008). Medulloblastoma can be initiated by deletion of Patched in lineage-restricted progenitors or stem cells. Cancer Cell *14*, 135–145.

Ying, Q.L., Nichols, J., Chambers, I., and Smith, A. (2003). BMP induction of Id proteins suppresses differentiation and sustains embryonic stem cell self-renewal in collaboration with STAT3. Cell *115*, 281–292.

Cancer Cell
Article

The *p53* mRNA-Mdm2 Interaction Controls Mdm2 Nuclear Trafficking and Is Required for p53 Activation following DNA Damage

Madhavsai Gajjar,[1,4] Marco M. Candeias,[1,4] Laurence Malbert-Colas,[1] Anne Mazars,[1] Jun Fujita,[2] Vanesa Olivares-Illana,[1,3,*] and Robin Fåhraeus[1,*]
[1]Cibles Therapeutiques, INSERM Unité 940, Institut de Génétique Moléculaire, Université Paris 7, IUH Hôpital St. Louis, 75010 Paris, France
[2]Department of Clinical Molecular Biology, Graduate School of Medicine, Kyoto University, Kyoto 606-8507, Japan
[3]Present address: Instituto de Fisica, Universidad Autonoma de San Luis Potosi, 78290 SLP, Mexico
[4]These authors contributed equally to this work
*Correspondence: vanesa.olivares-illana@inserm.fr (V.O.-I.), robin.fahraeus@inserm.fr (R.F.)
DOI 10.1016/j.ccr.2011.11.016

SUMMARY

The ATM kinase and p53 are key tumor suppressor factors that control the genotoxic stress response pathway. The ATM substrate Mdm2 controls p53 activity by either targeting p53 for degradation or promoting its synthesis by binding the *p53* mRNA. The physiological role and regulation of Mdm2's dual function toward p53 is not known. Here we show that ATM-dependent phosphorylation of Mdm2 at Ser395 is required for the *p53* mRNA-Mdm2 interaction. This event also promotes SUMO-conjugation of Mdm2 and its nucleoli accumulation. Interfering with the *p53* mRNA-Mdm2 interaction prevents p53 stabilization and activation following DNA damage. These results demonstrate how ATM activity switches Mdm2 from a negative to a positive regulator of p53 via the *p53* mRNA.

INTRODUCTION

ATM is a key regulator of genome stability and initiator of cellular signaling pathways required for the DNA damage response. Mutations in ATM cause ataxia telangiectasia and result in the development of cancers. Activation of ATM following double-stranded DNA break involves its autophosphorylation and monomerization and leads to phosphorylation of DNA damage checkpoint proteins, such as p53, Chk2, c-Abl, BRCA-1, and Mdm2 (Bartek et al., 2007; Kitagawa and Kastan, 2005; Shiloh, 2003). Different studies on ATM and the Wip1 phosphatase have shown that phosphorylation and dephosphorylation of p53 on Ser15 and Mdm2 on Ser395 are important for regulating p53 activity (Banin et al., 1998; Canman et al., 1998; Khanna et al., 1998; Lu et al., 2007; Maya et al., 2001).

Activation of p53 in response to stress leads to an early induction of Mdm2. Binding of Mdm2 to the N terminus of p53 promotes either p53 monoubiquitination and nuclear export or p53 polyubiquitination and degradation by the 26S proteasomal pathway (Honda et al., 1997; Li et al., 2003). Mdm2 also has the capacity to regulate *p53* mRNA translation indirectly via its interaction with L26 or directly by binding to the *p53* mRNA (Candeias et al., 2008; Naski et al., 2009; Ofir-Rosenfeld et al., 2008). Direct interaction with the mRNA also accounts for Mdm2's induction of XIAP synthesis (Gu et al., 2009). The *p53* mRNA-Mdm2 interaction is mediated by the C-terminal RING domain of Mdm2 and the *p53* mRNA sequence that encodes the Mdm2 binding site in the N terminus of p53. This interaction also controls Mdm2's E3 ligase activity (Candeias et al., 2008).

Mdm2-dependent regulation of p53 expression and activity is controlled via interactions with a number of different proteins that are linked to the nucleolus. Several ribosomal factors, such as L5, L11, and L23, have been shown to interact with the central region of Mdm2 that contains its acid and zinc domains (Deisenroth and Zhang, 2010). The central region of Mdm2 also binds $p14^{Arf}$, which can retain Mdm2 in the nucleolus

Significance

The presented results show the importance of the *p53* mRNA-Mdm2 interaction in activating p53 following DNA damage and describe an additional function for an mRNA. The *p53* mRNA binding changes Mdm2 activity and prevents Mdm2-mediated ubiquitination of p53 while it stimulates p53 synthesis and promotes Mdm2 nucleolar localization. These results help to explain the previous paradox of why Mdm2 is upregulated by p53 in response to genotoxic stress. As long as the ATM pathway is active, Mdm2 serves as a positive regulator of p53 while it rapidly degrades p53 when the DNA damage response is turned off. These results implicate a route for therapeutic intervention aimed at controlling Mdm2 activity toward p53.

and prevent its export to the cytoplasm (Tao and Levine, 1999; Weber et al., 1999). The localization of Mdm2 to nucleoli plays a key role in p53 activation and involves the interaction of Mdm2 with the PML (promyelocytic leukemia) tumor suppressor protein (Bernardi et al., 2004; Boulon et al., 2010; Lohrum et al., 2000; Weber et al., 1999). SUMOylation of PML, or of its interacting partners, helps to target a number of different proteins to PML nuclear bodies that are linked to a variety of different stress and damage pathways that control transcription and translation regulation, tumor suppression, DNA repair, and apoptosis (Bernardi and Pandolfi, 2007; Heun, 2007; Lallemand-Breitenbach and de Thé, 2010).

Here we investigated the physiological role of the *p53* mRNA-Mdm2 interaction in the well-described p53 tumor suppressor pathway triggered by genotoxic stress.

RESULTS

Mdm2 Is Required to Promote p53 Activity following DNA Damage in an ATM-Dependent Manner

Introduction of siRNA against Mdm2 in the human sarcoma cells MLS1765 that express endogenous wild-type p53 (p53wt) resulted in an increase in the number of cells undergoing apoptosis, in line with the notion that Mdm2 is a negative regulator of p53 activity under normal conditions. When MLS1765 cells were exposed to the DNA-damaging agent doxorubicin, the siRNA treatment against Mdm2 instead lead to a decrease in the apoptotic numbers, indicating that Mdm2 helps to activate apoptosis under conditions of genotoxic stress. siRNA against ATM also reduced the amount of cells undergoing apoptosis after doxorubicin treatment, and the strongest inhibition of apoptosis was observed when siRNA for both Mdm2 and ATM was introduced (Figure 1A; Figures S1A–S1C available online). Introduction of exogenous Mdm2 and p53 in the $p53^{-/-}$; $Mdm2^{-/-}$ double-KO (DKO) MEFs resulted in a four times higher rate of p53-dependent apoptosis following induction of DNA double-strand breaks by treating cells with etoposide (Figure 1B).

To further investigate the role of Mdm2 as an activator of the DNA damage-response pathway, we used the p53 null H1299 cell line, in which we introduced p53wt. Altering the levels of Mdm2 by either knocking down endogenous Mdm2 using siRNA or by overexpressing Mdm2 revealed an Mdm2-dependent inhibition of p53-induced apoptosis under normal conditions and an Mdm2-dependent augmented p53-dependent apoptosis in response to genotoxic stress. This proapoptotic effect of Mdm2 was significantly suppressed when the activity of endogenous ATM was diminished by siRNA or by overexpressing the Wip1 phosphatase (Figure 1C). The latter reverses ATM-mediated autophosphorylation and phosphorylation of p53 and Mdm2 (Lu et al., 2007, 2005; Shreeram et al., 2006; Yoda et al., 2008). Treatment of cells with an ATM kinase inhibitor (ATMi) prevented Mdm2 from inducing apoptosis upon doxorubicin treatment (Figure 1D; Figure S1D). Furthermore, we observed that ectopically expressed Mdm2 acted as a negative regulator of apoptosis in doxorubicin-treated cells expressing endogenous p53 and Mdm2 but deficient for ATM (AT5-BIVA cells) but acted as a positive regulator of apoptosis when exogenous ATM was introduced (Figure 1E). Taken together, these results indicate that Mdm2 acts as a positive regulator of p53 activity following genotoxic stress in an ATM-dependent fashion.

Phosphorylation of Mdm2 at Ser395 Induces p53 Activity Independently of the p53-Mdm2 Protein-Protein Interaction

ATM mediates phosphorylation, directly or indirectly, through Chk2 on several residues in the p53 N terminus (Shiloh, 2003), which harbors the *trans*-activating domains and the Mdm2-binding site (Oliner et al., 1993; Zhu et al., 1998). The current model on how phosphorylation at these sites suppresses Mdm2-dependent inhibition of p53 activity suggest that these events prevent the p53-Mdm2 protein-protein interaction (Cheng et al., 2009; Jimenez et al., 1999; Lu et al., 2007; Shieh et al., 1997). This cannot, however, explain our observations that Mdm2 not only stops being an inhibitor of p53 but in fact enhances its activity following genotoxic stress. Hence, other molecular mechanisms must be in place to explain Mdm2's switch from a negative to a positive regulator of p53. To test this hypothesis, we first used the p76 Mdm2 isoform (Mdm2p76), which lacks the N terminus and the capacity to bind the p53 protein (Perry, 2004). Expression of Mdm2p76 stimulated p53-dependent apoptosis following DNA damage in a similar way as the Mdm2wt, demonstrating that inhibition of the p53-Mdm2 protein-protein interaction is not required in order for Mdm2 to enhance p53 activity in response to DNA lesions (Figure 2A; Figure S2A).

Mdm2 is phosphorylated at Ser395 by ATM (Maya et al., 2001) and has been implicated in ATM-dependent activation of p53, so we tested whether the proapoptotic disposition of Mdm2 is dependent on the phosphorylation of Mdm2 at this residue. The introduction of the S395A mutation in Mdm2 caused a significant reduction in apoptosis in AT5-BIVA, H1299, and DKO cells expressing ATM and p53 in the presence of doxorubicin, confirming the importance of this site for p53 activation in response to DNA damage (Figure 2B). In each cell line, we observed a decrease in p53 expression in cells exposed to doxorubicin in the presence of Mdm2Ser395A, as compared to Mdm2wt (Figure S2B). As can be expected, the relative levels of apoptosis and p53 expression varies between cell lines depending on sensitivity to the drug and the levels of p53 expression. The binding of the *p53* mRNA to Mdm2 can stimulate p53 synthesis, and, because Ser395 is situated close to the RING domain, where the ability to bind *p53* mRNA lies, we next assessed whether the *p53* mRNA-Mdm2 interaction plays a role in Mdm2-mediated activation of p53 following DNA damage. We expressed p53wt protein from an mRNA that carries a single silent point mutation (*p53L22L*) and has a low affinity for Mdm2 (Candeias et al., 2008), or we expressed an Mdm2 protein that carries a point mutation that reduces its affinity to RNA (Mdm2G446S) (Elenbaas et al., 1996). Both mutants failed to induce p53-dependent apoptosis in H1299 cells treated with doxorubicin and, in fact, p53wt protein expressed from the *p53L22L* mRNA was unable to induce a significant amount of apoptosis in the presence of Mdm2wt (Figure 2C). On the contrary, introduction of the phospho-mimetic Mdm2S395D mutant caused an increase in apoptosis as compared to Mdm2wt. In addition, similar to what was observed in AT5-BIVA and DKO cells, the level of p53 was low in H1299 cells in which the *p53*

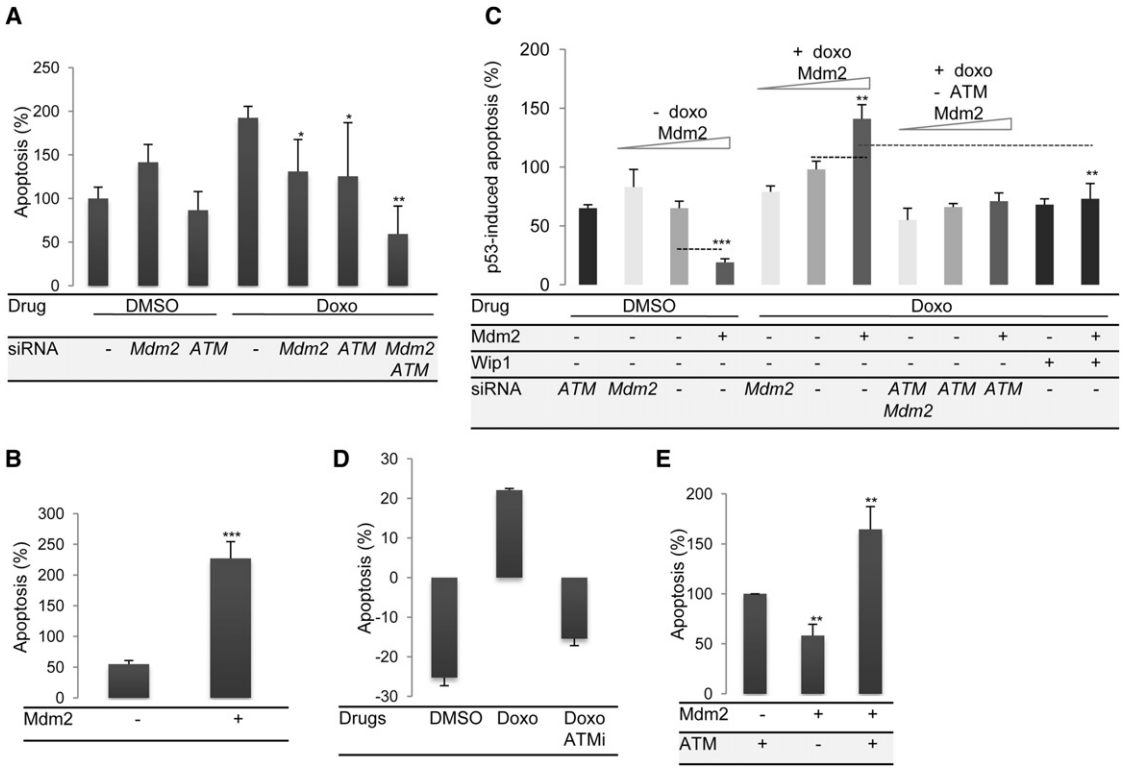

Figure 1. Mdm2 Is a Positive Regulator of p53 Activity in Response to DNA Damage in an ATM-Dependent Manner

Flow cytometry analyses show the levels of apoptosis in different cell lines treated, or not, with the genotoxic drugs doxorubicin (doxo) (0.1–1 μM for 6–16 hr as indicated below) or etoposide (5 μM for 20 hr).

(A) Suppression of Mdm2 and/or ATM using siRNA in MLS-1765 cells expressing endogenous wild-type p53 (p53wt) after treatment with 1 μM doxo for 8 hr. The data are normalized to the level of apoptosis in DMSO-treated cells with control siRNA (100%).

(B) Etoposide-induced apoptosis in $Mdm2^{-/-}$;$p53^{-/-}$ MEF cells expressing exogenous p53wt with, or without, exogenous Mdm2wt.

(C) The graph shows p53-induced apoptosis in $p53^{-/-}$ H1299 cells expressing exogenous p53wt. The levels of Mdm2 were altered using siRNA to knock down endogenous Mdm2 levels, or by overexpressing (+) Mdm2. p53-dependent apoptosis in DMSO- compared to doxo-treated cells (0.1 μM for 16 hr) is shown. Light bars (lanes 2, 5, and 8) represent low Mdm2 levels in cells treated with Mdm2 siRNA, light gray bars (lanes 3, 6, and 9) represent endogenous Mdm2 levels, and darker gray bars (lanes 4, 7, and 10) are cells overexpressing Mdm2.

(D) The relative levels of p53-dependent apoptosis in the presence of exogenous Mdm2 in H1299 cells treated with doxo (0.1 μM for 16 hr) and ATM inhibitor (ATMi, 10 μM for 20 hr).

(E) The levels of apoptosis in $ATM^{-/-}$ cells (AT5-BIVA) expressing exogenous Mdm2 and/or ATM in the presence of doxo (0.1 μM for 6 hr). The data are normalized to the level of apoptosis in cells expressing endogenous Mdm2 (100%). Data are means ± s.d. of at least three independent experiments (*$p < 0.05$, **$p < 0.01$, ***$p < 0.001$). P values are as compared with doxo and no siRNA (A), no Mdm2 (B and E), and as indicated (C). The data using H1299 cells (C and D) are normalized to the levels of apoptosis in mock-transfected cells (0%).

See also Figure S1.

mRNA-Mdm2 interaction was interrupted (Figure S2C). These results indicate that Mdm2's positive effect on p53 activity during genotoxic stress requires ATM-dependent phosphorylation of Mdm2 on Ser395 and the *p53* mRNA-Mdm2 interaction.

Phosphorylation of Mdm2 at Ser395 by ATM Promotes Its Interaction with the *p53* mRNA

We next tested whether ATM activity affects the *p53* mRNA-Mdm2 interaction. The binding of *p53* mRNA to Mdm2 was analyzed by immunoprecipitation (IP) of Mdm2 followed by quantitative RT-PCR (qRNA-coIP) (Candeias et al., 2008). An approximately three-fold induction in the amount of *p53* mRNA bound to Mdm2 was observed following treatment of cells with doxorubicin. This was prevented by the Mdm2S395A mutation or by treating the cells with ATMi or with the general PI3K inhibitor wortmannin. The *p53* mRNA-Mdm2 interaction was stabilized approximately five-fold by introducing the Mdm2S395D mutation in the absence of doxorubicin. Treatment with doxorubicin had no significant additional effect on the *p53* mRNA-Mdm2 interaction, indicating that the Ser395 site is sufficient and necessary. Mdm2 can also be phosphorylated on Y394 by the ATM substrate c-Abl (Goldberg et al., 2002). However, the binding of the *p53* mRNA to Mdm2S394A in response to genotoxic stress was similar to that of Mdm2wt, indicating that this site plays a minor role in controlling RNA binding and at the same time indicates the regulatory specificity of the Ser395 residue (Figure 3A; Figure S3A, left panel). To further test whether the binding of the *p53* mRNA to Mdm2 is controlled by ATM, we used the AT5-BIVA cells. qRNA-coIP using the 4B2 monoclonal Antibody (mAb), which is indifferent to Mdm2's Ser 395 phosphorylation status, revealed almost no *p53* mRNA bound to Mdm2 in these cells. The introduction of ATM restored *p53*

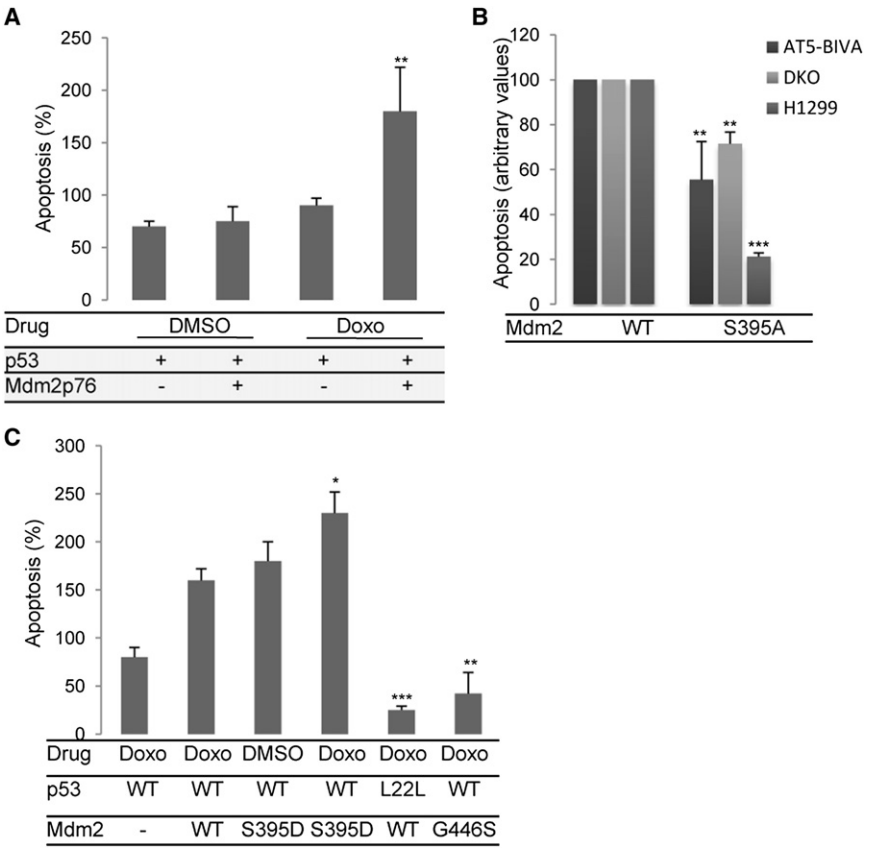

Figure 2. Phosphorylation of Mdm2 at Ser395 Induces p53-Dependent Apoptosis Independently of the p53–Mdm2 Protein-Protein Interaction

(A) The effect of the Mdm2p76 isoform on p53-dependent apoptosis was evaluated in H1299 cells in the presence or absence of genotoxic stress (doxo 0.1 μM for 16 hr). Doxo-treated and nontransfected cells were given the arbitrary value zero.

(B) The effect on p53-dependent apoptosis by Mdm2S395A in the presence of doxo in indicated cells. Cells were transfected with p53wt and with Mdm2wt or Mdm2S395A. The ATM$^{-/-}$ cells (AT5-BIVA) were also transfected with ATM. Apoptosis in the presence of Mdm2wt, p53wt and doxorubicin was given the arbitrary value 100. Mdm2$^{-/-}$;p53$^{-/-}$ double knock-out MEF cells (DKO).

(C) p53-dependent apoptosis in H1299 cells expressing indicated p53 and Mdm2 constructs in the absence, or presence, of doxo. Data are means ± s.d. of at least three independent experiments (*$p < 0.05$, **$p < 0.01$, ***$p < 0.001$). P values are as compared with doxo and no Mdm2 (A), Mdm2wt (B), and Mdm2wt and p53wt (C). The data using H1299 cells (A and C) are normalized to the levels of apoptosis in mock-transfected cells (0%).

See also Figure S2.

mRNA binding to Mdm2, and the affinity of this interaction increased by approximately four-fold after doxorubicin treatment. Importantly, when we instead used the 2A10 mAb, which does not recognize the phosphorylated Ser 395 epitope (Maya et al., 2001), we detected little *p53* mRNA in the qRNA-coIP even in the presence of ATM, indicating that nonphosphorylated Mdm2 has weak affinity to the *p53* mRNA (Figure 3B; Figure S3B). In order to investigate whether ATM-dependent phosphorylation at Mdm2Ser395 regulates Mdm2's binding to the *p53* mRNA, we performed in vitro binding experiments in which ATM immunoprecipitated from cell lysate was added to recombinant Mdm2 purified from Sf9 insect cells and in vitro transcribed *p53* mRNA (Figure S3C). Treatment of cells with doxorubicin prior to cell lysis resulted in an approximately four-fold increase in the amount of *p53* mRNA bound to Mdm2. This increase was suppressed by more than 50% if ATMi or wortmannin were added to the reaction mixture. We also tested the low-affinity *p53L22L* mRNA under these in vitro conditions and found that its interaction with Mdm2 in response to doxorubicin treatment was less than half of that of the wild-type message (Figure 3C). Furthermore, the ATM-dependent increase in the binding of *p53* mRNA to Mdm2 in vitro could be detected using the 4B2 but not the 2A10 mAb (Figure 3D).

Mdm2 is mainly detected in the nucleus in response to stress, but Mdm2-dependent synthesis and degradation of p53 takes place in the cytoplasm, so we wanted to know where the *p53* mRNA-Mdm2 interaction takes place. To address this question, we deleted the nuclear localization signal in Mdm2 (Mdm2ΔNLS). Interestingly, this protein is restricted to the cytoplasmic compartment and binds the *p53* mRNA in vitro (O'Keefe et al., 2003 and data not shown) but it only interacts with a fraction of the *p53* mRNA, as compared with the Mdm2wt, indicating that the *p53* mRNA-Mdm2 interaction mainly takes place in the nucleus (Figure 3E; Figure S3A, right panel).

We further characterized the *p53* mRNA-Mdm2 interaction using a biotinylated oligonucleotide corresponding to the Mdm2-binding sequence of *p53* mRNA (MBD-ES) and purified recombinant Mdm2 proteins expressed in bacteria (Figure S3D). The Mdm2wt showed low affinity for the *p53* MBD-ES, whereas the phospho-mimetic Mdm2S395D displayed a higher estimated affinity (Kdiss 160 nM) (Figures 3F and 3G). An Mdm2 construct that contains the C-terminal residues 322–491, Mdm2(322-491), showed a similar behavior as the full-length Mdm2 protein in that the 395D mutation enhances the RNA-binding capacity. However, a construct including the RING domain, but not Ser395, Mdm2(396-491), showed a similar affinity (Kdiss 400 nM) for the RNA as MdmS2395D, indicating that the RING domain alone is sufficient to bind the *p53* mRNA (Figure 3H). These results suggest that the RNA-binding capacity of Mdm2 takes place in the nuclear compartment and is located to the RING domain of Mdm2 and that the 395 residue is not part of the direct contact with the *p53* mRNA. This also indicates that phosphorylation of Ser395 by ATM promotes Mdm2's RNA-binding capacity via allosteric changes within the C terminus of Mdm2.

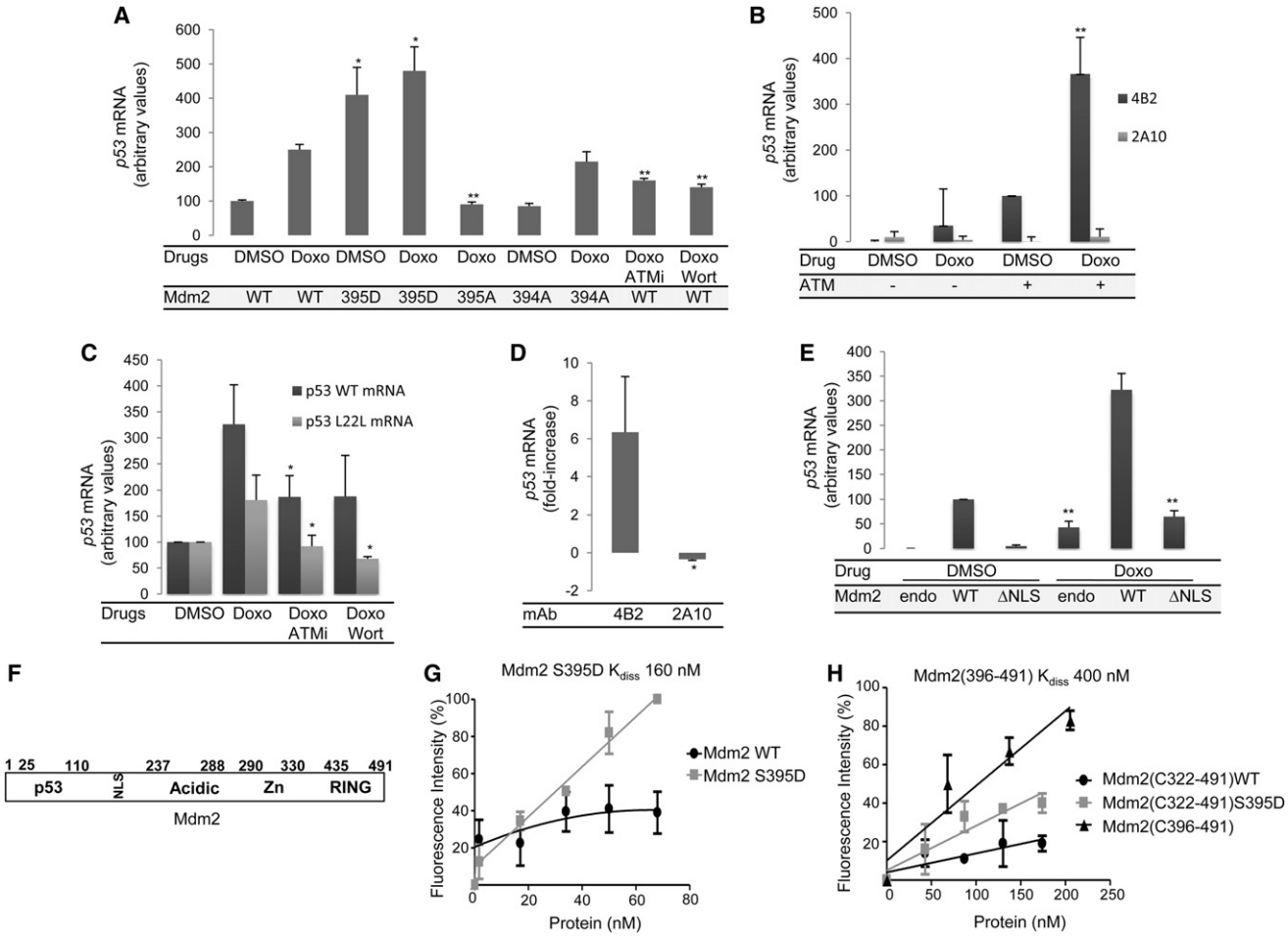

Figure 3. The Binding of the *p53* mRNA to Mdm2 Is Dependent on ATM Activity

(A) The binding of indicated Mdm2 constructs to the p53 mRNA in H1299 cells as estimated using qRNA-coIP. Cells (A–E) were treated with doxo (1 μM for 3 hr) or DMSO. ATM inhibitor (ATMi 10 μM) or the PI3K inhibitor wortmannin (wort. 5 μM) was added for 20 hr before RNA binding was determined.

(B) The binding of *p53* mRNA to Mdm2 in the ATM null AT5-BIVA cells with, or without, exogenous ATM using qRNA-coIP. The anti-Mdm2 monoclonal antibody (mAb) 4B2 is indifferent to phosphorylation, whereas 2A10 does not recognize the phosphorylated Ser395 Mdm2 epitope.

(C) ATM immunoprecipitated from H1299 cells treated, or not, with doxo was added to recombinant purified Mdm2 from Sf9 insect cells and in vitro-synthesized *p53wt* or *p53L22L* mRNAs in the presence or absence of ATMi (10 μM) or wortmannin (5 μM), and the amount of *p53* mRNA bound to Mdm2 was estimated following qRNA-coIP.

(D) ATM-dependent changes in the in vitro binding of *p53* mRNA to Mdm2 as in (C) using 4B2 and 2A10 mAbs.

(E) The binding of Mdm2 wild-type (WT) to the *p53* mRNA in H1299 cells or to an Mdm2 that lacks the nuclear localization signal (ΔNLS) as estimated using qRNA-coIP.

(F) Cartoon illustrating different domains of Mdm2.

(G) In vitro purified recombinant Mdm2wt or Mdm2S395D expressed in bacteria were tested for their binding to in vitro synthesized *p53* mRNA using RNA-ELISA.

(H) In vitro purified truncated recombinant Mdm2 proteins expressed in bacteria were tested for their binding to in vitro synthesized *p53* mRNA using RNA-ELISA.

Data are means ± s.d. of three independent experiments (*$p < 0.05$, **$p < 0.01$, ***$p < 0.001$). P values are as compared with Doxo and Mdm2wt (A, E), no Doxo and ATM (B), Doxo alone (C) and mAb 4B2 (D).

See also Figure S3.

The *p53* mRNA Is Required for Mdm2 SUMO-Conjugation and Nuclear Trafficking

After DNA damage, Mdm2 localizes to nucleoli and this plays an important role in p53's capacity to respond to DNA damage (Lohrum et al., 2000; Weber et al., 1999). Mdm2 also interacts with PML that is linked to RNA transport, and we tested whether the *p53* mRNA plays a role in Mdm2 nuclear translocation (Bernardi et al., 2004; Cohen et al., 2001; Ideue et al., 2004; Kurki et al., 2003). Treatment of p53wt-expressing cells with doxorubicin resulted in the localization of Mdm2 to nucleoli in conjunction with PML nuclear bodies, as reported previously (Figure 4A, top two rows; Figure S4) (Bernardi et al., 2004; Kurki et al., 2003). Interestingly, the localization of Mdm2 to nucleoli after genotoxic stress was abrogated by suppressing the interaction between Mdm2 and the *p53* mRNA using mutants Mdm2S395A or *p53L22L* (Figure 4A, lower panel). The expression of a silent p53 construct (*Sp53* mRNA) lacking initiation codons and that expresses no p53 protein (Candeias et al., 2008) revealed that

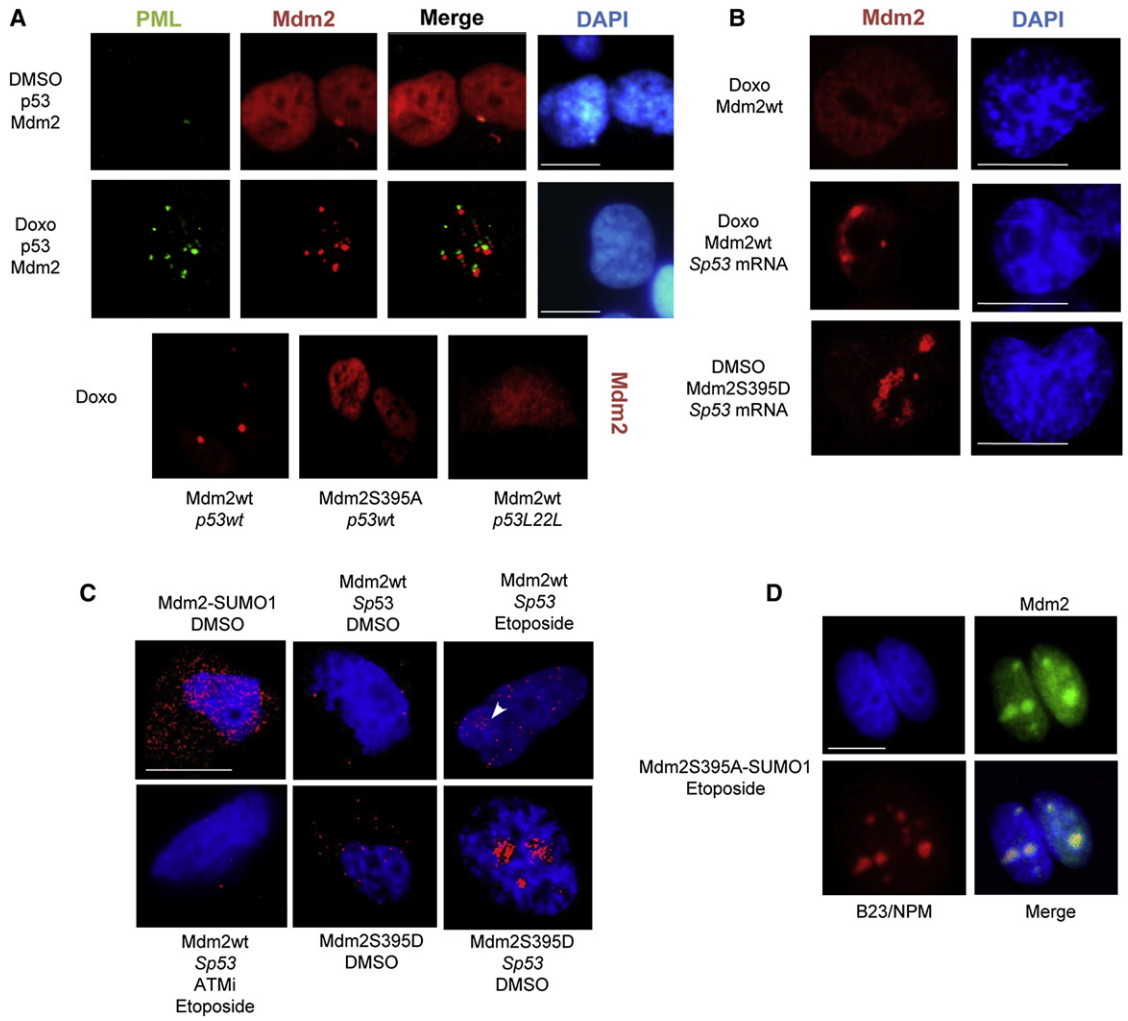

Figure 4. The *p53* mRNA Regulates Mdm2 SUMOylation and Nuclear Trafficking

H1299 cells were transfected with indicated constructs and Mdm2, PML, or B23/NPM was detected by indirect immunofluorescence microscopy staining. Cell nuclei were visualized with DAPI (blue). Fields were merged to assess protein colocalization.

(A) Cells expressing indicated p53 and Mdm2 constructs and treated with DMSO (upper panels) or doxo (middle panels) and stained for PML (green) and Mdm2 (red). The lower panels show staining of Mdm2 in cells overexpressing indicated Mdm2 and p53 constructs after treatment with doxo.

(B) Mdm2 staining in cells expressing indicated constructs and treated with doxo or DMSO.

(C) DuoLink using anti-SUMO1/2 and anti-Mdm2 specific mAbs. Fusion of SUMO1 to Mdm2 (Mdm2-SUMO1) serves as a positive control (upper left). Mdm2 conjugated to endogenous SUMO1/2 is shown in the other slides. Treatment with etoposide leads to an accumulation of SUMOylated Mdm2wt products in nucleoli (white arrow, top right).

(D) Double staining for Mdm2 using 4B2 mAb and anti-B23/NPM polyclonal sera. Data represent three similar independent experiments. Scale bars correspond to 10 μm.

See also Figure S4.

the *p53* mRNA, but not the p53 protein, is required for the nucleolar localization of Mdm2 following genotoxic stress. We also observed that the phosphomimetic S395D mutation resulted in an Mdm2 that, in the presence of the *Sp53* mRNA, localized to the nucleoli in the absence of genotoxic stress (Figure 4B).

SUMO modifications can play a role in nucleolar and PML-related nuclear trafficking, and we used the DuoLink method, which gives a single signal if two different antibody epitopes are localized within 40 nm of each other, to detect and visualize SUMO-conjugated Mdm2 under normal or genotoxic stress conditions. By using antibodies toward Mdm2 and SUMO, we could confirm positive signals throughout the cells using a control Mdm2-SUMO1 fusion construct. Mdm2 wild-type protein was weakly SUMOylated throughout nontreated cells in the presence of p53. Treating cells with etoposide (doxorubicin interferes with the DuoLink signal) in the presence of *Sp53* mRNA resulted in an increase in SUMOylated Mdm2 throughout the nucleus and an accumulation in nucleoli. This was prevented if the cells were treated with the ATMi. Introducing the S395D mutation resulted in an increase in the number of Mdm2-SUMO interactions in nontreated cells. Importantly, when the *Sp53* mRNA was coexpressed with the Mdm2S395D, the SUMOylation of Mdm2 in

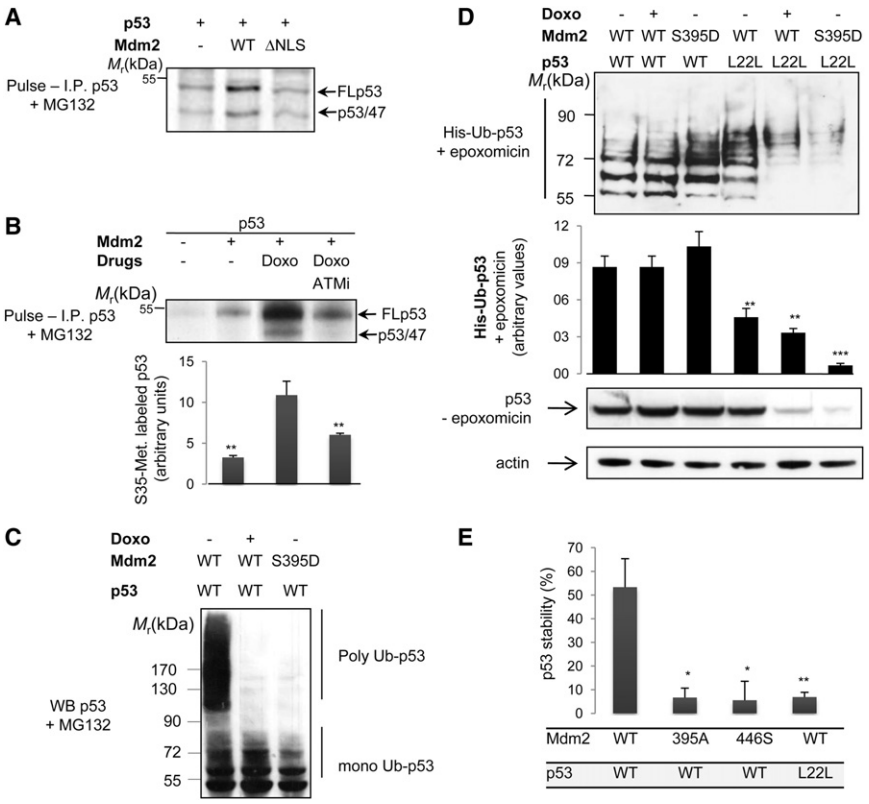

Figure 5. DNA Damage Stimulates ATM-Dependent *p53* mRNA Translation and p53 Polyubiquitination and Degradation

(A) Autoradiograph of a metabolic pulse label in H1299 cells expressing p53 and Mdm2wt or Mdm2ΔNLS in the presence of proteasome inhibitor (MG132 20 μM for 2 hr) followed by p53 IP.

(B) Metabolic pulse-label reveals synthesis of p53 in H1299 cells transfected with indicated constructs and treated, or not, with doxo (0.1 μM for 10 hr) and the specific ATM inhibitor (ATMi; 10 μM for 20 hr).

(C) Cells expressing indicated p53 and Mdm2 constructs were treated, or not, with doxo, and the p53 ubiquitination patterns were visualized after separation on a 7% SDS gel and blotted against p53 CM-1 polyclonal sera. Mono- and polyubiquitinated p53 forms are indicated.

(D) Cells were transfected with ubiquitin-His tag cDNA and indicated constructs in the presence or absence of genotoxic stress. Cells were treated with the proteasome inhibitor epoxomicin (5 μM 4 hr). Upper panel shows lower-molecular-weight ubiquitin-His conjugated p53 proteins after enrichment on Ni-Agarose beads, separated on SDS gels and blotted against p53 (CM-1 pAb). The graph below shows the relative values of three independent experiments as determined by ECL reader. Bottom panels shows corresponding p53 steady state levels (no proteasome inhibitors) and actin loading control.

(E) The graph shows the relative changes in p53 stability in the presence of indicated Mdm2 and p53 constructs after doxo treatment (0.1 μM for 10 hr) followed by cycloheximide for 1 hr prior to lysis. p53 levels in the absence of exogenous Mdm2 was set to 100%. Data are representative of three similar independent experiments and are expressed as means ± s.d. (*$p < 0.05$, **$p < 0.01$, ***$p < 0.001$). P values are as compared with doxo alone (B) and Mdm2wt and p53wt (E) and *p53wt* mRNA (D). See also Figure S5.

nontreated cells was enhanced over 10-fold and restricted to the nucleoli (Figure 4C). We also tested whether conjugation of SUMO1 to Mdm2 plays a direct role in the accumulation of Mdm2 in the nucleolus. Fusion of SUMO1 to Mdm2S395A (Mdm2S395A-SUMO1) resulted in a localization of the fusion protein to the nucleoli under stress conditions and without the presence of *p53* mRNA (Figure 4D). These results show that the *p53* mRNA plays an important role in directing Mdm2 SUMO modification and its nuclear trafficking.

ATM and the *p53* mRNA-Mdm2 Interaction Are Required to Induce p53 Expression following Genotoxic Stress

The binding of the *p53* mRNA to Mdm2 has been shown to promote p53 synthesis. Metabolic pulse-label experiments in the presence of proteasome inhibitors showed that the Mdm2 protein, which lacks the nuclear localization sequence (ΔNLS), does not support p53 synthesis (Figure 5A). This indicates that, even though synthesis of p53 takes place in the cytoplasm, the *p53* mRNA-Mdm2 interaction needs first to take place in the nucleus (Figure 3E). In line with the observation that ATM activity promotes the interaction between the *p53* mRNA and Mdm2, we found that Mdm2 induces more than three-fold increase in the rate of p53 synthesis after cells were exposed to doxorubicin, as compared to nontreated cells. This increase was suppressed by more than 60% if the cells were also treated with the ATMi. The induction of p53 synthesis by endogenous Mdm2 after doxorubicin treatment is approximately 50% (Figure 5B; Figure S5).

The degradation of p53 by Mdm2 involves p53 polyubiquitination, and managing Mdm2's E3 ligase activity toward p53 following DNA damage is important for p53 activation (Li et al., 2003; Thrower et al., 2000). The binding of the *p53* mRNA to the RING domain of Mdm2 can control Mdm2 E3 ligase activity (Candeias et al., 2008; Linares and Scheffner, 2003), we therefore investigated how Mdm2Ser395 phosphorylation and *p53* mRNA binding affects p53 ubiquitination. Treating cells with proteasome inhibitors prior to lysis revealed that the Mdm2-dependent polyubiquitination of p53 is compromised in cells treated with doxorubicin or when the 395D mutation is introduced in Mdm2 (Figure 5C). Monoubiquitination of p53, which can take place on several lysine residues, was relatively unaffected. We also enriched ubiquitinated p53 by expressing a His-ubiquitin construct followed by Ni^{+}-agarose purification. Using either method, we could not detect Mdm2-dependent polyubiquitinated p53 when p53wt protein was expressed from the *L22L* mRNA, but we could detect Mdm2-dependent His-ubiquitinated p53 of less than 90 kD (Figure 5D, upper and middle panel). Importantly, in the presence of genotoxic stress, or by introducing the 395D mutation in Mdm2, we observed a significant reduction in the amount of His-ubiquitinated p53 products of lower molecular weight when the p53wt protein was expressed from the *L22L* mRNA, as compared to the *p53wt*

mRNA, for which the ubiquitination pattern was relatively unchanged under these conditions. At the same time, we observed a sharp decrease in the steady-state levels of p53wt protein expressed from the *p53L22L* mRNA in the presence of either Mdm2S395D or Mdm2wt plus doxorubicin. The levels of p53wt protein expressed from the *p53wt* mRNA increased under these conditions (Figure 5D, lower panels). This shows that p53wt protein expressed from a non-Mdm2 binding mRNA is hyperunstable in the presence of Mdm2 during genotoxic stress. The importance of the *p53* mRNA-Mdm2 interaction in preventing p53 degradation following genotoxic stress was further underlined by introducing the Mdm2G446S and the Mdm2395A mutants, which both have a low affinity for the *p53wt* mRNA. Following doxorubicin and cycloheximide treatment (1 hr), we observed an approximately five-fold higher p53 turnover rate in cells expressing a dysfunctional combination of the *p53* mRNA-Mdm2 interaction (Figure 5E). These results support the notion that the increase in the *p53* mRNA-Mdm2 binding following genotoxic stress leads to both an increase in Mdm2-dependent p53 synthesis and a decrease in Mdm2-dependent degradation p53.

DISCUSSION

The results presented here describe the molecular mechanisms underlying ATM-dependent regulation of Mdm2 nuclear trafficking and p53 activation following genotoxic stress and offer an additional view on p53-dependent induction of Mdm2 expression. Our results support a model in which the induction of the *p53* mRNA-Mdm2 interaction takes place in the nuclear compartment in response to genotoxic stress via ATM-dependent phosphorylation of Mdm2 at Ser395. This event leads to a change of conformation in the Mdm2 RING domain that exposes the binding site for the *p53* mRNA. This, in turn, promotes Mdm2 SUMOylation and brings Mdm2 to the nucleolus and switches Mdm2 into a positive regulator of p53 by increasing p53 synthesis and, at the same time, suppresses Mdm2-dependent degradation of p53. When the DNA damage signaling cascade is turned off, ATM activity ceases and Mdm2 phosphorylation is reversed by Wip1 so that Mdm2 no longer binds the *p53* mRNA and switches to become a negative regulator of p53 activity by promoting p53 polyubiquitination and degradation (Figure 6). Disruption of the *p53* mRNA-Mdm2 interaction leads to a rapid decrease in p53 levels and to a failure in p53 activation in response to genotoxic stress.

Our results show that Mdm2p76 is a positive regulator of p53 activity in response to DNA damage, despite lacking the p53 interactive N-terminal domain, demonstrating that disrupting the p53-Mdm2 protein-protein interaction by ATM-dependent modifications of the p53 N terminus, or on Mdm2, are not required to induce p53 activity following ATM activation. Preventing the p53-Mdm2 protein-protein interaction could help to explain how ATM neutralizes the negative effect of Mdm2 but it cannot explain how Mdm2 actually stimulates p53 activity following genotoxic stress. Our data suggest that, in addition to preventing Mdm2-dependent degradation of p53, the *p53* mRNA-Mdm2 interaction also stimulates p53 synthesis and together these two effects can account for the positive outcome of Mdm2 on p53 expression and activity in response to DNA

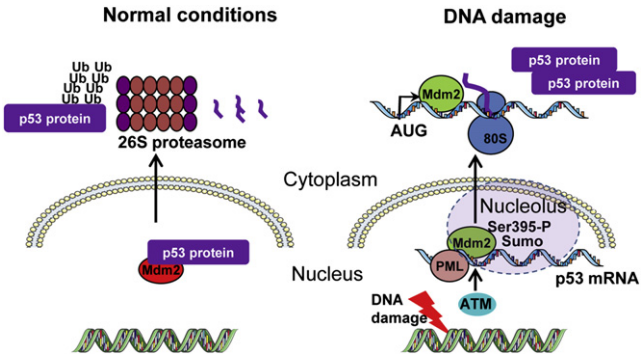

Figure 6. A Model for p53 Activation via ATM-Mdm2 in Response to Genotoxic Stress

Under normal conditions, Mdm2 translocates the p53 protein out of the nucleus for degradation via the ubiquitin-dependent pathway. Under conditions of genotoxic stress, ATM phosphorylates Mdm2 at Ser395. This results in allosteric changes in the C terminus of Mdm2 and opens up the Mdm2 RING domain for *p53* mRNA binding, which, in turn, promotes Mdm2 SUMO-conjugation and its accumulation in the nucleolus. The *p53* mRNA-Mdm2 interaction stimulates *p53* mRNA translation and suppresses Mdm2 E3 ligase activity toward p53 and is required for p53 activation following DNA damage. Suppressing the *p53* mRNA interaction, via either a single silent point mutation in the *p53* mRNA (p53L22L) or an amino acid substitution in Mdm2 (Mdm2S395A), leads to a decrease in p53 levels upon genotoxic stress and a failure to activate the p53 pathway. These results illustrate the importance of the *p53* mRNA in the genotoxic stress pathway and how it controls the activity of Mdm2 toward the p53 protein and offers an explanation to why Mdm2 is upregulated by p53 in response to DNA damage.

damage. The activation of p53 via DNA damaged-induced modifications on the p53 N terminus have been suggested, but we observed only a relative small additive effect on p53-dependent apoptosis after doxorubicin treatment in the presence of Mdm2S395D, as compared to the differences observed using the Mdm2wt. No significant difference with or without doxorubicin was found when we knock out Mdm2 in cells expressing endogenous p53wt. This indicates that under these conditions ATM-mediated phosphorylation of p53 plays a less important role in activating p53.

It is interesting to notice that expression of a p53wt protein from the *L22L* mRNA with low affinity for Mdm2, or expression of the wild-type *p53* mRNA in the presence of the non-RNA-binding Mdm2S395A mutant, results in an increase in p53 turnover rate following genotoxic stress, as compared to the stabilization observed using *p53wt* mRNA and Mdm2wt. More recently, it was suggested that phosphorylation of the C terminus of Mdm2 induces its monomerization and prevents p53 polyubiquitination (Cheng et al., 2009). Our results do not go against this model, but they show that the phosphorylation of Ser395 induces the *p53* mRNA-Mdm2, interaction which is necessary to inhibit p53 polyubiquitination. The molecular mechanism of the *p53* mRNA-mediated control of Mdm2 E3 ligase activity is not clear and might include a direct interference with the ligase activity, disruption of Mdm2 dimerization, or the interaction with proteins interacting with the C terminus of Mdm2, such as the ubiquitin protease HAUSP (Cummins et al., 2004; Li et al., 2004, 2002).

The localization of Mdm2 to the nucleoli is an important step in p53 activation, and the observation that Mdm2 requires

phosphorylation of Ser395 and the interaction with the *p53* mRNA to locate to nucleolar structures following genotoxic stress further adds to the important role of the *p53* mRNA in controlling Mdm2 functions. The RNA-binding capacity of other nucleolar factors such as nucleolin and NRF have been suggested to play a role in their respective nucleolar accumulation (Emmott and Hiscox, 2009; Niedick et al., 2004), suggesting that RNA-directed nucleolar trafficking is a more widespread concept. The requirement for Ser395 phosphorylation and *p53* mRNA-binding in order to translocate Mdm2 to the nucleolus becomes redundant if SUMO1 is conjugated to Mdm2, indicating that these two events precede SUMO-modification and translocation. In support of the idea that phosphorylation of Ser395 is the first step in this chain of events, we observed that the Mdm2S395D mutant does not localize to the nucleolus following genotoxic stress in the absence of the *p53* mRNA. Because phosphorylation of Ser395 is required for Mdm2's interaction with the *p53* mRNA in vitro and the Mdm2S395D binds *p53* mRNA with higher affinity in the cell, it is unlikely that *p53* mRNA binding to Mdm2 would be an indirect effect of SUMO-conjugation. The role of Mdm2-interacting factors in *p53* mRNA-mediated localization of Mdm2 to the nucleoli will be addressed separately (Poyurovsky et al., 2003; Tao and Levine, 1999).

Mdm2 binds to a region of the *p53* mRNA that has been shown to contain an IRES sequence (Candeias et al., 2008; Gu et al., 2009; Ray et al., 2006). Mdm2 requires nuclear localization to bind the *p53* mRNA and promote *p53* mRNA translation during genotoxic stress, indicating that the accumulation of Mdm2 in the nucleolus serves an important function in assembling the *p53* mRNA-Mdm2 translation complex. Because eukaryotic IRES *trans*-activating factors (ITAFs) are known to shuttle between nucleus and cytoplasm, and some to require expression in the nuclear compartment in order to promote translation in response to cellular stresses, it is possible that the *trans*-localization of Mdm2 within the nucleus to support synthesis of p53 during genotoxic stress reflects a more general aspects of stress-dependent mRNA translation.

Finally, an interesting aspect of these results is that they offer an explanation to the paradox of the rapid induction of Mdm2 by p53 in response to genotoxic stress (Mendrysa and Perry, 2000). As long as the ATM pathway is active and the interaction with the *p53* mRNA is present, Mdm2 serves as a positive regulator of p53 activity but as soon as this activity ceases, Mdm2 returns to be a negative regulator to ensure the suppression of p53 activity under normal conditions.

EXPERIMENTAL PROCEDURES

Cell Lines, Protein Labeling, and Expression

All cell-based assays were performed in $p53^{-/-}$ H1299, $p53^{WT}$ MLS-1765, $ATM^{-/-}$ AT5-BIVA, or $p53^{-/-}$;$Mdm2^{-/-}$ Double-KO MEF (DKO) cells. For all experiments, transfection efficiency and mRNA levels were verified using reverse transcription quantitative PCR (RT-qPCR). ^{35}S-methionine labeling was performed by culturing cells in methionine-free medium including 2% dialyzed FCS for 1 hr and 20 μM of the proteasome inhibitor MG132 (Merck Biosciences, UK). Cells were transfected using Genejuice (Novagen). Easytag Express Protein Labeling Mix (90 μCi; ^{35}S) (PerkinElmer, Boston, USA) was added for 20 min, and p53 proteins were immunoprecipitated using CM-1 antibody and separated by SDS-PAGE. In vitro transcribed capped mRNAs (Ambion, Austin, TX, USA) were prepared according to the manufacturer's protocol. Quantification of radioactively labeled products was determined using phosphoimager (Amersham) and Storm hardware together with Bio-1D software (Vilber-Lourmat). Cycloheximide (CHX, Calbiochem), Doxorubicin (Sigma), Etoposide (Sigma), ATM Kinase Inhibitor (ATMi, Calbiochem), and wortmannin (Calbiochem) or an equal volume of dimethylsuphoxide (DMSO) were used at the concentrations of 10 μg/ml, 0.1–1 μM (depending on the sensitivity of the cell type), 20 μM, 10 μM, and 5 μM, respectively, for the time durations indicated in the figure legends. CM-1, 4B2, 4B11, 2A10, and 1.2 antibodies were all kind gifts from Borek Vojtesek. siRNAs against Mdm2 and ATM were from QIAGEN and were applied according to the manufacturer's recommendations. Cells were transfected with 0.3 μg cDNA per 6-cm dish unless otherwise stated.

His-Ubiquitin Conjugation

Cells (1×10^6) were seeded on 10-cm tissue culture plates and transfected with 0.8 μg of plasmids encoding Mdm2, 6His-Ubiquitin, and p53. Twenty-eight hours after transfection, cells were treated with 0.1 μM of doxorubicin for 16 hr. Proteasome inhibitor MG-132 (25 μM) was added 4 hr before cells were washed twice with PBS and scraped in 1 ml of lysis buffer (6 M guanidinium-HCl, 0.1 M Na_2HPO_4/NaH_2PO_4, 0.01 M Tris-HCl [pH 8], 0.005 M imidazol, and 0.01 M β-mercaptoethanol). The cells were sonicated twice for 10 sec. After sonication, 4 ml of lysis buffer was added with 75 μl of Ni2+-NTA-agarose beads (Clontech) and was incubated for 4 hr at RT with gently agitation. The beads were washed once at RT in lysis buffers, once in wash buffer (8 M urea, 0.1 M Na_2HPO_4/NaH_2PO_4, 0.01 M Tris-HCl [pH 6.8], 0.005 M imidazol, and 0.01 M β-mercaptoethanol), and twice in wash buffer plus 0.1% Triton X-100. Products were eluted by incubating beads in 75 μl of 0.2 M imidazol, 0.15 M Tris-HCl (pH 6.8), 30% glycerol, 0.72 M β-mercaptoethanol, and 5% SDS for 20 min at RT with gentle agitation. Twenty-five microliters of 4× of Laemmeli buffer were added before being analyzed by western blot.

Flow Cytometry

The measurement of the percentage of apoptotic cells in a population was effectuated as described elsewhere (Vermes et al., 1995). Briefly, transfected cells were stained with annexin V-FITC and 7-Aminoactinomycin D (7-AAD) (Sigma, Missouri, USA) and were analyzed by flow cytometry with an LSR flow cytometer and CellQuest software (Becton Dickinson, San Jose, CA, USA). The test discriminates intact cells ($FITC^-/7\text{-}AAD^-$), apoptotic cells ($FITC^+/7\text{-}AAD^-$) and necrotic cells ($FITC^+/7\text{-}AAD^+$).

Quantitative RNA Coimmunoprecipitation

Quantitative RNA Coimmunoprecipitation (qRNAco-IP) assays were based on a previous protocol (Candeias et al., 2008; Tenenbaum et al., 2002). Briefly, transfected H1299 cells were lysed with a buffer containing RNase OUT (100 U/ml, Invitrogen) and centrifuged, and supernatants were precleared with mouse IgG followed by incubation with one of the monoclonal anti-Mdm2 antibodies: SMP14 (directed against amino-acids [aa] 154–167 of Mdm2), 4B2 (recognizes the N terminus of Mdm2) or 2A10 (directed against aa 393–395, cannot bind to Mdm2 that is phosphorylated at Ser395). The complexes were pulled-down using protein G–Sepharose beads (Amersham) treated with proteinase K (Sigma), and RNA was extracted and purified using TRIzol protocol (Invitrogen). RT-qPCR was performed using primers against p53 and control genes TATA Box-binding protein and β-actin. To ensure valid quantification of RNA binding to Mdm2, standard curves were used to attest for transfection, RT-PCR, and qPCR protocols' efficiency. RT-qPCRs on total RNA were realized, and qRNAco-IP values calculated according to the following formula: (qPCRvalue p53mRNA IP / qPCRvalue p53mRNA total) / (qPCRvalue controlmRNA IP / qPCRvalue controlmRNA total). A western blot anti-Mdm2 was done in parallel, and coimmunoprecipitation data were also normalized against total Mdm2 protein when needed.

In Vitro Quantitative RNA Coimmunoprecipitation

All binding reactions were performed for 15 min at 37°C in a binding buffer containing 50 mM Tris (pH 7.5), 150 mM NaCl, 0.02 mg/ml yeast tRNA, and 0.2 mg/ml BSA. ATM protein was included after being immunoprecipitated from H1299 cells using 10 μg of phosphorylation-specific antibody anti-phospho-ATM (Ser1981) (Millipore). One hundred twenty nanograms of hMdm2 protein purified from insect cells and a fixed amount (8.10^{-3} pmol) of WT or L22L p53 mRNA were used. ATM Kinase Inhibitor (10 μM; ATMi, Calbiochem) or 5 μM of

wortmannin (Calbiochem) were added to the reaction where indicated. After incubation, RNA-protein complexes were pulled-down using monoclonal anti-Mdm2 antibodies 4B2 or 2A10 and protein G beads (Amersham). The unbound fraction was recovered for later analysis, and the bound RNA was treated with proteinase K (Sigma). The bound and free RNA fractions were then extracted and purified using TRIzol protocol (Invitrogen). RT-qPCR was performed on these fractions using primers against p53. The binding results were expressed as a ratio between the bound and the total (bound+free) RNA.

Protein-RNA ELISA Assay

Ninety-six-well plates were coated with streptavidin (100 μg/ml in 0.1 M NaHCO3; 50 μl/well) overnight at 4°C. After incubation, plates were washed six times with 200 μl PBS-T and blocked with 50 μl of 3% BSA and 0.1 μg/ml of streptavidin in PBS overnight at 4°C. The plates were washed four times with 0.1% PBS-Tween. A mix of biotinylated RNA (5 pmol) and different amounts of protein previously incubated in a binding buffer containing 50 mM Tris (pH 7.5), 150 mM NaCl, 0.02 mg/ml yeast tRNA, and 0.2 mg/ml BSA for 30 min at 37°C were added to the plates (50 μl/well) and incubated 1 hr at RT. The plates were washed six times with 200μl/well PBS-T, and the 6His mAB/HRP conjugate (Clontech) in PBS 1:1000 (50 μl/well) was added and incubated for 1 hr at RT. Plates were washed six times with 200 μl/well PBS-T, and 50 μl/well of a mix of ECL was added and luminescence was measured. Biotinylated MS2 RNA oligonucleotide was used as a negative control to RNA binding specificity.

Immunofluorescence and Fluorescence Microscopy

H1299 cells were grown on coverslips and treated as indicated. Cells were fixed in 4% paraformaldehyde for 10 min before permeabilization in PBS containing 0.1% Triton X-100 for 2 min. The antibodies used for immunofluorescence microscopy were anti-PML (rabbit; Abcam), anti-Mdm2 (mouse; 4B2; gift from B. Vojtesek), anti-nucleolin (mouse; Abcam), and anti-SUMO1 anti-SUMO2 (sheep; gift from R.T. Hay). Double staining was performed as indicated. For detection, cells were incubated with Alexa-488-conjugated (Invitrogen) or Cy5-conjugated (Molecular probes) anti-rabbit antibodies and Alexa Fluor-568-conjugated (Invitrogen) or Alexa Fluor-633-conjugated (Invitrogen) anti-mouse antibodies.

Duolink

Duolink (Olink) was performed according to the manufacturer's instructions. Briefly, H1299 cells were grown on coverslips and then fixed in 4% paraformaldehyde for 10 min before permeabilization in PBS containing 0.1% Triton X-100 for 2 min. Cells were then blocked in 3% BSA/BPS and primary antibodies were incubated (anti-Mdm2, anti-SUMO1, and anti-SUMO2). After washing the cells, PLA probes were added, followed by hybridization, ligation, and amplification for 90 min at 37°C. DNA (blue) and Mdm2-SUMO interactions (red) were visualized after incubation with the Detection solution. Slides were analyzed by fluorescence microscopy.

SUPPLEMENTAL INFORMATION

Supplemental Information includes five figures and can be found with this article online at doi:10.1016/j.ccr.2011.11.016.

ACKNOWLEDGMENTS

We thank Niclas Zetterblad for confocal microscopy assistance, K. Komatsu for AT5-BIVA cells, Frank Toledo for Mdm2$^{-/-}$/p53$^{-/-}$ MEFs, Y. Shiloh for ATM, and Y. Minami for Wip1. Anti-p53 and anti-Mdm2 antibodies were a gift from B. Vojtesek, and anti-SUMO1 and -SUMO2 antibodies were from R.T. Hay. This work was supported by INSERM, La Ligue Contre le Cancer, and RECAMO CZ.1.05/2.1.00/03.0101. M.M.C. was supported by JSPS, AXA Research Fund, and Fundação para a Ciência e a Tecnologia of Portugal. M.G. was supported by a research fellowship from Indo-French Centre for the Promotion of Advanced Research (IFCPAR) and from the ARC.

Received: May 23, 2011
Revised: September 15, 2011
Accepted: November 23, 2011
Published: January 17, 2012

REFERENCES

Banin, S., Moyal, L., Shieh, S., Taya, Y., Anderson, C.W., Chessa, L., Smorodinsky, N.I., Prives, C., Reiss, Y., Shiloh, Y., and Ziv, Y. (1998). Enhanced phosphorylation of p53 by ATM in response to DNA damage. Science *281*, 1674–1677.

Bartek, J., Bartkova, J., and Lukas, J. (2007). DNA damage signalling guards against activated oncogenes and tumour progression. Oncogene *26*, 7773–7779.

Bernardi, R., and Pandolfi, P.P. (2007). Structure, dynamics and functions of promyelocytic leukaemia nuclear bodies. Nat. Rev. Mol. Cell Biol. *8*, 1006–1016.

Bernardi, R., Scaglioni, P.P., Bergmann, S., Horn, H.F., Vousden, K.H., and Pandolfi, P.P. (2004). PML regulates p53 stability by sequestering Mdm2 to the nucleolus. Nat. Cell Biol. *6*, 665–672.

Boulon, S., Westman, B.J., Hutten, S., Boisvert, F.M., and Lamond, A.I. (2010). The nucleolus under stress. Mol. Cell *40*, 216–227.

Candeias, M.M., Malbert-Colas, L., Powell, D.J., Daskalogianni, C., Maslon, M.M., Naski, N., Bourougaa, K., Calvo, F., and Fåhraeus, R. (2008). P53 mRNA controls p53 activity by managing Mdm2 functions. Nat. Cell Biol. *10*, 1098–1105.

Canman, C.E., Lim, D.S., Cimprich, K.A., Taya, Y., Tamai, K., Sakaguchi, K., Appella, E., Kastan, M.B., and Siliciano, J.D. (1998). Activation of the ATM kinase by ionizing radiation and phosphorylation of p53. Science *281*, 1677–1679.

Cheng, Q., Chen, L., Li, Z., Lane, W.S., and Chen, J. (2009). ATM activates p53 by regulating MDM2 oligomerization and E3 processivity. EMBO J. *28*, 3857–3867.

Cohen, N., Sharma, M., Kentsis, A., Perez, J.M., Strudwick, S., and Borden, K.L. (2001). PML RING suppresses oncogenic transformation by reducing the affinity of eIF4E for mRNA. EMBO J. *20*, 4547–4559.

Cummins, J.M., Rago, C., Kohli, M., Kinzler, K.W., Lengauer, C., and Vogelstein, B. (2004). Tumour suppression: disruption of HAUSP gene stabilizes p53. Nature *428*, 486.

Deisenroth, C., and Zhang, Y. (2010). Ribosome biogenesis surveillance: probing the ribosomal protein-Mdm2-p53 pathway. Oncogene *29*, 4253–4260.

Elenbaas, B., Dobbelstein, M., Roth, J., Shenk, T., and Levine, A.J. (1996). The MDM2 oncoprotein binds specifically to RNA through its RING finger domain. Mol. Med. *2*, 439–451.

Emmott, E., and Hiscox, J.A. (2009). Nucleolar targeting: the hub of the matter. EMBO Rep. *10*, 231–238.

Goldberg, Z., Vogt Sionov, R., Berger, M., Zwang, Y., Perets, R., Van Etten, R.A., Oren, M., Taya, Y., and Haupt, Y. (2002). Tyrosine phosphorylation of Mdm2 by c-Abl: implications for p53 regulation. EMBO J. *21*, 3715–3727.

Gu, L., Zhu, N., Zhang, H., Durden, D.L., Feng, Y., and Zhou, M. (2009). Regulation of XIAP translation and induction by MDM2 following irradiation. Cancer Cell *15*, 363–375.

Heun, P. (2007). SUMOrganization of the nucleus. Curr. Opin. Cell Biol. *19*, 350–355.

Honda, R., Tanaka, H., and Yasuda, H. (1997). Oncoprotein MDM2 is a ubiquitin ligase E3 for tumor suppressor p53. FEBS Lett. *420*, 25–27.

Ideue, T., Azad, A.K., Yoshida, J., Matsusaka, T., Yanagida, M., Ohshima, Y., and Tani, T. (2004). The nucleolus is involved in mRNA export from the nucleus in fission yeast. J. Cell Sci. *117*, 2887–2895.

Jimenez, G.S., Khan, S.H., Stommel, J.M., and Wahl, G.M. (1999). p53 regulation by post-translational modification and nuclear retention in response to diverse stresses. Oncogene *18*, 7656–7665.

Khanna, K.K., Keating, K.E., Kozlov, S., Scott, S., Gatei, M., Hobson, K., Taya, Y., Gabrielli, B., Chan, D., Lees-Miller, S.P., and Lavin, M.F. (1998). ATM associates with and phosphorylates p53: mapping the region of interaction. Nat. Genet. *20*, 398–400.

Kitagawa, R., and Kastan, M.B. (2005). The ATM-dependent DNA damage signaling pathway. Cold Spring Harb. Symp. Quant. Biol. *70*, 99–109.

Kurki, S., Latonen, L., and Laiho, M. (2003). Cellular stress and DNA damage invoke temporally distinct Mdm2, p53 and PML complexes and damage-specific nuclear relocalization. J. Cell Sci. *116*, 3917–3925.

Lallemand-Breitenbach, V., and de Thé, H. (2010). PML nuclear bodies. Cold Spring Harb. Perspect. Biol. *2*, a000661.

Li, M., Chen, D., Shiloh, A., Luo, J., Nikolaev, A.Y., Qin, J., and Gu, W. (2002). Deubiquitination of p53 by HAUSP is an important pathway for p53 stabilization. Nature *416*, 648–653.

Li, M., Brooks, C.L., Wu-Baer, F., Chen, D., Baer, R., and Gu, W. (2003). Mono- versus polyubiquitination: differential control of p53 fate by Mdm2. Science *302*, 1972–1975.

Li, M., Brooks, C.L., Kon, N., and Gu, W. (2004). A dynamic role of HAUSP in the p53-Mdm2 pathway. Mol. Cell *13*, 879–886.

Linares, L.K., and Scheffner, M. (2003). The ubiquitin-protein ligase activity of Hdm2 is inhibited by nucleic acids. FEBS Lett. *554*, 73–76.

Lohrum, M.A., Ashcroft, M., Kubbutat, M.H., and Vousden, K.H. (2000). Identification of a cryptic nucleolar-localization signal in MDM2. Nat. Cell Biol. *2*, 179–181.

Lu, X., Nannenga, B., and Donehower, L.A. (2005). PPM1D dephosphorylates Chk1 and p53 and abrogates cell cycle checkpoints. Genes Dev. *19*, 1162–1174.

Lu, X., Ma, O., Nguyen, T.A., Jones, S.N., Oren, M., and Donehower, L.A. (2007). The Wip1 Phosphatase acts as a gatekeeper in the p53-Mdm2 autoregulatory loop. Cancer Cell *12*, 342–354.

Maya, R., Balass, M., Kim, S.T., Shkedy, D., Leal, J.F., Shifman, O., Moas, M., Buschmann, T., Ronai, Z., Shiloh, Y., et al. (2001). ATM-dependent phosphorylation of Mdm2 on serine 395: role in p53 activation by DNA damage. Genes Dev. *15*, 1067–1077.

Mendrysa, S.M., and Perry, M.E. (2000). The p53 tumor suppressor protein does not regulate expression of its own inhibitor, MDM2, except under conditions of stress. Mol. Cell. Biol. *20*, 2023–2030.

Naski, N., Gajjar, M., Bourougaa, K., Malbert-Colas, L., Fåhraeus, R., and Candeias, M.M. (2009). The p53 mRNA-Mdm2 interaction. Cell Cycle *8*, 31–34.

Niedick, I., Froese, N., Oumard, A., Mueller, P.P., Nourbakhsh, M., Hauser, H., and Köster, M. (2004). Nucleolar localization and mobility analysis of the NF-kappaB repressing factor NRF. J. Cell Sci. *117*, 3447–3458.

O'Keefe, K., Li, H., and Zhang, Y. (2003). Nucleocytoplasmic shuttling of p53 is essential for MDM2-mediated cytoplasmic degradation but not ubiquitination. Mol. Cell. Biol. *23*, 6396–6405.

Ofir-Rosenfeld, Y., Boggs, K., Michael, D., Kastan, M.B., and Oren, M. (2008). Mdm2 regulates p53 mRNA translation through inhibitory interactions with ribosomal protein L26. Mol. Cell *32*, 180–189.

Oliner, J.D., Pietenpol, J.A., Thiagalingam, S., Gyuris, J., Kinzler, K.W., and Vogelstein, B. (1993). Oncoprotein MDM2 conceals the activation domain of tumour suppressor p53. Nature *362*, 857–860.

Perry, M.E. (2004). Mdm2 in the response to radiation. Mol. Cancer Res. *2*, 9–19.

Poyurovsky, M.V., Jacq, X., Ma, C., Karni-Schmidt, O., Parker, P.J., Chalfie, M., Manley, J.L., and Prives, C. (2003). Nucleotide binding by the Mdm2 RING domain facilitates Arf-independent Mdm2 nucleolar localization. Mol. Cell *12*, 875–887.

Ray, P.S., Grover, R., and Das, S. (2006). Two internal ribosome entry sites mediate the translation of p53 isoforms. EMBO Rep. *7*, 404–410.

Shieh, S.Y., Ikeda, M., Taya, Y., and Prives, C. (1997). DNA damage-induced phosphorylation of p53 alleviates inhibition by MDM2. Cell *91*, 325–334.

Shiloh, Y. (2003). ATM and related protein kinases: safeguarding genome integrity. Nat. Rev. Cancer *3*, 155–168.

Shreeram, S., Demidov, O.N., Hee, W.K., Yamaguchi, H., Onishi, N., Kek, C., Timofeev, O.N., Dudgeon, C., Fornace, A.J., Anderson, C.W., et al. (2006). Wip1 phosphatase modulates ATM-dependent signaling pathways. Mol. Cell *23*, 757–764.

Tao, W., and Levine, A.J. (1999). P19(ARF) stabilizes p53 by blocking nucleo-cytoplasmic shuttling of Mdm2. Proc. Natl. Acad. Sci. USA *96*, 6937–6941.

Tenenbaum, S.A., Lager, P.J., Carson, C.C., and Keene, J.D. (2002). Ribonomics: identifying mRNA subsets in mRNP complexes using antibodies to RNA-binding proteins and genomic arrays. Methods *26*, 191–198.

Thrower, J.S., Hoffman, L., Rechsteiner, M., and Pickart, C.M. (2000). Recognition of the polyubiquitin proteolytic signal. EMBO J. *19*, 94–102.

Vermes, I., Haanen, C., Steffens-Nakken, H., and Reutelingsperger, C. (1995). A novel assay for apoptosis: flow cytometric detection of phosphatidylserine expression on early apoptotic cells using fluorescein labelled Annexin V. J. Immunol. Methods *184*, 39–51.

Weber, J.D., Taylor, L.J., Roussel, M.F., Sherr, C.J., and Bar-Sagi, D. (1999). Nucleolar Arf sequesters Mdm2 and activates p53. Nat. Cell Biol. *1*, 20–26.

Yoda, A., Toyoshima, K., Watanabe, Y., Onishi, N., Hazaka, Y., Tsukuda, Y., Tsukada, J., Kondo, T., Tanaka, Y., and Minami, Y. (2008). Arsenic trioxide augments Chk2/p53-mediated apoptosis by inhibiting oncogenic Wip1 phosphatase. J. Biol. Chem. *283*, 18969–18979.

Zhu, J., Zhou, W., Jiang, J., and Chen, X. (1998). Identification of a novel p53 functional domain that is necessary for mediating apoptosis. J. Biol. Chem. *273*, 13030–13036.

Cancer Cell
Article

Bile Acid and Inflammation Activate Gastric Cardia Stem Cells in a Mouse Model of Barrett-Like Metaplasia

Michael Quante,[1,2,10,*] Govind Bhagat,[2,3] Julian A. Abrams,[1,2] Frederic Marache,[1,2] Pamela Good,[1,2] Michele D. Lee,[1,2] Yoomi Lee,[4] Richard Friedman,[5] Samuel Asfaha,[1,2] Zinaida Dubeykovskaya,[1,2] Umar Mahmood,[7] Jose-Luiz Figueiredo,[8] Jan Kitajewski,[2,6] Carrie Shawber,[2,6] Charles J. Lightdale,[1,2] Anil K. Rustgi,[9] and Timothy C. Wang[1,2,*]

[1]Division of Digestive and Liver Diseases, Department of Medicine
[2]Herbert Irving Comprehensive Cancer Center
[3]Department of Pathology and Cell Biology
[4]Division of Hematology and Oncology, Department of Medicine
[5]Department of Biomedical Informatics
[6]Department of Pathology, Obstetrics and Gynecology
Columbia University Medical Center, New York, NY 10032, USA
[7]Nuclear Medicine and Molecular Imaging
[8]Center for Systems Biology
Harvard Medical School and Massachusetts General Hospital, Boston, MA 02114, USA
[9]Division of Gastroenterology, Department of Medicine and Genetics, Abramson Cancer Center, University of Pennsylvania, Philadelphia, PA 19104, USA
[10]II. Medizinische Klinik, Klinikum rechts der Isar, Technische Universität München, 81675 Munich, Germany
*Correspondence: michael.quante@lrz.tum.de (M.Q.), tcw21@columbia.edu (T.C.W.)
DOI 10.1016/j.ccr.2011.12.004

SUMMARY

Esophageal adenocarcinoma (EAC) arises from Barrett esophagus (BE), intestinal-like columnar metaplasia linked to reflux esophagitis. In a transgenic mouse model of BE, esophageal overexpression of interleukin-1β phenocopies human pathology with evolution of esophagitis, Barrett-like metaplasia and EAC. Histopathology and gene signatures closely resembled human BE, with upregulation of TFF2, Bmp4, Cdx2, Notch1, and IL-6. The development of BE and EAC was accelerated by exposure to bile acids and/or nitrosamines, and inhibited by IL-6 deficiency. Lgr5^{+} gastric cardia stem cells present in BE were able to lineage trace the early BE lesion. Our data suggest that BE and EAC arise from gastric progenitors due to a tumor-promoting IL-1β-IL-6 signaling cascade and Dll1-dependent Notch signaling.

INTRODUCTION

Esophageal adenocarcinoma (EAC) has been linked to chronic inflammation of the esophagus and its incidence has increased by more than 500% since the 1970s (Corley et al., 2009) despite powerful acid suppressant medications (proton pump inhibitors) and a decline in the prevalence of *Helicobacter pylori* in the United States and Europe. The main risk factor for EAC is Barrett esophagus (BE), involving a progression from BE to low-grade/high-grade dysplasia (Falk, 2002). The precise origin of both EAC and BE has been difficult to discern in part because of the absence of useful experimental model systems that are genetically based.

BE has been attributed primarily to gastroesophageal reflux disease (GERD), leading to chronic inflammation of the esophagus. The link between inflammation and cancer is well established (Grivennikov et al., 2010); in particular, elevated IL-6 has been identified as a key mediator of tumorigenesis in murine models of cancer (Grivennikov and Karin, 2008). IL-1β, a pleiotropic pro-inflammatory cytokine upstream of IL-6 and

Significance

Using a transgenic mouse model of BE and EAC, that closely resembles the human disease, insights into the pathogenesis of BE are provided. A gastric cardia progenitor cell lineage appears to be activated by bile acid-induced and IL-1β- and IL-6-dependent inflammation, inducing migration into the distal esophagus where it gives rise to columnar-like metaplasia and dysplasia. Activated Notch signaling appears to regulate differentiation of the cardia progenitor into intestinal-type columnar cells instead of goblet cells, and is associated with a malignant transformation in mice and humans. Our findings challenge the common paradigms regarding the pathogenesis of BE and EAC.

TNF-α signaling cascades, has been demonstrated to induce tumorigenesis of the mouse stomach (Tu et al., 2008). IL-1β is overexpressed in BE, and clinical studies have suggested that polymorphisms in the *IL-1β* gene cluster are associated with BE (Fitzgerald et al., 2002; Gough et al., 2005; O'Riordan et al., 2005).

BE is defined as replacement of the stratified squamous epithelium in the distal esophagus with a metaplastic, intestinal-like columnar epithelium (Spechler et al., 2010). Whereas attention in the past has been focused on goblet cells (i.e., classical intestinal metaplasia [IM]) as the primary marker for BE, the recent change in the definition to include nongoblet, columnar lined esophagus ([CLE], resembling intestinal and cardia metaplasia) was made to acknowledge the more variable histologic presentation of BE. A major unanswered question that has been debated for decades, is whether the BE cell of origin derives from transdifferentiation of the esophageal squamous epithelium (Yu et al., 2005), or originates rather from a progenitor cell in the esophagus (Kalabis et al., 2008), the esophageal submucosal glands (Leedham et al., 2008), residual embryonic cells located at the squamocolumnar junction (Wang et al., 2011), or, as early investigators proposed, the gastric cardia (Allison and Johnstone, 1953; Barbera and Fitzgerald, 2010; Hamilton and Yardley, 1977; Nakanishi et al., 2007). However, prior to the development of IM, a regenerative intestinal-like columnar cell lineage appears in the esophagus that expresses TFF2, KRT8, KRT20, NOTCH, and CDX2 (Hanby et al., 1994; Menke et al., 2010; Stairs et al., 2008; Tatsuta et al., 2005). It is crucial to identify the progenitors responsible for BE, given the preneoplastic nature of the lesion.

Until recently, the primary animal model used to study BE has been a rat model comprising esophagojejunostomy that induces gastroduodenal reflux (Fein et al., 1998; Li and Martin, 2007). The observation that duodenesophageal reflux induces EAC in rats points to the importance of refluxed duodenal contents in the pathogenesis of BE. Bile acids, particularly unconjugated bile acids such as deoxycholate (DCA) that induce DNA damage, are one component of gastroduodenal reflux that have been linked strongly to the development of BE. Reflux injury in the esophagus results in chronic inflammation with upregulation of numerous cytokines, such as IL-1β, IL-6, and IL-8, that might contribute to the metaplastic and dysplastic conversion of BE (Fitzgerald et al., 2002). Here, we aimed to utilize a model of Barrett-like metaplasia, involving overexpression of IL-1β, to provide insights into the origins of Barrett esophagus.

RESULTS

Interleukin-1β Overexpression in the Mouse Esophagus Induces Esophagitis, Barrett-Like Metaplasia, and Neoplasia

To understand the pathogenesis of BE and EAC we generated a model of chronic esophageal inflammation, inserting the modified human *IL-1β* cDNA (Björkdahl et al., 1999) downstream of an Epstein-Barr virus (ED-L2) promoter that targets the oral cavity, esophagus, and squamous forestomach (Figure S1A available online) (Nakagawa et al., 1997). In two founder lines we observed high (Line 1) and low levels (Line 2) of specific esophageal (and forestomach) hIL-1β mRNA and protein expression (Figures 1A and 1B) that correlated with upregulated IL1-receptor-antagonist (IL1ra), indicative of IL-1 receptor signaling (Figure 1C). No hIL-1β mRNA and protein expression was observed in the glandular stomach or elsewhere (Figures 1A and 1D). *L2-IL-1β* mice developed splenomegaly (Figure S1C) that correlated with age dependent IL-1β expression levels (Figure 1B), consistent with a systemic inflammatory reaction and at least 10-fold elevated ($p < 0.05$) circulating levels of IL-1β, TNFα (Figure S1D), and IL-6 (Figure 1D).

The esophagus and squamous forestomach in the low and high expressing *L2-IL-1β* mice were markedly thickened with a mixed acute and chronic inflammatory infiltrate compared to age-matched wild-type (WT) mice (Figure S1B). However, the major histopathological changes in *L2-IL-1β* mice occurred at the squamocolumnar junction (SCJ), an anatomical location where the squamous and gastric columnar epithelium meet (Figure 1E) and where the esophagus enters the stomach. Compared to the human SCJ, the mouse esophagus enters the stomach at the midpoint of the lesser curvature of the stomach, at the junction between the glandular stomach and squamous forestomach, forming a SCJ that traverses the entire stomach and resembles the Z line in the human esophagus (Figure S1E). To determine whether the L2-IL-1β mice develop metaplasia resembling human BE, histological evaluation was performed on sagittal sections through the esophagus and stomach (Figure S1E, yellow line). Based upon previously described criteria (Fox et al., 2000), a histopathological scoring system for the mouse SCJ was developed. In 100% (10/10) of the 6-month-old *L2-IL-1β* mice, we observed moderate inflammation and profound epithelial hyperplasia (Figure 1F) that was never observed in age-matched WT mice. Proliferation was increased significantly in the esophageal basal compartment (Figure 2A).

In *L2-IL-1β* mice that were 12–15 months of age, 90% (9/10) developed severe columnar metaplasia (Figures 1E and 1F) with mucus producing (*Muc5ac*$^+$, PAS$^+$) cells (Figure 2A) at the SCJ, similar to human BE. Although classical goblet cells were not observed in *L2-IL-1β* mice, the mucus producing columnar cell types observed were consistent with Barrett-like metaplasia. *Tff2*, a marker for metaplasia in human BE (Van De Bovenkamp et al., 2003; Warson et al., 2002), and also an oxyntic progenitor cell marker in the gastric corpus (Quante et al., 2010), was not expressed in the WT esophagus but was upregulated above the SCJ of *L2-IL-1β* mice harboring metaplasia but not in dysplasia (Figure 2A). Electron microscopy studies revealed nearly identical ultrastructural features (columnar cell type, microvilli, granules, mucins) in human and mouse BE (Figure 2B). At 20–22 months of age, 20% (2/9) of *L2-IL-1β* mice developed high-grade dysplasia (HGD) or intramucosal EAC (Figures 1E–1G). These lesions were grossly visible within the distal end of the esophagus (Figure 1G) and were associated with significant weight loss (28% ± 4%, $p < 0.05$; data not shown). During this stepwise progression to cancer, we observed a gradual increase in αSMA$^+$ stromal myofibroblasts (Figure 2A) and increasing stroma global hypomethylation (Figure S2) in BE and HGD compared to WT, consistent with other models of inflammation-induced cancer (Jiang et al., 2008). Although hypomethylation was prominent in the stroma, we could not exclude (and

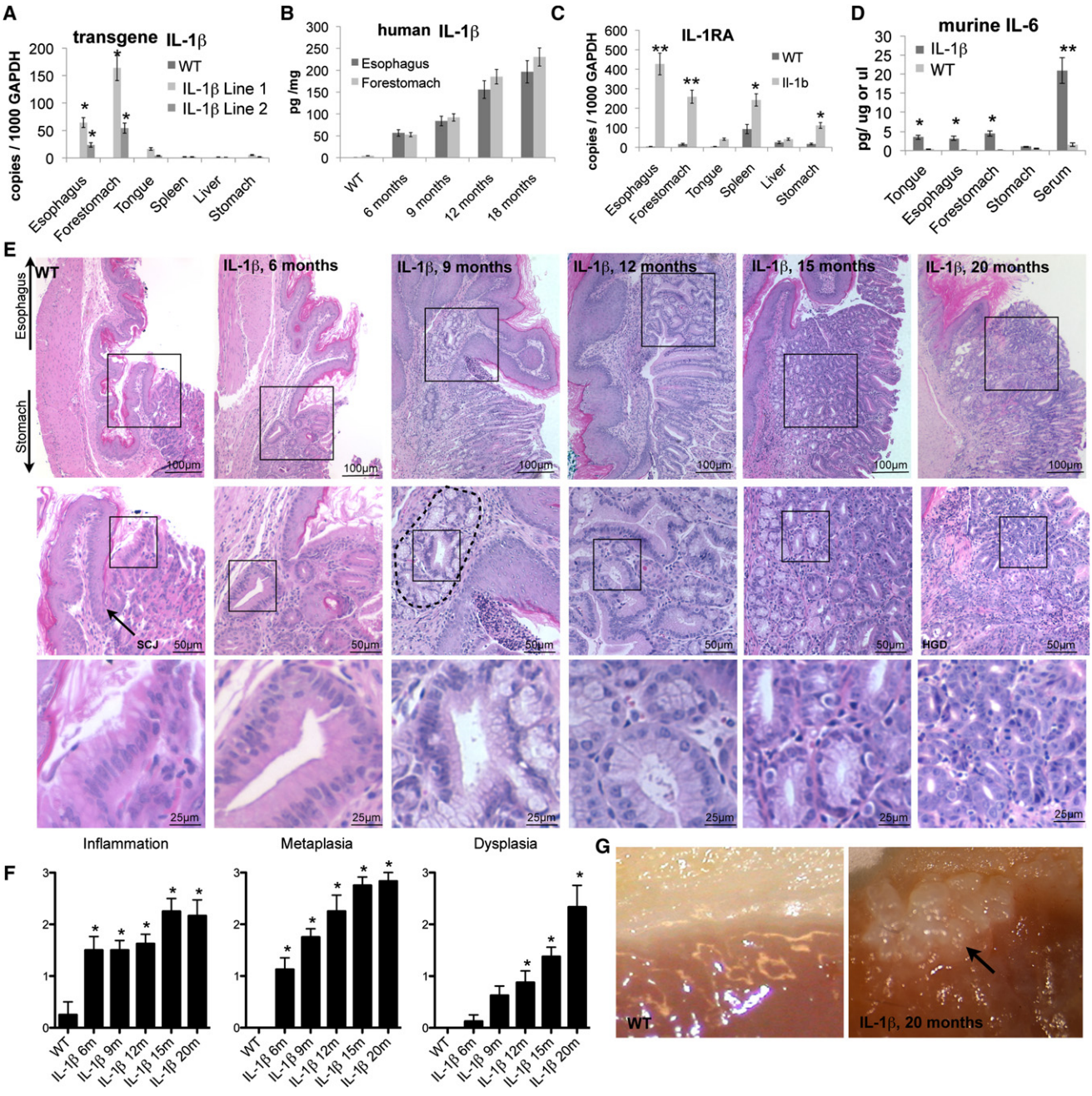

Figure 1. Overexpression of IL-1β-Induced Chronic Inflammation in the Murine Esophagus and Stepwise Development of Metaplasia and Dysplasia at the SCJ

(A) mRNA expression (RT-qPCR) in different organs of 3-month-old two founder *L2-IL-1β*-lines.

(B) ELISA for human (transgenic) IL-1β showed age dependent hIL-1β protein expression levels.

(C) mRNA expression (RT-qPCR) of IL1-receptor-antagonist (*IL1ra*) in different organs in 12-month-old *L2-IL-1β* mice compared to WT littermates.

(D) ELISA for serum levels and organ protein expression of mIL-6 in *L2-IL-1β* mice compared to WT (C57/B6) littermates.

(E) Histopathologic changes in *L2-IL-1β* mice occurred at the squamo-columnar junction (SCJ, arrow in WT). Representative pictures of WT and 6-, 9-, 12-, 15-, and 20-month-old *L2-IL-1β*, top panels show an overview of the SCJ, where the squamous esophagus epithelium meets the columnar cardia/stomach epithelium, second and third panels show inset magnifications of the stepwise progression to BE and EAC.

(F) Histopathologic scoring of 6-, 9-, 12-, 15-, and 20-month-old *L2-IL-1β* mice compared to WT (C57/B6) littermates.

(G) Representative gross pictures of the SCJ in WT and 20 months old *L2-IL-1β* mice with tumor (arrow). Data are represented as mean ± SEM. *$p < 0.05$, **$p < 0.01$. See also Figure S1.

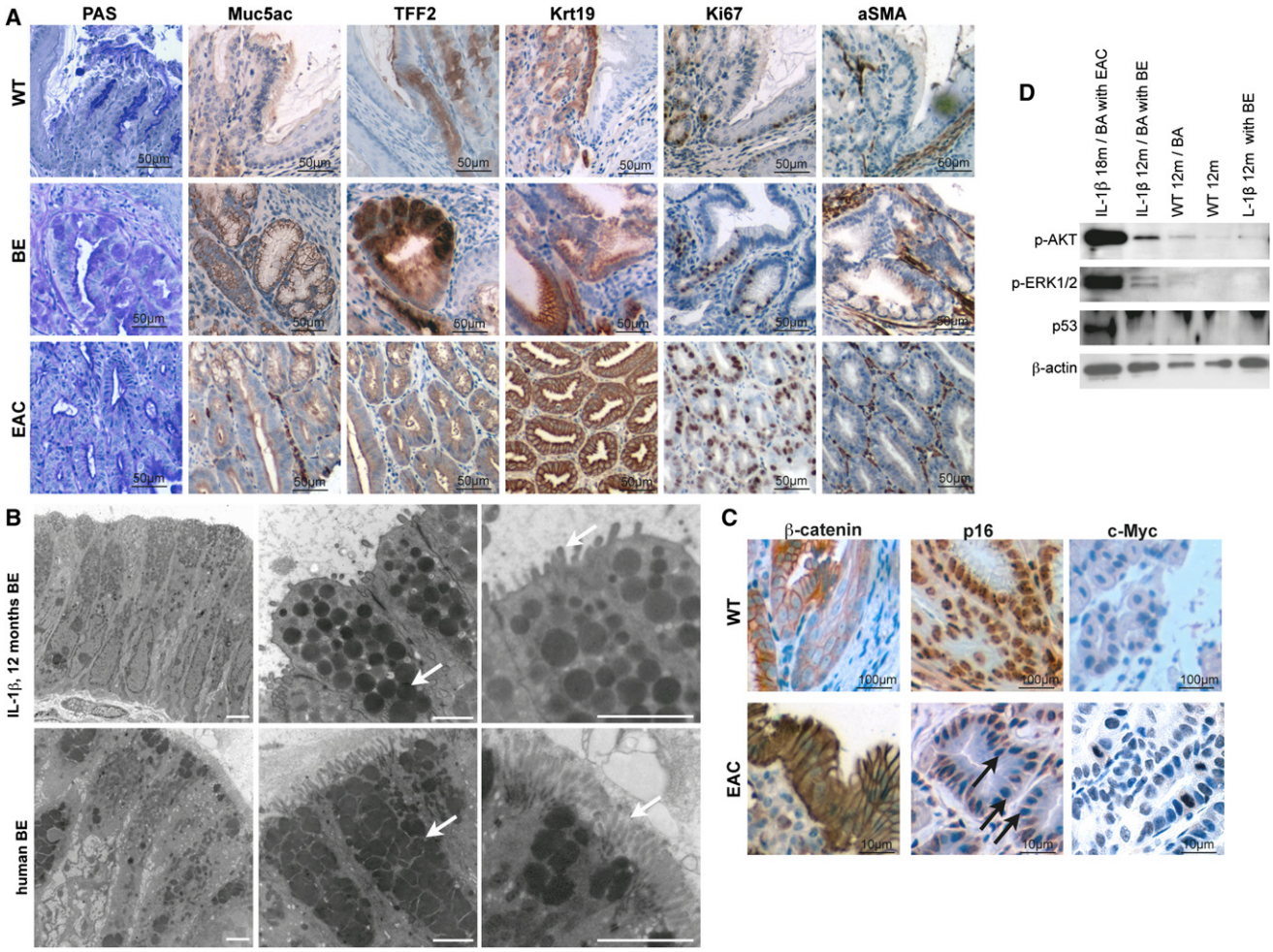

Figure 2. IL-1β Mouse Model Resembles the Human Disease

(A) Representative pictures of staining for PAS, Muc5ac, Krt19, Tff2, Ki67, and αSma of normal SCJ histology in WT (left panel), BE histology in 15-month-old *L2-IL-1*β mice (middle panel), and HGD histology in 22-month-old *L2-IL-1*β mice (right panel).

(B) Representative electron microscopy pictures of mouse (top panel) human (bottom panel) BE epithelium showing columnar cells (left), granules with mucin (middle), and microvilli (right). Scale bar represents 2 μm.

(C) Representative pictures of β-catenin, p16 and c-*myc* in WT mice and dysplastic tissue of 16-month-old BA-treated *L2-IL-1*β mice.

(D) Western blot for p53, p-Erk, and p-Akt in indicated tissues, showing p53 stabilization, and activation of Akt and Erk pathways in EAC- and BA-treated BE. See also Figure S2 and Table S1.

indeed suspect) gene specific hypermethylation in epithelial cells as described in humans (Sato and Meltzer, 2006).

Within the epithelial compartment, we observed stabilization of nuclear β-catenin (Figure 2C), a finding suggested by gene expression microarrays of WT and HGD tissue following laser capture microdissection (LCM) of metaplastic lesions in *L2-IL-1*β mice (Table S1). This microarray analysis confirmed an upregulation of β-*catenin*, *EVI1*, and *RRas* in the tumors, consistent with activation of these pathways. Pathway analysis also revealed markedly increased phosphorylation of Akt and Erk in HGD samples (Figure 2D), compared to only a slight increase in BE-like metaplasia, especially after bile acid treatment, and absent expression in WT cardia tissue (Figure 2D). We also observed occasional loss of p16 and increased c-Myc expression or stabilization of p53 in the neoplastic epithelium (Figures 2C and 2D), thus demonstrating involvement in our mouse model of BE/EAC of a number of pathways relevant to human BE and EAC.

Bile Acids and Carcinogens Accelerate the Development of Barrett-Like Metaplasia and Dysplasia that Can Be Diagnosed Endoscopically in the Mouse

BE and EAC have been attributed to acid reflux leading to chronic esophagitis. In our mouse model of chronic inflammation, Barrett-like metaplasia and dysplasia appeared to be more dependent upon IL-1β overexpression than acid exposure, because both WT mice and *L2-IL-1*β mice were kept on acidified water (pH $\leq$ 2.0) but pathological changes were evident only in the *EL2-IL-1*β mice. Unconjugated bile acids are another component of gastroduodenal reflux that has been linked to the development of BE. Consequently, we treated 2–3-month-old *L2-IL-1*β mice (line 2) and WT littermates with an unconjugated

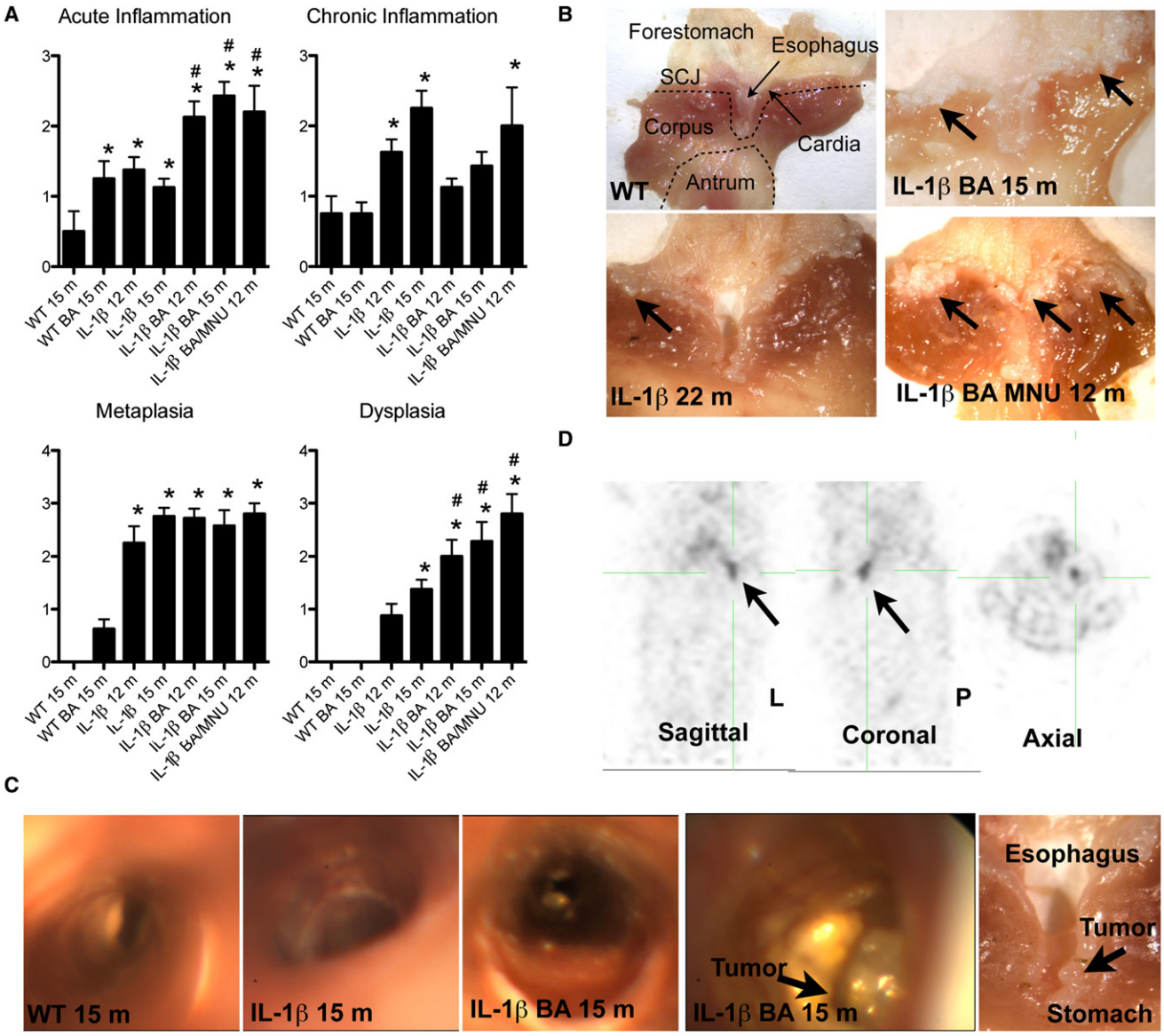

Figure 3. Bile Acids and Carcinogens Accelerate the Development of Barrett Metaplasia and Dysplasia

(A) Histopathological scoring of 6-, 9-, 12-, and 15-month-old BA-treated *L2-IL-1*β mice and combined 12 months old BA and N-methyl-N-nitrosourea (MNU)-treated *L2-IL-1*β mice compared to WT (C57/B6) littermates (*$p < 0.05$ compared to WT, #$p < 0.05$ compared to untreated *L2-IL-1*β mice).

(B) Representative gross pictures of the SCJ in WT, 22-month-old *L2-IL-1*β mice, 15-month-old BA-treated *L2-IL-1*β mice, and combined BA and MNU-treated 12-month-old *L2-IL-1*β mice with tumors at the SCJ.

(C) Representative pictures of the esophagus and SCJ during upper endoscopy in intact 15-month-old BA-treated or untreated *L2-IL-1*β mice and WT mice and corresponding gross macroscopic evaluation (right).

(D) PET imaging was performed on a rodent microPET scanner to measure glucose uptake in tumors relative to normal tissue. A representative picture of 15-month-old BA-treated *L2-IL-1*β mice is shown in sagittal, coronal, and axial position (arrow indicates the tumor that was macroscopically and histologically confirmed). Data are represented as mean ± SEM. See also Movies S1–S5 and Figure S3.

bile acid ([BA], 0.2% deoxycholate) in the drinking water (pH 7) and analyzed the mice at 6, 9, 12, and 15 months (Figure S3A). Due to issues of solubility, BA were administered in pH 7.0 water, thus eliminating the possibility of acid exposure.

Six-month-old BA-treated *L2-IL-1*β mice showed severe esophagitis with inflammatory infiltrates, but only moderate changes were observed in BA-treated WT mice (Figures 3A and 3B). Sixty percent (6/10) of 9-month-old BA-treated *L2-IL-1*β mice showed metaplastic changes at the SCJ, with higher overall metaplasia scores compared to untreated *L2-IL-1*β mice (2.7 versus 1.8, $p < 0.05$) (Figure 3A; Figure S3C), indicating a significant acceleration by BA of Barrett-like metaplasia. Moreover, we observed more severe metaplasia and dysplasia in BA-treated *L2-IL-1*β mice compared to untreated *L2-IL-1*β mice at both 12 months (dysplasia score 2.1 versus 1.0, $p < 0.05$) and 15 months (dysplasia score 2.4 versus 1.4,

$p < 0.01$) (Figure 3A; Figure S3C). Forty percent (4/9) of 15-month-old BA-treated *L2-IL-1β* mice presented with macroscopically visible tumors in the distal esophagus (Figure 3B), and exhibited significant weight loss consistent with partially obstructive lesions. These data suggest that BA play a significant role in the pathogenesis of BE and dysplasia, although we did not use bile acids at pH 2.0 and cannot rule out that gastric acid might also have a role in esophageal carcinogenesis.

N-nitrosamines are generated typically at the SCJ from reduction of salivary nitrite to nitric oxide in response to gastric juice (Winter et al., 2007) and might play a role in the pathogenesis of BE. N-methyl-N-nitrosourea (MNU) is a known gastric carcinogen for mice (Tomita et al., 2011), but does not appear to promote transformation of the noninflamed esophageal epithelium (Figures S3A and S3B). Mucosa that is chronically inflamed is thought to be more sensitive to the effects of luminal carcinogens (Winter et al., 2007). Thus, in comparison to BA+MNU-treated WT mice (Figure S3B), we observed a significant increase in tumor development in 12-month-old BA+MNU-treated *L2-IL-1β* mice (Figures 3A and 3B).

Patients with EAC lose weight due to luminal obstruction, typically diagnosed by endoscopy and/or noninvasive imaging. Upper endoscopy in intact 15-month-old BA-treated or untreated *L2-IL-1β* (Movies S1 and S2) and WT (Movie S3) mice after intubation and under constant ventilation (Figure 3C) revealed the luminal presence of BE-like metaplasia and tumor growth in the distal esophagus. The esophagi of *L2-IL-1β* mice showed circumferential erythema and edema with inflammatory exudates compared to the normal esophagus (Figure 3C), changes that were increased in BA-treated *L2-IL-1β* mice. The endoscopic appearance resembled human BE (Movie S4). In four of nine BA-treated *L2-IL-1β* mice (15 month) but no *L2-IL-1β* mice (15 month), we observed obstructing tumors at the SCJ (Figure 3C; Movies S1–S3). 18F-FDG PET scans of BA-treated *L2-IL-1β* mice with endoscopically detected tumors revealed markedly increased focal glucose uptake, consistent with the severe inflammation in the esophagus and forestomach, along with tumorigenesis confirmed histologically (Figure 3D; Movie S5). These imaging data provide support for the acceleration of neoplastic processes in *L2-IL-1β* mice by BA.

Bile Acids Induce an Acute and Chronic Immune Response and Activate Differential Gene Expression in BE

Previous studies of IL-1β-induced carcinogenesis suggested that recruitment of myeloid cells is crucial for the development of neoplasia (Tu et al., 2008; Yang et al., 2011). In 6-month-old *L2-IL-1β* mice with mild esophagitis, there was no change in the abundance of $CD4^+$ and $CD8^+$ T cells or $CD11b^+/F4/80^+$ monocytes/macrophages in esophageal tissue, but a significant accumulation of immature ($CD11b^+Gr1^+$) myeloid cells (Figure 4C). At 9, 12, and 15 months, there was an even greater accumulation in *L2-IL-1β* mice of $CD11b^+Gr1^+$ cells in the esophagus (Figure 4C) and spleen (not shown) associated with chronic esophagitis and metaplasia. $CD4^+$ T cells, $F4/80^+$ macrophages and $CD11b^-Gr1^+$ neutrophils were also significantly increased but to a lesser extent in *L2-IL-1β* mice at these later time points (Figure 4B). Inflammatory cytokines were increased (Figures 1A–1D; Figure S1D) and the *L2-IL-1β* mice developed splenomegaly, likely due to an accumulation of immature splenic myeloid cells (Figure S1C). BA treatment resulted in additional increases in $CD4^+$ T cells and $CD11b^-Gr1^+$ neutrophils, along with a slight decrease in $CD11b^+Gr1^+$ cells but no changes in $CD11b^+/F4/80^+$ macrophages (Figures 4A and 4B). These observations confirmed our histopathological scoring, showing more acute inflammation in BA-treated mice (Figure 3A). Our data suggest that BA may contribute to the development of BE by shifting the chronic inflammatory response toward an acute neutrophilic response. Recruited macrophages also suggest a role for tumor associated macrophages (TAMs) in BE.

In addition, 15 month BA-treated *L2-IL-1β* mice harboring metaplasia showed elevated levels of *Tff2*, *Cckbr*, *Muc5ac*, *Cdx2*, and *Krt19* (Figure 4D). *Bmp4*, *Cdx2*, and *Shh*, which are known to be involved in cellular differentiation and proliferation, were also associated with BA treatment (Figure 4D). Interestingly, we observed a significant upregulation of *Notch1* upon BA treatment, indicating a potentially important role for the Notch signaling pathway in BE and HGD (Figure 4D).

DLL1-Dependent Notch Signaling Regulates Differentiation and Correlates with Progression

Notch signaling is an essential factor in intestinal differentiation and seems to be required to maintain stem cells in an uncommitted state (Kim and Shivdasani, 2011). As with the intestinal epithelium, the Barrett epithelium contains proliferative crypt-like compartments, and the Notch pathway has been found to be active in BE (Menke et al., 2010). Indeed, *Notch1* was upregulated significantly in the epithelium at the SCJ of BA-treated *L2-IL-1β* mice, compared to WT and untreated *L2-IL-1β* mice (Figures 4D and 5A; Figure S4A), pointing to a role of Notch signaling during EAC pathogenesis. Notch inhibition by systemic treatment with a γ-secretase inhibitor (DBZ), as reported previously (Menke et al., 2010), markedly increased both PAS^+ cells and Alcian-Blue(+) goblet-like cells (Figures 5B and 5C), suggesting that inhibition of Notch signaling is associated with IM. Moreover, IHC for a general marker of activated Notch signaling (Notch intracellular domain or NICD; Figure S4A) revealed that NICD-expressing cells were predominantly found within columnar-lined esophagus (CLE) and dysplastic epithelial tissue at the SCJ, but not in IM at the SCJ, and were in general not present in DBZ-treated mice (Figure 5A; Figure S4A) where we observed increased numbers of goblet cells (Figure 5C). These findings suggest that Notch signaling might contribute to the development of dysplasia, whereas inhibition of Notch signaling results in goblet cell differentiation and may prevent malignant transformation, although in theory both processes could occur simultaneously in different regions of the metaplastic epithelium.

We also observed upregulation of the Notch ligand Delta-like1 (*Dll1*) in BE-like tissue (Figure 5D; Figures S4C and S4D), which correlated with increased Notch1 expression and proliferation in BE. Increasing numbers (Figure S4E) of *Dll1*-expressing cells could be found adjacent to Notch activated cells (Notch-IC), suggesting a possible intraepithelial crosstalk (Figure 5D). Most of the $Dll1^+$ cells also expressed Tff2, supporting a concept of an expansion of Dll^+ cells in the BE lineage (Figure S4F). In addition, we found downregulated Jagged2 gene expression in BE and EAC (Figure 6D; Table S1) and were able to confirm

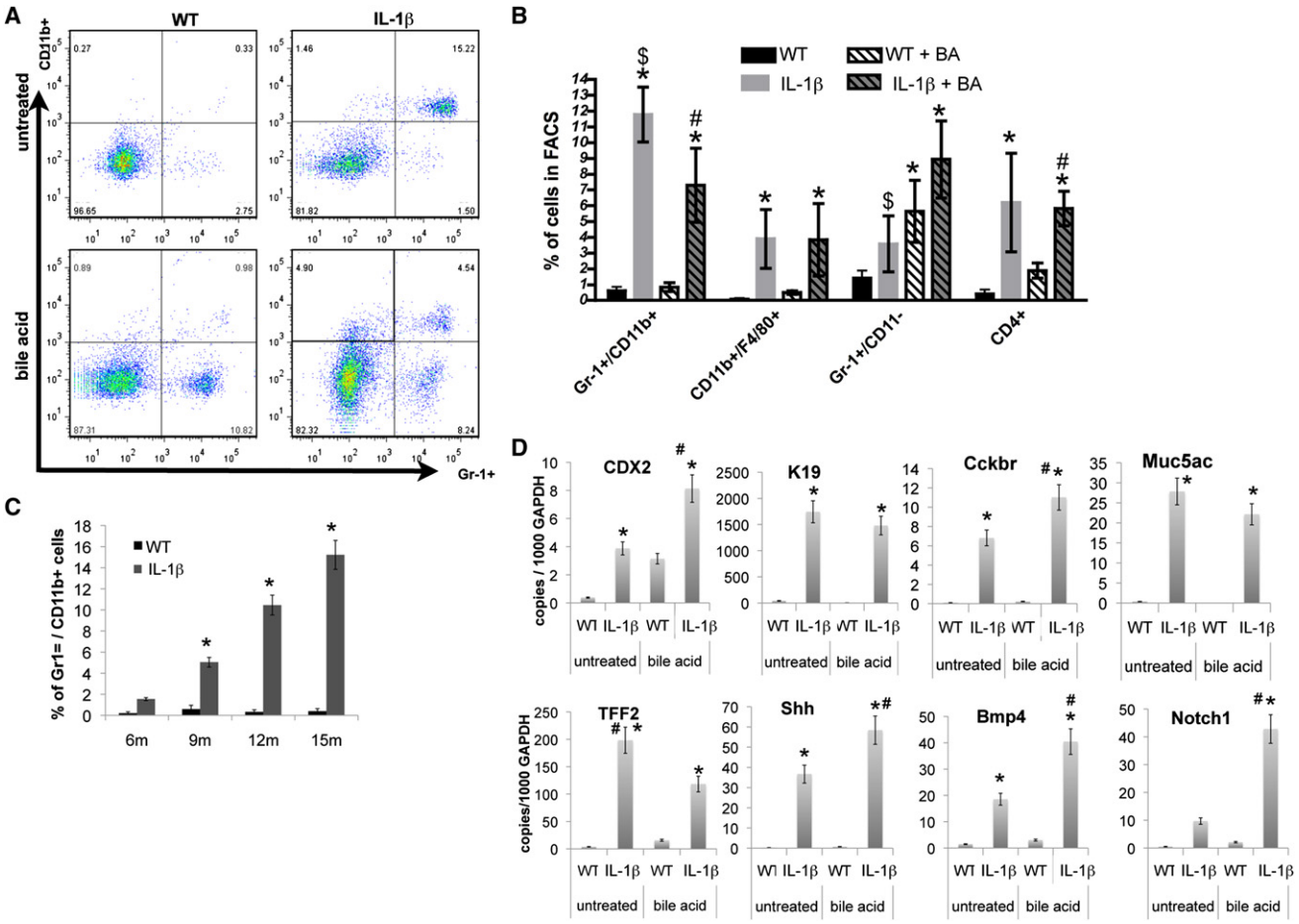

Figure 4. Bile Acids Induce an Acute and Chronic Immune Response and Activate Notch Signaling in BE

(A) The frequencies of lymphoid and myeloid cells in the esophagus from 12-month-old *L2-IL-1β* mice and age-matched WT mice were measured by FACS, and representative FACS blots for detecting immature ($CD11b^+Gr1^+$) myeloid cells in the esophagus from WT, *L2-IL-1β* mice, BA-treated WT, and BA-treated *L2-IL-1β* mice are shown.

(B) Quantitative analysis of FACS for immature ($CD11b^+Gr1^+$) myeloid cells, neutrophiles/granulocytes ($CD11b^-Gr1^+$), macrophages ($Cd11b^+/F4/80^+$), and T cells ($CD4^+$) (*$p < 0.05$ compared to WT, #$p < 0.05$ compared to BA-treated WT, \$$p < 0.05$ compared to untreated *L2-IL-1β* mice).

(C) Quantitative analysis of FACS for immature ($CD11b^+Gr1^+$) myeloid cells in 6-, 9-, 12-, 15-month-old *L2-IL-1β* mice compared to age-matched WT mice.

(D) mRNA expression (RT-qPCR) of Cdx2, K19, Cckbr, Muc5ac, TFF2, Shh, Bmp4, and Notch1 in the SCJ tissue of WT, *L2-IL-1β* mice, BA-treated WT, and BA-treated *L2-IL-1β* mice (*$p < 0.01$ compared to WT, # $p < 0.05$ compared to *L2-IL-1β* mice). Data are represented as mean ± SEM.

decreased Jagged2 as assessed by IHC (Figure S4B), suggesting that Dll1, not Jagged2, is the predominant ligand inducing Notch signaling in BE. The location of Dlll1 expression was associated with the normal stem cell zone in the gastric cardia (data not shown), whereas Jagged2 appeared to be expressed in more terminally differentiated areas of the gastric cardia glands (Figure S4B, data not shown).

To confirm these findings from our mouse model, we analyzed 46 human BE biopsy samples. Biopsies were taken from Barrett mucosa, evaluated by an expert gastrointestinal pathologist, and samples were classified histologically based on the highest degree of neoplasia present on any of the biopsies. *Notch1* was significantly upregulated in human biopsies of dysplastic tissues compared to BE tissue (Figure 5E), pointing to a role of Notch signaling in the development of EAC from BE. Overall, Notch activation appears to be associated with decreased goblet cell differentiation, as suggested by a lack of goblet cells in adjacent tissue of human EAC samples (unpublished data) and a review of the literature (Table S2). IHC for Notch intracellular domain (NICD) and Dll1 in human BE tissue showed a similar pattern, where expression of the receptor and ligand was found in adjacent but distinct cell types (Figure 5F).

Gene Expression Profiles of the IL-1β Mouse Esophagus Closely Resemble Those of Human Barrett Metaplasia and Esophageal Adenocarcinoma

The gene expression profile of human BE (Stairs et al., 2008) is only slightly more similar to small intestine than it is to normal esophagus, in contrast to the striking similarity of BE morphology to intestinal morphology. Nevertheless, we found in both human BE and our mouse model that a number of gastric and intestinal genes were significantly upregulated. LCM was applied to typical metaplastic lesions in *L2-IL-1β* mice (with or without BA), and to the squamous epithelium of WT mice (Figure 6A).

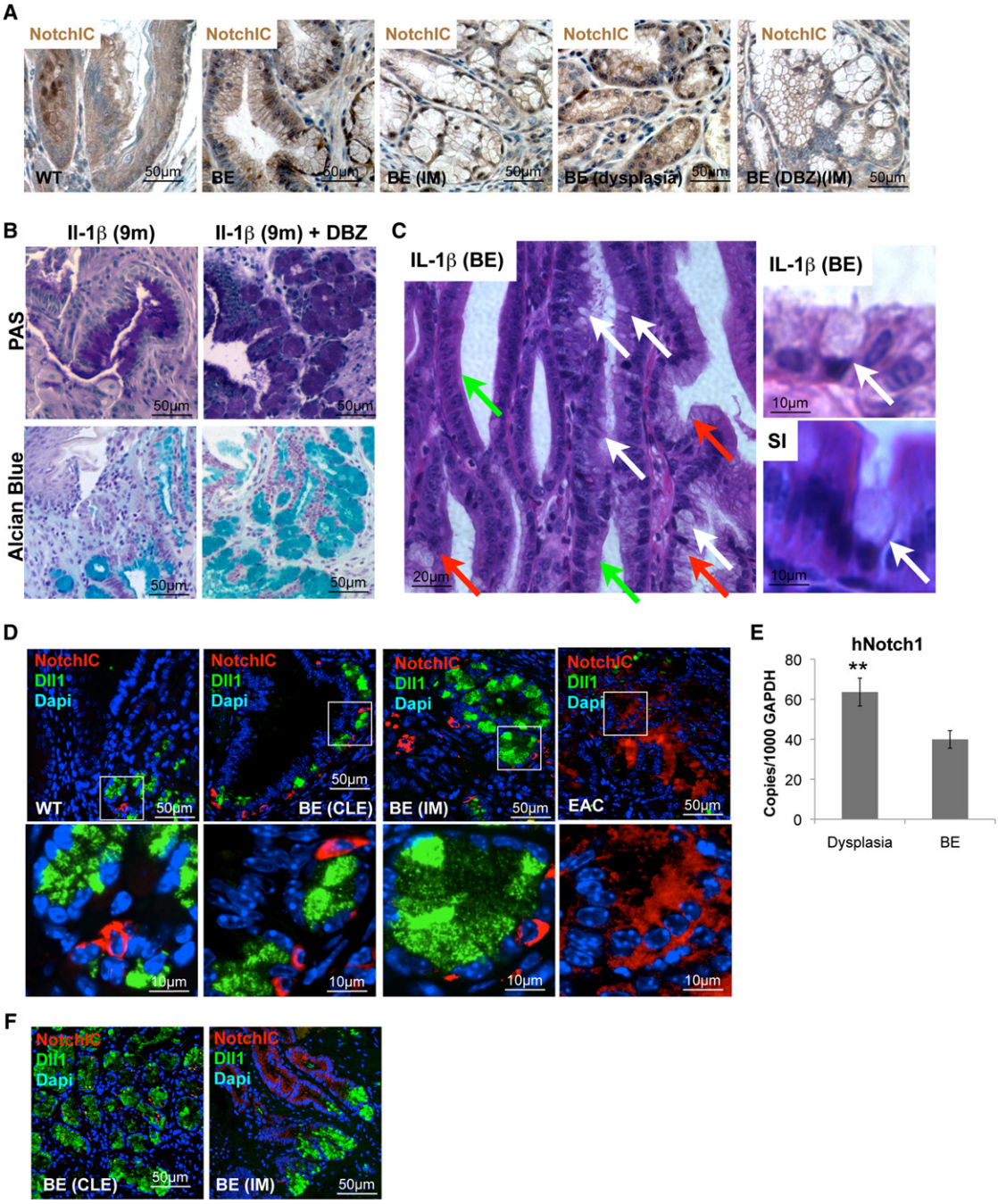

Figure 5. Notch Signaling in BE

(A) Representative pictures of NotchIC IHC in 15-month-old *L2-IL-1*β BA-treated mice and 9-month-old *L2-IL-1*β mice after γ-secretase inhibitor treatment (DBZ).

(B) Representative pictures of periodic acid-Schiff (PAS) and Alcian blue staining at the SCJ of 9-month-old *L2-IL-1*β without and with 10 days γ-secretase inhibitor treatment (right, Notch signaling inhibitor, DBZ).

(C) Representative picture of BE in γ-secretase-treated *L2-IL-1*β mice showing occasional true goblet cells (white arrows), CLE (green arrows), and goblet like cells (red arrows) on the left. On the right goblet cells in BE (top) and small intestine (SI, bottom) are shown to show similarities in intestinal metaplasia.

(D) Representative pictures of NotchIC (red) and Delta-Like1 (Dll1) (green) IHC in 9-month-old WT, 9-month-old *L2-IL-1*β with BE, and 15-month-old BA-treated *L2-IL-1*β with EAC (insets label magnified area below).

(E) mRNA expression (RT-qPCR) of *Notch1* in biopsies of esophageal tissue, obtained from 46 patients with BE with and without dysplasia. In each patient, biopsies were taken from Barrett mucosa and from dysplastic appearing mucosa.

(F) Representative pictures of NotchIC (red) and Delta-Like1 (Dll1) (green) IHC in human BE with CLE or IM. See also Figure S4 and Table S2. Data are represented as mean ± SEM. *$p < 0.05$.

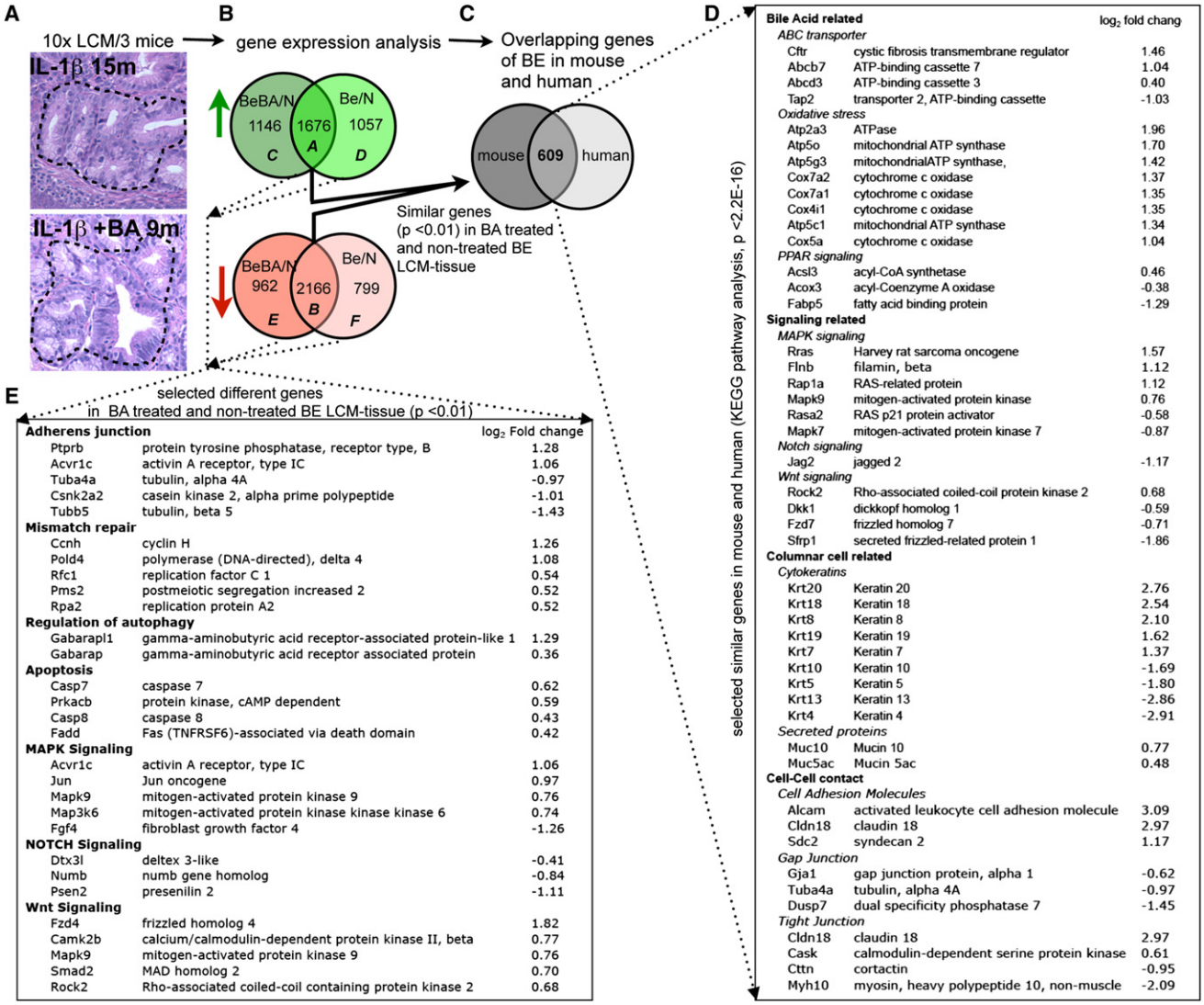

Adherens junction		log2 Fold change
Ptprb	protein tyrosine phosphatase, receptor type, B	1.28
Acvr1c	activin A receptor, type IC	1.06
Tuba4a	tubulin, alpha 4A	-0.97
Csnk2a2	casein kinase 2, alpha prime polypeptide	-1.01
Tubb5	tubulin, beta 5	-1.43
Mismatch repair		
Ccnh	cyclin H	1.26
Pold4	polymerase (DNA-directed), delta 4	1.08
Rfc1	replication factor C 1	0.54
Pms2	postmeiotic segregation increased 2	0.52
Rpa2	replication protein A2	0.52
Regulation of autophagy		
Gabarapl1	gamma-aminobutyric acid receptor-associated protein-like 1	1.29
Gabarap	gamma-aminobutyric acid receptor associated protein	0.36
Apoptosis		
Casp7	caspase 7	0.62
Prkacb	protein kinase, cAMP dependent	0.59
Casp8	caspase 8	0.43
Fadd	Fas (TNFRSF6)-associated via death domain	0.42
MAPK Signaling		
Acvr1c	activin A receptor, type IC	1.06
Jun	Jun oncogene	0.97
Mapk9	mitogen-activated protein kinase 9	0.76
Map3k6	mitogen-activated protein kinase kinase kinase 6	0.74
Fgf4	fibroblast growth factor 4	-1.26
NOTCH Signaling		
Dtx3l	deltex 3-like	-0.41
Numb	numb gene homolog	-0.84
Psen2	presenilin 2	-1.11
Wnt Signaling		
Fzd4	frizzled homolog 4	1.82
Camk2b	calcium/calmodulin-dependent protein kinase II, beta	0.77
Mapk9	mitogen-activated protein kinase 9	0.76
Smad2	MAD homolog 2	0.70
Rock2	Rho-associated coiled-coil containing protein kinase 2	0.68

Bile Acid related		log2 fold chang
ABC transporter		
Cftr	cystic fibrosis transmembrane regulator	1.46
Abcb7	ATP-binding cassette 7	1.04
Abcd3	ATP-binding cassette 3	0.40
Tap2	transporter 2, ATP-binding cassette	-1.03
Oxidative stress		
Atp2a3	ATPase	1.96
Atp5o	mitochondrial ATP synthase	1.70
Atp5g3	mitochondrialATP synthase,	1.42
Cox7a2	cytochrome c oxidase	1.37
Cox7a1	cytochrome c oxidase	1.35
Cox4i1	cytochrome c oxidase	1.35
Atp5c1	mitochondrial ATP synthase	1.34
Cox5a	cytochrome c oxidase	1.04
PPAR signaling		
Acsl3	acyl-CoA synthetase	0.46
Acox3	acyl-Coenzyme A oxidase	-0.38
Fabp5	fatty acid binding protein	-1.29
Signaling related		
MAPK signaling		
Rras	Harvey rat sarcoma oncogene	1.57
Flnb	filamin, beta	1.12
Rap1a	RAS-related protein	1.12
Mapk9	mitogen-activated protein kinase	0.76
Rasa2	RAS p21 protein activator	-0.58
Mapk7	mitogen-activated protein kinase 7	-0.87
Notch signaling		
Jag2	jagged 2	-1.17
Wnt signaling		
Rock2	Rho-associated coiled-coil protein kinase 2	0.68
Dkk1	dickkopf homolog 1	-0.59
Fzd7	frizzled homolog 7	-0.71
Sfrp1	secreted frizzled-related protein 1	-1.86
Columnar cell related		
Cytokeratins		
Krt20	Keratin 20	2.76
Krt18	Keratin 18	2.54
Krt8	Keratin 8	2.10
Krt19	Keratin 19	1.62
Krt7	Keratin 7	1.37
Krt10	Keratin 10	-1.69
Krt5	Keratin 5	-1.80
Krt13	Keratin 13	-2.86
Krt4	Keratin 4	-2.91
Secreted proteins		
Muc10	Mucin 10	0.77
Muc5ac	Mucin 5ac	0.48
Cell-Cell contact		
Cell Adhesion Molecules		
Alcam	activated leukocyte cell adhesion molecule	3.09
Cldn18	claudin 18	2.97
Sdc2	syndecan 2	1.17
Gap Junction		
Gja1	gap junction protein, alpha 1	-0.62
Tuba4a	tubulin, alpha 4A	-0.97
Dusp7	dual specificity phosphatase 7	-1.45
Tight Junction		
Cldn18	claudin 18	2.97
Cask	calmodulin-dependent serine protein kinase	0.61
Cttn	cortactin	-0.95
Myh10	myosin, heavy polypeptide 10, non-muscle	-2.09

Figure 6. Gene Expression Profiles of Mouse BE Resembles that of the Human Disease

(A) Laser capture microdissection (LCM) was applied to typical metaplastic lesions at the SCJ in 15-month-old *L2-IL-1β* mice or 9-month-old BA-treated *L2-IL-1β* mice and to the squamous epithelium of WT control mice. A schematic sequence of the experimental procedures is shown: (A) After LCM (a representative outlined area is shown) followed by RNA isolation and amplification, (B) Venn diagram mouse BE versus BA-treated mouse BE: gene expression of BE tissue from untreated *L2-IL-1β* mice (n = 3, BE versus N), and BA-treated *L2-IL-1β* mice (n = 3, BeBA versus N) was compared to WT squamous tissue (n = 3) in order to determine the overlapping up- and downregulated genes in both cohorts.

(C) Venn diagram mouse versus human. These 3,832 significantly different genes (1,676 up [Venn diagram: A] and 2,166 down [Venn diagram: B], $p < 0.01$) were than compared to the gene expression pattern of a human expression analysis (Stairs et al., 2008) where human BE tissue was compared to human esophageal squamous tissue. This comparison identified 606 genes, which were analyzed by KEGG pathway analysis.

(D) A list of these significantly identical genes in human and mouse is shown with the $\log_2$ fold change of the comparison of BA-treated *L2-IL-1β* mice compared to the squamous epithelium of WT control mice.

(E) KEGG pathway analysis also identified genes that were altered differentially in BE epithelium of *L2-IL-1β* mice versus BA-treated *L2-IL-1β* mice (Venn diagram: C–F). A list of significantly different genes is shown.

Compared to squamous epithelium, we observed 5,698 genes with a significance cutoff of <0.05, that were differentially regulated in BE tissue of 15-month-old *L2-IL-1β* mice and 5,950 genes in 9-month-old BA-treated *L2-IL-1β* mice. Direct comparison of these two groups identified 1,678 similarly upregulated (A in Venn diagram) and 2,166 similarly downregulated (B in Venn diagram) genes (Figure 6B). In KEGG pathway analysis, these transcripts were enriched for cell adhesion molecules, adherens junctions, tight junctions, biosynthesis of unsaturated fatty acids, PPAR signaling pathway, and protein export. When compared to the earlier human expression analysis (GSE13083) (Stairs et al., 2008), entire sets of genes in the mouse were altered in the same directions (Figure 6C). KEGG pathway analysis of those genes that were identically up- or downregulated in mouse and human, revealed changes in the expression of genes relevant for bile acid-induced

damage, signaling pathways (i.e., Notch), columnar cell related genes, and cell-cell contact genes (Figure 6D).

KEGG pathway analysis also identified genes that were altered differentially in BE-like epithelium of *L2-IL-1β* mice versus BA-treated *L2-IL-1β* mice (C–F in Venn diagram) with a significant overrepresentation of the biological processes of mismatch repair, adherens junction, apoptosis, and autophagy, as well as alterations in signaling pathways with importance for carcinogenesis (Figure 6E). These results are consistent with a role for bile acids in promoting metaplasia and cancer by loosening cell-cell contacts, inducing oncogenic pathways, and causing cell death by DNA damage and oxidative stress.

Barrett-Like Metaplasia and Dysplasia Correlate with Expansion of Gastric Cardia Progenitor Cells in Mice and Humans

The current paradigm suggests that BE derives from dedifferentiation or transdifferentiation of the squamous esophageal epithelium (Jankowski et al., 2000). To address the possible origins of BE in our mouse model, we examined the expression and localization of a number of putative stem cell or progenitor cell markers. Lgr5/GPR49 is a validated stem or progenitor cell marker for the mouse gut, but in the stomach it is expressed only in the gastric antrum and in the gastric cardia (Barker et al., 2010). Krt19 and Tff2 have been shown through lineage tracing studies to label different gastric progenitor cells (Means et al., 2008; Quante et al., 2010). Doublecortin and CaM like-kinase-1 (Dclk1), a microtubule-associated kinase expressed in neurons, has been postulated to be expressed in gut epithelial progenitors (Giannakis et al., 2006).

Although the above markers were absent from the normal squamous esophageal epithelium, they showed increased expression over time in our *L2-IL-1β* mouse model, with expression first in the gastric cardia and later above the SCJ. In qRT-PCR studies Lgr5 was expressed minimally in the WT cardia, but could easily be detected in the cardia in 15-month-old *L2-IL-1β* mice that showed features consistent with Barrett metaplasia (Figure 7B). Lgr5-labeled cells were present in the cardia of Lgr5-Cre-ERT mice crossed to Rosa-LacZ reporter mice shortly after tamoxifen induction, which within 7 days gave rise to lineage traced cardia epithelium in WT mice (Figure 7D), as previously shown (Barker et al., 2010). In *L2-IL-1β* mice crossed to Lgr5-Cre-ERT/Rosa-LacZ mice, we observed labeled BE metaplasia four months after tamoxifen induction followed by BA treatment at the age of 6–8 weeks (Figure 7D). These findings indicate that Lgr5$^+$ cells within the cardia may function as progenitor cells, and thus potentially as the cells of origin for BE and dysplasia. Furthermore, we observed an increase in protein and mRNA expression of the *Krt19* gene (Figures 2A and 4D), which is a known marker for surface mucus and gastric progenitor cells (Brembeck et al., 2001; Means et al., 2008), and of the *Tff2* gene, expressed in gastric and cardia mucus neck and progenitor cells (Quante et al., 2010), but not in the normal esophageal epithelium (Figures 2A and 4D). Finally, we found an accumulation of Dclk1$^+$ cells adjacent to the metaplastic mucus producing cells in BE tissue (Figures 7A and 7B). Dclk1$^+$ cells are typically present as rare scattered cells localized primarily to the isthmus of the gastric glands (data not shown), but Dclk1$^+$ cells are highly abundant in the gastric cardia, particularly just below the SCJ (Figure 7A). The gradual accumulation of Dclk1$^+$ cells just above the SCJ in *L2-IL-1β* mice positively correlated with the development of metaplasia at the SCJ; with progression to dysplasia, Dclk1 expression was downregulated.

In human BE, qRT-PCR analysis showed a highly significant upregulation of *LGR5* and *DCLK1* compared to normal squamous epithelium (Figure 7C). Moreover, IHC for DCLK1 showed increased expression in dysplastic BE and decreased (or absent) expression of DCLK1 in dysplasia or adenocarcinoma (Figure 7A), similar to the observation in *L2-IL-1β* mice. Consistent with previous reports, TFF2 was highly expressed in Barrett mucosa but not in biopsies of squamous esophageal epithelium (data not shown). Interestingly, LGR5 and DCLK1 were significantly elevated in the gastric cardia of BE patients (Figures 7E and 7F). The upregulation of gastric columnar progenitor cells in the region of the cardia and in BE suggest that the metaplastic lineage in BE lesions in mice and humans may derive from a gastric cardia lineage (Figure 4G).

IL-6 Deficiency Abolishes Inflammation, Metaplasia, and HGD in *L2-IL-1β* Mice

IL-1β is upstream of IL-6 and TNF-α, which are both upregulated in our models (Figure S1D) and overexpression of IL-1β has been shown to induce tumorigenesis of the stomach (Tu et al., 2008). Persistent activation of the transcription factor signal transducer and activator of transcription-3 (Stat3) occurs in a large number of solid malignancies and supports the proliferation and survival of malignant cells, mostly triggered by an autocrine-paracrine production of IL-6 and family members (Bollrath et al., 2009). We observed elevated IL-6 protein levels in the serum and the SCJ of *L2-IL-1β* mice (Figure 1D), and IL-6 could be upregulated further by BA treatment (Figure 8A). IHC revealed increased pStat3$^+$ cells during the progression from normal esophagus to BE and EAC (Figures 8B and 8C). Interestingly, we observed a significant upregulation of *IL-11Ra* and *Jak2*, and downregulation of *Socs3*, in our microarray analysis (Table S3). Given that we demonstrated increased levels of IL-6 and phosphorylated Stat3 in mouse BE-like and dysplasic tissues, *IL-11Ra* upregulation likely represents an inhibitory feedback mechanism. The finding of SOCS3 downregulation, as demonstrated recently (Watanabe et al., 2007), and increased levels of Jak2 with STAT3 activation, suggest a mechanism by which IL-1β and IL-6 could induce the development of cancer in our mouse model of BE/EAC (Lesina et al., 2011).

In human EAC samples qRT-PCR analysis showed a significant upregulation of IL-6 and IL-1β compared to BE samples (Figures 8D and 8E), supporting our hypothesis that both cytokines play an important role during EAC pathogenesis. When we crossed *L2-IL-1β* mice with *IL-6*$^{-/-}$ mice we observed a complete abolishment of the metaplastic and dysplastic phenotype in homozygous *L2-IL-1β*/IL-6$^{-/-}$ mice, and a partly diminished phenotype with little metaplasia and no dysplasia in heterozygous *L2-IL-1β*/*IL-6*$^{-/+}$ mice (Figure 8F). In *L2-IL-1β*/*IL-6*$^{-/-}$ mice, we observed only a minor inflammatory response, which was increased in *L2-IL-1β*/*IL-6*$^{-/+}$ mice, but no increase in pSTAT3$^+$ cells could be detected (data not shown). These data indicate that IL-1β mediates its carcinogenic effect in part through IL-6,

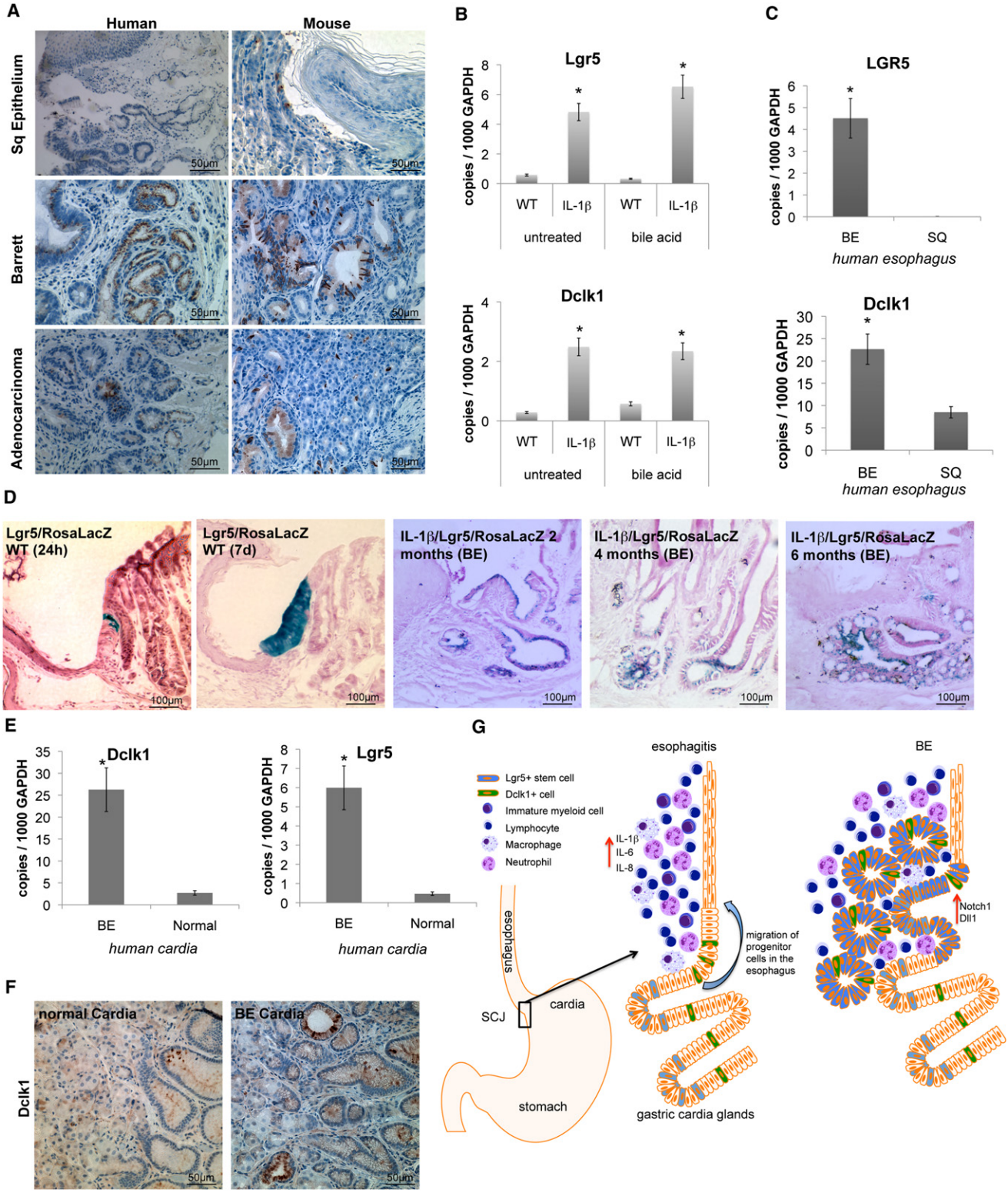

Figure 7. Barrett Metaplasia and Dysplasia Arise from Gastric Cardia Progenitor Cells in Mice and Humans

(A) Representative pictures of human (left) and mouse (right) SCJ, BE, and EAC tissue with doublecortin like kinase-1 (Dclk1) IHC.

(B) mRNA expression (RT-qPCR) of Lgr5 and Dclk1 in the SCJ tissue of WT, *L2-IL-1β* mice, BA-treated WT, and BA-treated *L2-IL-1β* mice.

(C) mRNA expression (RT-qPCR) of *Lgr5* and *Dclk1* in biopsies of esophageal tissue, obtained from 46 patients with BE. In each patient, biopsies were taken from Barrett mucosa and from normal-appearing squamous mucosa.

suggesting the presence of a tumor-promoting IL-1β-IL-6-pStat3 signaling cascade in mouse EAC.

DISCUSSION

Using a transgenic mouse model of esophageal inflammation, we demonstrate that increased IL-1β expression is sufficient for the induction of Barrett-like metaplasia and dysplasia at the SCJ, extending previous findings in the glandular stomach (Tu et al., 2008) and affirming a crucial role for IL-1β in carcinogenesis, which is highly upregulated in human BE and EAC (Fitzgerald et al., 2002). Gene expression analysis, IHC, EM, and endoscopy provided evidence that our IL-1β mouse model closely resembles human disease, despite the fact that the mouse stomach differs from the human stomach. Inflammation in the squamous esophagus resulted in migration of cardia progenitor cells (including $Lgr5^+$ cells) and their metaplastic descendants into the esophagus. We would conclude then that Barrett esophagus is derived from gastric cardia progenitors at the SCJ junction.

Although our L2-IL-1β mouse model exhibits a columnar-lined esophagus (CLE) but lacks abundant goblet cells (or classical IM), it is increasingly recognized that BE does not require classical IM to establish the diagnosis (Ogiya et al., 2008; Playford, 2006). Several studies have indicated that the risk of progression to EAC is the same in patients with CLE without goblet cells as it is in patients with IM (Gatenby et al., 2008; Goldblum, 2010; Kelty et al., 2007; Odze and Maley, 2010; Riddell and Odze, 2009; Takubo et al., 2009) (Table S2), and our clinical experience would support this broader premise. The findings that dysplasia tends to recur following radiofrequency ablation in the presence of CLE without classical IM would support this model (Vaccaro et al., 2011). Notch inhibition has been associated with goblet cell differentiation (Menke et al., 2010), and thus the absence of $Tff3^+$ or $Muc2^+$ goblet cells may be related to the high levels of Notch expression. Our study adds to the evidence challenging the notion that metaplastic nongoblet cell CLE is entirely benign, and we would even argue that TFF2 has many advantages as a marker for BE, because it seems to be expressed early in the development of CLE, a lesion we postulate is the primary precursor lesion for EAC. Nevertheless, further studies in patients are needed to clarify the prognostic and diagnostic value of IM and CLE, because at present it remains controversial as to which metaplastic epithelial subtype best defines BE (Chatelain and Fléjou, 2003), leading to controversial risk estimates for the development of HGD or EAC in BE patients (Hvid-Jensen et al., 2011).

IL-1β overexpression was able to induce metaplasia and dysplasia of the SCJ in part through recruitment of immature myeloid cells (IMC), which have been linked to carcinogenesis (Stairs et al., 2011; Tu et al., 2008; Yang et al., 2011). IMC were increased early in the distal esophagus and likely contribute to esophageal inflammation and carcinogenesis through secretion of pro-inflammatory cytokines (IL-6 and Tnf-α) and chemokines (Sdf1). With BA treatment, there was acceleration of dysplasia and a shift in the myeloid phenotype more toward granulocytic differentiation, pointing to the possible significance of a mixed acute/chronic inflammatory response in carcinogenesis (Fridlender et al., 2009). IL-6 levels were systemically elevated in *L2-IL-1β* mice, and IL-6 deficiency completely abrogated the IL-1β-induced phenotype, indicating the importance of systemic immune activation in the development of neoplasia. Persistent activation of Stat3 through IL-6 additionally supports the proliferation and survival of malignant cells in mouse and human EAC, in contrast to the importance of IL-11 in carcinogenesis of the antrum (Ernst et al., 2008; Howlett et al., 2009). IL-6 in most tissues is a critical mediator of cancer initiation and progression, and IL-6-Stat3 inhibition may be a useful target for prevention or treatment of BE and EAC.

Unconjugated BA, which are increased in the refluxate of patients with BE (Kauer et al., 1997) and in patients on a high fat diet (Theisen et al., 2000), accelerated the development of BE and dysplasia. Unconjugated BA can induce gene promoter demethylation leading to activation of *IL-6*, *Cdx2*, or *Notch1* gene expression in esophageal cells (Jankowski et al., 1999; Kazumori et al., 2006), a finding we can confirm in our BA-treated *L2-IL-1β* mice. Thus, through modulation of gene expression, unconjugated bile acids may promote an intestinal lineage commitment by progenitors. Pathway analysis of our gene expression studies confirm previously suggested carcinogenic roles for BA (Bernstein et al., 2005, 1999; Dvorak et al., 2007; Payne et al., 2005).

Although it is generally accepted that BE and EAC arise from a common progenitor cell, the precise type and location of this cell remained unresolved. Temporal analysis of the *L2-IL-1β* mouse SCJ at different stages of the disease showed an initial expansion of progenitors in the gastric cardia, followed by migration over time into the esophagus (Figure 4G). LgR5 cell lineage tracing studies demonstrated the likely origin of at least some of the metaplastic BE tissue from $Lgr5^+$ cells within the gastric cardia, where $Lgr5^+$ cells also serve as functional cardia stem or progenitor cells. Furthermore, progenitor markers were essentially absent from the normal esophageal squamous epithelium, but Lgr5 (Barker et al., 2010), Tff2 (Quante et al., 2010), Krt19 (Means et al., 2008), Cck2r (Jin et al., 2009), and Dclk1 (Giannakis et al., 2006) were all present in the normal mouse gastric cardia, and were significantly increased in BE. Analysis of a cohort of human patients with BE showed

(D) Left: Lgr5-Cre-ERT x RosaLacZ mice were treated with 3-OH tamoxifen and sacrificed 1 day or 7 days postinduction. Analysis at 1 day showed a small collection of $Xgal^+$ cells in the cardia at the squamocolumnar junction (SCJ), whereas analysis at 7 days showed complete lineage tracing of these columnar cardia glands. Right: lineage tracing of BE tissue in 6-month-old Lgr5-CreERT/IL-1b/RosaLacZ mice. Tamoxifen induction (6 mg in one dose) was performed prior to bile acid treatment at the age of 4 weeks. Mice were sacrificed at 2, 4, or 6 months after induction, indicating lineage tracing of developing BE suggesting that Lgr5 cells might migrate into the distal esophagus and give rise to BE.

(E) mRNA expression (RT-qPCR) of *LGR5* and *DCLK1* in biopsies of cardia tissue, obtained from five patients with BE and five patients without BE (normal).

(F) Representative DCLK1 IHC pictures of normal human cardia (left) and of cardia from patients with BE (right) with doublecortin-like kinase-1.

(G) In our model of the pathogenesis of BE and EAC in mice, bile acid treatment, and IL-1β-induced inflammation lead to migration of gastric cardia progenitor cells into the distal esophagus, giving rise to BE and EAC in association with increased Dll1-dependent Notch signaling that induced columnar cell differentiation.

Data are represented as mean ± SEM. *$p < 0.05$.

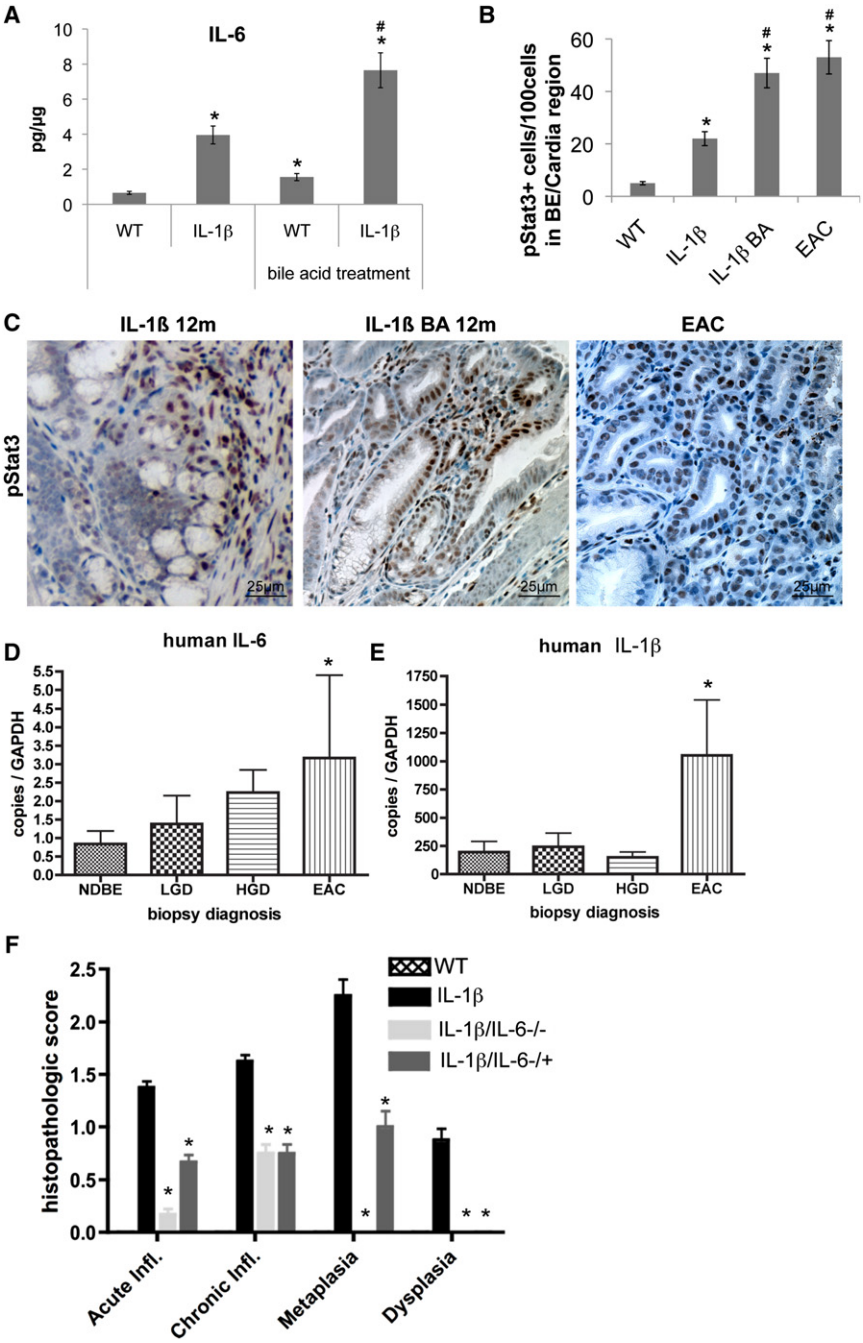

Figure 8. IL-6 Deficiency Abolishes IL-1β-Induced Metaplasia and Dysplasia

(A) mRNA expression (RT-qPCR) of IL-6 in the SCJ tissue of WT, *L2-IL-1*β mice, BA-treated WT, and BA-treated *L2-IL-1*β mice (*p < 0.01 compared to WT, # p < 0.05 compared to *L2-IL-1*β mice).

(B) Quantification of cells with phosphorylated STAT3 in WT, *L2-IL-1*β mice, BA-treated *L2-IL-1*β, and BA-treated *L2-IL-1*β mice with EAC (*p < 0.01 compared to WT, # p < 0.05 compared to *L2-IL-1*β mice).

(C) Representative pictures of pSTAT3 IHC in 12-month-old *L2-IL-1*β mice and BA-treated *L2-IL-1*β, and 15-month-old BA-treated *L2-IL-1*β mice with EAC.

(D and E) mRNA expression (RT-qPCR) of IL-6 (D) and IL-1β (E) in biopsies of esophageal tissue, obtained from 46 patients with BE.

(F) Histopathological scoring of 12-month-old *L2-IL-1*β mice and *L2-IL-1*β/IL-6$^{-/-}$ or *L2-IL-1*β/IL-6$^{-/+}$ mice and WT (C57/B6) littermates (*p < 0.05, compared to *L2-IL-1*β mice). Data are represented as mean ± SEM. See also Table S3.

a significant increase of identical progenitor markers in both gastric cardia and BE tissue.

However, our findings that Lgr5^{+} cardia cells can contribute to BE does not exclude contributions from other lineages. In addition, the use of mouse models to investigate the origins of human metaplasia has its limitations, given the anatomical differences. The predominant theory for the origins of Barrett esophagus is based on the notion of reflux-induced transdifferentiation of squamous epithelial cells (Barbera and Fitzgerald, 2010; Yu et al., 2005). In addition, genetic evidence has supported the possible origin from multipotent progenitors present in submucosal squamous gland ducts, which are not present in the mouse and thus could not be examined in our model (Jankowski et al., 2000; Leedham et al., 2008). A recent study of *p63 null* mice led to the proposal that Barrett-like metaplasia may arise from a population of Car4^{+}/Krt7^{+} embryonic progenitors at the squamocolumnar junction (Wang et al., 2011). However, each of these alternative hypotheses, although reasonable, is also limited to date by the absence of dynamic lineage tracing and the sort of mechanistic underpinnings provided by our model.

Notch signaling appears important in the regulation of stem cell differentiation, and our data suggest that Dll1 is the major ligand inducing activated Notch signaling in BE, whereas Jagged2 may acts as an inhibitor, similar to a model of antagonism between different Notch ligands suggested previously (Benedito et al., 2009). In the cardia, Dll1 was expressed at the bottom of the crypts adjacent to the location of Lgr5 cells. Notch activation in Lgr5^{+} cells has been shown to correlate with lineage tracing at the SCJ at the cardia (Kim and Shivdasani, 2011), consistent with our hypothesis that Lgr5 cells from the gastric cardia migrate into the distal esophagus to give rise to BE tissue with increased Notch activation and Lgr5 expression. With the expansion of progenitor cells in BE, we observe a similar expansion of Dll1^{+} cells immediately adjacent to Notch expressing cells within the metaplastic lineage. The strong correlation between Dll1 with the progenitor cell zone and proliferation, and Jagged2 with postmitotic, differentiated cells, suggests a potential mechanism for modulation of progenitor cell expansion and differentiation through Notch signaling. In this model, Dll1 promotes progenitor

cell maintenance and proliferation, and Jagged2 inhibits proliferation and promotes differentiation, both a consequence of intraepithelial crosstalk between progenitor cells and their progeny. We would further hypothesize, that the development of IM occurs in a low Notch signaling environment, whereas maintenance of the CLE phenotype and progression to dysplasia occurs in a high Notch signaling environment.

Taken together, our data strongly suggest that BE arises from a gastric cardia lineage, as originally suggested (Hamilton and Yardley, 1977). Indeed, it has been difficult to distinguish at the histopathological level between so-called esophagogastric "junctional tumors" that appear localized to the cardia and EAC, clearly present in the esophagus. The fact that BE always begins precisely at the SCJ has never otherwise been explained, and it now seems clear that special consideration should be given to "carditis," inflammation of the gastric cardia that may represent a precursor lesion of BE and EAC.

EXPERIMENTAL PROCEDURES

For a detailed description of all methods see Supplemental Experimental Procedures.

Mice

All mice studies and breeding were carried out under the approval of Institutional Animal Care and Use Committee of Columbia University. Human *IL-1β* transgenic mice were generated by targeting expression of hIL-1β to the esophagus using the Epstein-Bar virus promoter. Mice were placed on drinking water containing bile acids (0.3% DCA, pH 7.0) at the age of 3 months. Nine-month-old L2-IL-1β mice were subjected to a 5-day treatment regimen with the GSI (DBZ, 30 mmol/kg). Lineage tracing studies were performed with Lgr5-CreTM-IRES-GFP mice crossed to Rosa26R-LacZ reporter and L2-IL-1β mice. Tamoxifen (6 mg) was given at the age of 6–8 weeks prior to administration of BA.

Human Study

Esophageal tissue was obtained from 46 patients with BE, with and without dysplasia. Biopsies were taken for clinical and research purposes. This study was approved by the Columbia University Institutional Review Board and informed consent was obtained from all patients.

ACCESSION NUMBERS

Micro array information were deposited at the Gene Expression Omnibus database (http://www.ncbi.nlm.nih.gov/geo/) with the accession number GSE24931.

SUPPLEMENTAL INFORMATION

Supplemental Information includes four figures, three tables, Supplemental Experimental Procedures, and five movies and can be found with this article online at doi:10.1016/j.ccr.2011.12.004.

ACKNOWLEDGMENTS

These studies are supported by NIH (RO1DK060758, 1U54CA126513, and R01CA120979 to T.C.W; 5U01 CA143056 to A.K.R., T.C.W., U.M.). A.K.R. was further supported by NIH P01-CA098101 and P30-DK050306 grants. M.Q. was supported by a grant from the Mildred-Scheel-Stiftung, Deutsche Krebshilfe, Germany. J.A. is supported by a Career Development Award from the NCI (K07 CA132892) and by a Louis V. Gerstner, Jr. Scholars Award. We acknowledge the assistance of the Transgenic Mouse and Genomics Core of the Irving Cancer Research Center at Columbia University, and the Electronic Microscopy Core Facility at the University of Pennsylvania. We thank all members of the Wang lab for fruitful discussions.

Received: January 14, 2011
Revised: June 2, 2011
Accepted: December 1, 2011
Published: January 17, 2012

REFERENCES

Allison, P.R., and Johnstone, A.S. (1953). The oesophagus lined with gastric mucous membrane. Thorax *8*, 87–101.

Barbera, M., and Fitzgerald, R.C. (2010). Cellular origin of Barrett metaplasia and oesophageal stem cells. Biochem. Soc. Trans. *38*, 370–373.

Barker, N., Huch, M., Kujala, P., van de Wetering, M., Snippert, H.J., van Es, J.H., Sato, T., Stange, D.E., Begthel, H., van den Born, M., et al. (2010). Lgr5(+ve) stem cells drive self-renewal in the stomach and build long-lived gastric units in vitro. Cell Stem Cell *6*, 25–36.

Benedito, R., Roca, C., Sörensen, I., Adams, S., Gossler, A., Fruttiger, M., and Adams, R.H. (2009). The notch ligands Dll4 and Jagged1 have opposing effects on angiogenesis. Cell *137*, 1124–1135.

Bernstein, H., Payne, C.M., Bernstein, C., Schneider, J., Beard, S.E., and Crowley, C.L. (1999). Activation of the promoters of genes associated with DNA damage, oxidative stress, ER stress and protein malfolding by the bile salt, deoxycholate. Toxicol. Lett. *108*, 37–46.

Bernstein, H., Bernstein, C., Payne, C.M., Dvorakova, K., and Garewal, H. (2005). Bile acids as carcinogens in human gastrointestinal cancers. Mutat. Res. *589*, 47–65.

Björkdahl, O., Akerblad, P., Gjörloff-Wingren, A., Leanderson, T., and Dohlsten, M. (1999). Lymphoid hyperplasia in transgenic mice over-expressing a secreted form of the human interleukin-1beta gene product. Immunology *96*, 128–137.

Bollrath, J., Phesse, T.J., von Burstin, V.A., Putoczki, T., Bennecke, M., Bateman, T., Nebelsiek, T., Lundgren-May, T., Canli, O., Schwitalla, S., et al. (2009). gp130-mediated Stat3 activation in enterocytes regulates cell survival and cell-cycle progression during colitis-associated tumorigenesis. Cancer Cell *15*, 91–102.

Brembeck, F.H., Moffett, J., Wang, T.C., and Rustgi, A.K. (2001). The keratin 19 promoter is potent for cell-specific targeting of genes in transgenic mice. Gastroenterology *120*, 1720–1728.

Chatelain, D., and Fléjou, J.F. (2003). High-grade dysplasia and superficial adenocarcinoma in Barrett esophagus: histological mapping and expression of p53, p21 and Bcl-2 oncoproteins. Virchows Arch. *442*, 18–24.

Corley, D.A., Kubo, A., Levin, T.R., Block, G., Habel, L., Rumore, G., Quesenberry, C., and Buffler, P. (2009). Race, ethnicity, sex and temporal differences in Barrett oesophagus diagnosis: a large community-based study, 1994-2006. Gut *58*, 182–188.

Dvorak, K., Payne, C.M., Chavarria, M., Ramsey, L., Dvorakova, B., Bernstein, H., Holubec, H., Sampliner, R.E., Guy, N., Condon, A., et al. (2007). Bile acids in combination with low pH induce oxidative stress and oxidative DNA damage: relevance to the pathogenesis of Barrett oesophagus. Gut *56*, 763–771.

Ernst, M., Najdovska, M., Grail, D., Lundgren-May, T., Buchert, M., Tye, H., Matthews, V.B., Armes, J., Bhathal, P.S., Hughes, N.R., et al. (2008). STAT3 and STAT1 mediate IL-11-dependent and inflammation-associated gastric tumorigenesis in gp130 receptor mutant mice. J. Clin. Invest. *118*, 1727–1738.

Falk, G.W. (2002). Barrett esophagus. Gastroenterology *122*, 1569–1591.

Fein, M., Peters, J.H., Chandrasoma, P., Ireland, A.P., Oberg, S., Ritter, M.P., Bremner, C.G., Hagen, J.A., and DeMeester, T.R. (1998). Duodenoesophageal reflux induces esophageal adenocarcinoma without exogenous carcinogen. J. Gastrointest. Surg. *2*, 260–268.

Fitzgerald, R.C., Abdalla, S., Onwuegbusi, B.A., Sirieix, P., Saeed, I.T., Burnham, W.R., and Farthing, M.J. (2002). Inflammatory gradient in Barrett oesophagus: implications for disease complications. Gut *51*, 316–322.

Fox, J.G., Beck, P., Dangler, C.A., Whary, M.T., Wang, T.C., Shi, H.N., and Nagler-Anderson, C. (2000). Concurrent enteric helminth infection modulates inflammation and gastric immune responses and reduces Helicobacter-induced gastric atrophy. Nat. Med. *6*, 536–542.

Fridlender, Z.G., Sun, J., Kim, S., Kapoor, V., Cheng, G., Ling, L., Worthen, G.S., and Albelda, S.M. (2009). Polarization of tumor-associated neutrophil phenotype by TGF-beta: "N1" versus "N2" TAN. Cancer Cell *16*, 183–194.

Gatenby, P.A., Ramus, J.R., Caygill, C.P., Shepherd, N.A., and Watson, A. (2008). Relevance of the detection of intestinal metaplasia in non-dysplastic columnar-lined oesophagus. Scand. J. Gastroenterol. *43*, 524–530.

Giannakis, M., Stappenbeck, T.S., Mills, J.C., Leip, D.G., Lovett, M., Clifton, S.W., Ippolito, J.E., Glasscock, J.I., Arumugam, M., Brent, M.R., and Gordon, J.I. (2006). Molecular properties of adult mouse gastric and intestinal epithelial progenitors in their niches. J. Biol. Chem. *281*, 11292–11300.

Goldblum, J.R. (2010). Controversies in the diagnosis of Barrett esophagus and Barrett-related dysplasia: one pathologist's perspective. Arch. Pathol. Lab. Med. *134*, 1479–1484.

Gough, M.D., Ackroyd, R., Majeed, A.W., and Bird, N.C. (2005). Prediction of malignant potential in reflux disease: are cytokine polymorphisms important? Am. J. Gastroenterol. *100*, 1012–1018.

Grivennikov, S., and Karin, M. (2008). Autocrine IL-6 signaling: a key event in tumorigenesis? Cancer Cell *13*, 7–9.

Grivennikov, S.I., Greten, F.R., and Karin, M. (2010). Immunity, inflammation, and cancer. Cell *140*, 883–899.

Hamilton, S.R., and Yardley, J.H. (1977). Regenerative of cardiac type mucosa and acquisition of Barrett mucosa after esophagogastrostomy. Gastroenterology *72*, 669–675.

Hanby, A.M., Jankowski, J.A., Elia, G., Poulsom, R., and Wright, N.A. (1994). Expression of the trefoil peptides pS2 and human spasmolytic polypeptide (hSP) in Barrett metaplasia and the native oesophageal epithelium: delineation of epithelial phenotype. J. Pathol. *173*, 213–219.

Howlett, M., Giraud, A.S., Lescesen, H., Jackson, C.B., Kalantzis, A., Van Driel, I.R., Robb, L., Van der Hoek, M., Ernst, M., Minamoto, T., et al. (2009). The interleukin-6 family cytokine interleukin-11 regulates homeostatic epithelial cell turnover and promotes gastric tumor development. Gastroenterology *136*, 967–977.

Hvid-Jensen, F., Pedersen, L., Drewes, A.M., Sørensen, H.T., and Funch-Jensen, P. (2011). Incidence of adenocarcinoma among patients with Barrett esophagus. N. Engl. J. Med. *365*, 1375–1383.

Jankowski, J.A., Wright, N.A., Meltzer, S.J., Triadafilopoulos, G., Geboes, K., Casson, A.G., Kerr, D., and Young, L.S. (1999). Molecular evolution of the metaplasia-dysplasia-adenocarcinoma sequence in the esophagus. Am. J. Pathol. *154*, 965–973.

Jankowski, J.A., Harrison, R.F., Perry, I., Balkwill, F., and Tselepis, C. (2000). Barrett metaplasia. Lancet *356*, 2079–2085.

Jiang, L., Gonda, T.A., Gamble, M.V., Salas, M., Seshan, V., Tu, S., Twaddell, W.S., Hegyi, P., Lazar, G., Steele, I., et al. (2008). Global hypomethylation of genomic DNA in cancer-associated myofibroblasts. Cancer Res. *68*, 9900–9908.

Jin, G., Ramanathan, V., Quante, M., Baik, G.H., Yang, X., Wang, S.S., Tu, S., Gordon, S.A., Pritchard, D.M., Varro, A., et al. (2009). Inactivating cholecystokinin-2 receptor inhibits progastrin-dependent colonic crypt fission, proliferation, and colorectal cancer in mice. J. Clin. Invest. *119*, 2691–2701.

Kalabis, J., Oyama, K., Okawa, T., Nakagawa, H., Michaylira, C.Z., Stairs, D.B., Figueiredo, J.L., Mahmood, U., Diehl, J.A., Herlyn, M., and Rustgi, A.K. (2008). A subpopulation of mouse esophageal basal cells has properties of stem cells with the capacity for self-renewal and lineage specification. J. Clin. Invest. *118*, 3860–3869.

Kauer, W.K., Peters, J.H., DeMeester, T.R., Feussner, H., Ireland, A.P., Stein, H.J., and Siewert, R.J. (1997). Composition and concentration of bile acid reflux into the esophagus of patients with gastroesophageal reflux disease. Surgery *122*, 874–881.

Kazumori, H., Ishihara, S., Rumi, M.A., Kadowaki, Y., and Kinoshita, Y. (2006). Bile acids directly augment caudal related homeobox gene Cdx2 expression in oesophageal keratinocytes in Barrett epithelium. Gut *55*, 16–25.

Kelty, C.J., Gough, M.D., Van Wyk, Q., Stephenson, T.J., and Ackroyd, R. (2007). Barrett oesophagus: intestinal metaplasia is not essential for cancer risk. Scand. J. Gastroenterol. *42*, 1271–1274.

Kim, T.H., and Shivdasani, R.A. (2011). Notch signaling in stomach epithelial stem cell homeostasis. J. Exp. Med. *208*, 677–688.

Leedham, S.J., Preston, S.L., McDonald, S.A., Elia, G., Bhandari, P., Poller, D., Harrison, R., Novelli, M.R., Jankowski, J.A., and Wright, N.A. (2008). Individual crypt genetic heterogeneity and the origin of metaplastic glandular epithelium in human Barrett oesophagus. Gut *57*, 1041–1048.

Lesina, M., Kurkowski, M.U., Ludes, K., Rose-John, S., Treiber, M., Kloppel, G., Yoshimura, A., Reindl, W., Sipos, B., Akira, S., et al. (2011). Stat3/Socs3 activation by IL-6 transsignaling promotes progression of pancreatic intraepithelial neoplasia and development of pancreatic cancer. Cancer Cell *19*, 456–469.

Li, Y., and Martin, R.C., 2nd. (2007). Reflux injury of esophageal mucosa: experimental studies in animal models of esophagitis, Barrett's esophagus and esophageal adenocarcinoma. Dis. Esophagus *20*, 372–378.

Means, A.L., Xu, Y., Zhao, A., Ray, K.C., and Gu, G. (2008). A CK19(CreERT) knockin mouse line allows for conditional DNA recombination in epithelial cells in multiple endodermal organs. Genesis *46*, 318–323.

Menke, V., van Es, J.H., de Lau, W., van den Born, M., Kuipers, E.J., Siersema, P.D., de Bruin, R.W., Kusters, J.G., and Clevers, H. (2010). Conversion of metaplastic Barrett epithelium into post-mitotic goblet cells by gamma-secretase inhibition. Dis. Model Mech. *3*, 104–110.

Nakagawa, H., Wang, T.C., Zukerberg, L., Odze, R., Togawa, K., May, G.H., Wilson, J., and Rustgi, A.K. (1997). The targeting of the cyclin D1 oncogene by an Epstein-Barr virus promoter in transgenic mice causes dysplasia in the tongue, esophagus and forestomach. Oncogene *14*, 1185–1190.

Nakanishi, Y., Saka, M., Eguchi, T., Sekine, S., Taniguchi, H., and Shimoda, T. (2007). Distribution and significance of the oesophageal and gastric cardiac mucosae: a study of 131 operation specimens. Histopathology *51*, 515–519.

O'Riordan, J.M., Abdel-Latif, M.M., Ravi, N., McNamara, D., Byrne, P.J., McDonald, G.S., Keeling, P.W., Kelleher, D., and Reynolds, J.V. (2005). Proinflammatory cytokine and nuclear factor kappa-B expression along the inflammation-metaplasia-dysplasia-adenocarcinoma sequence in the esophagus. Am. J. Gastroenterol. *100*, 1257–1264.

Odze, R.D., and Maley, C.C. (2010). Neoplasia without dysplasia: lessons from Barrett esophagus and other tubal gut neoplasms. Arch. Pathol. Lab. Med. *134*, 896–906.

Ogiya, K., Kawano, T., Ito, E., Nakajima, Y., Kawada, K., Nishikage, T., and Nagai, K. (2008). Lower esophageal palisade vessels and the definition of Barrett esophagus. Dis. Esophagus *21*, 645–649.

Payne, C.M., Crowley-Weber, C.L., Dvorak, K., Bernstein, C., Bernstein, H., Holubec, H., Crowley, C., and Garewal, H. (2005). Mitochondrial perturbation attenuates bile acid-induced cytotoxicity. Cell Biol. Toxicol. *21*, 215–231.

Playford, R.J. (2006). New British Society of Gastroenterology (BSG) guidelines for the diagnosis and management of Barrett oesophagus. Gut *55*, 442.

Quante, M., Marrache, F., Goldenring, J.R., and Wang, T.C. (2010). TFF2 mRNA transcript expression marks a gland progenitor cell of the gastric oxyntic mucosa. Gastroenterology *139*, 2018–2027.

Riddell, R.H., and Odze, R.D. (2009). Definition of Barrett esophagus: time for a rethink—is intestinal metaplasia dead? Am. J. Gastroenterol. *104*, 2588–2594.

Sato, F., and Meltzer, S.J. (2006). CpG island hypermethylation in progression of esophageal and gastric cancer. Cancer *106*, 483–493.

Spechler, S.J., Fitzgerald, R.C., Prasad, G.A., and Wang, K.K. (2010). History, molecular mechanisms, and endoscopic treatment of Barrett esophagus. Gastroenterology *138*, 854–869.

Stairs, D.B., Nakagawa, H., Klein-Szanto, A., Mitchell, S.D., Silberg, D.G., Tobias, J.W., Lynch, J.P., and Rustgi, A.K. (2008). Cdx1 and c-Myc foster the initiation of transdifferentiation of the normal esophageal squamous epithelium toward Barrett esophagus. PLoS ONE *3*, e3534.

Stairs, D.B., Bayne, L.J., Rhoades, B., Vega, M.E., Waldron, T.J., Kalabis, J., Klein-Szanto, A., Lee, J.S., Katz, J.P., Diehl, J.A., et al. (2011). Deletion of p120-catenin results in a tumor microenvironment with inflammation and cancer that establishes it as a tumor suppressor gene. Cancer Cell *19*, 470–483.

Takubo, K., Aida, J., Naomoto, Y., Sawabe, M., Arai, T., Shiraishi, H., Matsuura, M., Ell, C., May, A., Pech, O., et al. (2009). Cardiac rather than intestinal-type background in endoscopic resection specimens of minute Barrett adenocarcinoma. Hum. Pathol. *40*, 65–74.

Tatsuta, T., Mukaisho, K., Sugihara, H., Miwa, K., Tani, T., and Hattori, T. (2005). Expression of Cdx2 in early GRCL of Barrett esophagus induced in rats by duodenal reflux. Dig. Dis. Sci. *50*, 425–431.

Theisen, J., Nehra, D., Citron, D., Johansson, J., Hagen, J.A., Crookes, P.F., DeMeester, S.R., Bremner, C.G., DeMeester, T.R., and Peters, J.H. (2000). Suppression of gastric acid secretion in patients with gastroesophageal reflux disease results in gastric bacterial overgrowth and deconjugation of bile acids. J. Gastrointest. Surg. *4*, 50–54.

Tomita, H., Takaishi, S., Menheniott, T.R., Yang, X., Shibata, W., Jin, G., Betz, K.S., Kawakami, K., Minamoto, T., Tomasetto, C., et al. (2011). Inhibition of gastric carcinogenesis by the hormone gastrin is mediated by suppression of TFF1 epigenetic silencing. Gastroenterology *104*, 879–891.

Tu, S., Bhagat, G., Cui, G., Takaishi, S., Kurt-Jones, E.A., Rickman, B., Betz, K.S., Penz-Oesterreicher, M., Bjorkdahl, O., Fox, J.G., and Wang, T.C. (2008). Overexpression of interleukin-1beta induces gastric inflammation and cancer and mobilizes myeloid-derived suppressor cells in mice. Cancer Cell *14*, 408–419.

Vaccaro, B.J., Gonzalez, S., Poneros, J.M., Stevens, P.D., Capiak, K.M., Lightdale, C.J., and Abrams, J.A. (2011). Detection of intestinal metaplasia after successful eradication of Barrett Esophagus with radiofrequency ablation. Dig. Dis. Sci. *56*, 1996–2000.

Van De Bovenkamp, J.H., Korteland-Van Male, A.M., Warson, C., Büller, H.A., Einerhand, A.W., Ectors, N.L., and Dekker, J. (2003). Gastric-type mucin and TFF-peptide expression in Barrett oesophagus is disturbed during increased expression of MUC2. Histopathology *42*, 555–565.

Wang, X., Ouyang, H., Yamamoto, Y., Kumar, P.A., Wei, T.S., Dagher, R., Vincent, M., Lu, X., Bellizzi, A.M., Ho, K.Y., et al. (2011). Residual embryonic cells as precursors of a Barrett-like metaplasia. Cell *145*, 1023–1035.

Warson, C., Van De Bovenkamp, J.H., Korteland-Van Male, A.M., Büller, H.A., Einerhand, A.W., Ectors, N.L., and Dekker, J. (2002). Barrett esophagus is characterized by expression of gastric-type mucins (MUC5AC, MUC6) and TFF peptides (TFF1 and TFF2), but the risk of carcinoma development may be indicated by the intestinal-type mucin, MUC2. Hum. Pathol. *33*, 660–668.

Watanabe, F., Iwasaki, Y., Ohashi, M., Nunobe, S., Iwagami, S., Takahashi, K., Yamaguchi, T., Matsumoto, H., and Yasutome, M. (2007). [A case report-the marked response to S-1 + CDDP chemotherapy for post-operative local recurrence of advanced gastric cancer]. Gan To Kagaku Ryoho *34*, 1970–1972.

Winter, J.W., Paterson, S., Scobie, G., Wirz, A., Preston, T., and McColl, K.E. (2007). N-nitrosamine generation from ingested nitrate via nitric oxide in subjects with and without gastroesophageal reflux. Gastroenterology *133*, 164–174.

Yang, X.D., Ai, W., Asfaha, S., Bhagat, G., Friedman, R.A., Jin, G., Park, H., Shykind, B., Diacovo, T.G., Falus, A., and Wang, T.C. (2011). Histamine deficiency promotes inflammation-associated carcinogenesis through reduced myeloid maturation and accumulation of CD11b+Ly6G+ immature myeloid cells. Nat. Med. *17*, 87–95.

Yu, W.Y., Slack, J.M., and Tosh, D. (2005). Conversion of columnar to stratified squamous epithelium in the developing mouse oesophagus. Dev. Biol. *284*, 157–170.

Cancer Cell
Article

Endothelial Cell HIF-1α and HIF-2α Differentially Regulate Metastatic Success

Cristina Branco-Price,[1] Na Zhang,[2] Moritz Schnelle,[4] Colin Evans,[1] Dörthe M. Katschinski,[4] Debbie Liao,[2] Lesley Ellies,[3] and Randall S. Johnson[1,*]
[1]Department of Physiology, Development and Neuroscience, University of Cambridge, CB2 3EG Cambridge, UK
[2]Department of Biology
[3]Department of Pathology
University of California, San Diego, La Jolla, CA 92093, USA
[4]Department of Cardiovascular Physiology, Universitätsmedizin Göttingen, Georg-August University Göttingen, D-37073 Göttingen, Germany
*Correspondence: rsj33@cam.ac.uk
DOI 10.1016/j.ccr.2011.11.017

SUMMARY

The hypoxia inducible transcription factors (HIFs) control many mediators of vascular response, including both angiogenic factors and small molecules such as nitric oxide (NO). In studying how endothelial HIF response itself affects metastasis, we found that loss of HIF-1α in endothelial cells reduces NO synthesis, retards tumor cell migration through endothelial layers, and restricts tumor cell metastasis, and that loss of HIF-2α has in each case the opposite effect. This results from differential regulation of NO homeostasis that in turn regulates vascular endothelial growth factor expression in an NO-dependent feedback loop. These opposing roles for the two HIF factors indicate that both they and endothelial cells regulate metastasis as malignancy progresses.

INTRODUCTION

There is a link between the metastatic process and oxygen deprivation (Brizel et al., 1996; Rofstad et al., 2010; Voss et al., 2011). Hypoxia itself triggers the induction of the hypoxia inducible (HIF) transcription factors; these in turn are linked to changes in the capacity of tumor cells to migrate, undergo epithelial to mesenchymal transition, and to a number of other processes intrinsic to metastasis (Chen et al., 2010; Haase, 2009; Liao et al., 2007; Yang et al., 2008). Hypoxic response via HIF activation also includes expression of factors such as vascular endothelial growth factor (*VEGF*), and inducible nitric oxide synthase (*iNOS*) that are known to facilitate both angiogenesis and tumor cell access to the circulatory system (Ambs et al., 1998; Claffey et al., 1996; Shweiki et al., 1992; Ziche and Morbidelli, 2009).

The role of the tumor cell in metastasis has been widely examined and discussed (Chambers et al., 2002; Gupta and Massagué, 2006). Significant evidence exists to indicate that migration of tumor cells during hematogenous metastasis is accelerated by a HIF-driven response (Liao et al., 2007; Lu et al., 2010; Zhong et al., 1999). This response in the metastatic cell may be driven in part by alterations in tumor oxygenation, which also impacts the tumor endothelium, and it follows that the hypoxic endothelial cell (EC), because of its location, could act as a gatekeeper to metastatic cell intravasation.

As intravasatory processes are related to the hypoxia found throughout many solid tumors, hypoxia is also tied to the extravasation process, through the arrest of migrating tumor cells in capillary beds. The resultant thrombus formation can also result in local hypoxia and ischemia, and reemergence of a growing tumor through a second endothelial barrier. Evidence to support this model includes the clear relationship between thrombus formation and metastatic success (Amirkhosravi et al., 2010; Cliffton and Grossi, 1974; Ostrowski et al., 1986; Palumbo et al., 2005; Saito et al., 1980).

Hypoxia has potent effects on regulation of nitric oxide (NO) (Melillo et al., 1995; Olson and van der Vliet, 2011; Takeda et al., 2010). NO can affect the overall vascular tension of tumor vessels, and also has numerous other localized effects on vascular function (Gunnett et al., 2005; Ignarro et al., 1987;

Significance

There is a central role for endothelial cells in the process of metastasis: they represent a critical barrier to the passage of tumor cells in their migration toward other organs. Vascular damage, clotting, and ischemia are correlated with tumor metastasis, and all involve hypoxic insult to the endothelium. This study demonstrates that the endothelial cell HIF response is complex, and can act to both promote and retard metastasis, dependent on the HIF isoform expressed and the overall regulation of endothelial nitric oxide production via hypoxic response.

Palmer et al., 1987). Previous work has demonstrated that NO synthesis in EC under normoxia is controlled primarily by endothelial NO synthase (eNOS) (Fukumura et al., 2001). However, hypoxic response induces NO chiefly via iNOS. Intriguingly, some reports have indicated that iNOS itself can positively regulate *VEGF* expression during tumorigenesis (Van der Wall and Palmer, 2006; Wang et al., 2001).

We have recently shown that in inflammatory cells, NO homeostasis is modulated by differential expression of the HIF isoforms HIF-1 and HIF-2 (Takeda et al., 2010) via regulation of two opposing uses of l-arginine: HIF-1α-induced expression of *iNOS*, and HIF-2α induced expression of arginase 1 (*ARG1*), which can remove l-arginine from NO synthetic pathways and thus reduce NO levels. The primary aim of this study was to investigate the effect of EC-specific deletion of HIF-1α or HIF-2α on NO homeostasis and metastatic progression.

RESULTS

Loss of HIF-1α in Endothelial Cells Reduces Metastatic Rate

To examine HIF function and endothelial hypoxic response in metastasis, metastatic success was assayed in murine progressive transgenic tumorigenesis, utilizing the *MMTV-PyMT* model of mammary cancer (Lin et al., 2003). These mice, maintained on a C57/Bl6 inbred background were crossed to mice carrying a conditional deletion of *HIF-1α* (Ryan et al., 2000) and the *TIE2CRE* transgenic strain (Kisanuki et al., 2001). The expression of the cre recombinase driven by the Tie2 promoter causes deletion in conditionally targeted endothelial cells and bone marrow-derived cells (Constien et al., 2001). In these first experiments, and in keeping with previously published results (Tang et al., 2004), overall effects on primary tumor growth were only moderate (Figure 1A); however, metastatic success was strongly reduced. At 16 weeks of age, when lung metastatic foci first become evident in this model, they are virtually absent in the *Tie2Cre+ HIF-1α^{df}* mice (Figure 1B, left). This reduction in metastasis is also evident at the endpoint of the model, where overall primary tumor burdens are similar in wild-type and mutant animals (Figure 1A); but where there is still an ~75% reduction in numbers of metastatic pulmonary foci (Figure 1B, right). At the terminal stage in this model, there was no significant difference in vascular density in the mutant mouse tumors relative to wild-type animals vascular density (data not shown).

Bone marrow transplantations of wild-type (*WT*) marrow were then introduced into control and mutant mice; this is necessary to circumvent bone marrow expression of the cre recombinase in *Tie2+cre* mice, and results in mice with a deletion solely in endothelial cells (Tang et al., 2004). When GFP-tagged Lewis lung carcinoma cells (LLC) were introduced into mammary fat pads and allowed to grow for 3 weeks, the size of the primary tumor in the different hosts was again identical as were vessel densities (data not shown), but the number of pulmonary foci was significantly reduced (Figure 1C, left). Further analysis of the number of circulating GFP-tagged tumor cells in the bloodstream at the time of sacrifice indicated tumor cells in the circulation were reduced by ~50% in tumor-bearing *HIF-1α* endothelial cell deletion mutants (Figure 1C, right). This indicates that HIF-1α in the endothelium plays a significant role in determining the number of intravasating tumor cells in this model.

Migration of Tumor Cells through Primary Endothelial Cell Layers Is Differentially Controlled by HIF-1α and HIF-2α

To better understand the mechanisms underlying HIF control of tumor cell migration in vivo, a tissue culture model of the movement of tumor cells through an endothelial layer was utilized. Primary murine lung endothelial cells were harvested from conditionally targeted mice and treated with cre recombinase-expressing or control adenovirus; they were then assayed for deletion efficacy, and subsequently cultured on an 8 μm filter insert. Labeled tumor cells were then introduced to the control or nullizygous endothelial cell layers and exposed to normoxia or hypoxia (1% O_2) for 9 hr, after which tumor cells that migrated through the endothelial cell layer were counted. As can be seen in Figure 1D, hypoxia acts to accelerate the migration of tumor cells through wild-type endothelial cells in this system. However, this increased migration is very significantly reduced when endothelial cells lack HIF-1α (Figure 1D). Conversely, endothelial cells lacking HIF-2α (Gruber et al., 2007) exhibit the opposite phenotype: there, migration of tumor cells through the mutant endothelial layer is accelerated relative to wild-type cells under both normoxic and hypoxic conditions.

Deletion of Both iNOS and VEGF Inhibits Tumor Cell Migration through Endothelial Cell Layers during Hypoxia

Two HIF target genes known to produce mediators of endothelial cell permeability are the angiogenic factor vascular endothelial growth factor-A, or *VEGF-A*, and the inducible NO synthase, or *iNOS* (or *NOS2*). To determine whether loss of either gene in endothelial cells affects the migration of tumor cells in this assay, primary lung *iNOS* null endothelial cells from global deletion animals, and VEGF-A conditional null (Gerber et al., 1999) primary lung endothelial cells (the latter treated ex vivo with cre recombinase-expressing virus, as above) were isolated. Loss of both endothelial *VEGF-A* and *iNOS* restricts the hypoxia-induced migration of tumor cells through the endothelial monolayer (Figure 1E).

Differential Regulation of VEGF Is Influenced by iNOS Expression during Hypoxia

As shown above, loss of either *iNOS* or *VEGF* in endothelial cells inhibits transmigration of tumor cells in a cell culture assay. To determine whether iNOS or VEGF is up- or downstream during hypoxic signaling in endothelial cells, *iNOS* mRNA expression was assayed in primary *VEGF null* endothelial cells during hypoxia (Figure 2A); and similarly, *VEGF-A* expression was assayed in *iNOS null* endothelial cells under the same conditions (Figure 2B). Loss of *VEGF* in endothelial cells has no significant effect on expression of *iNOS* in normoxia, but did affect hypoxic induction of iNOS (Figure 2A). However, loss of *iNOS* in endothelial cells suppresses *VEGF* expression in both normoxia and hypoxia (Figure 2B), as does specific inhibition of iNOS with 1400W in WT EC (Figure 2C). To determine whether this effect on *VEGF* expression in endothelial cells is NO-dependent, an NO donor (DETANONOate) was added to cultures to

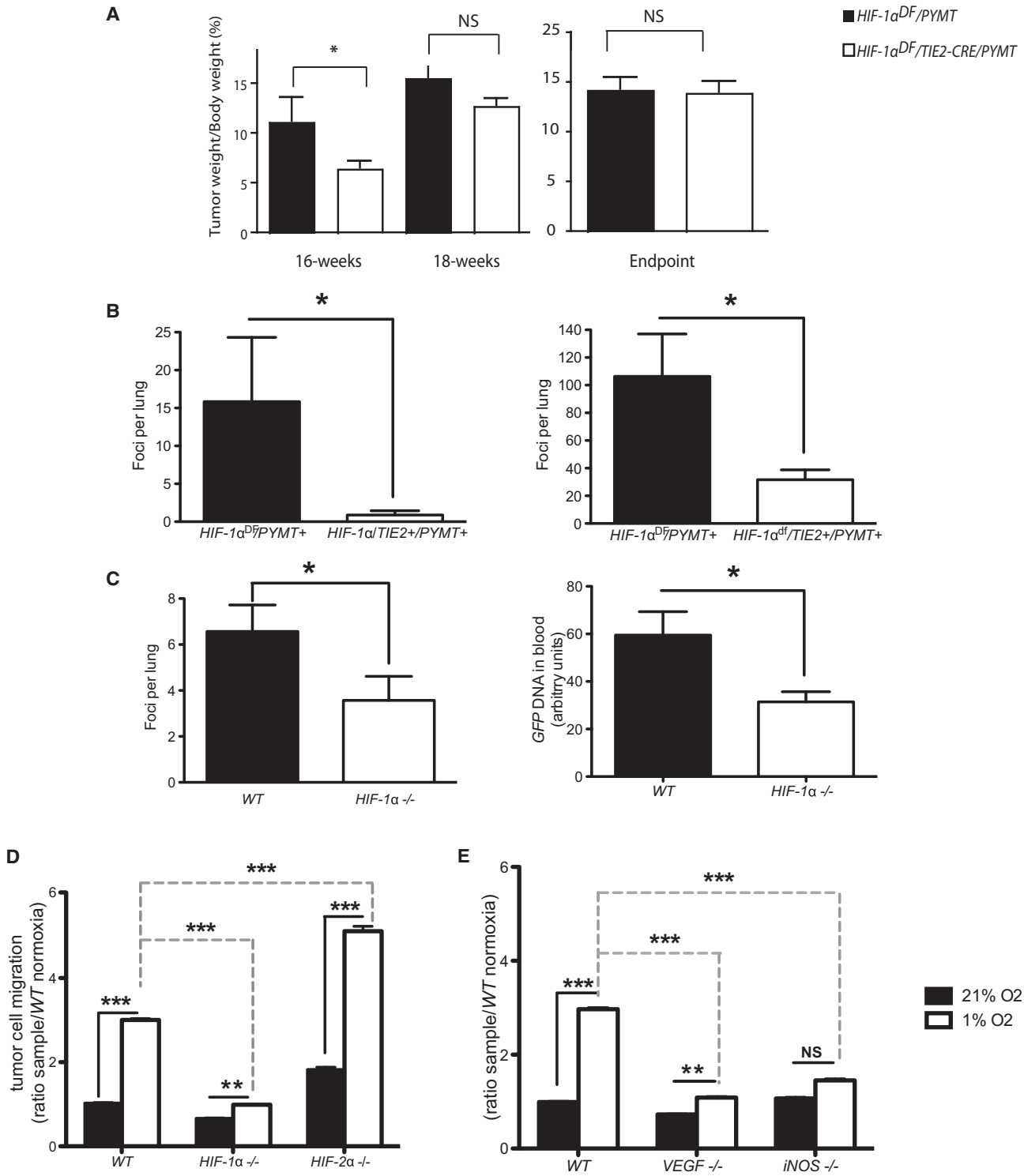

Figure 1. *HIF-1α* Deletion in Endothelial Cells Leads to Reduction in Metastatic Incidence in Transgenic and Xenograft Models

(A) Effect of Tie2-driven deletion of HIF-1α on primary tumor growth in the spontaneous breast tumor model PyMT (*HIF-1α^{df}/Tie2Cre/PyMT*) during different stages during tumor development, at 16 and 18 weeks, and at endpoint (when one tumor reaches diameter of 1 cm).

(B) Effect of Tie2-driven deletion of *HIF-1α* on spontaneous breast tumor model *PyMT* (*HIF-1α^{df}/Tie2Cre/PyMT*) tumor metastases at 16 wks of age (left panel), and at endpoint (when one tumor reaches diameter of 1 cm, right panel).

(C) LLC^{GFP} cells were implanted in cleared mammary pads of endothelial cell-specific deletion of *HIF-1α* (HIF-1α null) obtained by regenerating *WT* bone marrow into *HIF-1α^{df}/Tie2cre+* mice. Effect of endothelial *HIF-1α* deletion on frequency of lung metastasis 3 weeks after tumor cell implantation (left) and on blood genomic *GFP* levels, a measure of relative abundance of circulating tumor cells (right); Data in (A–C) are average ± SEM.

a concentration of 5 mM; this addition resulted in restored VEGF expression under hypoxia in *iNOS null* cells (Figure 2D). This demonstrates that the hypoxic induction of *VEGF* in endothelial cells is regulated by iNOS-mediated production of NO.

Endothelial Cell Expression of VEGF Is Suppressed by an iNOS-Specific Inhibitor in a Tissue-Specific Fashion

The inhibition of hypoxic induction of autocrine VEGF-A would be expected to reduce hypoxic activation of the Flk-1 (VEGFR2) receptor by phosphorylation, and this is indeed seen in *iNOS null* primary endothelial cells (Figure 2E, left, and phosphor imaging quantification, right). Immunoprecipitation of VEGFR2 from primary lung endothelial cells followed by detection of phosphotyrosine demonstrates that the hypoxic activation of VEGFR2 is significantly reduced in cells lacking iNOS.

VEGFR2 signaling is critical for the induction of tube formation in cultured endothelium (Zhang et al., 2010). To determine whether endothelial cell *iNOS* expression also affects this VEGF-A-dependent phenomenon, cultured EC were placed on collagen matrices, and as shown in Figure 2F, loss of EC *iNOS* reduced tube formation ~90%. Inhibition of iNOS protein activity by the iNOS-specific inhibitor 1400W (30 μM) also reduced tube formation significantly. These results indicate that iNOS is a critical determinant of function in endothelial cells in isolation.

Gene Expression Analysis of Hypoxic Endothelial Cells

It was recently shown that loss of *HIF-1α* and *HIF-2α* in macrophages has differential effects on the regulation of NO production; loss of *HIF-1α* resulting in decreased *iNOS* expression and decreased NO levels, and loss of *HIF-2α* in decreased *ARG1* expression and increased NO availability (Takeda et al., 2010). Examination of normoxic expression of *iNOS* and *ARG1* in *WT*, *HIF-1α*, and *HIF-2α null* endothelial cells reveals that the two HIF-α factors also regulate *iNOS* and *ARG1* differentially in these cells. Loss of either *HIF-1α* or *HIF-2α* reduced the expression of both *iNOS* and *VEGF* during hypoxia (Figure 3A); however, only the loss of HIF-2α significantly reduced the expression of Arginase1.

Hypoxic Induction of NO in Endothelial Cells Is HIF-1α and iNOS Dependent

A number of studies have determined that under normoxic circumstances, the primary factor in normoxic endothelial NO production is the endothelial NO synthase (*eNOS*) (Fukumura et al., 2001); however, *eNOS* is neither a HIF target nor a hypoxically responsive gene. To determine the role of iNOS in endothelial cell hypoxia-induced NO production, assays for NO metabolites were carried out on conditioned medium from normoxic or hypoxic endothelial cells. There is a significant increase in NO metabolites in hypoxically conditioned media, and this is dependent on HIF-1α (Figure 3B). HIF-2α loss causes an increase in NO metabolites under normoxic conditions when compared to wild-type cells.

Inhibition of VEGF Expression by Suppression of iNOS Is Specific to Endothelial Cells

To determine the endothelial specificity of the effects described above, primary lung murine endothelial cells (mEC), human umbilical vein endothelial cells (hUVEC), murine embryonic fibroblasts (mEF), and Lewis lung carcinoma cells (LLC) were treated with the iNOS inhibitor 1400W (Figure 4A). Hypoxically-induced *VEGF* expression was suppressed in both endothelial cell cultures (mEC and hUVEC) treated with 1400W; however, there was no suppression of *VEGF* mRNA by 1400W in the fibroblast (mEF) or carcinoma (LLC) lines (Figure 4A). Another hypoxia-induced HIF target, the glycolytic enzyme phosphoglycerate kinase (*PGK*), is not as strongly affected by suppression of iNOS in any of the cell types examined (Figure 4A). This indicates that the suppression of *VEGF* expression through inhibition of iNOS may not simply affect *HIF-1α* induction, but rather act through a more complex mechanism.

Inhibition of iNOS Reduces Tumor VEGF Expression In Vivo, but Does Not Significantly Affect Expression of Other HIF Target Genes

LLC xenograft tumors were assayed for net effects on gene expression when iNOS inhibitor was delivered at late stages of tumor growth. After 14 days of subcutaneous tumor expansion in wild-type animals, tumor-bearing mice received two injections with either a saline control or 1400W intraperitoneally. Four hours after the last injection, animals were sacrificed and tumors removed; the injection with 1400W caused a significant reduction in *VEGF* mRNA in the treated animals (Figure 4B). No statistically significant effect was seen in any of the other HIF targets assayed, including the two glycolytic enzymes lactate dehydrogenase (*LDH*) and *PGK*. This indicates that suppression of iNOS could be a useful modality for specifically suppressing VEGF expression in tumors, where it presumably acts at least in part on endothelial expression of the angiogenic factor.

Differential Tumor Cell Migration through Endothelial Cells Is Both HIF Isoform- and NO-Dependent

To determine whether iNOS is the critical factor that modulates differential tumor cell migration through endothelial cells, tumor cell migration was scored in endothelial layers treated with either vehicle or 15 μM 1400W for 3 hr prior to tumor cell seeding. Inhibitor and vehicle were removed and endothelial cells were washed immediately prior to tumor cell introduction, in order to limit the effects of the inhibitor compound solely to the endothelial cells (Figure 5A). 1400W strongly suppressed hypoxia-induced tumor cell migration through *WT* endothelial cells; however, it had no suppressive effect on *HIF-1α* and *VEGF* null endothelial cells. Suppression with 1400W had the strongest effect on *HIF-2α null* endothelial cell layers, where the degree of suppression indicates that altered NO levels are likely a primary cause of elevated tumor cell migration in this genotype.

(D and E) Boyden assay for tumor cell migration during 9h periods of normoxia (21% O_2) or hypoxia (1% O_2) through endothelial monolayers of *WT*, *HIF-1α null*, and *HIF-2α null* cells (D) and *VEGF null* and *iNOS null* cells (E). Data in (D) and (E) are average ± SD of ratio of cells migrated through endothelium divided by the mean number of migrated cells through *WT* endothelium during normoxic conditions. An asterisk is placed above differences with a significance exceeding $p < 0.05$; **$p < 0.01$; ***$p < 0.001$. NS indicates differences that do not reach a $p < 0.05$ level of significance.

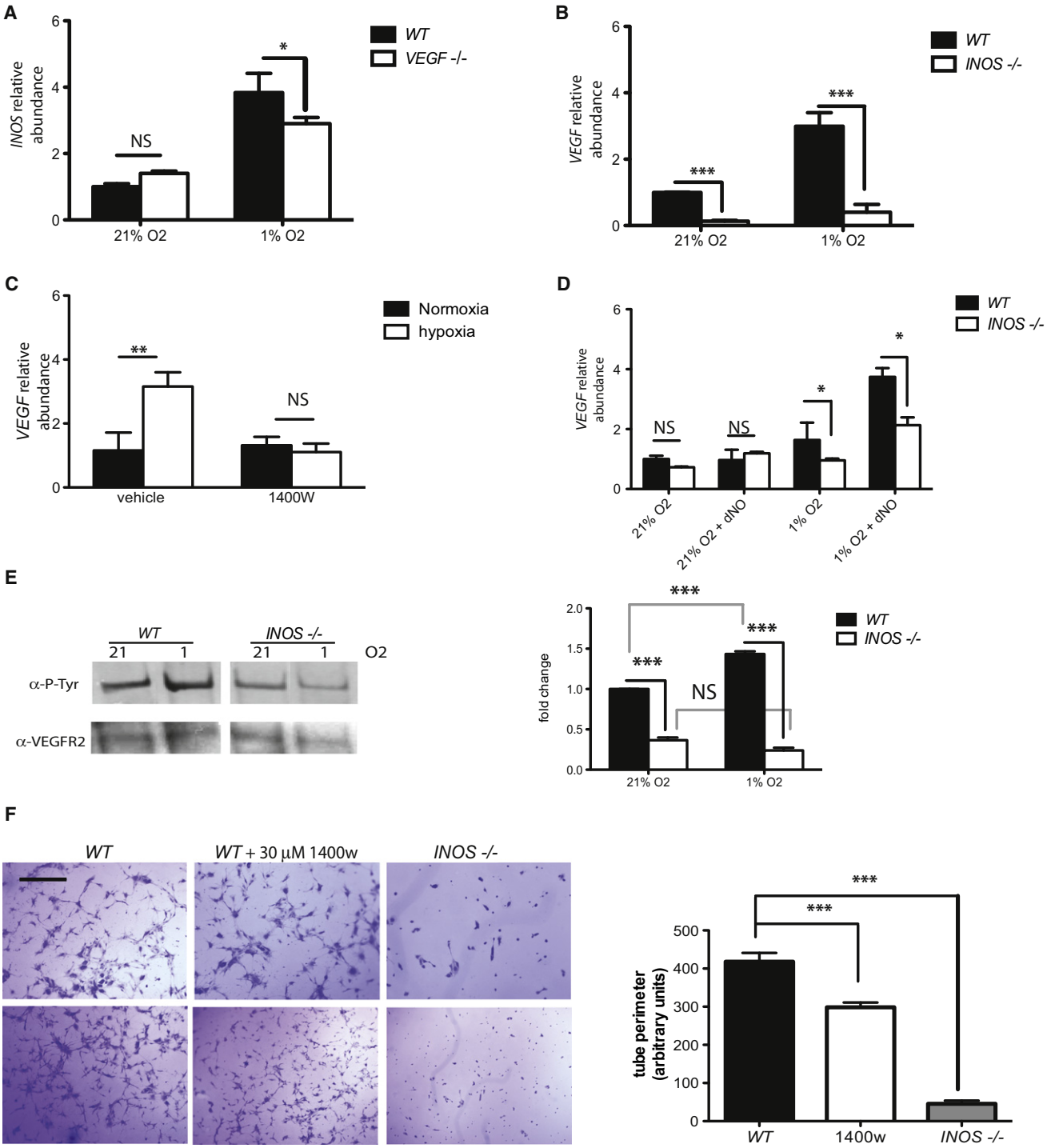

Figure 2. Deletion and Specific Inhibition of iNOS Result in Decreased VEGF Expression and Downstream Activity

(A–C) Quantification of relative abundance of *iNOS* mRNA in *VEGF null* endothelial cells (A) and *VEGF* mRNA abundance in *iNOS KO* cells (B) or *WT* cells treated with 15 μM of specific iNOS inhibitor 1400W (right panel) by quantitative RT-PCR (C).

(D) *VEGF* mRNA levels in *WT* and *iNOS null* endothelial cells upon addition of 5 mM NO donor DETA NONOate (dNO).

(E) Representative western blot of immunoprecipitated VEGFR2 (Flk1) probed for total Flk1 and P-tyrosine to detect activated form (left) and signal quantification of multiple blots (n = 3) by phosphor imaging (right).

(F) Tube formation assay in collagen I matrix, representative pictures of *WT*, *WT* + 30 μM 1400W, and *iNOS null* are shown (left) (scale bar represents 100 μm) and quantification of length of detected networks (right) was performed using ImageJ. Data is average ± SEM of lengths obtained from at least three pictures of at least three wells. Experiment shown is representative and was repeated three times with cells no older than passage 2. In this figure, data shown is average ± SEM, An asterisk is placed above differences with a significance exceeding $p < 0.05$; **$p < 0.01$; ***$p < 0.001$.

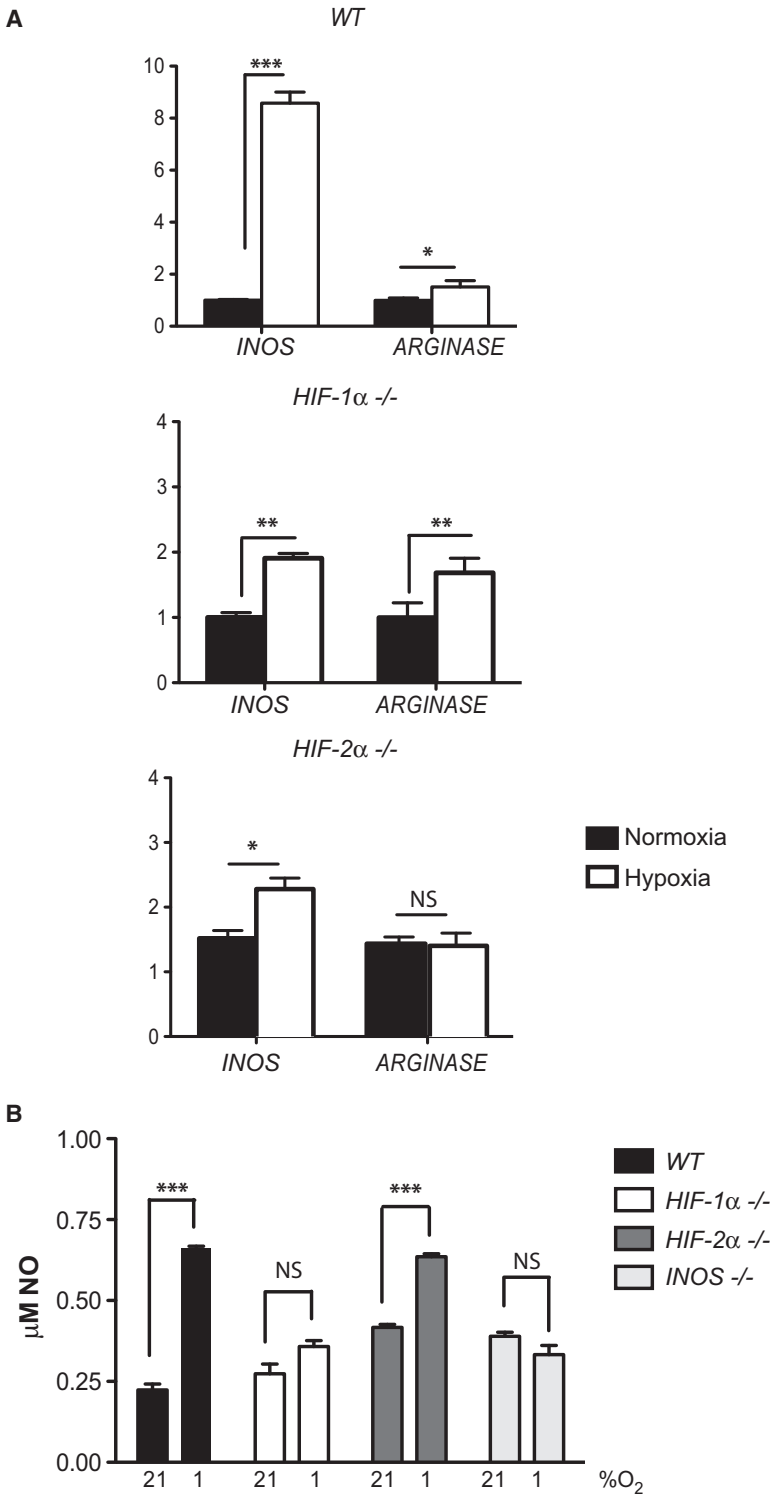

Figure 3. Endothelial Cells Generate NO through iNOS Activation during Hypoxia

(A) Relative abundance of *iNOS* and *ARG1* transcripts in *WT* (left), *HIF-1α null* (center), and *HIF-2α null* (right) endothelial cells exposed to 21% O_2 (normoxia) or 1% O_2 (hypoxia) for 9 hr. Data is average ± SEM of each sample; mRNA levels are compared to those observed in WT normoxia (that was defined as 1.0-fold).

(B) NO levels in endothelial cell conditioned medium from cells treated for 48 hr at 21% or 0.5% O_2; data presented are average ± SEM. An asterisk is placed above differences with a significance exceeding $p < 0.05$; **$p < 0.01$; ***$p < 0.001$.

Migration assays performed using *iNOS null* EC indicates that, as expected, *iNOS* deletion results in reduced endothelial permeability to tumor cells (Figure 5B). A number of groups have shown that inhibition or deletion of inducible NOS results in suppression of tumor growth and metastasis (Ohtsu et al., 2010; Thomsen et al., 1997); we also found that treatment with 1400W prior to intravenous injection of 1×10^6 LLC cells causes a significant reduction in metastatic success in vivo (Figure 5C).

Differential Migration and NO Regulation Correlate with Metastatic Success in EC-Specific HIF Isoform Null Mice

As shown above, the loss of *HIF-1α* in endothelial cells reduces metastasis in mouse tumor models, and reduces tumor cell migration through an endothelial layer under hypoxia. The loss of *HIF-2α* in endothelium accelerates tumor cell migration in an NO-dependent manner. It was thus important to determine whether these observations on the role of the different isoforms in cultured endothelial cells is correlated with metastatic success in vivo.

To model effects of this mutation on seeding of cells into the pulmonary endothelium and tumor cell extravasation, seeding of tumor cells into the tail vein in *WT*, *HIF-1α* EC null animals, and *HIF-2α* EC null animals was carried out. The mutant mice were created by *WT* bone marrow transplant into Tie2cre/conditional allele animals, as described above. Loss of endothelial cell *HIF-1α* significantly decreases metastatic success in this assay (Figure 6A). However, loss of *HIF-2α* in endothelial cells significantly increases both the number (Figure 6B) and size (Figure 6C) of pulmonary tumors in this experimental system.

DISCUSSION

The relationship of hypoxia to tumor progression has been well documented; hypoxia and hypoxia-associated necrosis have also been repeatedly linked to metastasis (De Jaeger et al., 1998). It is likely that hypoxic response is an intrinsic part of almost every stage of metastasis, through both hypoxia-induced tumor cell motility and increased vascular/endothelial permeability (Erler and Giaccia, 2006; Rofstad and Danielsen, 1999; Weis et al., 2004).

Clearly, a key to movement of tumor cells during hematogenous metastasis is transposition across endothelial barriers; the question being the degree to which this is influenced by

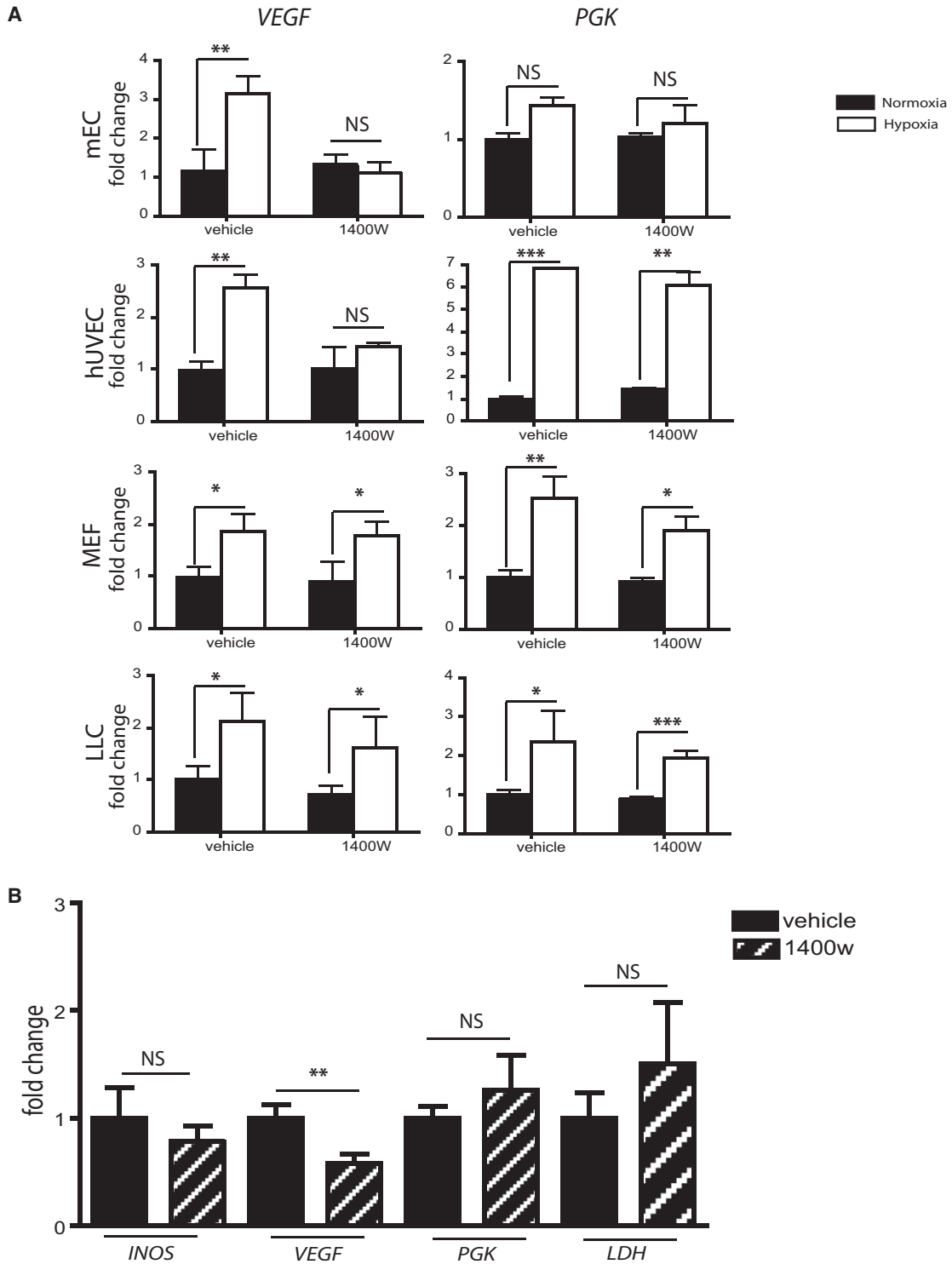

Figure 4. Inhibition of VEGF Expression upon iNOS Inhibition Is A Phenomenon Specific to Endothelial Cells

(A) Quantitative PCR of wild-type mouse endothelial cells (mEC), human umbilical vascular endothelial cells (hUVEC), mouse embryonic fibroblasts (MEF), and Lewis lung cancer cells (LLC) exposed to normoxia or hypoxia (21% or 1% O_2, respectively) in the presence or absence of 15 μM 1400W, to assess mRNA levels of VEGF and PGK (hypoxia and HIF-1α control). Data is average ± SEM of ratio of mRNA levels in sample compared to mRNA levels in WT untreated during normoxia.

(B) Quantitative PCR of RNA extracted from subcutaneous LLC^{GFP} tumors in WT mice. Mice were treated with two intraperitoneal injections: the first, a 15 mg/kg 1400W (or respective saline control of equal volume) at 8 hr before sacrifice, and the second, a 10 mg/kg injection at 4 hr prior to sacrifice. An asterisk is placed above differences with a significance exceeding $p < 0.05$; $^{**}p < 0.01$; $^{***}p < 0.001$.

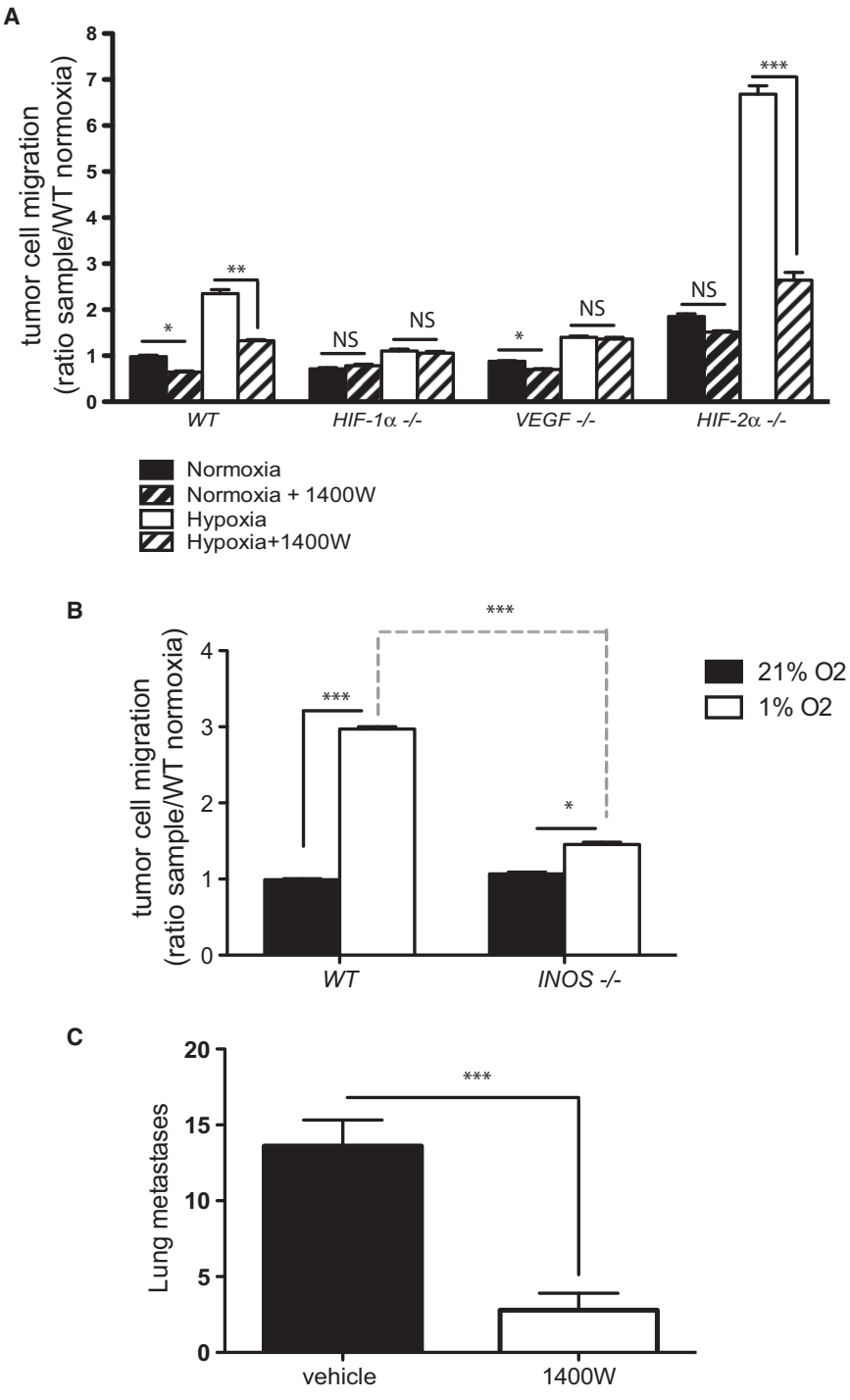

Figure 5. Hypoxia-Induced Tumor Cell Migration Is Inhibited in the Absence of Active iNOS

(A) Endothelial monolayers of different genotypes were incubated with 15 μM of 1400W for 3 hr, and then washed to remove inhibitor. They were then incubated with LLC cells (in the absence of inhibitor) for 9 hr at either 21% or 1% O_2, to assay for effects of inhibition of iNOS in endothelial cells on tumor cell migration.

(B) Migration assay using *WT* and *iNOS null* EC monolayers.

(C) Metastases in *WT* mice lungs 14 days posttail vein injection of 1 × 10^6 LLC^{GFP} cells. Experimental mice received a total of two intraperitoneal injections of either control saline or 1400W, one at 8 hr, and one at 4 hr (the first of 15 mg/kg followed by 10 mg/kg) immediately prior to tumor cell injections. In this figure, data presented is average ± SEM. An asterisk is placed above differences with a significance exceeding $p < 0.05$; $^{**}p < 0.01$; $^{***}p < 0.001$.

a hypoxic response in the blood vessel itself. The hypoxic response in the endothelium is controlled to a significant extent by two transcription factors, HIF-1α and HIF-2α (Liu et al., 2011; Skuli and Simon, 2009; Tang et al., 2004; Ten and Pinsky, 2002). These in turn control a number of EC effectors: receptors and signal transduction molecules that shape endothelial and vascular behavior. One of the most potent and wide-ranging of these is NO. In the work described here, it is clear that NO levels are modified in EC by hypoxia in a manner that is controlled differentially by the HIF isoforms. Surprisingly, we also show that this control in turn correlates with either suppression or enhancement of metastasis.

A number of studies have shown that HIF-1α is a powerful regulator of the *NOS2*, or *iNOS* gene (Melillo et al., 1997; Ortiz-Masiá et al., 2010; Tafani et al., 2010; Zhou et al., 2009). Hypoxia acts in many cell types to induce iNOS, and thus to increase NO levels via the action of the synthase. It was recently shown that macrophages regulate NO homeostasis in part through Th1 cytokine stimulation and induction of *HIF-1α* transcriptionally; this in turn activates iNOS expression and ultimately increases NO production (Doedens et al., 2010). It has also been recently shown that HIF-2α induces *ARG1* expression following Th2 cytokine stimulation in macrophages (Takeda et al., 2010). The combined actions of the two HIF-α factors can thus regulate NO homeostasis (Takeda et al., 2010). The present study demonstrates that this differential and antagonistic action of the two HIF-α factors is not limited to cytokine-induced responses in macrophages: loss of *HIF-1α* limits *iNOS* expression in EC, and thus restricts NO production, and loss of *HIF-2α* results in lower levels of *ARG1*, and increased NO production.

NO levels have well-documented effects on EC function. Substantial literature exists describing the roles of NO in EC, both from extrinsic sources and intrinsic ones (Fukumura et al., 2006; Mark et al., 2004; Ziche and Morbidelli, 2009). However, endothelial-derived NO was previously thought to be primarily

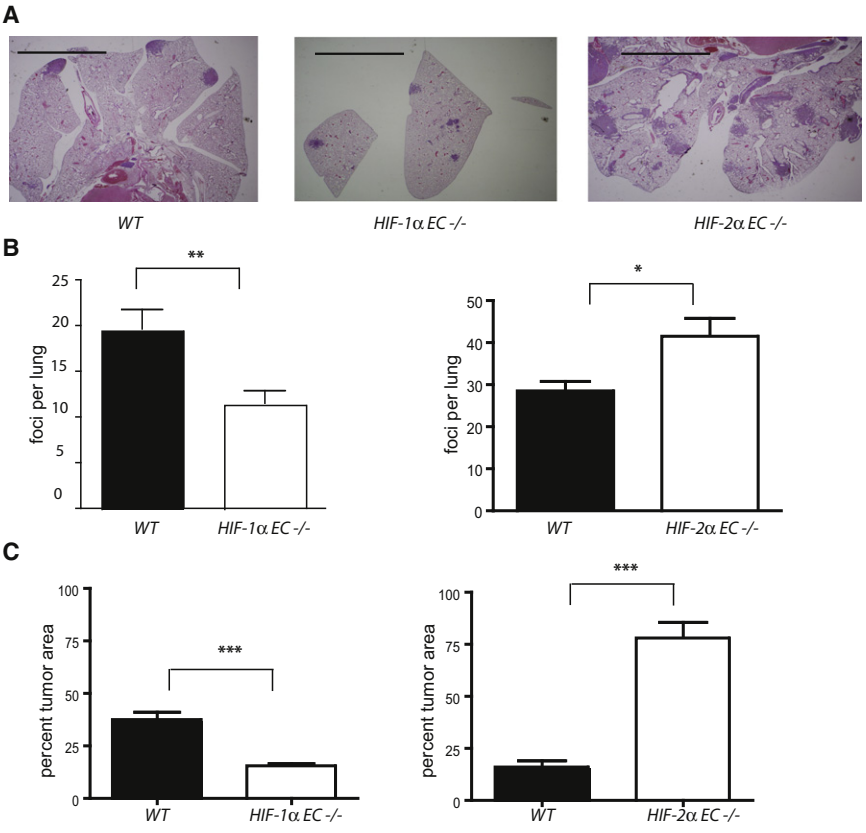

Figure 6. Endothelium-Specific Deletions of HIF-1α and HIF-2α Have Opposing Effects on Tumor Metastases

LLC^{GFP} cells (1×10^6) were injected via tail vein into HIF-$1\alpha^{df}$/Tie2Cre or *HIF-*$2\alpha^{df}$*/Tie2Cre* mice. All Cre-expressing and *WT* mice were lethally irradiated, and then received *WT* bone marrow, in order to ensure endothelial-exclusive deletion of gene of interest. Lungs were collected 14 days postinjection, fixed, and sectioned for hematoxylin and eosin staining.

(A) Representative images of mouse lungs 14 days post-LLC^{GFP} tail vein injection. Scale bars represent 5 mm.

(B) Number of metastases foci found in lungs of *HIF-1α null*, *HIF-2α null*, and their respective *WT* (i.e., df = double floxed/cre negative) controls.

(C) Average of relative tumor area in lung sections obtained by quantifying tumor area versus whole lung area in every third section of whole lungs. In this figure, data presented is average ± SEM. An asterisk is placed above differences with a significance exceeding $p < 0.05$; $^{**}p < 0.01$; $^{***}p < 0.001$.

due to NO production through the eNOS enzyme (Fukumura et al., 2001); it is clear from the results described here that iNOS is a key source of NO in a hypoxic EC.

We also show here that iNOS itself is a key regulator of *VEGF-A* expression in endothelium, and that in its absence, fundamental aspects of VEGF-A function are disturbed, including VEGFR2 activation and tube formation. Although a number of workers have shown that iNOS is important for metastasis and can be linked to *VEGF-A* expression (Davie et al., 2007; Hosogi et al., 2005; Van der Wall and Palmer, 2006), the demonstration that it has an endothelial-specific role in those processes represents an intriguing avenue for tissue-specific VEGF-A inhibition.

One recent study showed that NO could act as an inhibitor of the prolyl hydroxylases, which in turn would act to increase HIF isoform stability and expression, and that this can act by interceding in the feedback loop where HIF isoforms themselves induce the expression of prolyl hydroxylases (Berchner-Pfannschmidt et al., 2007). Loss of *iNOS* would thus lead to increased degradation of HIF isoforms via increased activity of the prolyl hydroxylases; current work is underway to determine the role of this feedback loop in EC hypoxic response.

It is shown here that in EC, there are specific and opposing roles for the two HIF isoforms in regulating NO. Previously published studies of *HIF-2α* loss in EC either did not examine metastasis (Yamashita et al., 2008), or only scored animals qualitatively as metastatic or not after xenografts, i.e., did not count metastases or overall metastatic tumor burden (Skuli et al., 2009). It is clear that quantitative metastatic success is differentially influenced by the two HIF isoforms in ECs.

Interestingly, deletion of prolyl hydroxylase activity has profound effects on overall vessel maturation and pericyte coverage, in turn affecting vessel permeability and function (Coulon et al., 2010; Mazzone et al., 2009; Schneider et al., 2010). As decreased or altered hydroxylation will affect availability and activity of both HIF isoforms, understanding the relationships between individual hydroxylases and individual HIF isoforms will be an essential parameter to completely understand, in order to ultimately predict the effect of pharmacological hydroxylase inhibitors on tumor progression and metastasis.

It should also be noted that we have demonstrated an important difference in the roles of HIF isoforms in regulating tumor progression, as shown in the model in Figure 7. The model indicates the differential effects of the HIF isoforms in endothelial cells: here, in a thrombotic focus of tumor cells clogging a tissue capillary. This vascular blockage would immediately cause localized drops in oxygen tension in both the tumor cells and surrounding stroma, including the local endothelial cells. Depending on how the thrombus resolves, the HIF isoforms in the endothelium could act to regulate NO homeostasis locally, and in turn affect metastatic success.

The homeostatic regulation of NO clearly depends on differential expression of HIF-1 and HIF-2; this expression may be regulated by temporal differences in the isoforms' response to hypoxia (Holmquist-Mengelbier et al., 2006), and/or by differing cytokine/growth factor responsiveness (Takeda et al., 2010) as well as other factors in the tumorigenic milieu. This model reinforces the still developing concept that these two HIF isoforms can act antagonistically, and not redundantly, to regulate biological processes in malignancy (Bertout et al., 2009; Gordan et al., 2007; Roberts et al., 2009).

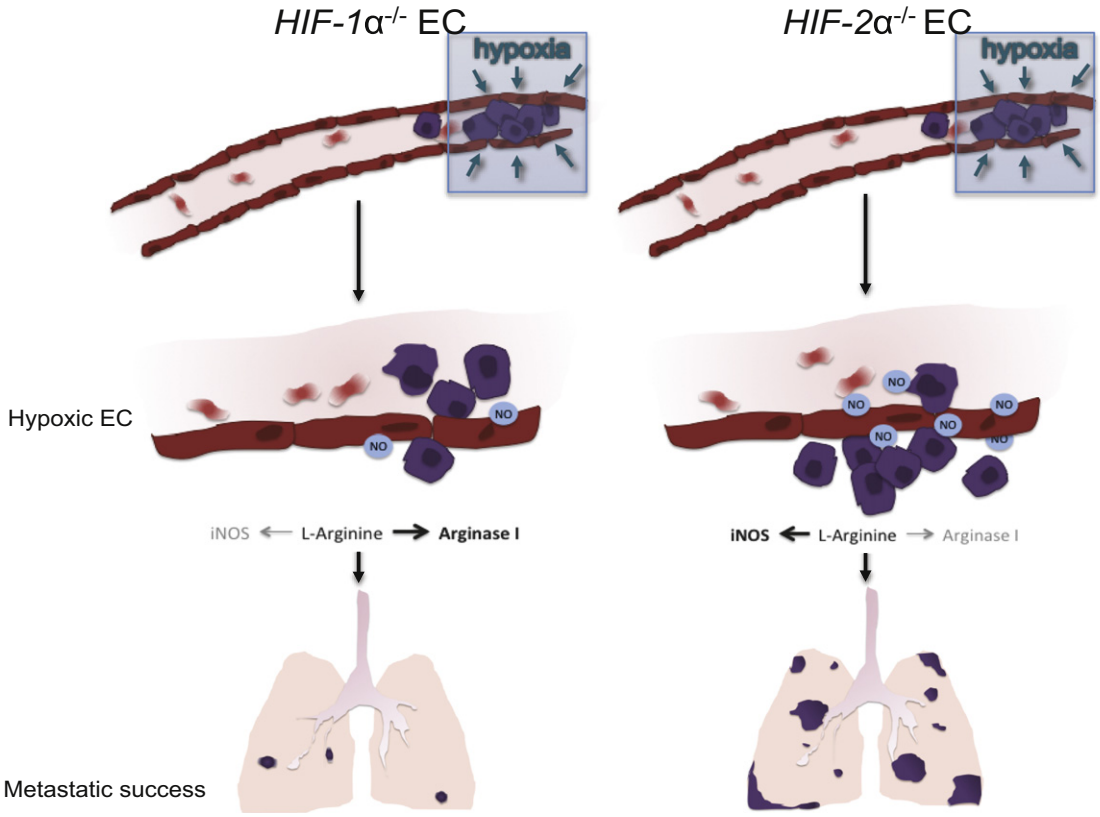

Figure 7. Differential Functions of HIF-1 and HIF-2 during Metastasis Depend on Differential NO Synthesis

As shown, HIF-1 and HIF-2 response in endothelial cells gives rise to differing levels of NO production following hypoxic induction of the factors: in this case, through hypoxic stress caused by tumor cell-induced blockage of a capillary. This, in turn, results in differing levels of metastatic success when one or the other HIF is genetically deleted from the endothelial cell. A remaining and important question is how hypoxic stress can cause differing levels of induction of the two HIF factors.

A number of studies have argued that in cancer, particularly in the context of VHL deletion, HIF-2α can act as the driver for malignant cell progression and tumor angiogenesis (Haase, 2006; Kondo et al., 2002; Smith et al., 2005). The data presented here indicate that the tumor stroma and malignant cells likely employ HIF isoforms differently, and as pharmacological manipulation of HIF factors is evaluated, their impact on HIF isoforms at a tissue-specific level should thus be considered and evaluated.

EXPERIMENTAL PROCEDURES

Animal Experiments

All animal studies were carried out according to the animal protocol approved by the UCSD Institutional Animal Care and Use Committee. Mice were maintained on a standard chow in a pathogen-free animal facility with 12 hr light and dark cycles.

Deletion of *HIF-1α* or *HIF-2α* in EC and myeloid cells was obtained by crossing *HIF-1α*^{df} or *HIF-2α*^{df} females (generated as previously described [Ryan et al., 1998 and Gruber et al., 2007, respectively]) to *HIF-1α*^{df}*/Tie2Cre+* or *HIF-2α*^{df}*/Tie2Cre+* males. Cre+ and Cre− females between 3 and 4 weeks of age were lethally irradiated (1,000 Rad) and received wild-type bone marrow (1×10^6 bone marrow [BM] cells per mouse) to restore genotype of hematopoietic cells and generate endothelial cell null mice and comparable df/wild-type controls.

Tie2-specific deletion of HIF-1α in polyoma middle T (*PyMT*) tumor model was obtained by crossing *HIF-1α*^{df} females with *HIF-1α*^{df}*/Tie2-Cre+/PyMT+* males. Only virgin females were used in this study. After weaning at 3 weeks of age, mice were palpated once per week. Tumor onset age was when a 2 × 2 mm palpable solid mass appeared. Tumors were measured in two dimensions using digital calipers. Mice were sacrificed when any tumor had reached 1 × 1 cm (endpoint).

C57Bl/6 *WT* and *iNOS*-deficient mice in the C57Bl/6 background were purchased from the Jackson Laboratory (Bar Harbor, ME) and used to purify endothelial cells lacking iNOS.

Histology and Immunohistochemistry

Lung and tumor tissues were fixed in 10% phosphate-buffered formalin (Fisher Scientific) for 16 hr and embedded in paraffin. Lung metastases were counted in hematoxylin and eosin (H&E) stained sections as previously described (Liao et al., 2007). Blood vessels in tumors were detected using rat anti-mouse CD34 antibody (1:100 dilution, NB600-1071, Novus). Secondary antibody for CD34 staining is biotinylated goat anti-rat IgG (1:200 dilution, sc-2041, Santa Cruz Biotechnology). Staining was revealed using Vectastain ABC kit (Vector Laboratories). Microvessel density was quantified using a Chalkley graticule eyepiece.

Generation of LLC^{GFP} Cells

Lewis lung carcinoma cells were infected with a lentivirus expressing GFP (made available by Dr. Cornelis Murre, University of California, San Diego) according to the standard protocol for retrovirus infection. Single clones from FACS-sorted GFP-positive cells were selected, and the clone used in this showing the highest GFP expression was used. LLC^{GFP} cells were cultured in DMEM (11965-092, Invitrogen) supplemented with 10% fetal bovine

serum (26140-079, Invitrogen), 100 U ml^{-1} penicillin, and 100μg ml^{-1} streptomycin.

Tumor Cell Extravasation

A total of 1 × 10^6 LLC^{GFP} cells in 200 μl sterile PBS were injected intravenously into bone marrow-reconstituted *WT* and *HIF-1α* and *HIF-2α EC null* mice. Lungs were excised 14 days postinjection and fixed in 10% formalin for histological analysis. The number of tumors were counted in H&E stained 10 μm serial lung sections of the whole lungs and compared between *WT* and *EC null* mice. The area of each lung tumor of every third section was measured and compared to the whole lung area in the section for an assessment of tumor burden, using ImageJ software.

Tumor Cell Intravasation

Right mammary gland pad 4 was surgically cleared in 3–4-week-old *HIF-1α^{df}* and *HIF-1α^{df}/Tie2-Cre+* female mice. Removal of ductal tree was confirmed by carmine whole-mount staining. Two months after surgery, bone marrow reconstitution was performed on these mice to obtain *WT* and *EC null* mice with cleared fat pads. Six weeks post-BM transplantation, 2.5 × 10^6 LLC^{GFP} cells in 50 μl sterile PBS were implanted into the cleared mammary gland. Mice were sacrificed 21 days later, and tumors were weighed, lungs removed and fixed for histological analysis of metastasis, and blood was collected by cardiac puncture. Relative abundance of genomic GFP in blood was determined by quantitative PCR to assess the presence of circulating tumor cells.

Quantitative Real-Time PCR

Genomic DNA was isolated using DNeasy Blood and Tissue Kit (QIAGEN). *GFP* DNA was quantified using an ABI Prism 7700 Sequence Detector (Applied Biosystems) and normalized to *VEGF* DNA levels. Conditions for the PCR: one 10-min incubation at 95°C, followed by 40 cycles of 15 s at 95°C and 1 min at 60°C. Primers used in this study include:

GFP forward, 5′-GGAGCGCACCATCTTCTTCA-3′;
GFP reverse, 5′-AGGGTGTCGCCCTCGAA-3′;
VEGF forward, 5′-CTATGGAGGCCAGAAGAGGGTAT-3′;
VEGF reverse, 5′-CCCACATCAGGTGGCTCATAA-3′; and
VEGF probe, 5′-(6FAM)AGATCCCTTGAAGCTAG(MGBNFQ)-3′.

For quantitative analysis of steady-state mRNA levels, total RNA was extracted from normoxia- and hypoxia-treated cells, using UltraClean Tissue and Cells RNA Isolation Kit (MoBio). cDNA was synthesized from 1 μg of total RNA, using Superscript III (Invitrogen) according to the manufacturer's instructions. Relative abundance of transcripts of interest was assessed by Q-PCR following normalization to β-*ACTIN* transcript levels. Primer pair and primer/probe sets used were as follows:

mb-actin forward, 5′-AGGCCCAGAGCAAGAGAGG-3′;
mb-actin reverse, 5′-TACATGGCTGGGGTGTTGAA-3′.
mVEGF total forward, 5′-ATCCGCATGATCTGCATGG-3′;
mVEGF total reverse, 5′-AGTCCCATGAAGTGATCAAGTTCA-3′;
mVEGF probe, 5′-[6∼FAM]-TGCCCACGTCAGAGAGCAACATCAC-[BHQ1a-Q]-3′.
mPGK forward, 5′-CAAATTTGATGAGAATGCCAAGACT-3′;
mPGK reverse, 5′-TTCTTGCTGCTCTCAGTACCACA-3′;
mPGK probe, 5′-[6∼FAM]-TATACCTGCTGGCTGGATGGGCTTGGACT-[BHQ1a-Q]-3′;
mArginase forward, 5′- AACACGGCAGTGGCTTTAACC-3′ (Takeda et al., 2010);
mArginase reverse, 5′ GGTTTTCATGTGGCGCATTC-3′ (Takeda et al., 2010);
miNOS: TaqMan Gene Expression Assay Mm00440488_m1 (Applied Biosystems); and
hiNOS: TaqMan Gene Expression Assay Hs01075521_m1 (Applied Biosystems).

Data are presented as average ± SEM of fold-change (ratio) between each sample and the WT normoxic control.

Isolation of Primary Endothelial Cells

Primary endothelial cells were isolated and cultured from lungs of *HIF-1α^{df}*, *HIF-2α^{df}*, *VEGF^{df}*, or *iNOS null* mice, as previously described (Dong et al., 1997; Tang et al., 2004) with the following modifications: the lungs were excised, minced, and digested for 90 min at 37°C in 2 mg/ml collagenase type I (Roche) in HBSS containing 2 mM $CaCl_2$, 2 mM $MgSO_4$, and 20 mM HEPES. The digest was filtered through a 70 μm nylon cell strainer and washed once in HBSS. Pellet was then resuspended in PBS containing 0.1% BSA and incubated with anti-CD31-coated magnetic beads (Dynal, Invitrogen) for 1 hr at 4°C. Cells and beads were plated in endothelial cell growth medium (ECGM) consisting of low glucose DMEM:F12 with 1% penicillin/streptomycin, 1% nonessential aminoacids, 2 mM sodium pyruvate, buffered with 20 mM HEPES and containing 20% FBS (Omega Scientific, Tarzana, CA), 20 μg/ml Heparin (Sigma, St. Louis, MO), and 75 μg/ml endothelial mitogens (Biomedical Technologies). Cell identity and culture purity were confirmed by immunodetection with anti-VE-cadherin (Santa Cruz Biotechnology, sc-6458), and LDL uptake.

Transendothelial Cell Migration Assay

After 12–14 days, cells from double-floxed genotypes, in the original isolates (p0) were infected with adenovirus expressing Cre recombinase (for *HIF-1α*, *HIF-2α*, or *VEGF* deletion) or adenovirus expressing β-gal, for control *WT* cells. All migration experiments shown were performed using endothelial cell monolayers generated from P1 or P2 cells. Endothelial cells (5 × 10^5) were seeded into COSTAR transwells (6.5 mm diameter, pore size 8 μm; Corning, NY) grown until confluent. Migration of tumor cells was examined by seeding 5 × 10^5 LLC^{GFP} cells onto the endothelial monolayer and the inserts incubated for 9 hr under 21% (kept in normoxic growth incubator) or 1% oxygen (transferred to hypoxic incubator), with media on both upper and lower chambers. Inserts were stained with 0.1% crystal violet in 10% ethanol and mounted onto glass slides. Migrated cells were counted in five random fields per insert at 100× magnification. Average was calculated from a minimum of three inserts per treatment. Data is expressed as average ± SEM of the ratio between migrated cells observed through each endothelial genotype and/or treatment and the migration observed through the WT endothelium under normoxic conditions.

Effect of iNOS inhibition in endothelial cells on tumor cell migration was done by preincubation of endothelial monolayer with 15 μM of 1400W for 3 hr prior to the migration experiment (normoxia and hypoxia for 9 hr), which occurred in the absence of the inhibitor.

Immunoprecipitation of VEGFR2

Subconfluent (∼80%) EC cultures in 6-well plate wells were incubated at 21% (normoxia) or 1% (hypoxia) for 9 hr, rinsed briefly with cold PBS, and immediately frozen in liquid N_2. Cells were lysed in RIPA buffer (Cell Signaling, 9806S) containing protease inhibitors (Minitab, Roche), and 100 mM PMSF. Protein was quantified in clarified lysates and equal amounts were used for pull down of VEGFR2 (Santa Cruz Biotechnologies, sc-504). Whole cell lysate and primary antibody were preincubated O/N in a final volume of 750 μL, at 4°C. Protein A/G Plus Agarose beads (Santa Cruz Biotechnologies, sc-2003) were added and incubated O/N with end-over-end tumbling at 4°C. A/G beads were washed and bound protein resolved by SDS-polyacrylamide gel electrophoresis, and transferred to PVDF membrane for immunoblotting with anti-VEGFR2 (sc-504) and antiphosphotyrosine antibody (4G10 Platinum, Millipore) to detect and quantify the activated form of VEGFR2.

Immunoblotting

Equal amounts of protein (15 μg) for normoxia- and hypoxia-treated cells were loaded onto 3%–8% acrylamide Tris-Glycine gels (Invitrogen) and transferred to PVDF membrane (Millipore), according to established western blotting procedures. Primary antibodies were used at 1:1,000 dilutions unless otherwise stated (iNOS [sc-651], eNOS [BD 610296], HIF-1α [Novus Biologicals NB-100-049], HIF-2α [R&D AF2997]). Proteins of interest were detected following secondary incubation with HRP-conjugated antibodies and ECL Plus chemiluminescence detection kit (Amersham).

NO Measurements

Endothelial cells were grown to confluence and incubated for 48 hr at 21% or 0.5% O_2 in growth media. Nitrate and nitrite levels were quantified in

conditioned media using Sievers Nitric Oxide Analyzer (NOA 280i) according to the manufacturer's instructions. EC production of NO during normoxia and hypoxia was quantified by measuring the nitrites in the growth medium, which is likely an underestimation of the NO produced. Because the EC growth medium is saturated with nitrates, the contribution of EC production of NO to this pool was undetectable.

Statistical Analyses

Statistical analysis in all cases (Q-PCR, NO levels, migration assays) was done using unpaired Student's t test, where values observed for each sample were routinely compared to the ones found in wild-type controls under normoxic/untreated conditions. Data are expressed as mean ± SEM unless otherwise stated.

ACKNOWLEDGMENTS

We acknowledge the support of a Wellcome Trust Principal Research Fellowship (to R.S.J.), a Gö4Med Fellowship from the Universitätsmedizin Göttingen (to M.S.), the National Institutes of Health (grants R01 CA82515 [to R.S.J.] and K22 CA118182 [to L.G.E.]), and a National Institutes of Health training grant minority supplement (T32 CA009523-27S2 [to C.B.P.]).

Received: August 9, 2011
Revised: October 3, 2011
Accepted: November 23, 2011
Published: January 17, 2012

REFERENCES

Ambs, S., Merriam, W.G., Bennett, W.P., Felley-Bosco, E., Ogunfusika, M.O., Oser, S.M., Klein, S., Shields, P.G., Billiar, T.R., and Harris, C.C. (1998). Frequent nitric oxide synthase-2 expression in human colon adenomas: implication for tumor angiogenesis and colon cancer progression. Cancer Res. *58*, 334–341.

Amirkhosravi, A., Mousa, S.A., Amaya, M., Meyer, T., Davila, M., Robson, T., and Francis, J.L. (2010). Assessment of anti-metastatic effects of anticoagulant and antiplatelet agents using animal models of experimental lung metastasis. Methods Mol. Biol. *663*, 241–259.

Berchner-Pfannschmidt, U., Yamac, H., Trinidad, B., and Fandrey, J. (2007). Nitric oxide modulates oxygen sensing by hypoxia-inducible factor 1-dependent induction of prolyl hydroxylase 2. J. Biol. Chem. *282*, 1788–1796.

Bertout, J.A., Majmundar, A.J., Gordan, J.D., Lam, J.C., Ditsworth, D., Keith, B., Brown, E.J., Nathanson, K.L., and Simon, M.C. (2009). HIF2alpha inhibition promotes p53 pathway activity, tumor cell death, and radiation responses. Proc. Natl. Acad. Sci. USA *106*, 14391–14396.

Brizel, D.M., Scully, S.P., Harrelson, J.M., Layfield, L.J., Bean, J.M., Prosnitz, L.R., and Dewhirst, M.W. (1996). Tumor oxygenation predicts for the likelihood of distant metastases in human soft tissue sarcoma. Cancer Res. *56*, 941–943.

Chambers, A.F., Groom, A.C., and MacDonald, I.C. (2002). Dissemination and growth of cancer cells in metastatic sites. Nat. Rev. Cancer *2*, 563–572.

Chen, J., Imanaka, N., Chen, J., and Griffin, J.D. (2010). Hypoxia potentiates Notch signaling in breast cancer leading to decreased E-cadherin expression and increased cell migration and invasion. Br. J. Cancer *102*, 351–360.

Claffey, K.P., Brown, L.F., del Aguila, L.F., Tognazzi, K., Yeo, K.T., Manseau, E.J., and Dvorak, H.F. (1996). Expression of vascular permeability factor/vascular endothelial growth factor by melanoma cells increases tumor growth, angiogenesis, and experimental metastasis. Cancer Res. *56*, 172–181.

Cliffton, E.E., and Grossi, C.E. (1974). The rationale of anticoagulants in the treatment of cancer. J. Med. *5*, 107–113.

Constien, R., Forde, A., Liliensiek, B., Gröne, H.J., Nawroth, P., Hämmerling, G., and Arnold, B. (2001). Characterization of a novel EGFP reporter mouse to monitor Cre recombination as demonstrated by a Tie2 Cre mouse line. Genesis *30*, 36–44.

Coulon, C., Georgiadou, M., Roncal, C., De Bock, K., Langenberg, T., and Carmeliet, P. (2010). From vessel sprouting to normalization: role of the prolyl hydroxylase domain protein/hypoxia-inducible factor oxygen-sensing machinery. Arterioscler. Thromb. Vasc. Biol. *30*, 2331–2336.

Davie, S.A., Maglione, J.E., Manner, C.K., Young, D., Cardiff, R.D., MacLeod, C.L., and Ellies, L.G. (2007). Effects of FVB/NJ and C57Bl/6J strain backgrounds on mammary tumor phenotype in inducible nitric oxide synthase deficient mice. Transgenic Res. *16*, 193–201.

De Jaeger, K., Merlo, F.M., Kavanagh, M.C., Fyles, A.W., Hedley, D., and Hill, R.P. (1998). Heterogeneity of tumor oxygenation: relationship to tumor necrosis, tumor size, and metastasis. Int. J. Radiat. Oncol. Biol. Phys. *42*, 717–721.

Doedens, A.L., Stockmann, C., Rubinstein, M.P., Liao, D., Zhang, N., DeNardo, D.G., Coussens, L.M., Karin, M., Goldrath, A.W., and Johnson, R.S. (2010). Macrophage expression of hypoxia-inducible factor-1 alpha suppresses T-cell function and promotes tumor progression. Cancer Res. *70*, 7465–7475.

Dong, Q.G., Bernasconi, S., Lostaglio, S., De Calmanovici, R.W., Martin-Padura, I., Breviario, F., Garlanda, C., Ramponi, S., Mantovani, A., and Vecchi, A. (1997). A general strategy for isolation of endothelial cells from murine tissues. Characterization of two endothelial cell lines from the murine lung and subcutaneous sponge implants. Arterioscler. Thromb. Vasc. Biol. *17*, 1599–1604.

Erler, J.T., and Giaccia, A.J. (2006). Lysyl oxidase mediates hypoxic control of metastasis. Cancer Res. *66*, 10238–10241.

Fukumura, D., Gohongi, T., Kadambi, A., Izumi, Y., Ang, J., Yun, C.O., Buerk, D.G., Huang, P.L., and Jain, R.K. (2001). Predominant role of endothelial nitric oxide synthase in vascular endothelial growth factor-induced angiogenesis and vascular permeability. Proc. Natl. Acad. Sci. USA *98*, 2604–2609.

Fukumura, D., Kashiwagi, S., and Jain, R.K. (2006). The role of nitric oxide in tumour progression. Nat. Rev. Cancer *6*, 521–534.

Gerber, H.P., Hillan, K.J., Ryan, A.M., Kowalski, J., Keller, G.A., Rangell, L., Wright, B.D., Radtke, F., Aguet, M., and Ferrara, N. (1999). VEGF is required for growth and survival in neonatal mice. Development *126*, 1149–1159.

Gordan, J.D., Bertout, J.A., Hu, C.J., Diehl, J.A., and Simon, M.C. (2007). HIF-2alpha promotes hypoxic cell proliferation by enhancing c-myc transcriptional activity. Cancer Cell *11*, 335–347.

Gruber, M., Hu, C.J., Johnson, R.S., Brown, E.J., Keith, B., and Simon, M.C. (2007). Acute postnatal ablation of Hif-2alpha results in anemia. Proc. Natl. Acad. Sci. USA *104*, 2301–2306.

Gunnett, C.A., Lund, D.D., McDowell, A.K., Faraci, F.M., and Heistad, D.D. (2005). Mechanisms of inducible nitric oxide synthase-mediated vascular dysfunction. Arterioscler. Thromb. Vasc. Biol. *25*, 1617–1622.

Gupta, G.P., and Massagué, J. (2006). Cancer metastasis: building a framework. Cell *127*, 679–695.

Haase, V.H. (2006). Hypoxia-inducible factors in the kidney. Am. J. Physiol. Renal Physiol. *291*, F271–F281.

Haase, V.H. (2009). Oxygen regulates epithelial-to-mesenchymal transition: insights into molecular mechanisms and relevance to disease. Kidney Int. *76*, 492–499.

Holmquist-Mengelbier, L., Fredlund, E., Löfstedt, T., Noguera, R., Navarro, S., Nilsson, H., Pietras, A., Vallon-Christersson, J., Borg, A., Gradin, K., et al. (2006). Recruitment of HIF-1alpha and HIF-2alpha to common target genes is differentially regulated in neuroblastoma: HIF-2alpha promotes an aggressive phenotype. Cancer Cell *10*, 413–423.

Hosogi, H., Ikai, I., Hatano, E., Taura, K., Fujii, H., Yamamoto, N., and Shimahara, Y. (2005). Complete response by a combination of 5-fluorouracil and interferon-alpha chemotherapy for lung metastasis of hepatocellular carcinoma after hepatic resection with portal and hepatic vein tumor thrombectomy. Hepatol. Res. *33*, 320–324.

Ignarro, L.J., Buga, G.M., Wood, K.S., Byrns, R.E., and Chaudhuri, G. (1987). Endothelium-derived relaxing factor produced and released from artery and vein is nitric oxide. Proc. Natl. Acad. Sci. USA *84*, 9265–9269.

Kisanuki, Y.Y., Hammer, R.E., Miyazaki, J., Williams, S.C., Richardson, J.A., and Yanagisawa, M. (2001). Tie2-Cre transgenic mice: a new model for endothelial cell-lineage analysis in vivo. Dev. Biol. *230*, 230–242.

Kondo, K., Klco, J., Nakamura, E., Lechpammer, M., and Kaelin, W.G., Jr. (2002). Inhibition of HIF is necessary for tumor suppression by the von Hippel-Lindau protein. Cancer Cell *1*, 237–246.

Liao, D., Corle, C., Seagroves, T.N., and Johnson, R.S. (2007). Hypoxia-inducible factor-1alpha is a key regulator of metastasis in a transgenic model of cancer initiation and progression. Cancer Res. *67*, 563–572.

Lin, E.Y., Jones, J.G., Li, P., Zhu, L., Whitney, K.D., Muller, W.J., and Pollard, J.W. (2003). Progression to malignancy in the polyoma middle T oncoprotein mouse breast cancer model provides a reliable model for human diseases. Am. J. Pathol. *163*, 2113–2126.

Liu, S., Guo, W., Shi, J., Li, N., Yu, X., Xue, J., Fu, X., Chu, K., Lu, C., Zhao, J., et al. (2011). MicroRNA-135a contributes to the development of portal vein tumor thrombus by promoting metastasis in hepatocellular carcinoma. J. Hepatol., [Epub ahead of print].

Lu, X., Yan, C.H., Yuan, M., Wei, Y., Hu, G., and Kang, Y. (2010). In vivo dynamics and distinct functions of hypoxia in primary tumor growth and organotropic metastasis of breast cancer. Cancer Res. *70*, 3905–3914.

Mark, K.S., Burroughs, A.R., Brown, R.C., Huber, J.D., and Davis, T.P. (2004). Nitric oxide mediates hypoxia-induced changes in paracellular permeability of cerebral microvasculature. Am. J. Physiol. Heart Circ. Physiol. *286*, H174–H180.

Mazzone, M., Dettori, D., Leite de Oliveira, R., Loges, S., Schmidt, T., Jonckx, B., Tian, Y.M., Lanahan, A.A., Pollard, P., Ruiz de Almodovar, C., et al. (2009). Heterozygous deficiency of PHD2 restores tumor oxygenation and inhibits metastasis via endothelial normalization. Cell *136*, 839–851.

Melillo, G., Musso, T., Sica, A., Taylor, L.S., Cox, G.W., and Varesio, L. (1995). A hypoxia-responsive element mediates a novel pathway of activation of the inducible nitric oxide synthase promoter. J. Exp. Med. *182*, 1683–1693.

Melillo, G., Taylor, L.S., Brooks, A., Musso, T., Cox, G.W., and Varesio, L. (1997). Functional requirement of the hypoxia-responsive element in the activation of the inducible nitric oxide synthase promoter by the iron chelator desferrioxamine. J. Biol. Chem. *272*, 12236–12243.

Ohtsu, N., Takaoka, K., Segawa, E., Hashitani, S., Noguchi, K., Kishimoto, H., and Urade, M. (2010). Antitumor effects of inhibitors of nitric oxide synthase or cyclooxygenase-2 on human KB carcinoma cells overexpressing COX-2. Oncol. Rep. *24*, 31–36.

Olson, N., and van der Vliet, A. (2011). Interactions between nitric oxide and hypoxia-inducible factor signaling pathways in inflammatory disease. Nitric Oxide *25*, 125–137.

Ortiz-Masiá, D., Hernández, C., Quintana, E., Velázquez, M., Cebrián, S., Riaño, A., Calatayud, S., Esplugues, J.V., and Barrachina, M.D. (2010). iNOS-derived nitric oxide mediates the increase in TFF2 expression associated with gastric damage: role of HIF-1. FASEB J. *24*, 136–145.

Ostrowski, L.E., Ahsan, A., Suthar, B.P., Pagast, P., Bain, D.L., Wong, C., Patel, A., and Schultz, R.M. (1986). Selective inhibition of proteolytic enzymes in an in vivo mouse model for experimental metastasis. Cancer Res. *46*, 4121–4128.

Palmer, R.M., Ferrige, A.G., and Moncada, S. (1987). Nitric oxide release accounts for the biological activity of endothelium-derived relaxing factor. Nature *327*, 524–526.

Palumbo, J.S., Talmage, K.E., Massari, J.V., La Jeunesse, C.M., Flick, M.J., Kombrinck, K.W., Jirousková, M., and Degen, J.L. (2005). Platelets and fibrin(ogen) increase metastatic potential by impeding natural killer cell-mediated elimination of tumor cells. Blood *105*, 178–185.

Roberts, A.M., Watson, I.R., Evans, A.J., Foster, D.A., Irwin, M.S., and Ohh, M. (2009). Suppression of hypoxia-inducible factor 2alpha restores p53 activity via Hdm2 and reverses chemoresistance of renal carcinoma cells. Cancer Res. *69*, 9056–9064.

Rofstad, E.K., and Danielsen, T. (1999). Hypoxia-induced metastasis of human melanoma cells: involvement of vascular endothelial growth factor-mediated angiogenesis. Br. J. Cancer *80*, 1697–1707.

Rofstad, E.K., Gaustad, J.V., Egeland, T.A., Mathiesen, B., and Galappathi, K. (2010). Tumors exposed to acute cyclic hypoxic stress show enhanced angiogenesis, perfusion and metastatic dissemination. Int. J. Cancer *127*, 1535–1546.

Ryan, H.E., Lo, J., and Johnson, R.S. (1998). HIF-1 alpha is required for solid tumor formation and embryonic vascularization. EMBO J. *17*, 3005–3015.

Ryan, H.E., Poloni, M., McNulty, W., Elson, D., Gassmann, M., Arbeit, J.M., and Johnson, R.S. (2000). Hypoxia-inducible factor-1alpha is a positive factor in solid tumor growth. Cancer Res. *60*, 4010–4015.

Saito, D., Sawamura, M., Umezawa, K., Kanai, Y., Furihata, C., Matsushima, T., and Sugimura, T. (1980). Inhibition of experimental blood-borne lung metastasis by protease inhibitors. Cancer Res. *40*, 2539–2542.

Schneider, M., Van Geyte, K., Fraisl, P., Kiss, J., Aragones, J., Mazzone, M., Mairbaurl, H., De Bock, K., Jeoung, N.H., Mollenhauer, M., et al. (2010). Loss or silencing of the PHD1 prolyl hydroxylase protects livers of mice against ischemia/reperfusion injury. Gastroenterology *138*, 1143–1154.

Shweiki, D., Itin, A., Soffer, D., and Keshet, E. (1992). Vascular endothelial growth factor induced by hypoxia may mediate hypoxia-initiated angiogenesis. Nature *359*, 843–845.

Skuli, N., and Simon, M.C. (2009). HIF-1alpha versus HIF-2alpha in endothelial cells and vascular functions: is there a master in angiogenesis regulation? Cell Cycle *8*, 3252–3253.

Skuli, N., Liu, L., Runge, A., Wang, T., Yuan, L., Patel, S., Iruela-Arispe, L., Simon, M.C., and Keith, B. (2009). Endothelial deletion of hypoxia-inducible factor-2alpha (HIF-2alpha) alters vascular function and tumor angiogenesis. Blood *114*, 469–477.

Smith, K., Gunaratnam, L., Morley, M., Franovic, A., Mekhail, K., and Lee, S. (2005). Silencing of epidermal growth factor receptor suppresses hypoxia-inducible factor-2-driven VHL-/- renal cancer. Cancer Res. *65*, 5221–5230.

Tafani, M., Russo, A., Di Vito, M., Sale, P., Pellegrini, L., Schito, L., Gentileschi, S., Bracaglia, R., Marandino, F., Garaci, E., and Russo, M.A. (2010). Up-regulation of pro-inflammatory genes as adaptation to hypoxia in MCF-7 cells and in human mammary invasive carcinoma microenvironment. Cancer Sci. *101*, 1014–1023.

Takeda, N., O'Dea, E.L., Doedens, A., Kim, J.W., Weidemann, A., Stockmann, C., Asagiri, M., Simon, M.C., Hoffmann, A., and Johnson, R.S. (2010). Differential activation and antagonistic function of HIF-alpha isoforms in macrophages are essential for NO homeostasis. Genes Dev. *24*, 491–501.

Tang, N., Wang, L., Esko, J., Giordano, F.J., Huang, Y., Gerber, H.P., Ferrara, N., and Johnson, R.S. (2004). Loss of HIF-1alpha in endothelial cells disrupts a hypoxia-driven VEGF autocrine loop necessary for tumorigenesis. Cancer Cell *6*, 485–495.

Ten, V.S., and Pinsky, D.J. (2002). Endothelial response to hypoxia: physiologic adaptation and pathologic dysfunction. Curr. Opin. Crit. Care *8*, 242–250.

Thomsen, L.L., Scott, J.M., Topley, P., Knowles, R.G., Keerie, A.J., and Frend, A.J. (1997). Selective inhibition of inducible nitric oxide synthase inhibits tumor growth in vivo: studies with 1400W, a novel inhibitor. Cancer Res. *57*, 3300–3304.

Van der Wall, H., and Palmer, A. (2006). On the AJR viewbox. Monomelic spread of metastatic disease due to proximal deep venous thrombosis. AJR Am. J. Roentgenol. *186*, 1797–1799.

Voss, M.J., Möller, M.F., Powe, D.G., Niggemann, B., Zänker, K.S., and Entschladen, F. (2011). Luminal and basal-like breast cancer cells show increased migration induced by hypoxia, mediated by an autocrine mechanism. BMC Cancer *11*, 158.

Wang, B., Xiong, Q., Shi, Q., Tan, D., Le, X., and Xie, K. (2001). Genetic disruption of host nitric oxide synthase II gene impairs melanoma-induced angiogenesis and suppresses pleural effusion. Int. J. Cancer *91*, 607–611.

Weis, S., Cui, J., Barnes, L., and Cheresh, D. (2004). Endothelial barrier disruption by VEGF-mediated Src activity potentiates tumor cell extravasation and metastasis. J. Cell Biol. *167*, 223–229.

Yamashita, T., Ohneda, K., Nagano, M., Miyoshi, C., Kaneko, N., Miwa, Y., Yamamoto, M., Ohneda, O., and Fujii-Kuriyama, Y. (2008). Hypoxia-inducible transcription factor-2alpha in endothelial cells regulates tumor neovascularization through activation of ephrin A1. J. Biol. Chem. *283*, 18926–18936.

Yang, M.H., Wu, M.Z., Chiou, S.H., Chen, P.M., Chang, S.Y., Liu, C.J., Teng, S.C., and Wu, K.J. (2008). Direct regulation of TWIST by HIF-1alpha promotes metastasis. Nat. Cell Biol. *10*, 295–305.

Zhang, Z., Neiva, K.G., Lingen, M.W., Ellis, L.M., and Nör, J.E. (2010). VEGF-dependent tumor angiogenesis requires inverse and reciprocal regulation of VEGFR1 and VEGFR2. Cell Death Differ. *17*, 499–512.

Zhong, H., De Marzo, A.M., Laughner, E., Lim, M., Hilton, D.A., Zagzag, D., Buechler, P., Isaacs, W.B., Semenza, G.L., and Simons, J.W. (1999). Overexpression of hypoxia-inducible factor 1alpha in common human cancers and their metastases. Cancer Res. *59*, 5830–5835.

Zhou, J., Dehne, N., and Brüne, B. (2009). Nitric oxide causes macrophage migration via the HIF-1-stimulated small GTPases Cdc42 and Rac1. Free Radic. Biol. Med. *47*, 741–749.

Ziche, M., and Morbidelli, L. (2009). Molecular regulation of tumour angiogenesis by nitric oxide. Eur. Cytokine Netw. *20*, 164–170.

Cancer Cell
Article

Pericyte Depletion Results in Hypoxia-Associated Epithelial-to-Mesenchymal Transition and Metastasis Mediated by Met Signaling Pathway

Vesselina G. Cooke,[1,5] Valerie S. LeBleu,[1,5] Doruk Keskin,[1,2] Zainab Khan,[1] Joyce T. O'Connell,[1] Yingqi Teng,[1] Michael B. Duncan,[1] Liang Xie,[1] Genta Maeda,[1] Sylvia Vong,[1,2] Hikaru Sugimoto,[1] Rafael M. Rocha,[3] Aline Damascena,[3] Ricardo R. Brentani,[3] and Raghu Kalluri[1,2,4,*]

[1]Division of Matrix Biology, Department of Medicine, Beth Israel Deaconess Medical Center and Harvard Medical School, Boston, MA 02115, USA

[2]Department of Biological Chemistry and Molecular Pharmacology, Harvard Medical School, Boston, MA 02115, USA

[3]Department of Oncology, Hospital A. C. Camargo, National Institute of Oncogenomics, Dundacao Antonio Prudente, 01509-010, Sao Paulo, Brazil

[4]Division of Health Sciences and Technology, Harvard-Massachusetts Institute of Technology, Boston, MA 02115, USA

[5]These authors contributed equally to this work

*Correspondence: rkalluri@bidmc.harvard.edu

DOI 10.1016/j.ccr.2011.11.024

SUMMARY

The functional role of pericytes in cancer progression remains unknown. Clinical studies suggest that low numbers of vessel-associated pericytes correlated with a drop in overall survival of patients with invasive breast cancer. Using genetic mouse models or pharmacological inhibitors, pericyte depletion suppressed tumor growth but enhanced metastasis. Pericyte depletion was further associated with increased hypoxia, epithelial-to-mesenchymal transition (EMT), and Met receptor activation. Silencing of *Twist* or use of a Met inhibitor suppressed hypoxia and EMT/Met-driven metastasis. In addition, poor pericyte coverage coupled with high Met expression in cancer cells speculates the worst prognosis for patients with invasive breast cancer. Collectively, our study suggests that pericytes within the primary tumor microenvironment likely serve as important gatekeepers against cancer progression and metastasis.

INTRODUCTION

Metastasis is the leading cause of death in cancer patients. The formation of secondary tumors or metastasis is greatly influenced by multifaceted tumor-stroma interactions, in which stromal components of the tumor microenvironment can influence the behavior of the cancer cells (Coussens et al., 2000; Joyce, 2005; Thiery, 2009). While cancer cell-autonomous changes are undoubtedly critical for cancer progression and metastasis, the functional contribution of stromal cells is still emerging.

Pericytes are an integral component of the tissue vasculature. As perivascular stromal cells, pericytes provide structural support to blood vessels and regulate tissue physiology via its influence on vascular stability (Dore-Duffy and Cleary, 2011; Kim et al., 2006). Due to their essential function in vascular development, pericytes are also speculated to play an important role in tumor angiogenesis. Angiogenesis is required for the growth of tumors, and VEGF-mediated proliferation and migration of endothelial cells is critical for the generation of new capillaries, which is further supported by the recruitment of pericytes (Raza et al., 2010). Some studies have explored strategies that target both endothelial cells and pericytes (Bergers et al., 2003; Lu et al., 2007) or pericytes alone (Lu et al., 2007; Ozerdem, 2006a) to inhibit tumor angiogenesis and tumor growth. However, clinical data correlates low pericyte coverage with poor patient prognosis (O'Keeffe et al., 2008; Stefansson et al., 2006; Yonenaga et al., 2005), and disruption of pericytes has also been suggested to enhance metastasis (Xian et al., 2006).

The growth of tumors is often associated with defective tumor vasculature that cannot keep up with the overall oxygen and metabolic needs, ultimately resulting in tumor hypoxia (Harris, 2002; Semenza, 2003). Diminished oxygen levels lead to the

Significance

Pericyte coverage and its relation to metastasis are poorly understood. This study suggests that pericyte coverage on tumor vasculature serves as a key negative regulator of metastasis. Clinical studies suggest that cancer patients with low numbers of vessel-associated pericytes exhibit a high mortality rate. Cancer cell autonomous changes cooperate with stromal changes to determine the rate of cancer progression and metastasis.

activation and stabilization of the transcription factor HIF1α (Pouysségur et al., 2006), and hypoxia and HIF1α expression are correlated with poor prognosis and metastasis in cancer patients (Birner et al., 2000; Bos et al., 2003; Brizel et al., 1997; Vleugel et al., 2005). Hypoxia induces epithelial-to-mesenchymal transition (EMT) of cells specifically via HIF1α activation of the master regulator of EMT *Twist* (Sun et al., 2009; Yang et al., 2008), which is suggested to play an essential role in promoting metastasis (Yang et al., 2004).

Met, the receptor for hepatocyte growth factor (HGF), is also a key promoter of EMT (Birchmeier et al., 2003). Furthermore, the *Met* promoter contains HIF1α binding sites and is regulated by both hypoxia and HIF1α (Hara et al., 2006; Hayashi et al., 2005; Pennacchietti et al., 2003). HGF/Met expression is also upregulated in many cancers (Di Renzo et al., 1991), correlating with disease progression and metastasis (Di Renzo et al., 1995; Kenworthy et al., 1992) (Natali et al., 1993).

Using genetically engineered mouse models (GEMMs) and pharmacological targeting of pericytes, we examined whether pericyte deficiency positively or negatively affects metastasis and explored possible underlying mechanisms.

RESULTS

Low Pericyte Coverage Is Associated with Invasive Breast Cancer and Correlates with Decreased Patient Survival

Pericyte coverage of the tumor vasculature was evaluated in tissue samples from breast cancer patients with invasive ductal carcinoma via immunostaining for NG2, a vascular pericytes marker (Bergers and Song, 2005; Jain, 2003; Ozerdem et al., 2002; Schlingemann et al., 1990; Sennino et al., 2007), and CD31, a marker for endothelial cells (Newman, 1994). The percentage of $CD31^+$ vessels associated with NG2 staining was quantified using morphometric analysis. Among various clinical characteristics, low pericyte coverage was significantly associated with the presence of distant metastasis (Table S1 available online). Moreover, the degree of pericyte coverage also significantly correlated with disease progression and overall survival (Figure S1A). Patients with no detectable pericyte coverage on tumor vessels exhibited a shorter disease-free survival and lower rate of overall survival than patients with greater pericyte coverage.

Pericyte Depletion Inhibited Tumor Growth but Produced Defective Tumor Vasculature and Increased Metastasis

To functionally assess the role of pericytes in tumor progression and metastasis, we generated transgenic mice that express viral thymidine kinase (tk) under control of the *NG2* promoter (NG2-tk mice) (Figure S1B). Ganciclovir (GCV) treatment of NG2-tk mice resulted in the selective ablation of proliferating $NG2^+$ cells due to incorporation of GCV nucleoside analog during replication leading to irreversible DNA synthesis arrest. To assess the specificity of the *NG2* promoter for expression in $NG2^+$ cells, we generated NG2-YFP transgenic mice that express yellow fluorescent protein (YFP) under the control of the same *NG2* promoter sequence and found that NG2-YFP expression colocalized with NG2 antibody staining in 4T1 mammary tumors (Figures S1B and S1C). To determine the efficacy of the NG2-tk transgene, in vitro culture of $NG2^+$ cells from NG2-tk and wild-type (WT) mice were treated with varying GCV concentrations (Figure S1D). Dose-dependent ablation of $NG2^+$ cells was observed, with 75% ablation at 500 μM GCV.

4T1-GFP cancer cells were implanted into the mammary fat pad of NG2-tk mice and wild-type littermates. Primary tumor growth was monitored and daily GCV injections were initiated when tumors reached ~500 mm^3 and continued until tumors reached ~2,000 mm^3 (Figure 1A). Tumor volumes decreased upon initiation of GCV treatment in the NG2-tk mice and remained significantly smaller until the experimental endpoint (Figure 1B). The number of $NG2^+$ cells, $CD31^+$ cells, and percent vessel-associated $NG2^+$ cells in the primary tumors of NG2-tk+GCV mice were significantly reduced when compared to control GCV-treated wild-type littermates (WT+GCV mice) (Figure 1C). To investigate whether pericyte depletion was associated with vascular abnormalities, we infused tumor-bearing mice with FITC-conjugated dextran and observed a greater amount of extravascular FITC-dextran in pericyte-depleted tumors (Figure 1D).

While pericyte ablation reduced primary tumor growth, 4T1 tumor-bearing NG2-tk+GCV mice exhibited increased lung metastasis when compared to WT+GCV mice (Figure 1E). FACS and quantitative PCR analysis of genomic DNA for the cancer cell-associated *GFP* gene revealed that the number of circulating cancer cells and metastatic cancer cells in the lungs was greater in NG2-tk+GCV mice than in WT+GCV mice. Reduced tumor size and increased metastasis were also observed when pericytes were ablated in the MMTV-PyMT spontaneous mammary tumor model using GCV-treated MMTV-PyMT/NG2-tk double transgenic mice (Figures 1F and 1G). However, upon intravenous injection of 4T1 cancer cells into NG2-tk+GCV and WT+GCV mice, pericyte ablation had no significant effects on metastasis in the absence of a primary tumor (Figure S1E).

PDGFRβ has also been used as a marker to identify pericytes (Dore-Duffy, 2008; Hellström et al., 1999; Liebner et al., 2000; Ozerdem et al., 2001a; Xian et al., 2006). To validate the prometastatic effects of pericyte depletion observed in NG2-tk+GCV mice, we generated PDGFRβ-tk mice in which viral thymidine kinase is expressed under the *PDGFRβ* promoter as an alternative model for pericyte depletion (Figure S2A). To assess the specificity of the *PDGFRβ* promoter, we also generated PDGFRβ-RFP mice in which red fluorescent protein (RFP) is expressed under the same *PDGFRβ* promoter element (Figures S2A and S2B) and found that PDGFRβ-RFP expression colocalized with PDGFRβ antibody staining in 4T1 tumors. To determine the efficacy of the PDGFRβ-tk transgene, in vitro culture of $PDGFR\beta^+$ cells from PDGFRβ-tk and WT mice were subjected to increasing concentrations of GCV (Figure S2C). Dose-dependent ablation of $PDGFR\beta^+$ cells was observed, with 60% ablation at 50 μM GCV.

4T1 cancer cells were implanted into the mammary fat pad of PDGFRβ-tk mice and WT littermates. Tumor volumes decreased upon initiation of GCV treatment in PDGFRβ-tk mice and remained significantly smaller until the experimental endpoint when compared to WT+GCV mice (Figures 2A and 2B). However, metastasis was greatly enhanced following ablation of $PDGFR\beta^+$ cells (Figure 2C). Immunostaining with PDGFRβ

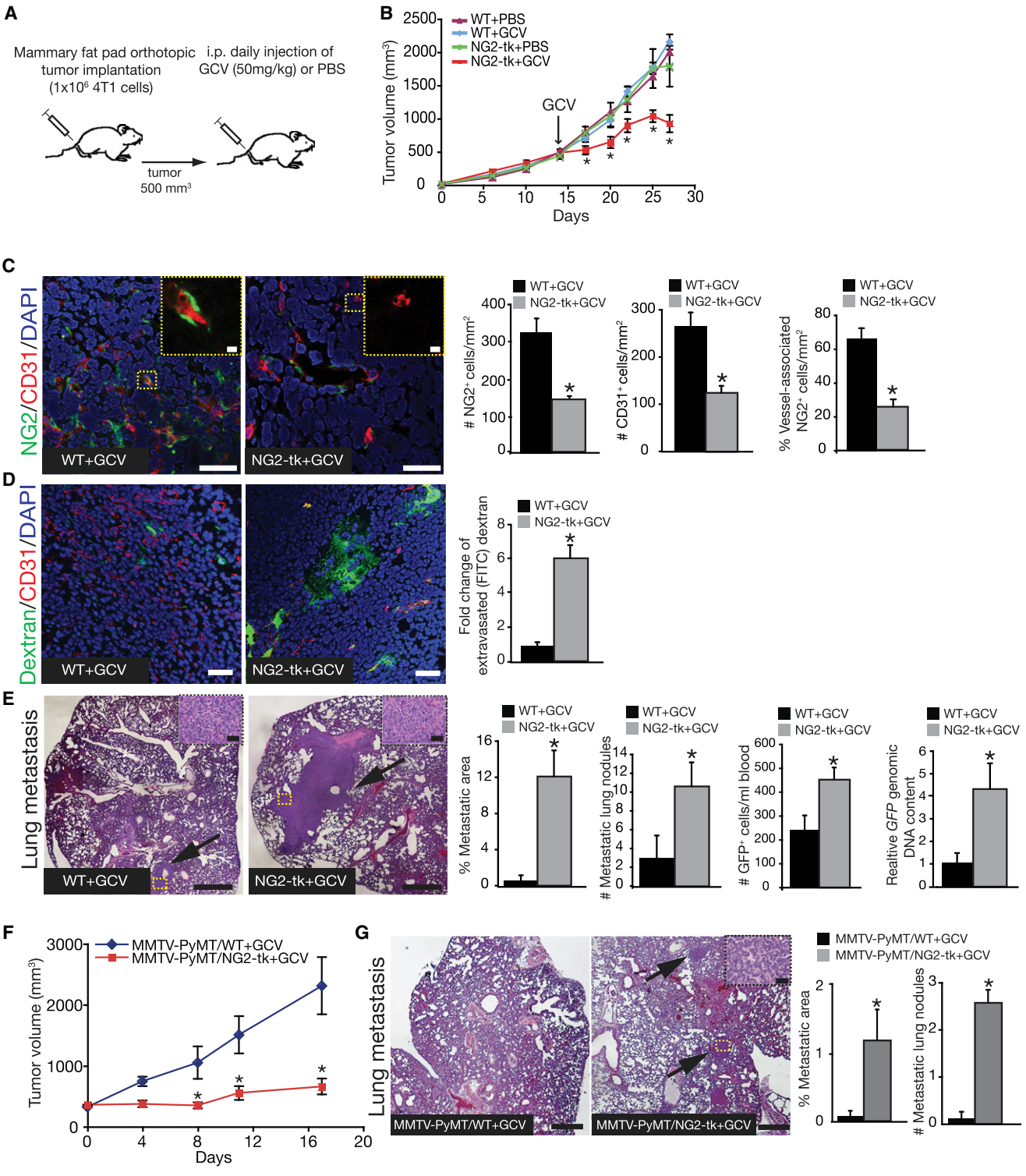

Figure 1. Reduced Tumor Growth and Increased Metastasis after Depletion of Vessel-Associated NG2⁺ Cells

(A) Orthotopic implantation of 4T1 cancer cells in NG2-tk mice and wild-type littermates, with daily ganciclovir (GCV) or saline (PBS) injections beginning when tumors reached ~500 mm³.

(B) Tumor volumes over the experimental time course.

(C) Representative images of tumor sections from WT+GCV and NG2-tk+GCV mice immunolabeled for NG2 (green)/CD31 (red), and quantification of number of NG2⁺ cells, CD31⁺ cells, and percent vessel-associated NG2⁺ cells in each group. DAPI = nuclei. Scale bar, 50 μm. High-magnification images are located in the upper right corner. Scale bar, 10 μm.

antibody in the tumors of PDGFRβ-tk+GCV mice revealed 80% reduction in vessel-associated PDGFRβ$^+$ cells (Figure 2D). PDGFRβ shares ~90% colocalization with NG2 on tumor vasculature (Sugimoto et al., 2006), and vessel-associated NG2$^+$ cells were also reduced by 80% in the tumors of PDGFRβ-tk+GCV mice (Figure 2D). The overall pericyte coverage (assessed by vessel-associated NG2$^+$/PDGFRβ$^+$ double-positive cells) and the number of CD31$^+$ cells were reduced in PDGFRβ-tk+GCV mice when compared to WT+GCV mice (Figure 2D).

As an alternative model for inhibiting PDGFRβ$^+$ cells, 4T1 tumor-bearing mice were treated with PDGFRβ-specific antibodies to suppress PDGFRβ activity. PDGFRβ antibody treatment significantly decreased tumor volume and increased metastatic burden (Figures 2E and 2F), in association with a significant reduction in the percent vessel-associated PDGFRβ$^+$ cells (Figure 2G).

Enhanced Hypoxia, HIF1α Expression, and EMT Program in Pericyte-Depleted Tumors

To gain insight into the molecular mechanisms associated with increased metastasis resulting from pericyte depletion, we performed gene expression profiling of tumors from NG2-tk+GCV and WT+GCV mice. We employed genealogy analysis to identify significantly upregulated genes [grouped as pathways (Table S2) and network processes (Table S3)] in NG2-tk+GCV mice when compared to WT+GCV mice. The overlapping processes identified were (1) response to hypoxia, (2) response to stress, and (3) cell motion/migration (Table S3). Reduced pericyte coverage can decrease vessel stability and increase hypoxia (Huang et al., 2010). In concordance, pericyte depletion in the NG2-tk+GCV mice induced a gene expression profile that reflected a hypoxic state. We assessed hypoxia levels by examining pimonidazole adduct formation in the tumors of NG2-tk+GCV and WT+GCV mice and found increased hypoxic levels in the NG2-tk+GCV pericyte-depleted tumors (Figure 3A). In addition, expression of the hypoxia-inducible transcription factor HIF1α was also significantly increased in the tumors of NG2-tk+GCV mice (Figure 3B).

The exact mechanism connecting hypoxia and cancer invasiveness remains unknown; however, several have been proposed (Dachs and Tozer, 2000; Gupta and Massagué, 2006; Rofstad, 2000; Yang et al., 2008). Because cell motion/migration was identified as one of the primary processes upregulated by NG2-tk+GCV tumors in the gene expression profiling analysis, we hypothesized that EMT may be a mechanism connecting hypoxia and cancer invasiveness. Further examination of the microarray data revealed that the expression of many EMT-associated genes were upregulated in NG2-tk+GCV tumors when compared to WT+GCV tumors (Table S4). To identify epithelial cells undergoing EMT, tumors from NG2-tk+GCV and WT+GCV mice were immunostained for the epithelial marker Cytokeratin-8 (CK8) and the mesenchymal marker αSMA; the number of CK8$^+$/αSMA$^+$ double-positive cells was significantly increased in NG2-tk+GCV pericyte-depleted tumors (Figure 3C). Next, we performed quantitative RT-PCR and confirmed that expression of *CK8* was significantly downregulated, while transcription factors associated with EMT induction, such as *Twist* and *Snail*, were significantly upregulated in NG2-tk+GCV tumors (Figure 3D). Other epithelial genes such as *E-cadherin* and *α-catenin* were also downregulated, while genes driving mesenchymal phenotype such as *Slug*, *Lox*, and *Fibronectin* were upregulated.

In agreement with the data from the NG2-tk+GCV mice, tumors from MMTV-PyMT/NG2-tk+GCV mice revealed increased hypoxia along with increased numbers of CK8$^+$/αSMA$^+$ double-positive cells, reduced *E-cadherin* expression, and increased *Twist* and *Snail* expression, when compared to tumors from MMTV-PyMT/WT+GCV mice (Figures 3E–3G). Tumors from PDGFRβ-tk+GCV mice also showed increased hypoxia, increased HIF1α expression, and acquisition of an EMT program shift when compared to control mice (data not shown).

The transcription factor Twist has been termed the master regulator of EMT (Yang et al., 2004). To evaluate whether inhibition of EMT via silencing of *Twist* abrogates the metastatic phenotype seen in NG2-tk+GCV mice, we orthotopically injected 4T1 cancer cells with stably-silenced *Twist* (two different clones of 4T1-twist shRNA) into NG2-tk+GCV and WT+GCV mice. Tumor volume in 4T1-twist shRNA tumor-bearing NG2-tk+GCV mice was reduced when compared to 4T1-twist shRNA tumor-bearing WT+GCV mice (Figure 4A). Moreover, metastatic burden was decreased in 4T1-twist shRNA tumor-bearing WT+GCV mice when compared to 4T1 tumor-bearing WT+GCV mice, while metastasis was further suppressed in 4T1-twist shRNA tumor-bearing NG2-tk+GCV mice (Figures 4B–4E).

Met Protooncogene Activation in Pericyte-Depleted Tumors

Quantitative RT-PCR for *Met* revealed significantly increased *Met* expression in NG2-tk+GCV tumors when compared to WT+GCV tumors (Figure 5A). Additionally, increased phosphorylation of Met was also observed in tumors from NG2-tk+GCV and MMTV-PyMT/NG2-tk+GCV mice when compared to tumors from control mice (Figures 5B and 5C), as well as in PDGFRβ-tk+GCV mice (data not shown).

Next, we explored whether pharmacological targeting of Met can suppress metastasis in pericyte-ablated mice. Treatment of MMTV-PyMT/NG2-tk mice with both GCV and the Met

(D) Representative images of tumor sections immunolabeled for CD31 (red) and quantitative analysis of extravascular FITC-dextran. DAPI = nuclei. Scale bar, 50 μm.

(E) Representative images of H&E-stained lung sections. Scale bar: 10 μm. Arrows point to metastatic nodules. High-magnification images of metastatic nodules are located in the upper right corner. Scale bar: 50 μm. Percent metastatic area, number of metastatic lung nodules, number of 4T1-GFP$^+$ cells in the blood, and relative GFP content in lungs of NG2-tk+GCV mice compared to WT+GCV mice.

(F) MMTV-PyMT/WT and MMTV-PyMT/NG2-tk female mice were treated with GCV when tumors reached ~500 mm^3 and tumor volumes measurements over time.

(G) Representative images of H&E-stained lung sections of MMTV-PyMT/WT+GCV and MMTV-PyMT/NG2-tk+GCV mice. Scale bar: 10 μm. Arrows point to metastatic nodules. Percent metastatic area and number of metastatic lung nodules. Error bars display SEM; asterisks denote significance (*$p \leq 0.05$). NS, nonsignificant.

See also Figure S1 and Table S1.

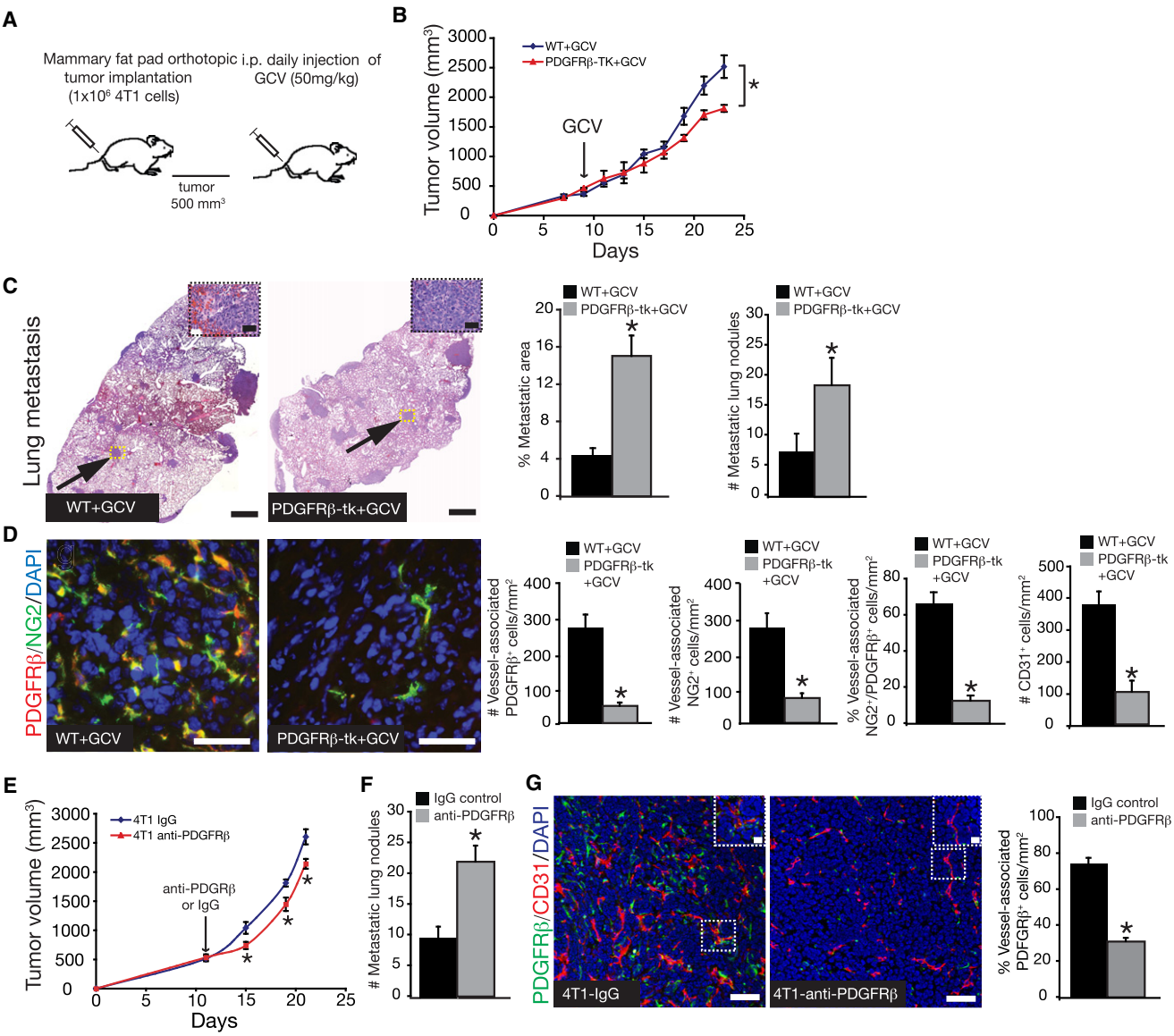

Figure 2. Reduced Tumor Growth and Increased Metastasis after Depletion of Vessel-Associated PDGFRβ⁺ Cells

(A) Orthotopic implantation of 4T1 cancer cells into PDGFRβ-tk mice and wild-type littermates, with daily ganciclovir (GCV) injections beginning when tumors reached ~500 mm³.

(B) Tumor volumes over the experimental time course.

(C) Representative images of H&E-stained lung sections. Scale bar, 10 μm. Arrows point to metastatic areas. High-magnification images of metastatic nodules are located in the upper right corner. Scale bar: 50 μm Percent metastatic area and number of metastatic lung nodules.

(D) Representative images of immunostaining for PDGFRβ (red) and NG2 (green) tumor sections. DAPI = nuclei. Scale bar, 50 μm. Quantitative assessment of vessel-associated PDGFRβ⁺, NG2⁺, PDGFRβ⁺/NG2⁺ double positive, and CD31⁺ cells in 4T1 tumors from PDGFRβ-tk+GCV and WT+GCV mice.

(E) Tumor volumes over the experimental time course in mice treated with anti-PDGFRβ antibody or control IgG.

(F) Number of metastatic lung nodules.

(G) Representative images of tumor sections immunolabeled for PDGFRβ (green)/CD31 (red) in IgG-treated and anti-PDGFRβ-treated mice, and quantification of vessel-associated PDGFRβ⁺ cells in the tumors; scale bar, 50 μm. Insets are magnified images of selected area.

Scale bar, 10 μm. Error bars display SEM; *p ≤ 0.05. See also Figure S2.

inhibitor PF2341066 completely suppressed the enhanced metastasis of MMTV-PyMT/NG2-tk mice treated with GCV alone (Figures 5D–5F). The baseline lung metastasis observed in the control tumors (without pericyte depletion, hypoxia, HIF-1α expression, Met activation, and EMT) did not respond to Met inhibition.

Enhanced Metastasis upon Pericyte Targeting Using Pharmacological Inhibitors Is Suppressed by Concomitant Met Inhibitor Treatment

Many studies have reported that imatinib (which targets pericytes via PDGFRβ) and sunitinib (which targets both endothelial cells and pericytes via VEGFR1, VEGFR2, VEGFR3, and

PDGFRβ), drugs currently in clinical use, can inhibit tumor progression (Bergers et al., 2003; Ebos et al., 2009; Lu et al., 2007; Mendel et al., 2003; Pàez-Ribes et al., 2009; Pietras and Hanahan, 2005); however, there have been limited studies examining their effects on metastasis. Treatment with sunitinib and another receptor tyrosine kinase inhibitor sorafenib have been demonstrated to increase metastasis in animal tumor models (Ebos et al., 2009; Pàez-Ribes et al., 2009); however, the molecular mechanism for which remains largely unknown. Therefore, we examined whether imatinib and sunitinib enhance metastasis due to mechanisms similar to shown above.

4T1 tumor-bearing mice were treated with either imatinib or sunitinib. Imatinib treatment reduced pericyte coverage (as determined by vessel-associated $NG2^+$/$PDGFR\beta^+$ double-positive cells) by more than 60% (Figure S3A). In concordance with previous reports (Lu et al., 2007), decreased pericyte coverage was not accompanied by net reduction of tumor vessels (Figure S3A). Quantitative RT-PCR showed negligible expression levels of *c-Kit* and *Abl1* (additional targets of imatinib) in 4T1 tumors, and their expression remained unchanged upon imatinib treatment (Figure S3A). Sunitinib treatment led to reduced numbers of both $NG2^+$/$PDGFR\beta^+$ double-positive cells and $CD31^+$ endothelial cells (Figure S3A).

4T1 tumor-bearing mice treated with sunitinib exhibited reduced tumor volume and growth with increased levels of apoptosis, while imatinib-treated tumor-bearing mice revealed similar tumor growth kinetics when compared to mice treated with PBS-vehicle (Figures 6A–6C). Analysis of lungs revealed a significantly higher level of metastatic burden in both the imatinib-treated and sunitinib-treated groups (Figure 6D). Quantification of FITC-dextran revealed increased amount of extravascular dextran in the tumors of imatinib-treated and sunitinib-treated mice (Figure 6E). Furthermore, tumors in imatinib-treated and sunitinib-treated mice showed significant increase in hypoxia as assessed by pimonidazole staining (Figure 6F), as well as increased expression of HIF1α (Figure 6G). Similar to results obtained with the transgenic mice, however, imatinib or sunitinib treatment had no significant effects on metastasis when 4T1 cells were injected intravenously (Figure S3B).

Next, we evaluated whether pharmacological targeting of pericytes also induced an EMT program in the cancer cells. Tumors from imatinib-treated and sunitinib-treated mice exhibited increased numbers of $CK8^+$/αSMA^+ double-positive cells when compared to tumors from PBS-treated mice (Figure 6H). In addition, quantitative RT-PCR showed significant downregulation of *E-cadherin*, while *Twist* and *Snail* were upregulated (Figure 6I). To address whether inhibition of EMT can suppress the increased metastatic phenotype seen after pharmacological targeting of pericytes, mice were implanted with 4T1-twist shRNA cells and treated with imatinib. Silencing of *Twist* was able to suppress the imatinib-induced EMT and metastasis without significant effects on primary tumor growth (Figure S3C).

Levels of Met and phosphorylated Met were also increased in tumors of imatinib-treated and sunitinib-treated mice when compared to PBS-treated mice (Figures S4A and S4B). Tumors from PBS-treated mice showed phosphorylated Met expression predominantly in the vascular wall, while tumors from imatinib-treated and sunitinib-treated mice exhibited significantly higher levels of phosphorylated Met in the cancer cells. Pharmacological targeting of Met using PF2341066 inhibited the EMT program shift and suppressed metastasis in imatinib-treated and sunitinib-treated mice (Figures 7A–7F), despite retaining the imatinib- or sunitinib-induced changes in vessel integrity and tumor hypoxia (Figures 7G–7I). PF2341066 treatment of imatinib-treated and sunitinib-treated mice successfully inhibited both Met and phosphorylated Met levels (Figure S4B). Although PF2341066 is also an inhibitor of ALK (Zou et al., 2007), quantitative RT-PCR (data not shown) and immunostaining revealed that ALK was not expressed in 4T1 tumors with or without PF2341066 treatment (Figure S4C). The baseline tumor weight and lung metastasis observed in the control tumors (without pericyte deficiency, hypoxia, HIF1α expression, Met activation, and EMT) did not respond to Met inhibition alone (Figure S4D).

To further investigate whether targeting pericytes leads to increased metastasis in other tumor types, we subcutaneously implanted B16F10 mouse melanoma cells into C57Bl6 mice (Figure S4E) and orthotopically implanted 786-O human renal cell carcinoma cells under the renal capsule of nude mice (Figure S4F). The mice were then treated with PBS, sunitinib, PF2341066 or a combination of both sunitinib and PF2341066. Sunitinib treatment led to reduced B16F10 tumor volume and weight but led to an increase in metastasis. Sunitinib-treated tumors also showed increase in hypoxia, phosphorylated Met, and induction of EMT. Treatment with PF2341066 did not affect primary tumor volume and weight; however, concomitant treatment with PF2341066 and sunitinib significantly suppressed metastasis, despite hypoxia remaining high in these tumors. Similarly, mice with RCC tumors treated with sunitinib showed increased lung metastasis, increased hypoxia, increased phosphorylated Met, and enhanced EMT program. Concomitant treatment of RCC tumor-bearing mice with sunitinib and PF2341066 suppressed metastasis and EMT despite high levels of hypoxia. Sunitinib-treated mice intravenously injected with RCC (to bypass the primary tumor), however, showed significantly reduced metastasis when compared to PBS-treated mice.

To explore the impact of targeting only endothelial cells on metastasis without targeting pericytes, RCC tumor-bearing mice were treated with anti-human VEGF-A blocking antibody (Bevacizumab) and 4T1 tumor-bearing mice with anti-mouse VEGF-A blocking antibody. Bevacizumab treatment led to decreased tumor volume; however, metastasis was unchanged (Figure S4G). Tumors from bevacizumab-treated mice did not show an increase in hypoxia or Met activation (Figure S4G). 4T1 tumor-bearing mice treated with VEGF-A antibody showed reduced tumor growth and metastasis when compared to control mice (Figure S4H). Similar results were obtained when pancreatic neuroendocrine (PNET) and RCC tumor-bearing mice were treated with endogenous inhibitors of angiogenesis that target endothelial cells, such as tumstatin and endostatin (data not shown; Xie et al., 2011).

Loss of Pericytes Coupled with High Met Expression Is Associated with Decreased Survival of Breast Cancer Patients

Our experiments with mice suggested that loss of pericytes leads to enhanced tumor hypoxia and metastasis via increased Met expression in cancer cells. We evaluated breast cancer

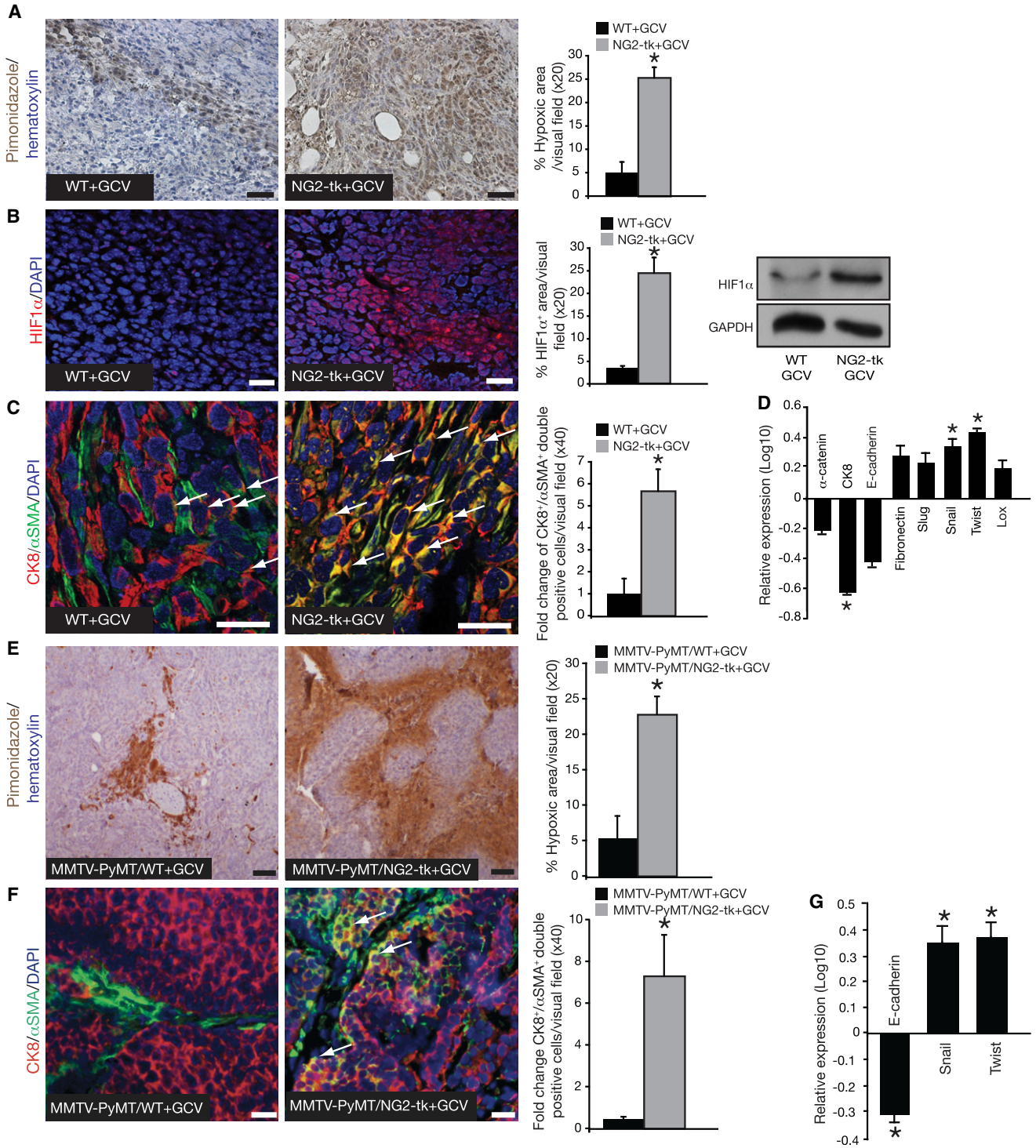

Figure 3. Increase in Hypoxia and EMT in Pericyte-Depleted Tumors

(A) Hypoxia was detected by immunohistochemistry staining of pimonidazole adducts in 4T1 tumor sections from NG2-tk+GCV and WT+GCV mice. Nuclear counterstain: hematoxylin stain. Quantitative analysis of the percent hypoxic area per visual field.

(B) Immunostaining for HIF1α. DAPI = nuclei. Quantification of HIF1α immunostaining and western blot analysis for HIF1α expression; GAPDH is used as an internal control.

(C) EMT as detected by immunofluorescent staining for Cytokeratin 8 (red) and αSMA (green). DAPI = nuclei. Arrows point to $CK8^+/\alpha SMA^+$ double-positive cells. Quantification of EMT is plotted as fold change in the number of $CK8^+/\alpha SMA^+$ double-positive cells per visual field.

(D) Quantitative RT-PCR for *α-catenin*, *Cytokeratin 8 (CK8)*, *E-cadherin*, *Fibronectin*, *Slug*, *Snail*, *Twist*, *and Lox* comparing expression levels in tumor tissues from NG2-tk+GCV mice relative to WT+GCV mice and plotted as log10 relative expression.

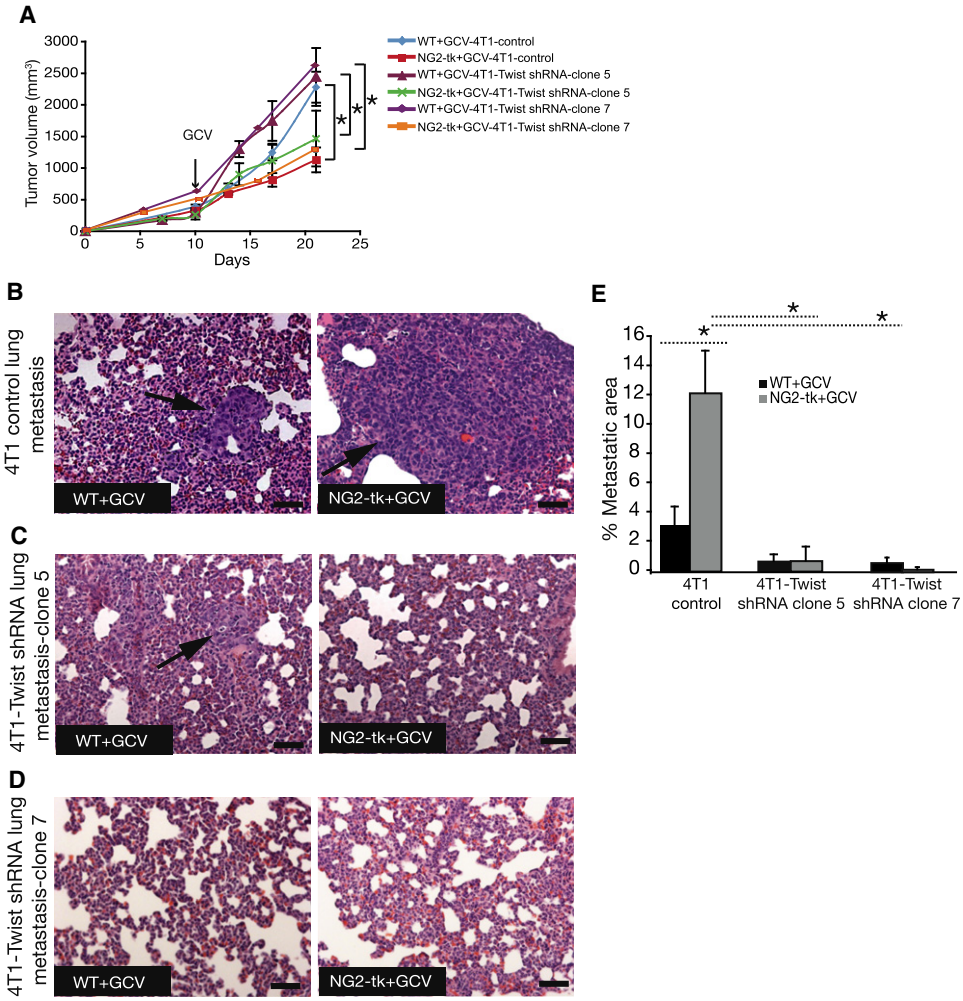

Figure 4. Decreased Metastasis in Mice with Pericyte-Depleted Tumors after Inhibition of EMT

(A) Tumor volumes over the experimental time course in WT+GCV and NG2-tk+GCV mice implanted with 4T1 or 4T1-Twist shRNA cells.

(B–D) Representative photomicrographs of H&E-stained lung sections of WT+GCV and NG2-tk+GCV mice implanted with (B) 4T1 cells, (C) 4T1-Twist shRNA cells-clone 5 and (D) 4T1-Twist shRNA cells-clone 7. Arrows point to metastatic nodules.

(E) Quantification of metastatic area.

Error bars display SEM; asterisks denote significance (*$p \leq 0.05$). NS, nonsignificant. Scale bar, 50 μm.

samples for pericyte coverage, HIF1α expression and Met expression. Invasive ductal carcinoma (IDC) patients with high levels of HIF1α exhibited poor prognosis with diminished disease-free survival, as has been also suggested by other studies (Baba et al., 2010; Koukourakis et al., 2002; Vleugel et al., 2005). While high Met expression in cancer cells was associated with a drop in disease-free and overall survival, the coupling of poor pericyte coverage together with high Met expression correlated with an additional drop in disease-free and overall survival (Figures 8A and 8B). Furthermore, pericyte coverage coupled with Met expression correlated with breast cancer stage, depth of invasion, and the presence of distant metastasis (Figure 8C).

DISCUSSION

Tumors induce angiogenesis to generate new blood vessels (Folkman, 1971, 1974, 1995; Hanahan and Weinberg, 2000), and pericytes are important structural and functional components of blood vessels (Dore-Duffy and Cleary, 2011). In normal

(E) Representative images of pimonidazole adducts staining (hypoxia). Nuclear counterstain: hematoxylin staining. Quantification of the percent hypoxic area per visual field.

(F) EMT as detected by immunofluorescent staining for Cytokeratin 8 (red) and αSMA (green). DAPI = nuclei. Arrows point to $CK8^+/\alpha SMA^+$ double-positive cells. Quantification of EMT plotted as the number of $CK8^+/\alpha SMA^+$ double-positive cells per visual field.

(G) Quantitative RT-PCR for *E-cadherin, Snail, and Twist* plotted as log10 relative expression. Error bars display SEM; asterisks denote significance (*$p \leq 0.05$). Scale bar, 50 μm. See also Tables S2–S4.

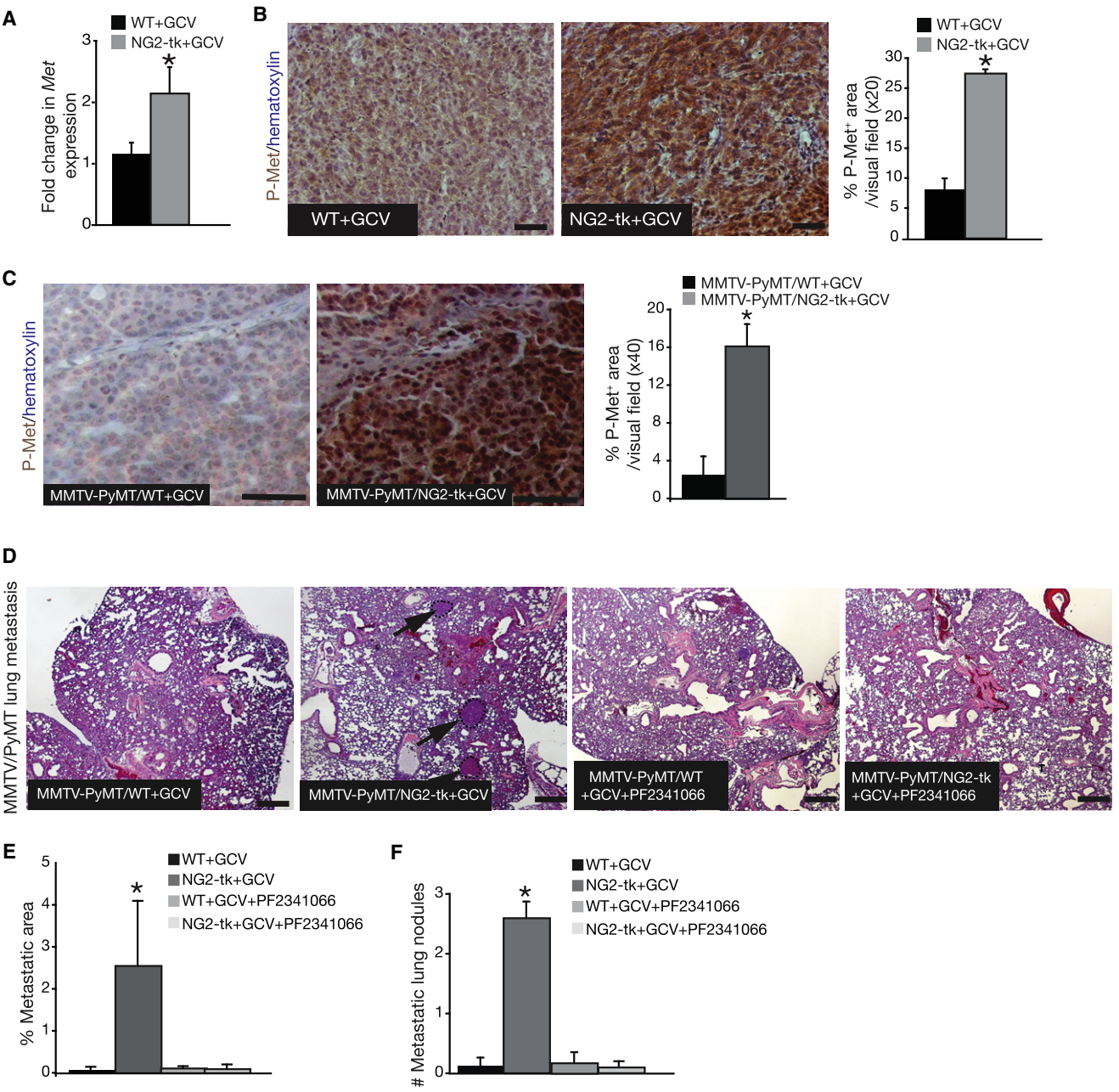

Figure 5. Suppression of Metastasis in Pericyte-Ablated Mice after Met Inhibition

(A) Quantitative RT-PCR for *Met* mRNA expression in tumors from NG2-tk+GCV and WT+GCV mice.

(B) Immunostaining of 4T1 tumor for phosphorylated Met (p-Met). Nuclear counterstain: hematoxylin. Scale bar, 50 μm. Quantification of p-Met expression.

(C) Immunostaining and quantification of p-Met (mammary tumors). Nuclear counterstain: hematoxylin. Scale bar, 50 μm.

(D) Representative images of H&E-stained lung sections from MMTV-PyMT/WT and MMTV-PyMT/NG2-tk mice treated with GCV or GCV+PF2341066. Arrows point to metastatic nodules. Scale bar, 50 μm.

(E) Percent lung metastatic area.

(F) Number of metastatic lung nodules before and after PF2341066 treatment.

Error bars display SEM; asterisks denote significance (*$p \leq 0.05$). Scale bar, 50 μm. See also Figure S4.

tissue, pericytes play an important role in regulating the physiological function of blood vessels; however, their precise role in the context of tumor vasculature is largely unexplored. Studies related to pericyte coverage on tumor blood vessels suggest that coverage can vary; some tumor types exhibit greater pericyte coverage whereas others exhibit limited and abnormal coverage (Eberhard et al., 2000). Many studies have suggested that targeting pericytes alone or in combination with endothelial cells might be beneficial to control tumor growth (Bergers et al., 2003; Lu et al., 2010; Ozerdem, 2006a, 2006b), while other

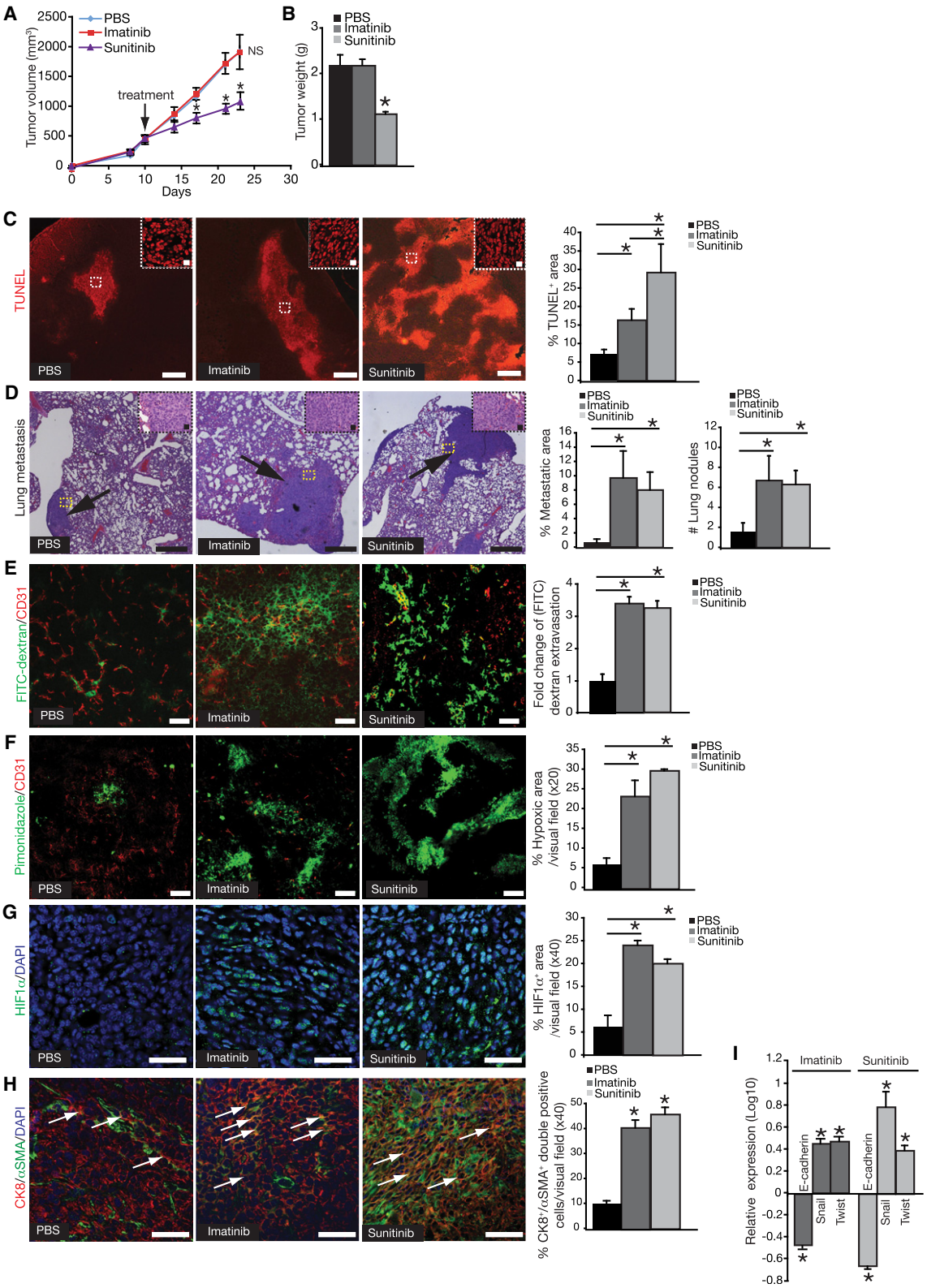

Figure 6. Decreased Pericyte Coverage, Altered Vasculature, Enhanced EMT, and Increased Metastasis in Imatinib- and Sunitinib-Treated Mice

(A) Orthotopic implantation of 4T1 cancer cells into PBS-, imatinib- and sunitinib-treated mice and tumor volumes over the experimental time course.

(B) Tumor weight at the experimental endpoint.

studies have suggested that pericyte deficiency may facilitate cancer metastasis (Xian et al., 2006). Our preliminary clinical studies with tissue samples from patients with invasive ductal carcinoma suggested that low numbers of vessel-associated pericytes significantly correlated with poor prognosis. Therefore, in this study, we explored the function of pericytes in cancer progression and metastasis.

Tumors in mice generally do not exhibit a significant drop in pericyte coverage until they reach a very large size (unpublished data). Therefore, we used multiple transgenic and pharmacological approaches to target pericytes and achieve their loss in tumors of reasonable size. Our data demonstrated that pericyte loss increased metastasis and was further associated with emergence of tumor hypoxia and increased expression of HIF1α. It is possible that such stromal changes can cooperate with cancer cell-autonomous changes to enhance metastasis. Met expression in cancer cells is detected in many advanced stage tumors including invasive breast cancer (Garcia et al., 2007). We propose that such induction of Met expression is a result of increased tumor hypoxia, among other possible mechanisms. In support of this notion, our results show that tumors without significant levels of hypoxia exhibit negligible expression levels of Met and treatment of these tumors with a Met inhibitor has little impact on their progression.

The reason why a drug such as sunitinib that targets both endothelial cells and pericytes leads to enhanced metastasis raises some questions. We speculate that regardless of their ability to target endothelial cells, drugs that can target pericytes in primary tumors, such as sunitinib and sorafenib (Ebos et al., 2009), may increase metastasis. More studies are required to clarify these observations, but our studies suggest that pericytes may serve as negative regulators of metastasis.

It is important to note that increased metastasis is associated with poor pericyte coverage in the primary tumor. However, if pericyte are targeted to mimic adjuvant therapy in the clinic, an increase in metastasis is not observed. In fact, sunitinib treatment of mice after intravenous introduction of RCC results in decreased metastatic colonization, consistent with the clinical experience of treating RCC patients with sunitinib as an adjuvant therapy to control metastasis (Motzer et al., 2007). Collectively, our data support the notion that sunitinib used in the adjuvant setting possibly helps to control metastasis of certain cancers but it might lead to increased metastasis when used in the neoadjuvant setting.

One of the challenges in studying the effect of pericyte ablation on tumor growth and metastasis is that pericytes are reported to express different markers such as NG2, PDGFRβ, αSMA, desmin, and RGS5 (Bergers and Song, 2005), and their expression may be tissue specific. During vascular morphogenesis, NG2 is exclusively present on pericytes (as determined by their perivascular location) (Ozerdem et al., 2001b), and NG2 and PDGFRβ share greater than 90% colocalization in the tumor microenvironment (Sugimoto et al., 2006). Additionally, NG2 and PDGFRβ have been repeatedly reported as reliable markers for pericytes (Bergers and Song, 2005; Hellström et al., 1999; Ozerdem et al., 2002; Schlingemann et al., 1990; Sennino et al., 2007; Xian et al., 2006). It should be noted that in our study we achieve pericyte ablation using different transgenic mouse models that use *NG2* and *PDGFRβ* promoters. While many studies have demonstrated the utility of NG2 and PDGFRβ to label pericytes in the tumor, it is possible that other cells are also identified by these markers. Therefore, despite using the most useful reagents currently available, one cannot rule out the possibility of nonpericyte cells contributing to the phenotype we observe in this study. Nevertheless, our approach of using multiple distinct strategies offers some confidence that our observations are related to pericyte targeting.

Our studies demonstrated that depletion of pericytes led to diminished primary tumor growth associated with decreased microvessel density (MVD) and hypoxia. Imatinib, which did not lead to reduced MVD, nevertheless, reduced the number of vessel-associated pericytes and also led to increased hypoxia possibly due to altered vascular integrity. The differential effects on MVD in the setting of the transgenic mouse models versus imatinib treatment raises the possibility that imatinib targeting of PDGFRβ is subtly distinct from strategies that eliminate proliferating pericytes. We speculate that imatinib treatment may induce an unknown proangiogenic response to compensate for the loss of pericytes, which may not be present in the transgenic mice. In this regard, we observed more non-vessel-associated $NG2^+$ cells in the imatinib-treated tumors when compared to tumors from NG2-tk+GCV and PDGFRβ-tk+GCV mice (data not shown). Such cells, while not associated with vasculature, may still potentially offer paracrine support to the defective vessels in imatinib-treated tumors, leading to vessel retention.

VEGF is a hypoxia and HIF1α-responsive gene and the pericyte-ablated tumors revealed defective vasculature associated with hypoxia, suggesting that any possible rebound angiogenic effect due to increased VEGF in these hypoxic tumors does not overcome the overall disruption of the tumor vasculature due to pericyte deletion. Interestingly, when VEGF-A is directly targeted using a mouse VEGF-A antibody in the 4T1 setting or

(C) Representative images of TUNEL immunofluorescent labeling and quantification of the percent $TUNEL^+$ area per visual field. Scale bar, 10 μm. High-magnification images are shown in the upper right corner. Scale bar, 50 μm.
(D) Representative photomicrographs of H&E-stained lung sections of control and treated mice. Scale bar, 10 μm. Arrows point to metastatic areas. High-magnification images of metastatic nodules are located in the upper right corner. Scale bar, 50 μm. Percent metastatic area and number of metastatic lung nodules.
(E) Representative images and quantitative analysis of extravascular FITC-dextran. Scale bar, 50 μm.
(F) Representative immunofluorescent images of staining for pimonidazole adducts in tumor sections and quantification. Scale bar, 50 μm.
(G) Representative immunofluorescent images and quantification of HIF1α expression. DAPI = nuclei. Scale bar, 50 μm.
(H) EMT was detected in 4T1 tumors of control and treated mice by immunofluorescent staining for Cytokeratin 8 (red) and αSMA (green). DAPI = nuclei. Arrows point to $CK8^+/\alpha SMA^+$ double-positive cells. Scale bar, 50 μm. Quantification of EMT plotted as percent of $CK8^+/\alpha SMA^+$ double-positive cells per visual field.
(I) Quantitative RT-PCR analysis for *E-cadherin*, *Snail*, *and Twist* mRNA expression from tumor tissues of control and treated mice and plotted as log10 relative expression.
Error bars display SEM; asterisks denote significance (*$p \leq 0.05$). NS, nonsignificant. See also Figure S3.

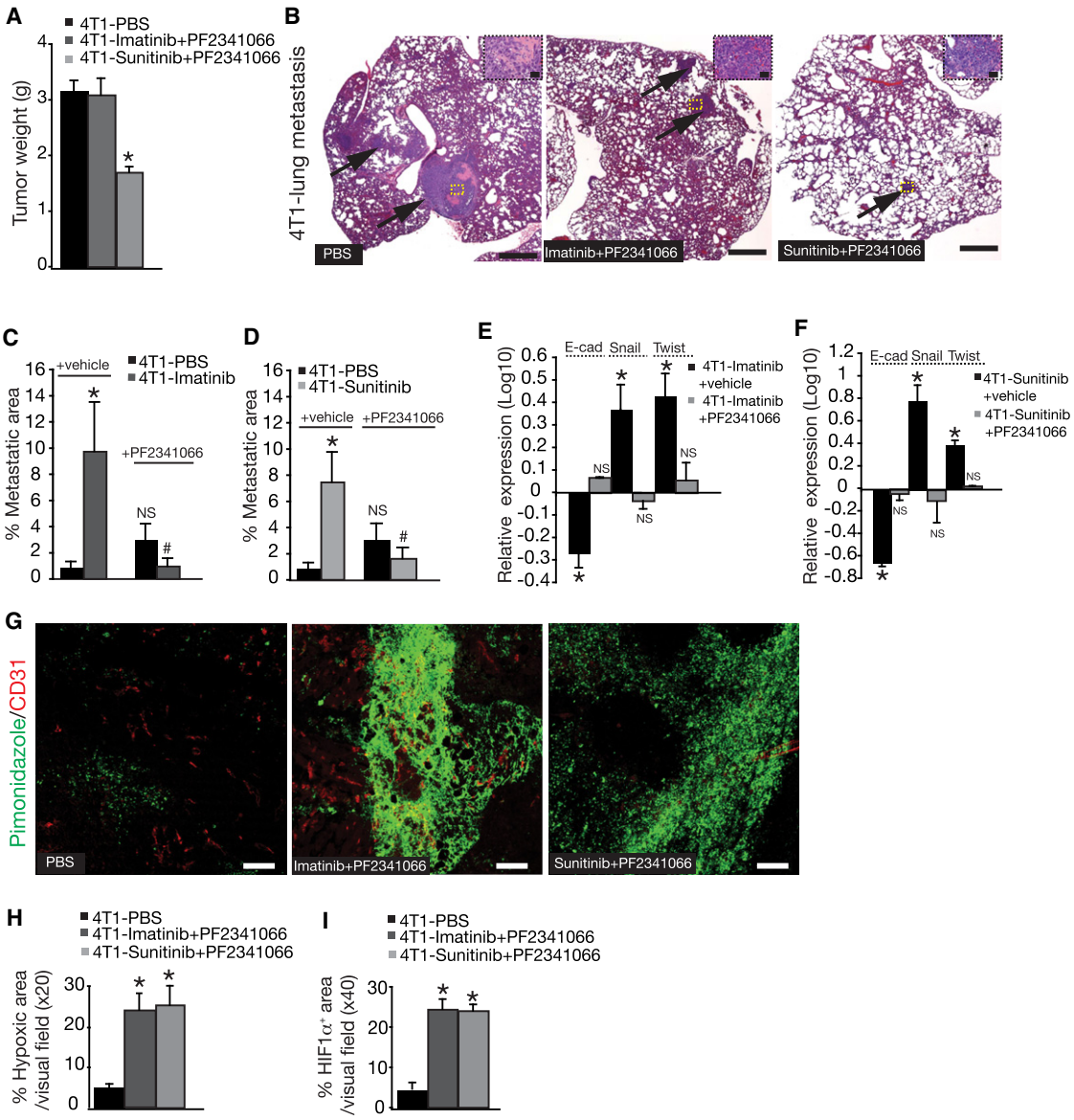

Figure 7. Suppression of Metastasis in Imatinib-Treated and Sunitinib-Treated Mice after Met Inhibition

(A) 4T1 tumor weight after drug treatment.

(B) Representative images of H&E-stained lung sections from tumor-bearing mice treated with PBS, imatinib+PF2341066, or sunitinib+PF2341066. Arrows point to metastatic nodules. Scale bar, 10 μm. High-magnification images of metastatic nodules are located in the upper right corner. Scale bar, 50 μm.

(C and D) Quantification of percent metastatic area in the lungs of these mice. Significance ($p \leq 0.05$) is denoted by * when comparing PBS+vehicle-treated mice versus imatinib/sunitinib+vehicle-treated mice and by # when comparing imatinib/sunitinib+vehicle-treated mice versus imatinib/sunitinib+PF2341066-treated mice.

(E and F) Quantitative RT-PCR for *E-cadherin*, *Twist*, and *Snail* in tumor tissues from imatinib-treated mice with and without PF2341066 treatment.

(G) Hypoxia was detected by immunofluorescent staining of pimonidazole adducts in tumor sections after PF2341066 treatment. Scale bar, 50 μm.

(H) Quantitative analysis of pimonidazole accumulation.

(I) Quantitative analysis of HIF1α expression.

Error bars display SEM; asterisks denote significance (*$p \leq 0.05$). NS, nonsignificant. See also Figure S4.

bevacizumab in the context of human renal cell carcinoma, tumor volume decreases due to the decrease in angiogenesis. Hypoxia, Met expression, and metastasis, however, are not increased in this setting. These results suggest that targeting endothelial cells alone may leave behind vessels that are normalized (appropriately pruned), while targeting pericytes (alone or in combination with endothelial cells) leads to leaky vasculature, increased hypoxia, increased Met, increased EMT, and enhanced metastasis (Carmeliet and Jain, 2011; Tong et al., 2004).

EMT is considered to be the first step in the metastatic cascade of carcinoma cells using the same response to migrate

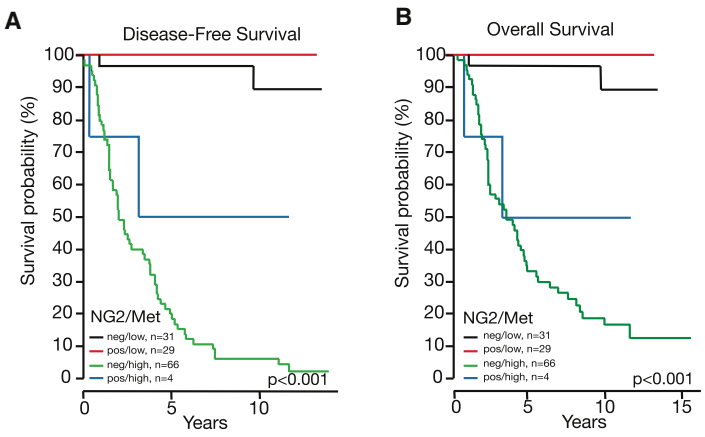

C

Clinical Characteristics

Variable	Number of patients (n=130), median age (range)-59yrs (26-96)				p value
	NG2 neg (n=97)		NG2 pos (n=33)		
	low Met (n=31)	high Met (n=66)	low Met (n=29)	high Met (n=4)	
Tumor size					0.043
<2.0cm	4	1	2	0	
2.0 to <5.0cm	18	37	21	1	
<or= 5.0cm	7	26	5	2	
unknown	2	2	1	1	
Stage					0.019
I	1	0	0	0	
IIA	9	13	14	0	
IIB	1	2	2	0	
IIIA	0	1	0	1	
IIIB	20	50	13	3	
IV	0	0	0	0	
Depth of invasion					0.009
pT1	3	0	2	0	
pT2	7	14	14	0	
pT3	0	1	0	0	
pT4	19	51	13	4	
pTX	2	0	0	0	
Lymph node metastasis					0.205
pN0	16	23	16	2	
pN1	11	25	8	0	
pN2	4	18	5	2	
Distant metastasis					<0.001
Yes	2	63	0	2	
No	29	3	29	2	

Figure 8. Poor Pericyte Coverage and High Met Expression Is Correlated with Decreased Survival of Breast Cancer Patients

(A and B) Disease-free (A) and overall survival (B) of invasive ductal carcinoma (IDC) patients with relation to $CD31^+$ vessel-associated NG2 expression together with Met expression.

(C) Baseline demographics and clinical characteristics associated with $CD31^+$ vessel-associated NG2 expression and Met expression.

away from the primary tumors as normal epithelial cells employ during the development (Acloque et al., 2009; Thiery et al., 2009). EMT is enhanced by hypoxia and has been implicated in tumor invasiveness (Kalluri, 2009; Kalluri and Weinberg, 2009; Thiery et al., 2009; Trimboli et al., 2008; Yang et al., 2008). Hypoxia is a classic stress-induced factor in the tumor microenvironment, and it promotes both cellular quiescence and induction of survival pathways (Xie and Huang, 2003). Hypoxia can tip a tumor to a more invasive phenotype via mechanisms of increased extracellular proteases such as MMP2 (Muñoz-Nájar et al., 2006), invoking induction of Met activation (Eckerich et al., 2007; Pennacchietti et al., 2003) and EMT (Chen et al., 2010; Erler et al., 2006). Our results suggest that pericyte depletion promotes leaky/hyperpermeable vessels, which may lead to increased interstitial plasma exudates, possibly increasing the concentration of plasma proteins (including albumin) in the intratumoral/interstitial region. Such increase in the intratumoral plasma volume may increase the interstitial pressure and alter fluid dynamics, which leads to compression of remaining tumor vessels and decreases the blood flow (Jain, 1987; Stohrer et al., 2000). Collectively, such changes lead to hypoxia and set in motion a series of events that lead to increased metastasis. Hypoxia-induced EMT can be prevented by Met targeting and thus our work suggests that pericyte targeting could be combined with Met inhibitors to achieve a synergistic benefit in controlling primary tumor growth and metastasis. This notion is in agreement with previously published reports where dual inhibitors of HGF and VEGFR (XL880 and XL184) were used (Qian et al., 2009; You et al., 2011). Patients with invasive ductal carcinoma who exhibit poor pericyte coverage coupled with high Met expression revealed a significant drop in disease-free and overall survival. Collectively, our results suggest that an analysis of pericyte coverage on tumor vessels coupled with Met expression can serve as a useful biomarker to inform patient prognosis. More in-depth clinical studies are required to further evaluate such potential clinical utility.

EXPERIMENTAL PROCEDURES

Cell Lines

4T1 BALB/c mammary tumor epithelial cells, B16F10 C57Bl6 melanoma cells, and 786-O human renal cell carcinoma cells were obtained from ATCC and grown in DMEM media supplemented with 10% fetal calf serum (FCS), 100 U/ml penicillin and 100 U/ml streptomycin. 4T1-twist shRNA cells (clones 5 and 7, a gift from Dr. Robert Weinberg, MIT) were cultured in DMEM media supplemented with 5% heat inactivated FCS, 5% heat activated FCS, 100 U/ml penicillin, and 100 U/ml streptomycin.

Animal Experiments and Immunohistochemistry

Generation of transgenic mice, tumor models, drug treatments, immunohistochemistry, and additional experimental procedures are described in Supplemental Experimental Procedures. All animal experiments were reviewed and approved by the Beth Israel Deaconess Medical Center Institutional of Animal Care and Use Committee.

Quantitative PCR Analysis

Expression was determined using the Applied Biosystems 7300 Sequence Detector System and SYBR green as the fluorescence reporter. Measurements were standardized to the housekeeping gene acidic ribosomal phosphoprotein PO (*ARP/36B4*). To assess the number of 4T1-GFP$^+$ cells in the lung, quantitative PCR for *GFP* was performed using genomic DNA as a template. Primer sequences are listed in Supplemental Experimental Procedures.

Clinical Study

Breast cancer patients were recruited for biopsy at the A. C. Carmargo Hospital in Sao Paulo, Brazil after approval by the institutional review board and informed consent. The analysis was performed on 130 biopsies from patients with invasive ductal carcinoma (IDC). The tissue microarrays (TMAs) were constructed from 1.50 mm cores of formalin-fixed paraffin-embedded breast tissue. Immunostaining and scoring of the TMAs for CD31, NG2, HIF1α, and Met are described in Supplemental Experimental Procedures.

Statistical Analysis

For comparison between two groups, a two-tailed unequal variance t test was used. Association between clinical characteristics and NG2 or Met expression levels was verified by a two-tailed Fisher's exact test. For survival analysis, Kaplan-Meier curves were drawn and differences between the curves were calculated by the log-rank test. Independent prognostic significance of HIF1α, Met and NG2 was computed by the Cox proportional hazards. *$p \leq 0.05$ was considered statistically significant. All data analysis was performed using R software version 2.13.0 (http://www.R-project.org).

ACCESSION NUMBERS

The microarray data have been deposited in the Array Express database under the accession number E-MTAB-525.

SUPPLEMENTAL INFORMATION

Supplemental Information includes four figures, four tables, and Supplemental Experimental Procedures and can be found with this article online at doi:10.1016/j.ccr.2011.11.024.

ACKNOWLEDGMENTS

This work was primarily supported by funds from NIH Grants CA125550, CA155370, CA151925, DK81576, CA163191, and DK55001. R.K. is funded by the Champalimaud metastasis programme and is a Champalimaud investigator. V.G.C. is funded by NRSA F32 Ruth Kirschstein Post-doctoral Fellowship from NIH/NIDDK (5F32DK082119-02). V.S.L. is funded from the NIH Research Training Grant in Gastroenterology (2T32DK007760-11), M.B.D. was funded by the NIH Research Training Grant in Cancer Biology (5T32CA081156-08), a NIH supplemental grant (CA125550) to support diversity, and the United Negro College Fund–Merck Postdoctoral Science Research Fellowship, H.S. is funded by the NIH Research Training Grant in Cardiovascular Medicine (5T32HL007374-30), J.T.O. is funded by the DoD Breast Cancer Research Predoctoral Traineeship Award (W81XWH-09-1-0008). We wish to thank J. Christensen of Pfizer, Inc. for providing us PF2341066.

Received: October 1, 2010
Revised: September 5, 2011
Accepted: November 29, 2011
Published: January 17, 2012

REFERENCES

Acloque, H., Adams, M.S., Fishwick, K., Bronner-Fraser, M., and Nieto, M.A. (2009). Epithelial-mesenchymal transitions: the importance of changing cell state in development and disease. J. Clin. Invest. *119*, 1438–1449.

Baba, Y., Nosho, K., Shima, K., Irahara, N., Chan, A.T., Meyerhardt, J.A., Chung, D.C., Giovannucci, E.L., Fuchs, C.S., and Ogino, S. (2010). HIF1A overexpression is associated with poor prognosis in a cohort of 731 colorectal cancers. Am. J. Pathol. *176*, 2292–2301.

Bergers, G., and Song, S. (2005). The role of pericytes in blood-vessel formation and maintenance. Neuro-oncol. *7*, 452–464.

Bergers, G., Song, S., Meyer-Morse, N., Bergsland, E., and Hanahan, D. (2003). Benefits of targeting both pericytes and endothelial cells in the tumor vasculature with kinase inhibitors. J. Clin. Invest. *111*, 1287–1295.

Birchmeier, C., Birchmeier, W., Gherardi, E., and Vande Woude, G.F. (2003). Met, metastasis, motility and more. Nat. Rev. Mol. Cell Biol. *4*, 915–925.

Birner, P., Schindl, M., Obermair, A., Plank, C., Breitenecker, G., and Oberhuber, G. (2000). Overexpression of hypoxia-inducible factor 1alpha is a marker for an unfavorable prognosis in early-stage invasive cervical cancer. Cancer Res. *60*, 4693–4696.

Bos, R., van der Groep, P., Greijer, A.E., Shvarts, A., Meijer, S., Pinedo, H.M., Semenza, G.L., van Diest, P.J., and van der Wall, E. (2003). Levels of hypoxia-inducible factor-1alpha independently predict prognosis in patients with lymph node negative breast carcinoma. Cancer *97*, 1573–1581.

Brizel, D.M., Sibley, G.S., Prosnitz, L.R., Scher, R.L., and Dewhirst, M.W. (1997). Tumor hypoxia adversely affects the prognosis of carcinoma of the head and neck. Int. J. Radiat. Oncol. Biol. Phys. *38*, 285–289.

Carmeliet, P., and Jain, R.K. (2011). Principles and mechanisms of vessel normalization for cancer and other angiogenic diseases. Nat. Rev. Drug Discov. *10*, 417–427.

Chen, J., Imanaka, N., Chen, J., and Griffin, J.D. (2010). Hypoxia potentiates Notch signaling in breast cancer leading to decreased E-cadherin expression and increased cell migration and invasion. Br. J. Cancer *102*, 351–360.

Coussens, L.M., Tinkle, C.L., Hanahan, D., and Werb, Z. (2000). MMP-9 supplied by bone marrow-derived cells contributes to skin carcinogenesis. Cell *103*, 481–490.

Dachs, G.U., and Tozer, G.M. (2000). Hypoxia modulated gene expression: angiogenesis, metastasis and therapeutic exploitation. Eur. J. Cancer *36* (13 Spec No), 1649–1660.

Di Renzo, M.F., Narsimhan, R.P., Olivero, M., Bretti, S., Giordano, S., Medico, E., Gaglia, P., Zara, P., and Comoglio, P.M. (1991). Expression of the Met/HGF receptor in normal and neoplastic human tissues. Oncogene *6*, 1997–2003.

Di Renzo, M.F., Olivero, M., Giacomini, A., Porte, H., Chastre, E., Mirossay, L., Nordlinger, B., Bretti, S., Bottardi, S., Giordano, S., et al. (1995). Overexpression and amplification of the met/HGF receptor gene during the progression of colorectal cancer. Clin. Cancer Res. *1*, 147–154.

Dore-Duffy, P. (2008). Pericytes: pluripotent cells of the blood brain barrier. Curr. Pharm. Des. *14*, 1581–1593.

Dore-Duffy, P., and Cleary, K. (2011). Morphology and properties of pericytes. Methods Mol. Biol. *686*, 49–68.

Eberhard, A., Kahlert, S., Goede, V., Hemmerlein, B., Plate, K.H., and Augustin, H.G. (2000). Heterogeneity of angiogenesis and blood vessel

maturation in human tumors: implications for antiangiogenic tumor therapies. Cancer Res. *60*, 1388–1393.

Ebos, J.M., Lee, C.R., Cruz-Munoz, W., Bjarnason, G.A., Christensen, J.G., and Kerbel, R.S. (2009). Accelerated metastasis after short-term treatment with a potent inhibitor of tumor angiogenesis. Cancer Cell *15*, 232–239.

Eckerich, C., Zapf, S., Fillbrandt, R., Loges, S., Westphal, M., and Lamszus, K. (2007). Hypoxia can induce c-Met expression in glioma cells and enhance SF/HGF-induced cell migration. Int. J. Cancer *121*, 276–283.

Erler, J.T., Bennewith, K.L., Nicolau, M., Dornhöfer, N., Kong, C., Le, Q.T., Chi, J.T., Jeffrey, S.S., and Giaccia, A.J. (2006). Lysyl oxidase is essential for hypoxia-induced metastasis. Nature *440*, 1222–1226.

Folkman, J. (1971). Tumor angiogenesis: therapeutic implications. N. Engl. J. Med. *285*, 1182–1186.

Folkman, J. (1974). Tumor angiogenesis. Adv. Cancer Res. *19*, 331–358.

Folkman, J. (1995). Angiogenesis in cancer, vascular, rheumatoid and other disease. Nat. Med. *1*, 27–31.

Garcia, S., Dalès, J.P., Charafe-Jauffret, E., Carpentier-Meunier, S., Andrac-Meyer, L., Jacquemier, J., Andonian, C., Lavaut, M.N., Allasia, C., Bonnier, P., and Charpin, C. (2007). Poor prognosis in breast carcinomas correlates with increased expression of targetable CD146 and c-Met and with proteomic basal-like phenotype. Hum. Pathol. *38*, 830–841.

Gupta, G.P., and Massagué, J. (2006). Cancer metastasis: building a framework. Cell *127*, 679–695.

Hanahan, D., and Weinberg, R.A. (2000). The hallmarks of cancer. Cell *100*, 57–70.

Hara, S., Nakashiro, K., Klosek, S.K., Ishikawa, T., Shintani, S., and Hamakawa, H. (2006). Hypoxia enhances c-Met/HGF receptor expression and signaling by activating HIF-1alpha in human salivary gland cancer cells. Oral Oncol. *42*, 593–598.

Harris, A.L. (2002). Hypoxia—a key regulatory factor in tumour growth. Nat. Rev. Cancer *2*, 38–47.

Hayashi, M., Sakata, M., Takeda, T., Tahara, M., Yamamoto, T., Okamoto, Y., Minekawa, R., Isobe, A., Ohmichi, M., Tasaka, K., and Murata, Y. (2005). Up-regulation of c-met protooncogene product expression through hypoxia-inducible factor-1alpha is involved in trophoblast invasion under low-oxygen tension. Endocrinology *146*, 4682–4689.

Hellström, M., Kalén, M., Lindahl, P., Abramsson, A., and Betsholtz, C. (1999). Role of PDGF-B and PDGFR-beta in recruitment of vascular smooth muscle cells and pericytes during embryonic blood vessel formation in the mouse. Development *126*, 3047–3055.

Huang, F.J., You, W.K., Bonaldo, P., Seyfried, T.N., Pasquale, E.B., and Stallcup, W.B. (2010). Pericyte deficiencies lead to aberrant tumor vascularizaton in the brain of the NG2 null mouse. Dev. Biol. *344*, 1035–1046.

Jain, R.K. (1987). Transport of molecules in the tumor interstitium: a review. Cancer Res. *47*, 3039–3051.

Jain, R.K. (2003). Molecular regulation of vessel maturation. Nat. Med. *9*, 685–693.

Joyce, J.A. (2005). Therapeutic targeting of the tumor microenvironment. Cancer Cell *7*, 513–520.

Kalluri, R. (2009). EMT: when epithelial cells decide to become mesenchymal-like cells. J. Clin. Invest. *119*, 1417–1419.

Kalluri, R., and Weinberg, R.A. (2009). The basics of epithelial-mesenchymal transition. J. Clin. Invest. *119*, 1420–1428.

Kenworthy, P., Dowrick, P., Baillie-Johnson, H., McCann, B., Tsubouchi, H., Arakaki, N., Daikuhara, Y., and Warn, R.M. (1992). The presence of scatter factor in patients with metastatic spread to the pleura. Br. J. Cancer *66*, 243–247.

Kim, J.A., Tran, N.D., Li, Z., Yang, F., Zhou, W., and Fisher, M.J. (2006). Brain endothelial hemostasis regulation by pericytes. J. Cereb. Blood Flow Metab. *26*, 209–217.

Koukourakis, M.I., Giatromanolaki, A., Sivridis, E., Simopoulos, C., Turley, H., Talks, K., Gatter, K.C., and Harris, A.L. (2002). Hypoxia-inducible factor (HIF1A and HIF2A), angiogenesis, and chemoradiotherapy outcome of squamous cell head-and-neck cancer. Int. J. Radiat. Oncol. Biol. Phys. *53*, 1192–1202.

Liebner, S., Fischmann, A., Rascher, G., Duffner, F., Grote, E.H., Kalbacher, H., and Wolburg, H. (2000). Claudin-1 and claudin-5 expression and tight junction morphology are altered in blood vessels of human glioblastoma multiforme. Acta Neuropathol. *100*, 323–331.

Lu, C., Kamat, A.A., Lin, Y.G., Merritt, W.M., Landen, C.N., Kim, T.J., Spannuth, W., Arumugam, T., Han, L.Y., Jennings, N.B., et al. (2007). Dual targeting of endothelial cells and pericytes in antivascular therapy for ovarian carcinoma. Clin. Cancer Res. *13*, 4209–4217.

Lu, C., Shahzad, M.M., Moreno-Smith, M., Lin, Y.G., Jennings, N.B., Allen, J.K., Landen, C.N., Mangala, L.S., Armaiz-Pena, G.N., Schmandt, R., et al. (2010). Targeting pericytes with a PDGF-B aptamer in human ovarian carcinoma models. Cancer Biol. Ther. *9*, 176–182.

Mendel, D.B., Laird, A.D., Xin, X., Louie, S.G., Christensen, J.G., Li, G., Schreck, R.E., Abrams, T.J., Ngai, T.J., Lee, L.B., et al. (2003). In vivo antitumor activity of SU11248, a novel tyrosine kinase inhibitor targeting vascular endothelial growth factor and platelet-derived growth factor receptors: determination of a pharmacokinetic/pharmacodynamic relationship. Clin. Cancer Res. *9*, 327–337.

Motzer, R.J., Hutson, T.E., Tomczak, P., Michaelson, M.D., Bukowski, R.M., Rixe, O., Oudard, S., Negrier, S., Szczylik, C., Kim, S.T., et al. (2007). Sunitinib versus interferon alfa in metastatic renal-cell carcinoma. N. Engl. J. Med. *356*, 115–124.

Muñoz-Nájar, U.M., Neurath, K.M., Vumbaca, F., and Claffey, K.P. (2006). Hypoxia stimulates breast carcinoma cell invasion through MT1-MMP and MMP-2 activation. Oncogene *25*, 2379–2392.

Natali, P.G., Nicotra, M.R., Di Renzo, M.F., Prat, M., Bigotti, A., Cavaliere, R., and Comoglio, P.M. (1993). Expression of the c-Met/HGF receptor in human melanocytic neoplasms: demonstration of the relationship to malignant melanoma tumour progression. Br. J. Cancer *68*, 746–750.

Newman, P.J. (1994). The role of PECAM-1 in vascular cell biology. Ann. N Y Acad. Sci. *714*, 165–174.

O'Keeffe, M.B., Devlin, A.H., Burns, A.J., Gardiner, T.A., Logan, I.D., Hirst, D.G., and McKeown, S.R. (2008). Investigation of pericytes, hypoxia, and vascularity in bladder tumors: association with clinical outcomes. Oncol. Res. *17*, 93–101.

Ozerdem, U. (2006a). Targeting of pericytes diminishes neovascularization and lymphangiogenesis in prostate cancer. Prostate *66*, 294–304.

Ozerdem, U. (2006b). Targeting pericytes diminishes neovascularization in orthotopic uveal melanoma in nerve/glial antigen 2 proteoglycan knockout mouse. Ophthalmic Res. *38*, 251–254.

Ozerdem, U., Freeman, W.R., Bartsch, D.U., and Clark, T.M. (2001a). A simple noncontact wide-angle fundus photography procedure for clinical and research use. Retina *21*, 189–190.

Ozerdem, U., Grako, K.A., Dahlin-Huppe, K., Monosov, E., and Stallcup, W.B. (2001b). NG2 proteoglycan is expressed exclusively by mural cells during vascular morphogenesis. Dev. Dyn. *222*, 218–227.

Ozerdem, U., Monosov, E., and Stallcup, W.B. (2002). NG2 proteoglycan expression by pericytes in pathological microvasculature. Microvasc. Res. *63*, 129–134.

Pàez-Ribes, M., Allen, E., Hudock, J., Takeda, T., Okuyama, H., Viñals, F., Inoue, M., Bergers, G., Hanahan, D., and Casanovas, O. (2009). Antiangiogenic therapy elicits malignant progression of tumors to increased local invasion and distant metastasis. Cancer Cell *15*, 220–231.

Pennacchietti, S., Michieli, P., Galluzzo, M., Mazzone, M., Giordano, S., and Comoglio, P.M. (2003). Hypoxia promotes invasive growth by transcriptional activation of the met protooncogene. Cancer Cell *3*, 347–361.

Pietras, K., and Hanahan, D. (2005). A multitargeted, metronomic, and maximum-tolerated dose "chemo-switch" regimen is antiangiogenic, producing objective responses and survival benefit in a mouse model of cancer. J. Clin. Oncol. *23*, 939–952.

Pouysségur, J., Dayan, F., and Mazure, N.M. (2006). Hypoxia signalling in cancer and approaches to enforce tumour regression. Nature *441*, 437–443.

Qian, F., Engst, S., Yamaguchi, K., Yu, P., Won, K.A., Mock, L., Lou, T., Tan, J., Li, C., Tam, D., et al. (2009). Inhibition of tumor cell growth, invasion, and metastasis by EXEL-2880 (XL880, GSK1363089), a novel inhibitor of HGF and VEGF receptor tyrosine kinases. Cancer Res. *69*, 8009–8016.

Raza, A., Franklin, M.J., and Dudek, A.Z. (2010). Pericytes and vessel maturation during tumor angiogenesis and metastasis. Am. J. Hematol. *85*, 593–598.

Rofstad, E.K. (2000). Microenvironment-induced cancer metastasis. Int. J. Radiat. Biol. *76*, 589–605.

Schlingemann, R.O., Rietveld, F.J., de Waal, R.M., Ferrone, S., and Ruiter, D.J. (1990). Expression of the high molecular weight melanoma-associated antigen by pericytes during angiogenesis in tumors and in healing wounds. Am. J. Pathol. *136*, 1393–1405.

Semenza, G.L. (2003). Angiogenesis in ischemic and neoplastic disorders. Annu. Rev. Med. *54*, 17–28.

Sennino, B., Falcón, B.L., McCauley, D., Le, T., McCauley, T., Kurz, J.C., Haskell, A., Epstein, D.M., and McDonald, D.M. (2007). Sequential loss of tumor vessel pericytes and endothelial cells after inhibition of platelet-derived growth factor B by selective aptamer AX102. Cancer Res. *67*, 7358–7367.

Stefansson, I.M., Salvesen, H.B., and Akslen, L.A. (2006). Vascular proliferation is important for clinical progress of endometrial cancer. Cancer Res. *66*, 3303–3309.

Stohrer, M., Boucher, Y., Stangassinger, M., and Jain, R.K. (2000). Oncotic pressure in solid tumors is elevated. Cancer Res. *60*, 4251–4255.

Sugimoto, H., Mundel, T.M., Kieran, M.W., and Kalluri, R. (2006). Identification of fibroblast heterogeneity in the tumor microenvironment. Cancer Biol. Ther. *5*, 1640–1646.

Sun, S., Ning, X., Zhang, Y., Lu, Y., Nie, Y., Han, S., Liu, L., Du, R., Xia, L., He, L., and Fan, D. (2009). Hypoxia-inducible factor-1alpha induces Twist expression in tubular epithelial cells subjected to hypoxia, leading to epithelial-to-mesenchymal transition. Kidney Int. *75*, 1278–1287.

Thiery, J.P. (2009). [Epithelial-mesenchymal transitions in cancer onset and progression]. Bull. Acad. Natl. Med. *193*, 1969–1978, discussion, 1978–1969.

Thiery, J.P., Acloque, H., Huang, R.Y., and Nieto, M.A. (2009). Epithelial-mesenchymal transitions in development and disease. Cell *139*, 871–890.

Tong, R.T., Boucher, Y., Kozin, S.V., Winkler, F., Hicklin, D.J., and Jain, R.K. (2004). Vascular normalization by vascular endothelial growth factor receptor 2 blockade induces a pressure gradient across the vasculature and improves drug penetration in tumors. Cancer Res. *64*, 3731–3736.

Trimboli, A.J., Fukino, K., de Bruin, A., Wei, G., Shen, L., Tanner, S.M., Creasap, N., Rosol, T.J., Robinson, M.L., Eng, C., et al. (2008). Direct evidence for epithelial-mesenchymal transitions in breast cancer. Cancer Res. *68*, 937–945.

Vleugel, M.M., Greijer, A.E., Shvarts, A., van der Groep, P., van Berkel, M., Aarbodem, Y., van Tinteren, H., Harris, A.L., van Diest, P.J., and van der Wall, E. (2005). Differential prognostic impact of hypoxia induced and diffuse HIF-1alpha expression in invasive breast cancer. J. Clin. Pathol. *58*, 172–177.

Xian, X., Håkansson, J., Ståhlberg, A., Lindblom, P., Betsholtz, C., Gerhardt, H., and Semb, H. (2006). Pericytes limit tumor cell metastasis. J. Clin. Invest. *116*, 642–651.

Xie, K., and Huang, S. (2003). Regulation of cancer metastasis by stress pathways. Clin. Exp. Metastasis *20*, 31–43.

Xie, L., Duncan, M.B., Pahler, J., Sugimoto, H., Martino, M., Lively, J., Mundel, T., Soubasakos, M., Rubin, K., Takeda, T., et al. (2011). Counterbalancing angiogenic regulatory factors control the rate of cancer progression and survival in a stage-specific manner. Proc. Natl. Acad. Sci. USA *108*, 9939–9944.

Yang, J., Mani, S.A., Donaher, J.L., Ramaswamy, S., Itzykson, R.A., Come, C., Savagner, P., Gitelman, I., Richardson, A., and Weinberg, R.A. (2004). Twist, a master regulator of morphogenesis, plays an essential role in tumor metastasis. Cell *117*, 927–939.

Yang, M.H., Wu, M.Z., Chiou, S.H., Chen, P.M., Chang, S.Y., Liu, C.J., Teng, S.C., and Wu, K.J. (2008). Direct regulation of TWIST by HIF-1alpha promotes metastasis. Nat. Cell Biol. *10*, 295–305.

Yonenaga, Y., Mori, A., Onodera, H., Yasuda, S., Oe, H., Fujimoto, A., Tachibana, T., and Imamura, M. (2005). Absence of smooth muscle actin-positive pericyte coverage of tumor vessels correlates with hematogenous metastasis and prognosis of colorectal cancer patients. Oncology *69*, 159–166.

You, W.K., Sennino, B., Williamson, C.W., Falcón, B., Hashizume, H., Yao, L.C., Aftab, D.T., and McDonald, D.M. (2011). VEGF and c-Met blockade amplify angiogenesis inhibition in pancreatic islet cancer. Cancer Res. *71*, 4758–4768.

Zou, H.Y., Li, Q., Lee, J.H., Arango, M.E., McDonnell, S.R., Yamazaki, S., Koudriakova, T.B., Alton, G., Cui, J.J., Kung, P.P., et al. (2007). An orally available small-molecule inhibitor of c-Met, PF-2341066, exhibits cytoreductive antitumor efficacy through antiproliferative and antiangiogenic mechanisms. Cancer Res. *67*, 4408–4417.

Cancer Cell
Article

Rapid Decrease in Delivery of Chemotherapy to Tumors after Anti-VEGF Therapy: Implications for Scheduling of Anti-Angiogenic Drugs

Astrid A.M. Van der Veldt,[1,*] Mark Lubberink,[1,6] Idris Bahce,[2] Maudy Walraven,[3] Michiel P. de Boer,[4] Henri N.J.M. Greuter,[1] N. Harry Hendrikse,[1,5] Jonas Eriksson,[1] Albert D. Windhorst,[1] Pieter E. Postmus,[2] Henk M. Verheul,[3] Erik H. Serné,[4] Adriaan A. Lammertsma,[1] and Egbert F. Smit[2]
[1]Department of Nuclear Medicine and PET Research
[2]Department of Pulmonology
[3]Department of Medical Oncology
[4]Department of Internal Medicine
[5]Department of Clinical Pharmacology and Pharmacy
VU University Medical Center, 1007 MB Amsterdam, The Netherlands
[6]PET Centre, Uppsala University Hospital, 751 85 Uppsala, Sweden
*Correspondence: aam.vanderveldt@vumc.nl
DOI 10.1016/j.ccr.2011.11.023

SUMMARY

Current strategies combining anti-angiogenic drugs with chemotherapy provide clinical benefit in cancer patients. It is assumed that anti-angiogenic drugs, such as bevacizumab, transiently normalize abnormal tumor vasculature and contribute to improved delivery of subsequent chemotherapy. To investigate this concept, a study was performed in non-small cell lung cancer (NSCLC) patients using positron emission tomography (PET) and radiolabeled docetaxel ([^{11}C]docetaxel). In NSCLC, bevacizumab reduced both perfusion and net influx rate of [^{11}C]docetaxel within 5 hr. These effects persisted after 4 days. The clinical relevance of these findings is notable, as there was no evidence for a substantial improvement in drug delivery to tumors. These findings highlight the importance of drug scheduling and advocate further studies to optimize scheduling of anti-angiogenic drugs.

INTRODUCTION

Angiogenesis is a critical component for growth and metastatic spread of tumors (Hanahan and Weinberg, 2000; Carmeliet, 2000). Vascular endothelial growth factor (VEGF), which is overexpressed in many human malignancies, is a key regulator of tumor angiogenesis, inducing proliferation, differentiation, and migration of endothelial cells (Ferrara et al., 2003). Consequently, numerous drugs have been developed to target the signaling pathways of VEGF and its receptors (VEGFR; Ferrara and Kerbel, 2005).

Bevacizumab is a humanized monoclonal antibody that targets circulating VEGF and subsequently prevents binding of VEGF to its receptors (Ferrara et al., 2004). Except for metastatic renal cell cancer (Yang et al., 2003), clinical efficacy of single-agent bevacizumab treatment has been very limited in the majority of advanced malignancies (Reese et al., 2001; Cobleigh et al., 2003). Combined with chemotherapy, however, additional value was shown in colorectal (Hurwitz et al., 2004), breast (Miller et al., 2007), and non-small cell lung cancer (NSCLC; Sandler et al., 2006).

In the past years, the normalization theory proposed by Jain (2001) has gained widespread acceptance for explaining additional antitumor effects of inhibitors of VEGF signaling, when combined with cytotoxic drugs. It is hypothesized that anti-angiogenic drugs normalize structurally and functionally abnormal tumor vasculature, thereby reducing interstitial fluid pressure, improving drug penetration, and subsequently

Significance

Optimal scheduling of anti-angiogenic drugs is important for improving efficacy of combination therapy in patients with advanced-stage cancer. In this study, effects of the anti-angiogenic drug bevacizumab on delivery of chemotherapy to non-small cell lung cancer (NSCLC) were investigated using positron emission tomography and ^{11}C-labeled docetaxel. Bevacizumab induced a rapid and significant reduction in delivery of chemotherapy to tumors in NSCLC patients. The study provides a framework for investigating effects of anti-angiogenic drugs on drug delivery to tumors in vivo. In addition, it highlights the importance of drug scheduling and advocates further studies to optimize scheduling of anti-angiogenic drugs.

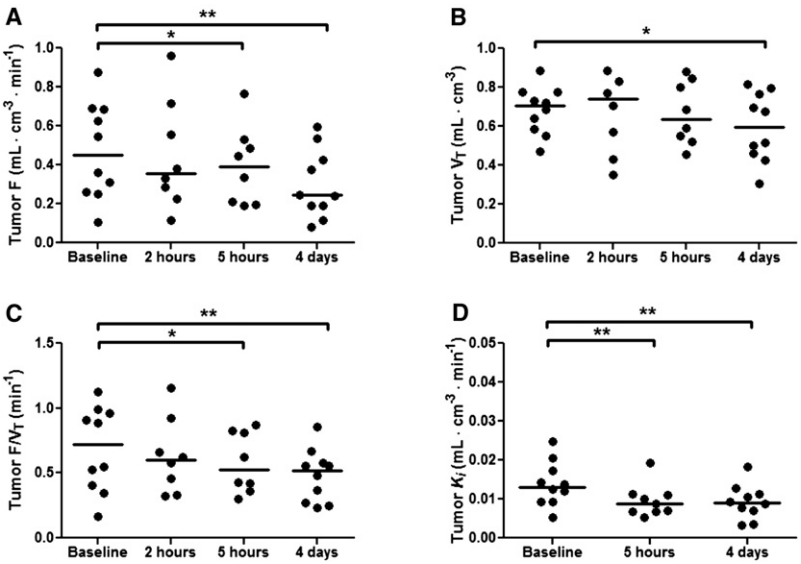

Figure 1. Tumor Measurements in 10 NSCLC Patients at Baseline and after Administration of Bevacizumab

Horizontal bars represent median values.
(A) Perfusion (F).
(B) Volume of distribution of water (V_T).
(C) F/V_T.
(D) Net rate of influx (K_i) of [^{11}C]docetaxel.
*p value < 0.05; **p value < 0.01.

enhancing efficacy of cytotoxic drugs. Exploration of the normalization window may be crucial for optimizing drug scheduling in order to improve clinical efficacy. To date, however, no clinical studies have been reported on the effects of anti-angiogenic agents on drug delivery in cancer patients.

Positron emission tomography (PET) is a noninvasive imaging technique that can be used to monitor drug pharmacokinetics and pharmacodynamics in vivo by radiolabeling drugs of interest with short-lived positron emitting radionuclides (Gambhir, 2002). Previously, the cytotoxic drug docetaxel, a taxane targeting the microtubular network, has been radiolabeled with the radionuclide C-11 ([^{11}C]docetaxel; van Tilburg et al., 2004), enabling in vivo quantification of docetaxel kinetics in lung cancer (Van der Veldt et al., 2011). In the latter study, feasibility of noninvasive PET measurements using radiolabeled water ([^{15}O]H_2O) and [^{11}C]docetaxel was demonstrated and uptake of [^{11}C]docetaxel in lung tumors was found to be associated with tumor perfusion, measured using [^{15}O]H_2O.

The purpose of the present study was to investigate the effects of anti-angiogenic drugs on tumor perfusion and [^{11}C]docetaxel delivery in patients with advanced-stage NSCLC using PET. To this end, bevacizumab was selected, as it is the most selective inhibitor of VEGF signaling among currently approved anti-angiogenic drugs. It was hypothesized that bevacizumab improves drug delivery by normalizing tumor vasculature, which should be reflected by a more homogeneous distribution of perfusion and [^{11}C]docetaxel delivery. A secondary objective of this study was to investigate (systemic) effects of bevacizumab on (1) circulating VEGF levels in plasma; (2) cardiovascular parameters, including blood pressure, cardiac output, and microcirculation in muscle and skin; (3) systemic exposure of [^{11}C]docetaxel; and (4) perfusion and [^{11}C]docetaxel uptake in normal tissues. For the latter, the thyroid gland and the vertebral body were selected. The thyroid gland is known to be highly sensitive to VEGF inhibition (Kamba et al., 2006), whereas the vertebral body may reflect effects of bevacizumab on [^{11}C]docetaxel uptake in bone marrow.

RESULTS

Bevacizumab Induces Rapid Reduction in Tumor Perfusion

To investigate the effect of anti-VEGF therapy on tumor perfusion (F), PET scans using [^{15}O]H_2O, which is a freely diffusible tracer (Hoekstra et al., 2002; Wilson et al., 1992), were performed at baseline and 2 hr, 5 hr, and 4 days after bevacizumab administration. Five hours after bevacizumab administration, there was a significant reduction in tumor perfusion, which persisted until day 4 (Figures 1A and 2A). In three out of eight patients, tumor perfusion already decreased 2 hr after the end of bevacizumab infusion. Accordingly, tumor perfusion showed median percentage changes of 8% (range −39 to +15%; N = 9; p value = 0.889), −20% (range, −39 to −7%; N = 8; p value = 0.012), and −38% (range, −55 to −4%; N = 10; p value = 0.005) at 2 hr, 5 hr, and 4 days after bevacizumab administration, respectively. In addition, the volume of distribution of water (V_T), a measure of the (viable) fraction of tissue that is able to exchange [^{15}O]H_2O, was decreased at 4 days after bevacizumab administration (Figure 1B), with a median percentage change of −7% (range, −52 to +2%; N = 10; p value = 0.022). Individually, eight out of ten patients showed a reduction in volume of distribution of water. Although both perfusion and volume of distribution of water showed an overall decrease, the reduction in perfusion was more severe, as illustrated by a significant decrease in the ratio of tumor perfusion over volume of distribution (F/V_T; (Figure 1C). Collectively, these findings indicate that the decrease in tumor perfusion is not due to a reduction in tumor tissue, which was confirmed by an unchanged tumor volume on subsequent computed tomography (CT) scans.

Bevacizumab Decreases the Net Influx Rate of [^{11}C]docetaxel in Tumors

To determine whether delivery of chemotherapy is affected by bevacizumab, PET scans using [^{11}C]docetaxel were performed at baseline and 5 hr and 4 days after bevacizumab administration. Kinetics of [^{11}C]docetaxel in tumor tissue are irreversible and can be quantified using Patlak graphical analysis, providing the net influx rate constant (K_i) of [^{11}C]docetaxel in tumor tissue (Patlak et al., 1983; Van der Veldt et al., 2011). Prior to bevacizumab infusion, tumors showed a variable K_i of [^{11}C]docetaxel (median K_i, 0.0132 $ml \cdot cm^{-3} \cdot min^{-1}$; range, 0.0054–0.0247 $ml \cdot cm^{-3} \cdot min^{-1}$; N = 10). After administration of bevacizumab, median K_i of [^{11}C]docetaxel significantly decreased (Figures 1D and 2B), resulting in a median percentage

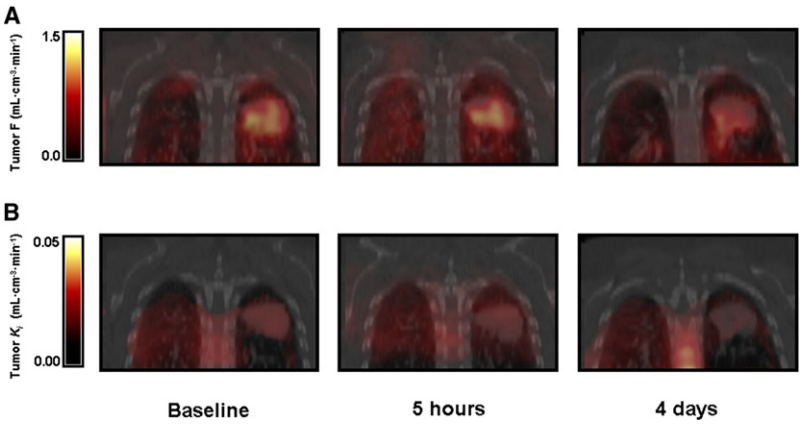

Figure 2. PET-CT Images of a 51-Year-Old Woman with Metastatic Non-Small Cell Lung Cancer

(A) Parametric perfusion images obtained at baseline and at 5 hr and 4 days after bevacizumab administration. In the whole tumor, the mean perfusion changed from 0.875 $ml \cdot cm^{-3} \cdot min^{-1}$ at baseline to 0.765 $ml \cdot cm^{-3} \cdot min^{-1}$ at 5 hr and 0.535 $ml \cdot cm^{-3} \cdot min^{-1}$ at 4 days.

(B) Patlak images of [^{11}C]docetaxel uptake obtained at baseline and at 5 hr and 4 days after bevacizumab administration. In the whole tumor, the mean K_i of [^{11}C]docetaxel changed from 0.0205 $ml \cdot cm^{-3} \cdot min^{-1}$ at baseline to 0.0193 $ml \cdot cm^{-3} \cdot min^{-1}$ at 5 hr and 0.0127 $ml \cdot cm^{-3} \cdot min^{-1}$ at 4 days.

F, perfusion; K_i, net influx rate constant.

change of −22% (range, −51 to −4%; N = 9; p value = 0.008) and −34% (range, −61 to −16%; N = 10; p value = 0.005) at 5 hr and 4 days, respectively. In line with the decrease in the volume of distribution of water, the distribution volume of [^{11}C]docetaxel, which can be obtained from the Patlak plot, also showed a decline on day 4 with a median percentage change of −14% (range, −24 to + 20%; N = 10; p value = 0.052). Before administration of bevacizumab, [^{11}C]docetaxel K_i was associated with tumor perfusion (Spearman's ρ = 0.626; N = 10; p value = 0.053). As two patients had one missing scan (either [^{11}C]docetaxel PET or [^{15}O]H_2O PET), this correlation could not be evaluated at 5 hr. At 4 days, the correlation between [^{11}C]docetaxel K_i and perfusion showed a slight decrease (Spearman's ρ 0.564; N = 10; p value = 0.090).

Tumor Heterogeneity of [^{11}C]docetaxel Uptake Is Not Affected by Bevacizumab

As it is assumed that normalization of tumor vasculature results in a more homogenous distribution of perfusion and drug delivery, spatial distributions of tumor perfusion, volume of distribution of water, and [^{11}C]docetaxel K_i were analyzed on a voxel-by-voxel basis using histogram analysis. For the K_i of [^{11}C]docetaxel, only the median kurtosis of the histograms showed a trend toward an increase from 2.60 at baseline to 3.11 (N = 9; p value = 0.051) and 2.97 (N = 10; p value = 0.059) at 5 hr and 4 days, respectively, whereas standard deviation and kurtosis of the other histograms (F and V_T) did not change. When histogram analysis was applied to separately analyze tumor center and rim, larger tumors showed lower perfusion and lower values of [^{11}C]docetaxel K_i in the center than in the rim. When all primary tumors were analyzed, median baseline values, however, were not significantly different (N = 10; p value = 0.739 and 0.579, respectively). At 5 hr and 4 days after bevacizumab administration, mean, median, minimum, and maximum values of tumor perfusion and [^{11}C]docetaxel K_i showed the same degree of reduction (p value < 0.05) in the whole tumor, as in the center and the rim separately. In addition, the volume of distribution of water showed a significant decrease in both center and rim at 4 days (N = 10; p value < 0.05). Standard deviation and kurtosis of all histograms (F, V_T, and [^{11}C]docetaxel K_i) did not change in the center and the rim, except for a decreased standard deviation of perfusion in the center at 5 hr (N = 8; p value = 0.028). Furthermore, changes in perfusion, volume of distribution of water, and [^{11}C]docetaxel K_i were not associated with baseline tumor volumes. Collectively, these results indicate that bevacizumab induces an overall decrease in perfusion, volume of distribution of water, and [^{11}C]docetaxel K_i in tumors without significantly affecting tumor heterogeneity.

Decrease in [^{11}C]docetaxel Delivery to Tumors Is Accompanied by Rapid Reduction in Circulating VEGF

Plasma levels of circulating VEGF were measured to evaluate whether the rapid decrease in [^{11}C]docetaxel K_i in tumors was supported by a rapid decrease in free VEGF. As VEGF is mainly transported by platelets (Verheul et al., 1997), circulating VEGF was assessed in both platelet-poor and platelet-rich plasma. At 3 hr, administration of bevacizumab resulted in a significant decrease in circulating VEGF in platelet-rich plasma (N = 7; p value = 0.018; Figure 3). In the majority of patients, free VEGF in plasma was completely neutralized within 3 hr and seemed to recover in part after 4 days. Comparable changes in VEGF levels were measured in platelet-poor plasma.

A Reduction in [^{11}C]docetaxel Delivery to Tumors Is Not Associated with Cardiovascular Parameters

Because arterial hypertension and cardiotoxicity are commonly reported side effects associated with inhibitors of VEGF/VEGFR-2 signaling (Chen and Cleck, 2009), it was investigated whether the rapid decrease in tumor perfusion and [^{11}C]docetaxel K_i was accompanied by early onset cardiovascular changes. A single infusion of bevacizumab did not affect systolic and diastolic blood pressure during the first 4 days (Figures 4A and 4B). Median cardiac output as derived from first pass dynamic [^{15}O]H_2O PET scans (Knaapen et al., 2008), however, showed a trend toward a reduction at day 4 (from 6.9 $l \cdot min^{-1}$ to 6.0 $l \cdot min^{-1}$; N = 9; p value = 0.051; Figure 4C). As inhibitors of VEGF/VEGFR-2 signaling may induce so-called rarefaction (Mourad et al., 2008), that is, a reduction in the number of arterioles or capillaries within vascular beds of various tissues (e.g., muscle and skin), muscle perfusion in the erector spinae, as well as capillary density in the skin, were measured. Muscle perfusion was obtained from the [^{15}O]H_2O images, whereas nailfold capillaries in the dorsal skin of the third finger were examined using a capillary microscope (Serné et al., 2001). Perfusion in the erector spinae muscle and capillary density in the skin did not change during the first 4 days after administration of

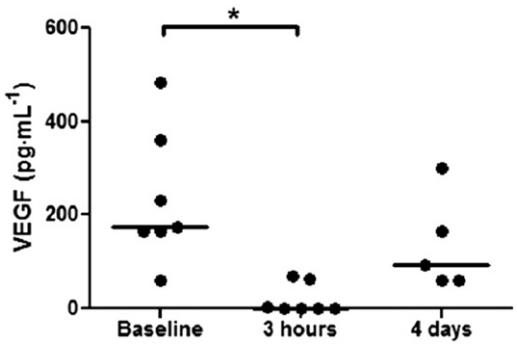

Figure 3. Platelet-rich Plasma Levels of VEGF in Seven Individual Patients at Baseline and after Administration of Bevacizumab

Vascular endothelial growth factor levels were corrected for platelet count and are expressed in pg·ml^{-1} per 200,000 platelets·μl^{-1}. Horizontal bars represent median values.

*p value < 0.05.

bevacizumab (Figures 4D, 4E, and 4F). Of note, [^{11}C]docetaxel K_i in muscle tissue (median K_i, 0.0072 ml·cm^{-3}·min^{-1}; range, 0.0029–0.0104 ml·cm^{-3}·min^{-1}) was lower than that in tumor tissue (N = 10; p value = 0.002). The K_i of [^{11}C]docetaxel in muscle tissue was neither associated with perfusion nor affected by bevacizumab.

Bevacizumab Increases Systemic Exposure of [^{11}C]docetaxel

To investigate whether decreased [^{11}C]docetaxel K_i in tumor tissue was associated with a change in systemic exposure of [^{11}C]docetaxel, plasma clearance of [^{11}C]docetaxel was determined. Four days after bevacizumab administration, plasma clearance of [^{11}C]docetaxel was significantly decreased (N = 10; p value = 0.037), as reflected by a shift to the right of the plasma curves (Figure 5). Consequently, bevacizumab increased the duration of [^{11}C]docetaxel exposure by a reduction in plasma clearance. However, this increased systemic exposure of [^{11}C]docetaxel did not result in increased [^{11}C]docetaxel accumulation in tumor tissue, as the retention index of [^{11}C]docetaxel still decreased after bevacizumab administration (from 0.0155 ml·cm^{-3}·min^{-1} at baseline to 0.0109 ml·cm^{-3}·min^{-1} at day 4; N = 10; p value = 0.005).

Bevacizumab Decreases Thyroid Perfusion

Because normal vessels of the thyroid gland are known for their extensive capillary regression after anti-VEGF therapy (Kamba et al., 2006), thyroid perfusion was also determined using parametric perfusion images. In four out of ten patients, the primary tumor was located in the upper lobes, enabling adequate analysis of thyroid perfusion at baseline and day 4. Four days after bevacizumab administration, median perfusion in the thyroid gland showed a decrease (from 1.316 ml·cm^{-3}·min^{-1} at baseline to 0.585 ml·cm^{-3}·min^{-1} at day 4; p value = 0.068), whereas the volume of distribution of water did not change (p value = 0.273).

[^{11}C]docetaxel Uptake in Bone Marrow Is Not Affected by Bevacizumab

As [^{11}C]docetaxel shows high uptake in bone marrow (Van der Veldt et al., 2010b) and anti-VEGF therapy can block rapid induction of viable circulating endothelial progenitor cells from bone marrow and can inhibit taxane-induced bone marrow colonization in tumors (Shaked et al., 2008), the effects of bevacizumab on [^{11}C]docetaxel uptake in bone marrow was also evaluated. To this end, perfusion and [^{11}C]docetaxel K_i were determined in the vertebral body. Perfusion values were significantly lower in the vertebral body than in tumors (N = 10; p value= 0.003), whereas K_i values of [^{11}C]docetaxel were significantly higher than those in tumors (N = 10; p value < 0.001; Figure 6). In contrast to tumor tissue, there was no association between [^{11}C]docetaxel K_i and perfusion in the vertebral body (Spearman's $\rho = -0.285$; N = 10; p value = 0.425). Perfusion and [^{11}C]docetaxel K_i did not change after bevacizumab administration (Figure 6).

DISCUSSION

Current strategies combining anti-angiogenic therapy with cytotoxic agents have shown proven efficacy in cancer patients, including those with advanced-stage NSCLC (Sandler et al., 2006). Pretreatment with anti-angiogenic drugs may transiently normalize abnormal tumor vasculature (Batchelor et al., 2007) and thereby contribute to improved delivery of subsequent chemotherapy, enhancing efficacy (Jain, 2005). Investigating this process of vasculature normalization in vivo is a major challenge, which is mainly restricted to imaging studies. Whereas conventional imaging studies, such as CT and magnetic resonance imaging, have concentrated on changes in tumor perfusion, the present concept of PET imaging using a radiolabeled drug to study drug delivery in patients after anti-VEGF therapy has not been reported yet. The humanized monoclonal antibody bevacizumab induced an overall decrease in both perfusion and K_i of [^{11}C]docetaxel in tumor tissue within a few hours after bevacizumab administration, a decrease that persisted for at least four days. These findings represent physiological changes in tumors, as measured changes were beyond the known test-retest variability (van der Veldt et al., 2010a and 2011). The large range of changes in perfusion and [^{11}C]docetaxel uptake is most likely due to interpatient differences in tumor response to bevacizumab and partly due to differences in interval between end of bevacizumab infusion and PET scans. Nevertheless, the results indicate a decrease in perfusion and [^{11}C]docetaxel uptake in tumor tissue of all patients. Based on these data, it can be concluded that anti-VEGF therapy is not able to improve drug delivery to tumors but rather has the opposite effect.

Results of the present study are at variance with those obtained by Willett et al. (2004), where improved drug delivery in rectal cancer was postulated partly based on human imaging studies. Tumor perfusion, as determined by dynamic contrast-enhanced CT scanning decreased, whereas the standardized uptake value of 2′-deoxy-2′-[^{18}F]fluoro-D-glucose ([^{18}F]FDG) remained unchanged at 12 days after bevacizumab administration. However, kinetics of [^{18}F]FDG are fundamentally different from those of anticancer drugs, as [^{18}F]FDG reflects glucose metabolism. In the present study, however, the decrease in standard deviation of tumor perfusion in the center of the tumor at 5 hr and the increase in kurtosis of [^{11}C]docetaxel histograms may reflect a more homogenous distribution as

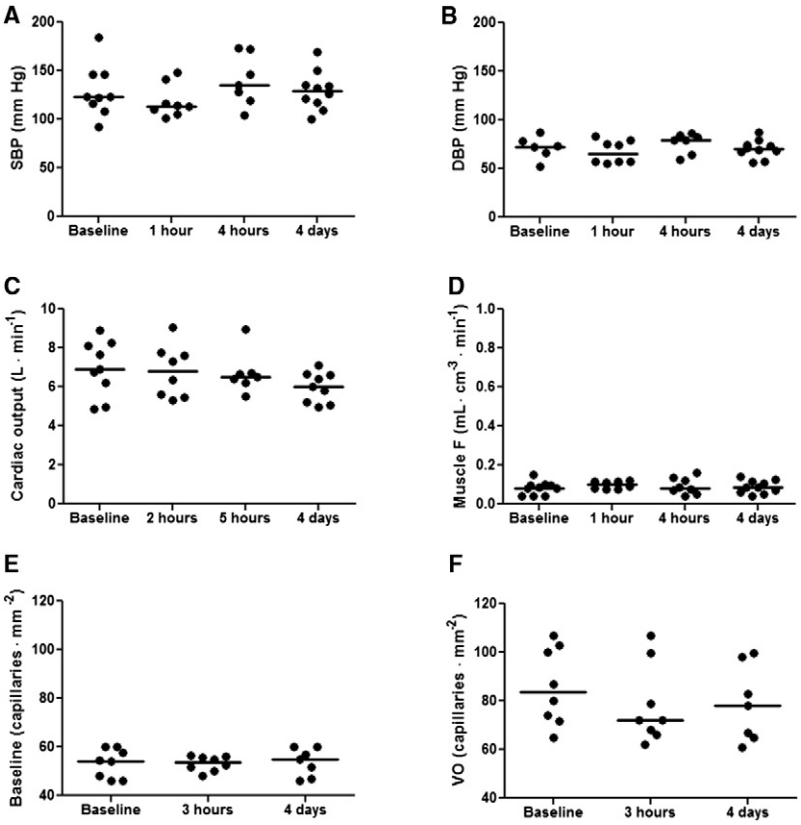

Figure 4. Cardiovascular Variables in Ten NSCLC Patients at Baseline and after Administration of Bevacizumab

Horizontal bars represent median values.
(A) Systolic blood pressure (SBP).
(B) Diastolic blood pressure (DBP).
(C) Cardiac output.
(D) Perfusion (F) in muscle tissue.
(E) Nailfold capillary density.
(F) Nailfold capillary density during venous occlusion (VO).

a result of certain normalization of tumor vasculature. Nevertheless, these possible changes in tumor heterogeneity did not result in improved drug delivery, as bevacizumab infusion caused a rapid and overall reduction in [^{11}C]docetaxel K_i in tumors. In addition, drug uptake may be further impaired by development of tumor necrosis, associated with extensive vascular damage, which usually develops after anti-VEGF therapy. Although it is not possible to define necrotic areas on low-dose CT, development of necrotic areas was possibly reflected by a reduction in the distribution volume of water after 4 days, despite an unchanged total tumor volume on low-dose CT.

Apart from tumor parameters, systemic effects after administration of bevacizumab were evaluated. The rapid changes in tumor perfusion and [^{11}C]docetaxel K_i were associated with an immediate reduction in plasma levels of VEGF, indicating an immediate inhibition of VEGF signaling in the whole body. This rapid neutralization of circulating VEGF also induced a decrease in perfusion of the thyroid gland, whereas perfusion and [^{11}C]docetaxel K_i in the vertebral body and muscle tissue were not affected. In addition, K_i values of [^{11}C]docetaxel in the vertebral body and muscle tissue were essentially different from that in tumor tissue and were not related to perfusion in these normal tissues. These findings imply that tumor tissue shows a difference in sensitivity to VEGF inhibition (Kamba et al., 2006) and in drug delivery as compared with normal tissues. Among the cardiovascular parameters, only cardiac output showed a decrease at day 4, whereas blood pressure and capillary density did not change during the first 4 days after bevacizumab infusion. These findings indicate that the rapid and significant changes in perfusion and [^{11}C]docetaxel K_i in tumors are not caused by immediate development of hypertension, microvascular rarefaction, or a rapid reduction in cardiac output. Consequently, it can be concluded that the decrease in perfusion and [^{11}C]docetaxel K_i in tumors can be attributed to rapid inhibition of VEGF signaling in tumors. As the decrease in perfusion and [^{11}C]docetaxel uptake in tumors is probably too rapid to be solely ascribed to inhibition of tumor angiogenesis, vasoconstrictive effects of anti-angiogenic drugs on tumor vessels, particularly those from the host, should be considered as a potential underlying mechanism. In this regard, inhibition of endothelial nitric oxide synthesis by VEGF inhibitors may be an important factor (Dhaun and Webb, 2010; Syrigos et al., 2011; Ng et al., 2007). Although plasma clearance of [^{11}C]docetaxel decreased slightly after bevacizumab administration, signifying prolonged duration of [^{11}C]docetaxel exposure, this decrease in clearance appeared to be too limited to result in an overall increase in [^{11}C]docetaxel uptake, that is, retention index, by tumors.

Bevacizumab was selected to investigate the effects of anti-angiogenic agents, as it is the most selective inhibitor of VEGF signaling among presently approved anti-angiogenic drugs, and it does not have multiple targets like most tyrosine kinase inhibitors. In addition, the long terminal half-life of 17–21 days (Ferrara et al., 2004) enables sequential measurements after a single administration of bevacizumab. The study was conducted in patients with advanced-stage NSCLC, as noninvasive PET-CT measurements using [^{15}O]H_2O and [^{11}C]docetaxel were previously found to be feasible in this patient group (Van der Veldt et al., 2011). As a result, [^{11}C]docetaxel measurements could be repeated in individual patients who acted as their own control. Although both docetaxel and bevacizumab are active agents for the treatment of advanced lung cancer (Sandler et al., 2006; Kudoh et al., 2006), single-agent bevacizumab is not considered effective for the treatment of NSCLC patients. Consequently, ethically it was not acceptable to prolong the study with PET measurements at later time points. In addition, the localization of the lung tumors did not enable invasive measurements of interstitial fluid pressure (Curti et al., 1993) or sequential biopsies for additional histopathological analyses. Furthermore, use of tracer amounts of docetaxel (microdoses)

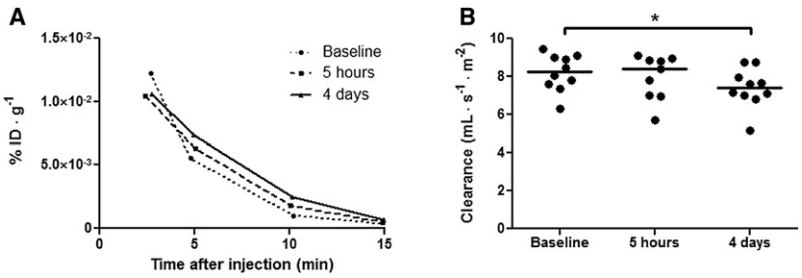

Figure 5. Plasma Clearance of [^{11}C]docetaxel at Baseline and after Administration of Bevacizumab

(A) Example of plasma activity curves of [^{11}C]docetaxel in a patient at baseline and after 5 hr and 4 days following bevacizumab administration. Plasma activity curves are divided by injected dose (ID).

(B) Plasma clearance of [^{11}C]docetaxel in 10 NSCLC patients at baseline and after administration of bevacizumab.

Horizontal bars represent median values.

*p values < 0.05.

may be a potential limitation of the present study, as it is conceivable that the effects of bevacizumab on [^{11}C]docetaxel delivery in tumors may not hold true for pharmacological drug concentrations. However, use of repeated therapeutic doses mixed with the radiolabeled drug, instead of microdoses, will obscure bevacizumab-induced effects, as cytotoxic drugs themselves also affect both tumor perfusion (Dunnwald et al., 2008) and interstitial fluid pressure (Griffon-Etienne et al., 1999) and may modulate the specific targets of the drug under study (Shalli et al., 2005). In a separate study, in which [^{11}C]docetaxel was given at tracer concentrations and during infusion of a therapeutic dose, albeit was possible to predict tumor uptake of (therapeutic) docetaxel from the tumor kinetics of (tracer) [^{11}C]docetaxel (data not shown), indicating that the present bevacizumab-induced decrease in [^{11}C]docetaxel uptake in tumors is likely to represent changes in tumor uptake of therapeutic doses of docetaxel.

The results of the present study pose a number of important issues relevant to anti-angiogenic drugs administered in combination with other anticancer drugs. In human tumors, bevacizumab induced a rapid decrease in perfusion and [^{11}C]docetaxel uptake. It is conceivable that other inhibitors of the VEGF signaling pathways may produce similar effects. In addition, it is likely that these effects may persist during continued treatment with these drugs. Therefore, administration of anti-angiogenic drugs can be considered after administration of the other anticancer agents, as the immediate decrease in tumor perfusion should decrease clearance of drugs from tumors. Hence, preclinical studies are warranted to investigate this concept for scheduling of anticancer drugs. To improve scheduling of combination therapy, other potential mechanisms need to be investigated to understand the synergistic effects with anti-angiogenic drugs. In this regard, it is important to explore the effects of anti-angiogenic drugs on proliferative activity of tumor cells (Ortholan et al., 2010) and their environment, such as mobilization of bone marrow-derived circulating endothelial progenitor cells (Shaked et al., 2008) and acute release of cytokines from the tumor microenvironment (Gilbert and Hemann, 2010).

The results of the present study may explain why several clinical trials have failed to show the additional value of anti-angiogenic drugs in specific populations of cancer patients. Clearly, more clinical studies are needed to assess whether administration schedules affect response and outcome of combination strategies. To this end, the optimal design to prove clinical relevance of drug scheduling would be a randomized controlled trial in which cancer patients are randomized to different administration schedules.

In conclusion, the results of this human study indicate a rapid and significant reduction in perfusion and [^{11}C]docetaxel uptake in NSCLC after administration of bevacizumab. The clinical relevance of these findings is notable, as the present study did not provide evidence for a substantial improvement in drug delivery to tumors but rather showed the opposite effect. These findings highlight the importance of drug scheduling and advocate further studies to optimize scheduling of anti-angiogenic drugs.

EXPERIMENTAL PROCEDURES

Patient Selection

Between October 2009 and September 2010, ten patients (six men and four women; median age 58 years; range, 47–70 years) with advanced-stage NSCLC were prospectively enrolled. Patients participated in this study prior to their scheduled therapy. The study was approved by the Medical Ethics Review Committee of the VU University Medical Center, Amsterdam. All patients signed a protocol-specific informed consent form prior to study enrollment.

Inclusion criteria were the following: age $\geq$18 years; a malignant lesion $\geq$1.5 cm in diameter within the chest; life expectancy of at least 12 weeks; Eastern Cooperative Oncology Group performance status <3; $\geq$4 weeks since any prior surgery or radiotherapy; no previous acute toxicities (>1) in accordance with Common Terminology Criteria for Adverse Events v3.0 (CTCAE); adequate organ function [hemoglobin $\geq$6.0 mmol·l^{-1}; absolute neutrophil count $\geq$1.5 × 10^9/l; absolute platelet count >100 × 10^9/l; total serum bilirubin $\leq$1.5 upper limit of normal (ULN); aspartate aminotransferase and alanine aminotransferase $\leq$2.5 x ULN (in case of liver metastases $\leq$ 5 x ULN); alkaline phosphatase $\leq$2.5 x ULN; serum creatinine $\leq$1.5 ULN or creatinine clearance $\geq$60 ml·min^{-1}; normal serum calcium; urine dipstick for proteinuria <2+]; and use of effective contraception.

Exclusion criteria were the following: squamous lung cancer; history of $\geq$ grade 2 hemoptysis; cavitary lesion; tumor invading major blood vessels; newly diagnosed and untreated central nervous system metastases; any unstable systemic disease (including but not limited to clinically significant cardiovascular disease and uncontrolled hypertension); major surgery or significant traumatic injury <28 days before study entry; prior treatment with taxanes or bevacizumab; concurrent treatment with other anticancer agents or experimental drugs; use of inhibitors or substrates of the efflux transporter ABCB1; serious nonhealing wound or ulcer; a history of documented hemorrhagic diathesis or coagulopathy; therapeutic anticoagulation; regular use of aspirin (>325 mg per day); planned radiotherapy or major surgery; pregnancy or lactation; metal implants (e.g., pacemakers); and claustrophobia.

Study Design

Patients received a single infusion of bevacizumab (15 mg·kg^{-1}, infused over 90 min). In the week prior to this infusion, patients underwent a dynamic PET-CT study with both [^{15}O]H_2O and [^{11}C]docetaxel. At 5 hr and 4 days after infusion of bevacizumab, the PET-CT protocol was repeated. In addition, 2 hr after infusion of bevacizumab, patients underwent an additional dynamic PET-CT scan with [^{15}O]H_2O. Sequential scans were possible because of the short half-lives of oxygen-15 and carbon-11, which are 2.0 and 20.3 min, respectively. Initially, the last time point for PET measurements was set at day 7. However, recruitment of patients seemed difficult, as patients were not willing

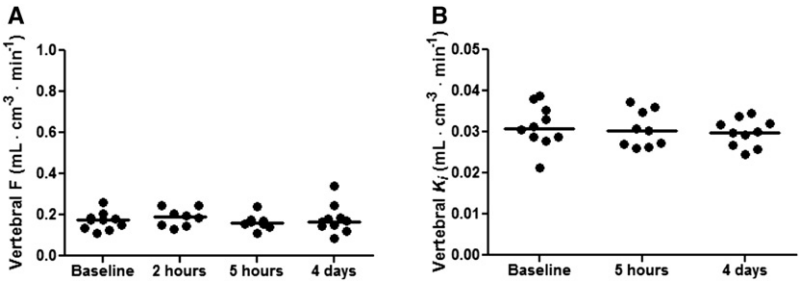

Figure 6. Perfusion and [^{11}C]docetaxel Uptake in the Vertebral Body, which Represents Bone Marrow, in Ten Individual Patients at Baseline and after Administration of Bevacizumab

Horizontal bars represent median values.

(A) Perfusion (F).

(B) Net rate of influx (K_i) of [^{11}C]docetaxel.

to postpone their planned chemotherapy for more than a few days. Hence, the protocol was amended and the last time point was set at day 4. Adverse events were graded in accordance with CTCAE v3.0. After the last PET-CT study, patients started with their scheduled therapy. In accordance with the guidelines of the Medical Ethics Review Committee of the VU University Medical Center, the total radiation burden of the study was estimated at <10 mSv. As efficacy was not an endpoint of the present study, response evaluation and data collection for survival were not performed.

Synthesis of Radiopharmaceuticals

The radiosyntheses of [^{15}O]H_2O and [^{11}C]docetaxel were performed in accordance with good manufacturing practice (GMP) standards (Jackson et al., 1993; van Tilburg et al., 2004 and 2008). Docetaxel, obtained from Green PlantChem Company (Hangzhou, China), was chemically modified and used as precursor in the synthesis of [^{11}C]docetaxel. ^{11}C-labeled docetaxel was obtained with an isolated decay-corrected radiochemical yield of 10 ± 2% and a radiochemical purity of >98%. [^{11}C]docetaxel has an identical molecular structure as the drug docetaxel. The identity of [^{11}C]docetaxel was confirmed by comparison of retention times on high-performance liquid chromatography with authentic docetaxel.

Scanning Protocol

Imaging studies were performed on a state-of-the-art three-dimensional (3D) PET-CT scanner (Gemini TF-64, Philips Medical Systems, Best, The Netherlands; Surti et al., 2007). This scanner has an axial field of view of 18 cm, divided into 45 contiguous planes. All patients underwent PET-CT scans with [^{15}O]H_2O and [^{11}C]docetaxel at baseline and at day 4. Nine patients underwent a [^{15}O]H_2O PET-CT scan at 2 hr and eight patients underwent combined [^{15}O]H_2O and [^{11}C]docetaxel PET-CT scans at 5 hr, whereas one patient underwent a single [^{11}C]docetaxel PET-CT scan at 5 hr. The median times from the end of the bevacizumab infusion to the first, second, and third scan sessions were 1.9 hr (range, 1.4–2.3 hr), 5.6 hr (range, 4.9–8.6 hr), and 4 days (range, 3–5 days). Sudden technical difficulties, clinical problems, and logistic issues were the reasons for missing scans and different time intervals.

Until 3 hr prior to scanning, food and drinks were allowed. On the day of a PET study, patients were asked to consume similar meals prior to scanning. All patients received two venous catheters, one for tracer injection and the other for blood sampling. Patients were positioned supine on the scanner bed, with both tumor and aortic arch located inside the axial field of view of the scanner. Elastic body-restraining bandages were used to minimize movement during scanning.

A 10 min dynamic scan was started simultaneously with an intravenous injection of 370 MBq [^{15}O]H_2O (5 ml at a rate of 0.8 ml·s^{-1}, followed by a 35 ml saline flush at a rate of 2 ml·s^{-1}). Thereafter, a 50 mAs low-dose CT scan was performed for attenuation correction purposes. At least 20 min after administration of [^{15}O]H_2O, a 60 min dynamic scan was started simultaneously with an intravenous injection of [^{11}C]docetaxel (dissolved in a maximum volume of 12 ml saline, infused at a rate of 0.8 ml·s^{-1}, and followed by a 35 ml saline flush at a rate of 2 ml·s^{-1}). The median injected dose of [^{11}C]docetaxel was 344 MBq (range, 122–388 MBq) with a median specific activity of 3.2 GBq·μmol^{-1} (range; 1.0–25.8 GBq·μmol^{-1}). During PET scanning, blood pressure was monitored with a Dinamap (Dash 4000, GE Medical Systems Information Technologies, Inc., Milwaukee, Wisconsin).

Data were normalized and all appropriate corrections for dead time, decay, randoms, scatter, and attenuation were applied. Using the 3D row action maximum likelihood reconstruction algorithm, [^{15}O]H_2O and [^{11}C]docetaxel scans were reconstructed into 26 (1x10, 8x5, 4x10, 2x15, 3x20, 2x30, and 6x60 s) and 36 (1x10, 8x5, 4x10, 2x15, 3x20, 2x30, 6x60, 4x150, 4x300, and 2x600 s) frames, respectively.

Blood Sampling

Sequential blood samples were collected in ACD vacutainers (8.5 ml, Becton Dickinson, Heidelberg, Germany; Cat. No. 364606) at baseline, and at 3 hr and 4 days after the end of the bevacizumab infusion. Prior to each sample, 3 ml–5 ml blood was discarded and the line was flushed with 2 ml saline after each sample. After collection, the blood samples were centrifuged immediately to obtain platelet-rich plasma (15 min; 20°C; 156 x *g*; N = 7 patients). Platelet-rich plasma was further centrifuged to obtain platelet-poor plasma (15 min; 20°C; 330 x *g*; N = 3 patients). Thereafter, plasma was stored at −20°C until analysis. Concentrations of VEGF (pg·ml^{-1}) were assessed in duplicate using a Quantikine enzyme-linked immunosorbent assay (ELISA) kit (R&D Systems, Minneapolis, Minnesota). Vascular endothelial growth factor concentrations in platelet-rich plasma were corrected for platelet count and were expressed in pg·ml^{-1} per 200,000 platelets·μl^{-1}.

After intravenous injection of [^{11}C]docetaxel, 10 ml discrete venous samples were collected manually at 2.5, 5, 10, 15, 20, 30, 40, and 60 min post-injection. Blood samples were analyzed for radioactivity concentrations in blood and plasma. Whole blood (0.5 ml) was weighted in duplicate and 0.05 ml 10% Triton X-100 solution was added. After centrifuging the remaining whole blood (5 min; room temperature; 4000 rpm), plasma was harvested and 0.5 ml plasma was weighted in duplicate, again adding 0.05 ml 10% Triton X-100 solution. A well-counter, cross-calibrated against the PET scanner, was used to determine activity concentrations. Samples were not analyzed for radiolabeled metabolites, as these were not detected previously (Van der Veldt et al., 2011).

Input Functions

Kinetic analyses of data were performed using dedicated programs written within the software environment Matlab (The MathWorks Inc., Natick, Massachusetts). The ascending aorta in the [^{15}O]H_2O and [^{11}C]docetaxel images was used to generate noninvasive image-derived input functions (IDIF), as validated previously (van der Veldt et al., 2010a and 2011). Volumes of interest (VOI) of 1 cm diameter were drawn over the ascending aorta in approximately ten consecutive image planes of the frame in which the first pass of the bolus was best visualized. Projection of these VOIs onto all image frames yielded the arterial time-activity curve (TAC) $C_A(t)$. A similar approach was used for the pulmonary artery in approximately five consecutive planes, thereby providing a TAC for the pulmonary circulation $C_V(t)$ (van der Veldt et al., 2010a). The [^{11}C]docetaxel plasma IDIF was obtained by multiplying $C_A(t)$ with a sigmoid function (Gunn et al., 1998), which was obtained by fitting the plasma/whole blood ratios derived from the venous samples. As the rapid [^{11}C]docetaxel clearance precludes reliable input functions at later time points, the generation of input functions of [^{11}C]docetaxel was limited to the first 10 min of data (Van der Veldt et al., 2011).

Analysis of Perfusion and [^{11}C]docetaxel Kinetics in Tumors

Scans were anonymized and randomly presented to an experienced observer (I.B.) who was blinded to patients' history and outcome. To delineate comparable tumor VOIs, this observer analyzed all scans from one patient in the same session. Low-dose CT images were converted to ECAT 7 format. Thereafter,

primary tumors were delineated on low-dose CT images using the CAPP software package (CTI/Siemens, Knoxville, Tennessee). Next, VOIs were projected onto the dynamic images of the corresponding [^{15}O]H_2O and [^{11}C]docetaxel scans, thereby generating tumor TACs for [^{15}O]H_2O and [^{11}C]docetaxel, respectively.

The standard single-tissue compartment model was used to derive tumor perfusion from [^{15}O]H_2O kinetics (Hermansen et al., 1998; van der Veldt et al., 2010a). Using nonlinear regression, [^{15}O]H_2O tumor TACs were fitted to the single-tissue compartment model using IDIF as arterial input function (van der Veldt et al., 2010a). The correction for pulmonary circulation blood volume was included, as it improves the quality of the fits without affecting tumor perfusion values. Using this approach, the absolute test-retest variability of tumor perfusion is 0.03 $ml \cdot cm^{-3} \cdot min^{-1}$ (van der Veldt et al., 2010a).

The kinetics of [^{11}C]docetaxel in tumors was described by a two-tissue irreversible compartment model, linearized using the Patlak method (Patlak et al., 1983). When applying the Patlak method to the first 10 min of dynamic PET data with the starting time at 2 min, the K_i of [^{11}C]docetaxel has an absolute test-retest variability of 0.003 $ml \cdot cm^{-3} \cdot min^{-1}$ (van der Veldt et al., 2011). In addition, the retention index of [^{11}C]docetaxel in tumor tissue was calculated by dividing the measured radioactivity concentration at 10 min post-injection by the integral of the plasma curve up to this time.

To analyze heterogeneity of tumor perfusion at the voxel level, parametric perfusion images were generated (van der Veldt et al., 2010a). Hence, IDIFs and a basis function implementation of the standard single-tissue compartment model were applied (Boellaard et al., 2005; Lodge et al., 2000; Watabe et al., 2005). Fifty logarithmically spaced, precomputed basis functions with F/V_T values, ranging from 0.1 to 2.0 min^{-1} were used and parametric perfusion images were postsmoothed with a Gaussian filter of 10 mm full width at half maximum. Then, VOIs previously defined on the low-dose CT scans were projected onto the parametric perfusion images. Next, voxel intensity histograms were generated for the whole VOI, its center and its rim. A voxel was considered to be part of the rim if at least one of the voxels in its 3D six-connected neighborhood was outside the defined VOI. In accordance with this method, the median baseline volume of the whole tumor VOI was 13.3 cm^3 (range, 1.7–278.5 cm^3) with center and rim accounting for median volumes of 2.5 cm^3 (range, 0.1–183.8 cm^3) and 9.1 cm^3 (range, 1.5–81.3 cm^3), respectively. Similarly, voxel intensity histograms were generated for the K_i of [^{11}C]docetaxel, applying the Patlak method on a voxel basis. The voxel intensity histograms were used to characterize tumor heterogeneity of perfusion and [^{11}C]docetaxel uptake, analyzing the following parameters: percentage of voxels, mean value, standard deviation, median value, minimal value, maximal value, kurtosis, and skewness of the distribution. More homogenous distributions are characterized by lower standard deviations and higher kurtosis (more peaked distribution) of corresponding histograms.

Cardiac Output

Using dynamic [^{15}O]H_2O PET data, the cardiac output can be estimated by the following equation (Knaapen et al., 2008):

$$\text{Cardiac output} = \frac{\text{ID}}{\int_0^t C_V \cdot dt}, \quad (1)$$

where the injected radioactivity (ID) of [^{15}O]H_2O is divided by the area under the curve of the blood activity in the pulmonary artery (C_V) multiplied by the duration of the first pass of the bolus. The TAC of the pulmonary artery was fitted with a linear upslope and followed by an exponential downslope, which was extrapolated to remove contamination of recirculating radioactivity.

Microcirculation in the Skin

In eight patients, microcirculation in the skin was investigated. At baseline, 3 hr and 4 days, nailfold capillaries in the dorsal skin of the third finger were visualized using a capillary microscope (Serné et al., 2001). Capillary density was defined as the number of erythrocyte-perfused capillaries $\cdot mm^{-2}$. First, baseline capillary density was recorded for 2 min. Thereafter, venous occlusion was applied to expose a maximal number of perfused capillaries. To this end, a digital cuff was inflated to 60 mmHg for 60 s. Recordings were presented randomly and in a blind fashion to an experienced investigator (M.P.d.B.), who counted number of capillaries off-line from a videotape. Using the same visual fields as used during baseline measurements, peak capillary density during venous congestion was counted in the 60 s recordings. Day-to-day variation of baseline capillary density and peak capillary density during venous congestion were 2.3% ± 1.8% (Serné et al., 2002) and 9.5 ± 7.1% (Serné et al., 2001), respectively.

Muscle Perfusion

On the low-dose CT scans, VOIs (diameter, 1 cm) were drawn over the erector spinae muscle in five consecutive image planes. Projection of these muscle VOIs onto the dynamic images of the corresponding [^{15}O]H_2O scan yielded a muscle TAC for [^{15}O]H_2O. The standard single-tissue compartment model was used to derive muscle perfusion (Hermansen et al., 1998) but without correction for pulmonary circulation blood volume:

$$C_T(t) = (1 - V_A) \cdot F \cdot C_A(t) \otimes e^{-\frac{F}{V_T} t} + V_A \, C_A(t), \quad (2)$$

where $C_T(t)$ is the total measured tissue signal in tumor as function of time, F is perfusion, V_A is arterial blood volume, and V_T is the volume of distribution or partition coefficient of water. To evaluate [^{11}C]docetaxel kinetics in normal tissue, muscle VOIs were also projected onto the corresponding [^{11}C]docetaxel image and those TACs were analyzed using the Patlak method (Patlak et al., 1983).

[^{11}C]docetaxel Clearance

To determine influence of bevacizumab on blood kinetics of [^{11}C]docetaxel, clearance of [^{11}C]docetaxel was calculated using the following equation:

$$\text{Clearance} = \frac{\text{ID}}{\int C_P(t) \cdot dt \cdot BSA}, \quad (3)$$

where the injected dose (ID) of [^{11}C]docetaxel is divided by the integral of the plasma (C_P) TAC multiplied by the body surface area.

Thyroid Perfusion

In those cases in which the thyroid gland was in the field of view, additional parametric perfusion images were generated, using 50 precomputed basis functions with F/V_T values, ranging from 0.1 to 15 min^{-1} and postsmoothing with a Gaussian filter of 10 mm in full width at half maximum. Then, the thyroid gland could be delineated on parametric perfusion images applying a semi-automatic threshold technique (50% of the maximum voxel value with correction for local background; van der Veldt et al., 2010a). Thereafter, these VOIs were projected onto the dynamic [^{15}O]H_2O images. Again, the standard single-tissue compartment model (Equation 2) was applied to calculate perfusion.

Perfusion and [^{11}C]docetaxel Kinetics in Bone Marrow

Perfusion and [^{11}C]docetaxel uptake were determined in the vertebral body, representing active bone marrow. From the level of the main carina to ten image planes downwards, VOIs (diameter, 1.5 cm) were defined in the vertebral body on low-dose CT scans. These VOIs were projected onto dynamic images of the [^{15}O]H_2O and [^{11}C]docetaxel scans, generating corresponding TACs.

Equation 2 was applied to calculate vertebral body perfusion, whereas the Patlak method (Patlak et al., 1983) was applied to determine [^{11}C]docetaxel uptake.

Statistics

Statistical analysis was performed using SPSS software (SPSS for Windows 16.0, SPSS, Inc., Chicago, IL). Correlations were explored using the Spearman's correlation coefficient. The Mann-Whitney test was used to compare between groups. The Wilcoxon signed-rank test was used to compare variables at 2 hr, 3 hr, 5 hr, and 4 days after bevacizumab administration with baseline values. A two-tailed probability value of p value < 0.05 was considered significant.

ACKNOWLEDGMENTS

The authors would like to thank all patients who participated in this study. In addition, the authors would like to thank Suzette van Balen, Amina

Elouahmani, Judith van Es, Robin Hemminga, Femke Jongsma, Nghi Pham, Nasserah Sais, and Jeroen Wilhelmus for scanning the patients, Emile Comans, Otto Hoekstra, Daniela Oprea-Lager, Pieter Raijmakers, Nafees Rizvi, Natasja Kok, Ilona Pomstra, Atie van Wijk, Sabri Duzenli, Martijn Groenendijk, Esther Nossent, Arifa Pašić, Suzy Samii, Serge van Wolferen, and Jennifer Benit for help with logistical planning and patient care, Ronald Boellaard, Dennis Boersma, Marc Huisman, Arthur van Lingen, and Maqsood Yaqub for technical assistance; Peter van de Ven for statistical advice; Bart Kuenen for help with the design of the study; Martien Mooijer, Anneloes Rijnders, and Dennis Laan for production of [^{11}C]docetaxel; Henk Dekker for help with the analyses of VEGF levels; and Marissa Rongen, Robert Schuit, and Kevin Takkenkamp for the production of [^{15}O]H_2O and the analysis of blood samples. This work was supported by a grant of the Cancer Center Amsterdam. This study was presented in part at the 2011 ASCO Annual Meeting, Chicago, IL, June 3–7, 2011, #3059; and at the 14th World Conference on Lung Cancer, Amsterdam, The Netherlands, July 3–7, 2011, #O18.02.

Received: July 23, 2011
Revised: November 2, 2011
Accepted: November 29, 2011
Published: January 17, 2012

REFERENCES

Batchelor, T.T., Sorensen, A.G., di Tomaso, E., Zhang, W.T., Duda, D.G., Cohen, K.S., Kozak, K.R., Cahill, D.P., Chen, P.J., Zhu, M., et al. (2007). AZD2171, a pan-VEGF receptor tyrosine kinase inhibitor, normalizes tumor vasculature and alleviates edema in glioblastoma patients. Cancer Cell *11*, 83–95.

Boellaard, R., Knaapen, P., Rijbroek, A., Luurtsema, G.J., and Lammertsma, A.A. (2005). Evaluation of basis function and linear least squares methods for generating parametric blood flow images using 15O-water and Positron Emission Tomography. Mol. Imaging Biol. *7*, 273–285.

Carmeliet, P. (2000). Mechanisms of angiogenesis and arteriogenesis. Nat. Med. *6*, 389–395.

Chen, H.X., and Cleck, J.N. (2009). Adverse effects of anticancer agents that target the VEGF pathway. Nat. Rev. Clin. Oncol. *6*, 465–477.

Cobleigh, M.A., Langmuir, V.K., Sledge, G.W., Miller, K.D., Haney, L., Novotny, W.F., Reimann, J.D., and Vassel, A. (2003). A phase I/II dose-escalation trial of bevacizumab in previously treated metastatic breast cancer. Semin. Oncol. *30* (*Suppl 16*), 117–124.

Curti, B.D., Urba, W.J., Alvord, W.G., Janik, J.E., Smith, J.W., 2nd, Madara, K., and Longo, D.L. (1993). Interstitial pressure of subcutaneous nodules in melanoma and lymphoma patients: changes during treatment. Cancer Res. (*Suppl*). *53*, 2204–2207.

Dhaun, N., and Webb, D.J. (2010). Receptor tyrosine kinase inhibition, hypertension, and proteinuria: is endothelin the smoking gun? Hypertension *56*, 575–577.

Dunnwald, L.K., Gralow, J.R., Ellis, G.K., Livingston, R.B., Linden, H.M., Specht, J.M., Doot, R.K., Lawton, T.J., Barlow, W.E., Kurland, B.F., et al. (2008). Tumor metabolism and blood flow changes by positron emission tomography: relation to survival in patients treated with neoadjuvant chemotherapy for locally advanced breast cancer. J. Clin. Oncol. *26*, 4449–4457.

Ferrara, N., and Kerbel, R.S. (2005). Angiogenesis as a therapeutic target. Nature *438*, 967–974.

Ferrara, N., Gerber, H.P., and LeCouter, J. (2003). The biology of VEGF and its receptors. Nat. Med. *9*, 669–676.

Ferrara, N., Hillan, K.J., Gerber, H.P., and Novotny, W. (2004). Discovery and development of bevacizumab, an anti-VEGF antibody for treating cancer. Nat. Rev. Drug Discov. *3*, 391–400.

Gambhir, S.S. (2002). Molecular imaging of cancer with positron emission tomography. Nat. Rev. Cancer *2*, 683–693.

Gilbert, L.A., and Hemann, M.T. (2010). DNA damage-mediated induction of a chemoresistant niche. Cell *143*, 355–366.

Griffon-Etienne, G.E., Boucher, Y., Brekken, C., Suit, H.D., and Jain, R.K. (1999). Taxane-induced apoptosis decompresses blood vessels and lowers interstitial fluid pressure in solid tumors: clinical implications. Cancer Res. *59*, 3776–3782.

Gunn, R.N., Sargent, P.A., Bench, C.J., Rabiner, E.A., Osman, S., Pike, V.W., Hume, S.P., Grasby, P.M., and Lammertsma, A.A. (1998). Tracer kinetic modeling of the 5-HT1A receptor ligand [carbonyl-11C]WAY-100635 for PET. Neuroimage *8*, 426–440.

Hanahan, D., and Weinberg, R.A. (2000). The hallmarks of cancer. Cell *100*, 57–70.

Hermansen, F., Rosen, S.D., Fath-Ordoubadi, F., Kooner, J.S., Clark, J.C., Camici, P.G., and Lammertsma, A.A. (1998). Measurement of myocardial blood flow with oxygen-15 labelled water: comparison of different administration protocols. Eur. J. Nucl. Med. *25*, 751–759.

Hoekstra, C.J., Stroobants, S.G., Hoekstra, O.S., Smit, E.F., Vansteenkiste, J.F., and Lammertsma, A.A. (2002). Measurement of perfusion in stage IIIA-N2 non-small cell lung cancer using H(2)(15)O and positron emission tomography. Clin. Cancer Res. *8*, 2109–2115.

Hurwitz, H., Fehrenbacher, L., Novotny, W., Cartwright, T., Hainsworth, J., Heim, W., Berlin, J., Baron, A., Griffing, S., Holmgren, E., et al. (2004). Bevacizumab plus irinotecan, fluorouracil, and leucovorin for metastatic colorectal cancer. N. Engl. J. Med. *350*, 2335–2342.

Jackson, J.R., Dembowski, B.S., Ehrenkaufer, R.L., McIntyre, E., and Reivich, M. (1993). [15O]H2O, [15O]O2 and [15O]CO gas production, monitoring and quality control system. Appl. Radiat. Isot. *44*, 631–634.

Jain, R.K. (2001). Normalizing tumor vasculature with anti-angiogenic therapy: a new paradigm for combination therapy. Nat. Med. *7*, 987–989.

Jain, R.K. (2005). Normalization of tumor vasculature: an emerging concept in antiangiogenic therapy. Science *307*, 58–62.

Kamba, T., Tam, B.Y., Hashizume, H., Haskell, A., Sennino, B., Mancuso, M.R., Norberg, S.M., O'Brien, S.M., Davis, R.B., Gowen, L.C., et al. (2006). VEGF-dependent plasticity of fenestrated capillaries in the normal adult microvasculature. Am. J. Physiol. Heart Circ. Physiol. *290*, H560–H576.

Knaapen, P., Lubberink, M., Rijzewijk, L.J., van der Meer, R.W., Unger, M., Germans, T., Bax, J.J., Smit, J.W., Lamb, H.J., van Rossum, A.C., et al. (2008). Stroke volume measurements with first-pass dynamic positron emission tomography: comparison with cardiovascular magnetic resonance. J. Nucl. Cardiol. *15*, 218–224.

Kudoh, S., Takeda, K., Nakagawa, K., Takada, M., Katakami, N., Matsui, K., Shinkai, T., Sawa, T., Goto, I., Semba, H., et al. (2006). Phase III study of docetaxel compared with vinorelbine in elderly patients with advanced non-small-cell lung cancer: results of the West Japan Thoracic Oncology Group Trial (WJTOG 9904). J. Clin. Oncol. *24*, 3657–3663.

Lodge, M.A., Carson, R.E., Carrasquillo, J.A., Whatley, M., Libutti, S.K., and Bacharach, S.L. (2000). Parametric images of blood flow in oncology PET studies using [15O]water. J. Nucl. Med. *41*, 1784–1792.

Miller, K., Wang, M., Gralow, J., Dickler, M., Cobleigh, M., Perez, E.A., Shenkier, T., Cella, D., and Davidson, N.E. (2007). Paclitaxel plus bevacizumab versus paclitaxel alone for metastatic breast cancer. N. Engl. J. Med. *357*, 2666–2676.

Mourad, J.J., des Guetz, G., Debbabi, H., and Levy, B.I. (2008). Blood pressure rise following angiogenesis inhibition by bevacizumab. A crucial role for microcirculation. Ann. Oncol. *19*, 927–934.

Ng, Q.S., Goh, V., Milner, J., Stratford, M.R., Folkes, L.K., Tozer, G.M., Saunders, M.I., and Hoskin, P.J. (2007). Effect of nitric-oxide synthesis on tumour blood volume and vascular activity: a phase I study. Lancet Oncol. *8*, 111–118.

Ortholan, C., Durivault, J., Hannoun-Levi, J.M., Guyot, M., Bourcier, C., Ambrosetti, D., Safe, S., and Pagès, G. (2010). Bevacizumab/docetaxel association is more efficient than docetaxel alone in reducing breast and prostate cancer cell growth: a new paradigm for understanding the therapeutic effect of combined treatment. Eur. J. Cancer *46*, 3022–3036.

Patlak, C.S., Blasberg, R.G., and Fenstermacher, J.D. (1983). Graphical evaluation of blood-to-brain transfer constants from multiple-time uptake data. J. Cereb. Blood Flow Metab. *3*, 1–7.

Reese, D., Fratesi, P., Corry, M., Novotny, W., Holmgren, E., and Small, E. (2001). A phase II trial of humanized anti-vascular endothelial growth factor antibody for the treatment of androgen-independent prostate cancer. The Prostate J. *3*, 65–70.

Sandler, A., Gray, R., Perry, M.C., Brahmer, J., Schiller, J.H., Dowlati, A., Lilenbaum, R., and Johnson, D.H. (2006). Paclitaxel-carboplatin alone or with bevacizumab for non-small-cell lung cancer. N. Engl. J. Med. *355*, 2542–2550.

Serné, E.H., Gans, R.O., ter Maaten, J.C., Tangelder, G.J., Donker, A.J., and Stehouwer, C.D. (2001). Impaired skin capillary recruitment in essential hypertension is caused by both functional and structural capillary rarefaction. Hypertension *38*, 238–242.

Serné, E.H., IJzerman, R.G., Gans, R.O., Nijveldt, R., De Vries, G., Evertz, R., Donker, A.J., and Stehouwer, C.D. (2002). Direct evidence for insulin-induced capillary recruitment in skin of healthy subjects during physiological hyperinsulinemia. Diabetes *51*, 1515–1522.

Shaked, Y., Henke, E., Roodhart, J.M., Mancuso, P., Langenberg, M.H., Colleoni, M., Daenen, L.G., Man, S., Xu, P., Emmenegger, U., et al. (2008). Rapid chemotherapy-induced acute endothelial progenitor cell mobilization: implications for antiangiogenic drugs as chemosensitizing agents. Cancer Cell *14*, 263–273.

Shalli, K., Brown, I., Heys, S.D., and Schofield, A.C. (2005). Alterations of beta-tubulin isotypes in breast cancer cells resistant to docetaxel. FASEB J. *19*, 1299–1301.

Surti, S., Kuhn, A., Werner, M.E., Perkins, A.E., Kolthammer, J., and Karp, J.S. (2007). Performance of Philips Gemini TF PET/CT scanner with special consideration for its time-of-flight imaging capabilities. J. Nucl. Med. *48*, 471–480.

Syrigos, K.N., Karapanagiotou, E., Boura, P., Manegold, C., and Harrington, K. (2011). Bevacizumab-induced hypertension: pathogenesis and management. BioDrugs *25*, 159–169.

van der Veldt, A.A., Hendrikse, N.H., Harms, H.J., Comans, E.F., Postmus, P.E., Smit, E.F., Lammertsma, A.A., and Lubberink, M. (2010a). Quantitative parametric perfusion images using 15O-labeled water and a clinical PET/CT scanner: test-retest variability in lung cancer. J. Nucl. Med. *51*, 1684–1690.

Van der Veldt, A.A., Hendrikse, N.H., Smit, E.F., Mooijer, M.P., Rijnders, A.Y., Gerritsen, W.R., van der Hoeven, J.J., Windhorst, A.D., Lammertsma, A.A., and Lubberink, M. (2010b). Biodistribution and radiation dosimetry of 11C-labelled docetaxel in cancer patients. Eur. J. Nucl. Med. Mol. Imaging *37*, 1950–1958.

Van der Veldt, A.A., Lubberink, M., Greuter, H.N., Comans, E.F., Herder, G.J., Yaqub, M., Schuit, R.C., Van Lingen, A., Rizvi, S.N., Mooijer, M.P., et al. (2011). Absolute quantification of [11C]docetaxel kinetics in lung cancer patients using positron emission tomography. Clin. Cancer Res. *15*, 4814–4824.

van Tilburg, E.W., Franssen, E.J., Van der Hoeven, J.J., Van der Meij, M., Elshove, D., Lammertsma, A.A., and Windhorst, A.D. (2004). Radiosynthesis of [11C]docetaxel. J. Labelled Comp. Rad. *47*, 763–777.

van Tilburg, E.W., Mooijer, M.P., Brinkhorst, J., van der Meij, M., and Windhorst, A.D. (2008). Improved and semi-automated GMP-compliant radiosynthesis of [11C]docetaxel. Appl. Radiat. Isot. *66*, 1414–1418.

Verheul, H.M., Hoekman, K., Luykx-de Bakker, S., Eekman, C.A., Folman, C.C., Broxterman, H.J., and Pinedo, H.M. (1997). Platelet: transporter of vascular endothelial growth factor. Clin. Cancer Res. *3*, 2187–2190.

Watabe, H., Jino, H., Kawachi, N., Teramoto, N., Hayashi, T., Ohta, Y., and Iida, H. (2005). Parametric imaging of myocardial blood flow with 15O-water and PET using the basis function method. J. Nucl. Med. *46*, 1219–1224.

Willett, C.G., Boucher, Y., di Tomaso, E., Duda, D.G., Munn, L.L., Tong, R.T., Chung, D.C., Sahani, D.V., Kalva, S.P., Kozin, S.V., et al. (2004). Direct evidence that the VEGF-specific antibody bevacizumab has antivascular effects in human rectal cancer. Nat. Med. *10*, 145–147.

Wilson, C.B., Lammertsma, A.A., McKenzie, C.G., Sikora, K., and Jones, T. (1992). Measurements of blood flow and exchanging water space in breast tumors using positron emission tomography: a rapid and noninvasive dynamic method. Cancer Res. *52*, 1592–1597.

Yang, J.C., Haworth, L., Sherry, R.M., Hwu, P., Schwartzentruber, D.J., Topalian, S.L., Steinberg, S.M., Chen, H.X., and Rosenberg, S.A. (2003). A randomized trial of bevacizumab, an anti-vascular endothelial growth factor antibody, for metastatic renal cancer. N. Engl. J. Med. *349*, 427–434.

Cancer Cell
Article

CREPT Accelerates Tumorigenesis by Regulating the Transcription of Cell-Cycle-Related Genes

Dongdong Lu,[1,2,8] Yinyuan Wu,[1,8] Yinyin Wang,[1,8] Fangli Ren,[1,8] Dianjun Wang,[3,8] Fuqin Su,[1] Yanquan Zhang,[1] Xi Yang,[1] Guihua Jin,[1] Xinbao Hao,[1] Dacheng He,[4] Yonggong Zhai,[4] David M. Irwin,[5] Jim Hu,[6] Joseph J.Y. Sung,[7] Jun Yu,[7] Baoqing Jia,[3,*] and Zhijie Chang[1,*]

[1]State Key Laboratory of Biomembrane and Membrane Biotechnology, School of Medicine, National Engineering Laboratory for Anti-tumor Therapeutics, Tsinghua University, Beijing 100084, China
[2]School of Life Sciences and Technology, Tongji University, Shanghai 200092, China
[3]Departments of Surgical Oncology and Pathology, Chinese PLA General Hospital, Beijing 100853, China
[4]School of Life Sciences, Beijing Normal University, Beijing 100874, China
[5]Department of Laboratory Medicine and Pathobiology, University of Toronto, 1 King's College Circle, Toronto M5S 1A8, Canada
[6]Physiology and Experimental Medicine Program, Hospital for Sick Children Research Institute, 555 University Avenue, Toronto M5G 1X8, Canada
[7]Institute of Digestive Disease and Department of Medicine and Therapeutics, Li Ka Shing Institute of Health Sciences, Chinese University of Hong Kong, Hong Kong, China
[8]These authors contributed equally to this work
*Correspondence: baoqingjia@126.com (B.J.), zhijiec@tsinghua.edu.cn (Z.C.)
DOI 10.1016/j.ccr.2011.12.016

SUMMARY

Tumorigenesis is caused by an uncontrolled cell cycle and the altered expression of many genes. Here, we report a gene *CREPT* that is preferentially expressed in diverse human tumors. Overexpression of CREPT accelerates tumor growth, whereas depletion of CREPT demonstrates a reversed effect. CREPT regulates cyclin D1 expression by binding to its promoter, enhancing its transcription both in vivo and in vitro, and interacting with RNA polymerase II (RNAPII). Interestingly, CREPT promotes the formation of a chromatin loop and prevents RNAPII from reading through the 3′ end termination site of the gene. Our findings reveal a mechanism where CREPT increases cyclin D1 transcription during tumorigenesis, through enhancing the recruitment of RNAPII to the promoter region, possibly, as well as chromatin looping.

INTRODUCTION

Tumor development is highly related to uncontrolled cell growth (Hanahan and Weinberg, 2000), a process where both oncogenes and tumor suppressors are involved (Gordon et al., 2005; Vogelstein and Kinzler, 2004). Oncogenes are upregulated or mutated with gain of function, whereas tumor suppressors are downregulated or lost in most tumors (Yamasaki and Pagano, 2004). Oncogenes encode growth factors, receptors, signal transducers, and nuclear proteins including transcriptional factors (Polsky and Cordon-Cardo, 2003; Zhang et al., 2005a, 2005b, 2005c), among these, cell-cycle-related proteins such as cyclin D and cyclin-dependent kinase (CDK)s have been demonstrated to play a major role in tumorigenesis (Johnson and Walker, 1999; Osborne et al., 2004; Semczuk and Jakowicki, 2004; Sherr, 1996).

Cell-cycle-related proteins precisely regulate cell proliferation. CDK4/6 and CDK2 pair with their cyclins (cyclin D, E) to control cell progression through G1 to S phase (Johnson and Walker, 1999; Lee and Yang, 2003; Sherr, 1996). Cyclin D/CDK4 or cyclin D/CDK6 complex forms in early G1 phase and functions during the whole G1 to S phase transition (Lee and

Significance

Many genes have been attributed to tumorigenesis; however, additional unknown genes are to be characterized in human tumors. In this study, we found a gene named *CREPT* that is highly expressed in human tumors and is correlated with short survival time of cancer patients. We revealed a mechanism where CREPT promotes cell proliferation by enhancing transcription of *CYCLIN D1*. CREPT prevents RNAPII from "reading through" and possibly promotes the recycling of RNAPII to the promoter of genes via the formation of a chromatin loop. We provided evidence that tumor cells with a high level of CREPT use "antiterminator" instead of "torpedo" model to accelerate transcription of *CYCLIN D1*. Our study provides insights on the mechanisms of tumorigenesis.

Yang, 2003), and phosphorylates the retinoblastoma protein (RB), which activates the transcription factor E2F. The cyclin E/CDK2 complex forms in mid to late G1 phase and is important for S phase entry (Obaya and Sedivy, 2002). Activities of these cyclins/CDKs can be regulated by CKIs (CDK inhibitors, such as $p15^{INK4b}$, $p16^{INK4a}$, $p21^{CIP1/WAF1}$, $p27^{KIP1}$, and $p57^{KIP2}$), which act as tumor suppressors, at the protein level (Lee and Yang, 2003; Obaya and Sedivy, 2002). The G1/S transition and progression in the S phase also requires the cyclin A/CDK2 complex. Furthermore, cyclin A2 and cyclin B1 form a complex with CDK1 and function in the G2/M transition.

Several oncoproteins positively regulate cyclins and CDKs but negatively regulate CKIs in tumor development (Felsher, 2003; Polsky and Cordon-Cardo, 2003; Zhang et al., 2005a, 2005b, 2005c). Great efforts have been put on the identification and characterization of these proteins (Felsher, 2003; Hunter and Pines, 1994; Massagué, 2004). To date, different screenings have been performed and numerous oncogenes have been found (Dickins et al., 2005; Gordon et al., 2005); however, additional unknown genes are likely involved in tumor development and it is important to identify and characterize novel genes that regulate tumorigenesis (Bonetta, 2005).

In a search for genes related to tumors, we performed a database homology screen using a recently isolated gene (*p15rs*), which is functionally linked to $p15^{INK4b}$ (Liu et al., 2002) and inhibits cell proliferation (Wu et al., 2010), and identified a gene *CREPT* (cell-cycle-related and expression-elevated protein in tumor). Here, we demonstrate the role of CREPT in tumorigenesis.

RESULTS

CREPT Is a Homolog of *Rtt103* and Highly Conserved across Species

Similarity searches of the NCBI protein database with a recently reported protein p15RS (Liu et al., 2002) identified a gene with no reported function. We named this gene *CREPT* (cell-cycle-related and expression-elevated protein in tumor) based on our later observation that this gene is related to the cell cycle and highly expressed in tumors (GenBank accession numbers DQ372938, DQ372939, DQ372940). Human (h) *CREPT* encodes a protein of 326 amino acids with a high similarity to p15RS (Figure S1A available online). CREPT contains an RPR domain (regulation of nuclear pre-mRNA, or CID, CTD-interacting domain) and is highly conserved across species (Figures S1B and S1C). In yeast, the homologous gene is called *Rtt103* (Scholes et al., 2001; Tong et al., 2001). A phylogenetic analysis indicates that two genes, *CREPT* and *p15RS*, in mammals, birds, fish, and *Arabidopsis* are homologs of yeast *Rtt103*, whereas in nematode, fly, and frog only one homolog is predicted (Figures S1B and S1C).

CREPT Is Highly Expressed in Human Tumor Tissues

To investigate the role of CREPT in human diseases, we screened samples from patients with cancers using a monoclonal antibody we generated (Figure S1D). We found that CREPT is more highly expressed in tumor tissues from colon cancer patients (Figure 1A), whereas in the paired noncancer tissues it is hardly (patients 1, 3, and 7) or weakly (patients 2, 4, 5, and 6) detected (Figure 1A, top panel). High levels of CREPT protein are in concordance with its mRNA levels in the tumor tissues (Figure 1A, bottom panel).

Elevated expression of CREPT is not limited just to the colon cancer, as we demonstrated that CREPT mRNA expression is elevated in other cancers including lung, liver, breast, prostate, stomach, uterine endometrium, and cervix cancers (Table 1). Patient samples (eight patients for each cancer are shown in Figure S1E) demonstrate that CREPT expression is dramatically enhanced in all cancer tissues compared to the paired noncancer tissues. In many cases, we could not detect the expression of CREPT in noncancer tissues but observed high levels in cancer tissues. In some cases, we detected relative high levels of CREPT expression in noncancer tissues, but the levels were always lower than those in the paired cancer sections (e.g., colon cancer patient 1, breast cancer patient 7, liver cancer patients 2 and 6 in Figure S1E).

Immunohistochemistry (IHC) analyses with an anti-CREPT antibody showed strong expression of CREPT in tumor regions compared to paired nontumor regions in the same patients (Figure 1B). The results also demonstrated that CREPT is highly expressed in the nucleus of tumor cells (Figure 1B, enlarged images). The nuclear localization was confirmed by overexpression of GFP-CREPT (Figure S1F) or immunostaining with an anti-CREPT antibody along with DAPI in HeLa and HEK293T cells (Figure S1G). Clearly, few CREPT positive staining cells can be observed in the nontumor regions, whereas most of the cells were negatively stained (Figure 1B).

In total, we examined 347 cases by RT-PCR and 466 cases by IHC analyses for patients with eight different types of cancers. Significantly elevated levels of CREPT mRNA or protein were found in 83.3% or 86.5%, respectively, in tumor compared to nontumor tissues from cancer patients (Table 1). Interestingly, a survival analysis of 117 stomach cancer patients indicated that positive CREPT staining was significantly correlated with shorter survival time of the patients after surgery and treatment (Figure 1C). CREPT is also highly expressed in most tumor cell lines examined (Figure S1H).

CREPT Promotes Cell Proliferation In Vitro

Elevated expression of CREPT in tumor cells suggests a role in cell proliferation. Since cells maintain high proliferation ability during embryonic development, we sought to examine the level of CREPT in different stages of the mouse embryos and young mice. An RT-PCR and a northern analysis indicated that CREPT was highly expressed during early stages of mouse embryonic development (Figure S1I). CREPT expression was observed in different normal tissues from mice after birth but remained at low levels in adult mouse tissues (Figure S1J). An IHC analysis showed that 10 days after birth tissues that highly expressed CREPT had correlated high levels of cyclin D1 and Ki67, two cell proliferation markers (Figure S1K). These results suggest that CREPT plays a critical role in cell proliferation during embryogenesis and mouse development.

To address whether CREPT affects cell proliferation, we stably overexpressed or depleted CREPT in MGC803 cells. The results showed that cells overexpressing CREPT proliferated more rapidly than the mock cells (Figure 2A), whereas cells

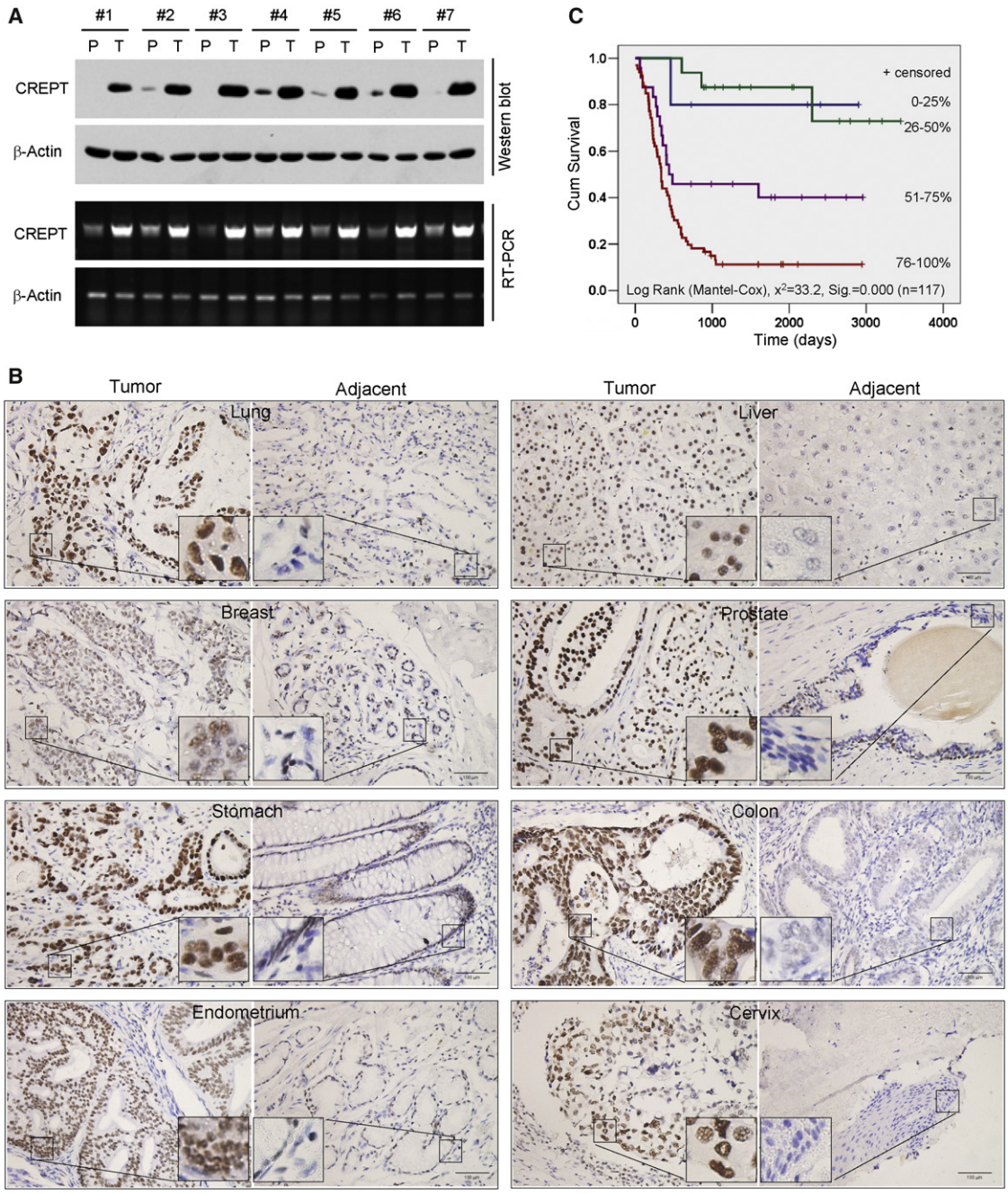

Figure 1. CREPT Is Highly Expressed in Tumor Tissues

(A) CREPT is highly expressed in colon cancer. RT-PCR and western blotting were performed in colon cancer samples. P refers to paired nontumor tissue and T tumor tissue from the same patient.

(B) CREPT is highly expressed in different tumor tissues. Immunohistological staining assays were performed with an anti-CREPT antibody (DAB staining, scale bars, 100 μm).

(C) Expression of CREPT correlates with the survival time of stomach cancer patients. A tissue array analysis was done in 117 cases of patients with the survival information. The percentage of CREPT-positive cells (%) was determined by counting five random views of each sample at 400-fold magnification.

See also Figure S1.

with depleted CREPT grew more slowly than the mock-si cells (Figure 2B). Consistently, overexpression or depletion of CREPT in HepG2 (Figure 2C) and HeLa (Figure S2A) cells led to accelerated or inhibited cell proliferation. In addition to HepG2 and HeLa cells, which are of tumor origin, we also observed similar results in a tetracycline induced CREPT-over-expression system in NIH 3T3 cells (Figure S2B), which are of fibroblast origin and expresses low endogenous CREPT

Table 1. Enhanced Expression of CREPT in Different Tumors Assessed by RT-PCR and Immunohistochemistry

	Upregulated Expression[a] (%)	
Tumor Organs	RT-PCR	Immunohistochemistry
Lung	57.1 (8/14)	75.9 (22/29)
Liver	86.9 (186/214)	73.8 (118/160)
Breast	75.0 (21/28)	77.1 (27/35)
Prostate	100.0 (8/8)	100.0 (8/8)
Stomach	70.0 (14/20)	88.3 (128/145)
Colon	75.0 (15/20)	80.9 (55/68)
Uterus endometrium	79.0 (15/19)	79.2 (19/24)
Uterine cervix	91.7 (22/24)	89.7 (26/29)
Total	83.3 (289/347)	86.5 (403/466)

[a] Upregulated expression was defined as those the expression of CREPT in tumor side is greater than that in paired nontumor side. The numbers in parentheses refer to number of tumors showing increased expression/total number of tumors.

(Figure S1I). Taken together, these results demonstrated that CREPT functions as a positive regulator of cell proliferation in both tumor-originated (epithelial) and nontumor-originated (fibroblastic) cells.

CREPT Promotes Tumorigenesis In Vitro and In Vivo

Since CREPT is highly expressed in tumors and promotes cell proliferation, we speculated that CREPT might enhance tumorigenesis. To examine this hypothesis, we first performed a colony formation assay in soft agar. The result showed that HepG2 cells stably overexpressing CREPT produced more colonies, whereas cells depleted of CREPT yielded fewer colonies than mock cells (Figure 2D). Similar results were observed with HeLa cells (Figures S2C and S2D).

To investigate whether CREPT accelerates tumorigenesis in vivo, we injected cells into nude mice and observed tumor growth. The result showed that CREPT-overexpressing cells generated larger tumors than control cells, whereas CREPT-depleted cells formed smaller tumors (Figures 2E and 2F). In addition, tumor appearance time (defined as the day when the tumors become palpable after injection) was shortened to 6 days when CREPT was overexpressed, whereas depleting CREPT expression delayed tumor appearance by additional 4.5 days (Figure 2G). Furthermore, we observed that tumors originating from cells with CREPT overexpression showed higher malignancy and much stronger proliferation ability as indicated by HE staining (Figure S2E) and immunostaining with an anti-PCNA antibody (stronger PCNA expression in CREPT overexpressed cells) (Figure S2F).

To address whether CREPT causes the transformation of cells, we overexpressed CREPT in tetracycline inducible NIH 3T3 cells. A soft agar experiment showed that cells with overexpressed CREPT formed colonies (Figure S2G). Consequently, NIH 3T3 cells overexpressing CREPT formed tumors in nude mice, whereas control cells had no ability to form tumors (Figure S2H). These data suggested that CREPT promotes tumor growth in vitro as well as cell transformation in NIH 3T3 cells.

CREPT Alters the Cell Cycle

A FACS analysis was performed to determine whether CREPT enhances cell growth and promotes tumorigenesis via alteration of the cell cycle. The size of the cell population in the S phase is significantly increased with overexpression of CREPT 12 hr after release from synchronization, whereas that in the G1 phase remains at a low level at this same time point in MGC803 cells (Figure 3A; Figure S3A). In contrast, the reversed effect was observed when CREPT was depleted (Figure 3B; Figure S3B). The proportion of cells in the G2/M phase was either slightly decreased or unchanged when CREPT was overexpressed (Figure 3A) or depleted (Figure 3B). Similar results were observed with HeLa (Figure S3C) and HepG2 (Figure S3D) cells. Furthermore, when CREPT was overexpressed in NIH 3T3 cells, we also observed more cells in the S phase (Figure 3C). By determining the length of each phase, we found that the overexpression of CREPT shortened the cell cycle in HeLa cells (Figure S3E). These results indicate that CREPT alters the cell cycle by promoting the G1 to S phase transition.

CREPT Regulates Expression of Genes Controlling the Cell Cycle

Given that the cell cycle was altered by the overexpression or depletion of CREPT, we addressed whether CREPT affects the expression of cell-cycle-related genes. Since CREPT affected the G1 to S phase transition (Figures 3A and 3B), we focused our attention on genes for activators (CDK4/6/cyclin D1 and CDK2/cyclin E/A), inhibitors ($p15^{INK4b}$/16^{INK4a} and $p21^{CIP1/WAF1}$/27^{KIP1}), as well as downstream genes such as RB, E2F1, and PCNA during cell-cycle regulation. An RT-PCR analysis indicated that the cyclin D1, CDK6, and CDK4 mRNA levels increased dramatically when CREPT expression was induced by the withdrawal of tetracycline in the NIH 3T3 cells (Figure 3D; Figure S3F). In contrast, cyclin A, $p21^{CIP1/WAF1}$, and $p27^{KIP1}$ remained constant and $p15^{INK4b}$, $p16^{INK4a}$, and RB decreased. Both cyclin E and CDK2 were also increased when CREPT was overexpressed (Figure 3D; Figure S3F). Similar results were observed when CREPT was overexpressed in HeLa cells (Figure S3G, left two lanes) and the reverse trend for the cell-cycle-related gene expression was observed when CREPT was depleted by an siRNA in HeLa cells (Figure S3G, right two lanes). Among these genes, we found that the *CYCLIN D1* gene, in particular, responded to the CREPT alteration quickly (Figure 3D). These data suggested that CREPT regulates expression of cell-cycle-related genes.

CREPT Enhances Gene Transcription Specifically

To examine whether changes in mRNA levels of genes that CREPT regulated are at the transcription level, we performed nuclear run-on experiments. The result indicated that transcription of CDK4/6, cyclin D1, CDK2, and cyclin E was enhanced when CREPT was overexpressed and almost completely abolished when CREPT was depleted (Figure 4A). In contrast, transcription of $p15^{INK4b}$, $p16^{INK4a}$, and RB was blocked by CREPT overexpression, and this inhibition was released when CREPT was depleted. These data suggest that CREPT regulates the expression of CDK4/6, cyclin D1, CDK2, and cyclin E at the transcriptional level. Moreover, the regulation is gene specific

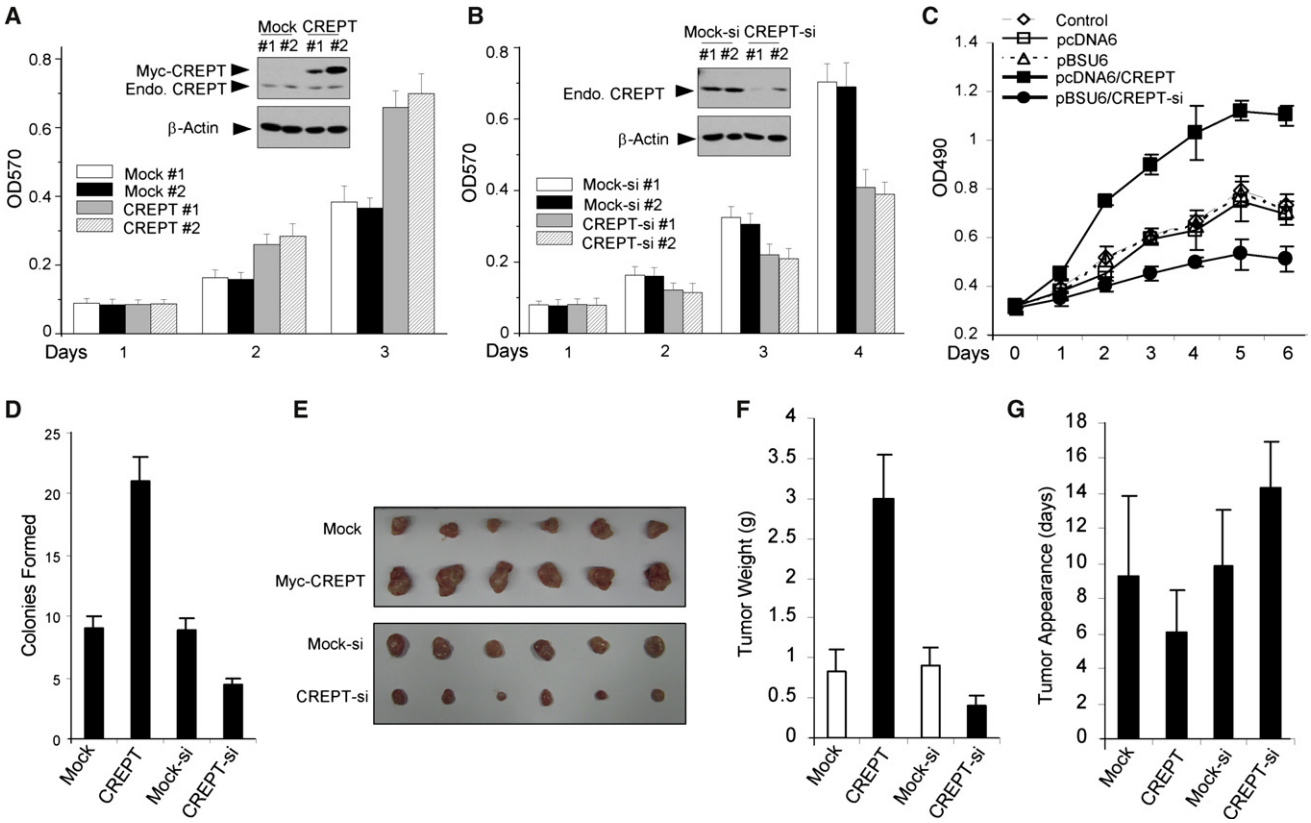

Figure 2. CREPT Promotes Cell Proliferation and Tumorigenesis

(A) Overexpression of CREPT enhances cell growth. Cell lines originating from the MGC803 cell line (a stomach cancer cell line) were established with stable overexpression of CREPT (western blot panels) and measured by an MTT assay. Endo. CREPT indicates the endogenous expression of CREPT. Error bars represent ±SD.

(B) Depletion of CREPT suppresses cell growth. MGC803 cells were stably transfected with an siRNA targeting CREPT.

(C) CREPT accelerates cell growth in HeLa cells. Cell proliferation was examined by MTT experiments in HeLa cells with stable overexpression (pcDNA/CREPT) or depletion (pBS/U6/CREPTi) of CREPT.

(D) CREPT promotes colony formation. One thousand cells from indicated cell lines based on HepG2 cells were seeded into soft agar. Colonies were stained with crystal violet and counted. Bars represent ±SD from three independent experiments.

(E–G) CREPT promotes tumor growth. Six nude mice were injected subcutaneously with 5×10^6 cells/mouse for each of the indicated stable cell lines. Results are shown as isolated tumors (E), tumor weights (F), and tumor appearance times (G). si refers to siRNA.

See also Figure S2.

because cyclin A, $p21^{CIP1/WAF1}$, and $p27^{KIP1}$ transcriptions were not affected (Figure 4A).

To investigate how CREPT activates the transcription of targeted genes, we selected the *CYCLIN D1* promoter (Herber et al., 1994) as this gene quickly responded to the elevation of CREPT expression (see Figure 3D). Assays of the luciferase reporter gene linked to the native *CYCLIN D1* promoter (Figure S4A) showed that overexpression of CREPT enhanced the luciferase activity, whereas depletion of CREPT decreased the activity (Figure 4B; Figure S4B, also Figures S4C and S4D). A nuclear run-off experiment with the *CYCLIN D1* promoter-luciferase reporter indicated that addition of nuclear extracts from CREPT-overexpressing cells increased transcription in vitro, whereas, in the presence of nuclear extracts from CREPT-depleted cells, no transcripts were detected (Figure 4C). In another nuclear run-off experiment using purified GST-CREPT protein (Figure S4E) together with nuclear extracts from HeLa cells, we observed that addition of GST-CREPT protein increased transcription in a dosage dependent manner in vitro (Figure 4D). Taken together, these data suggest that CREPT enhances the transcriptional activity of the *CYCLIN D1* promoter both in vivo and in vitro.

CREPT Interacts with RNAPII Physically

To reveal factors involved in transcription regulation by CREPT, we performed an immunoprecipitation (IP) experiment in HEK293T cells overexpressing Myc-CREPT. A mass spectrometry analysis identified RNAPII as an interacting protein with Myc-CREPT (Figure 5A). The interaction of CREPT with RNAPII occurred at the RPR domain as demonstrated by an IP experiment with Flag-tagged CREPT (Figure 5B), which is consistent with the observation that the RPR domain of yeast Rtt103 interacts with RNAPII (Kim et al., 2004). Furthermore, reciprocal IP analyses indicated that endogenous CREPT and RNAPII interacted (Figures 5C and 5D) and purified GST-CREPT protein pull-down RNAPII (Figure 5E), suggesting that CREPT

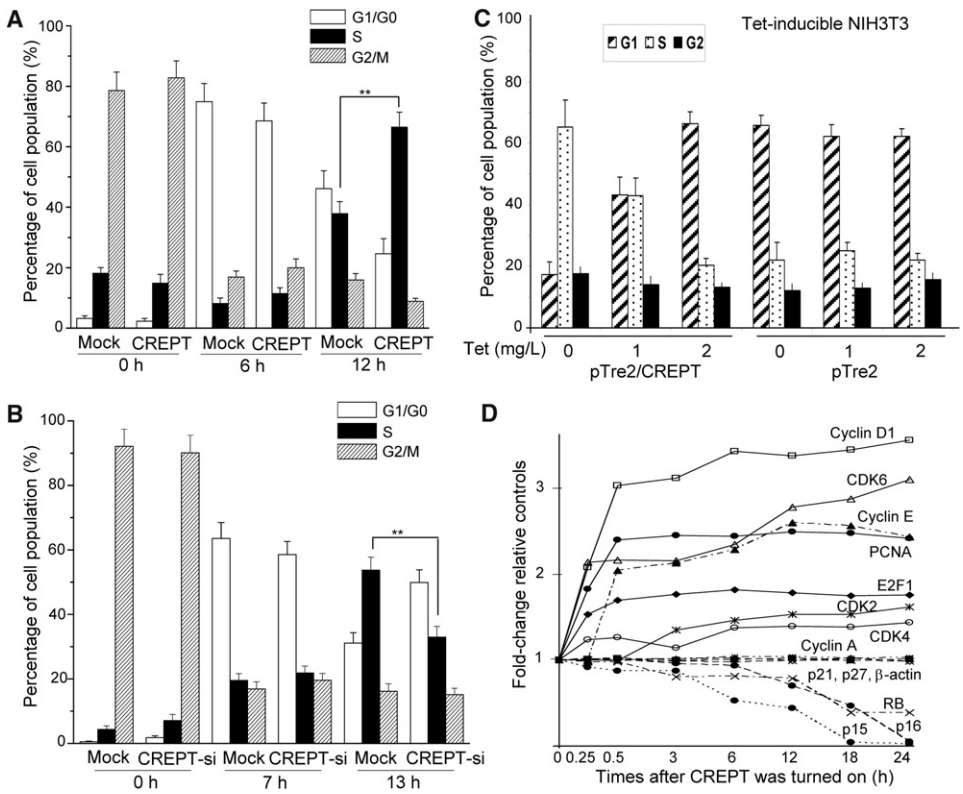

Figure 3. CREPT Alters the Cell Cycle and Cell-Cycle-Related Gene Expression

(A and B) Overexpression (A) and depletion (B) of CREPT in MGC803 cells alters the proportion of cells in the G1 and S phase. Cells were stained by propidium iodide at the indicated time after release from synchronization with nocodazole (200 ng/ml) for 18 hr. Sizes of cell populations averaged from three independent experiments with standard deviations. **$p < 0.01$.

(C) CREPT alters the cell cycle in a Tet-off system. A stable cell line was established for CREPT expression in NIH 3T3 cells under the control of tetracycline (Tet) off system. Ectopical CREPT expression is regulated by the withdrawal of Tet. pTRE2 is an empty vector. Cells were synchronized by starvation for 24 hr.

(D) CREPT alters the expression of cell-cycle-related genes. A quantitative representation of the time response to changes of gene expression as a consequence of ectopically expressed CREPT from a Tet-controlled expression system in NIH 3T3 cells. The complete withdrawal of Tet (Ectopic CREPT expression is turned on) was considered to be time point 0 and used for calculating fold change. The results are presented as fold changes relative to controls where ectopic CREPT is off.

See also Figure S3.

interacts with RNAPII in vivo and in vitro. These results imply that CREPT regulates the transcription of cyclin D1 via directly interacting with RNAPII.

CREPT Promotes RNAPII Occupancy on the *CYCLIN D1* Gene

To examine whether CREPT functions with RNAPII in the regulation of transcription of cyclin D1, we first addressed whether CREPT is involved in the *CYCLIN D1* promoter complex. Chromatin immunoprecipitation (ChIP) assays using different primers across the *CYCLIN D1* gene (Figure 6A) showed that promoter region B of *CYCLIN D1* was strongly precipitated down by an anti-CREPT antibody and that overexpression of CREPT enhanced the precipitation significantly, whereas depletion of CREPT abolished precipitation (Figures 6B and 6C). Although most of the other regions were not precipitated, region F, just before the poly(A) cleavage site, was precipitated in the presence of overexpressed CREPT, similar to the result for promoter region B (Figures 6B and 6C). These results suggest that CREPT crosslinks strongly to the *CYCLIN D1* promoter region, and also to a region related to transcription termination at the 3′ end of the gene.

Next, we analyzed the influence of CREPT on RNAPII binding density across the *CYCLIN D1* gene. A ChIP experiment indicated that strong binding of RNAPII to the promoter region B occurred in the presence of overexpressed CREPT, but only weak binding with the depletion of CREPT (Figures 6D and 6E), suggesting that CREPT enhances RNAPII binding to the *CYCLIN D1* promoter. However, CREPT did not affect RNAPII binding to regions C, D, and E of the *CYCLIN D1* gene, implying CREPT does not affect transcription elongation. Intriguingly, CREPT enhanced RNAPII binding to region F, a region before the poly(A) site, and reduced RNAPII binding to region G after the poly(A) site. In contract, depletion of CREPT resulted in less binding of RNAPII in regions B and F, but increased RNAPII binding to region G (Figures 6D and 6E). These results suggest that CREPT stops RNAPII from moving beyond the poly(A) site.

The enhanced binding of RNAPII in both the promoter (B) and termination (F) regions suggested that CREPT might promote recycling of RNAPII from the terminator to the promoter region.

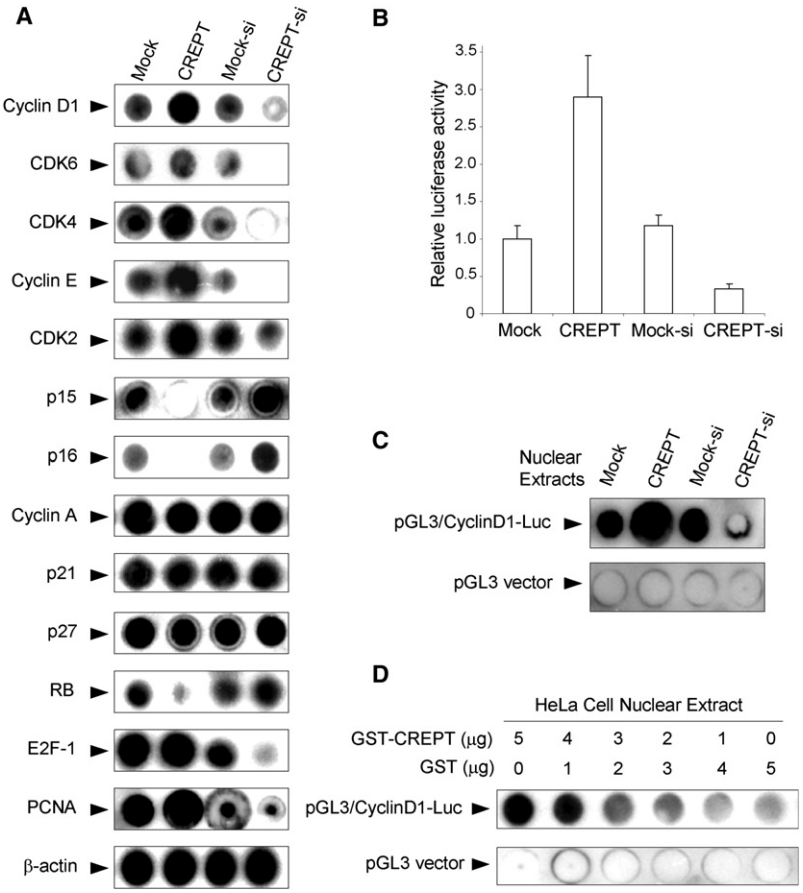

Figure 4. CREPT Accelerates *CYCLIN D1* Transcription

(A) CREPT regulates transcription of cell-cycle-related genes. Nuclear run-on assays, showing the transcriptional level of indicated genes in HepG2 cells where CREPT was stably overexpressed or depleted, were performed.

(B) CREPT activates transcription of *CYCLIN D1*. A luciferase reporter linked with the full-length native promoter of the *CYCLIN D1* gene was used for the luciferase assay. Results were normalized with internal controls and presented as averages with standard deviations from three repeats.

(C) CREPT enhances the transcriptional activity of the *CYCLIN D1* promoter. A nuclear run-off assay was performed with templates linearized from a luciferase reporter linked with a short fragment of the native *CYCLIN D1* promoter (186 bp). Nuclear extracts were from HEK293T cells transfected with indicated plasmids for overexpression or depletion of CREPT. Transcripts were dotted onto membranes and detected with a labeled probe from the luciferase reporter.

(D) CREPT activates transcription of CYCLIN D1 in vitro. Purified GST-CREPT proteins were added to the nuclear extract from HeLa cells and a nuclear run-off assay was performed using the same templates as in (C).

See also Figure S4.

To examine this hypothesis, we used a chromosome conformation capture (3C) experiment (Dekker et al., 2002) to test whether CREPT promotes RNAPII to drive the *CYCLIN D1* gene forming a chromatin loop (Figure 6F). For the 3C experiment, we chose primers that do not crossreact and have high specificity to observe loop formation. Indeed, a strong loop band was observed in cells when CREPT was overexpressed and the band was diminished when CREPT was depleted (Figures 6G and 6H). To avoid possible random ligation during the 3C experiment, we used DNA-protein complexes that were precipitated down by an anti-RNAPII antibody (8WG16) and performed the 3C experiment with and without ligation in combination with NcoI digestion. The results showed that the anti-RNAPII antibody precipitated down a strong cycled band when CREPT was overexpressed (Figure 6I). These data indicate that CREPT promotes loop formation to bring RNAPII physically close to the transcription start site, implying that CREPT may enhance RNAPII recycling from the terminator to the promoter region during transcription of the *CYCLIN D1* gene.

CREPT Regulates the Transcription of the *CYCLIN D1* Gene in Tumors

We have proposed a mechanism where CREPT enhances RNAPII binding to the *CYCLIN D1* promoter and terminator regions thereby driving the *CYCLIN D1* gene to form a chromatin loop. To examine whether CREPT functions to promote the chromatin loop formation in tumors, we investigated 12 cases of colon cancers. A western blot analysis showed a correlation of expression of CREPT and cyclin D1 in the tumor tissues where in most patients, elevated expression of CRPET is coupled with high levels of cyclin D1 (Figure 7A, patients 7 and 8 being the exceptions). The positive correlation of CREPT, cyclin D1, and Ki67 expression was confirmed, by IHC experiments, in these patient samples (Figure 7B), similar to that observed for several other cancers including stomach, lung, prostate, endometrium, liver, and breast cancers (Figure S5). Next, we performed a ChIP assay with tumor samples from three patients (2, 4, and 12) with the results showing that CREPT binds strongly to regions B and F of the *CYCLIN D1* gene (Figure 7C). These results are consistent with the results from cells overexpressing CREPT (Figure 6D), with RNAPII strongly binding to regions B and F and weakly to region G of the *CYCLIN D1* gene in tumor tissues (Figure 7D). Finally, we addressed whether the *CYCLIN D1* gene forms a chromatin loop in tumors. A 3C experiment showed a strong band in tumor tissues (Figure 7E), suggesting that a chromatin loop is formed in the cells of tumor tissues. All of the data indicate that CREPT promotes chromatin looping of the *CYCLIN D1* gene in tumor cells, which results in an increased binding of RNAPII to both the promoter and 3′ end regions.

DISCUSSION

Many genes are known to be associated with tumor formation; however, additional genes remain to be identified and characterized (Gordon et al., 2005). Here, we report a gene *CREPT* that is highly expressed in different tumors and is an oncogene

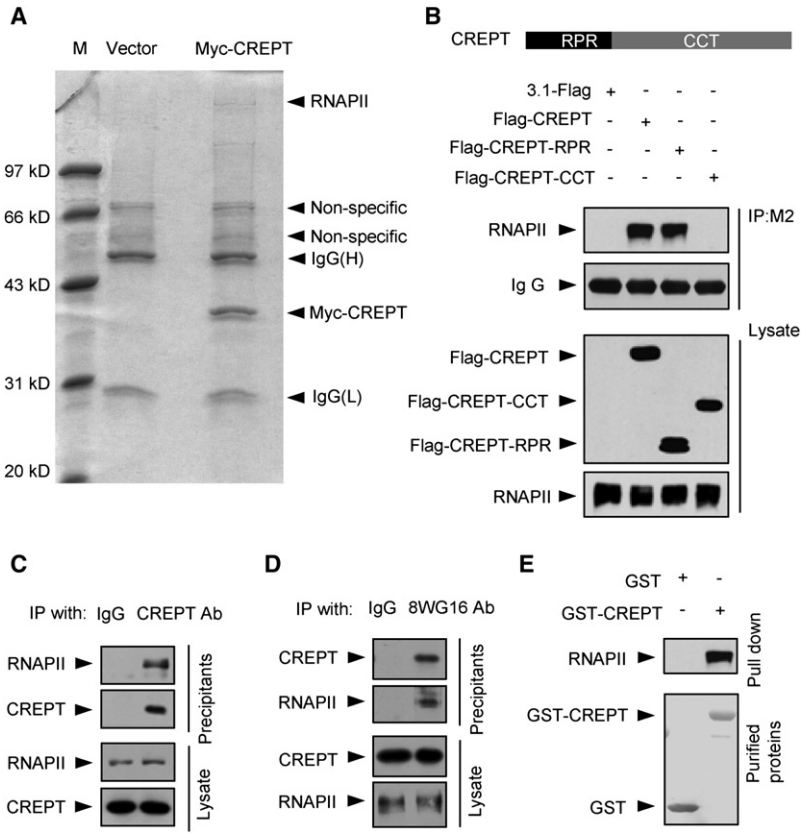

Figure 5. CREPT Interacts with RNAPII

(A) A mass spectrometry analysis of proteins associated with CREPT. HEK293T cells were transfected with pCDNA 3.1/Myc or Myc-CREPT and cell lysates were immunoprecipitated using an anti-Myc antibody. Precipitants were analyzed by an SDS-PAGE gel and stained with Coomassie blue. Bands were cut out and identified by a mass spectrometry analysis.

(B) CREPT interacts with RNAP II. Schematic illustration of CREPT and its deletions are presented on the top panel. RPR domain and CCT (coiled coil terminus) are shown. HEK293T cells were transfected with Myc-tagged full-length and two deletions of CREPT. Cell lysates were immunoprecipitated using an anti-Myc antibody and the precipitants were detected with an anti-RNAP II antibody (8WG16).

(C and D) Endogenous CREPT interacts with RNAP II in vivo. IP experiments were performed with an antibody against CREPT under the normal condition (C) and reciprocally with an antibody against RNAPII (8WG16) under fixation with formaldehyde (4%) (D).

(E) CREPT interacts with RNAP II in vitro. A GST pull-down assay was performed with purified GST or GST-CREPT protein.

based on the observations that CREPT accelerates the malignant cell growth and tumorigenesis. An anti-CREPT antibody clearly defined tumor boundaries, although a few positive staining cells were observed occasionally in the paired nontumor sections. These results suggest that CREPT could be used as a marker to diagnose tumors.

Cell-cycle alteration is a major feature of tumorigenesis (Johnson and Walker, 1999), which occurs by shortening the G1 phase (Hall and Peters, 1996; Hunter and Pines, 1994; Sherr, 1996). In this study, we observed that CREPT increased the proportion of cells in the S phase and, since no major change in the G2/M phase cell populations was observed when CREPT was overexpressed, we concluded that CREPT accelerates the G1 to S phase transition, and thus a shorter G1 phase, similar to the effects of many other oncogenes (Massague, 2004; Sherr, 1996). Consistently, we found that CREPT enhanced the expression of cell-cycle-related genes. Among the genes functioning during the G1 and S phase transition, we observed that the *CYCLIN D1* gene quickly responded to changes in CREPT expression; therefore, we used *CYCLIN D1* as an example to study the molecular mechanisms by which CREPT promotes cell proliferation.

CREPT contains an RPR domain, which is predicted to function in the 3′ end processing of mRNA (Doerks et al., 2002) and is a homolog of the yeast *Rtt103* gene. Previous studies implicated Rtt103 function in Ty1 transposition (Scholes et al., 2001) and in cell viability and growth (Tong et al., 2001). The Rtt103 protein was found in RNAPII complexes associated with other factors (Rat1, Pcf11) (Kim et al., 2004). Similar to the polyadenylation factors Rna14, Rna15, and Pcf11, Rtt103 was reported to strongly bind near the 3′ end of genes and to help Rat1 in degrading mRNA downstream of poly(A) site cleavage (Kim et al., 2004), supporting the "torpedo" model in the termination of transcription (Buratowski, 2009; Connelly and Manley, 1989; Moore and Proudfoot, 2009; Proudfoot, 1989). Previous IP experiment and structure-based analyses indicated that Rtt103 preferred to bind to Ser2P CTD of RNAPII (Kim et al., 2004; Lunde et al., 2010), downstream of the poly(A) site at the 3′ end of genes in yeast. To our surprise, we observed that CREPT bound not only to the region BEFORE the poly(A) site, but also to the promoter region of the *CYCLIN D1* gene. Interestingly, CREPT promotes RNAPII binding to both the promoter and the termination region before the poly(A) site and decreases RNAPII binding to the region after the poly(A) site. Together with our results from the 3C experiments, we propose that CREPT helps RNAPII recycle from the termination site to the promoter region of the *CYCLIN D1* gene through a chromatin loop (Figure 6F). CREPT binding to the 3′ end of the gene appears to prevent RNAPII from "reading through," and allows RNAPII to be recruited back to the promoter. The function of CREPT in binding to the 3′ end of *CYCLIN D*1 gene revealed in this study supports the allosteric (antiterminator) model for transcription termination (Luo and Bentley, 2004; Moore and Proudfoot, 2009), a model that explains the recycling of RNAPII from the termination to the promoter site (Mapendano et al., 2010).

Gene looping has been observed in the regulation of gene transcription in both yeast (O'Sullivan et al., 2004) and mammalian cells (Perkins et al., 2008; Tan-Wong et al., 2008). In this study, we observed that CREPT promotes loop formation at *CYCLIN D1*. We envisioned that this loop formation might

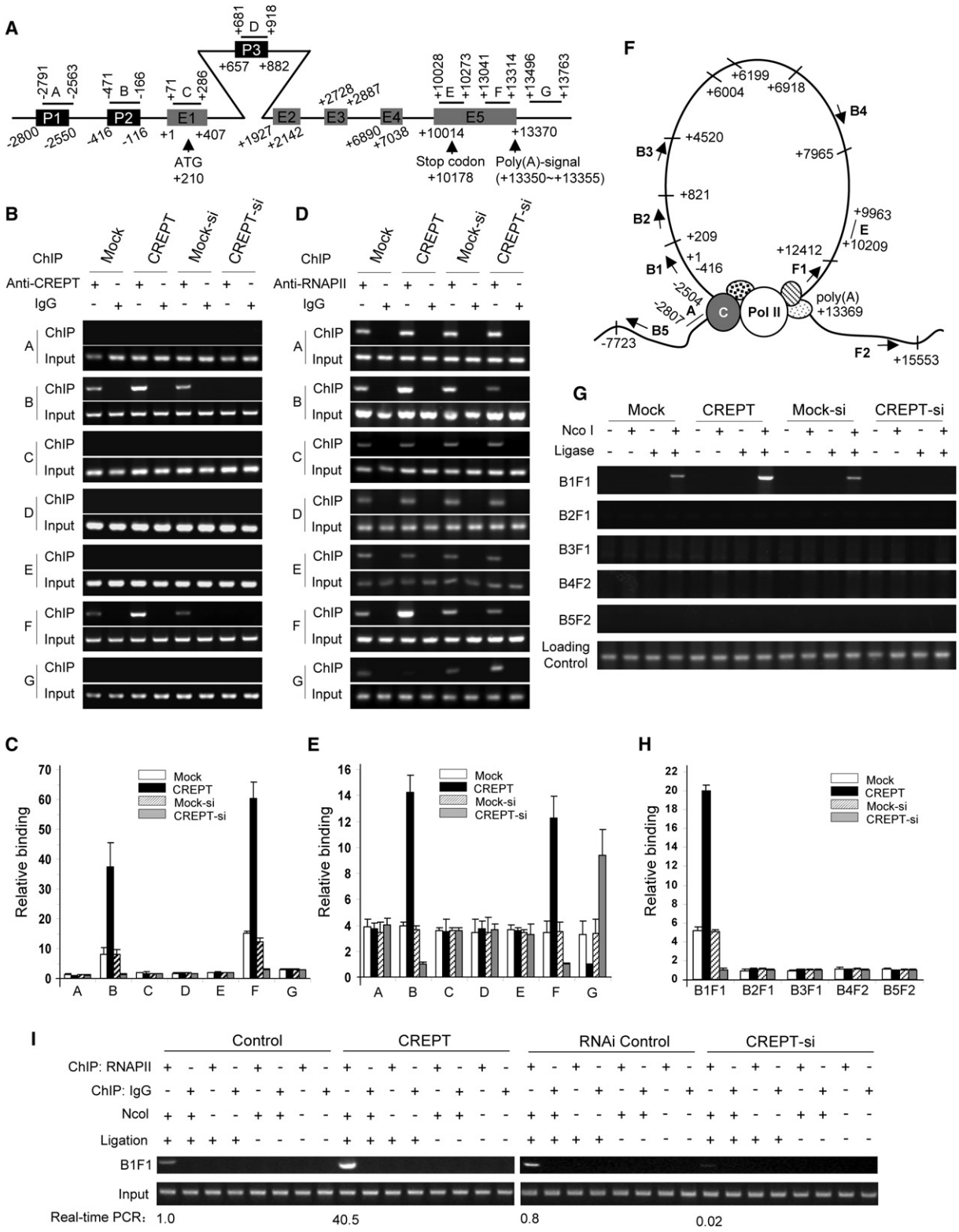

Figure 6. CREPT Promotes RNAPII Recycling in the *CYCLIN D1* Gene

(A) A graphic representation of the *CYCLIN D1* genomic structure. P1, P2, and P3 are predicated promoter regions. The P2 promoter has been functionally defined as the site of initiation of transcription of the *CYCLIN D1* gene. E1 to E5 represent exons. Numbers indicate the nucleotides counting from the primary transcription start site as +1. Fragments detected by PCR are shown as A to G.

facilitate the recycling of RNAPII and accelerate transcription. However, we could not exclude the possibility that CREPT has independent functions at the promoter region, as an activator, and the terminator. It is possible that CREPT may function directly in the promoter region to enhance the initiation of transcription and thereafter promote loop formation. We cannot exclude the possibility that the loop is required for enhanced transcription. It is possible that the loop functions as an enhancer, as has been observed for the estrogen receptor positive enhancer of the *CYCLIN D1* gene in breast cancer (Eeckhoute et al., 2006). In this study, we conclude that the loop formation is coupled with transcription initiation, possibly acting as an enhancer, as we found that CREPT associates with RNAPII.

Yeast Rtt103 appears to only function as a factor in transcriptional termination (Kim et al., 2004) as the RPR domain of Rtt103 binds to the Ser2P CTD of RNAPII in yeast (Lunde et al., 2010). Here, we observed that CREPT binds to both the promoter and the 3′ end of the *CYCLIN D1* gene. CREPT appears to help RNAPII stop at the poly(A) site, functioning as a terminator for the gene transcription, a role conceivable since yeast Rtt103 has been shown to function as a termination factor. However, the role of CREPT at the 5′ end of a gene, in the regulation of the gene transcription, seems different from that of its yeast ortholog Rtt103. A difference in the roles of CREPT appears not only in the binding to the promoter, where yeast Rtt103 does not, but also in the way it facilitates termination. We demonstrated that knocking down CREPT resulted in readthrough of RNAPII past the 3′ end of the *CYCLIN D1* gene, whereas yeast Rtt103 was shown to help Rat1 and Rai1 increase the degradation of nuclear mRNA after RNAPII reads through the poly(A) site (Kim et al., 2004). Interestingly, CREPT and p15RS are both homologs of Rtt103 in mammals. Our previous study indicated that p15RS functions as an intrinsic inhibitor of Wnt signaling mediated transcription (Wu et al., 2010), a function different from the role of CREPT as an oncoprotein observed in this study. p15RS (Wu et al., 2010) and CREPT together, therefore, may provide more regulatory functions to mammalian cells than are provided by Rtt103 to yeast (Kim et al., 2004).

Intriguingly, we observed that CREPT is highly expressed in human tumors. When CREPT is depleted, tumor cells grow slowly, an observation that echoes the role of Rtt103 in maintaining yeast viability and growth (Tong et al., 2001). The role of CREPT in cell-cycle regulation is attributed to the specific regulation of cell-cycle-related genes. We used *CYCLIN D1* as a model to demonstrate a mechanism where CREPT regulates gene transcription via interacting with RNAPII at both the termination and promoter regions. Consistent with cell experiments, we observed that cells from human tumors have a strong chromatin loop in the *CYCLIN D1* gene. Of importance, we found that RNAPII together with CREPT accumulate in the promoter region (region B) and region (F) before the poly(A) site but released from DNA after the poly(A) site (see binding in region G) (Figure 7) in human tumors. In the absence of excess CREPT, others have shown that RNAPII accumulates in the region after the poly(A) site of the *CYCLIN D1* gene (Eeckhoute et al., 2006) and RNAPII release generally occurs after the poly(A) site (Lian et al., 2008), observations that supports the torpedo model of transcription termination (Buratowski, 2009; Connelly and Manley, 1989; Moore and Proudfoot, 2009; Proudfoot, 1989). In this study, we observed that CREPT promotes the accumulation of RNAPII in the F region, a region just before the poly(A) site. Interestingly, when CREPT was depleted it appears that RNAPII reads through the poly(A) site, the situation that has generally been observed by others (Eeckhoute et al., 2006; Lian et al., 2008). Our results, therefore, describe conditions where both the torpedo and the antiterminator models are involved in the termination of gene transcription (Kim et al., 2004; Moore and Proudfoot, 2009). Cells appear to use the antiterminator mechanism to accelerate transcription of *CYCLIN D1* when CREPT is overexpressed in tumors and the torpedo model to maintain a lower level of cyclin D1 expression when CREPT is low as found in normal or slowly proliferating cells. This study illustrates a case where a gene can use different models for transcription termination (Buratowski, 2009).

Many questions remain concerning the function of CREPT. For example, what causes tumor cells to express CREPT at such high levels? How does CREPT enhance RNAPII binding to the *CYCLIN D1* promoter? Does CREPT enhance transcription termination by mechanisms similar to other RPR domain containing proteins (Kim et al., 2004)? How does CREPT specifically regulate gene expressions at the global genome level? Do other specific factors regulate the activity of CREPT? Answering these questions will help our understanding of the mechanisms of cell-cycle regulation, transcription control, and tumorigenesis. In conclusion, we reported that *CREPT* is a highly conserved

(B and C) CREPT crosslinks to a promoter region and the pre-poly(A) cleavage site in the *CYCLIN D1* gene. ChIP analyses were performed in MGC803 cells under stable overexpression or depletion of CREPT. Precipitation was performed using an anti-CREPT antibody. Results from PCR (B) and real-time PCR (C) using indicated primers are presented. Error bars represent ±SD from three repeats. Input indicates the PCR products from cell lysates without immunoprecipitation. Mouse IgG was used as a negative control in the precipitation experiment.

(D and E) CREPT enhances RNAPII crosslinking to the promoter and the pre-poly(A) cleavage site and decreases binding to the post-poly(A) cleavage site of the *CYCLIN D1* gene. ChIP analyses were performed in MGC803 cells under stable overexpression or depletion of CREPT using an anti-RNAPII antibody (8WG16) with indicated primers for PCR (D) and real-time PCR (E) analyses. Input indicates the PCR products from cell lysates without immunoprecipitation. Mouse IgG was used as a negative control in the precipitation experiment. Error bars represent ±SD from three repeats.

(F) Diagram of the primers used in the 3C assay of the human *CYCLIN D1* genomic region and a model of the chromatin loop of the *CYCLIN D1* gene by CREPT and RNAPII. Vertical lines indicate the Nco I restriction endonuclease sites, short arrows mark the positions of primers used in the 3C assay (labeled B1-5 and F1-2). C indicates CREPT and Pol II for RNAPII.

(G and H) CREPT promotes the formation of a chromatin loop at the *CYCLIN D1* gene. Products of amplifications with various primers with purified 3C DNA is shown in (G). Region E of *CYCLIN D1* is used as a loading control. Real-time PCR analyses of the products of the 3C assay are shown in (H). Error bars represent ±SD from three repeats.

(I) Specificity of the chromatin loop formation is shown by a ChIP-3C experiment. PCR analyses were performed on RNAPII-containing precipitated complexes. Real-time PCR result is shown as relative fold increases based on the level of the control normalized to the input.

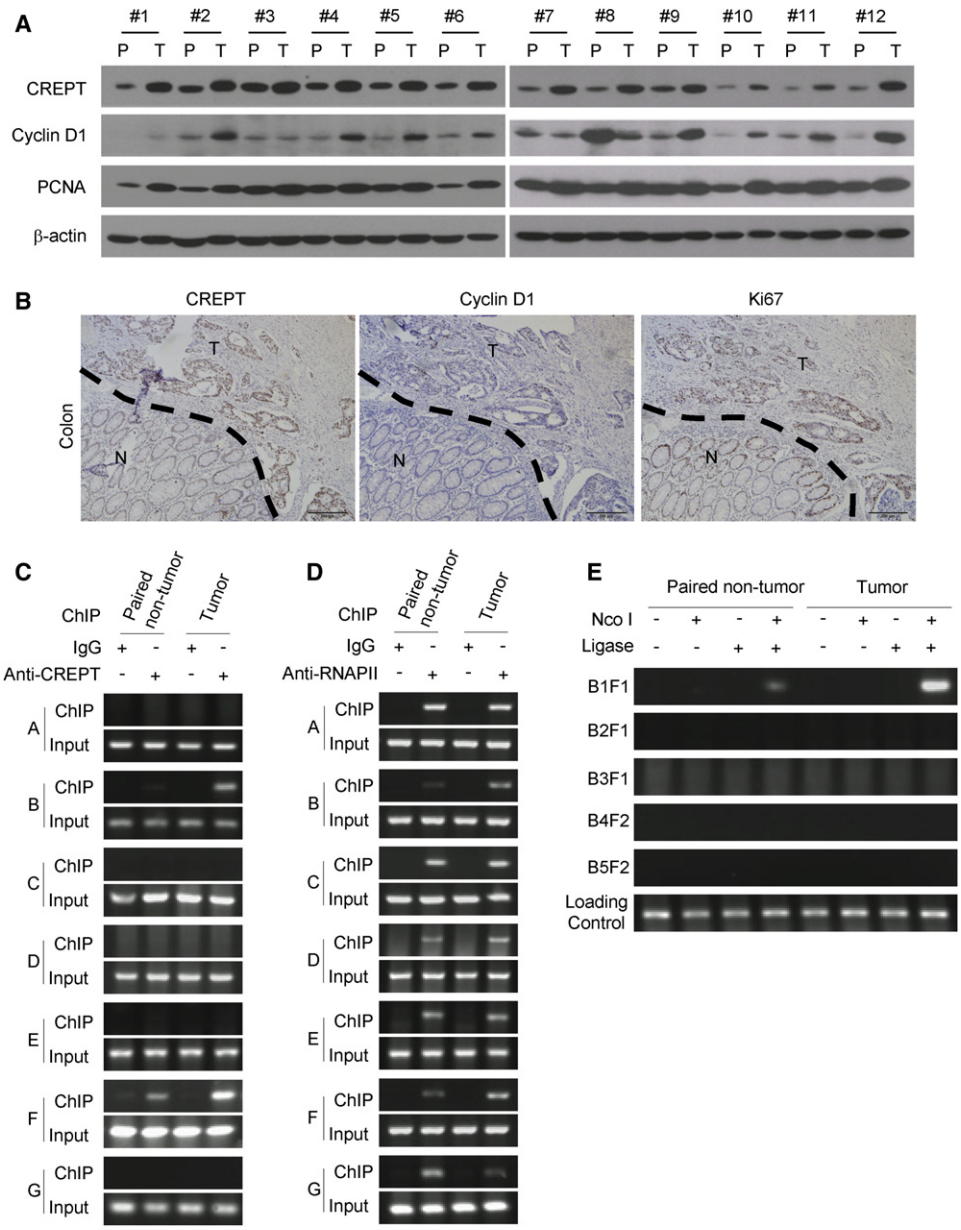

Figure 7. CREPT Promotes Chromatin Looping of the *CYCLIN D1* Gene in Tumors

(A) Correlation expression of cyclin D1, PCNA, and CREPT in colon cancers. A western blot was performed for samples from colon cancer patients. P refers to paired nontumor tissue and T refers to tumor tissue. # refers to the patient number.

(B) CREPT, cyclin D1, and Ki67 are elevated simultaneously in human colon tumor tissues. IHC was performed with colon cancer samples and a representative image (scale bar, 200 μm) is shown.

(C) CREPT binds to both the promoter and the 3′ end region of the *CYCLIN D1* gene in tumors. ChIP experiments were performed in tumor or paired nontumor tissues from three patients (1, 3, and 7).

(D) RNAPII strongly binds to both the promoter and the 3′ end region of the *CYCLIN D1* gene in tumors. ChIP experiments were performed as in (C).

(E) The *CYCLIN D1* gene forms stronger chromatin loops in tumors. 3C experiments were performed in the tumor and paired nontumor tissues from three patients. See also Figure S5.

oncogene that is highly expressed in tumors and accelerates tumor development. We reveal that the mechanism by which CREPT enhances tumor growth is by directly regulating cyclin D1 expression at the transcriptional level. We believe that CREPT should be another target for tumor diagnosis and therapy development.

EXPERIMENTAL PROCEDURES

Plasmids and Antibodies

Expression plasmids for human CREPT are pEGFPN1/Flag-CREPT, pGEX/5X-2/ GST-CREPT, pcDNA6/CREPT, pcDNA3.1/Myc-CREPT, pCMV/HA-CREPT, and pTre2/CREPT, which were constructed in our lab. The plasmid pBS/U6/CREPT-si was constructed according to a previous protocol (Sui

et al., 2002). The target sequence by an siRNA (CREPT-si), GGACCTGAATTC ACTAGAGA, is identical in human and mouse. Antibodies against Flag (M2), RNAPII (8WG16), Cyclin D1, PCNA, Ki67, and β-actin were purchased from Santa Cruz Biotechnology and Covance Research. An anti-CREPT antibody (3E10) was raised in our lab (see Figure S1D).

Human Tumor Specimens and Staining

Cancer tissues were collected in the Third People's Hospital of Qidong, Qi Dong Tumor Hospital, Wuxi 101 Hospital, the Chinese University of Hong Kong and the Chinese PLA General Hospital in China. Tissues were kept and stained according to routine protocols (Rong et al., 2006). The tissue collection procedure with informed consent was approved by the Ethic Affair Committee of the Third People's Hopspital of Qidong, the Ethic and Health Committee of Qi Dong Tumor Hospital, The Ethic Committee of Wuxi 101 Hospital, the Clinical Research Ethics Committee of the Chinese University of Hong Kong, and the Clinical Ethic Committee of the Chinese PLA General Hospital.

Western Blot, Immunoprecipitation, PCR, and RT-PCR

Experiments were performed according to protocols in the lab (Wu et al., 2010). CREPT cDNA was amplified using the primers: (forward) 5′-TATAGG TACCATGTCCTCCTTCTCTGAG-3′ and (reverse) 5′-TATACTCGAGCTAGT CAGTTGAAAACAGGTC-3′. Semiquantitative PCR products were quantified by Imagequant software (Amersham Pharmacia Biotechnology).

Cell Culture, Transfection, and Assays from Stable Cell Lines

Cells used for cell-cycle, growth, and luciferase experiments were cultured according to previous studies (Wu et al., 2010). Tumor formation assays were done according to a previous study (Rong et al., 2006) following the institutional guidelines and regulations on the animal health and ethics, approved by the animal health and ethics committee in Tsinghua University. All the experiments were performed in triplicate.

Chromatin Immunoprecipitation Assay

Cells were fixed at 37°C for 10 min with 1% formaldehyde for crosslinking (Wu et al., 2010). Sonication was done at 4°C for 30 s at level 2 (Ultrasonic Processor, Sonics) to yield fragments from 100 to 400 bps. Information of primers for PCR amplifications can be found in the Supplemental Information). The specificity of the primers to the different regions of the *CYCLIN D1* gene was examined and no crossreaction bands were observed. The efficiency of PCR in the chromatin immunoprecipitation (ChIP) experiments was greater than 20% when compared with the input. Real-time PCR was performed to quantify the data.

Nuclear Run-on and Run-off Assays

For nuclear run-on assays, nuclei prepared from the indicated cells were incubated in 2 × Transcription Mix, 10 × Nucleotide Mix, and 500 μCi [^{32}P]-dUTP at 37°C for 30 min. Labeled mRNA was hybridized to cDNA probes predotted onto membranes. For nuclear run-off assays, linearized pGL3/cyclin D1-Luc was incubated with purified GST-CREPT and HeLa cell nuclear extracts, or with nuclear extracts from the indicated cell lines. Transcript products were dotted on membranes and hybridized with [^{32}P]-CTP-labeled Luc cDNA probe.

Chromosome Conformation Capture Assay

Chromosome conformation capture (3C) assays were conducted essentially as described by Dekker et al. (2002) with some modifications (see Supplemental Information). Real-time PCR was performed to quantify the results.

ACCESSION NUMBERS

The GenBank accession numbers for human, murine, and chicken CREPT mRNAs are DQ372938, DQ372939, and DQ372930, respectively.

SUPPLEMENTAL INFORMATION

Supplemental Information includes five figures and Supplemental Experimental Procedures and can be found with this article online at doi:10.1016/j.ccr.2011.12.016.

ACKNOWLEDGMENTS

We thank Drs. Xiao-Fan Wang, Xin-Yuan Fu, and Robert Eisenman for their suggestions and discussions in this project. We thank Dr. Yang Shi for siRNA protocols and vectors. We thank Dr. Ya Gu in the Third People's Hospital of Qidong, Profs. Weibing Wang and Yaoyi Wu in Wuxi 101 Hospital in China for providing tumor samples, and Dr. Huijuan Zhang in the International Peace Maternity and Child Health Hospital, Shanghai Jiao Tong University for technical support. This work was supported by grants from the 973 Project (2006CB910102, 2011CB910502), the NSFC (31071225, 30228007, 30871286), the 863 project (2007AA021505), the MOST projects (2011ZX0811-006, 2009ZX08009, 2006CB910102) in China, a China-Canada Joint Health Research Initiative grant to J.H. (#CCI-82411) and Z.C. (#30611120522), and the Tsinghua Internal Foundation (20091081322).

Received: August 17, 2011
Revised: November 17, 2011
Accepted: December 16, 2011
Published: January 17, 2012

REFERENCES

Bonetta, L. (2005). Going on a cancer gene hunt. Cell *123*, 735–737.

Buratowski, S. (2009). Progression through the RNA polymerase II CTD cycle. Mol. Cell *36*, 541–546.

Connelly, S., and Manley, J.L. (1989). A CCAAT box sequence in the adenovirus major late promoter functions as part of an RNA polymerase II termination signal. Cell *57*, 561–571.

Dekker, J., Rippe, K., Dekker, M., and Kleckner, N. (2002). Capturing chromosome conformation. Science *295*, 1306–1311.

Dickins, R.A., Hemann, M.T., Zilfou, J.T., Simpson, D.R., Ibarra, I., Hannon, G.J., and Lowe, S.W. (2005). Probing tumor phenotypes using stable and regulated synthetic microRNA precursors. Nat. Genet. *37*, 1289–1295.

Doerks, T., Copley, R.R., Schultz, J., Ponting, C.P., and Bork, P. (2002). Systematic identification of novel protein domain families associated with nuclear functions. Genome Res. *12*, 47–56.

Eeckhoute, J., Carroll, J.S., Geistlinger, T.R., Torres-Arzayus, M.I., and Brown, M. (2006). A cell-type-specific transcriptional network required for estrogen regulation of cyclin D1 and cell cycle progression in breast cancer. Genes Dev. *20*, 2513–2526.

Felsher, D.W. (2003). Cancer revoked: oncogenes as therapeutic targets. Nat. Rev. Cancer *3*, 375–380.

Gordon, G.J., Rockwell, G.N., Jensen, R.V., Rheinwald, J.G., Glickman, J.N., Aronson, J.P., Pottorf, B.J., Nitz, M.D., Richards, W.G., Sugarbaker, D.J., and Bueno, R. (2005). Identification of novel candidate oncogenes and tumor suppressors in malignant pleural mesothelioma using large-scale transcriptional profiling. Am. J. Pathol. *166*, 1827–1840.

Hall, M., and Peters, G. (1996). Genetic alterations of cyclins, cyclin-dependent kinases, and Cdk inhibitors in human cancer. Adv. Cancer Res. *68*, 67–108.

Hanahan, D., and Weinberg, R.A. (2000). The hallmarks of cancer. Cell *100*, 57–70.

Herber, B., Truss, M., Beato, M., and Müller, R. (1994). Inducible regulatory elements in the human cyclin D1 promoter. Oncogene *9*, 1295–1304.

Hunter, T., and Pines, J. (1994). Cyclins and cancer. II: cyclin D and CDK inhibitors come of age. Cell *79*, 573–582.

Johnson, D.G., and Walker, C.L. (1999). Cyclins and cell cycle checkpoints. Annu. Rev. Pharmacol. Toxicol. *39*, 295–312.

Kim, M., Krogan, N.J., Vasiljeva, L., Rando, O.J., Nedea, E., Greenblatt, J.F., and Buratowski, S. (2004). The yeast Rat1 exonuclease promotes transcription termination by RNA polymerase II. Nature *432*, 517–522.

Lee, M.H., and Yang, H.Y. (2003). Regulators of G1 cyclin-dependent kinases and cancers. Cancer Metastasis Rev. *22*, 435–449.

Lian, Z., Karpikov, A., Lian, J., Mahajan, M.C., Hartman, S., Gerstein, M., Snyder, M., and Weissman, S.M. (2008). A genomic analysis of RNA

polymerase II modification and chromatin architecture related to 3′ end RNA polyadenylation. Genome Res. *18*, 1224–1237.

Liu, J., Liu, H., Zhang, X., Gao, P., Wang, J., and Hu, Z. (2002). Identification and characterization of P15RS, a novel P15(INK4b) related gene on G1/S progression. Biochem. Biophys. Res. Commun. *299*, 880–885.

Lunde, B.M., Reichow, S.L., Kim, M., Suh, H., Leeper, T.C., Yang, F., Mutschler, H., Buratowski, S., Meinhart, A., and Varani, G. (2010). Cooperative interaction of transcription termination factors with the RNA polymerase II C-terminal domain. Nat. Struct. Mol. Biol. *17*, 1195–1201.

Luo, W., and Bentley, D. (2004). A ribonucleolytic rat torpedoes RNA polymerase II. Cell *119*, 911–914.

Mapendano, C.K., Lykke-Andersen, S., Kjems, J., Bertrand, E., and Jensen, T.H. (2010). Crosstalk between mRNA 3′ end processing and transcription initiation. Mol. Cell *40*, 410–422.

Massagué, J. (2004). G1 cell-cycle control and cancer. Nature *432*, 298–306.

Moore, M.J., and Proudfoot, N.J. (2009). Pre-mRNA processing reaches back to transcription and ahead to translation. Cell *136*, 688–700.

O'Sullivan, J.M., Tan-Wong, S.M., Morillon, A., Lee, B., Coles, J., Mellor, J., and Proudfoot, N.J. (2004). Gene loops juxtapose promoters and terminators in yeast. Nat. Genet. *36*, 1014–1018.

Obaya, A.J., and Sedivy, J.M. (2002). Regulation of cyclin-Cdk activity in mammalian cells. Cell. Mol. Life Sci. *59*, 126–142.

Osborne, C., Wilson, P., and Tripathy, D. (2004). Oncogenes and tumor suppressor genes in breast cancer: potential diagnostic and therapeutic applications. Oncologist *9*, 361–377.

Perkins, K.J., Lusic, M., Mitar, I., Giacca, M., and Proudfoot, N.J. (2008). Transcription-dependent gene looping of the HIV-1 provirus is dictated by recognition of pre-mRNA processing signals. Mol. Cell *29*, 56–68.

Polsky, D., and Cordon-Cardo, C. (2003). Oncogenes in melanoma. Oncogene *22*, 3087–3091.

Proudfoot, N.J. (1989). How RNA polymerase II terminates transcription in higher eukaryotes. Trends Biochem. Sci. *14*, 105–110.

Rong, Y., Cheng, L., Ning, H., Zou, J., Zhang, Y., Xu, F., Liu, L., Chang, Z., and Fu, X.Y. (2006). Wilms' tumor 1 and signal transducers and activators of transcription 3 synergistically promote cell proliferation: a possible mechanism in sporadic Wilms' tumor. Cancer Res. *66*, 8049–8057.

Scholes, D.T., Banerjee, M., Bowen, B., and Curcio, M.J. (2001). Multiple regulators of Ty1 transposition in Saccharomyces cerevisiae have conserved roles in genome maintenance. Genetics *159*, 1449–1465.

Semczuk, A., and Jakowicki, J.A. (2004). Alterations of pRb1-cyclin D1-cdk4/6-p16(INK4A) pathway in endometrial carcinogenesis. Cancer Lett. *203*, 1–12.

Sherr, C.J. (1996). Cancer cell cycles. Science *274*, 1672–1677.

Sui, G., Soohoo, C., Affar, B., Gay, F., Shi, Y., Forrester, W.C., and Shi, Y. (2002). A DNA vector-based RNAi technology to suppress gene expression in mammalian cells. Proc. Natl. Acad. Sci. USA *99*, 5515–5520.

Tan-Wong, S.M., French, J.D., Proudfoot, N.J., and Brown, M.A. (2008). Dynamic interactions between the promoter and terminator regions of the mammalian BRCA1 gene. Proc. Natl. Acad. Sci. USA *105*, 5160–5165.

Tong, A.H., Evangelista, M., Parsons, A.B., Xu, H., Bader, G.D., Pagé, N., Robinson, M., Raghibizadeh, S., Hogue, C.W., Bussey, H., et al. (2001). Systematic genetic analysis with ordered arrays of yeast deletion mutants. Science *294*, 2364–2368.

Vogelstein, B., and Kinzler, K.W. (2004). Cancer genes and the pathways they control. Nat. Med. *10*, 789–799.

Wu, Y., Zhang, Y., Zhang, H., Yang, X., Wang, Y., Ren, F., Liu, H., Zhai, Y., Jia, B., Yu, J., and Chang, Z. (2010). p15RS attenuates Wnt/beta-catenin signaling by disrupting beta-catenin·TCF4 Interaction. J. Biol. Chem. *285*, 34621–34631.

Yamasaki, L., and Pagano, M. (2004). Cell cycle, proteolysis and cancer. Curr. Opin. Cell Biol. *16*, 623–628.

Zhang, Z., Li, M., Rayburn, E.R., Hill, D.L., Zhang, R., and Wang, H. (2005a). Oncogenes as novel targets for cancer therapy (part I): growth factors and protein tyrosine kinases. Am. J. Pharmacogenomics *5*, 173–190.

Zhang, Z., Li, M., Rayburn, E.R., Hill, D.L., Zhang, R., and Wang, H. (2005b). Oncogenes as novel targets for cancer therapy (part II): intermediate signaling molecules. Am. J. Pharmacogenomics *5*, 247–257.

Zhang, Z., Li, M., Rayburn, E.R., Hill, D.L., Zhang, R., and Wang, H. (2005c). Oncogenes as novel targets for cancer therapy (part III): transcription factors. Am. J. Pharmacogenomics *5*, 327–338.

Cancer Cell
Article

$Kras^{G12D}$-Induced IKK2/β/NF-κB Activation by IL-1α and p62 Feedforward Loops Is Required for Development of Pancreatic Ductal Adenocarcinoma

Jianhua Ling,[1] Ya'an Kang,[2] Ruiying Zhao,[1] Qianghua Xia,[1,4] Dung-Fang Lee,[5] Zhe Chang,[1,4] Jin Li,[6] Bailu Peng,[7] Jason B. Fleming,[2] Huamin Wang,[3,4] Jinsong Liu,[3,4] Ihor R. Lemischka,[5] Mien-Chie Hung,[1,4,8] and Paul J. Chiao[1,4,*]
[1]Department of Molecular and Cellular Oncology
[2]Department of Surgical Oncology
[3]Department of Pathology
The University of Texas M.D. Anderson Cancer Centre, Houston, TX 77030, USA
[4]The University of Texas Graduate School of Biomedical Sciences, Houston, TX 77030, USA
[5]Department of Developmental and Regenerative Biology, and the Black Family Stem Cell Institute, Mount Sinai School of Medicine, New York, NY 10029, USA
[6]Center for Applied Genomics, Children's Hospital of Philadelphia, Philadelphia, PA 19104, USA
[7]Guangdong Entomological Institute, Guangzhou, Guangdong 510260, China
[8]Center for Molecular Medicine and Graduate Institute of Cancer Biology, China Medical University, Taichung 447, Taiwan
*Correspondence: pjchiao@mdanderson.org
DOI 10.1016/j.ccr.2011.12.006

SUMMARY

Constitutive Kras and NF-κB activation is identified as signature alterations in pancreatic ductal adenocarcinoma (PDAC). However, how NF-κB is activated in PDAC is not yet understood. Here, we report that pancreas-targeted *IKK2/β* inactivation inhibited NF-κB activation and PDAC development in $Kras^{G12D}$ and $Kras^{G12D}$;*Ink4a/Arf*$^{F/F}$ mice, demonstrating a mechanistic link between *IKK2/β* and $Kras^{G12D}$ in PDAC inception. Our findings reveal that $Kras^{G12D}$-activated AP-1 induces IL-1α, which, in turn, activates NF-κB and its target genes *IL-1α* and *p62*, to initiate IL-1α/p62 feedforward loops for inducing and sustaining NF-κB activity. Furthermore, IL-1α overexpression correlates with *Kras* mutation, NF-κB activity, and poor survival in PDAC patients. Therefore, our findings demonstrate the mechanism by which IKK2/β/NF-κB is activated by $Kras^{G12D}$ through dual feedforward loops of IL-1α/p62.

INTRODUCTION

The mutational activation of *Kras* is an early event in PDAC development and has been detected in 80%–95% of PDAC, and mutational inactivation of *Ink4a/Arf* tumor suppressor genes can be identified in approximately 50%–75% of PDAC (Hruban et al., 2000). Several experimental animal models were established to determine the functions of mutated *Kras* in induction of pancreatic intraepithelial neoplasia (PanIN) and PDAC (Aguirre et al., 2003; Bardeesy et al., 2006; Hingorani et al., 2003). However, the key signaling pathways that function downstream of *Kras* remained unidentified.

Several previous studies have shown a key role of the NF-κB signaling pathway in Ras-driven cancers using animal models of cancer. For example, knockout of IKK2/β inhibited H-Ras-driven melanoma (Yang et al., 2010), inhibition of NF-κB bypassed restraints on oncogenic Ras-stimulated growth in induction of invasive human epidermal neoplasia (Dajee et al., 2003), and loss of IKK2/β in hepatocyte enhances inflammation, tumor promotion, and progression (He et al., 2010; Maeda et al., 2005). We previously showed that RelA/p50NF-κB is constitutively activated in almost 70% of pancreatic cancer specimens and inhibition of NF-κB activity by a mutant IκBα inhibited PDAC cell tumorigenesis (Fujioka et al., 2003; Wang et al.,

Significance

Pancreatic ductal adenocarcinoma (PDAC) is the fourth most common cause of adult cancer death in the US. The 5-year survival rate has remained 1%–3% for the past 25 years. Each year approximately 42,000 cases of PDAC are diagnosed; over 80% are therapy-resistant locally advanced or metastatic disease, and median survival is less than 6 months. Thus, PDAC remains a challenge in cancer research. To understand mechanisms of pancreatic tumorigenesis, we examined IKK2/β/NF-κB activation and $Kras^{G12D}$ mutation, two of the signature alterations in human PDAC, using genetically engineered mouse models. Our findings establish a pathway linking dual feedforward loops of IL-1α/p62 through which IKK2/β/NF-κB is activated by $Kras^{G12D}$; this suggests therapeutic targets for inhibiting $Kras^{G12D}$ signaling in PDAC.

1999). Thus, these studies demonstrated that IKK2/β/NF-κB has a distinct function in different types of cells. However, it was unclear whether IKK2/β/NF-κB has either prooncogenic or tumor suppressive role in mutant Kras-induced PDAC in mouse models.

Accumulating evidence shows that various signals, including mutant Kras and cytokines activate NF-κB, which, in turn, integrates proinflammatory signals and promote tumorigenesis (Staudt, 2010). For instance, binding of interleukin-1alpha (IL-1α) to its receptor induces K63-linked polyubiquitination of tumor necrosis factor (TNF) receptor-associated factor 6 (TRAF6) and activates transforming growth factor-β-activated kinase 1 (TAK1), which induces activation of IKK2/β, c-Jun N-terminal kinase, and p38 MAPK to activate NF-κB and AP-1 (Skaug et al., 2009; Wang et al., 2001). The turnover of signal-induced K63-polyubiquitination of TRAF6 is prevented by signaling adaptor p62 to prolong IKK2/β and NF-κB activation (Wooten et al., 2005), Furthermore, p62 is an important NF-κB mediator in lung tumorigenesis (Duran et al., 2008), However, the mechanisms that regulate p62 to control IKK2/β activation to the extent of stimulation were unknown. Another report showed that mutant Kras-driven transformation requires TBK1 kinase activation (Barbie et al., 2009). However, the work did not reveal the mechanisms for constitutive NF-κB activation by TBK1 in mutant *Kras*-driven tumor. Studies showed that mutant Kras-associated RAL guanine nucleotide exchange factors promote TBK1 kinase activation via an unknown mechanism, which, in turn, activates c-rel/p50NF-κB, (Chien et al., 2006), and that kinase-inactive TBK1 inhibits TANK-mediated alternative NF-κB activation pathway, but does not block canonical NF-κB activation induced by TNF-α or IL-1 (Pomerantz and Baltimore, 1999). Thus, the mechanisms through which oncogenic Kras activates the canonical NF-κB pathway in PDAC remained unknown.

In the present study, we investigated the role of IKK2/β/NF-κB activation and expression of IL-1α and p62 in *Kras*^{G12D}-induced PDAC development and explored the underlying mechanisms by which IKK2/β/NF-κB is activated by Kras^{G12D}.

RESULTS

Generation of Mutant Mouse Strains with Pancreas-Specific Expression of *Kras*^{G12D} and Inactivation of *IKK2/β* with or without Concurrent *Ink4a/Arf* Deletion

To determine the function of constitutive NF-κB activity in PDAC development, we targeted *IKK2/β* deletion in the pancreas of the *Kras*^{G12D} mice with and without *Ink4a/Arf* inactivation. The mouse strain with floxed *IKK2/β* alleles (*IKK2/β*$^{F/F}$) (Li et al., 2003) is utilized in breeding with the mice that harbors a *Pdx1-Cre* transgene (*Pdx1-Cre*) (Gu et al., 2002) and a latent *Kras*^{G12D} knockin allele (*Kras*$^{LSL-G12D}$) (Hingorani et al., 2003), and those that carry the floxed *Ink4a/ Arf* (*Ink4a/Arf* $^{F/F}$), *Kras*$^{LSL-G12D}$, and *Pdx1-Cre* alleles (Aguirre et al., 2003). Generation of *IKK2/β*$^{F/F}$ genotypes in *Pdx1-Cre;Kras*$^{LSL-G12D}$ and *Pdx1-Cre;Kras*$^{LSL-G12D}$*;Ink4a/Arf*$^{F/F}$ strains are schematically depicted in Figure 1A. *Cre*-mediated excision of the silencing cassette and subsequent recombination generated a single *LoxP* site was detected in the pancreas, but not in other organs such as liver in all of the mouse lines (Figure 1B). Consistent with expression of the mutant *Kras* allele at endogenous level, GTP-bound Ras protein was increased only in protein extracts from the pancreata of the mice carrying *Pdx1-Cre;Kras*$^{LSL-G12D}$ alleles (Figure 1C). The third coding exon-deleted *IKK2/β* alleles were detected in a mosaic pattern in the pancreata of all *Pdx1-Cre;IKK2/β*$^{F/F}$ mice (Figure 1D). As a result, NF-κB DNA binding activities were notably reduced in nuclear extracts from the pancreata of *Pdx1-Cre;Kras*$^{LSL-G12D}$*;IKK2/β*$^{F/F}$ mice, but not in those of *Pdx1-Cre;Kras*$^{LSL-G12D}$ mice (Figures 1E and 1F). Both *p16Ink4a* and *p19Arf* genes were specifically deleted in the pancreata of the mutant mice (Figure 1G). Thus, these results show that the *Pdx1-Cre* transgene concurrently deleted LoxP-containing alleles to target expression of *Kras*^{G12D} and inactivation of *IKK2/β*$^{F/F}$ and/or *Ink4a/Arf*$^{F/F}$ alleles specifically in the pancreata of these mutant mice.

IKK2/β Activity Required for Oncogenic Kras-Induced PanIN and PDAC

To examine the role of IKK2/β in PDAC development, we characterized a cohort of *Pdx1-Cre;Kras*$^{LSL-G12D}$*;IKK2/β*$^{F/F}$ and *Pdx1-Cre;Kras*$^{LSL-G12D}$*;Ink4a/Arf*$^{F/F}$*;IKK2/β*$^{F/F}$ mice and their control littermates. Our findings revealed that these mutant mice did not develop PDAC, unlike their control mice (Figures 2A and 2B). Chi-square analysis showed that the *Pdx1-Cre;Kras*$^{LSL-G12D}$ genotypes with IKK2/β are associated with the observed chronic pancreatis (CP), PanIN lesions, cystic ductal lesion (CDL), and PDAC (Figure 2B), suggesting IKK2/β plays a causal role in PDAC development. Consistent with these results, *Pdx1-Cre;Kras*$^{LSL-G12D}$*;Ink4a/Arf*$^{F/F}$*;IKK2/β*$^{F/F}$ mice remained free of PDAC for over 12 months, whereas the median survival of *Pdx1-Cre;Kras*$^{LSL-G12D}$*;Ink4a/Arf*$^{F/F}$ mice was about 3.5 months, as previously described (Aguirre et al., 2003; Figure 2C).

The littermates of all the mutant mice were born with mendelian frequencies and weight similar to those of wild-type controls. Organs appeared to be formed normally and no phenotypic differences were observed before the age of 2 months in *Pdx1-Cre;Kras*$^{LSL-G12D}$ mice and 6 weeks in *Pdx1-Cre;Kras*$^{LSL-G12D}$*;Ink4a/Arf*$^{F/F}$ mice. No pancreatic ductal lesions or other abnormalities were detected and the expression levels of glucagon, insulin, amylase, CK-19, and staining of duct-specific lectins, Dolichos biflorus agglutinin (DBA) in various *IKK2/β*$^{F/F}$ mice are consistent with those observed in the pancreas of wild-type mice (Figures 2E and 2F; Figure S1 available online). Altogether, the normal histology, marker gene expression, and life span suggest that knockout of IKK2/β in mouse pancreas did not result in abnormal pancreas development in acinar, ductal, and islet of the pancreas or apparent pathological phenotypes.

In *Pdx1-Cre;Kras*$^{LSL-G12D}$*;IKK2/β*$^{F/F}$ mice (Figures 2F and 2G), only 12% (10 of 84) of the mice developed stage 1 PanIN lesions, which consisted primarily of elongated mucinous ductal cells, and no PDAC was observed for over 12 months, whereas 19% (13 of 70) of *Pdx1-Cre;Kras*$^{LSL-G12D}$ mice had PDAC in 8–12 months (Figure 2M), 24% (17 of 70) had CDL during the same time period (Figure 2L), and 27% (19 of 70) had stage 1, 2, or 3 PanIN lesions (Figures 2I–2K) at about 3–6 months. Moreover, most CP was associated with all the PanIN and PDAC, and only 10% of *Pdx1-Cre;Kras*$^{LSL-G12D}$ mice (7 of 70) developed CP without PanIN or PDAC pathological lesions (Figures 2A and 2H). These findings suggest that inactivation of

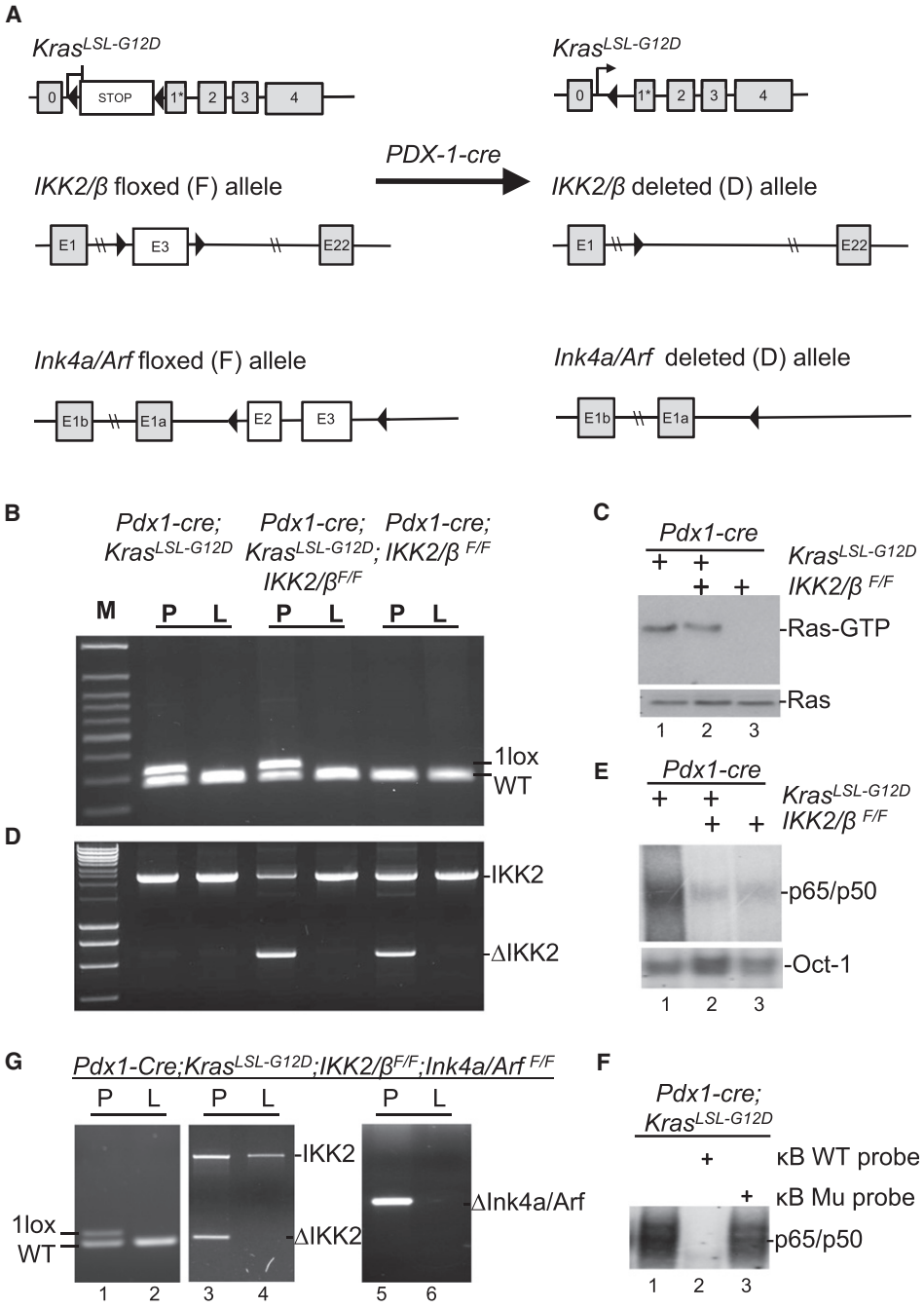

Figure 1. Generation of Mouse Strains with Pancreas-Specific *Kras^{G12D}* Expression and Inactivation of *IKK2/β* with or without Parallel Deletion of *Ink4a/Arf*

(A) Graphic representation of the targeted *Kras$^{LSL-G12D}$*, *IKK2/β*, and *Ink4a/Arf* alleles before and after *Cre*-mediated excision and recombination.

(B) The presence of recombined *Kras^{G12D}* allele in the pancreata (P) but not in the livers (L) of compound mutant mice was revealed by PCR.

(C) Ras-GTP and total Ras levels in whole pancreatic protein extracts of 3-month-old *Pdx1-Cre;Kras$^{LSL-G12D}$*, *Pdx1-Cre;Kras$^{LSL-G12D}$;IKK2/β$^{F/F}$*, and *Pdx1-Cre; IKK2/β$^{F/F}$* mice. Elevated levels of Ras-GTP were observed only in compound mutant mice with *Pdx1-Cre;Kras$^{LSL-G12D}$* alleles.

(D) The recombined *IKK2/β$^{F/F}$* allele was detected only in the pancreata (P), not in the livers (L), of mice carrying *Pdx1-Cre;IKK2/β$^{F/F}$* alleles.

(E) EMSA was performed to determine the levels of NF-κB DNA binding activity in the pancreata carrying *Pdx1-Cre;Kras$^{LSL-G12D}$*, *Pdx1-Cre;Kras$^{LSL-G12D}$;IKK2/β$^{F/F}$*, or *Pdx1-Cre;IKK2/β$^{F/F}$* alleles. Nuclear extracts from mouse pancreata were used in this analysis with a κB probe. Oct-1 probe was used as a loading control.

(F) EMSA was performed with ^{32}P-labeled κB probe in the presence and absence of both unlabeled wild-type (WT) and mutant (Mu) κB probes to determine the specificity of NF-κB DNA binding activity detected in the pancreata of *Pdx1-Cre;Kras$^{LSL-G12D}$* mice as indicated.

(G) Pancreas-specific deletion of *Ink4a/Arf* alleles was confirmed in *Pdx1-Cre; Kras$^{LSL-G12D}$;IKK2/β$^{F/F}$;Ink4a/Arf$^{F/F}$* mice. The presence of the recombined *Kras^{G12D}* allele and the exon 3-deleted *IKK2/β* allele in the pancreata (P) (lane 5) but not in the livers (L) (lane 6) of compound mutant mice was revealed by PCR.

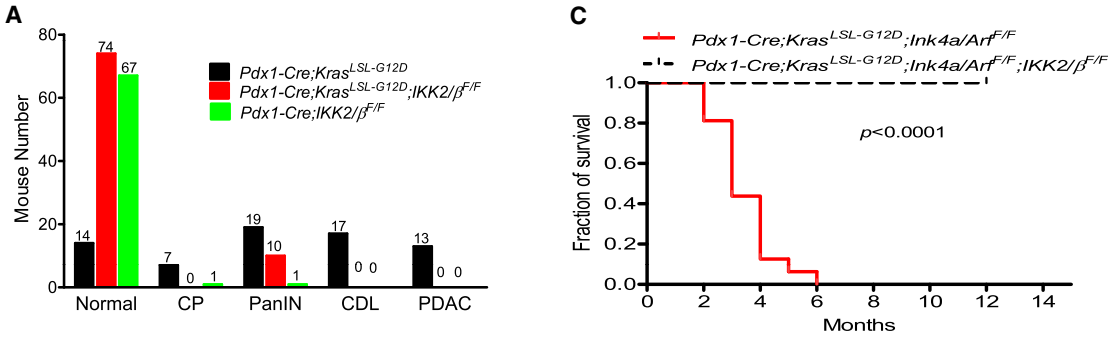

B

Genotype/observed pancreatic lesions	CP	No-CP	PanIN	NO-PanIN	CDL	NO-CDL	PDAC	No-PDAC
Pdx1-cre;Kras$^{LSL-G12D}$	56	14	49	21	30	40	13	57
Pdx1-cre;Kras$^{LSL-G12D}$;IKK2/β$^{F/F}$	10	74	10	74	0	84	0	84
Total mice	66	88	59	95	30	124	13	141
	X^2 = 72.29; p<0.0001		X^2 = 54.53; p<0.0001		X^2 = 44.71; p<0.0001		X^2 = 17.04; p<0.0001	

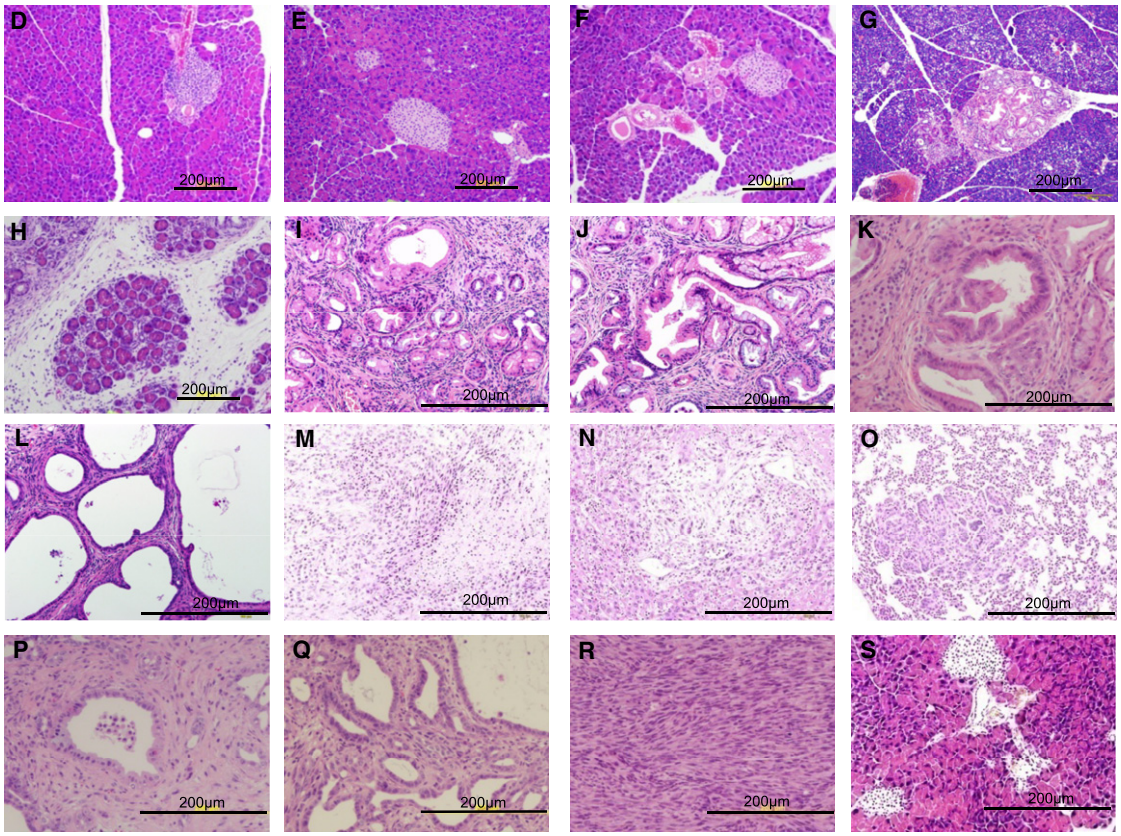

Figure 2. Suppression of Oncogenic *Kras^{G12D}*-Induced Histological Progression of PanIN and PDAC with or without Concurrent Deletion of *Ink4a/Arf* by Inactivation of *IKK2/β*

(A) Numbers of mutant mice that developed PDAC, cystic ductal lesions (CDL), PanIN, or chronic pancreatitis (CP), or remained healthy, in cohorts of *Pdx1-Cre;Kras$^{LSL-G12D}$*, *Pdx1-Cre;Kras$^{LSL-G12D}$;IKK2/$\beta^{F/F}$*, and *Pdx1-Cre;IKK2/$\beta^{F/F}$* mice.

(B) Chi-square analysis of the association between *Pdx1-Cre;Kras$^{LSL-G12D}$* and *Pdx1-Cre;Kras$^{LSL-G12D}$;IKK2/$\beta^{F/F}$*, and the observed phenotypes in (A). Note: CP was found in PanIN, CDL, and PDAC; PanIN was coexisted with CDL and PDAC; and CDL was observed in PDAC.

(C) Kaplan-Meier PDAC-free survival curve for *Pdx1-Cre;Kras$^{LSL-G12D}$;Ink4a/Arf$^{F/F}$* (n = 16) and *Pdx1-Cre;Kras$^{LSL-G12D}$;IKK2/$\beta^{F/F}$;Ink4a/Arf$^{F/F}$* mice (n = 15). According to the approved animal protocol, mice that presented in a moribund state were killed for autopsy.

IKK2/β inhibited PDAC and CP might be a precursor lesion in Kras-induced PDAC.

Serial histological surveys of the pancreas of all the mice are shown in Figures 2D–2S. *Pdx1-Cre;Kras$^{LSL-G12D}$* mice had PanIN at 3 months of age and had invasive tumors by 10 months of age, and 3 of 70 had liver or lung metastatic lesions by 8–12 months of age (Figures 2N and 2O). The progressive premalignant lesions with ductal histology and PDAC were observed (Figures 2M–2O and 2R). These PDAC histological lesions and incidences are consistent with those of the mice harboring *Kras$^{LSL-G12D}$* or *Kras$^{LSL-G12D}$;Ink4a/Arf$^{F/F}$* in earlier studies (Aguirre et al., 2003; Tuveson et al., 2004). These results demonstrate that IKK2/β is required for oncogenic Kras-induced PanIN and PDAC, thus establishing a definitive role of IKK2/β in PDAC development in vivo.

Attenuation of Inflammatory and Proliferative Responses by Pancreas-Targeted Inactivation of *IKK2/β*

To determine whether chronic inflammation and proliferative responses were inhibited in the pancreas of *Pdx1-Cre;Kras$^{LSL-G12D}$;IKK2/β$^{F/F}$* mice, immunohistochemical (IHC) analyses were performed. Levels of proliferation markers CyclinD1, Ki-67, and inflammatory marker COX-2 expression were substantially higher in PanIN and PDAC from *Pdx1-Cre;Kras$^{LSL-G12D}$* mice, than in histologically normal pancreas from *Pdx1-Cre;Kras$^{LSL-G12D}$;IKK2/β$^{F/F}$* mice (Figure 3A). This finding suggests that inactivation of IKK2/β interrupted mutant Kras-stimulated cell proliferation and inflammation.

The observation of CP or proinflammatory responses in *Pdx1-Cre;Kras$^{LSL-G12D}$* mice prompted us to examine whether these mutant mice developed lymphocytic infiltration around pancreatic lesions. IHC staining revealed that the infiltrating lymphocytes consisted of CD3-positive T cells, B220-positive B cells, F4/80-positive macrophages, and Ly6g-positive neutrophil (Figure 3B), whereas parallel staining did not reveal significant lymphocytic infiltration in the pancreata of *Pdx1-Cre;Kras$^{LSL-G12D}$;IKK2/β$^{F/F}$* mice (Figure 3B). This phenotype of lymphocytic infiltration in the pancreata of *Pdx1-Cre;Kras$^{LSL-G12D}$* mice has a close resemblance to those reported for various mouse strains with pancreatitis, such as *IκBα$^{m/m}$* mice defective in IκBα-mediated negative regulation of NF-κB (Peng et al., 2010). So, the absence of hallmarks of cancer-related inflammation in *Pdx1-Cre;Kras$^{LSL-G12D}$;IKK2/β$^{F/F}$* mice is due to inactivation of IKK2/β. This suggests chronic inflammation is a key factor in promoting PDAC development as observed in mouse models for other cancers (Karin, 2008), and one of the essential roles regulated by IKK2/β in Kras-induced PDAC inception.

Inhibition of Key Proinflammatory Cytokines in the Pancreas of *Pdx1-Cre;Kras$^{LSL-G12D}$;IKK2/β$^{F/F}$* Mice

To further analyze Kras-induced inflammatory responses, gene expression was profiled and a number of known and previously unknown NF-κB regulated genes were identified by Gene Set Enrichment analyses (GSEA) using gene ontology and NF-κB target gene sets (Figures 4A and 4B; Figures S2A–S2E). Importantly, GSEA of significant gene upregulation in *Pdx1-Cre;Kras$^{LSL-G12D}$* revealed that they are strongly associated to positive nodal status, high risk, higher tumor stage, and poor survival in PDAC patients by comparing with 102 PDAC cDNA microarray files (GSE21501) (Figure 4C). Two- and 5-fold enriched expression in *Pdx1-Cre;Kras $^{LSL-G12D}$;IKK2/β$^{F/F}$* is correlated to low risk (Figures S2A–S2E). These findings further indicate that the significant role of activated IKK2/β in PDAC development.

To further explore the role of IKK2/β in PDAC development, we compared additional gene expression profiles from *Pdx1-Cre;Kras$^{LSL-G12D}$* and *Pdx1-Cre;Kras$^{LSL-G12D}$;IKK2/β$^{F/F}$* mice using Affymetrix arrays. Our results showed that there is a little difference between the expression profiles of several IKK2/β/NF-κB-regulated genes, such as *IL-1α, IL-1β*, and *c-jun* in the histologically normal pancreas from *Pdx1-Cre;Kras$^{LSL-G12D}$* and *Pdx1-Cre;Kras$^{LSL-G12D}$;IKK2/β$^{F/F}$* mice, which might be due to the small fractions of Pdx1-targed cells (Figures S2F and S2G; Table S1). Furthermore, the analysis of the gene expression profiles among the normal pancreas, PanIN, and PDAC from *Pdx1-Cre;Kras$^{LSL-G12D}$* mice revealed that these profiles are consistent with those involved in PDAC development as those identified between *Pdx1-Cre;Kras$^{LSL-G12D}$* and *Pdx1-Cre;Kras$^{LSL-G12D}$;IKK2/β$^{F/F}$* mice (Figures 4A–4C; Table S2), and are associated with signaling pathways and cellular functions of genes in tumorigenesis (Figures S2H and S2I). The progressive increases in the expression of several NF-κB regulated genes from low expression in the histological normal pancreas to high expression levels in PanIN and PDAC suggest the involvement of the NF-κB-regulated genes in Kras-induced PDAC development.

Among 20 of the differentially expressed genes with a greater than 10-fold increases in expression in the pancreatic tissues of *Pdx1-Cre;Kras$^{LSL-G12D}$* mice (Figure 4A), most of them are cytokines, chemokines, and their receptors, suggesting a role of these molecules in Kras-induced PDAC in vivo. To substantiate the differences in cytokine gene expression between 5- to 12-month-old *Pdx1-Cre;Kras$^{LSL-G12D}$* and age-matched *Pdx1-Cre;Kras$^{LSL-G12D}$;IKK2/β$^{F/F}$* mice, we performed real-time PCR arrays with 84 cytokines and chemokines and validated 9 cytokines with highest expression levels, which includes *IL-1α*, *IL-1β*, and *IL-1 receptor type 2* (Figure 4D; Table S3).

We next investigate the expression of IL-1α and IL-1β, since the expression of both cytokines is among the highest. The levels of IL-1α were significantly elevated in pancreatic tissues and IL-1β levels were slightly higher in serum of *Pdx1-Cre;Kras$^{LSL-G12D}$* mice, but not in wild-type, *Pdx1-Cre;IKK2/β$^{F/F}$*, and *Pdx1-Cre;Kras$^{LSL-G12D}$;IKK2/β$^{F/F}$* mice (Figures 4E and 4F). These results, together with the lymphocytic infiltration, are consistent with chronic inflammation and the role of IKK2/β in cytokine

(D–S) Representative pancreatic histologic views. (D) Normal pancreas from a wild-type mouse. (E) Histologic appearance of normal pancreas from a *Pdx1-Cre;IKK2/β$^{F/F}$* mouse. (F) Histologic appearance of normal pancreas from a *Pdx1-Cre;Kras$^{LSL-G12D}$;IKK2/β$^{F/F}$* mouse. (G) A rare PanIN-1 from *Pdx1-Cre;Kras$^{LSL-G12D}$;IKK2/β$^{F/F}$* mouse. (H–O) *Pdx1-Cre;Kras$^{LSL-G12D}$* mice. (H) Chronic pancreatitis (I) PanIN-1. (J) PanIN-2. (K) PanIN-3. (L) Cystic ductal lesion. (M) PDAC. (N) PDAC liver metastasis. (O) PDAC lung metastasis. (P-R) *Pdx1-Cre;Kras$^{LSL-G12D}$;Ink4a/Arf$^{F/F}$* mice. (P) PanIN. (Q) Cystic ductal lesion. (R) PDAC. (S) Histologic appearance of normal pancreas from a *Pdx1-Cre;Kras$^{LSL-G12D}$;Ink4a/Arf$^{F/F}$;IKK2/β$^{F/F}$* mouse.
See also Figure S1.

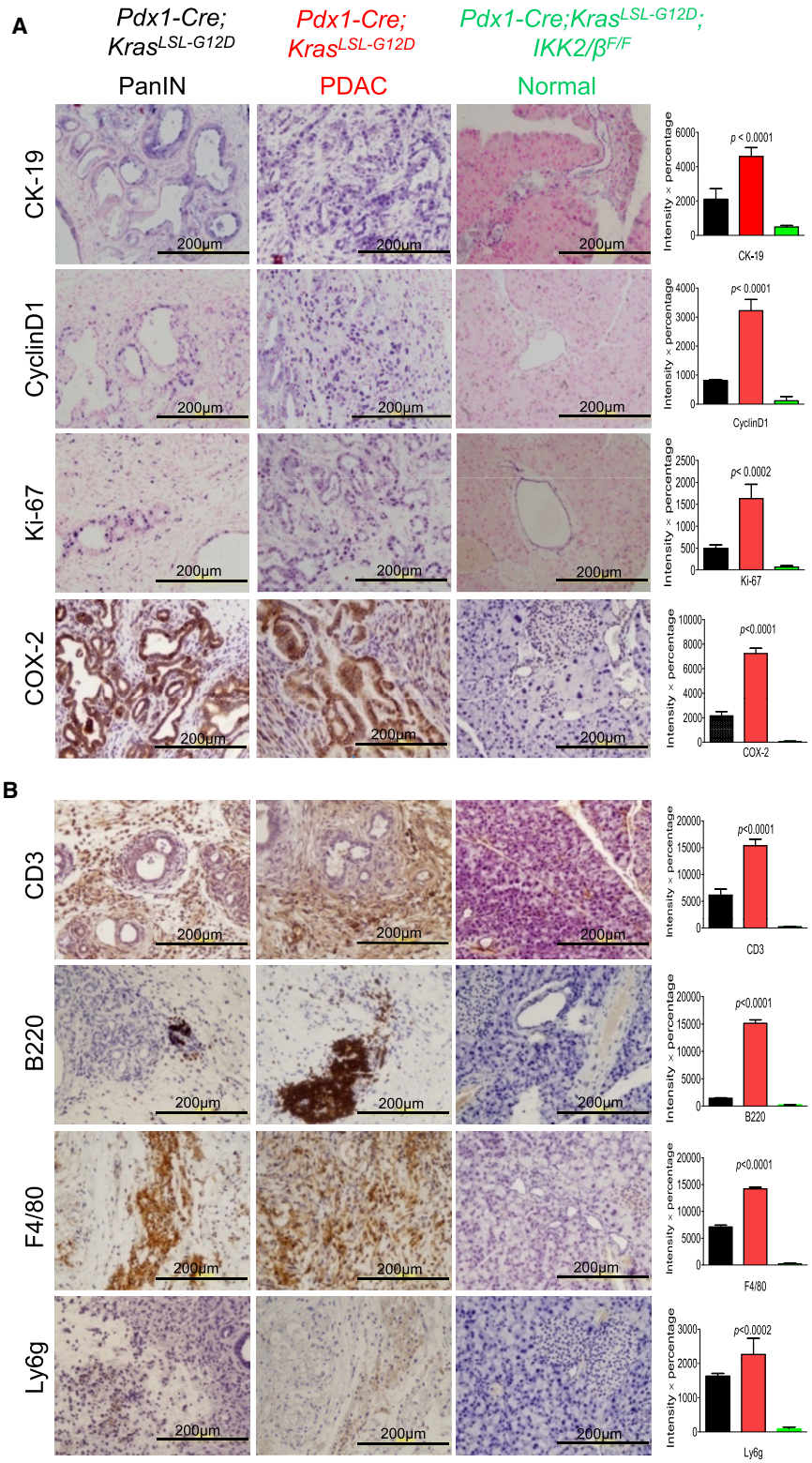

Figure 3. Comparison of the Cell Proliferation, Inflammation, and Immune Responses in the Pancreas between *Pdx1-Cre; Kras$^{LSL-G12D}$;IKK2/β$^{F/F}$* and *Pdx1-Cre; Kras$^{LSL-G12D}$* Mice

(A) Expression of CyclinD1, Ki-67, and COX-2 is elevated in PanIN and PDAC from *Pdx1-Cre; Kras$^{LSL-G12D}$* mice, but not in the normal pancreas of *Pdx1-Cre;Kras$^{LSL-G12D}$;IKK2/β$^{F/F}$* mice. Positive immunostaining for Cytokeratin-19 (CK-19) verifies the ductal phenotype of PanIN lesions, PDAC, and normal duct.

(B) Sections of formalin-fixed PanIN lesions and PDAC from 8-month old *Pdx1-Cre;Kras$^{LSL-G12D}$* and normal duct tissue from *Pdx1-Cre; Kras$^{LSL-G12D}$;IKK2/β$^{F/F}$* mice underwent IHC staining with anti-CD3 antibody as a T cell marker, anti-B220 as a B cell marker, anti-F4/80 as a macrophage marker, and anti-Ly6g as a neutrophil marker. Error bars represent ± standard deviation (SD) from the data of five mice for each of the two genotypes.

expression, which may, in turn, promote a protumorigenic microenvironment. *IL-1α* is an NF-κB target gene and a strong NF-κB inducer (Mori and Prager, 1996; Osborn et al., 1989), but *IL-1α* induction by Kras is previously unknown, suggesting a possible mechanistic link between *IL-1α* expression induced by the Kras^{G12D} and IKK2/β/NF-κB activation.

Downregulation of Expression of IKK2/β/NF-κB Upstream Signaling Molecules by Inactivation of IKK2/β

To elucidate the downstream pathways of mutant Kras that activate IKK2/β, we carried out IHC analysis of PanIN and PDAC to determine the status of inflammation related signaling pathways, including TAK1, p65/RelA, c-Fos, p62, IL-1α, and Rantes (Chemokine [C-C motif] ligand 5). Our results show that levels of c-Fos, TAK1, p62, activated-p65/RelA, IL-1α, and Rantes were substantially higher in PanIN and PDAC from *Pdx1-Cre;Kras$^{LSL-G12D}$* mice than in histologically normal pancreata from *Pdx1-Cre;Kras$^{LSL-G12D}$;IKK2/β$^{F/F}$* mice (Figure 5A). These results suggest that IKK2/β regulates the expression of TAK1, p62, c-Fos, IL-1α, and Rantes as well as NF-κB activation in the diseased pancreas of *Pdx1-Cre;Kras$^{LSL-G12D}$* mice. To determine whether the Kras-induced signaling pathways are also activated in human PDAC, IHC staining was performed using six different PDAC patient specimens with their adjacent normal tissues as controls for a pilot study. The increased levels of IL-1α, TAK1, c-Fos, nuclear p65/RelA recognized by a specific antiactivated p65/RelA antibody (Zabel et al., 1993), p62, and phosphorylated AKT were observed in human PDAC (Figure 5B). Taken together, these results suggest that inactivation of

IKK2/β interrupts oncogenic Kras-mediated pathways regulating expression of c-Fos, IL-1α, TAK1, and p62, and activation of AKT and NF-κB, but how these signaling molecules are regulated by oncogenic Kras through IKK2/β pathways remained largely unclear.

IL-1α Overexpression Correlates with Kras Mutation and NF-κB Activation in Human PDAC Specimens and Poor Survival in PDAC Patients

To determine whether IL-1α overexpression is correlated with mutant Kras in human PDAC specimens, and is induced by Kras^{G12D} in mouse PanIN and PDAC, we sequenced the *Kras* gene from paraffin sections of PDAC specimens from 14 patients who had not undergone neoadjuvant therapies, and from 9 PDAC patient specimens derived from the orthotopic xenograft mouse model implanted with freshly isolated patient pancreatic cancer for excluding normal human stromal cells (Kim et al., 2009). Ninety-three percent (13 of 14) Kras gene from PDAC paraffin sections has substitutional mutation at codon 12, from GGT (Gly) to GAT (Asp). 71% (5 of 7) Kras mutations identified in human PDAC tissue xenograft also have aspartic acid at codon 12, whereeas 29% (2 of 7) were changed to GTT (valine). The results of IL-1α expression, analyzed by chi-square test, showed that the presence of mutated *Kras* gene positively correlated with IL-1α overexpression in PDAC patient specimens (Figure 6A). Further study of IL-1α expression using human PDAC tissue microarray (TMA) demonstrated that IL-1α overexpression was found in most of the human PDAC tissues. Kaplan-Meier survival analysis indicated that high levels of IL-1α expression are associated with poor survival in PDAC patients ($p = 0.016$, log rank test) (Figure 6B).

To determine the association between NF-κB activity and expression levels of IL-1α in human PDAC for validating the relevance of the observations in *Pdx1-Cre;Kras$^{LSL-G12D}$* and *Pdx1-Cre; Kras$^{LSL-G12D}$;IKK2/β$^{F/F}$* mice, IHC staining for p65 and IL-1α in patient PDAC TMA was performed. 42 of 131 (32%) human PDAC samples showed very strong IL-1α staining and 47 (36%) had extremely intense staining for NF-κB activities (Figure 6C). Data analysis of these by Spearman's rank order correlation showed the positive correlation between NF-κB activities and expression levels of IL-1α (Figure 6D). Altogether, the results suggest that the oncogenic Kras-mediated pathway induced IL-1α overexpression, which triggered NF-κB activation. To determine how early activated NF-κB can be detected during PDAC development, we analyzed the staining of p65/RelA in our pancreatic TMA, and the results show 49% (20/41) positive staining in PanIN stage (Figures S3A and S3B), suggest that NF-κB activation is one of the earliest molecular alterations observed in the development of pancreatic cancer.

To determine whether expression of IL-1α and p62 was induced in by Kras^{G12D}, we examined the levels of IL-1α and p62 expression in human PDAC cell lines MDAPanc-28, AsPc-1, and in immortalized human pancreatic ductal cell lines HPDE and HPNE, with or without stable expression of mutant Kras. Expression of both IL-1α and p62 was elevated in MDAPanc-28 and AsPc-1 cells (Figure 6E) and in HPDE and HPNE cells expressing oncogenic Kras (Figure 6F). The expression of c-Fos and activation of Jun N-terminal kinase (JNK) was also induced in mutant *Kras* HPNE cells (Figure S3C).

To determine whether oncogenic Kras-induced AP-1 activity played a major role in the *IL-1α* and *p62* expression, we performed *IL-1α* and *p62* promoter analysis in mPDAC cells, an early passage mouse PDAC cell lines established from the PDAC of *Pdx1-Cre;Kras$^{LSL-G12D}$* mice. Our reporter gene assays show that *IL-1α* promoter with mutated *AP-1* sites had no responses, whereas activity of *IL-1α* promoter with wild-type *AP-1* sites was strongly inhibited by expression of a mutant of *ras* (RasN17), *c-fos* (*FosDN*), and *IκBα* (*IκBαM*), as well as kinase-dead *raf* and *jnk* (Figure 6G). Similarly, *p62* promoter was strongly inhibited by expression of *FosDN* and *IκBαM* (Figure 6H). The results showed that *IL-1α* and *p62* promoters in mPDAC cells were regulated by Kras through AP-1 and NF-κB transcription factors.

Identifying Feedforward Mechanisms that Sustain Constitutive NF-κB Activation in Oncogenic Kras^{G12D}-Induced PDAC

To determine whether IL-1α serves a mechanistic link between Kras^{G12D} and NF-κB activation, we utilized two human PDAC cell lines and two early passage mouse PDAC cell lines, mPDAC-1 and mPDAC-2, which were established from PDAC of *Pdx1-Cre;Kras$^{LSL-G12D}$* mice. These cells were treated with anti-IL-1α and anti-IL-1β neutralizing antibodies for 0, 4, and 8 hr and the nuclear extracts were analyzed. The results showed that anti-IL-1α, but not anti-IL-1β, neutralizing antibodies blocked constitutive NF-κB activation (Figures 7A and 7B). These findings suggest that secreted IL-1α from these cells activates NF-κB through autocrine mechanism.

Although p62 was induced by Kras to trigger IKK2/β activation in lung cancer cells (Duran et al., 2008), the mechanisms are still lacking. To determine whether and how p62 is involved in Kras^{G12D}-induced IKK2/β/NF-κB activation, we stimulated p62-knockdown cells and control cells expressing a puromycin resistant vector and scrambled shRNA with IL-1α for 0, 0.5, 2, or 8 hr and then analyzed NF-κB activity by EMSA (Figures 7C and 7D). The results revealed that constitutive NF-κB activity was decreased in both mPDAC and AsPc-1 *p62* knockdown cells (Figure 7D; Figures S4A and S4B). Interestingly, NF-κB activity was induced to the same peak level by IL-1α at 0.5 hr stimulation in the control and *p62* knockdown cells, remained at the same level at the end of 2 hr stimulation, and was inhibited at the end of 8 hr of IL-1α stimulation for the *p62* knockdown cells compared with their control cells (Figure 7D; Figures S4A and S4B). These findings suggest that p62 expression is dispensable for IL-1α-induced NF-κB activation at the early phase (Figure 7D, lanes 4–9; Figures S4A and S4B), but is required for IL-1α-induced long-term NF-κB activation (Figure 7D, lanes 10–12; Figures S4A and S4B). Since p62 expression was substantially increased in PanIN and PDAC from *Pdx1-Cre;Kras$^{LSL-G12D}$* mice in comparison to those from histologically normal pancreata from *Pdx1-Cre;Kras$^{LSL-G12D}$;IKK2/β$^{F/F}$* mice (Figures 5A and 5B), it is possible that *p62* is one of the previous unknown downstream target genes regulated by NF-κB. To test this possibility, we showed p62 expression was substantially inhibited in MDAPanc-28 and AsPc-1 cells by expressing *IκBαM* in comparison with their control cells (Figure 7E). Our results also show that both *p62* mRNA and protein levels were increased by IL-1α stimulation and reduced by the

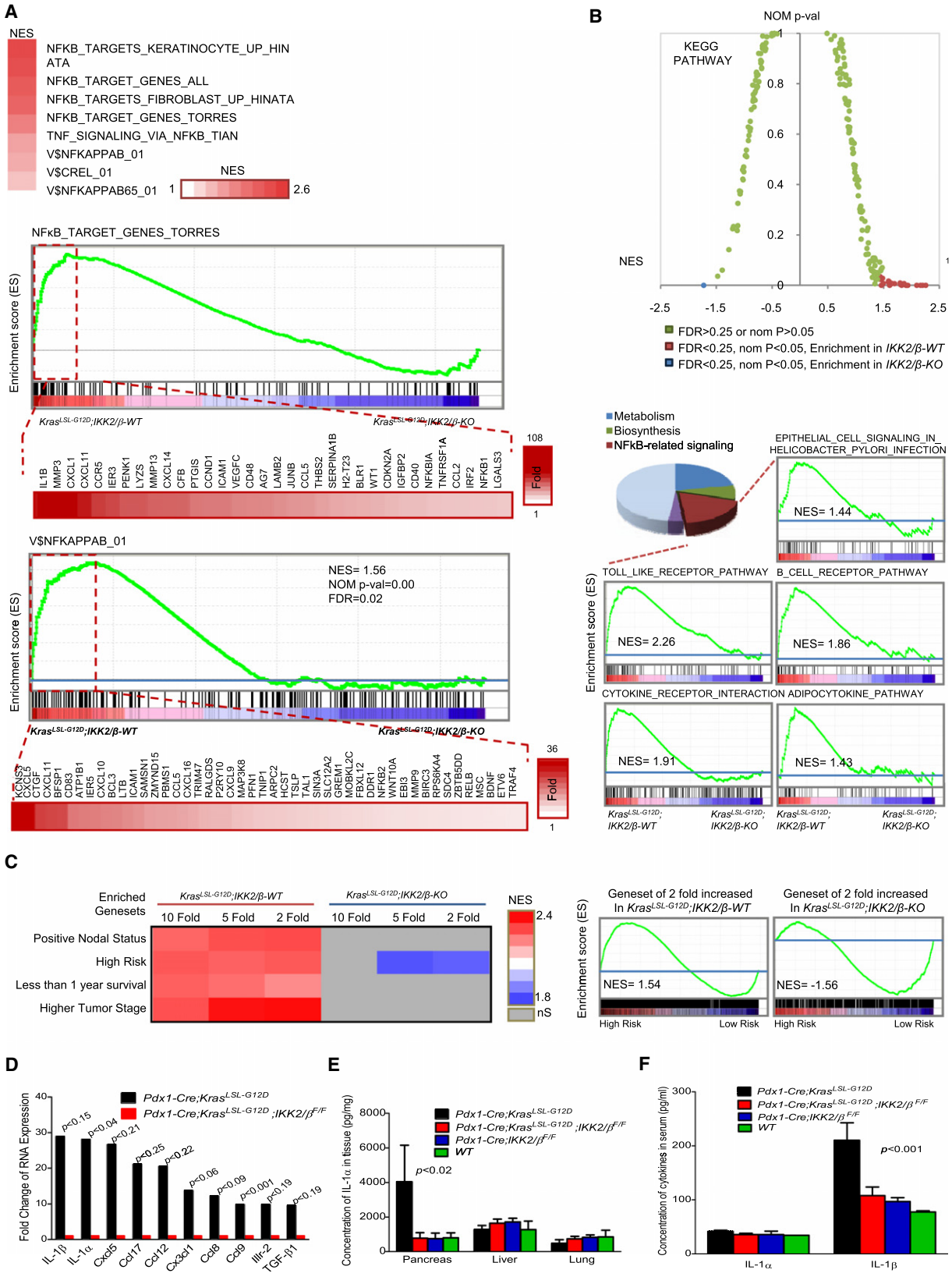
A
NES
NFKB_TARGETS_KERATINOCYTE_UP_HINATA
NFKB_TARGET_GENES_ALL
NFKB_TARGETS_FIBROBLAST_UP_HINATA
NFKB_TARGET_GENES_TORRES
TNF_SIGNALING_VIA_NFKB_TIAN
V$NFKAPPAB_01
V$CREL_01
V$NFKAPPAB65_01
NES
1
2.6
NFκB_TARGET_GENES_TORRES
Enrichment score (ES)
KrasLSL-G12D;IKK2/β-WT
KrasLSL-G12D;IKK2/β-KO
IL1B MMP3 CXCL1 CXCL11 CCR5 IER3 PENK1 LYZS MMP13 CXCL14 CFB PTGIS CCND1 ICAM1 VEGFC CD48 AG7 LAMB2 JUNB CCL5 THBS2 SERPINA1B H2-T23 BLR1 WT1 CDKN2A IGFBP2 CD40 NFKBIA TNFRSF1A CCL2 IRF2 NFKB1 LGALS3
108
Fold
1
V$NFKAPPAB_01
NES= 1.56
NOM p-val=0.00
FDR=0.02
KCNS3 CCL5 CTGF CXCL11 BFSP1 CD83 ATP1B1 IER5 CXCL10 BCL3 LTB ICAM1 SAMSN1 ZMYND15 PBMS1 CCL5 CXCL16 TRIM47 RALGDS P2RY10 CXCL9 MAP3K8 PFN1 TNIP1 ARPC2 HCST TSLP TAL1 SIN3A SLC12A2 GREM1 MOBKL2C FBXL12 DDR1 NFKB2 WNT10A EBI3 MMP9 BIRC3 RPS6KA4 SDC4 ZBTB5DD RELB MSC BDNF ETV6 TRAF4
36
Fold
1
B
NOM p-val
KEGG PATHWAY
NES
1
0.8
0.6
0.4
0.2
0
-2.5 -1.5 -0.5 0.5 1.5 2.5
FDR>0.25 or nom P>0.05
FDR<0.25, nom P<0.05, Enrichment in IKK2/β-WT
FDR<0.25, nom P<0.05, Enrichment in IKK2/β-KO
Metabolism
Biosynthesis
NFkB-related signaling
EPITHELIAL_CELL_SIGNALING_IN_HELICOBACTER_PYLORI_INFECTION
NES= 1.44
TOLL_LIKE_RECEPTOR_PATHWAY
NES= 2.26
B_CELL_RECEPTOR_PATHWAY
NES= 1.86
CYTOKINE_RECEPTOR_INTERACTION
NES= 1.91
ADIPOCYTOKINE_PATHWAY
NES= 1.43
Enrichment score (ES)
KrasLSL-G12D; IKK2/β-WT
KrasLSL-G12D; IKK2/β-KO
C
Enriched Genesets
KrasLSL-G12D;IKK2/β-WT
KrasLSL-G12D;IKK2/β-KO
10 Fold 5 Fold 2 Fold 10 Fold 5 Fold 2 Fold
Positive Nodal Status
High Risk
Less than 1 year survival
Higher Tumor Stage
NES
2.4
1.8
nS
Geneset of 2 fold increased In KrasLSL-G12D;IKK2/β-WT
NES= 1.54
Geneset of 2 fold increased In KrasLSL-G12D;IKK2/β-KO
NES= -1.56
Enrichment score (ES)
High Risk
Low Risk
D
Fold Change of RNA Expression
Pdx1-Cre;KrasLSL-G12D
Pdx1-Cre;KrasLSL-G12D ;IKK2/βF/F
p<0.15 p<0.04 p<0.21 p<0.25 p<0.22 p<0.06 p<0.09 p<0.001 p<0.19 p<0.19
IL-1β IL-1α Cxcl5 Ccl17 Ccl12 Cx3cl1 Ccl8 Ccl9 Il1r-2 TGF-β1
E
Concentration of IL-1α in tissue (pg/mg)
Pdx1-Cre;KrasLSL-G12D
Pdx1-Cre;KrasLSL-G12D ;IKK2/βF/F
Pdx1-Cre;IKK2/βF/F
WT
p<0.02
Pancreas Liver Lung
F
Concentration of cytokines in serum (pg/ml)
Pdx1-Cre;KrasLSL-G12D
Pdx1-Cre;KrasLSL-G12D ;IKK2/βF/F
Pdx1-Cre;IKK2/βF/F
WT
p<0.001
IL-1α IL-1β

anti-IL-1α neutralizing antibody and by silencing *IKK2/β* expression in MDAPanc-28, AsPc-1, mPDAC-1, and mPDAC-2 cells (Figures 7F–7H; Figure S4C), demonstrating that *p62* expression is regulated by NF-κB activity. To further demonstrate the regulation of *p62* expression by NF-κB, we identified two κB and three AP-1 binding sites in both 3.0 kb human and mouse *p62* promoters, which have extensive DNA sequence similarity (Figure 7I). The results from ChIP assays revealed that NF-κB BS2 and AP-1 BS3 sites showed higher binding activity upon IL-1α stimulation in mPDAC-1 cells (Figure 7J). EMSA showed that NF-κB BS2 site displayed the most κB binding activity, consistent with the results of ChIP assay, whereas the three AP-1 binding sites showed similar binding activity in mPDAC-1 cells (Figure S4D). The luciferase reporter gene assays, using different *p62* promoter constructs with and without mutated AP-1 or κB binding sites and controls, showed that *p62* expression is mainly regulated by NF-κB activity through NF-κB BS2 site and is also mediated by the three AP-1 sites in mPDAC cells, suggesting that *p62* is an NF-κB and AP-1 downstream target gene (Figure 7K). Furthermore, our results showed that NF-κB was activated in the *Kras^{G12D}* PDAC model in the presence of wild-type *p53* function (Figures S4E and S4F), and FOXO3a was stabilized and TSC1 was activated, whereas p70/S6K was not phosphorylated in *IKK2/β* knockdown cells (Figures S4G and S4H), suggesting that both TSC1 and FOXO3a pathways is also involved in Kras-induced PDAC development.

To demonstrated the role of IL-1α and p62 in mutant Kras-driven cancer cells, we knocked down *IL-1α* and *p62* expression in mPDAC cells and in LKP-13, a lung adenocarcinoma cell line derived from *Kras^{G12D}*(LA1) mice (Wislez et al., 2005; Figure 8A; Figures S5A and S5B), and showed significant reduction of tumorigenic potential in the *IL-1α* and *p62* knocked down cancer cells in orthotopic xenograft mouse and subcutaneous xenograft mouse models (Figures 8B-D). Knocking down *TRAF6*, which is essential for IKK2/β and JNK activation in the IL-1α and TLR pathways (Lomaga et al., 1999; Naito et al., 1999), decreased NF-κB activation in both mPDAC cells expressing *Kras^{G12D}* (Figures 8E–8G). Taken together, these results suggest that IL-1α and p62 play a key role in oncogenic Kras-induced tumors. Knocking down of *c-fos* expression inhibited *IL-1α* and *p62* expression and NF-κB activation (Figures 8H–8L). These results suggest that AP-1 activated by oncogenic Kras induced and sustained activation of RelA/p50 in PDAC development.

As illustrated in Figure 8M, our findings suggest a mechanism by which oncogenic Kras signaling pathway induced constitutive activation of NF-κB in PDAC development.

DISCUSSION

We have unequivocally demonstrated that the requirement of NF-κB pathway for PDAC development and the mechanism through which constitutive NF-κB activation and inflammatory responses were induced by oncogenic Kras during PDAC initiation. These findings suggest that the *primum movens* responsible for cancer-related inflammatory responses and the development of PanIN and PDAC is the mutant Kras-initiated constitutive activation of NF-κB. Importantly, our results suggest that mutant Kras may induce intrinsic inflammatory responses that promote a protumorigenic microenvironment through expressing inflammatory mediators such as chemokines and cytokines in tumor tissues, recruiting inflammatory cells, and inducing angiogenesis and tissue repair similar to those observed in hereditary pancreatitis, which has been firmly linked to the development of PDAC (Brentnall et al., 1999; Lowenfels et al., 1997). Thus, our findings further suggest that sporadic PDAC is also induced through a chronic inflammatory mechanism similar to those observed in hereditary pancreatitis related PDAC cases.

Although studies have demonstrated that mutant Ras was shown to activate NF-κB in several types of tumors in mouse models (Bassères et al., 2010; Meylan et al., 2009; Yang et al., 2010). Signaling pathways leading to the constitutive NF-κB activity in cancer cells were not clear at all. Duran et al. (2008) showed that mutant Ras induced p62 expression through AP-1 to activate IKK2/β and NF-κB. However, the requirement for p62 in NF-κB activation is not completely understood considering the reported function of p62 as an adaptor for regulating E3 ubiquitin-protein ligase TRAF6 and deubiquitination enzyme CYLD to balance the turnover of K63-polyubiquitination (Sanz et al., 2000; Wooten et al., 2005). Our results clearly demonstrated that p62 expression is not required for rapid and early NF-κB activation induced by IL-1α, but it is essential for

Figure 4. Gene Ontology and Gene Set Enrichment Analyses between Pancreata from *Pdx1-Cre;Kras$^{LSL-G12D}$* and *Pdx1-Cre;Kras$^{LSL-G12D}$;IKK2/β$^{F/F}$* Mice and Profiling Cytokine Expression

(A) Enriched expression of NF-κB downstream target gene sets in *Pdx1-Cre;*Kras$^{LSL-G12D}$*;IKK2/β^{WT}* compared to *Pdx1-Cre;Kras$^{LSL-G12D}$;IKK2/β$^{F/F}$*. The heat map represents top enriched genes in *Pdx1-Cre;*Kras$^{LSL-G12D}$*;IKK2/β^{WT}*. NES, normalized enrichment score; NOM p value, nominal p value; FDR, false discovery rate q value. (red, high expression; blue, low expression).

(B) GSEA analyses identify the enriched gene sets expressed either in *Pdx1-Cre; Kras$^{LSL-G12D}$;IKK2/β^{WT}* or *Pdx1-Cre;Kras$^{LSL-G12D}$;IKK2/β$^{F/F}$* using 198 KEGG pathway gene sets. One gene set are enrich in *Pdx1-Cre;Kras$^{LSL-G12D}$;IKK2/β^{WT}* and twenty seven gene sets are enriched in *Pdx1-Cre;Kras$^{LSL-G12D}$;IKK2/β$^{F/F}$*. Five NF-κB pathway-related gene sets are noteworthy enriched in *Pdx1-Cre;Kras$^{LSL-G12D}$; IKK2/β^{WT}*. Enriched gene sets were selected based on statistical significance (FDR q value < 0.25 and normalized p value < 0.05).

(C) GSEA analyses of significant gene upregulation in *Pdx1-Cre;Kras$^{LSL-G12D}$* revealed that they are strongly correlated to positive nodal status, high risk, higher tumor stage, and poor survival in PDAC patients by using 102 PDAC cDNA microarray data (GSE21501). Two- and 5-fold enriched expression in *Pdx1-Cre;Kras$^{LSL-G12D}$; IKK2/β$^{F/F}$* is correlated to low risk. ns, not significant (FDR q value > 0.25 and/or normalized p value > 0.05).

(D) Analysis of differential cytokine gene expression between pancreatic cancer and normal pancreas (from 5- to 12-month-old *Pdx1-Cre;Kras$^{LSL-G12D}$* mice and age-matched *Pdx1-Cre;Kras$^{LSL-G12D}$;IKK2/β$^{F/F}$* mice) by real-time PCR arrays.

(E) Determination of IL-1α expression levels in pancreas, liver, and lung from *Pdx1-Cre;Kras$^{LSL-G12D}$*, *Pdx1-Cre;Kras$^{LSL-G12D}$;IKK2/β$^{F/F}$*, *Pdx1-Cre;IKK2/β$^{F/F}$*, and *wild-type* (*WT*) mice.

(F) Evaluation of IL-1α and IL-1β expression levels in sera from *Pdx1-Cre;Kras$^{LSL-G12D}$*, *Pdx1-Cre;Kras$^{LSL-G12D}$;IKK2/β$^{F/F}$*, *Pdx1-Cre;IKK2/β$^{F/F}$*, and *wild-type* (*WT*) mice. Error bars represent ±SD of the data from three mice in each genotype as indicated. See also Figure S2 and Tables S1–S3.

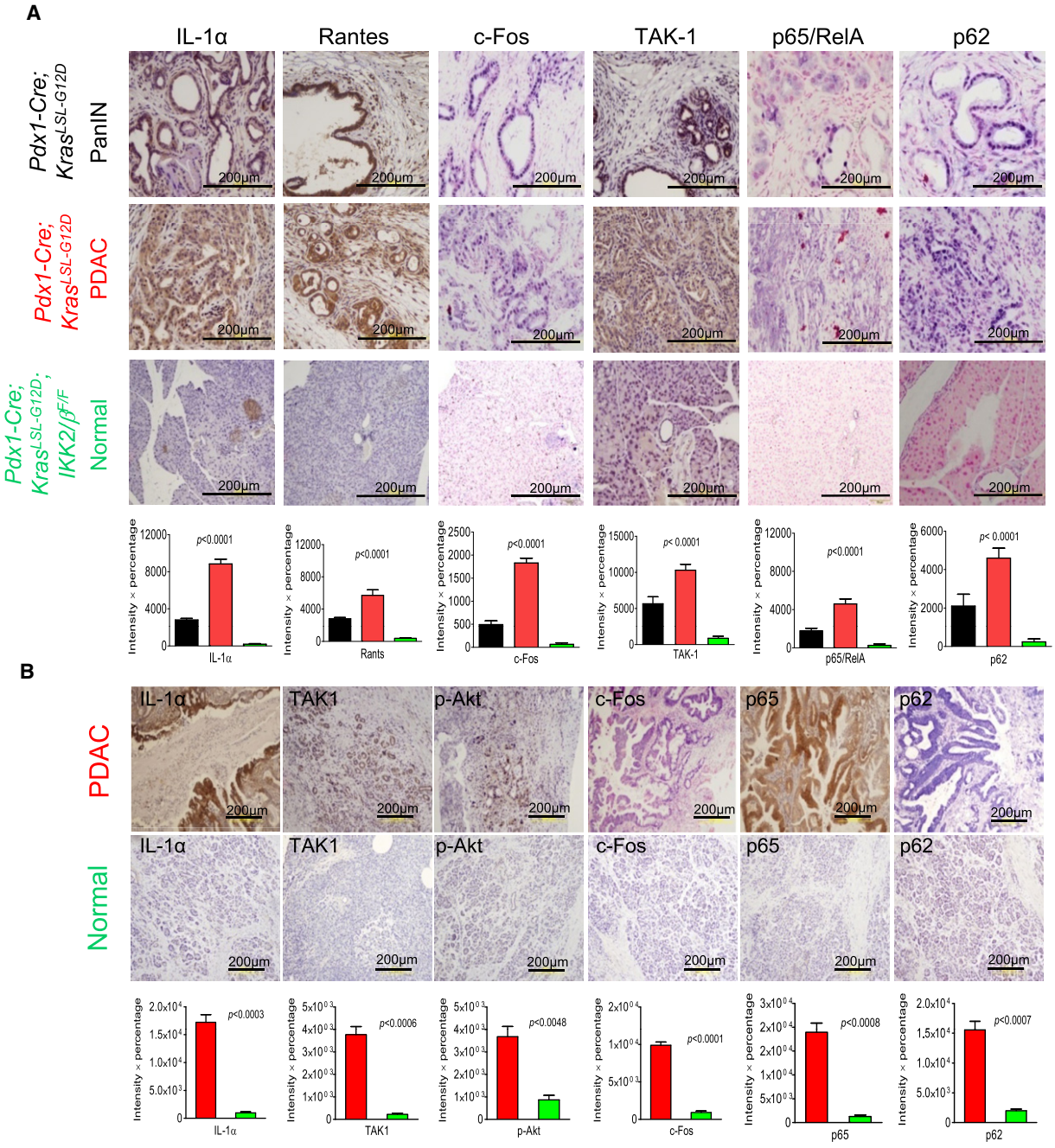

Figure 5. Analysis of Signaling Pathways in PanIN, PDAC, and Histologically Normal Pancreas from Compound Mutant Mice and Human PDAC Patients

(A) Immunohistochemical analysis with anti-IL-1α, anti-Rantes (Chemokine [C-C motif] ligand 5), anti-c-Fos, anti-TAK1, anti-p62, and anti-p65 antibodies in sections of formalin-fixed PanIN lesions and PDAC from *Pdx1-Cre;*$Kras^{LSL-G12D}$ mice, and of normal duct tissues from *Pdx1-Cre;*$Kras^{LSL-G12D}$*;IKK2/*$\beta^{F/F}$ mice. Error bars represent ±SD from the data of five mice for each of the three genotypes.

(B) Immunohistochemical staining for IL-1α, TAK1, pAKT, c-Fos, p65, and p62 in sections of formalin-fixed human PDAC and adjacent histologically normal pancreatic tissues. Error bars represent ±SD from six human PDAC specimens.

constitutive NF-κB activation (Figure 7D; Figures S4A and S4B), which is consistent with the function of p62 as an adaptor for regulating the turnover of K63-polyubiquitinated proteins, including TRAF6, to maintain IKK2/β and NF-κB activation (Sanz et al., 2000; Wooten et al., 2005). Our results show that expression of *p62* is induced by NF-κB activation during IL-1α stimulation of mouse and human PDAC cell lines (Figures 7E–7J), suggesting the existence of an autoregulatory loop whereby NF-κB regulates *p62* expression, which, in turn, extends NF-κB activation.

A

PDAC Patient Specimens	*Kras* Status		IL-1α Expression	% of IL-1α Positive Specimens
PDAC Paraffin Sections	Lymphocyte DDA: N.D.	Wide-type in PDAC DNA (1)	High: 0	0
			Low: 1	100%
		Mutant in PDAC DNA (13)	High: 9	69.2%
			Low: 4	30.8%
PDAC Xenograft Tissues	Lymphocyte DNA: Wide-type	Wide-type in PDAC DNA (2)	High: 0	0
			Low: 2	100%
		Mutant in PDAC DNA (7)	High: 5	71.4%
			Low: 2	28.6%

IL-1α expression vs Kras Mutant: $p<0.05$, $X^2=5.37$

B

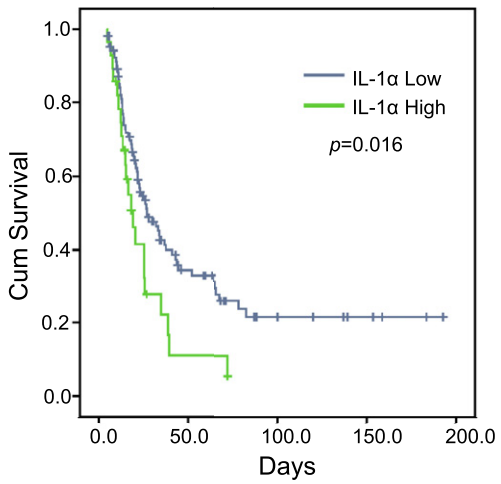

C

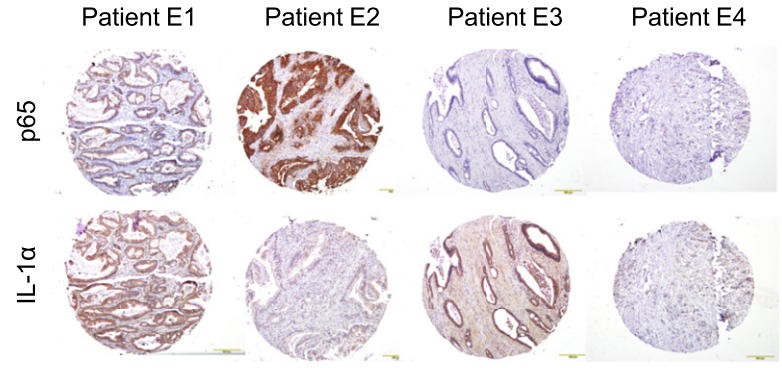

D

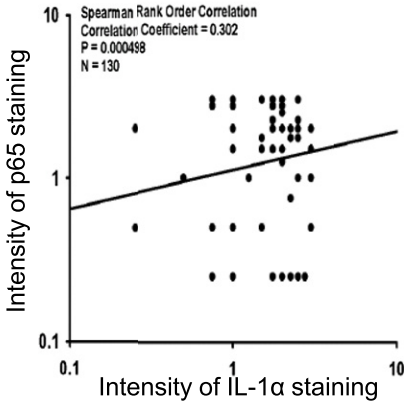

E

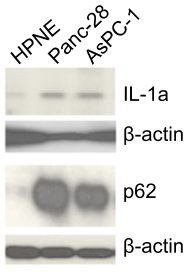

F

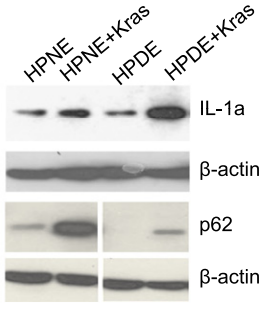

G

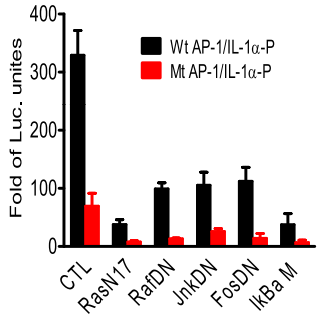

H

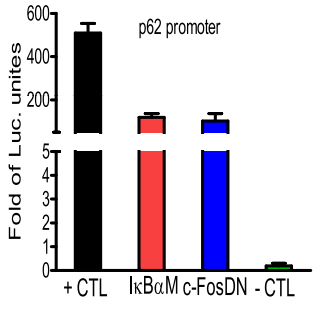

Figure 6. Clinical Correlations among Mutant *Kras*, IL-α Overexpression, and NF-κB Activation in Human PDAC

(A) The percentages of IL-1α positivity in PDAC tissues carrying a mutant *Kras* gene. Chi-square test was used to demonstrate the positive correlation between overexpression of IL-1α and the presence of a mutant *Kras* in PDAC tissues.

(B) Kaplan-Meier survival analysis of PDAC patients with and without high levels of IL-1α expression using TMA.

(C) Immunohistochemical staining for p65 and IL-1α in human PDAC tissue microarrays. Representative IHC stainings are shown, with four combinations of immunostaining patterns, E1: p65 high, IL-1α high; E2: p65 high, IL-1α low; E3: p65 low, IL-1α high; E4: p65 low, IL-1α low.

(D) Scores of activated NF-κB are plotted against those of IL-1α overexpression. Spearman's rank order correlation was used to demonstrate the positive correlation between NF-κB activity and expression levels of IL-1α in TMA.

(E) Western blot analysis showing IL-1α and p62 overexpression in pancreatic cancer cell lines MDAPanc-28 and AsPc-1.

(F) Western blot analysis of IL-1α and p62 expression in hTERT-immortalized human pancreatic ductal HPNE and HPDE cell lines.

(G) Reporter gene assay for analyzing *IL-1α* promoter regulation by Kras, AP-1, and NF-κB pathways using mPDAC cells.

(H) Reporter gene assay for analyzing the regulation of *p62* promoter by AP-1 and NF-κB pathways using mPDAC cells. Error bars represent ±SD from three independent experiments. See also Figure S3.

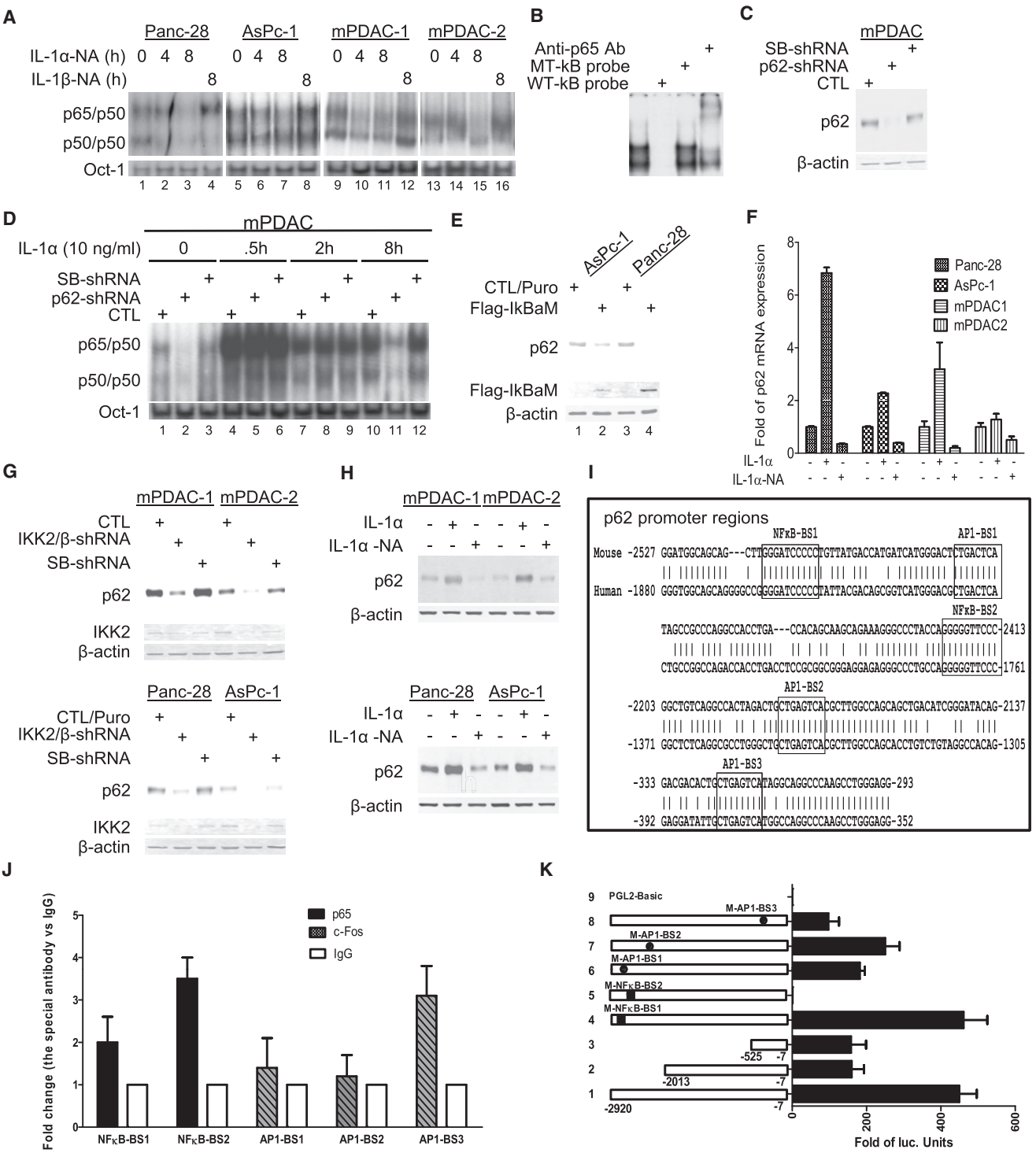

Figure 7. Elucidation of Feedforward Signaling Pathways that Sustain Constitutive NF-κB Activation in Oncogenic *Kras^{G12D}*-Induced PDAC

(A) Nuclear extracts of human PDAC cell lines MDAPanc-28 and AsPc-1 and mouse PDAC cell lines mPDAC-1 and mPDAC-2 (derived from *Pdx1-Cre; Kras$^{LSL-G12D}$*), treated with anti-IL-1α neutralizing antibody (2 μg/ml) for 0, 4, or 8 hr or with anti-IL-1β neutralizing antibody (2 μg/ml) for 0 or 8 hr as indicated, were analyzed by EMSA to determine NF-κB activity using a probe containing an NF-κB DNA binding site. Oct-1 DNA binding activities were determined as loading controls.

(B) EMSA was performed to determine the specificity of inducible RelA/p50 NF-κB DNA binding activity. Competition and supershift assays were performed using 20 μg of nuclear protein from mPDAC-2 cells as indicated.

(C) Western blot was performed to determine the expression of p62 in mPDAC cells (CTL), mPDAC cells (*p62-shRNA*) expressing *p62shRNA*, and mPDAC cells (*SB-shRNA*) expressing scrambled control shRNA with anti-p62 antibody. Relative protein loading was determined by the use of anti-β-actin antibody.

Our results show that TSC1 and FOXO3a pathways are involved in Kras-induced PDAC (Figures S4G and S4H), consistent with the studies showing that IKK2/β phosphorylates TSC1 at Ser^{487} and Ser^{511} and FOXO3a for promoting tumorigenesis (Hu et al., 2004; Lee et al., 2007). Interestingly, expression of both IL-1α and IL-1β was inhibited in our *Pdx1-Cre;Kras$^{LSL-G12D}$; IKK2/β$^{F/F}$* mouse model (Figures 4E–4F), pointing out different regulatory mechanisms of IL-1β in pancreas as NF-κB activity inhibits the release of IL-1β from macrophage (Greten et al., 2007).

In summary, we report here constitutive NF-κB activation is required for PDAC development and proposed the mechanism for NF-κB activation by Kras^{G12D} through AP-1-induced IL-1α overexpression. Since IL-1α overexpression correlates with poor survival in PDAC patients, and since it is found in other diseases, such as chronic inflammation autoimmune disorders (Gabay et al., 2010), pharmacologic targeting IL-1α overexpression may represent a potential therapy for PDAC.

EXPERIMENTAL PROCEDURES

Generation of Mouse Strain

The genetically engineered mouse strains used in our study were kindly and generously provided by the following laboratories: floxed *IKK2/β* (*IKK2/β$^{F/F}$*) mice by Michael Karin's laboratory (Li et al., 2003); floxed Ink4a/Arf (*Ink4a/Arf$^{F/F}$*) mice by Ronald Depinho's laboratory (Aguirre et al., 2003); *Kras$^{LSL-G12D}$* mice by Tyler Jacks' laboratory (Johnson et al., 2001); and *Pdx1-Cre* transgenic mice by Douglas Melton's laboratory (Gu et al., 2002). These strains were interbred to generate the experimental cohorts, which include the following genotypes: *Pdx1-Cre;Kras$^{LSL-G12D}$*, *Pdx1-Cre;IKK2/β$^{F/F}$*, *Pdx1-Cre;Kras$^{LSL-G12D}$; IKK2/β$^{F/F}$*, *Pdx1-Cre;Kras$^{LSL-G12D}$;Ink4a/Arf$^{F/F}$* and *Pdx1-Cre;Kras$^{LSL-G12D}$;Ink4a/Arf$^{F/F}$; IKK2/β$^{F/F}$*. These mutant mouse strains were genotyped by PCR as previously described by the laboratories that generated them. All animal experiments were conducted under the protocol that was approved for this study by the Institutional Animal Care and Use Committee (IACUC) at the University of Texas MD Anderson Cancer Center.

Patient Pancreatic Ductal Adenocarcinoma and Adjacent Normal Tissues

Patient pancreatic cancer tissue microarray (TMA) was constructed and paraffin sections were obtained using the paraffin blocks from primary pancreatic ductal adenocarcinoma and paired adjacent normal tissues of 131 pancreatic cancer patients, which were collected within 1 hr after surgery under the protocol approved by the Institutional Review Board at M.D. Anderson Cancer Center, and written informed consent was obtained from patients in all cases at time of enrollment.

Cell Lines and Reagents

The human pancreatic cancer cell line AsPC-1 was purchased from the American Type Culture Collection. MDAPanc-28 was established by Marsha Frazier and Douglas B. Evans (M.D. Anderson Cancer Center). Immortalized/nontumorigenic HPDE and the hTERT-HPNE cells were described (Lee et al., 2005; Qian et al., 2005). Panc-28/ IκBαM, AsPc-1/IκBαM, HPNE/Kras, and HPDE/Kras cell lines were established in Chiao's laboratory (Qian et al., 2005). Anti-human IL-1α and IL-1β, anti-mouse IL-1α and IL-1β neutralizing antibodies, and IL-1α were obtained from R&D Systems.

Knockdown of *IKK2/β*, *p62*, *IL-1α*,*Traf6*, and *c-Fos*

To silence *IKK2/β*, *p62*, *and IL-1α* expression, DNA sequences encoding shRNAs and a scramble sequence were chosen to clone into the FG12 lentiviral vector. The mouse primary pancreatic cancer cell lines mPDAC-1 and mPDAC-2 and human PDAC cell lines Panc28 and AsPc-1 were infected by lentivirus containing the shRNA. The infected cells were sorted by green fluorescent protein after infection 4 days. The levels of target gene knockdown by shRNA were determined using immunoblotting.

Statistical Analysis

Mean values between groups were compared by Excel. Survival curves were plotted by the Kaplan-Meier method and compared by the log-rank test using GraphPad Prism. The correlative relationships between two quantitative measurements were investigated using Spearman rank-order correlation and the chi-square statistic. Data were analyzed by the Student t test and results were considered significant at a p value < 0.05.

ACCESSION NUMBERS

Microarray data has been deposited in the Gene Expression Omnibus (GEO) database (accession number GSE33323).

SUPPLEMENTAL INFORMATION

Supplemental Information includes five figures, three tables, and Supplemental Experimental Procedures and can be found with this article online at doi:10.1016/j.ccr.2011.12.006.

ACKNOWLEDGMENTS

We thank Dr. Michael Karin for the *IKK2/β$^{F/F}$* mice, Dr. Douglas Melton for the *Pdx1-Cre* transgenic mice, Dr. Tyler Jacks for the *Kras$^{LSL-G12D}$* mice,

(D) NF-κB activities in the nuclear extracts of mPDAC cells (*CTL*), mPDAC cells (*p62-shRNA*) expressing *p62shRNA*, and mPDAC cells (*SB-shRNA*) expressing scrambled control shRNA stimulated with IL-1α for the times indicated were determined by EMSA. Oct-1 DNA binding activities were determined as loading controls in (A) and (D).

(E) NF-κB-dependent expression of p62 was determined by western blot analysis in protein extracts from MDAPanc-28 and AsPc-1 cells expressing a Flag-tagged IκBα mutant (*Flag-IκBαM*) and their control cells expressing a puromycin resistance vector (*CTL/Puro*). Flag-IκBαM expression was verified by using anti-Flag antibody. Relative protein loading was determined by the use of anti-β-actin antibody.

(F) IL-1α-regulated p62 expression was determined by real-time PCR in MDAPanc-28, AsPc-1, mPDAC-1, and mPDAC-2 treated with anti-IL-1α neutralizing antibody (2 μg/ml) for 8 hr or IL-1α (10 ng/ml) for 1 hr as indicated.

(G) IKK2/β-induced p62 expression was determined by western blot analysis using MDAPanc-28, AsPc-1, mPDAC-1, and mPDAC-2 cells expressing *IKK2/β-shRNA* (*IKK2-shRNA*) and their control cells expressing a puromycin resistance vector (*CTL/Puro*) and scrambled shRNA (*CTL-shRNA*). IKK2/β expression was verified by using anti-IKK2/β antibody. Relative protein loading was determined by the use of anti-β-actin antibody.

(H) IL-1α-regulated p62 expression was determined by western blot analysis in protein extracts of MDAPanc-28, AsPc-1, mPDAC-1, and mPDAC-2 cells treated with anti-IL-1α neutralizing antibody (2 μg/ml) for 8 hr or IL-1α (10 ng/ml) for 1 hr as indicated. Relative protein loading was determined by using anti-β-actin antibody.

(I) The sequence alignment between mouse and human *p62* promoter regions was presented with AP-1 and NF-κB binding sites indicated.

(J) The activities of the AP-1 and κB binding sites in mouse *p62* promoter were determined. mPDAC cells were stimulated with IL-1α for one hour and ChIP assays were performed with anti-c-Fos and anti-p65/NF-κB antibodies and IgG as negative control by using real-time PCR.

(K) Analysis of p62 promoter activities in mPDAC-1 cells. The luciferase reporter gene activities are presented with the schematic illustration of the different luciferase reporter constructs of the p62 promoter constructs with mutated AP-1 and κB binding sites and control plasmids as indicated. Luciferase activity was measured as described in Experimental Procedures. Error bars represent ±SD from three independent experiments. See also Figure S4.

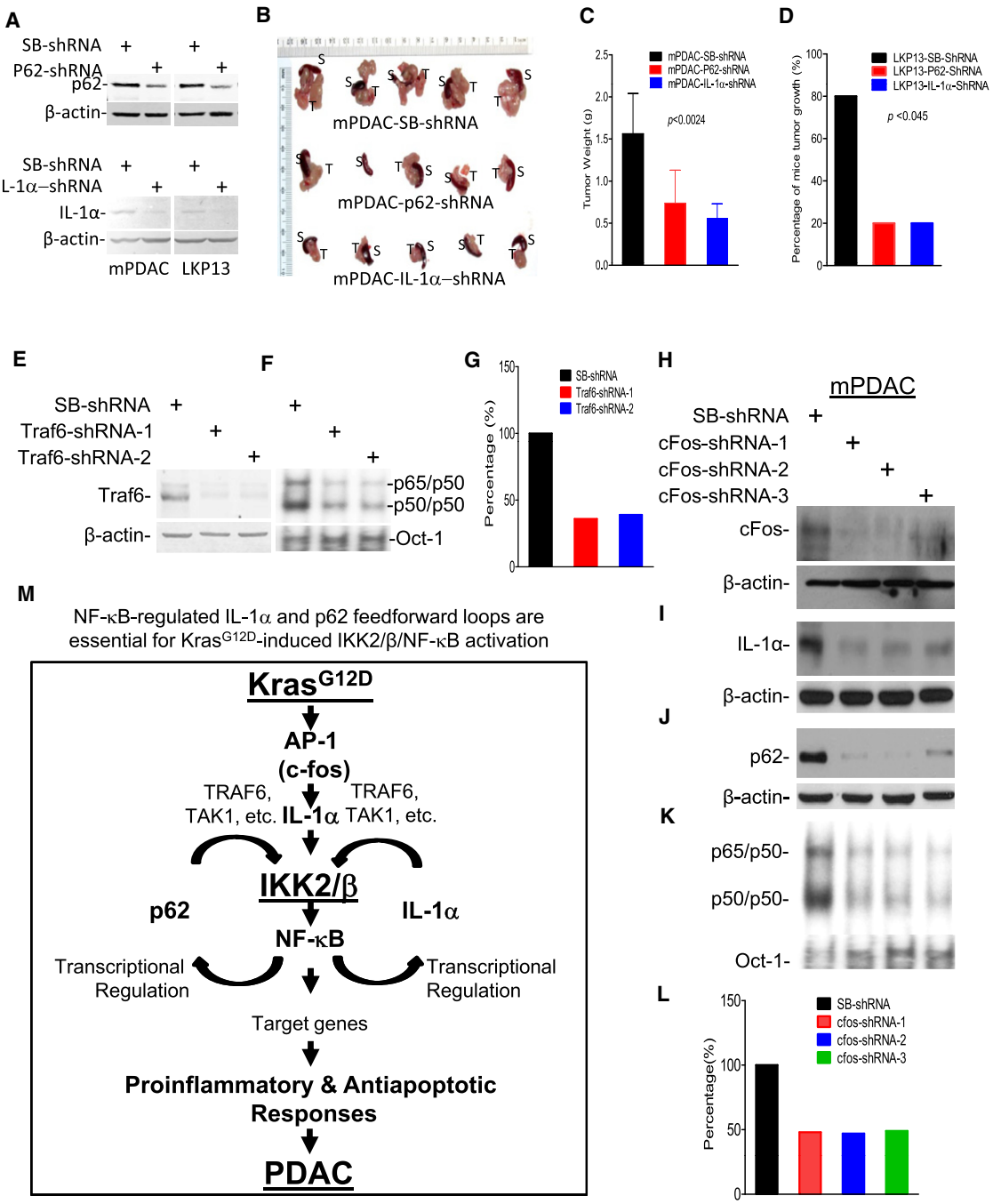

Figure 8. AP-1 Induced by Oncogenic *Kras^{G12D}* Initiates Feedforward Loops of IL-1α and p62 to Induce and Sustain Constitutive NF-κB Activation and the Working Model

(A) Knocked down expression of IL-1α and p62 in mPDAC and LKP-13 cells. The expression levels of p62 and IL-1α in mPDAC *and* LKP-13 cells expressing scrambled shRNA (*SBshRNA*), *p62shRNA,* and IL-1α*shRNA* was determined using anti-p62 or anti- IL-1α antibody in western blot with β-actin as relative protein loading controls.

(B) The resected orthotopic tumors attached to spleen in fifteen C57B6 mice injected with mPDAC-*SBshRNA*, mPDAC-*p62shRNA*, and mPDAC-*IL-1αshRNA* cells (n = 5 per group) were shown at week 5. S: spleen; T: tumor.

(C) Tumor weight in C57B6 mice orthotopically injected with mPDAC-*SBshRNA*, mPDAC-*p62shRNA*, and mPDAC-*IL-1αshRNA* cells. Columns: mean of all individual tumors in each group. Error bars: ±SD of the pancreatic tumor from five mice in each of the three groups as indicated.

(D) Percentage of C57B6 mice that developed subcutaneous tumors after injection of *LKP-13-SB-shRNA, LKP-13-p62shRNA*, and *LKP-13-IL-1αshRNA* cells. Columns: percentage of the mice that grew tumor in each group (n = 5). The statistical significance was determined by Fisher's exact test.

(E) Expression of TRAF6 in mPDAC cells expressing scrambled Traf6 shRNA (*SB-shRNA*) and two Traf6-shRNA (*Traf6-shRNA-1 and 2*) was determined by anti-TRAF6 antibody with β-actin as loading control.

Dr. Ronald DePinho for the *Ink4a/Arf* $^{F/F}$ mice, and Dr. Kenneth Hess in the Department of Biostatistics, M.D. Anderson Cancer Center, for statistical analysis, Dr. Chang-gong Liu in Sequencing & Non-coding RNA Program and Dr. Wei Zhang at Genomic Core, M.D. Anderson Cancer Center, for microarray analysis. We also thank Yu (June) Cao for technical assistance and Kathryn Hale for editorial assistance. The work was supported in part by grants from the National Cancer Institute (CA109405 and CA142674 to P.J.C.), a Cancer Center Core Supporting grant (CA16672), and Sister Institution Fund of China Medical University and Hospital and MD Anderson Cancer Center to M. C. H.

Received: June 20, 2011
Revised: November 2, 2011
Accepted: December 13, 2011
Published: January 17, 2012

REFERENCES

Aguirre, A.J., Bardeesy, N., Sinha, M., Lopez, L., Tuveson, D.A., Horner, J., Redston, M.S., and DePinho, R.A. (2003). Activated Kras and Ink4a/Arf deficiency cooperate to produce metastatic pancreatic ductal adenocarcinoma. Genes Dev. *17*, 3112–3126.

Barbie, D.A., Tamayo, P., Boehm, J.S., Kim, S.Y., Moody, S.E., Dunn, I.F., Schinzel, A.C., Sandy, P., Meylan, E., Scholl, C., et al. (2009). Systematic RNA interference reveals that oncogenic KRAS-driven cancers require TBK1. Nature *462*, 108–112.

Bardeesy, N., Aguirre, A.J., Chu, G.C., Cheng, K.H., Lopez, L.V., Hezel, A.F., Feng, B., Brennan, C., Weissleder, R., Mahmood, U., et al. (2006). Both p16(Ink4a) and the p19(Arf)-p53 pathway constrain progression of pancreatic adenocarcinoma in the mouse. Proc. Natl. Acad. Sci. USA *103*, 5947–5952.

Bassères, D.S., Ebbs, A., Levantini, E., and Baldwin, A.S. (2010). Requirement of the NF-kappaB subunit p65/RelA for K-Ras-induced lung tumorigenesis. Cancer Res. *70*, 3537–3546.

Brentnall, T.A., Bronner, M.P., Byrd, D.R., Haggitt, R.C., and Kimmey, M.B. (1999). Early diagnosis and treatment of pancreatic dysplasia in patients with a family history of pancreatic cancer. Ann. Intern. Med. *131*, 247–255.

Chien, Y., Kim, S., Bumeister, R., Loo, Y.M., Kwon, S.W., Johnson, C.L., Balakireva, M.G., Romeo, Y., Kopelovich, L., Gale, M., Jr., et al. (2006). RalB GTPase-mediated activation of the IkappaB family kinase TBK1 couples innate immune signaling to tumor cell survival. Cell *127*, 157–170.

Dajee, M., Lazarov, M., Zhang, J.Y., Cai, T., Green, C.L., Russell, A.J., Marinkovich, M.P., Tao, S., Lin, Q., Kubo, Y., and Khavari, P.A. (2003). NF-kappaB blockade and oncogenic Ras trigger invasive human epidermal neoplasia. Nature *421*, 639–643.

Duran, A., Linares, J.F., Galvez, A.S., Wikenheiser, K., Flores, J.M., Diaz-Meco, M.T., and Moscat, J. (2008). The signaling adaptor p62 is an important NF-kappaB mediator in tumorigenesis. Cancer Cell *13*, 343–354.

Fujioka, S., Sclabas, G.M., Schmidt, C., Niu, J., Frederick, W.A., Dong, Q.G., Abbruzzese, J.L., Evans, D.B., Baker, C., and Chiao, P.J. (2003). Inhibition of constitutive NF-kappa B activity by I kappa B alpha M suppresses tumorigenesis. Oncogene *22*, 1365–1370.

Gabay, C., Lamacchia, C., and Palmer, G. (2010). IL-1 pathways in inflammation and human diseases. Nat. Rev. Rheumatol. *6*, 232–241.

Greten, F.R., Arkan, M.C., Bollrath, J., Hsu, L.C., Goode, J., Miething, C., Göktuna, S.I., Neuenhahn, M., Fierer, J., Paxian, S., et al. (2007). NF-kappaB is a negative regulator of IL-1beta secretion as revealed by genetic and pharmacological inhibition of IKKbeta. Cell *130*, 918–931.

Gu, G., Dubauskaite, J., and Melton, D.A. (2002). Direct evidence for the pancreatic lineage: NGN3+ cells are islet progenitors and are distinct from duct progenitors. Development *129*, 2447–2457.

He, G., Yu, G.Y., Temkin, V., Ogata, H., Kuntzen, C., Sakurai, T., Sieghart, W., Peck-Radosavljevic, M., Leffert, H.L., and Karin, M. (2010). Hepatocyte IKKbeta/NF-kappaB inhibits tumor promotion and progression by preventing oxidative stress-driven STAT3 activation. Cancer Cell *17*, 286–297.

Hingorani, S.R., Petricoin, E.F., Maitra, A., Rajapakse, V., King, C., Jacobetz, M.A., Ross, S., Conrads, T.P., Veenstra, T.D., Hitt, B.A., et al. (2003). Preinvasive and invasive ductal pancreatic cancer and its early detection in the mouse. Cancer Cell *4*, 437–450.

Hruban, R.H., Goggins, M., Parsons, J., and Kern, S.E. (2000). Progression model for pancreatic cancer. Clin. Cancer Res. *6*, 2969–2972.

Hu, M.C., Lee, D.F., Xia, W., Golfman, L.S., Ou-Yang, F., Yang, J.Y., Zou, Y., Bao, S., Hanada, N., Saso, H., et al. (2004). IkappaB kinase promotes tumorigenesis through inhibition of forkhead FOXO3a. Cell *117*, 225–237.

Johnson, L., Mercer, K., Greenbaum, D., Bronson, R.T., Crowley, D., Tuveson, D.A., and Jacks, T. (2001). Somatic activation of the K-ras oncogene causes early onset lung cancer in mice. Nature *410*, 1111–1116.

Karin, M. (2008). The IkappaB kinase - a bridge between inflammation and cancer. Cell Res. *18*, 334–342.

Kim, M.P., Evans, D.B., Wang, H., Abbruzzese, J.L., Fleming, J.B., and Gallick, G.E. (2009). Generation of orthotopic and heterotopic human pancreatic cancer xenografts in immunodeficient mice. Nat. Protoc. *4*, 1670–1680.

Lee, D.F., Kuo, H.P., Chen, C.T., Hsu, J.M., Chou, C.K., Wei, Y., Sun, H.L., Li, L.Y., Ping, B., Huang, W.C., et al. (2007). IKK beta suppression of TSC1 links inflammation and tumor angiogenesis via the mTOR pathway. Cell *130*, 440–455.

Lee, K.M., Yasuda, H., Hollingsworth, M.A., and Ouellette, M.M. (2005). Notch 2-positive progenitors with the intrinsic ability to give rise to pancreatic ductal cells. Lab. Invest. *85*, 1003–1012.

Li, Z.W., Omori, S.A., Labuda, T., Karin, M., and Rickert, R.C. (2003). IKK beta is required for peripheral B cell survival and proliferation. J. Immunol. *170*, 4630–4637.

Lomaga, M.A., Yeh, W.C., Sarosi, I., Duncan, G.S., Furlonger, C., Ho, A., Morony, S., Capparelli, C., Van, G., Kaufman, S., et al. (1999). TRAF6 deficiency results in osteopetrosis and defective interleukin-1, CD40, and LPS signaling. Genes Dev. *13*, 1015–1024.

Lowenfels, A.B., Maisonneuve, P., DiMagno, E.P., Elitsur, Y., Gates, L.K., Jr., Perrault, J., and Whitcomb, D.C.; International Hereditary Pancreatitis Study

(F) NF-κB activities in the nuclear extracts of mPDAC cells expressing scrambled Traf6 shRNA (*SB-shRNA*) and two *Traf6-shRNAs* were determined by EMSA. Oct-1 DNA binding activities were determined as loading controls.
(G) Quantitation of NFκB activities in EMSA by Image Analysis Software (ImageQuant TL 7.0).
(H) c-Fos expression in mPDAC expressing a scrambled control shRNA (*SB-shRNA*) and three different cFos-shRNAs (*cfos-shRNA-1, 2, 3*) was determined with anti-cFos antibody in western blot analysis.
(I) The levels of IL-1α in mPDAC cytoplasmic extracts expressing a scrambled control shRNA (*SB-shRNA*) and three different cFos-shRNAs (c-*fos*-shRNA-1, 2, 3) were analyzed by anti-IL-1α western blot with β-actin as loading control.
(J) p62 expression in mPDAC cells expressing a scrambled control shRNA(*SB-shRNA*), and three different cFos-shRNAs (*cfos-shRNA-1, 2, 3*) were analyzed by anti-p62 western blot with β-actin as loading control.
(K) NF-κB activity from mPDAC expressing a scrambled control shRNA(*SB-shRNA*) and three different cFos-shRNAs (*cfos-shRNA-1, 2, 3*) were analyzed by EMSA. Oct-1 DNA binding activities were determined as loading controls
(L) Quantitation of NFκB activities in EMSA by Image Analysis Software (ImageQuant TL 7.0).
(M) A proposed working model illustrates the potential mechanism through which *Kras^{G12D}* oncogenic signaling induces feedforward loops of IL-1α and p62 to sustain constitutive IKK2/β/NF-κB activation in PDAC development. See also Figure S5.

Group. (1997). Hereditary pancreatitis and the risk of pancreatic cancer. J. Natl. Cancer Inst. *89*, 442–446.

Maeda, S., Kamata, H., Luo, J.L., Leffert, H., and Karin, M. (2005). IKKbeta couples hepatocyte death to cytokine-driven compensatory proliferation that promotes chemical hepatocarcinogenesis. Cell *121*, 977–990.

Meylan, E., Dooley, A.L., Feldser, D.M., Shen, L., Turk, E., Ouyang, C., and Jacks, T. (2009). Requirement for NF-kappaB signalling in a mouse model of lung adenocarcinoma. Nature *462*, 104–107.

Mori, N., and Prager, D. (1996). Transactivation of the interleukin-1alpha promoter by human T-cell leukemia virus type I and type II Tax proteins. Blood *87*, 3410–3417.

Naito, A., Azuma, S., Tanaka, S., Miyazaki, T., Takaki, S., Takatsu, K., Nakao, K., Nakamura, K., Katsuki, M., Yamamoto, T., and Inoue, J. (1999). Severe osteopetrosis, defective interleukin-1 signalling and lymph node organogenesis in TRAF6-deficient mice. Genes Cells *4*, 353–362.

Osborn, L., Kunkel, S., and Nabel, G.J. (1989). Tumor necrosis factor alpha and interleukin 1 stimulate the human immunodeficiency virus enhancer by activation of the nuclear factor kappa B. Proc. Natl. Acad. Sci. USA *86*, 2336–2340.

Peng, B., Ling, J., Lee, A.J., Wang, Z., Chang, Z., Jin, W., Kang, Y., Zhang, R., Shim, D., Wang, H., et al. (2010). Defective feedback regulation of NF-kappaB underlies Sjogren's syndrome in mice with mutated kappaB enhancers of the IkappaBalpha promoter. Proc. Natl. Acad. Sci. USA *107*, 15193–15198.

Pomerantz, J.L., and Baltimore, D. (1999). NF-kappaB activation by a signaling complex containing TRAF2, TANK and TBK1, a novel IKK-related kinase. EMBO J. *18*, 6694–6704.

Qian, J., Niu, J., Li, M., Chiao, P.J., and Tsao, M.S. (2005). In vitro modeling of human pancreatic duct epithelial cell transformation defines gene expression changes induced by K-ras oncogenic activation in pancreatic carcinogenesis. Cancer Res. *65*, 5045–5053.

Sanz, L., Diaz-Meco, M.T., Nakano, H., and Moscat, J. (2000). The atypical PKC-interacting protein p62 channels NF-kappaB activation by the IL-1-TRAF6 pathway. EMBO J. *19*, 1576–1586.

Skaug, B., Jiang, X., and Chen, Z.J. (2009). The role of ubiquitin in NF-kappaB regulatory pathways. Annu. Rev. Biochem. *78*, 769–796.

Staudt, L.M. (2010). Oncogenic activation of NF-kappaB. Cold Spring Harb. Perspect. Biol. *2*, a000109.

Tuveson, D.A., Shaw, A.T., Willis, N.A., Silver, D.P., Jackson, E.L., Chang, S., Mercer, K.L., Grochow, R., Hock, H., Crowley, D., et al. (2004). Endogenous oncogenic K-ras(G12D) stimulates proliferation and widespread neoplastic and developmental defects. Cancer Cell *5*, 375–387.

Wang, C., Deng, L., Hong, M., Akkaraju, G.R., Inoue, J., and Chen, Z.J. (2001). TAK1 is a ubiquitin-dependent kinase of MKK and IKK. Nature *412*, 346–351.

Wang, W., Abbruzzese, J.L., Evans, D.B., Larry, L., Cleary, K.R., and Chiao, P.J. (1999). The nuclear factor-kappa B RelA transcription factor is constitutively activated in human pancreatic adenocarcinoma cells. Clin. Cancer Res. *5*, 119–127.

Wislez, M., Spencer, M.L., Izzo, J.G., Juroske, D.M., Balhara, K., Cody, D.D., Price, R.E., Hittelman, W.N., Wistuba, I.I., and Kurie, J.M. (2005). Inhibition of mammalian target of rapamycin reverses alveolar epithelial neoplasia induced by oncogenic K-ras. Cancer Res. *65*, 3226–3235.

Wooten, M.W., Geetha, T., Seibenhener, M.L., Babu, J.R., Diaz-Meco, M.T., and Moscat, J. (2005). The p62 scaffold regulates nerve growth factor-induced NF-kappaB activation by influencing TRAF6 polyubiquitination. J. Biol. Chem. *280*, 35625–35629.

Yang, J., Splittgerber, R., Yull, F.E., Kantrow, S., Ayers, G.D., Karin, M., and Richmond, A. (2010). Conditional ablation of Ikkb inhibits melanoma tumor development in mice. J. Clin. Invest. *120*, 2563–2574.

Zabel, U., Henkel, T., Silva, M.S., and Baeuerle, P.A. (1993). Nuclear uptake control of NF-kappa B by MAD-3, an I kappa B protein present in the nucleus. EMBO J. *12*, 201–211.

Cancer Cell
Article

Polycomb-Mediated Loss of miR-31 Activates NIK-Dependent NF-κB Pathway in Adult T Cell Leukemia and Other Cancers

Makoto Yamagishi,[1,3] Kazumi Nakano,[1] Ariko Miyake,[1] Tadanori Yamochi,[1] Yayoi Kagami,[1] Akihisa Tsutsumi,[1] Yuka Matsuda,[1] Aiko Sato-Otsubo,[4] Satsuki Muto,[1,4] Atae Utsunomiya,[5] Kazunari Yamaguchi,[6] Kaoru Uchimaru,[2] Seishi Ogawa,[4] and Toshiki Watanabe[1,*]
[1]Graduate School of Frontier Sciences
[2]Institute of Medical Science
The University of Tokyo, Tokyo, 108-8639, Japan
[3]Japan Foundation for AIDS Prevention, Tokyo, 101-0061, Japan
[4]Cancer Genomics Project, Graduate School of Medicine, The University of Tokyo, Tokyo, 113-8655, Japan
[5]Department of Haematology, Imamura Hospital, Bun-in, Kagoshima, 890-0064, Japan
[6]Department of Safety Research on Blood and Biologics, NIID, Tokyo, 208-0611, Japan
*Correspondence: tnabe@ims.u-tokyo.ac.jp
DOI 10.1016/j.ccr.2011.12.015

SUMMARY

Constitutive NF-κB activation has causative roles in adult T cell leukemia (ATL) caused by HTLV-1 and other cancers. Here, we report a pathway involving Polycomb-mediated miRNA silencing and NF-κB activation. We determine the miRNA signatures and reveal miR-31 loss in primary ATL cells. MiR-31 negatively regulates the noncanonical NF-κB pathway by targeting NF-κB inducing kinase (NIK). Loss of miR-31 therefore triggers oncogenic signaling. In ATL cells, miR-31 level is epigenetically regulated, and aberrant upregulation of Polycomb proteins contribute to miR-31 downregulation in an epigenetic fashion, leading to activation of NF-κB and apoptosis resistance. Furthermore, this emerging circuit operates in other cancers and receptor-initiated NF-κB cascade. Our findings provide a perspective involving the epigenetic program, inflammatory responses, and oncogenic signaling.

INTRODUCTION

Adult T cell leukemia (ATL) is an aggressive T cell neoplasm with very poor prognosis (Yamaguchi and Watanabe, 2002). Human T cell leukemia virus type I (HTLV-I) is recognized as an etiological factor in T cell malignancy. Although mounting molecular evidence has contributed to our ability to cure several cancers and other diseases, the genetic background of ATL leukemogenesis is not yet fully understood. Thus, it is an urgent request to clarify the molecular mechanism of ATL development.

Constitutive activation of nuclear factor-κB (NF-κB) is observed in the ATL cell lines and primary isolated tumor cells from ATL patients, although the viral oncoprotein Tax, a powerful activator of NF-κB, is not expressed in these malignant cells (Hironaka et al., 2004; Watanabe et al., 2005). NF-κB activation aberrantly contributes to cell propagation and anti-apoptotic responses in ATL and other cancers (Prasad et al., 2010). In our previous study, inhibition of NF-κB activity with a specific inhibitor, DHMEQ, drastically impaired the levels of ATL cell growth and resistance to apoptosis (Watanabe et al., 2005), suggesting that the molecular background of aberrant NF-κB activation may give us potential therapeutic targets. A recent report provided a new readout that NF-κB-inducing kinase (NIK) has a causal role in tumor progression and the aggressive phenotypes of various cancers, including ATL (Saitoh et al., 2008). NIK plays a pivotal role in the noncanonical (alternative) NF-κB pathway as a crucial kinase in receptor-initiating signaling, including signaling from CD40, LTBR, and BAFFR.

Significance

Here, we propose a molecular perspective of the onset of oncogenic signaling. NIK overexpression is a major driving force for constitutive NF-κB activation in various types of cancers. Using ATL cells as a model of NF-κB-addiction, we identified miR-31 as a suppressor of NIK that is completely silenced in ATL cells. Furthermore, an oncogenic function of a subset of Polycomb is implicated in NF-κB signaling via miRNA regulation. This study introduces a fundamental link between the Polycomb-mediated epigenetic regulation and the NF-κB signaling, allowing us to attribute the constitutive activation of NF-κB to epigenetic reprogramming.

Several studies have recently implicated another functional significance of NIK protein in epithelial cell proliferation, inflammatory response, and oncogenic signaling (for review, see Thu and Richmond, 2010). Although the expression level of NIK is strictly maintained by proteasomal degradation in normal cells (Liao et al., 2004), increased level of NIK transcript are observed in some cancers, causing inappropriate accumulation of NIK protein without stimuli (Annunziata et al., 2007; Saitoh et al., 2008). Overexpression of NIK leads to aberrant phenotypes in several cell types; however, little is known about the abnormal accumulation of NIK in malignant cells.

Recent advances have led to deeper understanding of a new aspect of posttranscriptional gene regulation, i.e., regulation by a class of noncoding RNAs. MicroRNAs (miRNAs) are functional RNAs with 18–25 nt in length that contribute to a class of cellular functions by negatively controlling targeted gene expression via base-pairing to 3′ untranslated region (3′ UTR). A single miRNA regulates the expression of multiple genes, and the functions of miRNAs therefore need to be orchestrated for cellular homeostasis (Ventura and Jacks, 2009). In the context of cancer pathology, many studies have provided evidences that miRNAs can act as either oncogenes or tumor suppressors. Although the relationship between miRNA deregulation and oncogenes has been clarified in several cancer cells, there has been no integrated analysis of gene expression in ATL. Since miRNAs have important functions in living cells, miRNA expression needs to be tightly regulated. Our knowledge about the regulatory mechanisms of miRNA expression is very inadequate because research effort has focused mainly on the role of miRNAs, which remains one of the most intriguing questions. miRNA regulation involves multiple steps. miRNA maturation has been identified as an important step, and its deregulation leads to progression and development of cancer (Davis et al., 2008; Trabucchi et al., 2009). Genetic deletion in cancer cells has also been reported to account for specific miRNA defect (Varambally et al., 2008). In addition, miRNA expression seems to be epigenetically programmed. DNA methylation and histone modification are strong candidates for miRNA regulation and their abnormalities, therefore, have causal roles in cancer initiation, development, and progression. In particular, Polycomb group proteins have central functions in cellular development and regeneration by controlling histone methylation, especially at histone H3 Lys27 (H3K27), which induces chromatin compaction (Simon and Kingston, 2009). Recent studies have revealed that the amount of Polycomb family is closely associated with cancer phenotypes and malignancy in breast cancer, prostate cancer, and other neoplasms (Sparmann and van Lohuizen, 2006). However, the substantial status of Polycomb family and their epigenetic impact in ATL cells have not been documented. Furthermore, the general roles of Polycomb proteins in miRNA regulation are mostly unknown. As described above, since miRNAs are multifunctional molecules in gene regulation, it is of pivotal importance to clarify the miRNAs functions and their regulatory circuit in order to formulate therapeutic strategies.

In the present study, we first performed global miRNA and mRNA profilings of the ATL cells derived from patients to precisely define the significance of miRNA expressions and functions.

RESULTS

miRNA Expression Signature in Primary ATL Cells

To characterize the miRNA expression signature in the primary ATL cells, we first performed an miRNA expression microarray analysis. For results with physiological significance, we used total RNA prepared from clinical ATL samples (n = 40, Table S1 available online) and control CD4+ T cells from healthy donors (n = 22) aged 50–70 years. A strict threshold ($p < 1 \times 10^{-5}$) and two-dimensional hierarchical clustering analysis revealed 61 miRNAs that showed significantly altered levels of expression in ATL cells compared with those of control CD4+ T cells (Figure 1A). It is noteworthy that 59 miRNAs out of 61 (96.7%) showed decreased expression in the primary ATL cells. Among them, we identified miR-31 as one of the most profoundly repressed miRNAs in all ATL individuals (fold change, 0.00403; Figure 1B). miR-31 was recently reported as a tumor suppressor and/or metastasis-associated miRNA in metastatic breast cancer. However, the biological functions of miR-31 in lymphocytes have not been studied. We therefore focused on the biological significance and regulatory mechanisms of miR-31 expression in T cells as well as in solid cancers.

miR-31 Negatively Regulates NF-κB Signaling via NIK Expression

To study the functional significance of miR-31 loss, we attempted to identify the target genes of miR-31 using four computational algorithms. We also performed gene expression microarray analysis of the primary ATL cells (n = 52, Table S1) and normal CD4+ T cells (n = 21) in order to detect aberrations in gene expression. Selected putative target genes are known to be involved in cell-cycle regulation and T cell development (Table S2). To experimentally identify the target genes, we performed reporter-based screens as described below. Luciferase-3′ UTR reporter assays demonstrated a remarkable negative effect against upstream gene expression by the *MAP3K14* 3′ UTR sequence (Figure S1B), which is consistent with an initial cloning report (Malinin et al., 1997). MAP3K14, also known as NIK, has a central role in noncanonical NF-κB signaling by phosphorylation of IKKα. A previous report (Saitoh et al., 2008) and the present results (Table S2) show that NIK is overexpressed in ATL cells, leading to constitutive NF-κB activation. As shown in Figure 2A, treatment with a miR-31 inhibitor increased *NIK* 3′ UTR reporter activity, suggesting the involvement of endogenous miR-31 in NIK downregulation. A computational search predicted one site each of miR-31 and miR-31 antisense (miR-31*) binding sites in the *NIK* 3′ UTR (Figure 2B). To identify the regulatory sequence in 3′ UTR of *NIK*, we established additional two reporters with mutated sequence in each potential seed region (Figure 2C; Figure S1C). Mutant 1, which contains mutated sequence in the miR-31 seed region, partially canceled the negative effect of endogenous miR-31 (Figure S1D) and prevented the effect of Anti-miR-31 treatment (Figure 2D). On the contrary, our results suggest that miR-31* does not participate in NIK regulation. miR-31-mediated reporter regulation was also observed in T cell lines (Figure S1E). To confirm the results, we repeated the experiment to examine whether miR-31 could inhibit NIK expression through seed sequence. We made expression plasmid vectors carrying NIK, NIK-3′

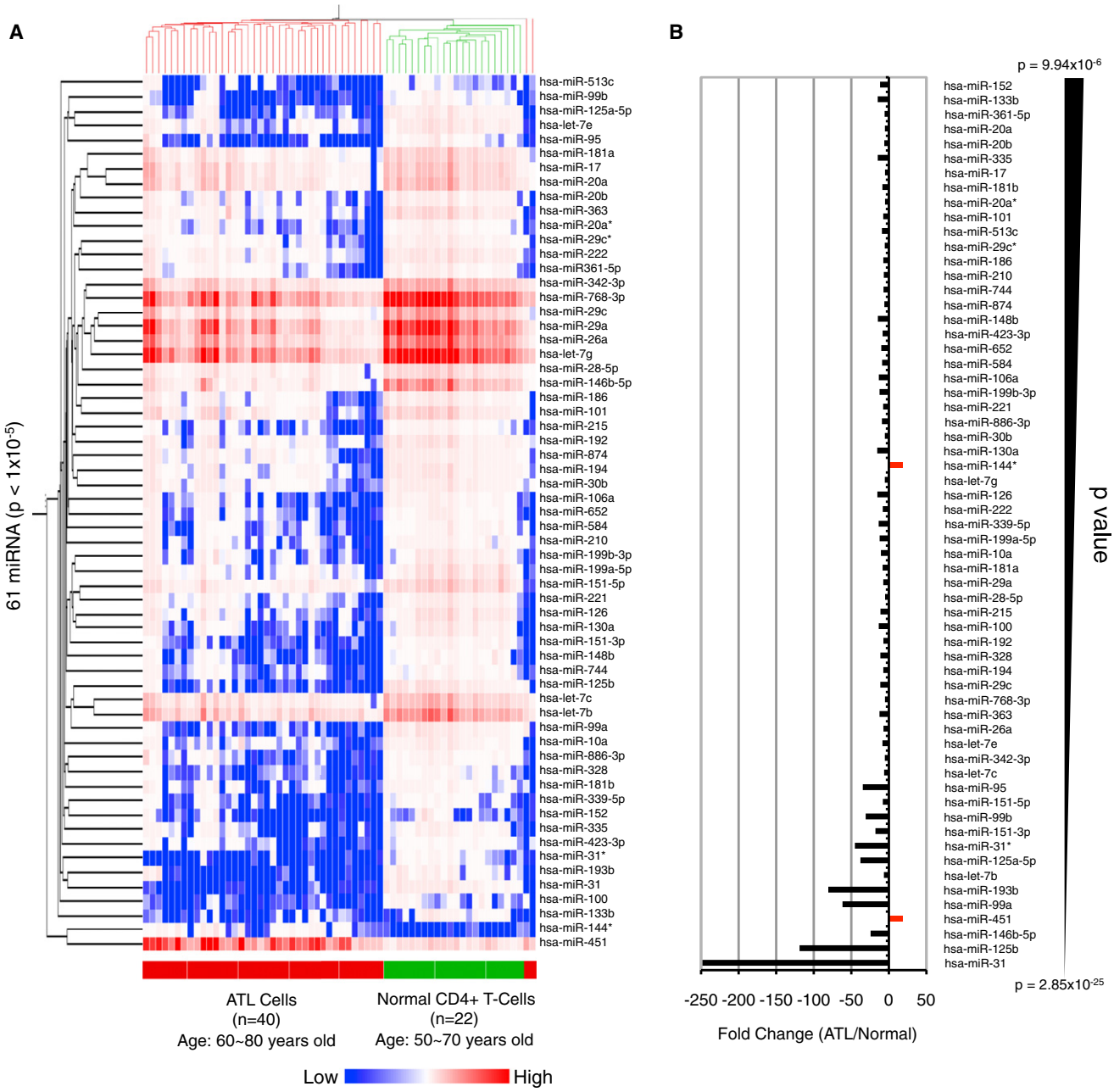

Figure 1. Global Profiling of Cellular miRNA on Primary ATL Cells

(A) Two-dimensional hierarchical clustering analysis and Pearson correlation as similarity measure on the miRNAs expressed at significantly different levels between the ATL (n = 40) and the control (n = 22) groups. Sixty-one miRNAs were identified ($p < 1 \times 10^{-5}$) and by filtering on more than 5-fold changes. A vertical branch shows the expression pattern of the selected miRNAs in each individual.

(B) Fold changes in the 61 miRNAs between ATL and Normal ($p < 10^{-5}$, fold change >5-fold). Selected miRNAs are arranged according to p values. See also Table S1.

UTRWT, or NIK-3′ UTRMu1 and tested their expressions in 293T cells. Results demonstrated that expression of NIK-3′ UTRWT was inhibited by simultaneous introduction of miR-31 (Figure 2E). miR-31 inhibition inversely rescued the NIK level, revealing that the cellular miR-31 level negatively affected that of the NIK protein through its 3′ UTR sequence. These lines of evidence collectively demonstrated that miR-31 recognizes and regulates *NIK* mRNA through specific binding to its 3′ UTR.

Transient introduction of the miR-31 precursor in TL-Om1 cells, which were established from an ATL patient, resulted in downregulation of NIK at the mRNA and protein levels, associated with downregulation of the phospho-IKKα/β level and NF-κB activity (Figures S1F and S1G). In contrast, miR-31 inhibition resulted in accumulation of NIK mRNA and protein in HeLa cells (Figure 2F). Manipulation of the miR-31 level clearly indicated that the miR-31 level negatively correlates with cellular

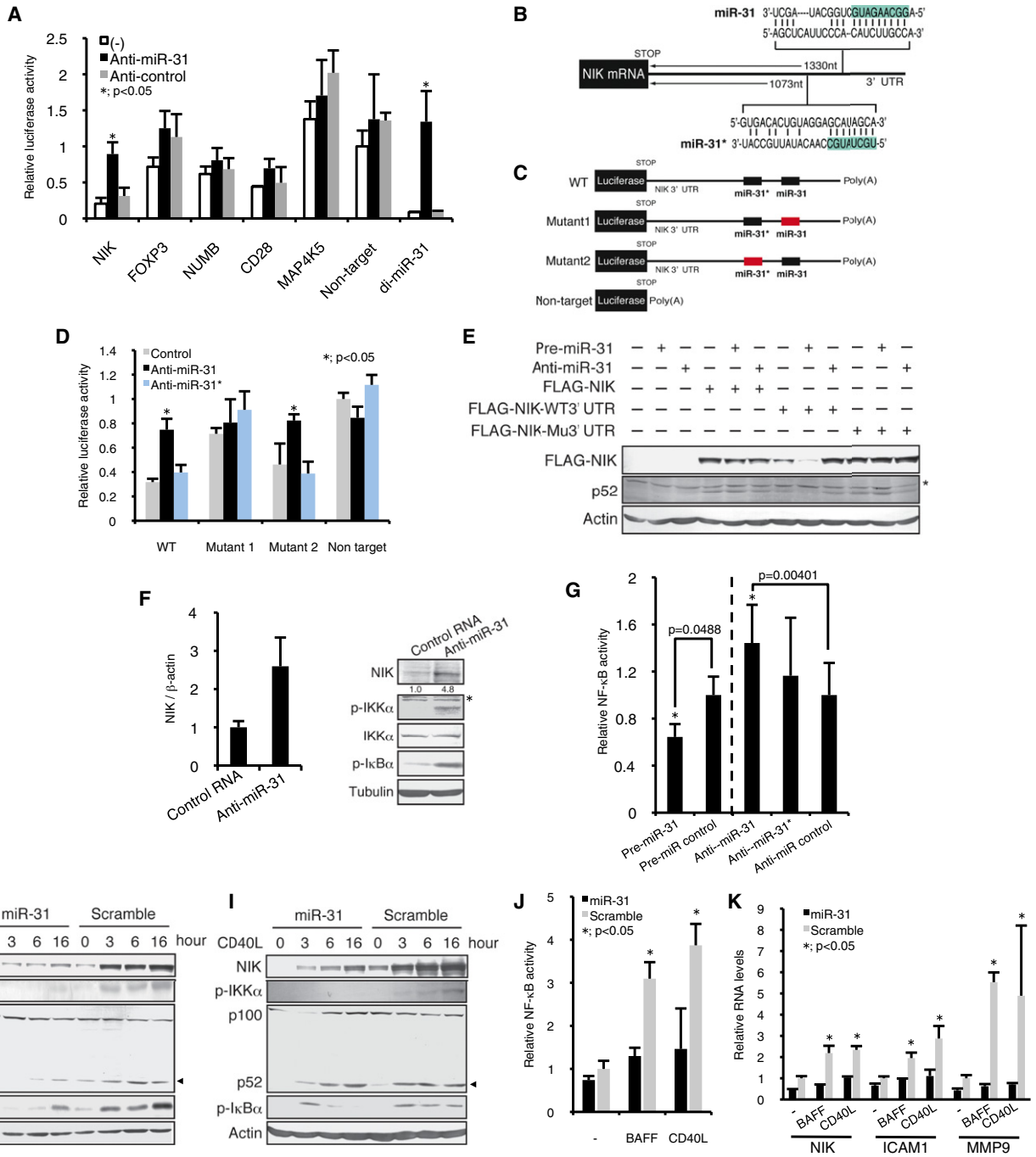

Figure 2. miR-31 Is a Negative Regulator of NF-κB Pathway by Inhibiting NIK Expression

(A) Reporter-based miR-31's target gene screening. A series of 3′ UTR-luciferase reporters was transfected in HeLa cells together with or without miR-31 specific inhibitory RNA (Anti-miR-31) or control RNA (Anti-control). Relative values of Dual-luciferase assay are presented. "Non-target" represents reporter without any 3′ UTR. "di-miR-31" reporter contains two perfect match sequences. The data are presented as mean ± SD of three independent experiments.

(B) Schematic of miR-31 target sites in the *NIK* 3′ UTR.

(C) Mutation-induced reporters. Red box stands for mutated target region (see Figure S1C).

(D) miR-31 negatively regulates *NIK* 3′ UTR analyzed by reporter assay (n = 4, mean ± SD). Luciferase activities of reporter series were tested in a presence or absence of miR-31 inhibitor.

(E) FLAG-tagged NIK protein is negatively regulated through its 3′ UTR and miR-31 binding. Plasmid vectors and miR-31 precursor or miR-31 inhibitor are cotransfected in 293T cells. Western blots showed levels of NIK and endogenous p52. Asterisk indicates nonspecific bands.

(F) NIK mRNA (left) and protein (right) levels in HeLa cells measured by quantitative RT-PCR (n = 3, mean ± SD) and western blotting, respectively. Treatment of miR-31 inhibitor resulted in NIK accumulation. Result of densitometry is shown in the bottom panel. Asterisk indicates nonspecific bands.

(G) Cellular NF-κB activity in HeLa cells (n = 5, mean ± SD) in a presence or absence of miR-31 precursor or inhibitor.

NF-κB activity (Figure 2G). Furthermore, enforced miR-31 expression in B cells attenuated both BAFF and CD40L-mediated NIK accumulation and the subsequent NF-κB signaling (Figures 2H–2K). Consistent with previous reports (Ramakrishnan et al., 2004; Zarnegar et al., 2008b), we also found decreased levels of IκBα phosphorylation. On the other hand, TNF-α-triggered canonical NF-κB activation was not affected by miR-31 in Jurkat cells (Figures S1H–S1K). These results collectively show that miR-31 inhibits the basal and receptor-initiated activities of noncanonical NF-κB pathway. With genetic evidence and an experimental approach, we further demonstrated that the function of miR-31 is well conserved among several classes of species (Figures S1L–S1O). Taking together all these results, miR-31, which is almost completely absent in primary ATL cells, appears to play a critical role in negative regulation of the NF-κB pathway by manipulating the expression of NIK.

miR-31 Suppresses ATL Cell Growth and Promotes Apoptosis by Inhibiting NF-κB

Although it was documented that abnormal NIK accumulation in ATL cells acts as a constitutive activator of the NF-κB pathway, the mechanism underlying overproduction of NIK remains to be elucidated. The results described in the previous section indicated that the amount of miR-31 is linked to the level of NIK, and we therefore speculated that downregulation of miR-31 expression is at least partially responsible for the constitutive activation of NF-κB in ATL cells. Quantitative RT-PCR revealed that *NIK* mRNA levels were negatively correlated with miR-31 levels in primary ATL cell samples (Figure 3A). To investigate the functional roles of NIK and miR-31, we established TL-Om1 cells stably expressing the miR-31 or NIK specific shRNA (shNIK) by retroviral vectors. RT-PCR and western blots showed that expression of miR-31 or shNIK reduced NIK at mRNA and protein levels as well as the levels of phospho-IKKα/β, p52, and IκBα (Figures 3B and 3C). Decreased levels of nuclear RelA and RelB are considered to represent repressed activities of the canonical and noncanonical NF-κB pathways, respectively (Figure 3D). EMSA and NF-κB reporter assays also revealed the repressive function of miR-31 and shNIK on the NF-κB activity (Figures 3E and 3F; Figures S2A, S2B, S5B, and S5C). Re-expression of NIK led to NF-κB activation that was inhibited by miR-31, suggesting a reciprocal relationship between the level of miR-31 and that of NIK.

We and others previously showed that constitutive NF-κB activation is a strong driver of ATL proliferation and prosurvival properties. Here, we examined the effects of miR-31 loss on ATL cell growth. We found that TL-Om1 cells expressing miR-31 or shNIK showed a significant attenuation of cell proliferation compared with control cells. In addition, serum starvation experiments showed greater sensitivity to induced cell death in NIK-repressed cells (Figure 3G). miR-31 expression showed the same phenotypic results in other ATL-derived cell lines (Figures S2C, S2D, and S5E). Jurkat cells do not have significant basal activity of NF-κB, and showed no significant difference in cell growth with or without induced expression of miR-31 (Figure S2E).

Next, we hypothesized that miR-31-mediated NF-κB modulation may affect cellular apoptosis, because numerous studies have demonstrated that NF-κB activation is a strong antiapoptotic factor in ATL and other cancer cells. We found that repression of NIK by miR-31 or shNIK resulted in downregulation of a subset of genes involved in resistance to apoptosis such as BCL-XL, XIAP, and FLIP (Figure 3H), suggesting that miR-31 has a role in proapoptosis through inhibition of NF-κB activity. To assess the biological function of miR-31 in apoptosis signals, we utilized a lentivirus gene transfer system for cell lines and freshly isolated tumor cells. The lentivirus vector is competent to infect nondividing cells and the infected cells can be monitored by the fluorescence of Venus. We found that lentivirus-mediated miR-31 expression promoted basal and Fas-directed apoptosis in TL-Om1 cells (Figure 3I). Venus-negative population showed no significant changes, demonstrating the specificity of miR-31 activity. To confirm the relationship among miR-31, NIK, and NF-κB signaling, we also prepared another retroviral vector encoding NIK without its 3′ UTR sequence. As results, re-expression of NIK reversed the miR-31-mediated apoptosis. In addition, miR-31 expression led to caspase 3 activation (Figure 3J). Collectively, these findings indicate that miR-31 mediates apoptosis through repression of NIK in ATL cell lines.

Tumor cells from ATL patients primarily represent the malignant characteristics. In fact, miR-31 loss is found from patient samples (Figures 1 and 3A). To demonstrate the responsibility of miR-31 for tumor cell survival, we tested whether lentivirus-mediated miR-31 expression has a killing effect against tumor cells. After establishment of lentivirus infection, the apoptotic cells were determined by flow cytometry. The results revealed that expression of miR-31 facilitated tumor cell death. Since NIK repression by shRNA lentivirus also showed a strong killing effect, NIK and NF-κB activity are suggested as crucial players for survival in ATL tumor cells (Figure 3K). Strong toxicities were not observed in normal resting lymphocytes that express low levels of NIK. Taken together, these lines of experimental evidence, including data from cell lines and primary ATL cells, definitively support two notions that (1) miR-31 acts as a tumor suppressor in T cells, and (2) NIK-regulated NF-κB has pivotal importance in cancer cell survival.

Loss of miR-31 Occurs in T Cells with Genetic and Epigenetic Abnormalities

The results described above together with previous publications indicate that regulation of miR-31 expression has profound impacts on multiple functions in human tumors as well as in normal cells. However, little is known about the regulatory mechanism of miR-31 expression. The human gene that encodes miR-31, *hsa-miR-31*, is located at 9p21.3, which is

(H–K) miR-31 attenuates signal-dependent NF-κB activation in B cells. (H and I) BJAB cells expressing miR-31 or control RNA were treated with BAFF (0.2 μg/ml) or CD40L (0.5 μg/ml) for indicated time periods. The protein levels of NIK, phospho-IKKα/β, p100/p52 (arrowheads indicate active p52), and phospho-IκBα were shown. Actin was detected as control. (J) NF-κB activity (n = 5, mean ± SD) evaluated by NF-κB-luciferase reporter assay at 24 hr after cytokine treatments. (K) NF-κB-dependent gene expressions were inhibited by miR-31 (n = 3, mean ± SD). See also Table S2 and Figure S1.

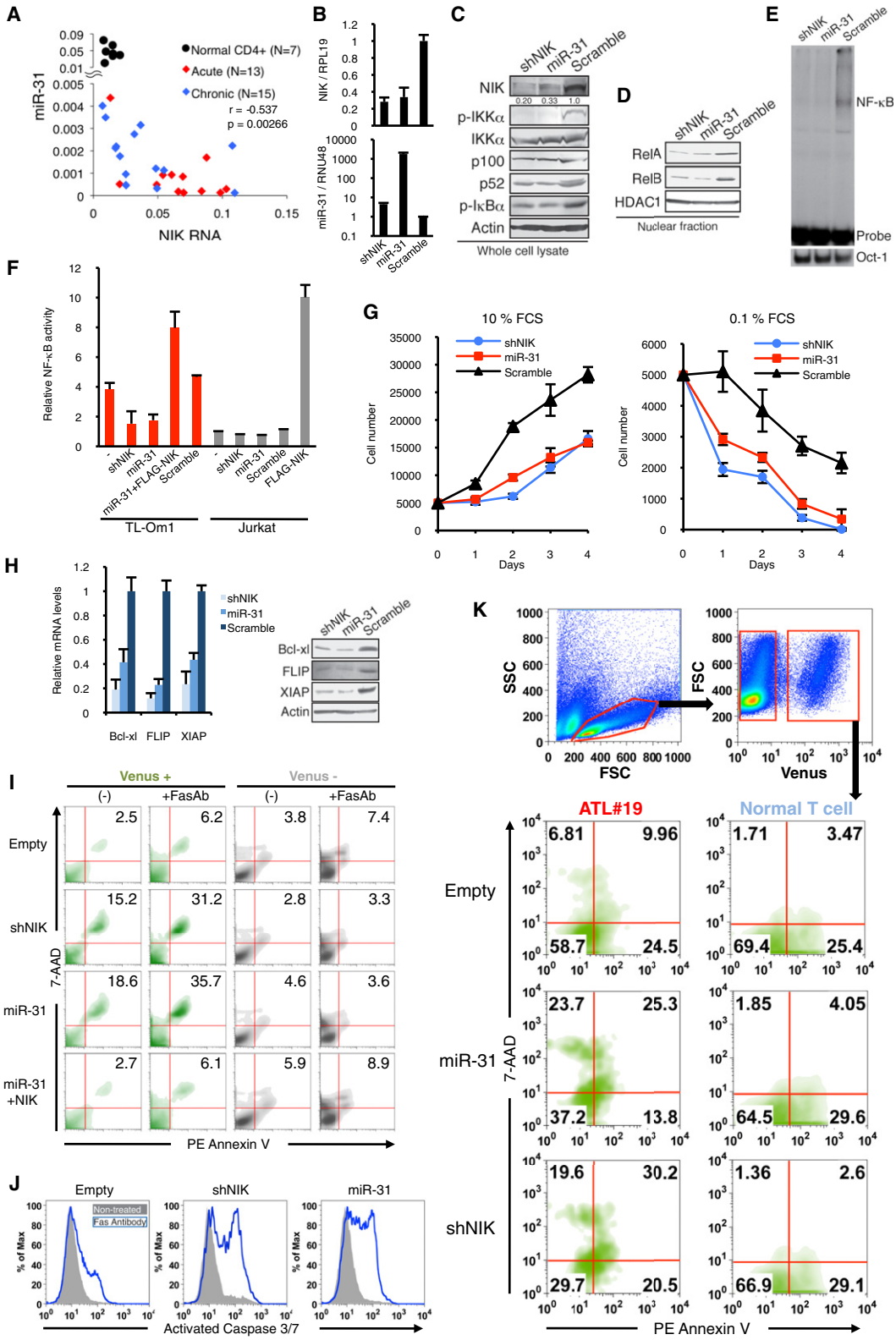

Figure 3. Loss of miR-31 Is Responsible for Constitutive NF-κB Activation, Abnormal Cell Growth, and Resistance to Apoptotic Cell Death in ATL Cells

(A) Expression levels of miR-31 and *NIK* in individual ATL patients and normal controls using data set obtained by quantitative RT-PCR. Pearson's correlation coefficient within ATL samples was described in the graph.

adjacent to clusters of the *CDKN2* and *IFNA* families, and is a well-known hotspot of genomic loss in several types of human cancers. We performed genome-wide scans of genetic lesions in 168 ATL samples and demonstrated that 21 ATL cases (12.5%) had genomic deletion of 9p21.3 containing the *hsa-miR-31* coding region (Figure 4A; Figure S3A). All of these cases also have genomic defect in *CDKN2A* region. A major proportion of ATL cases that are without genetic deletion and somatic mutation in the *hsa-miR-31* region showed remarkable loss of miR-31 expression (Figure 4B). Detailed expression profiling revealed drastic downregulation of *Pri-miR-31* transcription in the primary ATL cells (Figure 4C). There was a strong correlation between the levels of mature miR-31 and primary transcript ($r = 0.9414$, $p = 5.45 \times 10^{-8}$). *hsa-miR-31* is located in intronic region of *LOC554202* gene. However, *LOC554202* mRNA levels were very low in primary T cells and there was no significant difference between ATL and normal cells, strongly suggesting that loss of miR-31 expression is due to specific transcriptional suppression in ATL cells. Using computational analysis, we identified a putative TATA box and transcriptional start site (TSS) 2500 bp upstream of the miR-31 coding region (Figure 4D). Although no CpG islands were found in this region, we unexpectedly discovered an assembly of YY1-binding motifs upstream of the miR-31 region in human and mouse (Figure 4D; Figure S3C). YY1 is a pivotal transcription factor and a recruitor of the Polycomb repressive complex (PRC) (Simon and Kingston, 2009). Convergence of the YY1 binding sequence, especially the repressive motif (Figure S3D), seems to be evolutionarily conserved, suggesting that YY1 is important in the regulation of miR-31 transcription. We further performed chromatin immunoprecipitation (ChIP) to evaluate repressive histone hallmarks, including di- and trimethylated H3K9 (H3K9me2 and H3K9me3) and trimethylated H3K27 (H3K27me3). The results showed higher levels of methylation at H3K9 and H3K27 in a broad area containing the miR-31 coding region (Figure 4E). As shown in Figures S3E–S3G, there was an inverse correlation between the levels of miR-31 expression and repressive histone methylation. These data allowed us to hypothesize that histone methylation, especially that of Polycomb family-dependent H3K27me3, may contribute to miR-31 repression. To confirm our hypothesis, we performed a YY1 knockdown experiment using a specific shRNA (Figures 4F–4I). As expected, knockdown of YY1 led to an increase in the levels of *Pri-miR-31* and mature miR-31 (Figures 4F and 4G). Furthermore, ChIP assays showed that YY1 occupied the miR-31 region, especially in the upstream region of TSS, where there is an array of YY1 binding sites (Figures 4D and 4H). The results also demonstrated that decreased occupancy of YY1 and concomitant derecruitment of EZH2, a key component of PRC2, were induced by YY1 knockdown, indicating involvement of EZH2 in the repressive complex recruited to the miR-31 region (Figures 4H and 4I; Figure S3H). These results collectively suggest that YY1 regulates PRC2 localization and initiates miR-31 suppression. Indeed, we found significant escalation of methylated histone H3K9 and H3K27 at the miR-31 locus of peripheral blood lymphocytes of ATL patients (Figure 4J), indicating that aberrant abundance of suppressive histone methylation may be responsible for the loss of miR-31 in the primary ATL cells.

Overexpression of PRC2 Components Leads to miR-31 Repression

Given that Polycomb-mediated repressiveness affects miR-31 level, our findings imply that the amount of EZH2 is related to miR-31 expression (Figure 4I; Figures S3G and S4A). We found a significantly upregulated expression of PRC2 components, especially EZH2 and SUZ12, in the primary ATL cells (Figures 5A and 5B; Table S3). Quantitative RT-PCR revealed that miR-31 levels inversely correlated with both *EZH2* and *SUZ12*, respectively (Figure 5C). miR-101 and miR-26a, which are putative negative regulators of EZH2, seem to be associated with this relationship in ATL cells (Figures S4B–S4E). To further confirm our hypothetical mechanism linking the epigenetic machinery and miR-31 expression, we performed a "loss-of-PRC2-function" assay. Retroviral delivery of shSUZ12 and shEZH2 in the ATL cell lines resulted in a great increase in the levels of *Pri-miR-31* and its mature form (Figure 5D; Figure S4F). Knockdown of PRC2 induced histone demethylation at H3K27 in the miR-31 region, which is concomitant with the decrease in H3K9me3 levels, EZH2 occupancy, and HDAC1 recruitment (Figure 5E), suggesting that this multimeric complex leads to a completely closed chromatin architecture as a result of histone modifications in the miR-31 genomic region.

To further examine whether the proposed mechanism holds true in other human cancers, we analyzed a couple of carcinoma cell lines, including HeLa cells and nonmetastatic and metastatic breast carcinoma cell lines, MCF7 and MDA-MB-453 cells, respectively. qRT-PCR revealed that expression of *EZH2* and *SUZ12* inversely correlated with miR-31 levels (Figure S4G).

(B) miR-31 restoration by retroviral vector inhibits *NIK* RNA accumulation in TL-Om1 cells. The results of *NIK* and mature miR-31 quantifications are shown (n = 3, mean ± SD).
(C) miR-31 or shNIK expression downregulates NIK protein expression and inhibits downstream pathway of noncanonical NF-κB in TL-Om1 cells.
(D) Reduced nuclear translocation of RelA and RelB proteins in miR-31- or shNIK-expressing TL-Om1 cells.
(E) miR-31-dependent downregulation of NF-κB activity in TL-Om1 cells examined by EMSA.
(F) NF-κB-luciferase reporter assays (n = 5, mean ± SD). FLAG-NIK plasmid was transiently introduced 48 hr prior to the assay.
(G) miR-31 level is relevant to proliferation of ATL cells. Cell proliferation curve of TL-Om1 cells were evaluated in two FCS conditions (n = 3, mean ± SD).
(H) Apoptosis-related gene expression in TL-Om1 cells analyzed by qRT-PCR (n = 3, mean ± SD) and western blots.
(I) Lentivirus-mediated NIK depletion promotes basal and Fas antibody-mediated apoptosis. Venus-positive population represented lentivirus-infected cells. Apoptotic cells were determined by PE-Annexin V / 7-AAD stainings (n = 4). Representative FACS analyses are shown.
(J) miR-31 activates Caspase 3/7 determined by FACS (n = 3).
(K) miR-31 expression and NIK depletion induce tumor cell death. Primary tumor cell from ATL patient and healthy CD3+ T cells were infected with lentivirus and analyzed by FACS. The apoptotic cells were defined by sequential gating beginning with FSC-SSC to select intact lymphocytes, subgating on the Venus-positive population, and calculating the PE-Annexin V and 7-AAD profilings. Representative result is shown and summarized data are presented in Figure 6J. See also Figure S2.

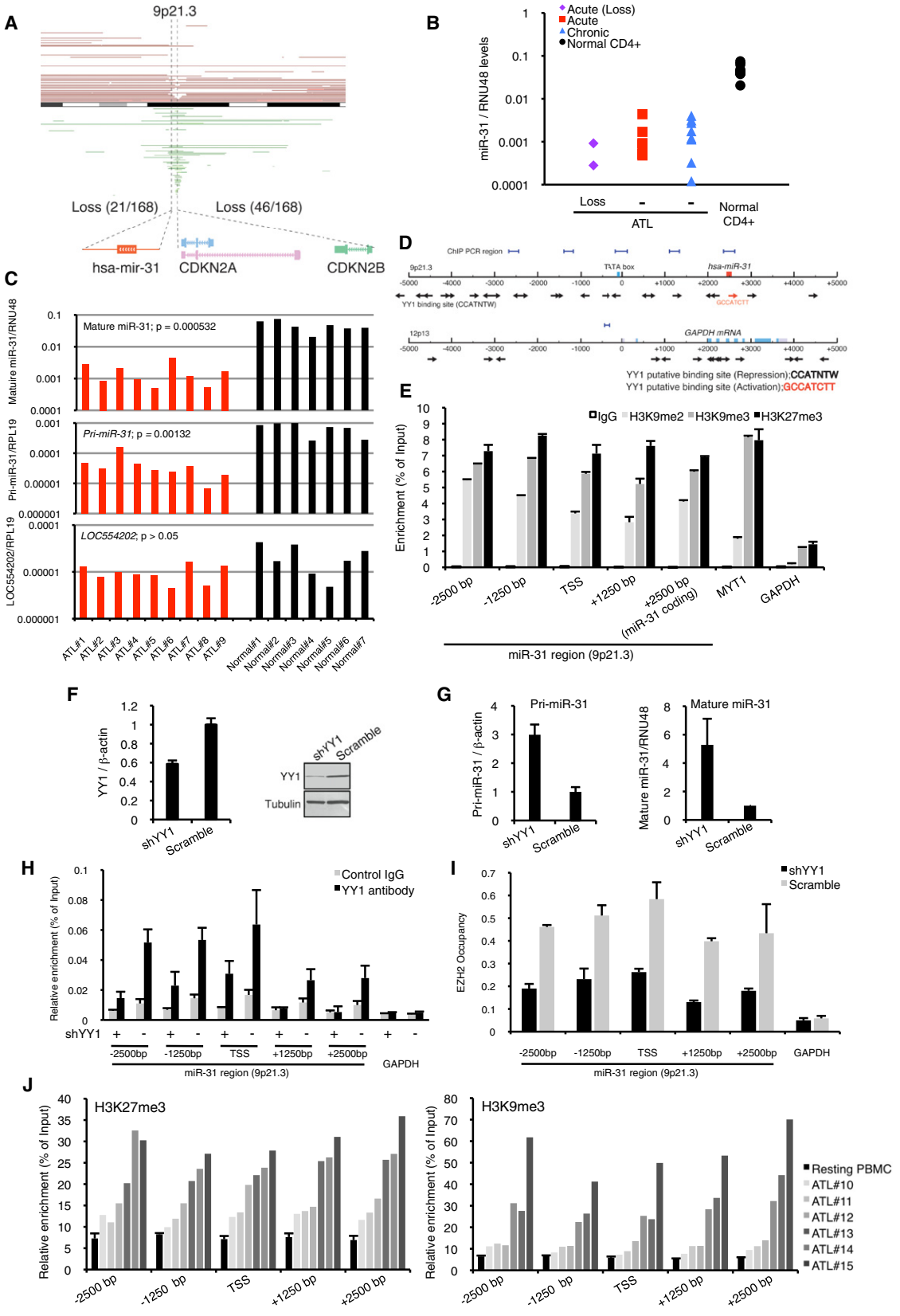
A
9p21.3
Loss (21/168)
Loss (46/168)
hsa-mir-31
CDKN2A
CDKN2B
B
Acute (Loss)
Acute
Chronic
Normal CD4+
miR-31 / RNU48 levels
Loss
ATL
Normal CD4+
C
Mature miR-31; p = 0.000532
Pri-miR-31; p = 0.00132
LOC554202; p > 0.05
Mature miR-31/RNU48
Pri-miR-31/RPL19
LOC554202/RPL19
ATL#1 ATL#2 ATL#3 ATL#4 ATL#5 ATL#6 ATL#7 ATL#8 ATL#9
Normal#1 Normal#2 Normal#3 Normal#4 Normal#5 Normal#6 Normal#7
D
ChIP PCR region
9p21.3
TATA box
hsa-miR-31
YY1 binding site (CCATNTW)
GCCATCTT
12p13
GAPDH mRNA
YY1 putative binding site (Repression):CCATNTW
YY1 putative binding site (Activation):GCCATCTT
E
IgG H3K9me2 H3K9me3 H3K27me3
Enrichment (% of Input)
-2500 bp
-1250 bp
TSS
+1250 bp
+2500 bp (miR-31 coding)
MYT1
GAPDH
miR-31 region (9p21.3)
F
YY1 / β-actin
shYY1
Scramble
YY1
Tubulin
G
Pri-miR-31
Mature miR-31
Pri-miR-31 / β-actin
Mature miR-31/RNU48
H
Control IgG
YY1 antibody
Relative enrichment (% of Input)
shYY1
-2500bp -1250bp TSS +1250bp +2500bp GAPDH
miR-31 region (9p21.3)
I
shYY1
Scramble
EZH2 Occupancy
-2500bp -1250bp TSS +1250bp +2500bp GAPDH
miR-31 region (9p21.3)
J
H3K27me3
H3K9me3
Relative enrichment (% of Input)
-2500 bp -1250 bp TSS +1250 bp +2500 bp
Resting PBMC
ATL#10
ATL#11
ATL#12
ATL#13
ATL#14
ATL#15

ChIP assays detected higher levels of trimethylated H3K27 and EZH2 occupancy in cells showing lower expression levels of miR-31 (Figure S4H). Furthermore, knockdown of EZH2 or SUZ12 restored miR-31 transcription in MDA-MB-453 and MCF7 cells (Figures 5F and 5G; Figure S4K, respectively), which are consistent with the results obtained with ATL cells. These results indicate a link between Polycomb-mediated epigenetic regulation and miR-31 transcription in ATL and breast cancer cell lines.

Polycomb Group Regulates NF-κB Pathway by Controlling miR-31 Expression

Based on our findings, we considered an aspect of the biological communication between epigenetic silencing and the NF-κB pathway through miR-31 regulation. The microarray data sets showed positive correlations between PRC2 components and miR-31 target gene, *NIK* expression (Figure 6A). The results also suggested that these factors tend to show higher levels in the aggressive subtype (acute type) than in the indolent subtypes (chronic and smoldering types), implying that these genes may play important roles in the clinical phenotype and prognosis of ATL. To examine this notion, we performed PRC2 knockdown in ATL cell lines. Western blots of these cells demonstrated decreased levels of NIK, p52, and phospho-IκBα (Figure 6B; Figure S5A), suggesting suppression of both canonical and noncanonical NF-κB cascade and activity (Figure 6C; Figures S5B and S5C). These results are consistent with those of miR-31 overexpression (Figures 3C–3F). Then, we tested whether exogenous manipulation of miR-31 could restore the effect of PRC2 loss. Anti-miR-31 treatment rescued impaired NF-κB activity in PRC2-disrupted cells (Figure 6D). On the other hand, overexpression of EZH2 induced NF-κB activation, which was partially canceled by the introduction of miR-31 precursor (Figure 6E; Figure S5D). These results suggest that Polycomb-mediated miR-31 suppression leads to NF-κB activation. Indeed, knockdown of the PRC2 complex led to reduced levels of cell proliferation and greater sensitivity to serum deprivation in ATL cells (Figure 6F; Figure S5E). In addition, PRC2 disruption showed a reduction in cell migration (Figure S5F).

To gain further insight into this general network, we studied the functions of miR-31 and the PRC2 complex in breast cancer cell lines. NF-κB activity was downregulated by knockdown of PRC2 components in MDA-MB-453 cells (Figure 6G; Figures S5G and S5H), although no significant differences were observed in cell proliferation (data not shown). Repression of NF-κB activity induced by knockdown of PRC2 components was partially restored by treatment with a miR-31 inhibitor, suggesting that PRC2 knockdown-mediated relief of NF-κB repression is at least a part of the result of the miR-31 induction. In addition, knockdown of PRC2 components resulted in a reduced level of receptor-initiated accumulation of NIK in B cells (Figure 6H). Our findings indicate a common molecular mechanism comprising Polycomb-mediated epigenetic regulation, miR-31 expression and the NF-κB signaling pathway.

Regulation of NF-κB by Polycomb family may in turn control the cellular apoptosis responses. We found that lentivirus-mediated EZH2 knockdown led to increased apoptotic sensitivity in TL-Om1 cells (Figure 6I). Additional expression of NIK inhibited the cell death induced by EZH2 knockdown, suggesting the reciprocal relationship between Polycomb and NF-κB cascades. By using primary tumor cells from patient, we tested the killing effect induced by miR-31, NIK knockdown, and EZH2 knockdown (Figure 6J; Figures S5I and S5J). All tested samples showed strong death response, demonstrating that survival of ATL cells was closely associated with miR-31, NIK, and EZH2, all of which show deregulated expression in ATL cells.

By qRT-PCR we finally examined the expression levels of some genes involved in the noncanonical NF-κB pathway. As shown in Figure 6K, the results clearly demonstrated higher expression levels of positive regulators such as *NIK*, *CD40,* and *LTBR*, and lower expression levels of the negative regulators such as *BIRC2/3* (cIAP1/2), which are involved in proteasomal degradation of NIK (Zarnegar et al., 2008a). These observations are in line with a previous report on Multiple Myeloma cells (Annunziata et al., 2007). In addition to these data, we obtained convincing evidence for a molecular aspect of NIK accumulation in ATL cells. Polycomb-dependent epigenetic gene silencing may be associated with miR-31 loss, followed by NF-κB activation and other signaling pathways (Figure 7).

DISCUSSION

Constitutive activation of NF-κB contributes to abnormal proliferation and inhibition of apoptotic cell death in cancer cells,

Figure 4. Genetic and Epigenetic Abnormalities Cause miR-31 Loss in ATL Cells

(A) Genomic loss of chromosome 9p21.3 in primary ATL cells. Copy number analyses revealed tumor-associated deletion of miR-31 region (21/168) and *CDKN2* region (46/168). Recurrent genetic changes are depicted by horizontal lines based on CNAG output of the SNP array analysis.

(B) miR-31 expression in various sample sets. Expression levels were evaluated by real-time PCR.

Loss, samples with genomic loss of the miR-31 region; (−) samples without genomic loss of the miR-31 region.

(C) PCR-based miR-31 quantifications in primary ATL samples. ATL samples without genetic loss in miR-31 region (n = 9, Figure S3B), and normal CD4+ T cells (n = 7) were tested. p values (ATL versus normal) are shown.

(D) YY1 binding motif cluster around transcriptional start site (TSS) of miR-31 region. Arrows represent positions of the motifs. Regions of PCR amplification for ChIP assay are shown.

(E) Repression-associated histone methylation in miR-31 region determined by ChIP assay (n = 3, mean ± SD). The results of relative enrichment against input control are presented and distance from miR-31 TSS is described. *MYT1* and *GAPDH* promoters are as positive or negative controls, respectively.

(F–I) YY1-dependent EZH2 occupancy in miR-31 locus. (F) YY1 knockdown in TL-Om1 cells. qRT-PCR (left, n = 3, mean ± SD) and western blotting (right) showed decreased YY1 level. (G) YY1 knockdown led to both primary and mature miR-31 restoration in TL-Om1 cells (n = 3, mean ± SD). (H) YY1 occupancy in miR-31 region analyzed by ChIP (n = 3, mean ± SD). YY1 occupancy in miR-31 locus was reduced by YY1 knockdown. (I) EZH2 occupancy in miR-31 region analyzed by ChIP (n = 3, mean ± SD). YY1 knockdown inhibited EZH2 recruitment in miR-31 region.

(J) Aberrant accumulation of repression-associated histone methylations widely in miR-31 region of primary ATL cells. PBMCs freshly isolated from ATL patients (n = 6) were analyzed by ChIP assay. PBMC from healthy adults were used for normal controls. See also Figure S3.

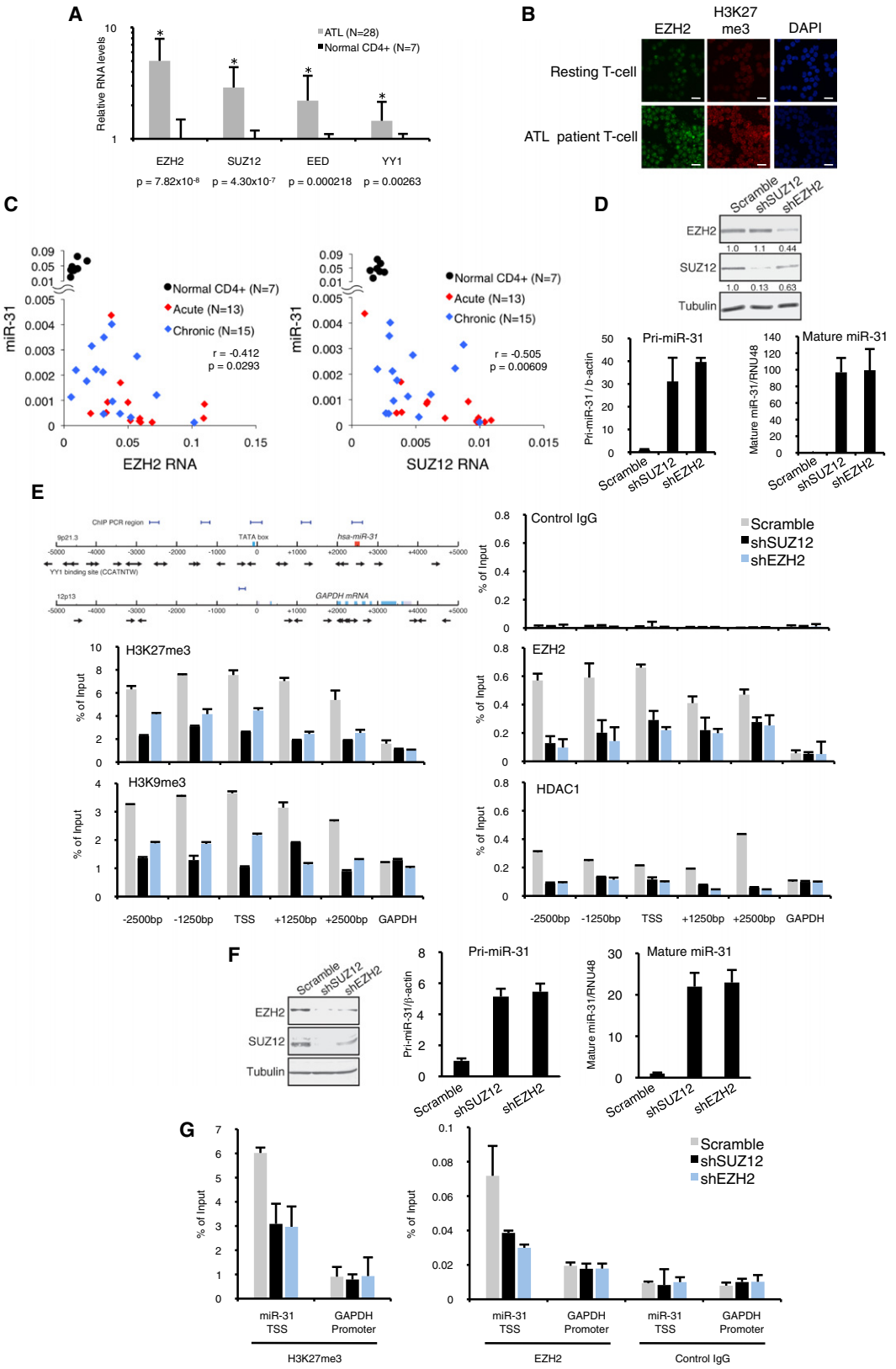
A
Relative RNA levels
ATL (N=28)
Normal CD4+ (N=7)
EZH2
SUZ12
EED
YY1
p = 7.82x10-8
p = 4.30x10-7
p = 0.000218
p = 0.00263
B
H3K27 me3
EZH2
DAPI
Resting T-cell
ATL patient T-cell
C
miR-31
Normal CD4+ (N=7)
Acute (N=13)
Chronic (N=15)
r = -0.412
p = 0.0293
r = -0.505
p = 0.00609
EZH2 RNA
SUZ12 RNA
D
Scramble
shSUZ12
shEZH2
EZH2
SUZ12
Tubulin
Pri-miR-31
Pri-miR-31 / b-actin
Mature miR-31
Mature miR-31/RNU48
E
ChIP PCR region
TATA box
hsa-miR-31
YY1 binding site (CCATNTW)
GAPDH mRNA
Control IgG
Scramble
shSUZ12
shEZH2
% of Input
H3K27me3
EZH2
H3K9me3
HDAC1
-2500bp
-1250bp
TSS
+1250bp
+2500bp
GAPDH
F
Scramble
shSUZ12
shEZH2
EZH2
SUZ12
Tubulin
Pri-miR-31
Pri-miR-31/β-actin
Mature miR-31
Mature miR-31/RNU48
G
% of Input
miR-31 TSS
GAPDH Promoter
H3K27me3
EZH2
Control IgG
Scramble
shSUZ12
shEZH2

including ATL, diffuse large B cell lymphoma (DLBCL), Hodgkin lymphoma, breast cancer, prostate cancer and others (Prasad et al., 2010). NF-κB is also essential for various cell functions, including inflammation, innate immunity, and lymphocytic development (Hayden and Ghosh, 2008). Identification of NF-κB determinants will lead to marked progress in understanding molecular pathology.

Our global analyses demonstrated an interesting miRNA expression signature as well as an aberrant mRNA expression profile, which may be associated with leukemogenesis in the primary ATL cells (Figures 1 and 6A). We revealed downregulation of tumor-suppressive miRNA including Let-7 family, miR-125b, and miR-146b, which can contribute to aberrant tumor cell signaling. Recent studies have suggested unique expression profiles of miRNAs in ATL (Yeung et al., 2008; Bellon et al., 2009), but loss of miR-31 has not been focused. Cellular amount of miRNAs may be susceptible to various environments such as transcriptional activity, maturation processing, and also epigenetic regulation. The end results appear to be affected by methodology employed and conditions and types of samples used. Our integrated expression profiling of primary ATL cells are based on a significantly larger number of samples and fruitfully provides intriguing information that may be useful in improving the understanding of T cell biology as well as in the identification of biomarkers for diagnosis.

Pleiotropy of miR-31 was first reported by Valastyan et al. (2009). The authors elegantly demonstrated the function of miR-31 in vivo and also identified several target genes that contribute to cell migration and invasiveness. In the present study, we focused on the functional significance of miR-31 in the regulation of NF-κB signaling that contributes to tumor cell survival.

Overexpression of NIK acts as an oncogenic driver in various cancers. In the present study, NIK was identified as a miR-31 target based on several lines of evidence. First, luciferase-3′ UTR reporter assay showed that *NIK* 3′ UTR sequence has a role for negative regulation (Figure S1B). By combining a specific inhibitor and mutations in miR-31-binding site, we demonstrated that miR-31 recognizes and negatively regulates the *NIK* 3′ UTR (Figures 2A and 2D). Second, by introducing a miR-31 precursor or inhibitor, we showed that amount of miR-31 inversely correlates with levels of NIK expression and downstream signaling (Figures 2E–2K). Third, genetic evidence indicated strong base pairing and biological conservation (Bartel, 2009) (Figures S1L–S1O). Our experimental approach illustrated that mmu-miR-31 regulates mouse *Map3k14* gene. Fourth, individual assessments using gene expression data clearly revealed an inverse correlation between the expression levels of miR-31 and *NIK* (Figure 3A). Collectively, we provide definitive evidence for the notion that miR-31 negatively regulates NIK expression and activity.

It is well known that the NIK level directly regulates NF-κB activity in various cell types (Thu and Richmond, 2010). We experimentally showed that miR-31 regulates noncanonical NF-κB activation stimulated by BAFF and CD40L, both of which are major B cell activating cytokines. Since signals from receptors are essential for the development and activity of B cells, the negative role of miR-31 in cytokines-induced NIK accumulation appears to be widely important in the noncanonical regulation of NF-κB in B cells and other cell types (Figures 2H–2K). Again, our findings revealed the role of NIK in the regulation of canonical NF-κB pathway. Strict regulation of NIK appears to be closely associated with the fate of lymphocytes.

The level of miR-31 was drastically suppressed in all tested primary ATL cells, and its magnitude is greater than that which has been reported in other cancers. Our results demonstrated a profound downregulation of miR-31 (fold change, 0.00403; Figure 1B) in all ATL cases, suggesting that miR-31 loss is a prerequisite for ATL development. Restoration of miR-31-repressed NF-κB activity in ATL cells, resulting in impairment of the proliferative index and apoptosis resistance (Figure 3). Furthermore, our results demonstrate that inhibition of NF-κB promotes tumor cell death in cell lines and also primary tumor cells from ATL patients (Figures 3 and 6), which are consistent with our previous observation (Watanabe et al., 2005). Since it is highly possible that miR-31 and relevant factors are pivotal in cancers, their expressions would have a great importance in view of biomarkers for the aberrant signaling and clinical outcomes.

By studying clinical samples and in vitro and ex vivo models, we obtained several biologically interesting results. First, we identified the Polycomb protein complex as a strong suppressor of miR-31. Generally, the Polycomb group constitutes a multimeric complex that negatively controls a large number of genes involved in cellular development, reproduction, and stemness (Sparmann and van Lohuizen et al., 2006). However, the key molecules involved in cancer development, progression, and prognosis are not yet fully understood. In breast and prostate cancers, oncogenic functions of EZH2 and NF-κB activation were reported independently (Kleer et al., 2003; Varambally et al., 2002; Suh and Rabson, 2004). Interestingly, these tumors show low miR-31 levels (Valastyan et al., 2009; Schaefer et al., 2010). Recently, Min et al. (2010) reported that EZH2 activates NF-κB by silencing the DAB2IP gene in prostate cancer cells.

Figure 5. Amount of PRC2 Components Epigenetically Links to miR-31 Expression in T Cells and Epithelial Cells

(A) Overexpression of PRC2 components in primary ATL cells measured by qRT-PCR (ATL, n = 28; normal, n = 7; mean ± SD). These results were supported by the data of gene expression microarray (Table S3).

(B) Escalation of EZH2 protein and trimethylated H3K27 levels in primary ATL cells illustrated by immunocytostaining (n = 4, a representative result is shown). Resting T cells were as normal control. Scale bars = 20 μm.

(C) Statistical correlation among the levels of miR-31, *EZH2*, and *SUZ12* in individual ATL samples. Correlation coefficients within ATL samples are shown in the graphs.

(D and E) Loss of PCR2 function causes chromatin rearrangement and miR-31 upregulation. (D) TL-Om1 cells expressing shSUZ12, shEZH2, and scrambled RNA were established by retroviral vector. The levels of EZH2, SUZ12, *Pri-miR-31*, and mature miR-31 were measured by western blotting and qRT-PCR (n = 3, mean ± SD). (E) Results of ChIP assays with indicated antibodies (n = 3, mean ± SD). Amounts of immunoprecipitated DNA were analyzed by region-specific PCR. *GAPDH* promoter served as a region control.

(F and G) Knockdown of Polycomb family proteins in MDA-MB-453 cells. (F) EZH2 and SUZ12 are shown by western blot. miR-31 level was examined by qRT-PCR (n = 3, mean ± SD). (G) Histone methylation and EZH2 occupancy evaluated by ChIP assay (n = 3, mean ± SD). See also Table S3 and Figure S4.

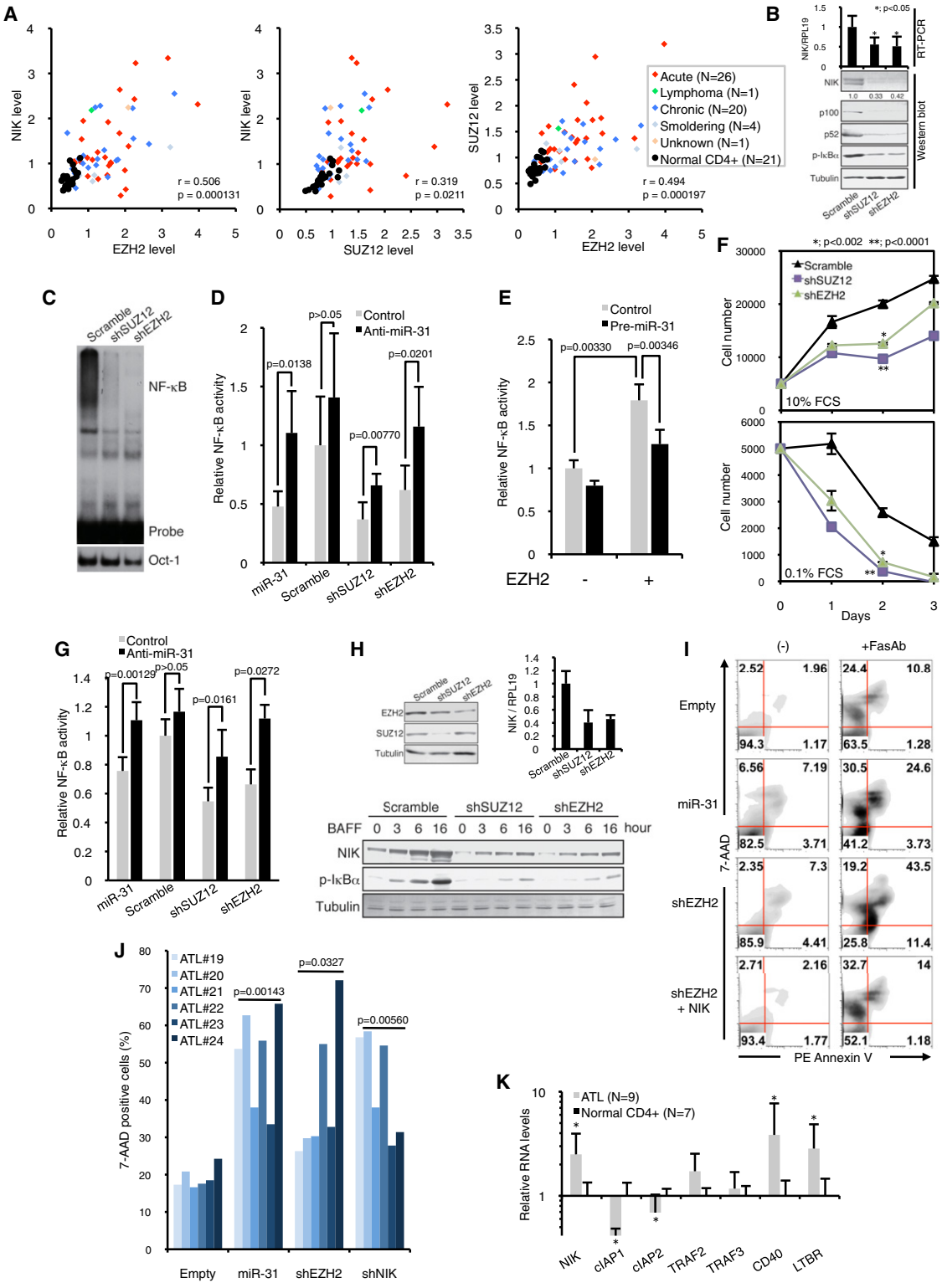

Figure 6. Epigenetic Change Driven by Polycomb Group Mediates NF-κB Signaling through miR-31 Regulation

(A) Reciprocal relationship of mRNA expression between *NIK* and Polycomb group in primary samples. Pearson's correlation coefficients among ATL samples are shown.

(B) PRC2 knockdown negatively affects NF-κB signaling in TL-Om1 cells. After establishment of PRC2 knockdown, the levels of *NIK* RNA (n = 4, mean ± SD) and proteins of NIK, p52/p100, and phospho-IκBα were examined.

(C) Downregulation of NF-κB activity in PRC2-disrupted cells detected by EMSA.

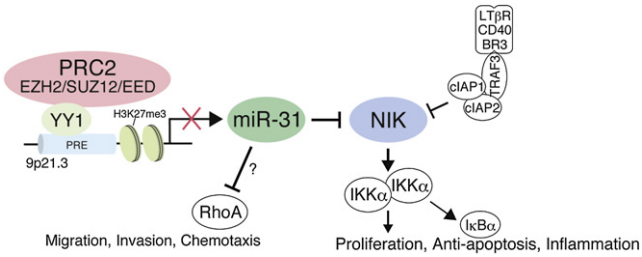

Figure 7. Proposed Model for ATL and Other Tumor Cells
Polycomb repressive factors are linked to NIK-dependent NF-κB activation via miR-31 regulation.

In the present study, we found that the Polycomb group regulates miR-31 expression and that elevated expression of EZH2 leads to NF-κB activation via NIK-miR-31 regulation in ATL and breast cancer cells (Figure 6). We also showed that restoration of miR-31 partially impaired Polycomb-mediated NF-κB operation (Figures 6D, 6E, and 6G), suggesting that miR-31 is involved in this relationship. Furthermore, a connection between NIK and PRC2 was observed in B cells (Figure 6H). Polycomb group proteins are essential in lymphocyte development and activation (Su et al., 2003, 2005). Further, given the NF-κB is a pivotal transcription regulator in normal and oncogenic functions, practical participations of epigenetic regulators and miR-31 in NF-κB signaling will increase our understanding of the molecular mechanisms of T cell functions. For generalization of the molecular axis in other cancers and normal cells, further study will be needed.

Second, YY1 is a recruiter of PRC2 to the miR-31 region. In humans, the Polycomb response element (PRE) has not been precisely identified. A good candidate for a mammalian recruiter of PRC2 is YY1, the homolog of *D. melanogaster* PHO (Simon and Kingston, 2009). We found an assembly of the YY1 binding motif in the miR-31 locus and demonstrated that YY1 knockdown dislodged EZH2 in this region (Figure 4I), which supports previous findings (Caretti et al., 2004). The detailed mechanism by which YY1 mediates recruitment of the Polycomb family may be important in the context of epigenetic regulation of orchestrated gene expression and T cell functions.

Third, Polycomb family proteins can control miRNA expression in an epigenetic fashion. The amount of PRC2 factors strongly influenced the degree of suppression of miR-31 expression (Figure 5). We speculate that, in addition to controlling the transcription, the Polycomb group can modulate translation via miRNA regulation. Furthermore, miR-101 and miR-26a are known to regulate EZH2 expression (Sander et al., 2008; Varambally et al., 2008), which is supported by our observation (Figure S4C). This signaling circuit will permit multiple gene regulation. Whereas genetic loss at the miR-31 locus is observed in some cases of ATL (Figure 4A), no genetic deletion in the miR-101-1 or miR-101-2 region was detected in ATL, which is not consistent with a previous finding in prostate cancer. Our results also suggested putative association between Let-7 family and EZH2 (Figure S4). Aberrant downregulations of these miRNAs in the primary ATL cells will be the next important questions to be addressed in efforts to improve understanding of the oncogenic signaling network.

By collaborative profiling of miRNA and mRNA expression, we identified a notable relationship between ATL subtypes and a gene cluster that contains miR-31, NIK, EZH2, and SUZ12. This finding suggests that an aberrant gene expression pattern correlates with the malignant phenotype, and this provides important clues about clinical manifestations and may help identify therapeutic targets against ATL cells (Figure 6A). Although HDAC inhibitors did not show effective responses (Figures S4I and S4J), emerging epigenetic drug such an EZH2 inhibitor (Fiskus et al., 2009) may pave a pathway leading to cures for various malignancies that involve constitutive activation of NF-κB.

In summary, we show that genetic and epigenetic loss of miR-31 is responsible for oncogenic NF-κB activation and malignant phenotypes in ATL. This provides evidence for the idea that miR-31 is an important tumor suppressor. An emerging pathway involving an epigenetic process, miR-31, and NF-κB will provide a conceptual advance in epigenetic reprogramming, inflammatory signaling, and oncogenic addiction.

EXPERIMENTAL PROCEDURES

Cell Lines and Primary ATL Cells

The primary peripheral blood mononuclear cells (PBMCs) from ATL patients and healthy volunteers used in the present work were a part of those collected with an informed consent as a collaborative project of the Joint Study on Prognostic Factors of ATL Development (JSPFAD). The project was approved by the Institute of Medical Sciences, the University of Tokyo (IMSUT) Human Genome Research Ethics Committee. Additional ATL clinical samples for copy number analysis were provided by Drs. Y. Yamada, Nagasaki University,

(D) NF-κB activity evaluated by reporter assays in the presence or absence of miR-31 inhibitor (n = 5, mean ± SD). Anti-miR-31 treatment partially rescued the NF-κB activity in PRC2 knockdowned TL-Om1 cells.
(E) Overexpressed EZH2 activates NF-κB via miR-31. Jurkat cells were transfected with an EZH2 plasmid together with miR-31 precursor or control RNA (n = 5, mean ± SD).
(F) PRC2 dysfunction changes TL-Om1 cell proliferation and response to serum starvation. Under conditions of 10% or 0.1% of FCS, cell growth curves were examined (n = 3, mean ± SD). PRC2 downregulation decreased cell growth with statistical significance.
(G) NF-κB activity in PRC2-knockdowned MDA-MB-453 cells in the presence or absence of miR-31 inhibitor were examined (n = 5, mean ± SD).
(H) PRC2 disruption inhibits BAFF-dependent NIK accumulation and IκBα phosphorylation in BJAB cells.
(I) Apoptotic cell death induced by lentivirus-mediated EZH2 knockdown in TL-Om1. Venus-positive populations were analyzed by Annexin V/7-AAD stainings (n = 3) and representative of FACS data are shown.
(J) Summary of primary tumor cell death. Lentivirus-based miR-31 expression, NIK knockdown, and EZH2 knockdown showed killing effects in six primary ATL samples. Statistical significances are shown in the graph. Results of FACS and qRT-PCR are shown in Figures S5I and S5J.
(K) Expression levels of genes involved in noncanonical NF-κB pathway in primary ATL cells (ATL, n = 9; normal, n = 7; mean ± SD). Relative expression levels were tested by qRT-PCR (*$p < 0.05$). See also Figure S5.

and K. Ohshima, Kurume University, where the projects were approved by the Research Ethics Committees of Nagasaki University and Kurume University, respectively. PBMC were isolated by Ficoll separation. ATL cells, primary lymphocytes, and all T cell lines were maintained in RPMI1640 supplemented with 10% of FCS and antibiotics. Clinical information of ATL samples is provided in Table S1.

Expression Analyses

Clinical samples for microarrays were collected by a collaborative study group, JSPFAD (Iwanaga et al., 2010). Gene expression microarray was used 4x44K Whole Human Genome Oligo Microarray (Agilent Technologies) and miRNA microarray was used Human miRNA microarray kit v2 (Agilent Technologies), respectively. Quantitative RT-PCR was performed with SYBRGreen (TAKARA). Mature miRNA assays were purchased from Applied Biosystems.

Copy Number Analyses

Genomic DNA from ATL patients was provided from the material bank of JSPFAD, Nagasaki University, and Kurume University, and was analyzed by Affymetrix GeneChip Human Mapping 250K Nsp Array (Affymetrix). Obtained data were analyzed by CNAG/AsCNAR program (Chen et al., 2008).

Oligonucleotides, Plasmids, and Retrovirus Vectors

All RT-PCR primers and oligonucleotides are described in Supplemental Experimental Procedures. miRNA precursor and inhibitor were from Applied Biosystems. Transfection of small RNA and other plasmid DNA were performed by Lipofectamine2000 (Invitrogen). For miRNA or shRNA expression, retroviral vectors (pSINsi-U6, TAKARA) were used.

3′ UTR-Conjugated miR-31 Reporter Assay

HeLa cells were cotransfected with 3′ UTR-inserted pMIR-REPORT firefly plasmid (Ambion), RSV-Renilla luciferase plasmid, and miRNA inhibitor. The cells were collected at 24 hr posttransfection, and Dual-luciferase reporter assay was performed (Promega).

Analysis of NF-κB Pathway

NF-κB activity was evaluated by EMSA and reporter assays as previously described (Horie et al., 2004). Antibodies for western blots are described in supplemental information. Cell proliferative assay was performed by Cell Counting Kit-8 (Dojindo).

Lentivirus Vectors and Apoptosis Analysis

A lentivirus vector (CS-H1-EVBsd) was provided from RIKEN, BRC, Japan. Lentivirus solution was produced by cotransfection with packaging plasmid (pCAG-HIVgp) and VSV-G- and Rev-expressing plasmid (pCMV-VSV-G-RSV-Rev) into 293FT cells. After infection of lentivirus, the apoptotic cell was evaluated by PE Annexin V / 7-AAD staining (BD PharMingen) and analyzed by FACS Calibur (Becton, Dickinson). Collected data were analyzed by FlowJo software (Tree Star).

ChIP Assay

ChIP assay was previously described (Yamagishi et al., 2009). Briefly, cells were crosslinked with 1% of formaldehyde, sonicated, and subjected to chromatin-conjugated IP using specific antibodies. Precipitated DNA was purified and analyzed by real-time PCR with specific primers (see Supplemental Experimental Procedures).

Computational Prediction

To identify miR-31 target genes, we integrated the output results of multiple prediction programs; TargetScan, PicTar, miRanda, and PITA. RNAhybrid was for secondary structure of miRNA-3′ UTR hybrid. TSSG program was for TATA box and TSS predictions. DNA methylation site was predicted by CpG island Searcher.

Statistical Analyses

Data were analyzed as follows: (1) Welch's t test for Gene Expression Microarray (p value cutoff at 10^{-6}) and miRNA Microarray (p value cutoff at 10^{-5}); (2) Pearson's correlation for two-dimensional hierarchical clustering analysis and individual assessment of microarray data sets; (3) two-tailed pared Student's t test with $p < 0.05$ considered statistically significant for in vitro cell lines and primary cells experiments, including luciferase assay, RT-PCR, ChIP assay, cell growth assay, and migration assay. Data are presented as mean ± SD.

ACCESSION NUMBERS

Coordinates have been deposited in Gene Expression Omnibus database with accession numbers, GSE31629 (miRNA microarray), GSE33615 (gene expression microarray), and GSE33602 (copy number analyses).

SUPPLEMENTAL INFORMATION

Supplemental Information includes three tables, five figures, and Supplemental Experimental Procedures and can be found with this article online at doi:10.1016/j.ccr.2011.12.015.

ACKNOWLEDGMENTS

We thank Dr. M. Iwanaga, Mr. M. Nakashima, and Ms. T. Akashi for support and maintenance of JSPFAD. We thank Drs. H. Miyoshi and A. Miyawaki for providing the Venus-encoding lentivirus vectors. We also thank Dr. R. Horie for experimental advices, and Drs. T. Kanno and T. Ishida for providing the MDA-MB-453. Grant support: Grants-in-Aid for Scientific Research from Ministry of Education, Culture, Sports, Science, and Technology of Japan to T.W. (No. 23390250) and by Grants-in-Aid from the Ministry of Health, Labour and Welfare to T.W. (H21-G-002 and H22-AIDS-I-002).

Received: November 3, 2010
Revised: August 12, 2011
Accepted: December 19, 2011
Published: January 17, 2012

REFERENCES

Annunziata, C.M., Davis, R.E., Demchenko, Y., Bellamy, W., Gabrea, A., Zhan, F., Lenz, G., Hanamura, I., Wright, G., Xiao, W., et al. (2007). Frequent engagement of the classical and alternative NF-kappaB pathways by diverse genetic abnormalities in multiple myeloma. Cancer Cell *12*, 115–130.

Bartel, D.P. (2009). MicroRNAs: target recognition and regulatory functions. Cell *136*, 215–233.

Bellon, M., Lepelletier, Y., Hermine, O., and Nicot, C. (2009). Deregulation of microRNA involved in hematopoiesis and the immune response in HTLV-I adult T-cell leukemia. Blood *113*, 4914–4917.

Caretti, G., Di Padova, M., Micales, B., Lyons, G.E., and Sartorelli, V. (2004). The Polycomb Ezh2 methyltransferase regulates muscle gene expression and skeletal muscle differentiation. Genes Dev. *18*, 2627–2638.

Chen, Y., Takita, J., Choi, Y.L., Kato, M., Ohira, M., Sanada, M., Wang, L., Soda, M., Kikuchi, A., Igarashi, T., et al. (2008). Oncogenic mutations of ALK kinase in neuroblastoma. Nature *455*, 971–974.

Davis, B.N., Hilyard, A.C., Lagna, G., and Hata, A. (2008). SMAD proteins control DROSHA-mediated microRNA maturation. Nature *454*, 56–61.

Fiskus, W., Wang, Y., Sreekumar, A., Buckley, K.M., Shi, H., Jillella, A., Ustun, C., Rao, R., Fernandez, P., Chen, J., et al. (2009). Combined epigenetic therapy with the histone methyltransferase EZH2 inhibitor 3-deazaneplanocin A and the histone deacetylase inhibitor panobinostat against human AML cells. Blood *114*, 2733–2743.

Hayden, M.S., and Ghosh, S. (2008). Shared principles in NF-kappaB signaling. Cell *132*, 344–362.

Hironaka, N., Mochida, K., Mori, N., Maeda, M., Yamamoto, N., and Yamaoka, S. (2004). Tax-independent constitutive IkappaB kinase activation in adult T-cell leukemia cells. Neoplasia *6*, 266–278.

Horie, R., Watanabe, M., Ishida, T., Koiwa, T., Aizawa, S., Itoh, K., Higashihara, M., Kadin, M.E., and Watanabe, T. (2004). The NPM-ALK oncoprotein

abrogates CD30 signaling and constitutive NF-kappaB activation in anaplastic large cell lymphoma. Cancer Cell *5*, 353–364.

Iwanaga, M., Watanabe, T., Utsunomiya, A., Okayama, A., Uchimaru, K., Koh, K.R., Ogata, M., Kikuchi, H., Sagara, Y., Uozumi, K., et al; Joint Study on Predisposing Factors of ATL Development investigators. (2010). Human T-cell leukemia virus type I (HTLV-1) proviral load and disease progression in asymptomatic HTLV-1 carriers: a nationwide prospective study in Japan. Blood *116*, 1211–1219.

Kleer, C.G., Cao, Q., Varambally, S., Shen, R., Ota, I., Tomlins, S.A., Ghosh, D., Sewalt, R.G., Otte, A.P., Hayes, D.F., et al. (2003). EZH2 is a marker of aggressive breast cancer and promotes neoplastic transformation of breast epithelial cells. Proc. Natl. Acad. Sci. USA *100*, 11606–11611.

Liao, G., Zhang, M., Harhaj, E.W., and Sun, S.C. (2004). Regulation of the NF-kappaB-inducing kinase by tumor necrosis factor receptor-associated factor 3-induced degradation. J. Biol. Chem. *279*, 26243–26250.

Malinin, N.L., Boldin, M.P., Kovalenko, A.V., and Wallach, D. (1997). MAP3K-related kinase involved in NF-kappaB induction by TNF, CD95 and IL-1. Nature *385*, 540–544.

Min, J., Zaslavsky, A., Fedele, G., McLaughlin, S.K., Reczek, E.E., De Raedt, T., Guney, I., Strochlic, D.E., Macconaill, L.E., Beroukhim, R., et al. (2010). An oncogene-tumor suppressor cascade drives metastatic prostate cancer by coordinately activating Ras and nuclear factor-kappaB. Nat. Med. *16*, 286–294.

Prasad, S., Ravindran, J., and Aggarwal, B.B. (2010). NF-kappaB and cancer: how intimate is this relationship. Mol. Cell. Biochem. *336*, 25–37.

Ramakrishnan, P., Wang, W., and Wallach, D. (2004). Receptor-specific signaling for both the alternative and the canonical NF-kappaB activation pathways by NF-kappaB-inducing kinase. Immunity *21*, 477–489.

Saitoh, Y., Yamamoto, N., Dewan, M.Z., Sugimoto, H., Martinez Bruyn, V.J., Iwasaki, Y., Matsubara, K., Qi, X., Saitoh, T., Imoto, I., et al. (2008). Overexpressed NF-kappaB-inducing kinase contributes to the tumorigenesis of adult T-cell leukemia and Hodgkin Reed-Sternberg cells. Blood *111*, 5118–5129.

Sander, S., Bullinger, L., Klapproth, K., Fiedler, K., Kestler, H.A., Barth, T.F., Möller, P., Stilgenbauer, S., Pollack, J.R., and Wirth, T. (2008). MYC stimulates EZH2 expression by repression of its negative regulator miR-26a. Blood *112*, 4202–4212.

Schaefer, A., Jung, M., Mollenkopf, H.J., Wagner, I., Stephan, C., Jentzmik, F., Miller, K., Lein, M., Kristiansen, G., and Jung, K. (2010). Diagnostic and prognostic implications of microRNA profiling in prostate carcinoma. Int. J. Cancer *126*, 1166–1176.

Simon, J.A., and Kingston, R.E. (2009). Mechanisms of polycomb gene silencing: knowns and unknowns. Nat. Rev. Mol. Cell Biol. *10*, 697–708.

Sparmann, A., and van Lohuizen, M. (2006). Polycomb silencers control cell fate, development and cancer. Nat. Rev. Cancer *6*, 846–856.

Su, I.H., Basavaraj, A., Krutchinsky, A.N., Hobert, O., Ullrich, A., Chait, B.T., and Tarakhovsky, A. (2003). Ezh2 controls B cell development through histone H3 methylation and Igh rearrangement. Nat. Immunol. *4*, 124–131.

Su, I.H., Dobenecker, M.W., Dickinson, E., Oser, M., Basavaraj, A., Marqueron, R., Viale, A., Reinberg, D., Wülfing, C., and Tarakhovsky, A. (2005). Polycomb group protein ezh2 controls actin polymerization and cell signaling. Cell *121*, 425–436.

Suh, J., and Rabson, A.B. (2004). NF-kappaB activation in human prostate cancer: important mediator or epiphenomenon? J. Cell. Biochem. *91*, 100–117.

Thu, Y.M., and Richmond, A. (2010). NF-κB inducing kinase: a key regulator in the immune system and in cancer. Cytokine Growth Factor Rev. *21*, 213–226.

Trabucchi, M., Briata, P., Garcia-Mayoral, M., Haase, A.D., Filipowicz, W., Ramos, A., Gherzi, R., and Rosenfeld, M.G. (2009). The RNA-binding protein KSRP promotes the biogenesis of a subset of microRNAs. Nature *459*, 1010–1014.

Valastyan, S., Reinhardt, F., Benaich, N., Calogrias, D., Szász, A.M., Wang, Z.C., Brock, J.E., Richardson, A.L., and Weinberg, R.A. (2009). A pleiotropically acting microRNA, miR-31, inhibits breast cancer metastasis. Cell *137*, 1032–1046.

Varambally, S., Dhanasekaran, S.M., Zhou, M., Barrette, T.R., Kumar-Sinha, C., Sanda, M.G., Ghosh, D., Pienta, K.J., Sewalt, R.G., Otte, A.P., et al. (2002). The polycomb group protein EZH2 is involved in progression of prostate cancer. Nature *419*, 624–629.

Varambally, S., Cao, Q., Mani, R.S., Shankar, S., Wang, X., Ateeq, B., Laxman, B., Cao, X., Jing, X., Ramnarayanan, K., et al. (2008). Genomic loss of microRNA-101 leads to overexpression of histone methyltransferase EZH2 in cancer. Science *322*, 1695–1699.

Ventura, A., and Jacks, T. (2009). MicroRNAs and cancer: short RNAs go a long way. Cell *136*, 586–591.

Watanabe, M., Ohsugi, T., Shoda, M., Ishida, T., Aizawa, S., Maruyama-Nagai, M., Utsunomiya, A., Koga, S., Yamada, Y., Kamihira, S., et al. (2005). Dual targeting of transformed and untransformed HTLV-1-infected T cells by DHMEQ, a potent and selective inhibitor of NF-kappaB, as a strategy for chemoprevention and therapy of adult T-cell leukemia. Blood *106*, 2462–2471.

Yamagishi, M., Ishida, T., Miyake, A., Cooper, D.A., Kelleher, A.D., Suzuki, K., and Watanabe, T. (2009). Retroviral delivery of promoter-targeted shRNA induces long-term silencing of HIV-1 transcription. Microbes Infect. *11*, 500–508.

Yamaguchi, K., and Watanabe, T. (2002). Human T lymphotropic virus type-I and adult T-cell leukemia in Japan. Int. J. Hematol. *76* (*Suppl 2*), 240–245.

Yeung, M.L., Yasunaga, J., Bennasser, Y., Dusetti, N., Harris, D., Ahmad, N., Matsuoka, M., and Jeang, K.T. (2008). Roles for microRNAs, miR-93 and miR-130b, and tumor protein 53-induced nuclear protein 1 tumor suppressor in cell growth dysregulation by human T-cell lymphotrophic virus 1. Cancer Res. *68*, 8976–8985.

Zarnegar, B.J., Wang, Y., Mahoney, D.J., Dempsey, P.W., Cheung, H.H., He, J., Shiba, T., Yang, X., Yeh, W.C., Mak, T.W., et al. (2008a). Noncanonical NF-kappaB activation requires coordinated assembly of a regulatory complex of the adaptors cIAP1, cIAP2, TRAF2 and TRAF3 and the kinase NIK. Nat. Immunol. *9*, 1371–1378.

Zarnegar, B.J., Yamazaki, S., He, J.Q., and Cheng, G. (2008b). Control of canonical NF-kappaB activation through the NIK-IKK complex pathway. Proc. Natl. Acad. Sci. USA *105*, 3503–3508.